

# Experimental Characterization and Numerical Simulation of Differential PEM Fuel Cells

Von der Fakultät Energie-, Verfahrens- und Biotechnik der Universität  
Stuttgart zur Erlangung der Würde eines Doktors der  
Ingenieurwissenschaften (Dr.-Ing.) genehmigte Abhandlung

Vorgelegt von  
**Christophe Gerling**  
aus Haguenau, Frankreich

Hauptberichter: Prof. Dr. rer. nat. K. Andreas Friedrich  
Mitberichter: Prof. Dr.-Ing. Ulrike Krewer  
Prüfungsvorsitzender: Prof. Dr. rer. nat. André Thess

Tag der mündlichen Prüfung: 4. April 2024

Institut für Gebäudeenergetik, Thermotechnik und Energiespeicherung  
der Universität Stuttgart



# Vorwort

Im Folgenden möchte ich mich bei allen bedanken, die mich während meiner Zeit als Doktorand in der zentralen Forschung der Robert Bosch GmbH unterstützt und somit zum erfolgreichen Gelingen dieser Arbeit beigetragen haben.

Meinem Doktorvater Herrn Prof. Dr. K. Andreas Friedrich danke ich für die hilfreiche Begleitung während meiner Promotionszeit. Besonders dankbar bin ich für die Bereitschaft, mich als externen Doktoranden zu betreuen sowie für das Vertrauen und die wissenschaftliche Freiheit. Die einfache und schnelle Kommunikation hat mir ein zügiges Vorankommen ermöglicht. Prof. Dr. Ulrike Krewer möchte ich zudem für die Übernahme des Korreferats danken.

Ganz herzlich möchte ich mich bei meinen internen Betreuern, Dr. Matthias Hanauer und Dr. Ulrich Berner, für die hervorragende Zusammenarbeit und uneingeschränkte moralische Unterstützung bedanken. Sowohl mit experimentellen als auch mit theoretischen Fragestellungen war ich immer bestens bei ihnen aufgehoben. Ihre wertvollen Anregungen und Ideen haben meine Arbeit wesentlich vorangetrieben. Vor allem haben mich ihre konstruktive Kritik und wichtigen Hinweise beim Schreiben meiner Publikationen immer wieder auf den richtigen Weg gebracht.

Außerdem gilt Dr. Jörg Ziegler, Dr. Ulrich Sauter und Dr. Jean-Claude Njodzefon mein Dank für die geschätzten konstruktiven fachlichen und nicht-fachlichen Diskussionen. Dass sie ihre Erfahrung mit mir teilten und mich in schwierigen Zeiten mit ihrer guten Laune aufheitern und antreiben konnten, weiß ich sehr zu schätzen.

Meinen Kollegen Dr. Stefan Schönbauer und Helmut Marx danke ich für die effektive Starthilfe im Labor bei der Inbetriebnahme des ersten Subscale-Teststands für die Charakterisierung von PEM-Brennstoffzellen. Weiterhin gilt mein Dank den Kolleginnen und Kollegen des PEM- und SOFC/SOEC-Laborteams für die angenehme Zusammenarbeit und die tatkräftige Unterstützung. Auch den Studentinnen und Studenten, die im Rahmen diverser Praktika sowie Abschlussarbeiten unterstützt haben, möchte ich hiermit danken.

Des Weiteren möchte ich Andreas Häffelin und Dr. Thilo Lehre dafür danken, dass sie mir damals als elektrochemie-fremdem Masterranden die Möglichkeit boten, meine Promotion in der Gruppe CR/ARC2 (mittlerweile CR/ATC2) zu realisieren. Zudem bedanke ich mich bei Dr. Raphaëlle Satet und Dr. Bernd Reinsch, die mir stets den Rücken freihielten und mich in meiner persönlichen und fachlichen Entwicklung begleitet haben.

Ein besonderes Dankeschön möchte ich an Dr. Peter Wolfangel für die Übernahme des Mentorings meiner Arbeit und an Dr. Jürgen Rapp für die Hilfe bei der Vermittlung an die Brennstoffzellen-Stack-Entwicklung zu meiner jetzigen Anstellung aussprechen.

Meinen Mitdotorandinnen und Mitdotoranden danke ich für die großartige Arbeitsatmosphäre und besonders gute Stimmung. Vor allem meinen PEM-Mitdotoranden, Tobias Schmitt und Wolfgang Olbrich, danke ich herzlich. Ihre Unterstützung, die gemeinsamen Pausen und unsere unterhaltsamen Gespräche haben diese Arbeit ein ganzes Stück angenehmer gemacht.

Mein größter Dank gilt meiner Familie, meinen beiden Eltern sowie meinen beiden Schwestern, die immer an mich geglaubt und mich schon mein Leben lang motiviert haben, meine Träume zu verwirklichen. Nicht zuletzt danke ich meiner Frau Isabelle für ihre Liebe, Geduld und aufbauenden Worte in diesen anspruchsvollen Zeiten. Ohne ihren Rückenwind hätte ich es nicht schaffen können.

Christophe Gerling,  
am 04. April 2024

# Declaration

I certify that the dissertation entitled

”*Experimental Characterization and Numerical Simulation of Differential PEM Fuel Cells*”

is entirely my own work. Passages and ideas from other sources have been clearly marked.

# Erklärung

Ich versichere, dass ich die vorliegende Dissertation mit dem Titel

”*Experimental Characterization and Numerical Simulation of Differential PEM Fuel Cells*”

selbstständig verfasst und keine anderen als die angegebenen Quellen und Hilfsmittel benutzt habe. Passagen und Gedanken aus fremden Quellen sind als solche kenntlich gemacht.

---

Christophe Gerling

Stuttgart, 04.04.2024



# Contents

<b>Abstract / Kurzfassung</b>	<b>ix</b>
<b>List of Abbreviations</b>	<b>xv</b>
<b>List of Symbols and Indices</b>	<b>xix</b>
<b>1 Introduction</b>	<b>1</b>
<b>2 PEMFC Fundamentals</b>	<b>5</b>
2.1 Components of PEM Fuel Cells . . . . .	6
2.1.1 Membrane - Electrolyte . . . . .	6
2.1.2 Porous Electrodes . . . . .	8
2.1.3 Gas Diffusion Layers . . . . .	9
2.1.4 Flow Fields and Bipolar Plates . . . . .	10
2.2 Working Principles . . . . .	11
2.2.1 Thermodynamics - Equilibrium Conditions . . . . .	11
2.2.2 Reaction Kinetics Overpotential . . . . .	16
2.2.3 Ohmic Overpotential . . . . .	23
2.2.4 Mass Transport Overpotential . . . . .	24
2.3 Ageing Mechanisms . . . . .	25
2.3.1 Irreversible Degradation . . . . .	25
2.3.2 Reversible Degradation . . . . .	26
<b>3 Experimental and Methods</b>	<b>27</b>
3.1 Setup and Materials . . . . .	27
3.2 Characterization Methods . . . . .	29
3.2.1 Voltammetry Techniques . . . . .	29
3.2.2 Polarization Curve . . . . .	33
3.2.3 Limiting Current and Heliox Measurements . . . . .	39
3.2.4 Electrochemical Impedance Spectroscopy . . . . .	41
3.3 Experimental Procedure . . . . .	47
<b>4 Published Work</b>	<b>57</b>
4.1 Publication I . . . . .	58
4.2 Publication II . . . . .	74
4.3 Publication III . . . . .	91

---

<b>5</b>	<b>Significance of the Studies in the Literature Context</b>	<b>109</b>
<b>6</b>	<b>Conclusion and Outlook</b>	<b>119</b>
<b>7</b>	<b>Bibliography</b>	<b>125</b>
<b>A</b>	<b>Supplementary Material</b>	<b>137</b>
A.1	Supplementary Information Publication I . . . . .	137
A.2	Supplementary Information Publication II . . . . .	144
A.3	Supplementary Information Publication III . . . . .	160
	<b>Publications and Supervised Theses</b>	<b>189</b>
	<b>Curriculum Vitae</b>	<b>191</b>



# Abstract

To accomplish a global market entry with polymer electrolyte membrane fuel cells, several challenges have to be tackled. One of them is finding the right compromise between functionality, lifetime and costs. For this purpose, understanding the influence of design, materials and operating conditions on the fuel cell behavior is essential. In this work, the focus is set on the operating conditions. The first aim is to address the lack of consistent datasets for electrochemical parameters of state-of-the-art materials in the literature by using in situ characterization techniques. The second aim is to propose a new, simple but complete parameterized performance model. When a fuel cell is operated, several loss mechanisms can be observed. Close attention is paid to the oxygen reduction reaction (ORR) since it represents the highest contribution, even though other mechanisms are also characterized in order to deconvolute the performance signatures. In order to ensure high data quality and minimize unwanted in-plane effects, single cells under differential conditions are used. The base of this work consists of a comprehensive dataset containing polarization, electrochemical impedance spectroscopy (EIS), limiting current and voltammetry data obtained from systematic parameter variations in  $\text{H}_2/\text{O}_2$ ,  $\text{H}_2/\text{N}_2$  and  $\text{H}_2/\text{H}_2$  configurations.

In the first publication, the hydrogen crossover and the protonic resistances of both the cathode catalyst layer (CCL) and the membrane are characterized. First, the equivalency of cyclic voltammetry (CV) and linear sweep voltammetry (LSV) to determine the hydrogen crossover is demonstrated and validated with an online gas analysis. Then, an  $\text{H}_2/\text{N}_2$  measurement campaign with a full factorial variation of the relative humidity  $RH$  and the temperature  $T$  is carried out. Based on the CV data, a model for the hydrogen permeation coefficient is parameterized and with the EIS spectra the parameters of a specific transmission line model (TLM) for blocking electrodes are fitted. Especially the membrane and cathodic ionomer resistances  $R_{\text{PEM}}$  and  $R_{\text{p}}$  are thereby fitted as functions of  $RH$  and  $T$  and then used to parameterize models of the ionomer conductivities. Although the values that are measured are comparable to values reported in the literature, distinct deviations and trends can be observed which highlights the need for specific characterization of new materials. Finally, the change of the ionomer conductivity caused by modified water management under load ( $\text{H}_2/\text{O}_2$ ) is investigated and an approach to estimate the local CCL relative humidity is discussed. The deviations of the ionomer resistances under load from those in the  $\text{H}_2/\text{N}_2$  state reveal that a correction of polarization data for ohmic contributions based on  $\text{H}_2/\text{N}_2$  data is not recommended.

In the second publication, proton pump ( $\text{H}_2/\text{H}_2$ ) measurements provide a quantification of the anode loss contributions which are strongly dependent on  $RH$  and the hydrogen partial pressure  $p_{\text{H}_2}$ . Within these  $\text{O}_2$ -free experiments, carbon monoxide (CO) poisoning on the catalysts from trace impurities in the gas feed is observed. Thus, a new recovery

procedure to counter CO poisoning is presented which allows for a reliable parameterization of the hydrogen oxidation reaction (HOR) based on linearized Butler-Volmer (BV) kinetics. Then, a dataset containing polarization curves for a full factorial variation of  $T$ ,  $RH$  and the oxygen partial pressure  $p_{O_2}$  is created and corrected by the ionomer resistances and hydrogen crossover. This dataset is used to parameterize the ORR reaction based on a Tafel law and allows to prove that  $RH$  has no significant influence on the ORR performance. Subsequently,  $O_2$  mass transport contributions are discussed based on limiting current techniques and heliox measurements and a global loss analysis is performed. The latter shows that up to  $0.1 \text{ A cm}^{-2}$ , anode and oxygen transport contributions do not interfere with the parameterization of the ORR. Moreover, the analysis reveals that the simple Tafel law with one intrinsic slope of  $-70 \text{ mV/dec}$  is sufficient to capture the ORR kinetics at half-cell potentials above  $0.8 \text{ V}$ . Below  $0.8 \text{ V}$ , the data deviates from the Tafel line. Furthermore, the EIS spectra under load show trends that are not covered by the Tafel law even at very small current densities. Deviations between Tafel slopes obtained from polarization data and EIS charge transfer resistances hint at more complex kinetics, which is investigated further in the third publication.

In the third publication, the low-frequency inductive loop in EIS and its responsibility for the discrepancies in the Tafel slopes between polarization curves ( $-70 \text{ mV/dec}$ ) and the charge transfer resistance ( $\leq -100 \text{ mV/dec}$ ) is demonstrated. Based on the  $H_2/O_2$  test run, the low-frequency contributions are deciphered by subtracting the local slopes of the polarization curves (calculated by numerical derivation) from the low-frequency real-axis-intercepts of the capacitive EIS that occur at approximately  $1 \text{ Hz}$ . Based on this knowledge and on the ionomer resistances under load, the slow humidification effects leading to inductivities can be separated from the platinum oxidation contributions. Therewith, a new simple representation of the cathode kinetics containing the ORR and platinum poisoning effects that result in a low-frequency inductive loop is parameterized. This reaction kinetics is integrated into a transient 1D through-plane membrane electrode assembly (MEA) model which is used for an extensive parameter study. This model yields consistent results and both polarization curves and EIS match the experiments well at high humidity conditions, thus reconciling steady-state and dynamic performance signatures of PEMFCs.

In Chapter 5, the link between the publications and their significance in the literature context are discussed. Additionally, the MEA model is extended by ionomer hydration dynamics. The parameterizations of  $R_{PEM}$  and  $R_p$  depending on  $RH$  and the current density  $j$  is obtained by fitting polynomials to selected data of the  $H_2/O_2$  test run. This final MEA model is now able to simulate all humidity conditions meaningfully and even slightly enhances the predictions at high  $RH$  compared to the model from the third publication. Finally, an extensive loss analysis containing both overpotentials and differential resistances is carried out and depicts the most important loss mechanisms in state-of-the-art PEMFCs depending on the operating parameters.

# Kurzfassung

Um einen globalen Markteintritt mit Polymer-Elektrolyt-Membran-Brennstoffzellen (engl. polymer electrolyte membrane fuel cells, PEMFC) zu erreichen, gilt es noch diverse Herausforderungen zu meistern. Eine davon ist die Erarbeitung des besten Kompromisses zwischen Funktionalität, Lebensdauer und Kosten. Hierfür ist es essenziell, den Einfluss von Design, Materialien und Betriebsbedingungen auf das Brennstoffzellen-Verhalten zu verstehen. In dieser Arbeit wird deshalb der Fokus auf die Untersuchung der Betriebsbedingungen gesetzt. Die erste Zielsetzung ist hierbei, den Mangel an konsistenten Datensätzen für elektrochemische Parameter von Stand-der-Technik Materialien in der Literatur zu beheben, indem In-Situ-Charakterisierungs-Techniken angewandt werden. Das zweite Ziel besteht darin, ein neues, simples, aber vollständiges Performance-Modell bereitzustellen, das mit überschaubarem Aufwand parametrisiert werden kann. Beim Betrieb einer Brennstoffzelle können mehrere Verlust-Mechanismen beobachtet werden, wobei die Sauerstoff-Reduktions-Reaktion (engl. oxygen reduction reaction, ORR) in der Kathode meist den größten Beitrag ausmacht. Deshalb kommt der ORR in dieser Arbeit besondere Aufmerksamkeit zu, es werden jedoch auch andere Mechanismen untersucht, um sämtliche Performance-Merkmale zu erschließen. Als Test-Hardware kommen Einzelzellen unter differentiellen Bedingungen zum Einsatz, um eine hohe Datenqualität zu gewährleisten und gleichzeitig unerwünschte In-Plane-Effekte zu minimieren. Diese Arbeit baut auf einem umfangreichen Datensatz auf, der unter anderem Messdaten zu Polarisation, elektrochemischer Impedanzspektroskopie (engl. electrochemical impedance spectroscopy, EIS), Grenzstrom und Voltammetrie enthält, die durch systematische Parameter-Variationen in  $\text{H}_2/\text{O}_2$ ,  $\text{H}_2/\text{N}_2$  und  $\text{H}_2/\text{H}_2$  Konfigurationen erzielt wurden.

In der ersten Publikation wird der Schwerpunkt auf die Charakterisierung der Wasserstoffpermeation sowie der Protonen-Widerstände der Kathoden-Katalysatorschicht (engl. cathode catalyst layer, CCL) und der Membran gesetzt. Eine vergleichende Studie zwischen zyklischer Voltammetrie (engl. cyclic voltammetry, CV) und linearer Voltammetrie (engl. linear sweep voltammetry, LSV) sowie eine Validierung basierend auf einer Online-Gas-Analyse zeigen im ersten Schritt die Äquivalenz beider Methoden hinsichtlich der Bestimmung des Wasserstoff-Crossovers auf. Darauf folgend wird eine Messkampagne in  $\text{H}_2/\text{N}_2$  Konfiguration mit voll faktorieller Variation der relativen Feuchte  $RH$  und der Temperatur  $T$  evaluiert. Mit den resultierenden CVs wird ein Modell für den Wasserstoffpermeations-Koeffizienten parametrisiert und mit den EIS-Spektren werden Parameter eines Kettenleitermodells (engl. transmission line model, TLM) für blockierende Elektroden bestimmt. Besonders die Membran- und kathodischen Ionomer-Widerstände  $R_{\text{PEM}}$  und  $R_{\text{p}}$  werden hierbei als Funktionen von  $RH$  und  $T$  gefittet und im Anschluss für die Parametrisierung von Modellen der Ionomerleitfähigkeiten verwendet. Obwohl die hier gemessenen Werte in der gleichen Größenordnung wie bestehende

Literatur-Referenzdaten liegen, können deutliche Abweichungen und Trends beobachtet werden, die die absolute Notwendigkeit hervorheben, neue Materialien tiefergehend zu charakterisieren. Abschließend werden die Änderungen der Ionomerleitfähigkeiten unter Last ( $\text{H}_2/\text{O}_2$ ), verursacht durch das sich ändernde Wasser-Management, untersucht und ein Ansatz zur Abschätzung der lokalen Feuchtigkeit der CCL, vorgestellt. Die Abweichungen der Ionomer-Widerstände unter Last von jenen im  $\text{H}_2/\text{N}_2$  Zustand enthüllen, dass eine Korrektur der Polarisations-Daten um die Ohm'schen Beiträge basierend auf  $\text{H}_2/\text{N}_2$  Messungen nicht empfehlenswert ist.

In der zweiten Publikation liefern Messungen im Modus „Protonenpumpe“ ( $\text{H}_2/\text{H}_2$ ) eine Quantifizierung der Anoden-Verlustmechanismen, die, wie sich zeigt, stark von  $RH$  und dem Wasserstoffpartialdruck  $p_{\text{H}_2}$  abhängig sind. Innerhalb dieser  $\text{O}_2$ -freien Experimente wird eine CO-Vergiftung des Katalysators durch Spurenverunreinigungen in der Gas-Zufuhr beobachtet. Um diese CO-Vergiftung zu verhindern, wird eine neue Recovery-Prozedur vorgestellt, die eine zuverlässige Parametrierung der  $\text{H}_2$ -Oxidationsreaktion (engl. hydrogen oxidation reaction, HOR) basierend auf der linearisierten Butler-Volmer-Kinetik (BV) erlaubt. Nachfolgend wird ein Datensatz mit stationären Polarisationskurven für eine voll faktorielle Variation von  $RH$ ,  $T$  und dem Sauerstoffpartialdruck  $p_{\text{O}_2}$  erstellt und um die Ionomer-Widerstände und Wasserstoff-Crossover-Werte korrigiert. Dieser Datensatz wird für die Parametrierung einer auf einem einfachen Tafel-Gesetz basierenden ORR-Reaktion eingesetzt und ermöglicht somit den Beweis, dass  $RH$  keinen signifikanten Einfluss auf die ORR-Performance hat. Weiterhin werden  $\text{O}_2$ -Massentransport-Beiträge, beruhend auf Grenzstrom-Techniken und Heliox-Messungen, diskutiert und eine globale Verlust-Analyse durchgeführt. Die Letztere zeigt, dass Anoden- sowie Sauerstofftransport-Beiträge bis zu  $0.1 \text{ A/cm}^2$  nicht mit der Parametrierung der ORR interferieren. Die Analyse enthüllt zudem, dass das Tafel-Gesetz mit einer einzelnen intrinsischen Steigung von  $-70 \text{ mV/dec}$  ausreicht, um die ORR-Kinetik bei Halbzellenpotentialen von über  $0.8 \text{ V}$  zu beschreiben, während die Daten unterhalb von  $0.8 \text{ V}$  von der Tafel-Linie abweichen. Des Weiteren zeigen sich Trends in den EIS-Spektren unter Last, die nicht von dem Tafel-Gesetz abgedeckt werden, sogar bei sehr kleinen Stromdichten. Abweichungen zwischen Tafel-Steigungen, die durch Polarisations-Daten bestimmt wurden, und jener, die mittels EIS Ladungstransfer-Widerständen gewonnen wurden, weisen auf eine komplexere Kinetik hin, die innerhalb der dritten Publikation weiter untersucht wird.

In der dritten Publikation wird der Einfluss des niederfrequenten induktiven Loops der EIS auf die Diskrepanzen der Tafel-Steigungen zwischen Polarisationskurven ( $-70 \text{ mV/dec}$ ) und Ladungstransfer-Widerständen ( $\leq -100 \text{ mV/dec}$ ) demonstriert. Anhand der  $\text{H}_2/\text{O}_2$  Daten werden die Niederfrequenz-Beiträge entschlüsselt. Hierfür werden die lokalen Steigungen der Polarisationskurven, berechnet durch numerische Ableitung, vom niederfrequenten Schnittpunkt der kapazitiven EIS mit der Realachse bei ca.  $1 \text{ Hz}$  abgezogen. Basierend auf dieser Erkenntnis und auf den Ionomerwiderständen unter Last, können die langsamen Befeuchtungseffekte, die zu einem induktiven Verhalten führen, von den Platin-Oxidations-Beiträgen unterschieden werden. Hiermit wird eine neue einfache Darstellungsweise der Kathoden-Kinetik parametrisiert, die die ORR- und Platin-Vergiftungseffekte enthält, welche in einem niederfrequenten induktiven Loop resultieren. Die daraus folgende Reaktionskinetik wird dann in ein vereinfachtes transientes 1D-Through-Plane-Modell der Membran-Elektroden-Einheit (engl. membrane electrode assembly, MEA) integriert, das im Anschluss für eine extensive Parameterstudie verwendet wird. Dieses Modell

erzielt konsistente Ergebnisse, wobei sowohl Polarisationskurven als auch EIS mit den Experimenten bei hoher Feuchte übereinstimmen. Somit vereint es grundlegend stationäre und impedanzspektroskopische Performance-Merkmale von PEM-Brennstoffzellen.

Im Kapitel 5 wird schließlich der Zusammenhang der einzelnen Publikationen ausgearbeitet und ihre Signifikanz im aktuellen Literatur-Kontext diskutiert. Zusätzlich wird das MEA-Modell um die Ionomer-Befeuchtungsdynamik erweitert. Die Parametrierung von  $R_{\text{PEM}}$  und  $R_{\text{p}}$ , abhängig von  $RH$  und der Stromdichte  $j$ , wird durch das Anfitten von Polynomen an ausgewählte Daten des  $\text{H}_2/\text{O}_2$  Testlaufs erreicht. Dieses finale MEA-Modell ermöglicht nun die sinnvolle Simulation aller Feuchte-Bedingungen und steigert sogar leicht die Vorhersage-Güte bei hohem  $RH$ . Abschließend wird eine umfangreiche Verlustanalyse durchgeführt, sowohl hinsichtlich der Überspannung, als auch für die differentiellen Widerstände, welche die wichtigsten Verlust-Mechanismen von State-of-the-Art PEMFCs, abhängig von den Betriebsparametern, abbildet.



# List of Abbreviations

<b>ACL</b>	anode catalyst layer
<b>ASR</b>	area specific resistance
<b>BPP</b>	bipolar plate
<b>BEV</b>	battery electric vehicle
<b>BV</b>	Butler-Volmer
<b>CCL</b>	cathode catalyst layer
<b>CCM</b>	catalyst coated membrane
<b>CL</b>	catalyst layer
<b>CO</b>	carbon monoxide
<b>CO<sub>2</sub></b>	carbon dioxide
<b>COR</b>	carbon oxidation reaction
<b>CPE</b>	constant phase element
<b>CV</b>	cyclic voltammetry
<b>DFT</b>	density functional theory
<b>DOE</b>	design of experiments
<b>DPT</b>	dew point temperature
<b>DRT</b>	distribution of relaxation times
<b>ECM</b>	equivalent circuit model
<b>ECP</b>	electrochemical potential
<b>ECSA</b>	electrochemical surface area
<b>EIS</b>	electrochemical impedance spectroscopy
<b>EOD</b>	electroosmotic drag

<b>EW</b>	equivalent weight
<b>FC</b>	fuel cell
<b>FCEV</b>	fuel cell electric vehicle
<b>FEM</b>	finite element method
<b>FF</b>	flow field
<b>GDB</b>	gas diffusion backbone
<b>GDL</b>	gas diffusion layer
<b>GHG</b>	greenhouse gas
<b>HER</b>	hydrogen evolution reaction
<b>HFR</b>	high-frequency resistance
<b>HHV</b>	higher heating value
<b>HOR</b>	hydrogen oxidation reaction
<b>HUPD</b>	hydrogen under potential deposition
<b>ICE</b>	internal combustion engine
<b>LHV</b>	lower heating value
<b>LSV</b>	linear sweep voltammetry
<b>MEA</b>	membrane electrode assembly
<b>MPL</b>	micro-porous layer
<b>OCV</b>	open circuit voltage
<b>OER</b>	oxygen evolution reaction
<b>ORR</b>	oxygen reduction reaction
<b>PDE</b>	partial differential equation
<b>PEEK</b>	polyether ether ketone
<b>PEM</b>	proton exchange membrane
<b>PEMFC</b>	polymer electrolyte membrane, or proton exchange membrane, fuel cell
<b>PEN</b>	polyethylene naphtalate
<b>PFSA</b>	perfluorinated sulfonic acid
<b>PTFE</b>	polytetrafluoroethylene



## LIST OF ABBREVIATIONS

---

<b>RDE</b>	rotating disc electrode
<b>RDS</b>	rate determining step
<b>SHE</b>	standard hydrogen electrode
<b>SLC</b>	steady-state limiting current
<b>SOEC</b>	solid oxide electrolyzer cell
<b>SOFC</b>	solid oxide fuel cell
<b>SOH</b>	state of health
<b>STP</b>	standard temperature and pressure
<b>TLC</b>	transient limiting current
<b>TLM</b>	transmission line model
<b>TPB</b>	triple phase boundary
<b>TS</b>	Tafel slope



# List of Symbols and Indices

The units might deviate from the SI standard and some symbols might be assigned multiple times depending on the circumstances.

## Latin symbols

Symbol	Description	Unit
$a$	chemical activity	-
$A$	area	$\text{cm}^2$
ASR	area specific resistance	$\Omega \text{cm}^2$
$b$	Tafel slope	V or mV dec <sup>-1</sup>
$c$	exponent - fitting parameter	-
$C$	concentration	$\text{mol cm}^{-3}$
$C_{\text{dl}}$	area specific double layer capacitance	$\text{mF cm}^{-2}$
	volumetric double layer capacitance	$\text{mF cm}^{-3}$
$d$	diameter	$\mu\text{m}$ or $\text{nm}$
$D$	diffusion coefficient	$\text{cm}^2 \text{s}^{-1}$
DPT	dew point temperature	$^{\circ}\text{C}$ or $\text{K}$
$e$	exponent - fitting parameter	-
$E$	energy	$\text{kJ mol}^{-1}$
ECSA	electrochemical surface area	$\text{m}_{\text{Pt}}^2 \text{g}_{\text{Pt}}^{-1}$
EW	equivalent weight	$\text{g mol}^{-1}$
$f$	frequency	$\text{Hz}$
$f_v$	water vapor volume fraction in the membrane	-
$\Delta G$	Gibbs free energy	$\text{kJ mol}^{-1}$
$\Delta H$	reaction enthalpy	$\text{kJ mol}^{-1}$
$i(x)$	volumetric current density at position $x$	$\text{A cm}^{-3}$
$I$	current	$\text{A}$
$j, j^*$	current density, complex current density	$\text{A cm}^{-2}$
$j_0$ or $j^0$	exchange current density	$\text{A cm}_{\text{geo}}^{-2}$ or $\text{A cm}_{\text{Pt}}^{-2}$
$k$	reaction rate constant	$\text{A cm}_{\text{geo}}^{-2}$ or $\text{A cm}_{\text{Pt}}^{-2}$
$l$	length or thickness	$\mu\text{m}$ or $\text{cm}$
$m$	reaction order of the ORR	-
	$p_{\text{H}_2\text{O}}$ -dependency exponent of $j_{\text{ORR}}^0$ (Tafel+PtOx)	-

Symbol	Description	Unit
$M$	molar mass	$\text{g mol}^{-1}$
$n$	amount of substance	mol
$n$	valency - number of elementary charges	-
	$p_{\text{H}_2\text{O}}$ -dependency exponent of $j_{\text{ORR}}^0$ (Tafel)	-
$N$	molar flux	$\text{mol cm}^{-1} \text{s}^{-1}$
$p$	pressure or partial pressure	bar or Pa
$P$	power density	$\text{W cm}^{-2}$
$q$	charge	C
$Q$	capacitance of constant phase element	$\text{mF cm}^{-2}$
$rf$	roughness factor	$\text{m}_{\text{Pt}}^2 \text{m}_{\text{geo}}^{-2}$
rH or RH	relative humidity	% or -
$R_{\Omega}$ or $R_0$	ohmic resistance, HFR	$\Omega \text{cm}^2$
$R_{\text{ct}}$	charge transfer resistance	$\Omega \text{cm}^2$
$R_{\text{p}}$	catalyst layer proton resistance	$\Omega \text{cm}^2$
$R_{\text{p}}^{\text{eff}}$	effective catalyst layer proton resistance	$\Omega \text{cm}^2$
$R_{\text{O}_2}$	oxygen transport resistance	$\text{s cm}^{-1}$
$\Delta S$	reaction entropy	$\text{J mol}^{-1} \text{K}^{-1}$
$t$	time	s, min or h
$T$	temperature	$^{\circ}\text{C}$ or K
$U, U^*$	voltage, complex voltage	V
$\dot{V}$	volume flow	$\text{Nl min}^{-1}$ or sccm
$w$	kinetic reaction order of the HOR	-
$x$	position in through-plane	$\mu\text{m}$ or mm
$x_i$	mole fraction of the species $i$	-
$y$	equation of fitting equation	-
$z$	valency - number of elementary charges	-
$Z$ or $Z^*$	impedance	$\Omega \text{cm}^2$

## Greek symbols

Symbol	Description	Unit
$\Delta\phi$	difference of electric and protonic potential	V
$\alpha$	transfer coefficient	-
$\beta$	symmetry coefficient	-
$\gamma$	kinetic reaction order of the ORR (Tafel)	-
$\gamma$	distribution of relaxation times	$\Omega \text{cm}^2$
$\Gamma$	volumetric density of surface platinum sites	$\text{mol cm}_{\text{geo}}^{-3}$
$\Gamma_{\text{Pt}}$	surface density of platinum sites	$\text{mol cm}_{\text{Pt}}^{-2}$

LIST OF SYMBOLS AND INDICES

---

Symbol	Description	Unit
$\delta$	infinitesimal variation of a quantity	-
$\Delta$	difference operator	-
$\epsilon$	porosity	-
$\zeta$	stoichiometry factor	-
$\eta$	overpotential	V
$\theta_{\square}$	fraction of free platinum surface	-
$\lambda$	stoichiometry	-
$\lambda_{\text{ionomer}}$	ionomer water content	-
$\mu$	chemical potential	J mol <sup>-1</sup>
$\bar{\mu}$	electrochemical potential	J mol <sup>-1</sup>
$\nu$	reaction rate	A cm <sup>-2</sup>
$\sigma$	conductivity	S cm <sup>-1</sup>
$\tau$	time constant	s
$\phi$	electric or protonic potential	V
$\Phi$	phase shift	° or rad
$\psi$	structure parameter	-
$\Psi$	permeation coefficient	A cm <sup>-2</sup> MPa <sup>-1</sup>
$\omega$	angular frequency	s <sup>-1</sup>

### Subscripts and superscripts

Syntax	Description
0	equilibrium conditions or ohmic
a or ACL	anode or anode catalyst layer
act	activation
app	apparent
c or CCL	cathode or cathode catalyst layer
DC	base load
dl	double layer
DRT	distribution of relaxation times
e	electronic
eff	effective
$i$ and/or $j$	component variable
Im	imaginary part
$jR$ -free	corrected by ohmic contributions
lim	limiting
liq	liquid
max	maximum

---

**Syntax    Description**


---

min	minimum
MT	mass transport
ox	oxidized
p	protonic or products
PEM	membrane
r	reactants
Re	real part
red	reduced
ref	reference
SLC	steady-state limiting current
TLC	transient limiting current
vap	vapor
$\Omega$	ohmic
$\circ$	standard state
$\ominus$	STP conditions
$\ddagger$	activated state

**Functions**


---

**Syntax    Description**


---

$\exp(X)$	exponential of $X$
$\text{Im}(X)$	imaginary part of the complex number $X$
$\ln(X)$	natural logarithm of $X$
$\log(X)$	decimal logarithm of $X$
$\text{Re}(X)$	real part of the complex number $X$
$\tilde{X}$	water partial-pressure-dependent

**Constants**


---

Symbol	Description	Value	Unit
$F$	Faraday constant	96485.39	C mol <sup>-1</sup>
$M_{\text{H}_2}$	molar mass of H <sub>2</sub>	2	g mol <sup>-1</sup>
$M_{\text{H}_2\text{O}}$	molar mass of H <sub>2</sub> O	18	g mol <sup>-1</sup>
$M_{\text{O}_2}$	molar mass of O <sub>2</sub>	32	g mol <sup>-1</sup>
$p^\circ$	pressure at standard state conditions	101 325	Pa
$p^\ominus$	pressure at STP conditions	101 325	Pa

LIST OF SYMBOLS AND INDICES

---

Symbol	Description	Value	Unit
$p_{\text{ref}}$	reference pressure	100 000	Pa
$R$	molar gas constant	8.31	J mol <sup>-1</sup> K <sup>-1</sup>
$T^{\ominus}$	temperature at STP conditions	298.15	K
$T_{\text{ref}}$	reference temperature	273.15	K
$\Delta G_{\text{liq}}^{\ominus}$	Gibbs free energy for liquid product water	-237.1	kJ mol <sup>-1</sup>
$\Delta G_{\text{vap}}^{\ominus}$	Gibbs free energy for vapor product water	-228.6	kJ mol <sup>-1</sup>





# 1 Introduction

Between the 1950s and today, human population on Earth has quadrupled from 2 billion to 8 billion inhabitants [1]. Combined with wealth growth in many countries, this has led to rapidly rising energy demands that are mainly satisfied by the combustion of fossil fuels. The latter drastically accelerated the anthropogenic greenhouse gas (GHG) emissions to the atmosphere and therewith the global climate change [2].

To slow down the climate change and prevent likely challenges caused by fossil fuel shortages, moving towards sustainable energy supply solutions seems inevitable. One possibility is the creation of a sustainable economy articulated around renewable energy sources and hydrogen to carry the energy. In this scenario, hydrogen is mainly generated with electricity coming from renewables by water electrolysis and can be stored in pressurized tanks or bound in metal hydrides. This stored energy can then be converted again by fuel cells into electrical energy, heat and water. Therewith, fluctuation in the available renewable energies can be compensated [3, 4].

Particularly in the industry and transportation sectors, which together represent over 40% of the total carbon dioxide (CO<sub>2</sub>) emissions [2, 5], a change in paradigm is necessary to reach carbon neutrality. In transportation, aside from battery electric vehicles (BEVs), fuel cell electric vehicles (FCEVs) represent a promising alternative to classical vehicles containing internal-combustion-engine-based powertrains in the quest to zero emission mobility. Especially in the long-haul domain, where fast refueling and high energy densities are needed to guarantee the necessary ranges, fuel cells have significant advantages over batteries. Also, the latter are currently still heavier and bulkier than fuel cell power modules, thus allowing less payload capacity [6]. Recently, the European Union has sharpened its goals for climate protection with the *Fit-For-55* target of saving 55% GHG emissions until 2030 and becoming climate-neutral until 2050 [7–9]. To reach these goals, one important measure is to increase the share of BEVs and FCEVs on the roads and even ban the sales of emissions-emitting engines starting from 2035 [10, 11].

The polymer electrolyte membrane, or proton exchange membrane, fuel cell (PEMFC) stands out for its capability of high-dynamic-operation and high power densities, its scalability and its high level of maturity. Since it operates mainly with hydrogen at low temperatures, it emits neither GHGs nor other pollutants such as NO<sub>x</sub>. The latter are emitted by internal combustion engines (ICEs) and represent a growing threat to human health in densely inhabited areas. PEMFC systems can easily reach high electric efficiencies of above 50%<sub>LHV</sub><sup>1</sup> and therefore lie between classical powertrains and pure-battery powertrains [6].

---

<sup>1</sup> Efficiency referenced to the lower heating value (LHV) of H<sub>2</sub>, see section 2.2.1.

The history of proton exchange membrane (PEM) fuel cells has been described in multiple works and goes back to the years 1838/1839 and the experiments of Professor Christian Friedrich Schönbein and Sir William Grove on platinum electrodes under hydrogen and oxygen atmospheres (see Fig. 1.1) [3, 4, 12]. Afterwards, fuel cells were mainly used in combination with coal gas in technical applications but remained rather discreet until the late 1950s and early 1960s, when Willard T. Grubb invented a fuel cell comprising a polymer membrane assuring ion transport. PEMFCs as they are known nowadays started being developed in collaborations between NASA and industry partners such as General Electric (GE) mainly for space mission purposes. However, the PEMFCs employed in the NASA Gemini spacecraft used hydrocarbon membranes (polystyrene sulfonate, PSS) which were not as stable as current membranes [3]. Since then, research and development underwent several time periods with more or less interest and thus investments. First, the NASA opted for an alkaline fuel cells solution for the Apollo program and GE also abandoned PEMFCs. Then, significant improvements were made possible with the introduction of perfluorinated sulfonic acid (PFSA) membranes (Nafion<sup>®</sup>) by Dupont and with the reduction of platinum needed per square centimeter of electrode by more than two orders of magnitude while increasing performance [4]. This progress was initiated in the 1980s by the regrowing interest for instance from Ballard Power Systems and the LANL [4]. Since the early 2000s, research was accelerated by growing government support through fundings all over the world. Investments by the automakers have also strongly increased such that a first generation of FCEVs has been launched successfully in small series (e.g. Honda *Clarity*, Toyota *Mirai*, Hyundai *ix35 Fuel Cell* or Mercedes-Benz *GLC F-Cell*) [13–17].

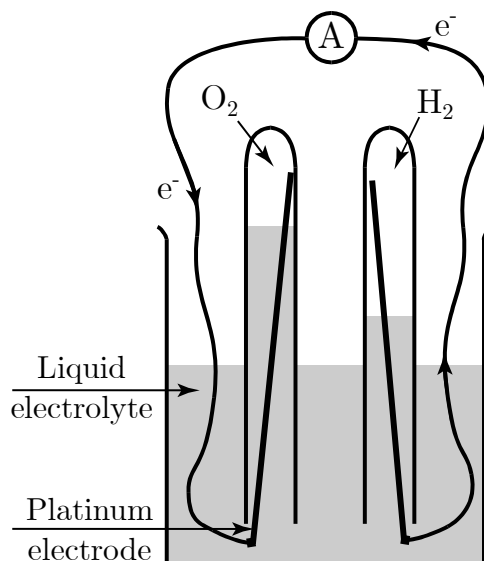


**Figure 1.1:** Grove's first fuel cell.  
Adapted from [4].

Despite the higher range of FCEV and the faster refueling process (less than 5 min) compared to BEV, to reach global market readiness, the infrastructure of refueling stations has to be expanded in Europe as it is still limited and unevenly distributed. In Germany, the hydrogen fueling station coverage with its 95 currently available stations is already good [18], while most other countries are still lacking a comparable infrastructure. In France for instance, there are only 29 hydrogen filling stations open to the public [19], even though the country is roughly 1.5 times larger (area-wise) than Germany [20]. Furthermore, the functionality, lifetime and costs of PEM fuel cell systems must be optimized for a wide commercialization and process steps in fabrication need to be reduced and simplified for the sake of upscalability and economic viability. Since the fuel cell stack is the major component of an FCEV and as the MEA represents up to 50% of the total stack expenses (40% for the electrodes alone) [21], one important way of optimization lies in enhancing this component with respect to performance, lifetime as well as costs. To do so, the fuel-cell-internal loss mechanisms during operation and their dependencies on the operating parameters must be understood as they control performance and lifetime. This

thesis particularly focuses on the influence of the operating conditions on the steady-state and *electrochemical impedance spectroscopy* (EIS) response of PEM single cells under differential conditions.

## Aim and Scope of the Thesis

This thesis focuses on analyzing the influence of the operating conditions of PEM fuel cells on steady-state as well as electrochemical impedance spectroscopy (EIS) signatures and proposes well-parameterized models for the most important physics. This is relevant as even recent models and analyses in the literature often rely on parameterizations that become progressively outdated [22]. Thus, this lack of up-to-date datasets was addressed first in this work. To do so, an extensive dataset measured in fuel cell ( $\text{H}_2/\text{O}_2$ ) configuration containing polarization and EIS data was gathered, completed by blocking cathode ( $\text{H}_2/\text{N}_2$ ) and proton pump ( $\text{H}_2/\text{H}_2$ ) experiments. Especially in the fuel cell mode, the operating parameters were varied systematically in a full factorial manner. Special care was taken to get consistent data by ensuring long hold times for stabilization of the conditions before the measurements and by performing regular quality checks. A small cell which allows for differential conditions, i.e. cell inlet state equals cell outlet state, was chosen to minimize the influence of cell design and in-plane effects in the measurements. With this dataset, material laws were parameterized which allowed to dive deep into the cathode kinetics, i.e. the oxygen reduction reaction (ORR), which is still responsible for the major loss contribution at typical operating conditions. The final aim was to propose a model for MEA steady-state and EIS response which represents a good compromise between accuracy and usability, i.e. that can be parameterized with manageable effort based on in situ measurements. In the following, the structure of this work is presented.

A general overview on the most important PEMFC fundamentals is given in **Chapter 2**, including a description of the working principle and thermodynamics as well as a description of PEMFC components and their functions. **Chapter 3** describes the setup which was used in this work and explains the experimental characterization methods to extract the data needed for the parameterization of material laws. Subsequently, the three peer-reviewed publications of this work are presented in chronological order of publication in **Chapter 4**. The order of publication can also be seen as a seamless transition between the parameterization and modeling of the most important performance physics going from low time constant to high time constant processes. Thereafter, the link between these three studies is deepened and their integration in the current literature context discussed in **Chapter 5**. Beyond this, the model published in the last paper is extended by ionomer hydration effects in order to enable the simulation of dry conditions. With this final model, an extensive loss separation study based on both steady-state overpotentials and differential resistances is presented. Finally, a summary and an outlook are given in **Chapter 6**.

This thesis is composed of three peer-reviewed articles which have been published in the *Journal of the Electrochemical Society*. These articles are shown in full detail in Chapter 4; however, a brief summary of each article is given below:

- **Full factorial in situ characterization of ionomer properties in differential PEM fuel cells** [23]

This paper deals with the full factorial experimental characterization of the ionomer-related quantities including hydrogen crossover and protonic conductivity/resistance of the membrane and the cathode electrode. Based on the gathered data, simple models are parameterized that can be used in the analysis of performance data or directly be implemented into more detailed physical models.

- **PEM single cells under differential conditions: full factorial parameterization of the ORR and HOR<sup>2</sup> kinetics and loss analysis** [24]

The article presents an extensive characterization of both the anode and cathode kinetics in PEM fuel cells based on Butler-Volmer and Tafel's laws. The humidity dependency of the cathode kinetics is investigated extensively. Additionally, a complete loss mechanism analysis is performed and oxygen mass transport contributions are discussed.

- **Experimental and numerical investigation of the low-frequency inductive features in differential PEM fuel cells: ionomer humidification and platinum oxide effects** [25]

The low-frequency inductive signatures in EIS spectra are investigated in this third article. These low-frequency features are ascribed to slow ionomer hydration and slow platinum oxides (PtOx) which lead to discrepancies in the apparent Tafel slopes obtained by the steady-state polarization response and the EIS capacitive response. Based on the consistent dataset from the two first publications, both effects were disentangled and a simple but effective model for the cathode kinetics extended by PtOx kinetics is proposed and parameterized.

---

<sup>2</sup> HOR: hydrogen oxidation reaction

## 2 PEMFC Fundamentals

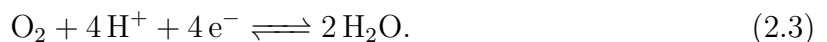
Fuel cells are galvanic cells which transform the chemical energy contained by two reactants to electrical energy and heat. In such devices, the oxidation and reduction reactions are spatially separated by the electrolyte. A catalyst facilitates these reactions within the electrodes which represent the interface between the ionic, electronic and reactant phases. On the free active sites of this catalyst, a species  $s$  is adsorbed in its reduced ( $s_{\text{red}}$ ) or oxidized ( $s_{\text{ox}}$ ) state and  $n$  electrons are transferred in the redox reaction according to



In automotive applications, PEMFCs are preferred over other types of fuel cells due to their low operating temperatures ( $T < 100^{\circ}\text{C}$ ), high power density ( $P > 0.5 \text{ W cm}^{-2}$ ), dynamic behavior and cold start capabilities. In the PEMFC, the membrane exchanges protons and separates the mixed-conducting porous electrodes by blocking electrons and gas transport. The cathode and anode are defined as the electrodes where the reduction and oxidation occur, respectively. Thus, the hydrogen oxidation reaction (HOR) proceeds on the anode side, i.e. molecular hydrogen  $\text{H}_2$  is oxidized into protons  $\text{H}^+$  and electrons  $\text{e}^-$ :



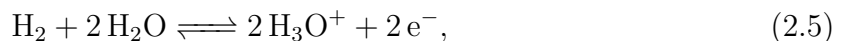
Since the membrane is largely electronically insulating, the electrons reach the cathode side by passing through an external circuit, this provides an electrical current and therefore electrical work. Meanwhile, the  $\text{H}^+$  protons are transported to the cathode across the membrane, where they come into play in the oxygen reduction reaction (ORR) together with the electrons and oxygen:



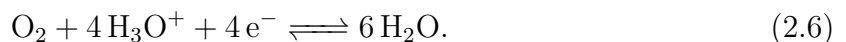
The sum of these two half-cell reactions leads to the total PEMFC reaction equation, which is spontaneous (thermodynamically favored) from the left to the right as the free energy of the reactants is higher than it is of the products:



As the protons formed during the HOR do not prevail alone but are bonded to water molecules within the electrolyte, the equations are sometimes written in the form containing oxonium ions (in this case hydronium,  $\text{H}_3\text{O}^+$ ) instead of  $\text{H}^+$  protons. Thus, the HOR can be found written as:



which leads to the following modified ORR equation:



## 2.1 Components of PEM Fuel Cells

In this section, the typical layout of a single PEMFC is presented and discussed based on Fig. 2.1, depicting the polymer electrolyte membrane (PEM) in the center and the cathode and anode parts respectively on the top and bottom. The sandwich of the membrane and both electrodes, namely the anode catalyst layer (ACL) and cathode catalyst layer (CCL), is referred to as catalyst coated membrane (CCM), which is the heart of the fuel cell hosting the electrochemistry. The MEA is obtained by adding a gas diffusion layer (GDL) on top of each catalyst layer for homogeneous reactant and electron transport. Typically, a GDL is made of a gas diffusion backbone (GDB) supplemented by a micro-porous layer (MPL) which is meant to ensure a well-balanced water management.

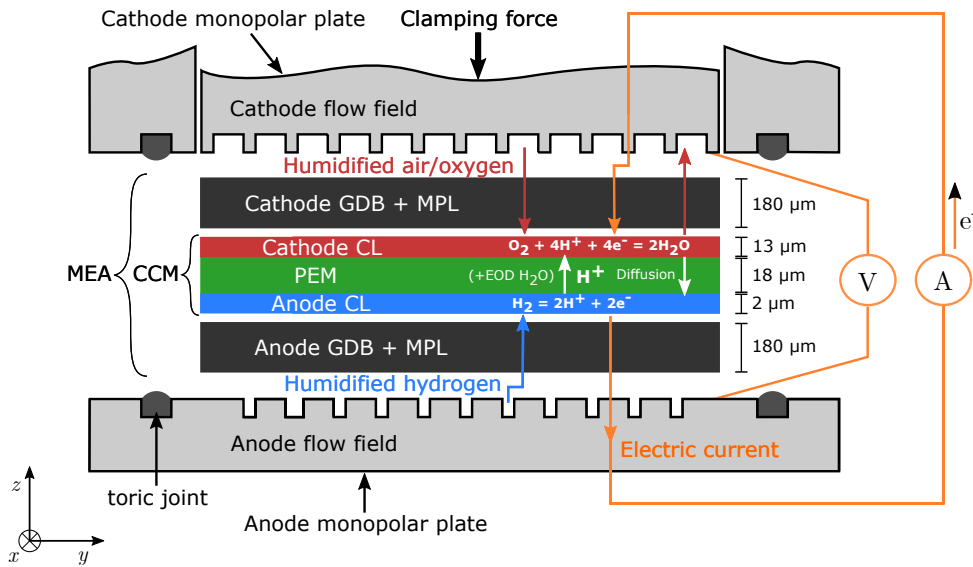


**Figure 2.1:** Schematics of the working principle of a single PEMFC as used in this work (not to scale). Gas permeation and electrical shorts are not represented. Gaskets and/or subgaskets are not shown.

### 2.1.1 Membrane - Electrolyte

Liquid water could be a suitable electrolyte as it allows protons to easily migrate through the aqueous solutions when a concentration gradient or electrical field is applied. In PEMFC however, additionally to transporting ions, the electrolyte also has to assure electrical insulation and to separate the anode and cathode reactant gas compartments from each other [26]. Therefore, polymer membranes, or proton exchange membranes (PEMs), come into play rather than liquid electrolytes. Such a membrane is represented exemplarily in the schematics of Fig. 2.1 by the green component in the center and is typically less than  $50 \mu\text{m}$  thick. Furthermore, the electrolyte is also needed within the porous three-dimensional electrode networks (blue and red components in Fig. 2.1) in order to provide pathways for the protons to reach or leave the reaction sites in the whole depth. Typically, the electrolyte is referred to as ionomer and is made of perfluorinated sulfonic acid (PFSA). It is a co-polymer that consists of a hydrophobic and chemically inert backbone (usually polytetrafluoroethylene (PTFE)-like) for mechanical stability and

of hydrophilic side chains made of perfluorinated ethers ending with sulfonic acid groups for the protonic conductivity, as shown in Fig. 2.2. The main advantages of this material type are [27]:

- mechanical strength, allowing thin membranes ( $\leq 50 \mu\text{m}$ )
- chemical stability, allowing high lifetime ( $> 10000 \text{ h}$ )
- high macroscopic proton conductivities between  $0.01$  and  $10 \text{ S m}^{-1}$
- low gas permeabilities between  $10^{-12}$  and  $10^{-10} \text{ mol cm}^{-1} \text{ s}^{-1} \text{ bar}^{-1}$

The equivalent weight (EW) describes the weight of polymer per quantity of sulfonic acid groups and is one of the most important characteristics of ionomers. Typically, it varies between  $700$  to  $1500 \text{ g}_{\text{polymer}}/\text{mol}_{\text{SO}_3^-}$ . On the one hand, lower EWs lead to higher protonic conductivity. On the other hand, a higher tendency towards swelling or dissolution can limit the applicability of ionomers with low EW.

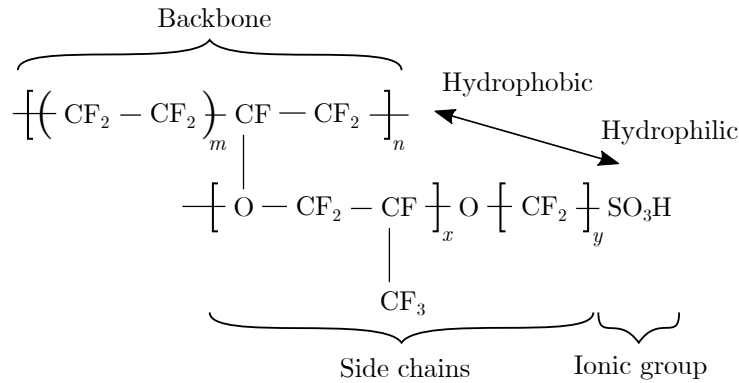


**Figure 2.2:** Typical chemical structure of Nafion<sup>®</sup>, a PFSA ionomer:  $m = 5 - 13.5$ ,  $x \geq 1$ ,  $y = 2$ , values may vary depending on the ionomer type [27].

However, swelling is mainly linked to exposure of the ionomer to water, which is needed in a certain range. The uptake of water by the hydrophilic regions of the ionomer is usually followed by swelling and the formation of an interconnected protonic conductive phase. The most important quantity in this process is the amount of water per amount of  $\text{SO}_3^-$  end groups, also called water content  $\lambda_{\text{ionomer}}$ . This emphasizes the importance of a constantly sufficient humidification during operation. Under too dry conditions, the ionic side chains can become isolated and as a result the protonic conductivity drops drastically, thus leading to higher resistances and locally increased temperature. Too much swelling, or swelling and shrinking cycles caused by humidity and temperature cycles, are not wanted since they provoke constructive and mechanical issues and accelerate chemo-mechanical ionomer ageing. Aside from this, ionomer swelling in the catalyst layer might reduce the pore size and therefore increase the reactant transport resistance. Thus, local conditions such as relative humidity  $RH$  and temperature  $T$  can also affect the conductivity apart from the EW.

The interconnected protonic conductive phase builds water pathways between both electrodes in which the protons can be transported either by the vehicle mechanism

(molecular diffusion) or by the Grotthuss mechanism (proton-hopping or structural diffusion). In the first mechanism, transport is driven by a concentration gradient or by an electrical field and the protons are bound as  $\text{H}_3\text{O}^+$  molecules enclosed inside hydration shells. In the second, hydrogen bridges in between the water molecules are formed, followed by a rearrangement of the local ionomer structure [12, 28].

### 2.1.2 Porous Electrodes

The porous electrode, often referred to as catalyst layer (CL), is a complex three-dimensional structure containing the active sites for the electrochemical reaction, the so-called triple phase boundaries (TPBs). These are the points where all three phases converge (see Fig. 2.3): the carbon phase for the electron transport, the ionomer phase for the proton transport, and the reactant gas phase [3]. The carbon phase, or more generally electronically conductive phase, is typically based on carbon black and transports electrons from and to the catalyst nanoparticles it supports, which also represent the reaction centers. These catalyst particles are dispersed on the support and reduce the activation barrier between the oxidized and reduced state of the reactants, thus increasing the reaction rate, without being consumed themselves. They are commonly made of platinum-group metals (PGMs), although platinum-based alloys (e.g. Pt-Ni or Pt-Co), with their own advantages and drawbacks, can also be employed. Possible PGM loadings lie in the range of 0.1 to 0.5  $\text{mg Pt cm}^{-2}$  [12] while the current target given by the Department of Energy is 0.125  $\text{mg Pt cm}^{-2}$  [21]. It is on these PGM catalyst particles that the charge transfer steps of both the HOR and ORR happen.

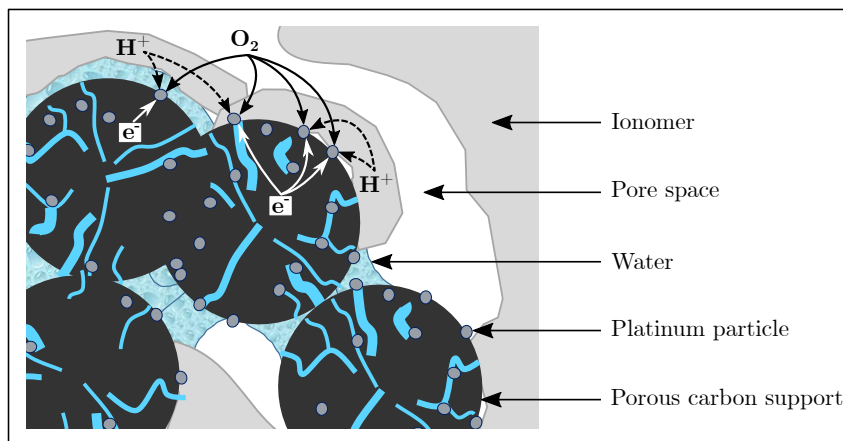


**Figure 2.3:** Porous electrode structure of a partly water-saturated cathode hosting several triple-phase boundaries. Product water transport is not shown here.

As mentioned above, the catalyst layer is also infiltrated by ionomer to ensure protonic connection between the membrane ionomer and the active reaction sites. In order to guarantee sufficient reactant gas feed to the electrodes as the liquid saturation of the porous structure increases during operation, a certain porosity has to be maintained to ensure sufficient pore void space (secondary pores). Nevertheless, species supply to the TPB is a complex process which involves multiple transport paths such as molecular and Knudsen diffusion in the void of the porous structure, diffusion through the ionomer thin film and dissolution and diffusion inside liquid water. All the transport properties strongly



depend on the humidification and the liquid water saturation of the porous matrix, thus emphasizing how essential a reliable water management is for the performance. State-of-the-art electrodes have a porosity of around 50% and pore sizes of around 30 nm.

The protons produced during the HOR in the ACL are transported through the ionomer of the electrode and the membrane to the CCL, where they are consumed in the ORR. Meanwhile, the electrons from the HOR are conducted in the opposite direction in the carbon phase through the GDL to the bipolar plate (BPP). There, they leave the fuel cell and travel via an external circuit to the cathode side where they rejoin the protons and together with oxygen molecules form water in the ORR at the reaction centers.

Typical electrode thicknesses in PEMFC applications range from 1 to 15  $\mu\text{m}$  and depend strongly on the carbon support type and on the catalyst loading. While thin electrodes with low catalyst loadings are sufficient for the anode side, the cathode side generally needs higher loadings and therefore thicknesses in order to get meaningful Pt/C ratios. This has mainly two origins: Firstly, the HOR on platinum is several orders of magnitude more effective than the ORR on platinum and thus requires less catalyst loading. Secondly, the oxidative conditions on the cathode side and the high half-cell potentials are harsher for the electrode and lead to higher degradation rates, meaning that a bigger reservoir of catalyst material is required.

### 2.1.3 Gas Diffusion Layers

The gas diffusion layer (GDL) is a highly porous sheet which is sandwiched between the CL and the bipolar plate (BPP). Its primary functions are to homogeneously distribute the reactant gases over the cell area, to transport heat and electrons, to remove excess liquid water and to ensure mechanical stability. The transportation of heat in the GDL occurs both through conduction in the solid phase and through media transport in the gaseous and liquid phases in the pore network. State-of-the-art GDLs are composed of

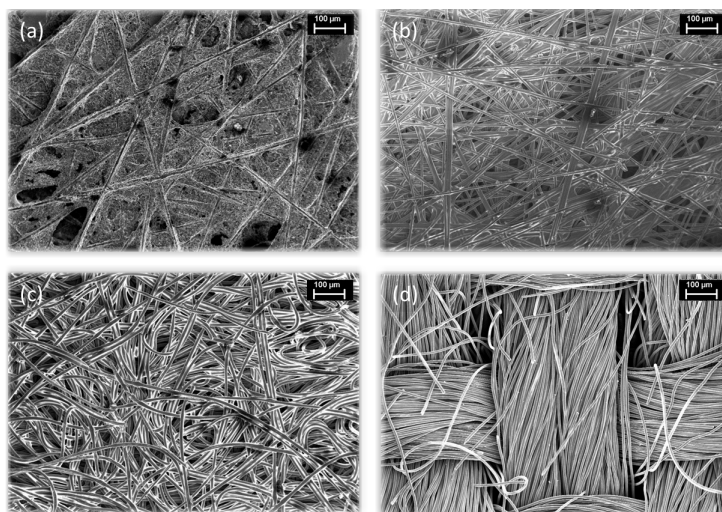


**Figure 2.4:** Scanning electron microscope (SEM) recordings of three GDL substrate types: Paper type from SGL<sup>®</sup> Carbon and Toray<sup>®</sup> in a) and b), respectively; Non-woven type from Freudenberg<sup>®</sup> in c); Carbon cloth type in d). Recordings from ref. [29].

two interplaying layers: the substrate, or GDB, and the MPL.

Usually, the GDB is made of a carbon fiber sheet which ensures high electrical and thermal transport properties as well as mechanical stability. It has a porosity higher than 70% and a thickness ranging from 100 to 200  $\mu\text{m}$ . In order to enhance water management, a hydrophobic coating such as PTFE is applied onto its carbon structure which increases the capillary pressure in the pores. The carbon structure can be based on a carbon fiber paper, non-woven carbon or carbon cloth as shown in Fig. 2.4.

The MPL is a compound typically made of carbon black, a binder and PTFE and most of the time coated on top of the substrate so as to penetrate some of it, thus creating an hybrid transition structure. Unlike the GDB, the MPL has a quite low porosity below 50% and is thinner with a thickness below 50  $\mu\text{m}$ . The smaller pore size of 50-100 nm leads to a good electrical and thermal contact with the catalyst layer while reducing the mechanical stress and protecting the membrane from the stiff carbon fibers. Even though gas transport in the GDB could mainly be modeled by molecular diffusion, Knudsen diffusion should also be taken into account in the MPL. Aside from this, convective gas transport may also play a non-negligible role and the complex two-phase behavior including liquid water transport with its effect on the saturation of the porous media must be taken into account. Due to the small pore size, high capillary pressures are required to push liquid water through according to the Young-Laplace equation. Nevertheless, preferential water pathways can be added by cracks/holes coming from the fabrication process. These pathways enable the removal of liquid water from the CL to the flow channel and keep the porous matrix free for the reactant gas transport in the opposite direction. Generally, pathways are created by pores with a high pore radius and a low contact angle.

#### 2.1.4 Flow Fields and Bipolar Plates

As can be seen in Fig. 2.1, the outmost component of a fuel cell sandwich is the flow field (FF) containing small flow channels for the reactant gases distribution across the cell area and the transport of water. Another important function is the conduction of electrons and heat, which is mainly done through the contact area with the GDL, also called lands, even though part of the heat is also transported by the gaseous and liquid phases through media transport. Moreover, the FF provides mechanical stability and supports the cell since it is the most thick and rigid part of the cell assembly. Most of the time, the FF designates a channel and land structure which is molded, milled or stamped into a stainless-steel-, aluminum- or titanium-based metal sheet or block. Sometimes, graphite-based plates can also be used instead of metal [30,31].

The ensemble composed of FF and plate or sheet is the so-called monopolar plate or bipolar plate (BPP), depending on the setup. In this work, single cells are characterized according to the setup shown schematically in Fig. 2.1 which uses one monopolar plate on each side (see section 3.1 for the full details on the setup). When stacking several cells, BPPs come into play. Then, in state-of-the-art setups, each plate has one side with an anode FF, one side with a cathode FF and coolant flows in between to remove the heat and control the cell temperature. The geometry and arrangement of the flow channels influences the media distribution and hence the performance of the fuel cell. The most common layout for flow fields in PEMFCs are straight [32–34], serpentine [35–39]

and interdigitated [40, 41] channels. Sometimes, other inventive geometries come into play [42]. Furthermore, the flow direction of the gases and coolant with respect to each other also plays a major role. The most known configurations are co-, counter- and cross-flow, although other flow configurations or constructive solutions to replace the *GDL + flow field* pair such as metal foams or meshes can be found [43]. Each configuration has its own advantages and drawbacks, which have already been extensively discussed in the literature based on both experiments and numerical simulations [31, 44–48].

## 2.2 Working Principles

Fuel cells are electrochemical energy converters which transform the high chemical energy contained within the reactants to electrical energy, thermal energy and products with lower chemical energy. In the case of PEM fuel cells, it is the energy contained within the hydrogen and oxygen that is converted during the electrochemical reaction to water, as shown in Fig. 2.5.

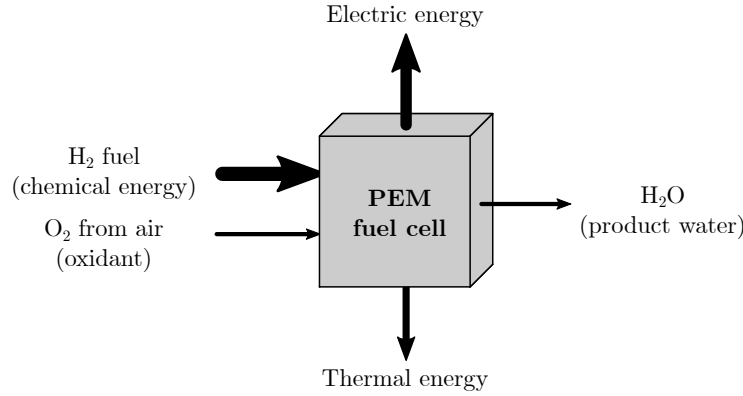


**Figure 2.5:** Energy fluxes entering and leaving the PEM fuel cell which is represented as a black box.

The fuel cell voltage which depends on current density can be computed theoretically based on the reversible (or equilibrium) cell voltage  $U_{\text{eq}} = U_0$  and the voltage losses caused by the different physicochemical processes. Such a voltage loss is commonly called *overpotential*  $\Delta U = \eta$  and is the driving force of the electrochemical reaction. In the following sections, the basics of the thermodynamics of PEMFCs as well as the major irreversibilities during operation, i.e. the loss mechanisms, are explained. The importance of these losses increases with cell current and they are mainly composed of kinetic overpotentials due to charge transfer resistances at the TPBs, ohmic losses caused by electron and proton transport and concentration or mass transport overpotentials.

### 2.2.1 Thermodynamics - Equilibrium Conditions

The chemical energy liberated or bound during a reaction, called enthalpy of reaction (sometimes calorific value), is simply the difference between the total reactant and total product molar enthalpies of formation

$$\Delta H_{\text{reaction}} = \Delta H_{\text{products}} - \Delta H_{\text{reactants}} = \sum_{\text{products, p}} \zeta_{\text{p}} \cdot H_{\text{p}} - \sum_{\text{reactants, r}} \zeta_{\text{r}} \cdot H_{\text{r}}, \quad (2.7)$$

with  $\zeta_i$  the stoichiometry factor of component  $i$  for the given reaction. Regarding the global PEM reaction (2.4), this enthalpy of reaction  $\Delta H_{\text{reaction}}$  corresponds to the heat measured when burning hydrogen in presence of oxygen in a calorimeter and is negative since energy is released. In tables of thermodynamic quantities, the values are often given for substances in their standard state<sup>1</sup>. However, the temperature is not officially part of this definition and therefore specifically needs to be mentioned. Most commonly, the reference is 25 °C, which leads to the definition called standard temperature and pressure (STP)<sup>2</sup> conditions in the following. Depending on whether the product water is condensed back to liquid or not during the overall PEMFC reaction (2.4),  $\Delta H$  can take two distinct values, both dependent on the temperature as shown in Fig. 2.6a. The difference between both values is the molar latent heat of water of 44.01 kJ mol<sup>-1</sup> at STP conditions [4, 49]:

- water vapor as product:  $\Delta H_{\text{vapor}}^{\circ} = -241.8 \text{ kJ mol}^{-1} = \text{LHV}^3$
- liquid water as product:  $\Delta H_{\text{liquid}}^{\circ} = -285.8 \text{ kJ mol}^{-1} = \text{HHV}^4$

The negative sign denotes the exothermic nature of the reaction. In a fuel cell, however, the maximum usable work  $w_{\text{max}}$  is lower than the reaction enthalpy and is given by the *Gibbs free energy* of reaction<sup>5</sup>, which represents the maximum chemical energy that can be converted to electrical energy. It is composed of an enthalpy and an entropy term  $\Delta H$  and  $\Delta S$ , respectively, and can be written as

$$\Delta G = \Delta H - T\Delta S = w_{\text{max}}, \quad (2.8)$$

where  $\Delta G$  is negative and thus the process is spontaneous. In electrical systems, the work provided is the product of charge  $Q$  and voltage  $U$  and the correlation between transferred charge and converted amount of substance  $n$  can easily be introduced by Faraday's law under constant current conditions:

$$w_{\text{electric}} = -Q \cdot U \stackrel{\text{Faraday}}{=} -n \cdot z \cdot F \cdot U. \quad (2.9)$$

In this equation,  $F = 96485 \text{ C mol}^{-1}$  is Faraday's constant and  $z = 2$  is the valency for the global PEMFC reaction. In the case where no current is drawn, the system is at equilibrium (or reversible, no losses occur) and thus the Gibbs free energy can be converted into an equilibrium voltage  $U_0$ , which is obtained by combining (2.8) and (2.9) ( $\Delta G = w_{\text{max}} = w_{\text{electric}}$ ) and normalizing to  $n = 1 \text{ mol}$ . This results in

$$U_0 = \frac{-\Delta G}{2 \cdot F}, \quad (2.10)$$

which is also called *open circuit voltage* (OCV) and is the voltage that should be measured between the solid phases of the anode and cathode electrodes when no electric current

<sup>1</sup> Standard state, marked with a degree sign (°):  $p^{\circ} = 101\,325 \text{ Pa} \approx 1 \text{ bar}$  and  $n^{\circ} = 1 \text{ mol}$ .

<sup>2</sup> STP, marked with a Plimsoll character (°):  $T^{\circ} = 298.15 \text{ K} = 25 \text{ °C}$ ,  $p^{\circ} = p^{\circ}$  and  $n^{\circ} = n^{\circ}$ .

<sup>3</sup> LHV: lower heating value.

<sup>4</sup> HHV: higher heating value.

<sup>5</sup> Similar to the reaction enthalpy in (2.7)  $\Delta G$ , the reaction Gibbs free energy equals the difference between the total reactant and total product molar Gibbs free energies of formation. For the PEMFC reaction equation (2.4), this results in  $\Delta G = G_{\text{H}_2\text{O}} - (G_{\text{H}_2} + \frac{1}{2}G_{\text{O}_2})$ .

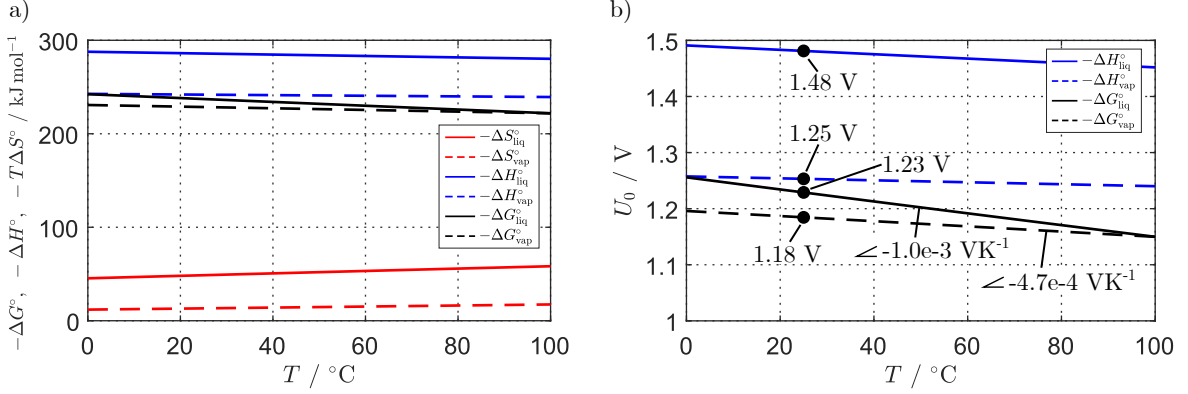


**Figure 2.6:** a) Representation of the energy terms at standard pressure conditions over temperature. b) Resulting theoretical OCV over temperature according to (2.10). The calculations are done based on data tabulated in ref. [50].

flows through the external circuit, i.e. the net reaction rate of (2.4) equals zero. Typical values of open circuit voltage (OCV) at standard conditions are shown in Fig. 2.6b. Generally, it is the Gibbs free energy of reaction which is determined by the experimental measurement of the voltage. Just as the enthalpy of reaction, the Gibbs free energy is tabulated for standardized conditions (see Fig. 2.6a) [4, 49]:

- water vapor as product:  $\Delta G_{\text{vapor}}^\ominus = -228.6 \text{ kJ mol}^{-1} \xrightarrow{\text{Eq. (2.10)}} U_0^\ominus = 1.18 \text{ V}$
- liquid water as product:  $\Delta G_{\text{liquid}}^\ominus = -237.1 \text{ kJ mol}^{-1} \xrightarrow{\text{Eq. (2.10)}} U_0^\ominus = 1.23 \text{ V}$

In real PEM fuel cells, such voltages can never be measured. In fact, even if no external current is drawn, small electrode internal currents in the range of 1 to 10  $\text{mA cm}^{-2}$  which are caused by fuel and oxidant permeation through the PEM reduce the observed OCV.

To calculate fuel cell efficiencies, the voltages measured are typically compared to those that would be obtained if the limit of the maximum electric work was given by the total enthalpy of reaction instead of the Gibbs free energy of reaction. This is custom since fuels are typically burnt to convert their chemical energy. Numerically, this is obtained by introducing the higher heating value (HHV) and the lower heating value (LHV) into (2.10). These theoretical voltages are given by  $U_{\text{LHV}}^\ominus = 1.25 \text{ V}$  and  $U_{\text{HHV}}^\ominus = 1.48 \text{ V}$  for the LHV and the HHV, respectively. Generally, if not specified, it is to expect that the LHV is used. Therewith, depending on whether liquid water or vapor is assumed as being the sole product of the reaction, the maximum reachable efficiency at STP conditions would be given by

$$\text{Max. efficiency} = \frac{\Delta G_{\text{liquid}}^\ominus}{\Delta H_{\text{liquid}}^\ominus} = \frac{\Delta G_{\text{liquid}}^\ominus}{\text{HHV}} = 83\% \text{ or } \frac{\Delta G_{\text{vapor}}^\ominus}{\Delta H_{\text{vapor}}^\ominus} = \frac{\Delta G_{\text{vapor}}^\ominus}{\text{LHV}} = 94\%. \quad (2.11)$$

In a real-life cell, more fuel and oxidant are fed at an actual current than needed as expected by the stoichiometry in order to avoid local undersupply. The unused amounts of fuel and oxidant leaving the cell are either recirculated by specific components or lost at the exhaust. This must be taken into account when calculating fuel cell system efficiencies.

### Effect of temperature on the equilibrium

Based on the assumption that the standard molar enthalpy and standard molar entropy are both approximately constant over temperature, the influence of temperature on the reversible cell voltage can be computed by partial derivation of (2.10) at constant pressure  $p$  and amount of substance  $n$  [12]:

$$\left(\frac{\partial U_0}{\partial T}\right)_{p,n} = \frac{\Delta S^\circ}{2 \cdot F} = -8.5 \cdot 10^{-4} \text{ V K}^{-1}. \quad (2.12)$$

Defining the standard temperature and pressure state as the reference condition now allows to get the equilibrium voltage at any temperature, provided that the pressure and the amount of substance remain constant:

$$U_0 = U_0^\circ + (T - T^\circ) \cdot \frac{\Delta S^\circ}{z \cdot F}. \quad (2.13)$$

This is a common approach used in the literature; however, as can be seen Fig. 2.6a, neither of the quantities is really constant over the temperature, which leads to slightly deviating slopes of the curves  $U_0 = f(T)$ . This effect should be taken into account when computing expected OCVs. As can be seen from (2.12), OCV decreases when the temperature increases. Nevertheless, when operating a PEM fuel cell under load, various processes are intertwined such that the tendency of the general performance with temperature is not trivial. While many physico-chemical processes including reaction kinetics and mass transport follow Arrhenius-like laws and thus are enhanced at higher temperatures, proper ionomer humidification likely gets more difficult and might affect performance in a negative way.

### Effect of partial pressure on the equilibrium

In order to investigate the variation of the equilibrium voltage with partial pressures of species, the potentials and reactions occurring at a single electrode are considered instead of looking at the complete PEMFC voltage and its global reaction. Hence, the voltage which equals the difference of cathode and anode electric potentials  $U = \phi_{\text{e,cathode}} - \phi_{\text{e,anode}}$  is substituted with the difference of electric and ionic potentials  $\Delta\phi = \phi_{\text{e}} - \phi_{\text{p}}$  applied at the given electrode. The global reaction (2.4) is first replaced by (2.3) for the ORR, then by (2.2) for the HOR.

In PEM fuel cells as in every other electrochemical system, the *electrochemical potential* (ECP)  $\bar{\mu}_i$  of a component  $i$  combines the chemical potential  $\mu_i$  and the contribution from the electrical potential  $\phi$  as in  $\bar{\mu}_i = \mu_i + z_i \cdot F \cdot \phi$ . The second term of the latter equation represents the electrical work performed to transport the charged component inside an electric field. At constant temperature  $T$ , pressure  $p$  and amount of substance of all other components  $n_{j \neq i}$ , the definition of the chemical potential of the substance  $i$  can be given as [51]:

$$\mu_i = \mu_i^\circ + R \cdot T \cdot \ln(a_i), \quad (2.14)$$

where  $R$  is the ideal gas constant,  $\mu_i^\circ$  the standard chemical potential of  $i$  and  $a_i$  its activity. The correction for the activity is needed when deviating from the standard conditions since intermolecular interactions cannot be neglected in concentrated solutions (non-ideal solutions). Based on this, the electrochemical potential can be written as

$$\bar{\mu}_i = \mu_i + z_i \cdot F \cdot \phi = \mu_i^\circ + R \cdot T \cdot \ln(a_i) + z_i \cdot F \cdot \phi. \quad (2.15)$$

The second term in (2.15) shows the simple proportionality of the electrical work per mole to the charge of this mole and the applied electric or electrolytic potential. Depending on the signs of the charge carrier and the potential, this second term increases or decreases the electrochemical potential. When no external current flows and the components' concentrations are constant in time, an electrode reaches the equilibrium between reduced and oxidized state. Thus, the sum of the electrochemical potential contributions of all the species present at this electrode is zero:

$$\sum_i (\zeta_i \cdot \bar{\mu}_i) = 0. \quad (2.16)$$

Based on the stoichiometry factors  $\zeta_i$  from (2.3), the equilibrium condition for a PEMFC cathode can be expressed by

$$\bar{\mu}_{\text{O}_2} + 4\bar{\mu}_{\text{H}^+} + 4\bar{\mu}_{\text{e}^-} = 2\bar{\mu}_{\text{H}_2\text{O}}, \quad (2.17)$$

with the electrochemical potentials  $\bar{\mu}_{\text{O}_2}$  of gaseous oxygen,  $\bar{\mu}_{\text{H}^+}$  of protons  $\text{H}^+$  in aqueous solution,  $\bar{\mu}_{\text{e}^-}$  of electrons  $\text{e}^-$  in the solid phase and  $\bar{\mu}_{\text{H}_2\text{O}}$  of liquid water. Applying (2.15) to (2.17) results in

$$\begin{aligned} [\mu_{\text{O}_2}^\circ + R \cdot T \cdot \ln(a_{\text{O}_2})] + 4 \cdot [\mu_{\text{H}^+}^\circ + R \cdot T \cdot \ln(a_{\text{H}^+}) + z_{\text{H}^+} \cdot F \cdot \phi_{\text{p}}^0] \\ + 4 \cdot [\mu_{\text{e}^-} + z_{\text{e}^-} \cdot F \cdot \phi_{\text{e}}^0] = 2 \cdot [\mu_{\text{H}_2\text{O}}^\circ + R \cdot T \cdot \ln(a_{\text{H}_2\text{O}})], \end{aligned} \quad (2.18)$$

where  $a_{\text{O}_2}$ ,  $a_{\text{H}^+}$  and  $a_{\text{H}_2\text{O}}$  represent the chemical activities and  $\mu_{\text{O}_2}^\circ$ ,  $\mu_{\text{H}^+}^\circ$  and  $\mu_{\text{H}_2\text{O}}^\circ$  the standard chemical potentials of oxygen, protons and water, respectively. The chemical potential of electrons in the solid electrode phase is represented by  $\mu_{\text{e}^-}$  and the valencies of the protons and electrons by  $z_{\text{H}^+} = +1$  and  $z_{\text{e}^-} = -1$ . Equation (2.18) also contains the equilibrium potentials  $\phi_{\text{p}}^0$  and  $\phi_{\text{e,cathode}}^0 = \phi_{\text{e}}^0$  of the protonic and electronic phases. In fact, it is the difference between the electrochemical potentials of reactants and products that represents the driving force for the electrode reaction. Therefore, it is advantageous to rearrange (2.18) in a way to express the *Galvani potential*  $\Delta\phi_{\text{cathode}}^0 = \Delta\phi_{\text{c}}^0$  by the well-known *Nernst equation*

$$\Delta\phi_{\text{c}}^0 = \phi_{\text{e}}^0 - \phi_{\text{p}}^0 = \frac{\mu_{\text{O}_2}^\circ + 4 \cdot \mu_{\text{H}^+}^\circ - 2 \cdot \mu_{\text{H}_2\text{O}}^\circ + 4 \cdot \mu_{\text{e}^-}}{4 \cdot F} + \frac{R \cdot T}{4 \cdot F} \cdot \ln \left( \frac{a_{\text{O}_2} \cdot (a_{\text{H}^+})^4}{(a_{\text{H}_2\text{O}})^2} \right), \quad (2.19)$$

which cannot be determined directly. Instead, the difference to the well-defined potential of a so-called *reference electrode* must be measured, which typically consists of a hydrogen/platinum electrode. In the case of PEMFC, the anode can be used as the reference electrode at equilibrium conditions. The Nernst equation of the anode electrode for its Galvani potential  $\Delta\phi_{\text{anode}}^0 = \Delta\phi_{\text{a}}^0$  can be written similarly to (2.19) and leads to

$$\Delta\phi_{\text{a}}^0 = \phi_{\text{e}}^0 - \phi_{\text{p}}^0 = \frac{2 \cdot \mu_{\text{H}^+}^\circ - \mu_{\text{H}_2}^\circ + 2 \cdot \mu_{\text{e}^-}}{2 \cdot F} + \frac{R \cdot T}{2 \cdot F} \cdot \ln \left( \frac{(a_{\text{H}^+})^2}{a_{\text{H}_2}} \right), \quad (2.20)$$

with  $\phi_{\text{e}}^0 = \phi_{\text{e,anode}}^0$  the potential of the electric phase,  $a_{\text{H}_2}$  the chemical activity of hydrogen and  $\mu_{\text{H}_2}^\circ$  its standard chemical potential. The Galvani potential of a *standard hydrogen electrode* (SHE) without any phase activity influence ( $a_i = 1$ ) is defined as the origin of the potential scale:

$$\Delta\phi_{\text{a}}^0 := 0 \text{ V}_{\text{SHE}}. \quad (2.21)$$

Now, knowing that the overall cell voltage is measured experimentally between the electric phase of the anode  $\phi_{e,\text{anode}}$  and the cathode  $\phi_{e,\text{cathode}}$ , the equilibrium cell voltage  $U_0$  can be obtained by combining both electrode equilibrium potentials (2.20) and (2.19) as

$$U_0 = \phi_{e,\text{cathode}}^0 - \phi_{e,\text{anode}}^0 = \Delta\phi_c^0 - \Delta\phi_a^0. \quad (2.22)$$

Since the standard chemical potential  $\mu_i^\circ$  of a pure species  $i$  is equal to its standard Gibbs free energy of formation  $\Delta G_i^\circ$ , the OCV equation (2.22) can finally be written as

$$U_0 = \frac{\Delta G_{\text{O}_2}^\circ + 2 \cdot \Delta G_{\text{H}_2}^\circ - 2 \cdot \Delta G_{\text{H}_2\text{O}}^\circ}{4 \cdot F} + \frac{R \cdot T}{4 \cdot F} \cdot \ln \left( \frac{a_{\text{O}_2} \cdot (a_{\text{H}_2})^2}{(a_{\text{H}_2\text{O}})^2} \right). \quad (2.23)$$

While the Gibbs free energy of formation of oxygen  $\Delta G_{\text{O}_2}^\circ$  and hydrogen  $\Delta G_{\text{H}_2}^\circ$  are zero, the temperature dependency of  $\Delta G_{\text{H}_2\text{O}}^\circ$  is exactly as in (2.12). The most known form of (2.23) which can be found in literature contains the gas partial pressures  $p_i$  and is as follows [52, 53]:

$$U_0 = 1.23 \text{ V} - 8.5 \cdot 10^{-4} \text{ V K}^{-1} \cdot (T - 298.15 \text{ K}) + \frac{R \cdot T}{4 \cdot F} \cdot \ln \left[ \left( \frac{p_{\text{O}_2}}{p_{\text{ref}}} \right) \left( \frac{p_{\text{H}_2}}{p_{\text{ref}}} \right)^2 \left( \frac{p_{\text{H}_2\text{O}}}{p_{\text{ref}}} \right)^{-2} \right]. \quad (2.24)$$

Equation (2.24) explicitly contains the dependency of the PEMFC equilibrium voltage on the temperature and the partial pressures of the involved species  $p_i$ . In this case, it is assumed that the product water is in the liquid form.

## 2.2.2 Reaction Kinetics Overpotential

Once an *overpotential* is applied to an electrochemical half-cell, it is driven away from its equilibrium state and carries current. Hence, there is a net mass conversion which means that the forward and backward rates of the the half-cell reactions involved are not equal anymore. In this case, the Galvani potential is different from the equilibrium potential and this difference is the definition of the overpotential  $\eta$ :

$$\eta = \phi_e - \phi_p - \Delta\phi^0 = \Delta\phi - \Delta\phi^0. \quad (2.25)$$

As above,  $\Delta\phi$  represents the difference between the electric and ionic potentials  $\phi_e$  and  $\phi_p$ , respectively.  $\Delta\phi^0$  is the half-cell equilibrium potential at given conditions. Mostly but not necessarily, a positive overpotential  $\eta > 0 \text{ V}$  defines a dominant forward reaction, meaning that an oxidation of the corresponding reactant happens. The latter is called an anodic reaction and electrons and protons are released. Accordingly, a negative overpotential  $\eta < 0 \text{ V}$  stands for a dominant cathodic (backward) reaction, where the reactant is reduced by consuming protons and electrons. In the literature, another term for the overpotential and the deviation from the equilibrium it produces is the *polarization*. The well-known polarization curve shows nothing else than the relation between the applied current and the resulting overpotential, or vice-versa. This is discussed in more detail in section 3.2.2. To properly describe an electrochemical system under load, the electrode kinetics have to be taken into account. In the following, the derivation of simple electrode kinetics leading to the *Butler-Volmer* relation between electrode current and overpotential is demonstrated.



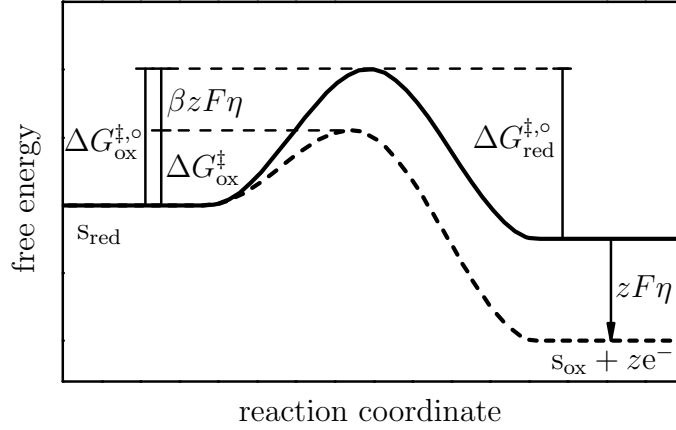


**Figure 2.7:** Effects of an electrode overpotential on the standard free energies of activation. The solid line represents the equilibrium case and the dashed line shows the activation characteristics when an overpotential is applied [12,51].

Typically, the assumption of a rate determining first order reaction with one single electron transfer such as in (2.1) is made. With the rate constants  $k_{\text{ox}}$  and  $k_{\text{red}}$  for the oxidation and reduction reaction and the concentrations of the species  $c_{\text{ox}}$  and  $c_{\text{red}}$ , the rate law of the forward and backward reactions can be written by using Faraday's law:

$$\frac{dc_{\text{red}}}{dt} = k_{\text{red}} \cdot c_{\text{ox}} = \frac{I_{\text{red}}}{z \cdot F}, \quad (2.26)$$

$$\frac{dc_{\text{ox}}}{dt} = k_{\text{ox}} \cdot c_{\text{red}} = \frac{I_{\text{ox}}}{z \cdot F}. \quad (2.27)$$

Then, the transition state theory can be invoked to describe a given rate constant  $k$  as a function of the rate constant at standard conditions  $k^\circ$  and the standard Gibbs free energy of activation for the activated complex  $\Delta G^\ddagger$ :

$$k = k^\circ \cdot \exp\left(-\frac{\Delta G^\ddagger}{R \cdot T}\right). \quad (2.28)$$

As shown above in (2.9) and (2.10), the Gibbs free energy can be linked with the electrochemical potential. Introducing the symmetry factor  $\beta$  to take into account the fraction of the total Gibbs free energy change in the system to the Gibbs energy of activation when applying an overpotential  $\eta$  leads to

$$\Delta G_{\text{red}}^\ddagger = \Delta G_{\text{red}}^{\ddagger, \circ} + (1 - \beta) \cdot z \cdot F \cdot \eta, \quad (2.29)$$

$$\Delta G_{\text{ox}}^\ddagger = \Delta G_{\text{ox}}^{\ddagger, \circ} - \beta \cdot z \cdot F \cdot \eta, \quad (2.30)$$

which is sketched in Fig. 2.7. Both these equations can now be combined with (2.28) to get expressions for the rate constants depending on the overpotential:

$$k_{\text{red}} = k_{0, \text{red}} \cdot \exp\left(\frac{-\Delta G_{\text{red}}^{\ddagger, \circ} - (1 - \beta) \cdot F \cdot \eta}{R \cdot T}\right), \quad (2.31)$$

$$k_{\text{ox}} = k_{0, \text{ox}} \cdot \exp\left(\frac{-\Delta G_{\text{ox}}^{\ddagger, \circ} + \beta \cdot F \cdot \eta}{R \cdot T}\right). \quad (2.32)$$

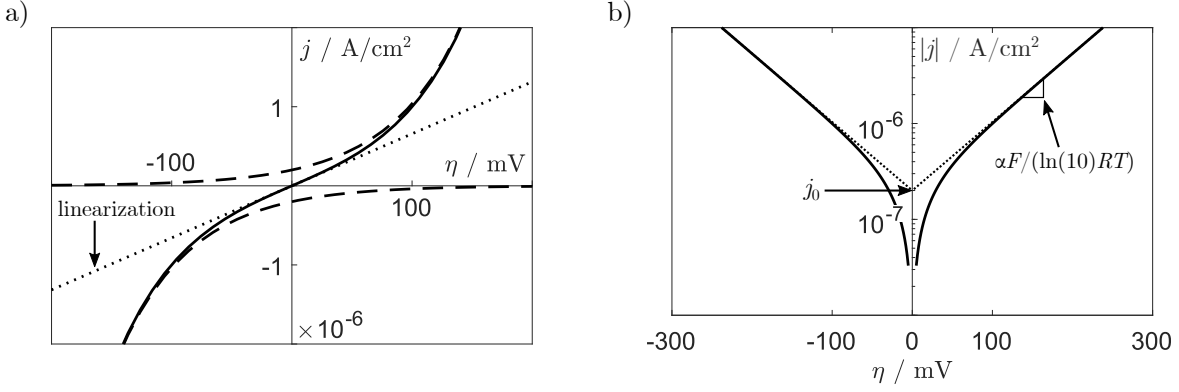


**Figure 2.8:** a) Zoom on the low overpotential zone of the current-overpotential curve based on the equation (2.37). The solid line represents the Butler-Volmer kinetics, the dashed lines the anodic and cathodic branches and the dotted line the linearization based on the equation (2.42). b) Tafel plot for the anodic and cathodic branches of the current-overpotential curve. The conditions in both diagrams are  $\alpha = 0.5$ ,  $T = 80^\circ\text{C}$  and  $j_0 = 2 \cdot 10^{-7} \text{ A/cm}^2$ .

Then, these rate constants are inserted into (2.27) and (2.26) to obtain the equations of the anodic and cathodic currents of an electrode. The current  $I$  is thereby replaced by the current density  $j$ , which is the surface-normalized current. This leads to

$$j_{\text{red}} = z \cdot F \cdot c_{\text{ox}} \cdot k_{0,\text{red}} \cdot \exp\left(\frac{-\Delta G_{\text{red}}^{\ddagger,\circ} - (1 - \beta) \cdot F \cdot \eta}{R \cdot T}\right), \quad (2.33)$$

$$j_{\text{ox}} = z \cdot F \cdot c_{\text{red}} \cdot k_{0,\text{ox}} \cdot \exp\left(\frac{-\Delta G_{\text{ox}}^{\ddagger,\circ} + \beta \cdot F \cdot \eta}{R \cdot T}\right). \quad (2.34)$$

At equilibrium conditions, both forward and backward reactions occur at the same rate. This means that both current densities have the same value, that the overpotential equals zero and the concentrations equal their equilibrium concentrations  $c_{\text{red}} = c_{\text{red}}^0$  and  $c_{\text{ox}} = c_{\text{ox}}^0$ :

$$j_{\text{red}} = j_{\text{ox}} = j_0 = z \cdot F \cdot c_{\text{ox}}^0 \cdot k_{0,\text{red}} \cdot \exp\left(\frac{-\Delta G_{\text{red}}^{\ddagger,\circ}}{R \cdot T}\right) \quad (2.35)$$

$$= z \cdot F \cdot c_{\text{red}}^0 \cdot k_{0,\text{ox}} \cdot \exp\left(\frac{-\Delta G_{\text{ox}}^{\ddagger,\circ}}{R \cdot T}\right). \quad (2.36)$$

In this context,  $j_0$  is the well-known exchange current density and quantifies the rate of reduction and oxidation in equilibrium when no net current flows. It is generally an indicator for catalytic activity and should be as high as possible. In non-equilibrium conditions, the net current is the difference between anodic and cathodic current. By neglecting any transport processes and thus considering that the concentrations are equal to their equilibrium concentrations, the famous *Butler-Volmer* (BV) equation can finally be derived as

$$j = j_{\text{ox}} - j_{\text{red}} = j_0 \cdot \left[ \exp\left(\frac{\beta \cdot z \cdot F \cdot \eta}{R \cdot T}\right) - \exp\left(\frac{-(1 - \beta) \cdot z \cdot F \cdot \eta}{R \cdot T}\right) \right]. \quad (2.37)$$

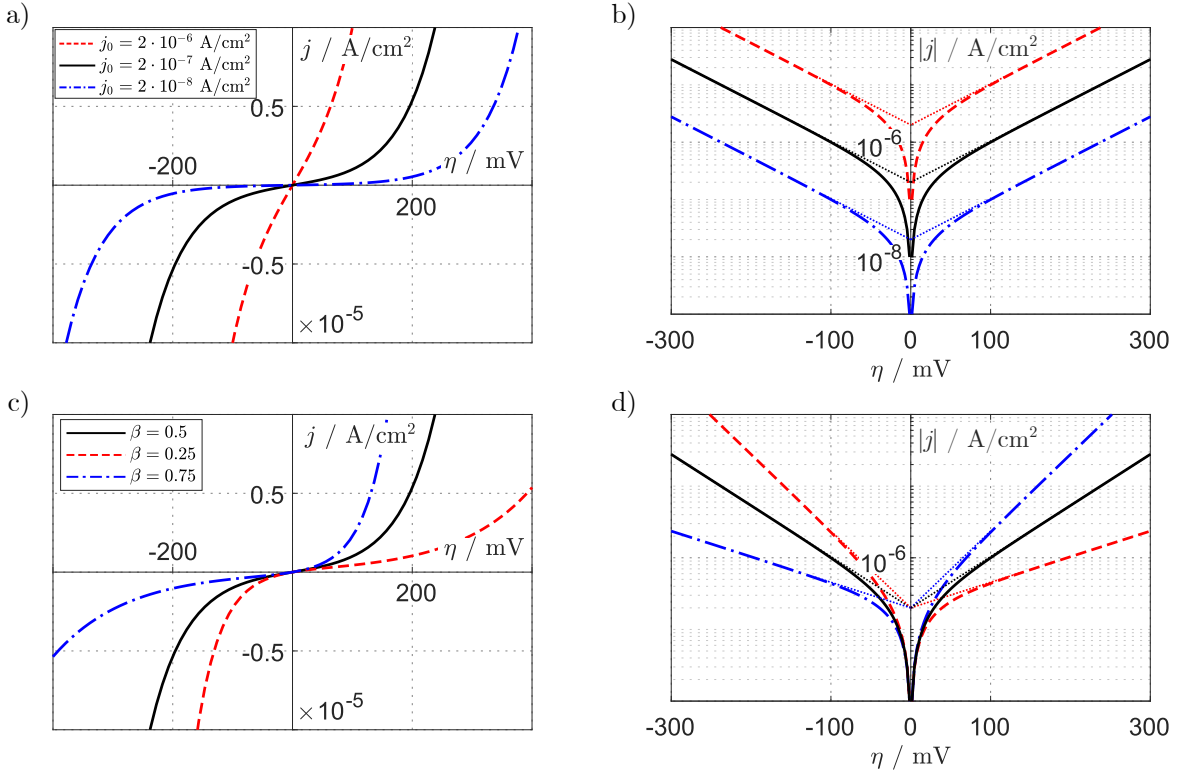


**Figure 2.9:** Effect of the exchange current density  $j_0$  on the kinetic overpotential required to produce net current in a linear diagram (a) and in the Tafel representation (b). Effect of the symmetry coefficient  $\beta$  on the kinetic overpotential required to produce net current in a linear diagram (c) and in the Tafel representation (d). The baseline conditions (solid black lines) in both diagrams are  $\alpha = 0.5$ ,  $T = 80^\circ\text{C}$  and  $j_0 = 2 \cdot 10^{-7} \text{ A/cm}^2$ .

The shape of this equation is shown exemplarily in Fig. 2.8a with a zoom on the low overpotential zone. It can be seen that at very low overpotentials, a linearization seems reasonable. In this range, both branches play an important role in the net current. At higher overpotentials, the current produced by one branch becomes negligibly small. Figure 2.8b shows both branches in a so-called Tafel plot, which is useful for the evaluation of kinetic parameters. Especially the exchange current density can be gained by extrapolating the linear regime to zero overpotential, and the *transfer coefficient*  $\alpha = z \cdot (1 - \beta)$  can be obtained by evaluating the slope. Figure 2.9 depicts the influence of both these parameters on the polarization in a linear representation as well as in a Tafel plot (logarithmic current scale). In the following, famous simplifications of the BV equation are presented and discussed.

### High overpotentials - Tafel approximation

One simplification of the BV equation often encountered in the literature is the expression of the famous *Tafel kinetics*, which can legitimately be applied with sluggish kinetics, i.e. when the absolute value of the overpotential is high for current densities of interest. This holds for instance whenever the ratio of back current to forward current is less than 1%, that is  $\exp(\frac{F}{RT}\eta) < 0.01$  [51]. At  $25^\circ\text{C}$ , this leads to  $|\eta| > 118 \text{ mV}$  and at  $80^\circ\text{C}$  it leads to  $|\eta| > 140 \text{ mV}$ . Depending on the sign of the overpotential, one term of the Butler-Volmer

equation (2.37) can be neglected in this case, see Figs. 2.8a and b. In the case of a high negative overpotential as it usually is the case with the ORR kinetics on platinum, this leads to

$$j = -j_0 \cdot \exp\left(\frac{-(1-\beta) \cdot z \cdot F \cdot \eta}{R \cdot T}\right). \quad (2.38)$$

A common transformation of (2.38) is its inversion to represent the overpotential as a function of the current density. This transformation is widely used to fit experimental polarization curves and is given by the expression

$$\eta = -\frac{R \cdot T}{\alpha \cdot F} \cdot \ln\left(\frac{j}{j_0}\right) = b \cdot \ln\left(\frac{j}{j_0}\right). \quad (2.39)$$

An approach to make the model and experimental curves match is to fix the *Tafel slope* (TS)  $b$  and the exchange current density  $j_0$ . While  $j_0$  gives insights into the catalytic performance,  $b$  yields mechanistic insights about the reaction. The expression of the electrochemical impedance spectroscopy (EIS) response of a kinetics law is called *charge transfer resistance*  $R_{ct}$  and can be calculated by derivation of the overpotential  $\eta$  according to the current density  $j$ . In the special case of Tafel kinetics, this yields:

$$-\frac{\partial \eta}{\partial j} = R_{ct} = \frac{R \cdot T}{\alpha \cdot F \cdot j} = \frac{b}{j}, \quad (2.40)$$

Equation (2.40) proves that the Tafel slope is accessible from EIS measurements, even though the exchange current density is not and thus must be gained from fitting polarization data.

### Low overpotentials - Linearized kinetics

The second simplification of the BV kinetics is exactly the opposite from the first and therefore only applies if the absolute value of the overpotential is so small ( $|\eta| \ll 118$  mV) as to allow a linearization of (2.37) (see Fig. 2.8). To do so, the exponential function is approximated via its Taylor series expansion:

$$e^x = 1 + \sum_{n=1}^{+\infty} \frac{x^n}{n!} = 1 + x + \frac{x^2}{2!} + \frac{x^3}{3!} + \dots \quad (2.41)$$

which must be applied to (2.37). All the terms with an order higher than one are neglected as a linear relationship is assumed between current density and overpotential:

$$j \approx j_0 \cdot \left[ \left(1 + \frac{\beta \cdot z \cdot F \cdot \eta}{R \cdot T}\right) - \left(1 + \frac{-(1-\beta) \cdot z \cdot F \cdot \eta}{R \cdot T}\right) \right] = -\frac{j_0 \cdot z \cdot F}{R \cdot T} \cdot \eta. \quad (2.42)$$

Here, the impedance response is constant over the current density and is simply the slope of the polarization curve when the overpotential is very small, i.e. at conditions near the equilibrium. Hence, the charge transfer resistance  $R_{ct}$  can be expressed via

$$-\frac{\partial \eta}{\partial j} = R_{ct} = \frac{R \cdot T}{z \cdot F \cdot j_0}. \quad (2.43)$$

This shows that the evaluation of  $j_0$  from polarization data is straightforward with linearized kinetics. However, the Tafel slope cannot directly be determined at such conditions.

### Symmetrical Butler-Volmer

Another special case arises when the exponential terms in (2.37) are symmetrical, i.e. if the symmetry coefficient takes the exact value  $\beta = 0.5$  (baseline case in Figs. 2.9c and d). In this case, the properties of the exponential function can be exploited and the equation takes the mathematical form

$$j = j_0 \cdot \left[ \exp\left(\frac{z \cdot F \cdot \eta}{2 \cdot R \cdot T}\right) - \exp\left(-\frac{z \cdot F \cdot \eta}{2 \cdot R \cdot T}\right) \right] = 2 \cdot j_0 \cdot \sinh\left(\frac{z \cdot F \cdot \eta}{2 \cdot R \cdot T}\right). \quad (2.44)$$

Again, this equation can be inverted in order to express the overpotential  $\eta$  as a function of the current density  $j$ . Here, this inversion yields the following expression:

$$\eta = \frac{2 \cdot R \cdot T}{z \cdot F} \cdot \sinh^{-1}\left(\frac{j}{2 \cdot j_0}\right). \quad (2.45)$$

Hence, an analytical expression can be derived for the charge transfer resistance which would be expected in transient measurements, e.g. in EIS recordings:

$$-\frac{\partial \eta}{\partial j} = R_{ct} = \frac{2 \cdot R \cdot T}{z \cdot F \cdot j_0 \cdot \sqrt{\frac{j^2}{j_0^2} + 4}}. \quad (2.46)$$

This special case of symmetrical kinetics branches was sometimes used in studies to simplify the equations, e.g. by Kulikovskiy and Reshetenko, who used it in several polarization curve and EIS investigations [54–61].

### More sophisticated kinetics

Even though the Butler-Volmer (BV) equation or its simplifications as shown above are typically employed in PEMFC performance analysis and modeling, it is clear that neither the HOR nor the ORR are simple single step reactions with one electron transfer such as in (2.1). Generally, multiple steps occur including species adsorption on the catalyst, surface diffusion, splitting or formation of molecular bonds and several distinct electron transfers. According to literature sources, the HOR and hydrogen evolution reaction (HER) on platinum in acidic environment supposedly follows either the Tafel-Volmer or Heyrovsky-Volmer mechanism [12, 62]. The first involves a dissociative adsorption of molecular hydrogen onto platinum (Tafel), followed by an electrochemical oxidation of the adsorbed species (Volmer). The second involves first a partially oxidative adsorption of hydrogen (Heyrovsky), then again an oxidation of the adsorbed species (Volmer) [12, 62]. In the past, different studies aimed at unraveling the exact mechanisms and parameterized them based on rotating disc electrode (RDE) as well as MEA measurements [62–67]. In their experimental and simulative studies of hydrogen electrodes and humidity effects, Wiezell et al. also integrated a water dependency in the Volmer step (hydration of protons) as originally proposed by Andreaus and Scherer [68–72]. They showed that the features of the simulations closely matched their experimental results and that the water dependency in the HOR yielded a low-frequency inductive loop in EIS. Usually, the HOR is very fast and produces very small overpotentials with common PEMFC materials, thus only small amounts of Pt (0.025 - 0.05 mg<sub>Pt</sub>/cm<sub>geo</sub><sup>2</sup>) are required to facilitate the reaction. However, with low loadings, degradation phenomena can play an important role and

provoke noticeable performance losses even if they lead only to modest electrochemical surface area (ECSA) losses. Therefore, understanding the kinetics seems essential to derive mitigation strategies and develop improved next generation materials.

In contrast to this, the ORR and oxygen evolution reaction (OER) kinetics at platinum-based catalyst are sluggish and lead to high overpotentials. At typical PEMFC operating conditions, the cathode kinetics are often responsible for the highest overpotential of all the loss mechanisms. Some groups modeled the ORR with simple descriptions based on Tafel or Butler-Volmer laws complemented by platinum oxide coverage-dependent effects and assumed a single equivalent rate determining step (RDS). The assumption is that chemisorbed species on the catalyst surface have a poisoning effect leading to dual Tafel slopes and dual reaction orders which are predicted for instance by RDE or microelectrode measurements [73–76]. Such considerations were probably triggered by the early work of Damjanovic et al. [77–79]. Nevertheless, the potential-dependent change in the Tafel slope is very challenging to detect in full cells since they are mainly operated at conditions where the half-cell potential of the ORR electrode corrected by the ohmic contributions remains high. Hence, simple models with a single RDS and a single Tafel slope were considered as being sufficiently accurate to describe ORR kinetics-related performance losses in many PEMFC studies. Subramanian et al. proposed a steady-state oxide coverage-dependent model and parameterized it pragmatically based on polarization and cyclic voltammetry data gathered with real MEAs of PEMFCs, although they only detected a potential-dependent change the Tafel slope with their low-loaded cathode sample which showed decreased performance and therefore lower cathode half-cell potentials [80].

Other authors previously used comparable models in transient studies to explain the mismatch between the steady-state apparent Tafel slopes and those obtained from the charge transfer resistance in capacitive EIS, which was detected early by Antoine et al. [81] and was sometimes also explained completely or partially by ionomer hydration/dehydration and/or along-the-channel effects [34, 82–90] or catalyst poisoning [91, 92]. Early studies by Roy et al. and Mathias et al. considered ORR mechanisms containing one or more intermediates and took the slow poisoning effect of platinum by oxide growth into account, which leads to low-frequency inductive contributions [93–95]. Therein, the oxide growth models were derived from the one of Darling and Meyers [96]. Other comparable approaches used more detailed modeling of the platinum oxide layer formation and reduction containing a fast chemisorbed oxide and two slow place-exchanged oxides (planar-site and edge-site) which block chemisorption and progressively replace the initial fast and reversible chemisorbed oxide with slow irreversible place-exchanged oxides [97, 98]. Based on steady-state and EIS computations, they also showed that their oxide model produces low-frequency inductive loops which need to be taken into account to get Tafel slopes consistent with those obtained from polarization curves. Currently, it is understood that even in differential cells where no along-the-channel effects are expected, the low-frequency inductive loop contains multiple processes that can at least partially be traced to slow humidification and oxide reduction effects [90, 99–101].

Another perspective is the ORR representation in terms of microkinetics which replaces the simple Tafel law and can consist of two distinct mechanisms [102]. The first is a direct reduction of adsorbed molecular oxygen to water in a four-electron-step. The second is a series pathway likely to include the creation of hydrogen peroxide ( $\text{H}_2\text{O}_2$ ) and other intermediate species such as adsorbed  $\text{O}_2$ ,  $\text{O}$ ,  $\text{OH}$ ,  $\text{OOH}$ ,  $\text{O}$ , and  $\text{H}_2\text{O}$  in individual

elementary reactions. In such microkinetics considerations, there is no single RDS as the importance of the individual rate equations generally varies with the potential [103–105]. This absence of a single RDS leads to variable apparent Tafel slopes over the potential. However, since all the kinetics are supposedly fast, no low-frequency inductive features are expected from such considerations. Finally, even though several work groups have worked on the exact mechanistic description of the ORR on Pt based on density functional theory (DFT) calculations and sophisticated experiments over the years, there still is no final consensus as discussions are ongoing and further work needs to be done [106–108].

### 2.2.3 Ohmic Overpotential

Loss contributions which are proportional to the load drawn from a PEMFC are commonly called ohmic losses as they behave almost perfectly like a simple resistor at first glance. Different overlapping resistances contribute to the overall ohmic contribution:

- the electronic resistance of the setup containing the BPP and GDL bulk resistances as well as the contact resistances between the individual layers
- the protonic resistance of the catalyst layers (CL)
- the protonic resistance of the membrane (PEM)

Usually, the electronic bulk and contact resistances as well as the membrane resistance are measured simultaneously by EIS techniques and are therefore summarized under the name high-frequency resistance (HFR),  $R_0$  or  $R_\Omega$ . The contribution of proton transport within the electrodes is named  $R_p^{\text{eff}}$  and comes mainly from the cathode side as the anode impedance is usually negligible at typical automotive operating conditions. Together, these resistances lead to the overpotential given by

$$\eta_{\text{Ohm}}^{\text{total}} = \eta_\Omega + \eta_{\text{CCL}}^{\text{H}^+} = (R_\Omega + R_p^{\text{eff}}) \cdot j, \quad (2.47)$$

with  $\eta_{\text{CCL}}^{\text{H}^+}$  the voltage drop due to proton transport resistance in the CCL  $R_p^{\text{eff}}$ ,  $\eta_\Omega$  the voltage drop caused by the HFR  $R_\Omega$  and  $j$  the current density. The bulk electronic resistances are often small compared with the contact resistances which are influenced by the nature of the contact and the clamping pressure. The protonic resistances are correlating with the corresponding layer thickness  $L$ , the surface area  $A$  and the ionic conductivity  $\sigma$  and can be expressed as

$$R = \frac{L}{A \cdot \sigma}. \quad (2.48)$$

The local conductivity is mostly dependent on the temperature and the humidification level, which can both be influenced by the operating conditions. Often, EIS measurements under load ( $\text{H}_2/\text{O}_2$ ) or with a blocking cathode ( $\text{H}_2/\text{N}_2$ ) are performed to access this property as they enable a proper separation between membrane and electrode contribution [109, 110]. Sometimes, these properties are extracted by fitting the parameters of a specific model to polarization curves [58]. This is less precise however since it does not allow for a current-dependent evaluation of the parameters as they are mostly assumed to

be constant over the load range in such analyses. By partial derivation of (2.47) according to  $j$ , the general impedance response is obtained as follows:

$$\frac{\partial \eta_{\text{Ohm}}^{\text{total}}}{\partial j} = R_{\text{PEM}} + R_{\text{p}}^{\text{eff}} + j \cdot \left( \frac{\partial R_{\text{PEM}}}{\partial j} + \frac{\partial R_{\text{p}}^{\text{eff}}}{\partial j} \right), \quad (2.49)$$

where the first two resistances can be determined from the high frequencies of EIS and the third term contains the change of the resistances with the load, which comes mainly from changed humidification during operation.

## 2.2.4 Mass Transport Overpotential

Reactant gas transport from the gas channels of the BPP through the GDL and the catalyst layer to the reaction centers can be described by diffusion and convection processes. The resistance to this transport leads to a concentration gradient between the gas channel and the electrode which in turn leads to a drop of the OCV and a decrease of the kinetics exchange current density. The latter effect provokes a higher kinetics overpotential as shown in (2.39). Therefore, the voltage drop caused by reactant transport is a combination of an effect on the local Nernst potential and the local kinetics overpotential and is strictly speaking not an overpotential according to (2.25). However, it is mostly called diffusion or mass transport overpotential in the literature, or diffusion polarization sometimes. At typical PEM operating conditions, the combination of high hydrogen concentrations on the anode side and the advantageous hydrogen transport properties yields negligibly small performance losses. Thus, when talking about mass transport losses in PEMFCs, mostly oxygen transport is addressed. By combining the laws of Nernst, Tafel and Ficks law of diffusion with an equivalent oxygen transport resistance  $R_{\text{O}_2}$ , the steady-state performance loss caused by oxygen transport from the cathode gas channels to the reaction sites in the CCL can be calculated by (2.50) [111]:

$$\Delta U_{\text{O}_2, \text{MT}}(j) = \frac{R \cdot T}{F} \cdot \left( \frac{1}{4} + \frac{\gamma}{\alpha_{\text{ORR}}} \right) \cdot \ln \left( \frac{p_{\text{O}_2}^{\text{channel}} - \frac{R \cdot T}{4 \cdot F} \cdot R_{\text{O}_2} \cdot j}{p_{\text{O}_2}^{\text{channel}}} \right). \quad (2.50)$$

Here,  $\alpha_{\text{ORR}}$  is the ORR transfer coefficient as described above in (2.39) and  $\gamma$  is its reaction order which describes the dependency of the exchange current density  $j_0$  on oxygen partial pressure. The most difficult part resides in the determination of  $R_{\text{O}_2}$  which is strongly depending on the actual load. Mostly, the oxygen transport resistance is obtained by fitting polarization curves [58] or by the measurement of the limiting current density which enables the separation of pressure-dependent and pressure-independent resistances [112, 113]. Both methods however only yield a single load-independent value of the transport resistance. At limiting current density  $j_{\text{lim}}$ , the amount of available reactant at the catalyst surface drops to zero. Knowing the oxygen concentration in the flow channel and the molar flux to the electrode which is given by Faraday's law, this condition can be put into Fick's law of diffusion to give the expression of the total oxygen transport resistance

$$R_{\text{O}_2} = \frac{p_{\text{O}_2}^{\text{channel}} \cdot 4 \cdot F}{R \cdot T \cdot j_{\text{lim}}}. \quad (2.51)$$



Since the resistance obtained by classical limiting current techniques does not necessarily paint a representative picture due to altered heat generation and water management, other derived methods were investigated such as limiting current measurements in proton-pumping configuration [114–116]. Sometimes, EIS techniques are also used to get a rough estimation of the differential transport resistance at a given load point, either by directly fitting the parameters of a physical model to spectra [59–61, 117, 118], or by fitting the parameters of an equivalent circuit model (ECM), which can be supported by distribution of relaxation times (DRT) analyses [86, 119–123]. Isolating the pure oxygen transport contributions from EIS where several processes overlap frequency-wise remains challenging nonetheless.

## 2.3 Ageing Mechanisms

PEM fuel cells, like every other component or system, are subject to various degradation phenomena. While some of them directly lead to a loss of performance over lifetime, others do not and thus are only detected during specific service protocols or when failure occurs. The contributions of catalyst and ionomer degradation are considered as being the most important ones. However, other effects such as BPP degradation by thermo-mechanical and corrosive stress and GDL hydrophilicity alteration as well as structural degradation can be important.

Comparably to every other physico-chemical process, degradation mechanisms strongly depend on the chosen materials, the conditions of operation, the surroundings and time. Hence, understanding detrimental operating conditions is of utmost importance in this work since they need to be avoided in the process of characterizing performance signatures with the aim of parameterizing appropriate models. In the following sections, the most known irreversible and reversible ageing mechanisms in PEMFCs are briefly itemized and a glimpse of some corresponding mitigation solutions is given.

### 2.3.1 Irreversible Degradation

#### Platinum degradation

One major non-reversible performance decay of the electrode can be attributed to ageing of its Pt, which is accelerated at high half-cell potentials, high humidity and high temperature and is also dependent on the pH. Such noxious conditions mainly arise within the cathode of PEMFCs, leading to several degradation appearances [124, 125]:

- Electrochemical Ostwald ripening and coalescence, caused by dissolution of small Pt particles and redeposition on bigger particles (growth/coarsening to more stable particles).
- Pt dissolution, migration and precipitation in the ionomer of the CL or the membrane, where the diffusion is caused by the gradient in concentration of dissolved Pt between the cathode and the anode. Migrating dissolved Pt ions get in contact with crossover hydrogen in the membrane and are reduced to elemental Pt.
- Loss of electrically connected Pt by detachment from the carbon support caused by its corrosion at high potential.

### Carbon corrosion

The corrosion of the support, i.e. oxidation to CO and CO<sub>2</sub> accompanied by morphological and structural changes of the CL, occurs mainly at high local potential. At normal potentials of fuel cell operation, carbon corrosion can be neglected due to its slow kinetics. However, during highly transient phenomena like air/air startup as well as global or local fuel starvation, unusually high potentials can arise locally and strongly accelerate the corrosion process. Aside from the loss of Pt, a loss in the conductivity as well as an increase in the oxygen transport resistance can also be observed [124–126].

### Ionomer deterioration

The electrode and membrane electrolyte are typically subject to two ageing modes: chemical and thermomechanical. The first one is amplified at dry conditions and high potentials, where gas permeation leads to the formation of H<sub>2</sub>O<sub>2</sub> forming free radicals by Fenton's reactions which directly attack the PFSA chains. The radical formation can also be accelerated by metal cations coming for instance from the corrosion of the bipolar plates. Furthermore, there is an ongoing debate as to whether Pt precipitation in the membrane globally has a positive or a negative effect. Thermomechanical stress mainly comes from load dynamics leading to dynamics in local temperature and water management. These conditions provoke ionomer redistribution, cracks and pinhole formation as well as delamination [26, 124, 125, 127].

## 2.3.2 Reversible Degradation

When operated, fuel cells are subject to several reversible performance loss phenomena. Similarly to the irreversible effects, the reversible processes also depend on the operating conditions. However, a major difference is that even though these reversible effects provoke much larger performance losses in time, they are recoverable either during operation or by specific service protocols. The most important reversible losses which are known are [128]:

- Pt oxidation and/or carbon support surface oxidation, triggered at normal operation by high half-cell potential ( $> 0.6 V_{\text{SHE}}$ ) and accelerated by temperature and humidity.
- Sulfate adsorption, caused by adsorption of irreversible ionomer degradation product on the catalyst. Accelerated at low load or OCV and high temperature and low humidity.
- Ionomer humidification effects, caused by dry out or flooding due to disadvantageous operating conditions.
- Contaminants adsorption (e.g. CO, NO<sub>x</sub>, ...) on the catalyst coming from the fuel and/or oxidant gas feed.

Most of these effects can be recovered by quite simple measures such as operation at high or low half-cell potential and by advantageous operating conditions in terms of humidity, temperature and reactant stoichiometry. Reversible effects linked to contaminants might need specific protocols aside from a clean gas feed. Reversible loss mechanisms in PEMFCs need to be understood and handled in order to be able to determine meaningful ageing rates and thus control lifetime [128, 129].

## 3 Experimental and Methods

To investigate MEA properties and derive material law parameters, a test station was commissioned and automated and several measurement methods came into play. In this chapter, the setup used in this work is presented in detail, the design of experiments depicted and the *in situ* characterization techniques explained in depth. Further details concerning specific tests can be found in the respective publications in Chapter 4.

### 3.1 Setup and Materials

To gather the measurement data needed in this work a FuelCon Evaluator C50 test station was employed, which is represented schematically in Fig. 3.1 together with the single cell setup. The control of this test station was completely automatized such that the operating conditions could be controlled by Visual-Basic-based scripts.

As can be seen in Fig. 3.1, a completely separate conditioning of the anode and cathode gas streams was possible upstream of the fuel cell. On the cathode side (red lines), either dry air or dry O<sub>2</sub> could freely be mixed with dry N<sub>2</sub> and similarly, dry H<sub>2</sub> could be mixed with N<sub>2</sub> on the anode side (blue lines). The quantity of each species was regulated by mass flow controllers and the resulting gas stream on each side could be humidified by flowing through a heated bubbler with an adjusted water temperature determining the dew point temperature (DPT). The gas lines between the bubbler and the fuel cell inlet were heated to control the inlet gas temperature and avoid unwanted condensation. Downstream of the fuel cell, the gases were cooled down to remove the water by condensation within condensate traps before flowing through the back pressure valves which allow to adjust the system pressure. The cell temperature was measured by a type K thermocouple which was fixed onto the back of the graphite plate of the fixed flow field. The temperature regulation was done by gold-coated copper plates which were fixed directly onto both graphite flow fields and flowed through by de-ionized water whose temperature was controlled by a Huber Ministat 125 thermostat. The equivalent clamping pressure of 1.3 MPa on the active area was obtained by a pneumatic cylinder, where the force applied by the latter was controlled by adjusting the pressure in a buffer vessel (see path at the bottom of Fig. 3.1).

The electronic load integrated in the test station could handle up to 600 W at a maximum of 100 A. Considering that single cells with 25 cm<sup>2</sup> and 12 cm<sup>2</sup> were characterized, this means that current densities up to 4 A/cm<sup>2</sup> (100 A with 25 cm<sup>2</sup>) and 8.33 A/cm<sup>2</sup> (100 A with 12 cm<sup>2</sup>) could be drawn, respectively. To conduct EIS and voltammetry measurements, a combination of Gamry reference 3000 potentiostat/galvanostat plus Booster 30 K came into play in addition to the load of the test station. High data quality was

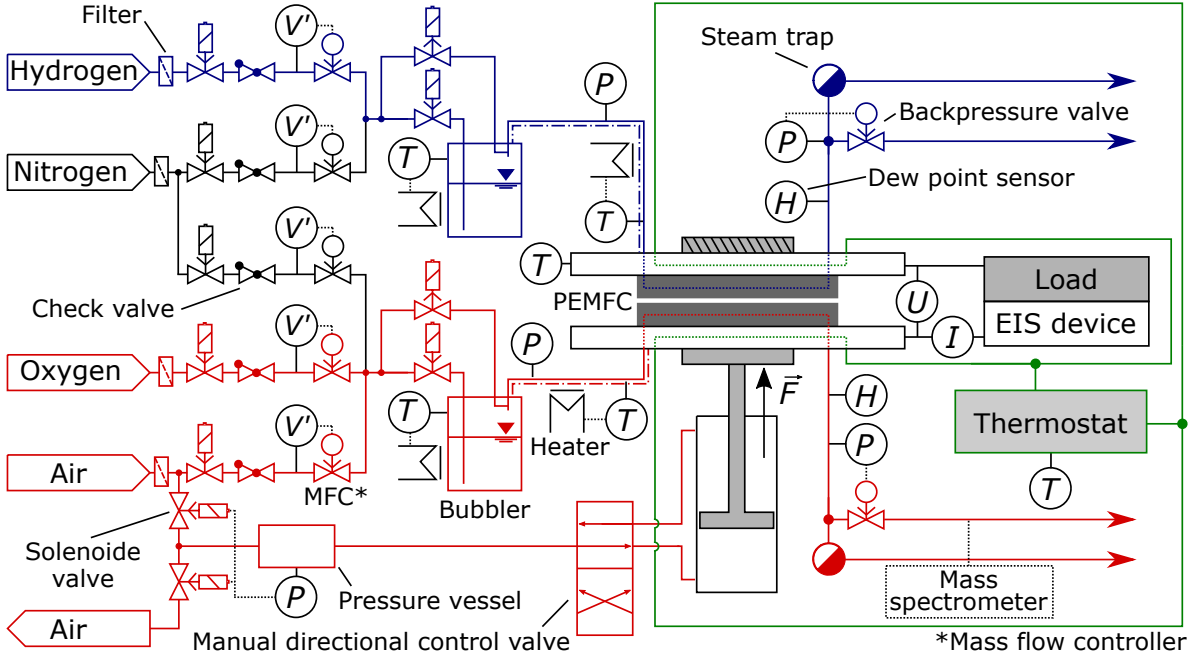


**Figure 3.1:** P&ID (non-standardized) of the test station and cell setup used in this work. The list of symbols is as follows:  $T$  for temperature,  $P$  for pressure,  $H$  for humidity,  $\dot{V}$  for volume flow,  $\vec{F}$  for force,  $I$  for current and  $U$  for voltage.

ensured thanks to a four-point measurement configuration with twisted cable pairs. While the connection of the sense wires was realized as close as possible to the electrodes by directly contacting the graphite, the load cables were connected to the copper plates behind the graphite (farther away). Generally, for the tests under load, the test station load was taken for the current offset (DC current) and the Gamry devices applied the AC signal on top for the sake of simpler software implementation. Furthermore, this constellation of the loads permitted higher cell currents (Gamry and Booster alone were limited to 30 A). Before starting the whole measurement campaign, it was made sure that the test station load did not interfere with the measurements in the frequency range which is relevant for typical EIS ( $f < 20$  kHz).

The baseline MEA of this work was a Gore<sup>®</sup> PRIMEA<sup>®</sup> (W.L. Gore & Associates, Elkton, MD, USA) with 18  $\mu\text{m}$  membrane thickness and loadings of 0.4/0.05  $\text{mg}_{\text{Pt}} \text{cm}^{-2}$  in the cathode/anode. For the permeation study, especially CV and LSV, an MEA with a 50- $\mu\text{m}$ -thick membrane (Nafion<sup>®</sup> N212, 0.4  $\text{mg}_{\text{Pt}} \text{cm}^{-2}$  on the cathode and 0.2  $\text{mg}_{\text{Pt}} \text{cm}^{-2}$  on the anode side) was used for comparison. The roughness factors  $rf$  were calculated by integrating the  $H_{\text{UPD}}$ -areas in CV and averaging over the adsorption and desorption process (see section 3.2.1 for more details). The results for the baseline MEA were  $rf_{\text{cathode}} = 166 \pm 11 \text{ m}_{\text{Pt}}^2 \text{ m}_{\text{geo}}^{-2}$  and  $rf_{\text{anode}} = 30 \pm 3 \text{ m}_{\text{Pt}}^2 \text{ m}_{\text{geo}}^{-2}$ , determined over at least 10 CVs of each electrode.

The MEAs were prepared by cutting CCM material in the right dimensions and then laminating it into polyethylene naphthalate (PEN) frames at 100°C to get better mechanical properties and thereby enhance handling. These prepared CCMs were sandwiched between Sigracet<sup>®</sup> 22BB GDLs from SGL<sup>®</sup> Carbon to form the final MEAs and mounted in a differential cell setup from Baltic FuelCells (quickConnect<sup>®</sup>) which can be seen in

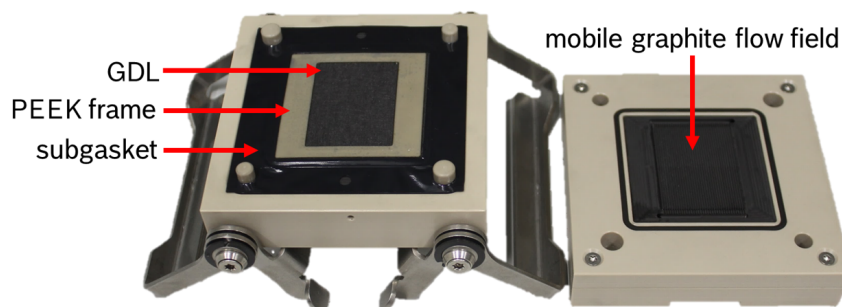


**Figure 3.2:** Cell holder quickConnect<sup>®</sup> from Baltic FuelCells used in this work. As can be seen in Fig. 3.1, the mobile graphite flow field for the application of the clamping force was used on the cathode side. The anode GDL and CCM are located beneath the cathode GDL which is visible here.

Fig. 3.2. Unless stated otherwise, the results which are discussed in this work were obtained from single cells with an active area of  $12 \text{ cm}^2$ . On rare occasions, the cell format was  $25 \text{ cm}^2$ .

With the cell setup shown in Fig. 3.2, the combination of high gas flow rates (differential conditions, cell inlet = cell outlet) and the cathode flow field containing wide straight channels (channel/land ratio of approximately 0.7/0.3) enable only small in-plane inhomogeneities during operation. The two clamps which can be seen in this figure enabled a compression to reach external gas tightness, whereas the subgasket prevented internal gas leakage between the anode and cathode gas compartments. The equivalent clamping pressure on the active area of about 1.3 MPa was obtained by a pneumatic cylinder which applied a constant force onto the mobile cathode flow field represented on the right side of the figure. The gas line and pressure vessel providing the necessary energy to the pneumatic cylinder can be seen at the bottom of Fig. 3.1.

## 3.2 Characterization Methods

In this section, the most important characterization techniques used in this work are presented. First, the voltammetry techniques *cyclic voltammetry* (CV) and *linear sweep voltammetry* (LSV) are illustrated. Then, *polarization curve* as well as *limiting current* measurements are explained in detail. Finally, *electrochemical impedance spectroscopy* (EIS) is described depending on the mode of operation.

### 3.2.1 Voltammetry Techniques

#### Cyclic voltammetry

One of the most prominent diagnostic tools for the characterization of electrochemical cells is cyclic voltammetry since it can provide valuable information about their kinetics and thermodynamics [130]. Usually, CV is accomplished by using a two- or three electrode setup: the potential at the working electrode is recorded relative to a reference electrode while monitoring the current going through the counter electrode. In the case of the PEMFC, the anode is flushed with humidified hydrogen during the experiment and serves as both counter and reference electrode, whereas the cathode is either flushed with

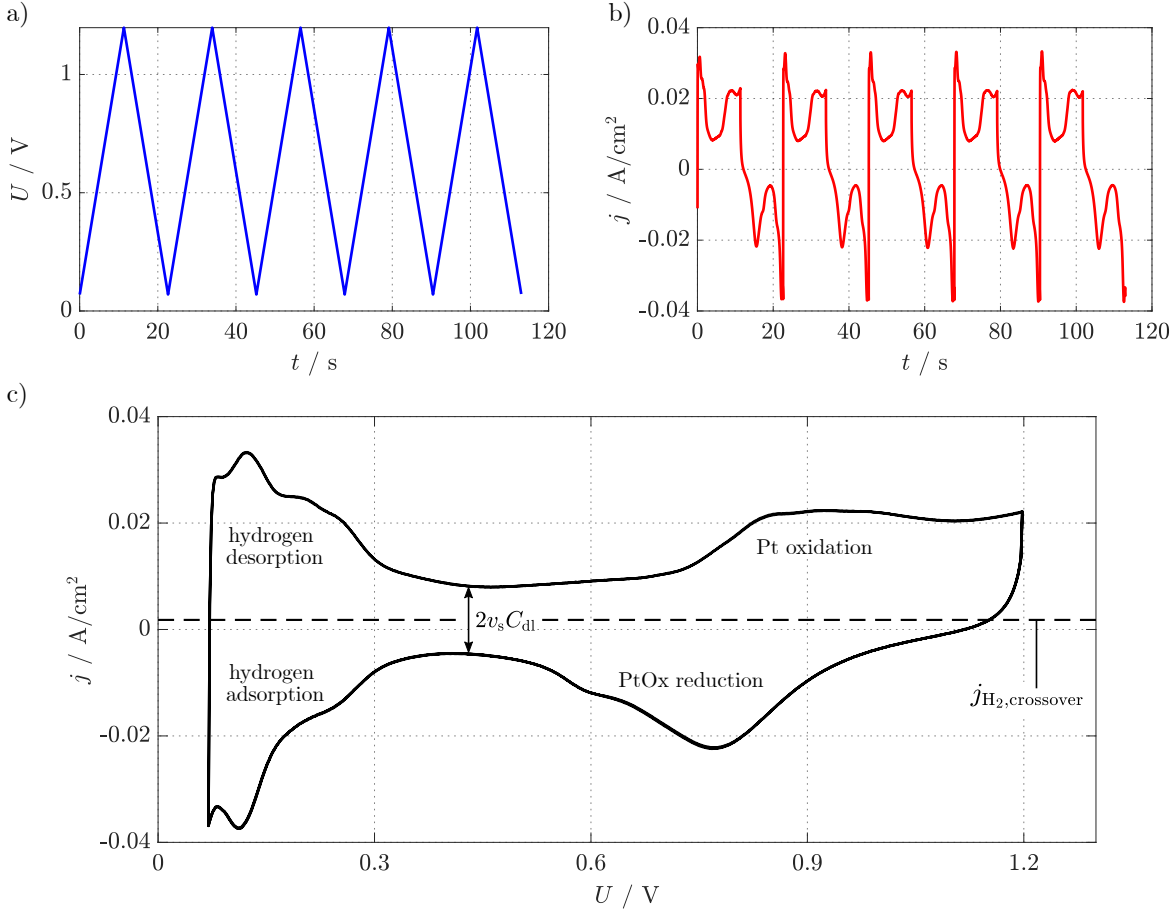


**Figure 3.3:** Cyclic voltammetry recorded at  $T = 40^\circ\text{C}$ ,  $RH = 100\%$  and  $p_{\text{total}} = 1 \text{ bar}_a$  from 0.07 V to 1.20 V cell voltage with a sweep rate of 100 mV/s. a) time trace of the input voltage, b) time trace of the resulting current, and c) Voltammogram containing the two last cycles.

humidified nitrogen or not flushed at all. Figure 3.3 depicts a CV experiment carried out with the baseline materials used in this work (see section 3.1). Figure 3.3a shows the five consecutive voltage cycles that were applied to the cell from 0.07 to 1.20 V and back, i.e. between HER and OER. The cycling was done at a rate of 100 mV/s and the resulting non-trivial cell current is shown in Fig. 3.3b. However, the most important representation is the corresponding voltammogram of current density over voltage depicted in Fig. 3.3c, where the upper and lower branches are named anodic and cathodic sweep, respectively. Therein, it can be seen that the complete voltammogram is slightly shifted towards positive currents, which is caused by the parasitic transport-controlled HOR in the CCL coming from the *crossover* of molecular hydrogen through the membrane. For state-of-the-art membranes, typical crossover rates  $j_{\text{H}_2, \text{crossover}}$  lie between 1 and 10  $\text{mA cm}^{-2}$  and depend also on the thickness. Since aged membranes show elevated gas permeation,  $j_{\text{H}_2, \text{crossover}}$  is a good state of health (SOH) indicator for the PEM.

Further important information can be extracted from this diagram, which can be subdivided into at least three distinct regions. At low voltage, i.e. below 0.4 V, the adsorption and desorption of a hydrogen monolayer ( $\text{H}_{\text{UPD}}$ ) on the platinum catalyst occurs, leading to almost symmetrical peaks with respect to the  $j_{\text{H}_2, \text{crossover}}$  line. By integrating the

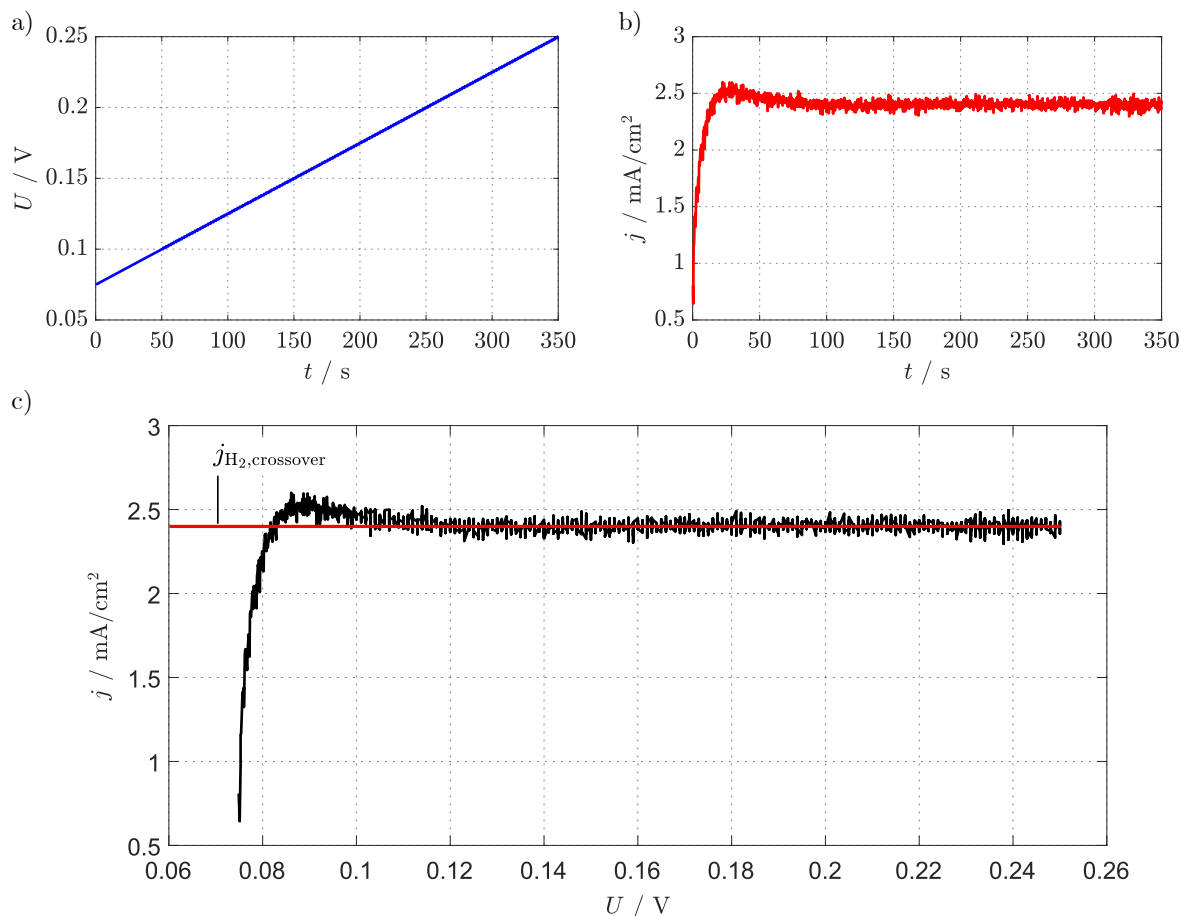


**Figure 3.4:** Linear sweep voltammetry recorded at  $T = 70^\circ\text{C}$ ,  $RH = 70\%$  and  $p_{\text{total}} = 1.5 \text{ bar}_a$  from 0.07 V to 0.25 V cell voltage with a sweep rate of 0.5 mV/s. a) time trace of the input voltage, b) time trace of the resulting current, and c) Voltammogram.

current over either one of the peaks in this area, the charge needed to create or remove a hydrogen monolayer in this specific catalyst layer is obtained. Based on this charge and knowing the specific charge of a hydrogen monolayer on polycrystalline platinum of  $210 \mu\text{C cm}_{\text{Pt}}^{-2}$  [131,132], the roughness factor  $rf$  in  $\text{cm}_{\text{Pt}}^2/\text{cm}_{\text{geo}}^2$  can be determined. Subsequently, an area around 0.45 V with a small and almost constant current in both branches is observed. In this range, the catalyst is free of adsorbates and the measured current is attributed to the charge or discharge of the double layer (capacitive currents). The distance between cathodic and anodic branches equals two times the double layer capacitance multiplied with the sweep rate, i.e.  $\text{distance} = 2\nu_s C_{\text{dl}}$ . Above 0.6 V, the formation and reduction of platinum oxides such as  $\text{Pt-O}_{\text{ad}}$  and  $\text{Pt-OH}_{\text{ad}}$  is observed.

### Linear sweep voltammetry

LSV is typically conducted in the same way as explained above for CV, i.e. with one humidified hydrogen counter and reference electrode and the working electrode which is either flushed with an inert gas, e.g. with nitrogen, or not flushed at all during the scan. Actually, the sole difference compared to CV is the fact that LSV consists of a single very slow voltage sweep from low to high voltage. Figure 3.4 depicts an LSV experiment done with the baseline materials of this work (see section 3.1). The applied slow voltage

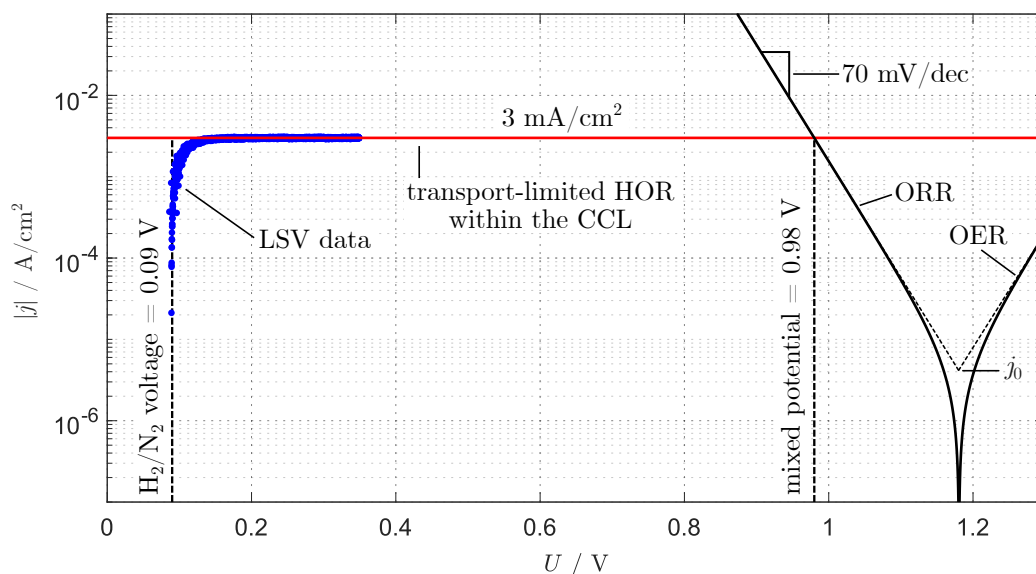


**Figure 3.5:** Tafel plot of the internal-current-induced mixed-potential on the cathode side caused by  $\text{H}_2$  crossover. An exemplary LSV measurement showing a transport-limited HOR of  $3 \text{ mA/cm}^2$  in the CCL due to crossover is shown overlapping with the ORR ( $j_0 = 4.1 \cdot 10^{-6} \text{ A/cm}^2$ ). This causes a deviation of the OCV from the theoretical value.

ramp which can be seen in Fig. 3.4a yields the current response depicted in Fig. 3.4b and comparably to the CV technique, the corresponding voltammogram showing current over voltage can be drawn as in Fig. 3.4c. From the latter, mainly the transport-controlled hydrogen crossover rate  $j_{\text{H}_2, \text{crossover}}$  can be determined from the  $y$ -axis intercept of the red linear regression curve. Additionally, the membrane electric short resistance can be determined from the inverse slope of this regression curve. This resistance was always very high in this work, pointing out negligible short currents in the analyses. Compared to CV, LSV is slower and does not yield electrode-specific information; however, crossover and membrane shorts can be determined more precisely.

### Influence of crossover ( $j_0$ ) on OCV

Aside from determining the membrane SOH, measuring hydrogen crossover is also important to understand OCV under  $\text{H}_2/\text{O}_2$  conditions. In fact, since the cathode half-cell potential is favorable to the HOR in such conditions, hydrogen permeating through the membrane is completely oxidized within the CCL even at OCV, i.e. when no net external current is measured. Hence, internal currents are induced, which lowers the observed OCV by shifting the polarization current by  $j_{\text{H}_2, \text{crossover}}$ . This mixed-potential effect is pictured in Fig. 3.5 by the overlap of LSV data representing the transport-controlled HOR as well as the ORR polarization curve, both happening within the CCL. As the rate of ORR compensates the rate of HOR, the ORR polarization curve is shifted by the crossover current ( $3 \text{ mA/cm}^2$  in this case) on the current axis, leading to a drop of the observed OCV (approximately 200 mV here). Of course, the ACL can be subject to a comparable mixed-potential phenomenon caused by oxygen permeation. However, oxygen permeates less than hydrogen and the exchange current density of the HOR is so high (higher by several orders of magnitude than for the ORR) that this effect is almost absent. In the



literature, other effects likely to contribute to the mixed-potential in the CCL were discussed such as the oxidation of the platinum catalyst. However, in this work the parasitic  $H_2$  crossover is considered as being the major responsible for the OCV drop.

### 3.2.2 Polarization Curve

When an electrochemical cell is operated under load, the voltage measured between the anode and cathode deviates from the equilibrium voltage due to several loss mechanisms as explained in section 2.2. Measuring the steady-state current (or current density) versus voltage characteristics, i.e. the polarization curve, is always part of the characterization process since it is the first step towards unraveling the contributions caused by the different loss mechanisms. At a given current density, the cell voltage can be calculated by subtracting all the overpotentials from the equilibrium voltage  $U_0$  according to:

$$U_{\text{cell}} = U_0 - |\eta_{\text{ORR}}| - |\eta_{\text{HOR}}| - j \cdot (R_{\Omega} + R_p^{\text{eff}}) - |\Delta U_{\text{MT}}|, \quad (3.1)$$

where  $|\eta_{\text{ORR}}|$  and  $|\eta_{\text{HOR}}|$  are the overpotentials caused by cathode and anode kinetics, respectively,  $j \cdot (R_{\Omega} + R_p^{\text{eff}})$  the contribution from electron and proton transport and  $|\Delta U_{\text{MT}}|$  the overall loss contribution caused by reactant transport from the channels to the TPBs. Figure 3.6 depicts a typical polarization curve which was modeled based on the laws detailed in section 2.2. It can be seen that the oxygen kinetics on the cathode side (ORR) by far generate the highest voltage loss over the complete current density range. As explained in section 2.2.2, this loss mainly depends on the Tafel slope  $b$  and on the effective exchange current density  $j_{\text{c,eff}}^0$  and can be described by

$$\eta_{\text{ORR}} = -\frac{R \cdot T}{\alpha_{\text{ORR}} \cdot F} \cdot \ln \left( \frac{j}{j_{\text{c,eff}}^0} \right) = b \cdot \ln \left( \frac{j}{j_{\text{c,eff}}^0} \right). \quad (3.2)$$

While the Tafel slope depends on the intrinsic nature of the ORR on the platinum catalyst itself, the effective exchange current density can be influenced by the CCL design as well as by the operating conditions. It is usually written as

$$j_{\text{c,eff}}^0 = r f_c \cdot j_{\text{c,ref}}^0 \cdot \left( \frac{p_{\text{O}_2}}{p_{\text{ref}}} \right)^{\gamma} \cdot \exp \left[ \frac{-E_{\text{act}}^{\text{ORR}}}{RT} \left( 1 - \frac{T}{T_{\text{ref}}} \right) \right]. \quad (3.3)$$

Thus, cathode kinetics can be influenced by the amount and accessibility of Pt, which is reflected in  $r f_c$ , by the oxygen partial pressure  $p_{\text{O}_2}$  and the temperature  $T$ . In contrast to the ORR, the HOR is way faster since its exchange current density is typically higher by several orders of magnitude ( $10^{-1}$  A/cm $^2_{\text{Pt}}$  to  $10^{-8}$  A/cm $^2_{\text{Pt}}$ , see section 4.2). Hence, the ACL causes only very small losses in PEMFCs. Therefore, the HOR mainly operates in the linear regime as in

$$\eta_{\text{HOR}} = \frac{R \cdot T}{j_{\text{a,eff}}^0 \cdot F} \cdot j. \quad (3.4)$$

Comparably to the ORR, the exchange current density of the HOR can be written dependent on the ACL-specific roughness factor  $r f_a$ , the hydrogen partial pressure  $p_{\text{H}_2}$  and the temperature:

$$j_{\text{a,eff}}^0 = r f_a \cdot j_{\text{a,ref}}^0 \cdot \left( \frac{p_{\text{H}_2}}{p_{\text{ref}}} \right)^w \cdot \exp \left[ \frac{-E_{\text{act}}^{\text{HOR}}}{RT} \left( 1 - \frac{T}{T_{\text{ref}}} \right) \right]. \quad (3.5)$$

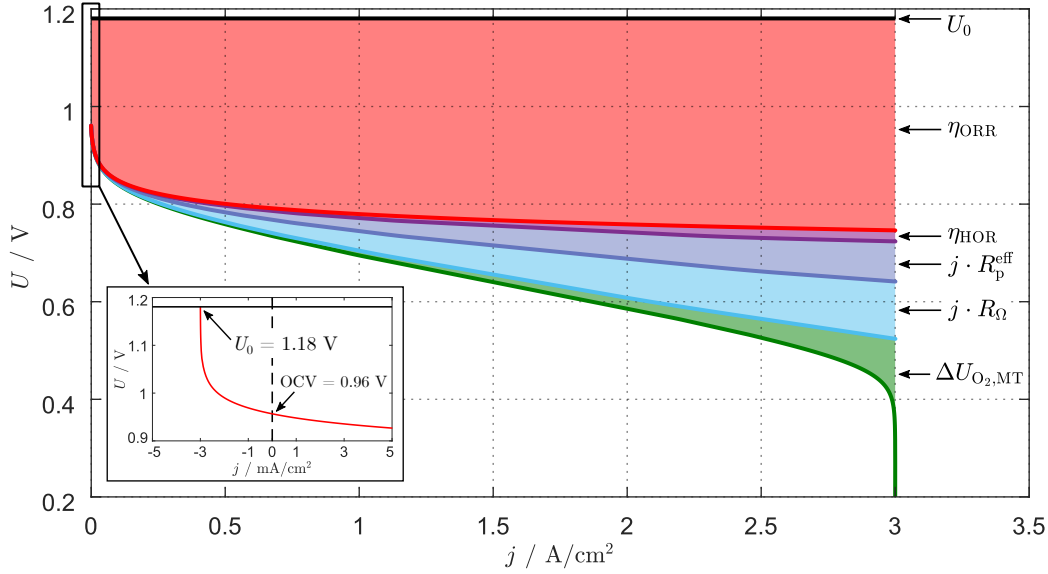


**Figure 3.6:** Model fuel cell polarization curve and corresponding voltage loss breakdown. The model parameters are:  $T = 80^\circ\text{C}$ ,  $U_0 = 1.18\text{ V}$ ,  $j_{\text{H}_2, \text{crossover}} = 3\text{ mA/cm}^2$ ,  $p_{\text{O}_2} = 0.21\text{ bar}_a$ ,  $\alpha_{\text{ORR}} = 1$ ,  $j_{\text{c,eff}}^0 = 1.88 \cdot 10^{-6}\text{ A/cm}^2$ ,  $R_\Omega = 40\text{ m}\Omega\text{ cm}^2$ ,  $R_p^{\text{eff}} = 27\text{ m}\Omega\text{ cm}^2$ ,  $R_{\text{anode}} = 8\text{ m}\Omega\text{ cm}^2$  (linearized kinetics), and  $R_{\text{O}_2} = 0.92\text{ s/cm}$ . Cathode kinetics were modeled with both branches of Butler-Volmer’s law.

The contributions from electronic and protonic transport within the CLs and PEM, i.e.  $j \cdot (R_\Omega + R_p^{\text{eff}})$ , are proportional to the cell current and typically represent the second biggest performance loss within PEMFCs (after the ORR) at meaningful operating conditions. As explained above in section 2.2.3, the electronic resistances depend on the setup (GDL and BPP materials and nature of contact as well as test bench hardware) and are approximately constant (slight temperature dependence) provided that cell clamping remains constant. On the other hand, protonic resistance contributions strongly depend on local ionomer hydration, thus on gas channel relative humidity  $RH$  and on the cell current density  $j$ . Finally, mass transport contributions  $\Delta U_{\text{O}_2, \text{MT}}$  from reactant transport to the TPBs also depend on the design and materials, e.g. on the geometry and materials of the gas channels but also on the porosity, tortuosity and materials of the porous media. However, they are also heavily influenced by the operating conditions such as the partial pressure of oxygen in the gas channels as can be seen in (2.50). At given transport resistance, the lower the reactant partial pressure in the channels, the higher the mass-transport-related voltage loss. As such losses increase logarithmically with the cell current, they only become noticeable at high load in most instances. It is necessary to emphasize again that as previously mentioned, Fig. 3.6 only shows a theoretical curve with constant parameters, whereas some of these parameters might strongly depend on the cell current in real setups because of changing water and thermal management. Hence, additional characterization methods such as limiting current techniques and EIS are needed to get deeper insights. For instance, kinetics can be investigated by polarization curves corrected for reactant transport and ohmic contributions. The latter methods are explained in the following sections.

In addition to the voltage loss breakdown depicted in the polarization curve in Fig. 3.6, Fig. 3.7 shows typical through-plane distributions of the potentials (a) and currents (b)

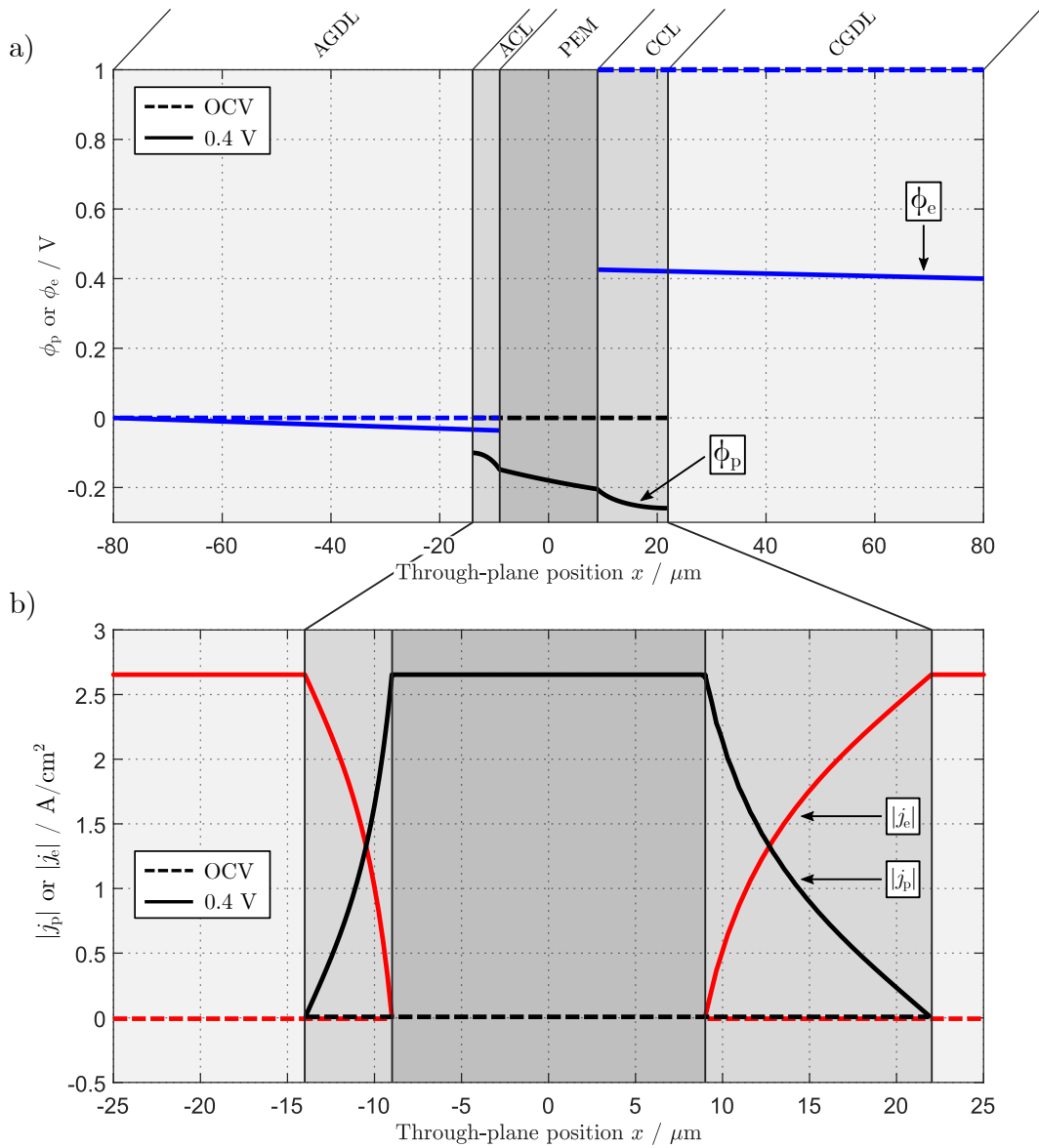


**Figure 3.7:** a) Through-plane distribution of electronic and ionic potentials  $\phi_e$  and  $\phi_p$  within the MEA at equilibrium OCV and under load. b) Corresponding through-plane distribution of absolute electronic and ionic current densities  $|j_e|$  and  $|j_p|$ . In both plots, neither electric shorts nor crossover were considered.

within the MEA from anode to cathode gas channel at OCV and under load at 0.4 V cell voltage. Figure 3.7a shows the distribution of the electric potential  $\phi_e$  which can be sensed in the carbon or metallic phase and the protonic potential  $\phi_p$  which would be obtained from the voltage measurement between a standard hydrogen electrode (SHE) and the ionomer at a given location. It is worth emphasizing that this plot gives a macrohomogeneous view and does not resolve the complex Helmholtz double layer effects. At equilibrium, the bulk potentials within each phase are constants. However, when current is drawn, protons are transported within the electrolyte through a potential gradient between the anode and the cathode and electrons are transported within the electrodes and GDLs. The electric potential gradient is very small compared to the gradient in

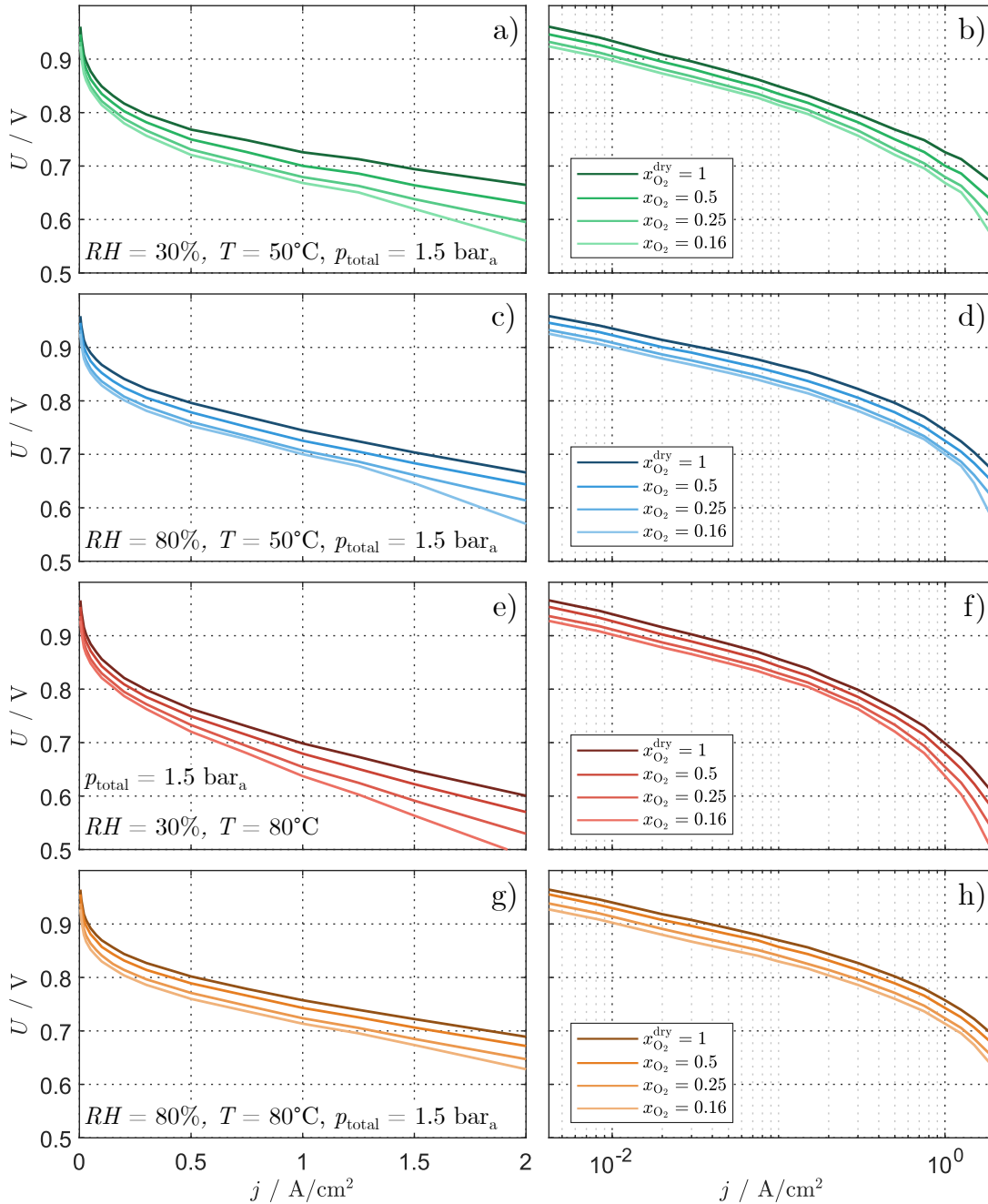


**Figure 3.8:** Polarization curves measured for an oxygen partial pressure variation in linear (left plots) and Tafel (right plots) representation. a) and b) cold and dry conditions. c) and d) cold and wet conditions. e) and f) hot and dry conditions. g) and h) hot and wet conditions.

the protonic potential due to the high conductivity of the carbon phase compared to the protonic conductivity of the ionomer. Furthermore, Fig. 3.7b depicts the corresponding electronic and protonic current densities  $j_e$  and  $j_p$ , respectively. Here, the role of the mixed-conducting catalyst layers becomes clear: namely to transform the external current which arrives completely as an electronic current from the GDL to a protonic current which can travel through the PEM. Within the CLs, both currents must add up

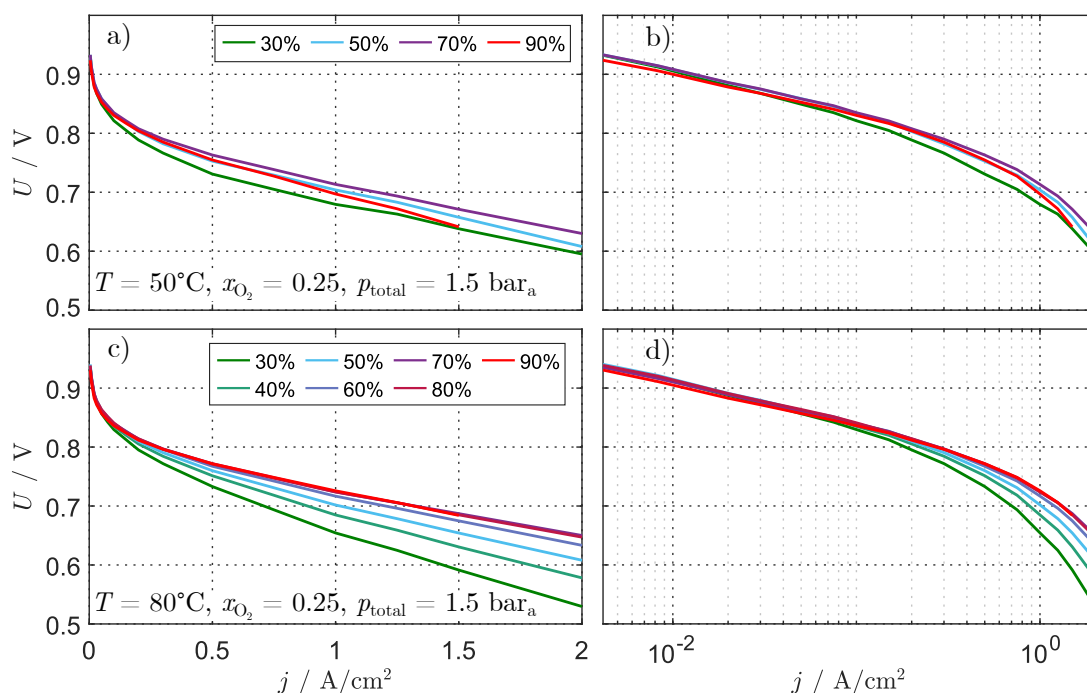


**Figure 3.9:** Polarization curves measured for a variation of the relative humidity in linear (left plots) and Tafel (right plots) representation. a) and b) cold conditions. c) and d) hot conditions.

to the complete external current due to charge conservation. To model such behavior, the minimal model solution requires solving at least Ohm's law and charge conservation. Moreover, mass transport is often added by Fick's law of diffusion. Under given circumstances, this system of partial differential equations (PDEs) admits an analytical solution. At most conditions however, specific solvers are needed. Way more sophisticated models which are thus way more complex to parameterize also compute two-phase water and heat transport. Such models are referred to as *complete MEA models* in the following.

### Influence of operating parameters

The influence of two of the most important parameters on the polarization curve are depicted in the following: oxygen partial pressure and relative humidity of the gas stream. Figure 3.8 provides a glimpse into the influence of an oxygen partial pressure variation at given system pressure of 1.5 bar<sub>a</sub> by mixing O<sub>2</sub> and N<sub>2</sub>. It can be seen that at wet conditions (c, d, g and h), the polarization curves are shifted by an almost constant offset over the complete range of current densities, which proves that the variation of partial pressure solely affects the cathode kinetics by modifying the effective exchange current density. The latter effect simply shifts the polarization curve on the voltage axis. Only the lowest-partial-pressure curve at cold and wet conditions (c and d) deviates from this behavior at high current density, which is likely caused by an increased oxygen mass transport resistance at such conditions. At dry conditions (a, b, e and f) the previous shift of the curves on the voltage axis can be observed at low current densities; however, at medium to high current densities the curves spread probably due to different water management, e.g. channel/land effects. In the same fashion, Fig. 3.9 shows a variation

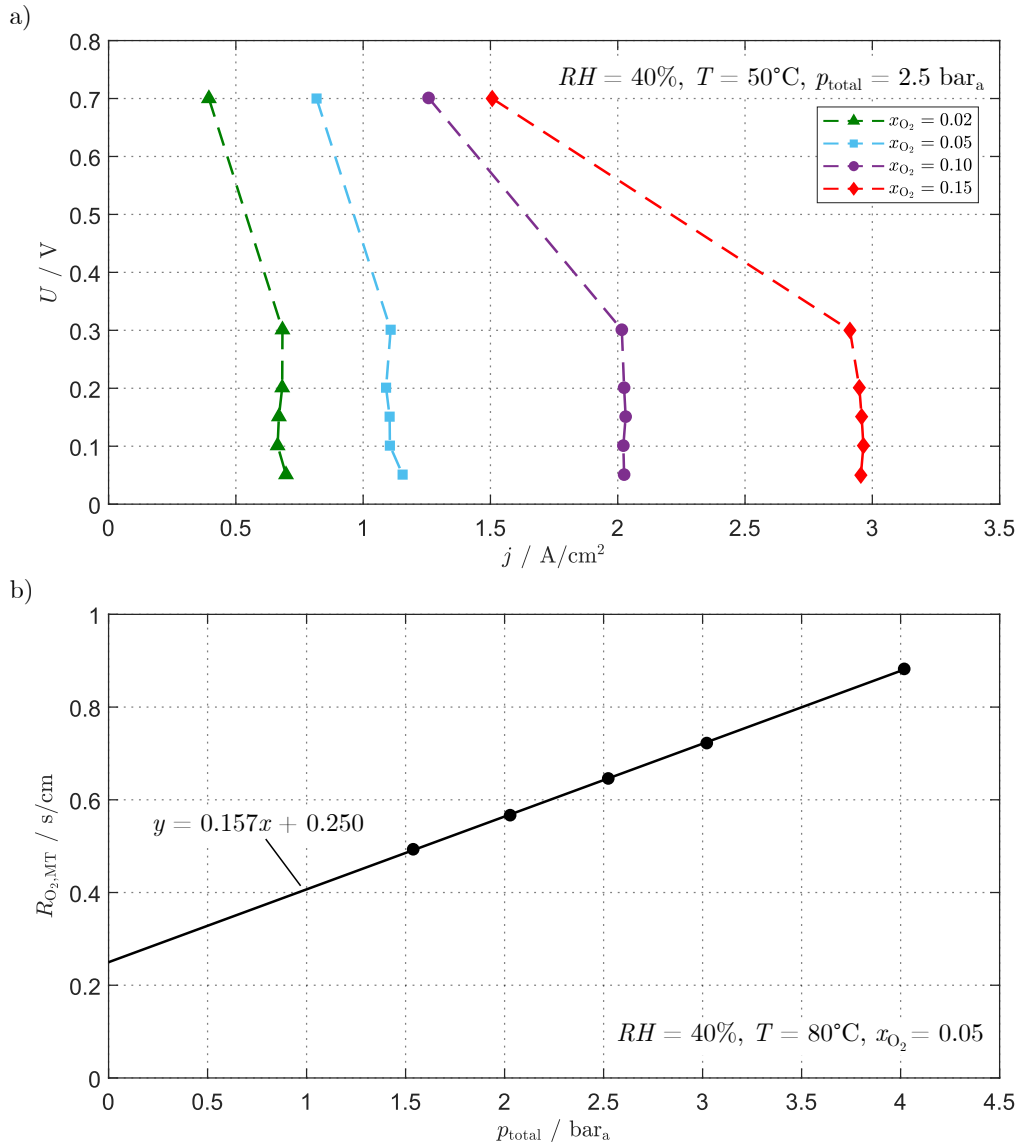


**Figure 3.10:** a) Steady-state limiting current measurement for four different oxygen mole fractions at  $RH = 40\%$ ,  $T = 50^\circ C$  and  $p_{total} = 2.5 \text{ bar}_a$ . b) Oxygen transport resistance  $R_{O_2,MT}$  as a function of the total system pressure  $p_{total}$  and corresponding regression curve to determine the pressure-dependent (slope) and pressure-independent ( $y$ -axis intercept) resistances. Conditions:  $RH = 40\%$ ,  $T = 80^\circ C$  and  $x_{O_2} = 0.05$ .

of the gas channel relative humidity. The two upper plots represent the cold conditions and the two lower plots depict hot conditions. At low current densities, the humidity does not seem to have a significant impact (see mainly the Tafel representations on the right side); however, at medium to high loads there is a noticeable influence of humidity on performance. Obviously, the gas channel relative humidity strongly affects the slope of the curves (ohmic contributions) at hot conditions, which points at changing ohmic contributions caused by ionomer humidification. At cold conditions, the effect is present but way softer up to  $RH = 70\%$ . At higher humidity, the tendency is inverted and performance decreases due to reactant transport issues caused by the presence of more

liquid water and lower diffusion coefficients compared with hot conditions.

### 3.2.3 Limiting Current and Heliox Measurements

As explained in section 2.2.4, mass transport processes in fuel cells can significantly affect the performance. In PEMFCs, it is mainly oxygen transport from the cathode gas channels to the TPBs in the catalyst layer which is causing a voltage drop depending on the operating conditions. *Limiting current density* measurements, also called steady-state limiting current (SLC), are a well-known tool to study such effects [112, 133]. At cathode limiting current density conditions, the ORR is exclusively controlled by the limitation in  $O_2$  mass transport. Hence, the current does not depend on other overpotentials such as activation or ohmic contributions from ionic transport. This can be identified by a vertical voltage drop in the polarization curve, i.e. when the current is independent of the applied voltage. In the model polarization curve shown in Fig. 3.6, the limiting current density is approximately  $3 \text{ A/cm}^2$ . Under meaningful operating conditions, limiting currents are not pursued in order to avoid drastic efficiency drops. Furthermore, kinetic or ohmic contributions would often limit performance before mass transport when the inlet oxygen concentration in the dry gas is as high as in air ( $\approx 21\% O_2$  in  $N_2$ ) or higher.

For the specific measurement of oxygen transport resistances based on limiting current densities, oxygen has to be diluted in order to reach only low currents and thus avoid too unrealistic cell-internal conditions. An example is given in Fig. 3.10a, where the limiting current density measurement as performed in this work is shown for four different oxygen concentrations at low inlet humidity conditions of 40%. The conditioning point at  $0.7 \text{ V}$  prior to the measurement can be seen in this diagram and points out the potentiostatic nature of the measurement. Precise information about the technical implementation can be found in section 3.3. Based on these limiting current densities, transport resistances be can computed according to (2.51) and the voltage loss during operation can be estimated

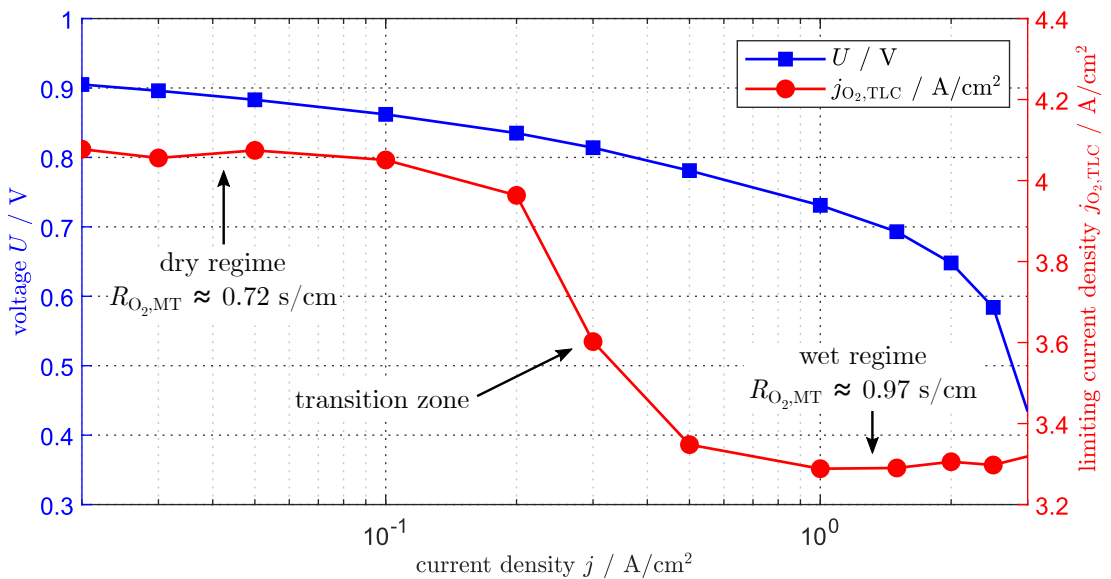


**Figure 3.11:** Polarization curve and corresponding transient limiting current density recorded for  $RH = 80\%$ ,  $T = 60^\circ\text{C}$  and  $x_{O_2} = 0.16$ .

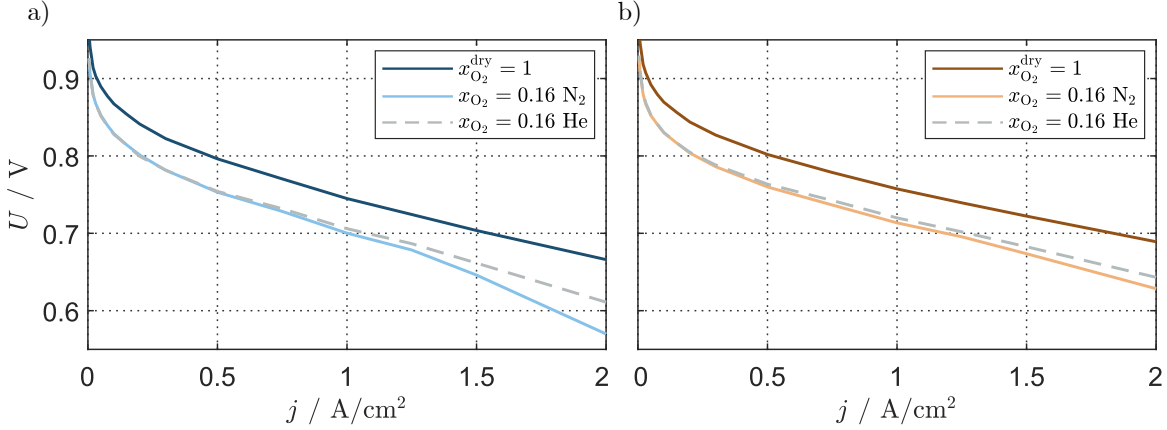


**Figure 3.12:** Polarization curves measured for  $x_{O_2}^{dry} = 1$  and  $x_{O_2} = 0.16$  in the  $\{O_2, H_2O, N_2\}$  and  $\{O_2, H_2O, He\}$  mixtures. a) cold and wet conditions,  $RH = 80\%$  and  $T = 50^\circ C$ . b) hot and wet conditions,  $RH = 80\%$  and  $T = 80^\circ C$ .

by (2.50). Unless mentioned otherwise, the diffusion resistance was modeled as proposed in the second publication of this work based on measurements for  $x_{O_2} = 0.15$  [24]:

$$R_{O_2,MT} = R_{O_2,MT}^{ref} \cdot (RH)^c \cdot \left(\frac{p_{total}}{p_{ref}}\right)^e \cdot \exp\left(\frac{E_{act}^{O_2,MT}}{RT}\right), \quad (3.6)$$

with a constant prefactor  $R_{O_2,MT}^{ref}$ , two exponents  $c$  and  $e$  for the dependency on relative humidity and absolute pressure, and  $E_{act}^{O_2,MT}$  the activation energy. Figure 3.10b depicts the separation between pressure-dependent and pressure-independent transport resistance, which is obtained by varying the system pressure at otherwise constant conditions. The slope of the fitting line represents the pressure-dependent resistance, which is mostly linked to molecular diffusion in the GDL (bulk diffusion) and the  $y$ -axis intercept which represents the pressure-independent resistance and can be attributed to Knudsen and thin film diffusion mainly in the CL.

A variant of the classical method is the transient limiting current (TLC) [134], which aims at providing a different transport resistance for each load point instead of a single value and thus be more realistic. It consists of conditioning the cell at a given current or voltage prior to going only briefly to the limiting current density in potentiostatic mode as shown in Fig. 3.11. Aside from the polarization curve resulting from the conditioning, the corresponding limiting current density is shown. Three distinct regions are observed. At low current density, the limiting current is at its highest since the liquid water saturation of the porous layers is small and thus oxygen transport to the electrode is facilitated. At medium load, there is a transition zone where the limiting current density drops. Then, a low limiting current density regime is reached at high load, likely caused by a high liquid water saturation of the porous media.

Finally, another possibility to directly approximate the voltage drop caused by mass transport is the measurement of performance with heliox, i.e. by mixing oxygen with helium instead of nitrogen. With heliox, losses caused by molecular diffusion (bulk losses) are reduced to almost zero since the diffusivity of  $O_2$  in  $He$  is roughly four times higher compared to  $O_2$  in  $N_2$  [135]. Furthermore, the non-bulk losses can be estimated by the difference between the heliox and the pure oxygen curves since the higher partial pressure



in the pure oxygen case strongly reduces the losses in the CL. However, it has to be remembered that the difference between the curves in nitrogen and those in helium might partly be due to the higher vapor diffusivity in helium which can lead to a different hydration state of the ionomer. Hence, the equality of the ohmic contributions has to be verified by EIS in order to avoid interpretation mistakes (see next section). Moreover, due to the better performance of the heliox curves, the cathode half-cell potential is higher which might cause a reduced catalyst activity due to a higher oxide coverage. This has to be considered during evaluation. Figure 3.12 shows such measurements for cold and wet (a) as well as hot and wet (b) conditions for pure oxygen and the  $x_{\text{O}_2} = 0.16$  case. It can be seen that the curves in helium are parallel to the pure oxygen curves almost over the complete load range, whereas the curves in nitrogen show lower performance at high load due to mass transport contributions.

### 3.2.4 Electrochemical Impedance Spectroscopy

To investigate the nature of the loss mechanisms locally at a given load point and to get information about the time constant and extent of physico-chemical processes in an electrochemical device, the advanced characterization method electrochemical impedance spectroscopy (EIS) comes into play. It is a very powerful technique since it provides the frequency-dependent differential resistance and thus quantifies the loss-resistances which

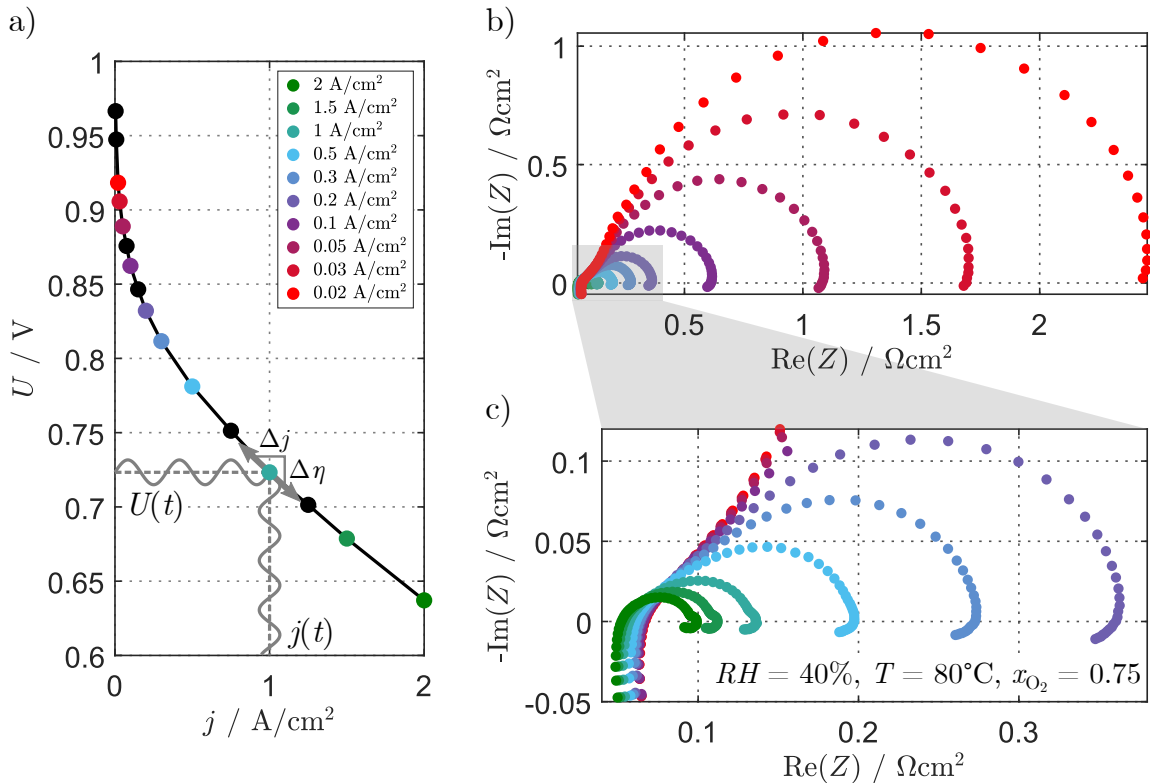


**Figure 3.13:** a) Polarization curve recorded at  $RH = 40\%$ ,  $T = 80^\circ\text{C}$  and  $x_{\text{O}_2}^{\text{dry}} = 1$  and schematic representation of the principle of EIS. The points at which EIS was conducted are colored and the corresponding spectra are depicted in b) and c) in the Nyquist representation.

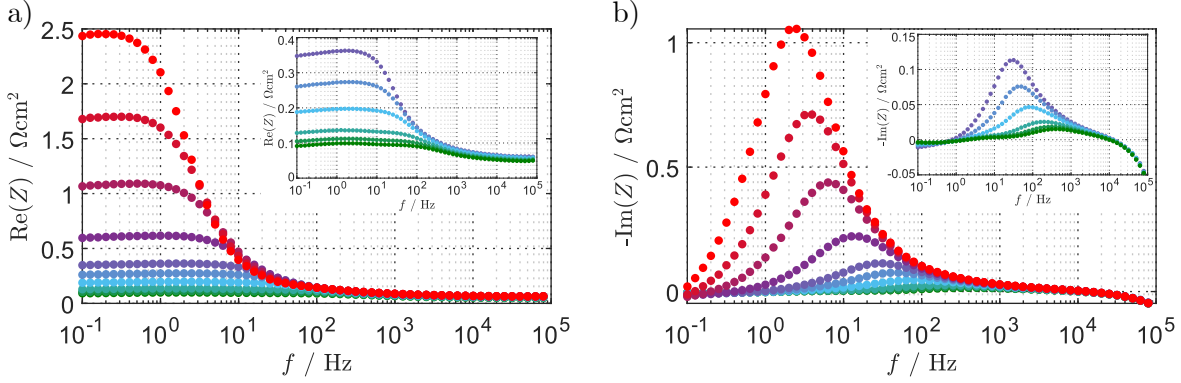


**Figure 3.14:** Bode representation of the EIS spectra shown in Fig. 3.13. a) Real part of the impedance. b) Imaginary part of the impedance. The boxes inside the plots represent a zoom on the high current density conditions.

correlate with the corresponding overpotentials. This information can be used directly for targeted optimization; however, as in the present work, it is often used to get a proper separation of the loss mechanisms and access specific overpotentials that are not directly available otherwise. The principle of EIS can be explained based on Fig. 3.13 which shows a typical polarization curve of this work in a), where the points at which spectra were recorded are marked by a specific color. The corresponding spectra can then be found in b) and c) under the same color. As shown exemplarily for the  $1 \text{ A/cm}^2$  point, EIS consist in overlaying a sinusoidal AC signal over the steady-state DC load point and recording the system's response. In other words, the stationary state is disturbed and excited by a small sinusoidal change of potential or current, which results in a phase shifted sinusoidal response of the non-excited quantity, i.e. current or voltage, respectively. The impedance  $Z(\omega)$ , which is the complex resistance of the cell at the angular frequency  $\omega = 2\pi f$ , can be calculated analogously to Ohm's law as the fraction of voltage and current. For the example of EIS where the voltage is controlled, the equations are

$$U(t) = \hat{U} \cdot \sin(\omega \cdot t), \quad (3.7)$$

$$j(t) = \hat{j} \cdot \sin(\omega \cdot t + \Phi), \quad (3.8)$$

$$Z(\omega) = \frac{U(t)}{j(t)} = \frac{\hat{U}}{\hat{j}} \cdot e^{i\Phi} = |Z| \cdot e^{i\Phi} = \text{Re}(Z) + i \cdot \text{Im}(Z), \quad (3.9)$$

where the hats represent the amplitude of the quantities,  $i$  the imaginary unit and  $\Phi$  the phase shift between the excitation and the response. By determining the impedance for a range of frequencies, the impedance spectrum is obtained. This can be done either by controlling the current, i.e. in galvanostatic mode, the voltage, i.e. in potentiostatic mode, or for instance by controlling the DC current and overlaying a specific voltage signal. The latter is often called hybrid mode. It has further to be emphasized that since  $Z$  is the cell impedance, its limit when the frequency goes towards zero represents the local slope of the polarization curve, i.e.

$$Z(\omega \rightarrow 0) = -\frac{\partial U}{\partial j}. \quad (3.10)$$

Hence,  $Z$  is often called *differential resistance*. The two plots on the right side in Fig. 3.13 show the spectra in the Nyquist plane resulting from the EIS measurements along the

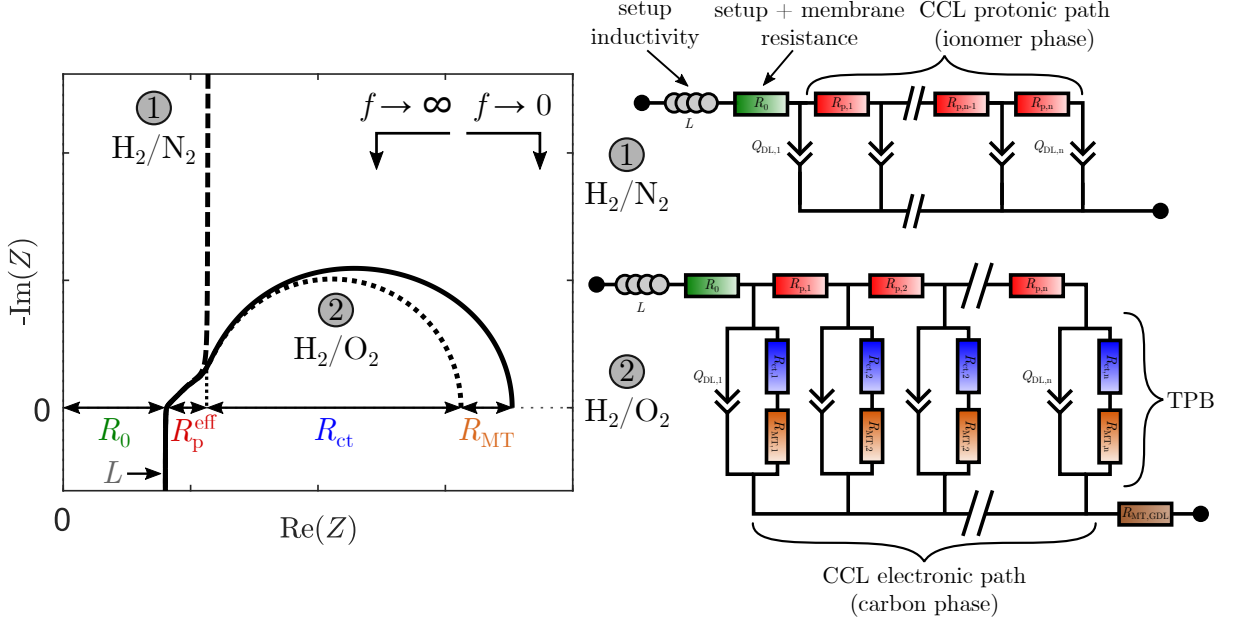


**Figure 3.15:** Modeled EIS spectra in the Nyquist plane (left) for a blocking electrode (1) and for a mixed-conducting electrode under load (2) and corresponding TLMs (right). In the Nyquist plane, the quantities that can be extracted are shown.

polarization curve shown in the plot on the left side. Additionally, Fig. 3.14 depicts the same spectra in the so-called Bode plane, which represents the real part (a) as well as the imaginary part (b) of the impedance over the frequency. In EIS, negative imaginary parts are generally called capacitive, whereas positive imaginary parts are called inductive. An explanation of what information is contained within such a spectrum is given in Fig. 3.15, which represents a simplified theoretical spectrum for the blocking electrode (1) and the charge transfer electrode (2) configuration and the corresponding ECMs in the form of TLMs. The anode electrode contributions are neglected in this case. At the highest frequencies, an inductive behavior ( $L$ ) coming mainly from the setup is typically observed in the form of a vertical line with a positive imaginary part. The  $x$ -axis intercept at high frequencies represents  $R_0$  containing the membrane resistance  $R_{\text{PEM}}$  as well as bulk and contact electrical resistances. Continuing towards lower frequencies, a  $45^\circ$  branch can be seen. This comes from distributed through-plane proton transport within the catalyst layer  $R_p$ , which is inversely proportional to the ionic conductivity. The projection of this branch on the  $x$ -axis yields the effective proton conductivity  $R_p^{\text{eff}} \approx (1/3) \cdot R_p$  which can be treated as an ohmic contribution to the performance loss. Generally, both ionomer-related resistances  $R_{\text{PEM}}$  and  $R_p$  are mostly dependent on  $RH$  and  $T$  at or near equilibrium, i.e. if the load is zero or small enough not to influence the conductivities by product water. In this case, such a resistance can be written in the form

$$R_{\text{ionic}} = R_{\text{ionic}}^{\text{ref}} \cdot (RH)^{-c} \cdot \exp\left(\frac{E_{\text{act}}^{\text{ionic}}}{RT}\right), \quad (3.11)$$

with a constant prefactor  $R_{\text{ionic}}^{\text{ref}}$ , a dimensionless exponent  $c$  for the dependency on relative humidity and an activation energy  $E_{\text{act}}^{\text{ionic}}$ . When large current is drawn, i.e. the cell is far from its equilibrium, the protonic resistances might strongly deviate and must be determined separately. Then, in the case of an electrode hosting an electrochemical

reaction, there is a capacitive charge transfer loop coming from the distributed resistor-capacitor (RC) or resistor-constant phase element (RQ) circuits. In the case of a blocking electrode, there is simply a vertical capacitive line. In the first case, the diameter of the capacitive charge transfer loop equals  $R_{ct} = -b/j$  if the kinetics follows Tafel's law with a slope  $b$  and if the ratio  $R_{ct}/R_p$  is large, i.e. the electrode is working homogeneously. If one of these two conditions does not apply, more sophisticated models must be chosen for the analyses. At low frequencies, losses by reactant transport within the CL (close to the reaction centers) and through the GDL can occur, which enlarges the capacitive loop by a certain amount. Under specific condition, the time constants of charge transfer and reactant transport can be such that two loops are observed instead of only one. It is worth mentioning that in this work mostly constant phase elements Q were used to take deviations from the ideal capacitance behavior of the C-element into account. These deviations are typically small at well-humidified conditions and increase at dry conditions (see the first publication in section 4.1).

### EIS data quality

Special care was taken in all our measurements to ensure stable test bench conditions before recording the needed data, which is explained in detail in section 3.3. Furthermore, it is important to emphasize that different conditions have to be fulfilled in order to get proper meaningful spectra [136]:

- linearity:  $Z$  is independent of the perturbation and no harmonic is created.
- causality: The response is only due to the applied perturbation.
- time-invariance/stability: The system does not change with time and returns to its original state after the experiment.
- $Z$  is finite-valued at  $\omega \rightarrow 0$  and  $\omega \rightarrow \infty$  and continuous and finite-valued everywhere else.

To verify these preconditions the Kramers-Kronig relations were applied [137]. If the aforementioned requirements are met by the data, the real and imaginary parts of the impedance are linked by the following relations:

$$Z_{\text{Re}}(\omega) = \frac{2}{\pi} \cdot \int_0^{\infty} \frac{\omega' \cdot Z_{\text{Im}}(\omega')}{\omega^2 - \omega'^2} d\omega' \quad (3.12)$$

$$Z_{\text{Im}}(\omega) = \frac{-2}{\pi} \cdot \int_0^{\infty} \frac{\omega \cdot Z_{\text{Re}}(\omega')}{\omega^2 - \omega'^2} d\omega' \quad (3.13)$$

A tool according to the linear Kramers-Kronig test by Schönleber et al. [138] was used to compute the errors and thus verify the data quality. The result of this test for most of the spectra recorded in this work is given in section A.2.

### Distribution of relaxation times

In order to get deeper insights into parameter dependencies and time characteristics by deconvoluting the physicochemical processes, the distribution of relaxation times (DRT) was computed. The principle behind it lies in the fact that every impedance function

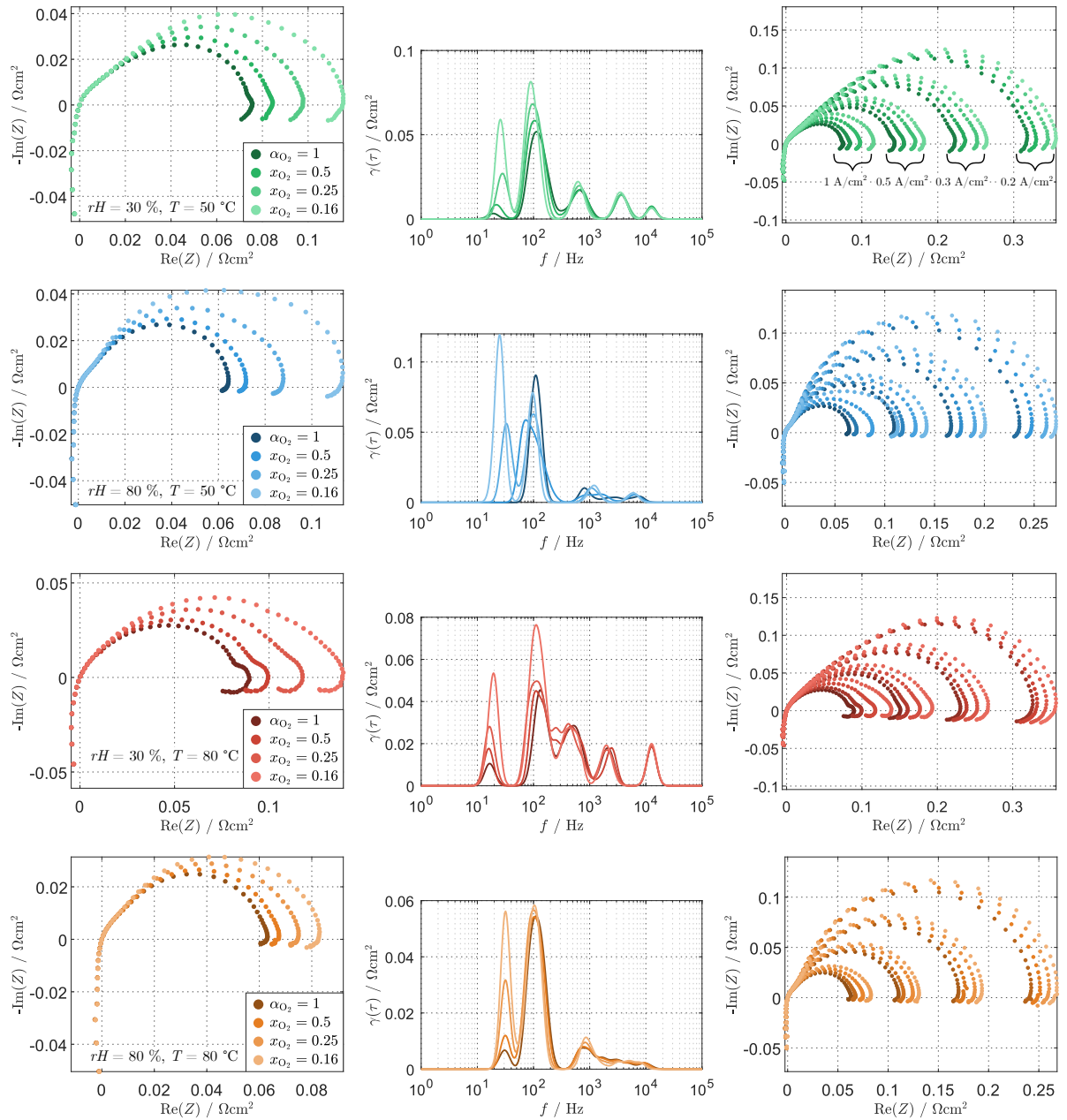


**Figure 3.16:** EIS spectra and corresponding DRTs for an oxygen partial pressure variation at  $1 \text{ A/cm}^2$  (left and middle columns) as well as a representation for the same variation at different current densities (right column). From top to bottom: cold and dry, cold and wet, hot and dry, and hot and wet conditions. All the spectra were shifted so that they have their high-frequency  $x$ -axis intercept at  $\text{Re}(Z)=0$ .

meeting the quality criteria from above and thus being conform with the Kramers-Kronig relations can be expressed as a sum of infinitesimal small RC-elements [136]. The integral form of the DRT is given by

$$Z_{\text{DRT}}(f) = R_0 + \int_{-\infty}^{+\infty} \frac{\gamma(\ln \tau)}{1 + i \cdot 2 \cdot \pi \cdot f \cdot \tau} d(\ln \tau), \quad (3.14)$$

with  $\gamma(\ln \tau)$  being the density function that has to be determined. For this, the tool by

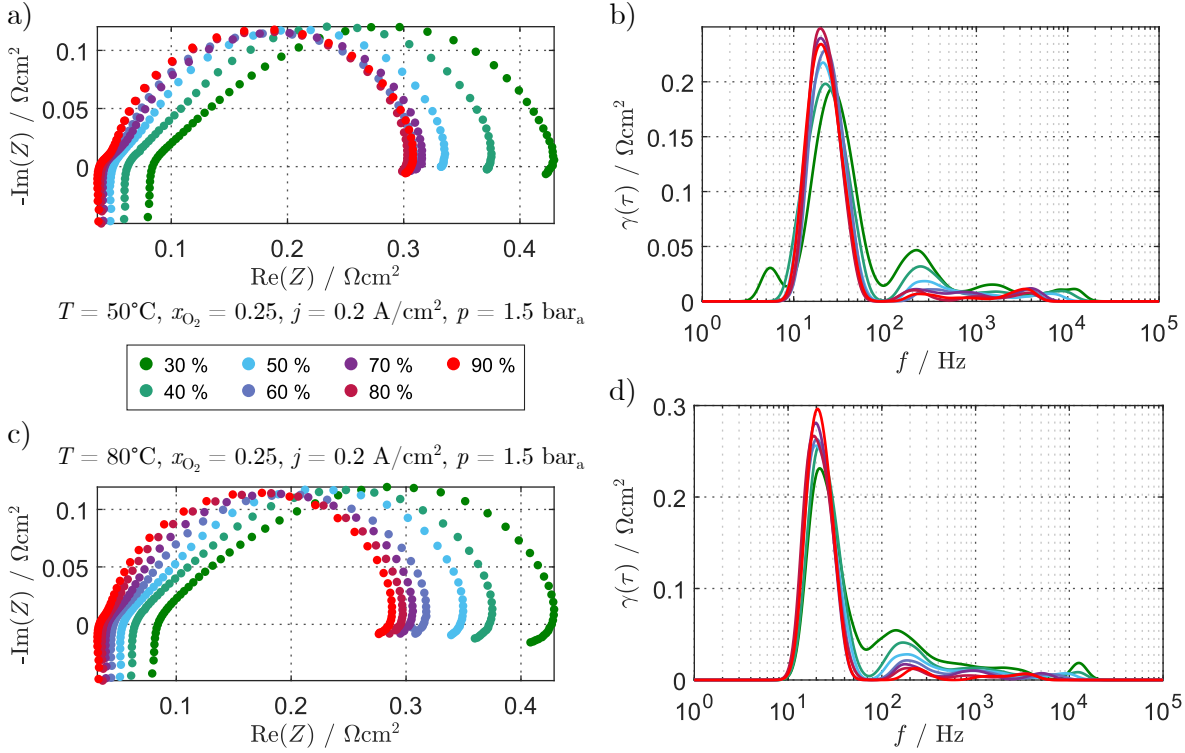


**Figure 3.17:** EIS spectra (left) and corresponding DRT (right) for a variation of the relative humidity at  $0.2 \text{ A/cm}^2$ . a) and b) cold ( $50^\circ\text{C}$ ) conditions. c) and d) hot ( $80^\circ\text{C}$ ) conditions.

Wang et al. [139] was used in this work and adapted to allow an automated evaluation of multiple spectra at the same time.

### Influence of operating parameters

Some of the most important parameter variations are shown in the Figs. 3.16 to 3.18. Figure 3.16 depicts an oxygen partial pressure variation at  $1 \text{ A/cm}^2$  in the Nyquist representation on the left and the corresponding DRTs in the center. From the top to the bottom, the conditions were cold and dry, cold and wet, hot and dry, and hot and wet. Additionally, the same variations are shown in the Nyquist representation for different current densities on the right side. Globally, it can be seen that the capacitive loop increases at low frequencies when the oxygen partial pressure is reduced, which is reflected in the two peaks with the lowest frequencies in the DRT. These peaks are expected to contain the mass transport and charge transfer contributions. At both dry conditions, the two peaks are affected by the change in partial pressure. At cold and wet conditions, there seems to be a drastic increase of the impedance and a shift towards lower frequencies. This might hint at poor oxygen transport conditions which could be caused by increased liquid water saturation and decreased transport properties at cold conditions. At hot and dry conditions, only the lowest-frequency-peak seems to be significantly affected by the changes. On the right side, it can be seen that the tendency with changing oxygen partial pressure is comparable for all conditions and that even at low current densities, EIS permits to probe such effects. In Fig. 3.17, a symmetrical variation of the gas channel relative humidity  $RH$  is shown at low current density for cold (a and b) and for hot (c

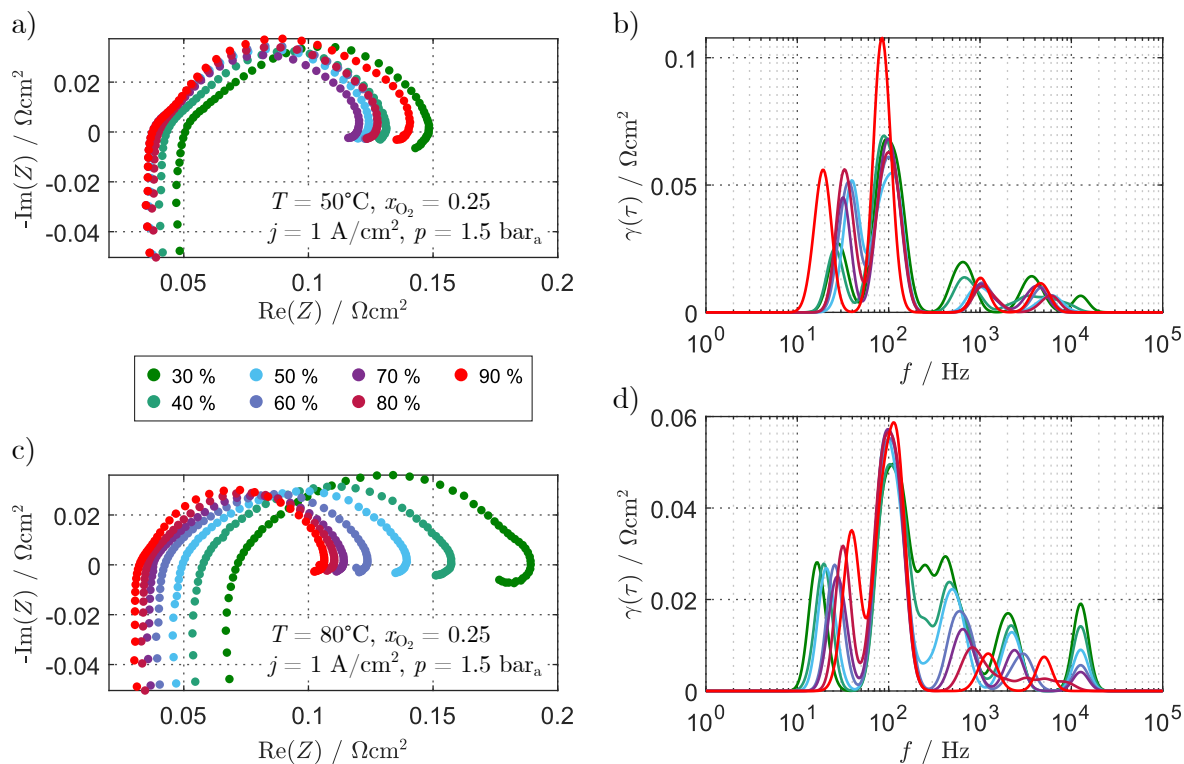


**Figure 3.18:** EIS spectra (left) and corresponding DRT (right) for a variation of the relative humidity at  $1 \text{ A/cm}^2$ . a) and b) cold ( $50^\circ\text{C}$ ) conditions. c) and d) hot ( $80^\circ\text{C}$ ) conditions.

and d) conditions. As expected, the change mainly affects the ionomer conductivity of the membrane and the catalyst layer, which is reflected by the fact that the  $x$ -axis intercept is shifted to the right and the  $45^\circ$ -slope increases in the Nyquist plots (left side) when the humidity decreases. In the DRTs on the right side this is confirmed as merely the high-frequency part is affected by a change in  $RH$ . A similar investigation is shown in Fig. 3.18 for  $1 \text{ A/cm}^2$ . There, the water produced by the electrochemical reactions also plays a role and it can be seen that the tendencies are not so trivial anymore. At cold conditions, humidification enhances the performances until a certain threshold after which it decreases again, likely because of the presence of too much water and poor transport properties. This is also reflected in the DRT which shows that at high humidity, it is the contributions of the low-frequency processes which drastically increase. At hot conditions, the tendency is easier as it can nicely be seen that an increased humidification always improves the performance.

### 3.3 Experimental Procedure

In this section, a typical test run of this work is presented, which was mostly carried out for a full factorial variation of the operating conditions. The experiments were usually carried out in four in four distinct stages:

- Cell conditioning by voltage cycling under load
- Proton pumping ( $\text{H}_2/\text{H}_2$ ) and blocking cathode ( $\text{H}_2/\text{N}_2$ ) experiments including

voltammetry and EIS measurements

- Fuel cell (H<sub>2</sub>/O<sub>2</sub>) measurements including polarization curves and EIS. Second separate run with heliox (O<sub>2</sub> and He mixture in the cathode)
- Limiting current test run in H<sub>2</sub>/O<sub>2</sub> mode

After a cell was prepared according to the information given in section 3.1 and mounted in the cell holder, the latter was mounted on the test station and the operation could start. First, the gas tightness of the setup was tested by applying 2.5 bar<sub>a</sub> pressure with N<sub>2</sub> on both sides, turning off the flows and monitoring the pressure decay over at least 2 min. After that, the cell was heated up to 80°C while humidified N<sub>2</sub> flew on both sides until a stable equilibrium was reached. Then, the cell was conditioned under load in H<sub>2</sub>/air configuration with flows of 1250/3000 sccm in the anode and cathode, respectively. During this conditioning process, the cell performance was cycled in potentiostatic mode, i.e. the voltage was the controlled electric quantity, as can be seen in Fig. 3.19. The voltage profile was set according to Harzer et al. [140]: 0.6 V during 45 min, OCV during 5 min, and 0.85 V during 10 min. To reach a stable cell performance, this was repeated ten times ( $\approx 10$  h) and then followed by a recovery procedure featuring a voltage hold under load at 0.3 V for 2 h (not shown in Fig. 3.19). After conditioning, an extensive test run was carried out containing blocking cathode (H<sub>2</sub>/N<sub>2</sub>) and proton pump (H<sub>2</sub>/H<sub>2</sub>) measurements. The first set of conditions allowed to characterize proton conductivities and hydrogen permeation, whereas the second set of conditions was used to investigate anode performance signatures. The operating conditions were varied in a full factorial fashion from  $RH = 30\%$  to  $RH = 100\%$  and  $T = 50\text{ }^\circ\text{C}$  to  $T = 80\text{ }^\circ\text{C}$  at  $p_{\text{total}} = 1.5\text{ bar}_a$ , leading to 32 operating conditions (proton pump measurements under load excluded). For each of these conditions, EIS, CV and LSV were recorded in the H<sub>2</sub>/N<sub>2</sub> cell and EIS and polarization curves in the H<sub>2</sub>/H<sub>2</sub> cell. At such conditions, the CCL acts as working electrode and the ACL as counter and reference electrode. For each condition, the sequence was the following:

1. Setting temperatures and dew points (from low to high dew points) in H<sub>2</sub>/N<sub>2</sub> mode and leaving 2 h equilibration time before starting the measurements to guarantee steady-state conditions. Thereafter, it was assumed that the gas and ionomer phases were at thermodynamic equilibrium.
2. Carrying out potentiostatic EIS at 0.5 V DC in the frequency range of  $f = 100\text{ kHz}$  to  $f = 1\text{ Hz}$  with ten points per decade to determine  $R_\Omega$  and  $R_p$ . All measurement amplitudes between 3 mV rms and 12 mV rms showed identical results and each measurement was carried out twice. The parameters of an ECM were fitted to the experimental data such that the model impedance matched the measured impedance, see section 3.2.4.
3. Recording CV and LSV to determine the hydrogen permeation coefficient, the roughness factor  $rf$  (or ECSA) and the double layer capacity  $C_{\text{dl}}$ . CV was typically recorded by sweeping the cell voltage from 70 mV to 900 mV with 50, 100 or 150 mV/s and a step rate of 2 mV. Each measurement yielded three to five voltammograms and was repeated twice. The anode was continuously flushed with



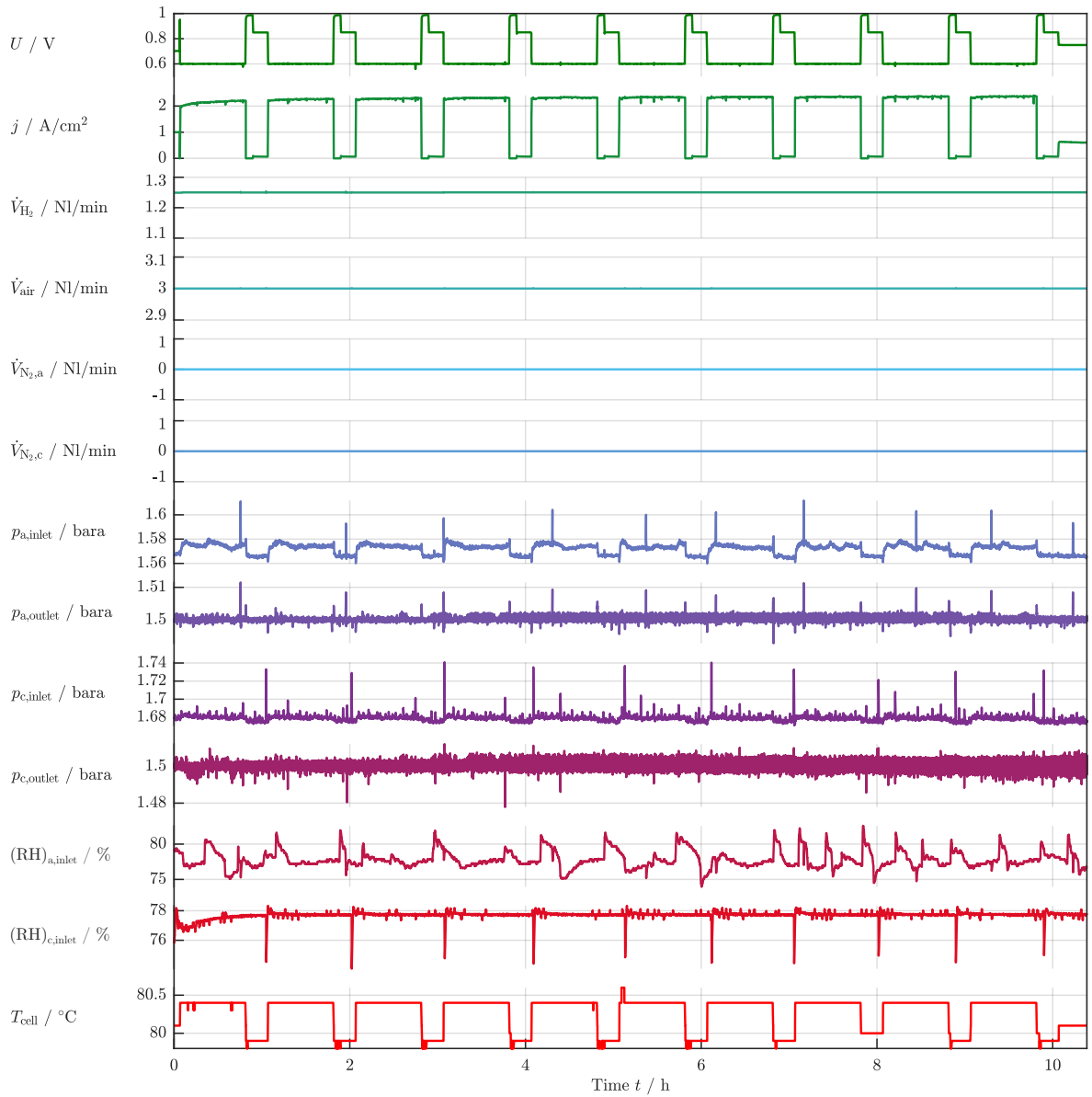


**Figure 3.19:** Fuel cell operating parameters over time for the conditioning procedure containing the voltage profile according to ref. [140]. This was followed by two hours voltage hold at 0.3 V under load ( $\text{H}_2/\text{air}$ ) which is not shown here.

500 sccm  $\text{H}_2$  and the  $\text{N}_2$  flow of 500 sccm on the cathode side was interrupted during the measurement. LSV was done under similar conditions with a single slow voltage sweep with a rate of 5 mV/s.

- Recording polarization curves and potentiostatic EIS at OCV in  $\text{H}_2/\text{H}_2$  mode (proton pump) from  $f = 100$  kHz to  $f = 0.1$  Hz with 10 points per decade and an amplitude of 4 mV to investigate the performance signatures. Hereafter, switching back to  $\text{H}_2/\text{N}_2$  conditions and going back to the first step with the next humidity and temperature condition.

In a separate measurement campaign in  $\text{H}_2/\text{H}_2$  mode, a recovery step was developed to avoid CO-poisoning of the catalyst layers when operating PEMFCs in  $\text{O}_2$ -free conditions

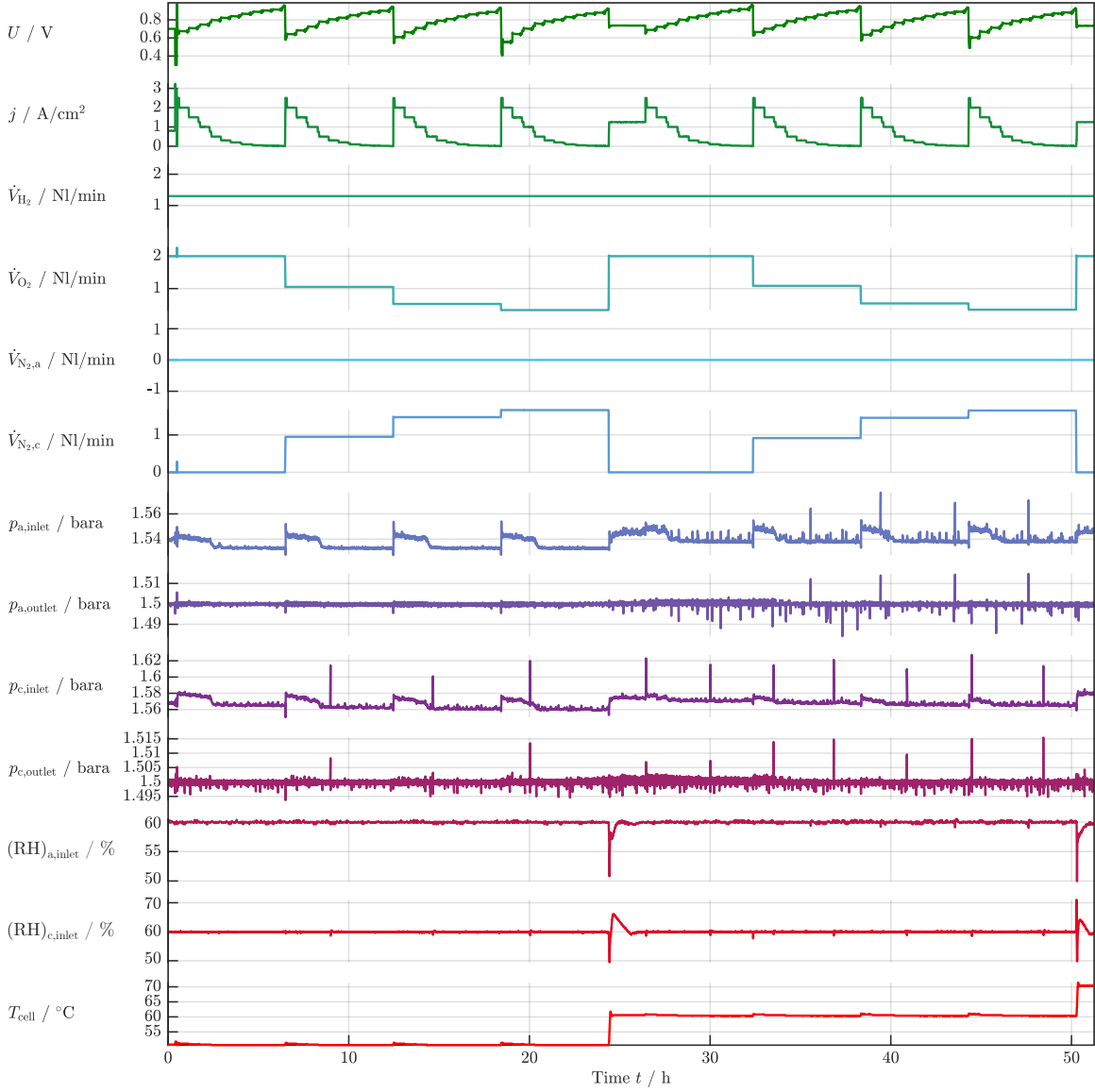


**Figure 3.20:** Exemplary extract of the fuel cell operating parameters over time during the main DOE run in  $\text{H}_2/\text{O}_2$  mode for  $50^\circ\text{C}$  and  $60^\circ\text{C}$  at 60% relative humidity.

(see the second publication in section 4.2). Then, the central test run under load in fuel cell mode ( $\text{H}_2/\text{O}_2$ ) was performed with seven relative humidity levels, from  $RH = 30\%$  to  $RH = 100\%$ , four temperatures ( $T = 50^\circ\text{C}$  to  $T = 80^\circ\text{C}$ ), four oxygen concentrations on the cathode side ( $x_{\text{O}_2}^{\text{dry}} = 1$ ,  $x_{\text{O}_2} = 0.5$ ,  $x_{\text{O}_2} = 0.25$ ,  $x_{\text{O}_2} = 0.16$ ), and sixteen current densities ( $j = 2 \text{ A/cm}^2$  to  $j = 4 \text{ mA/cm}^2$ ). This lead to 1792 operating points and ten out of the sixteen current density levels were selected for an EIS characterization in addition to the steady-state polarization, which yielded 1120 spectra. Pressure drops  $\Delta p < 100 \text{ mbar}$  were reached for all the conditions by using constant dry flow rates of 1300 sccm on the anode side and 2000 sccm on the cathode side at a system pressure of  $p_{\text{total}} \approx 1.5 \text{ bar}_a$ .  $\text{O}_2$  was mixed with  $\text{N}_2$  ahead of the humidification bubbler to vary  $p_{\text{O}_2}$  and heliox measurements were conducted additionally in a separate experiment for  $RH = 30\%$  and  $RH = 80\%$ . The conditions were chosen in the order of increasing

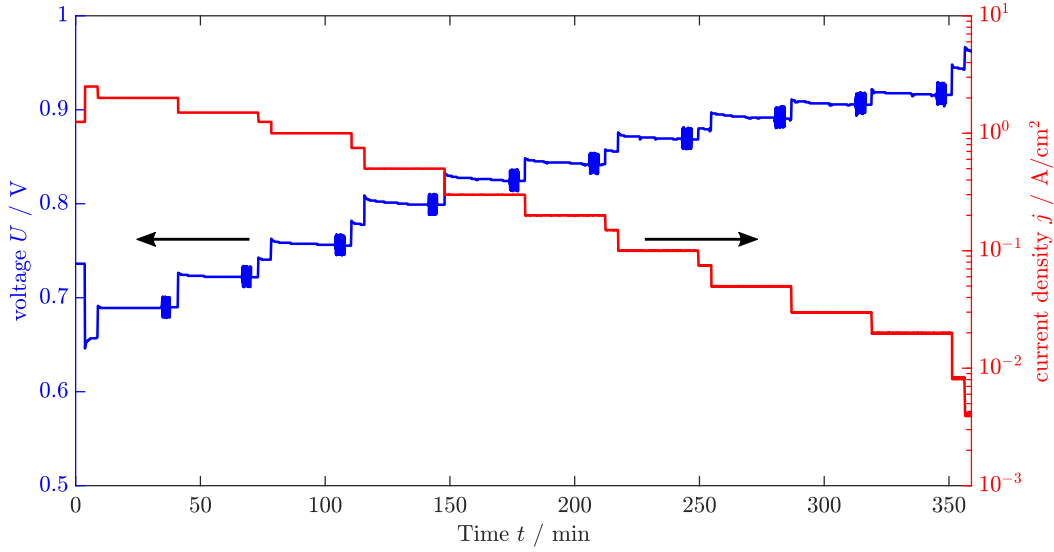


**Figure 3.21:** Zoom on typical raw data obtained from the main DOE run in  $\text{H}_2/\text{O}_2$  mode leading to a polarization curve. Conditions:  $RH = 60\%$ ,  $T = 60^\circ\text{C}$ ,  $x_{\text{O}_2}^{\text{dry}} = 1$ ,  $p_{\text{out}} = 1.5 \text{ bar}_a$ .

dew points and from high currents to low currents. Moreover, the operating conditions were stabilized under  $\text{H}_2/\text{air}$  conditions at 0.7 V for at least 2 h whenever temperature or dew point was changed. An extract of this run showing the complete current density and oxygen partial pressure variation for the four cell temperatures at 60% relative humidity is shown in Fig. 3.20. Furthermore, exemplary raw data showing the current sweep leading to a complete polarization curve including the voltage transients caused by EIS are depicted in Fig. 3.21. This figure shows also that prior to recording each EIS spectrum, a stabilization time of 25 min was implemented to ensure high measurement quality, whereas the current density conditions without EIS were held for 5 min. The impedance measurements were performed in pseudo-galvanostatic (hybrid) mode (DC load is fixed and AC voltage sweep is performed) with 11 mV AC amplitude from  $f = 100 \text{ kHz}$  to  $f = 0.1 \text{ Hz}$  and with 10 points per decade. The EIS spectra of some selected conditions were recorded down to  $f = 10 \text{ mHz}$ . For data evaluation, the parameters of different

**Table 3.1:** Values taken by the operating parameters during the main experiments ( $\text{H}_2/\text{H}_2$  run excluded). The values for  $x_{\text{O}_2}$  and  $j$  only apply for the test run in fuel cell mode. Bold text indicates current densities at which EIS was conducted.

Parameter	Values
$RH / \%$	{30, 40, 50, 60, 70, 80, 90, 100}
$T / ^\circ\text{C}$	{50, 60, 70, 80}
$x_{\text{O}_2}^{\text{dry}}$ or $x_{\text{O}_2} / -$	{1} or {0.5, 0.25, 0.16}
$j / \text{A}/\text{cm}^2$	{ <b>2</b> , <b>1.5</b> , 1.25, 1, 0.75, <b>0.5</b> , <b>0.3</b> , <b>0.2</b> , 0.15, <b>0.1</b> , ... 0.075, <b>0.05</b> , <b>0.03</b> , <b>0.02</b> , 0.008, 0.004}

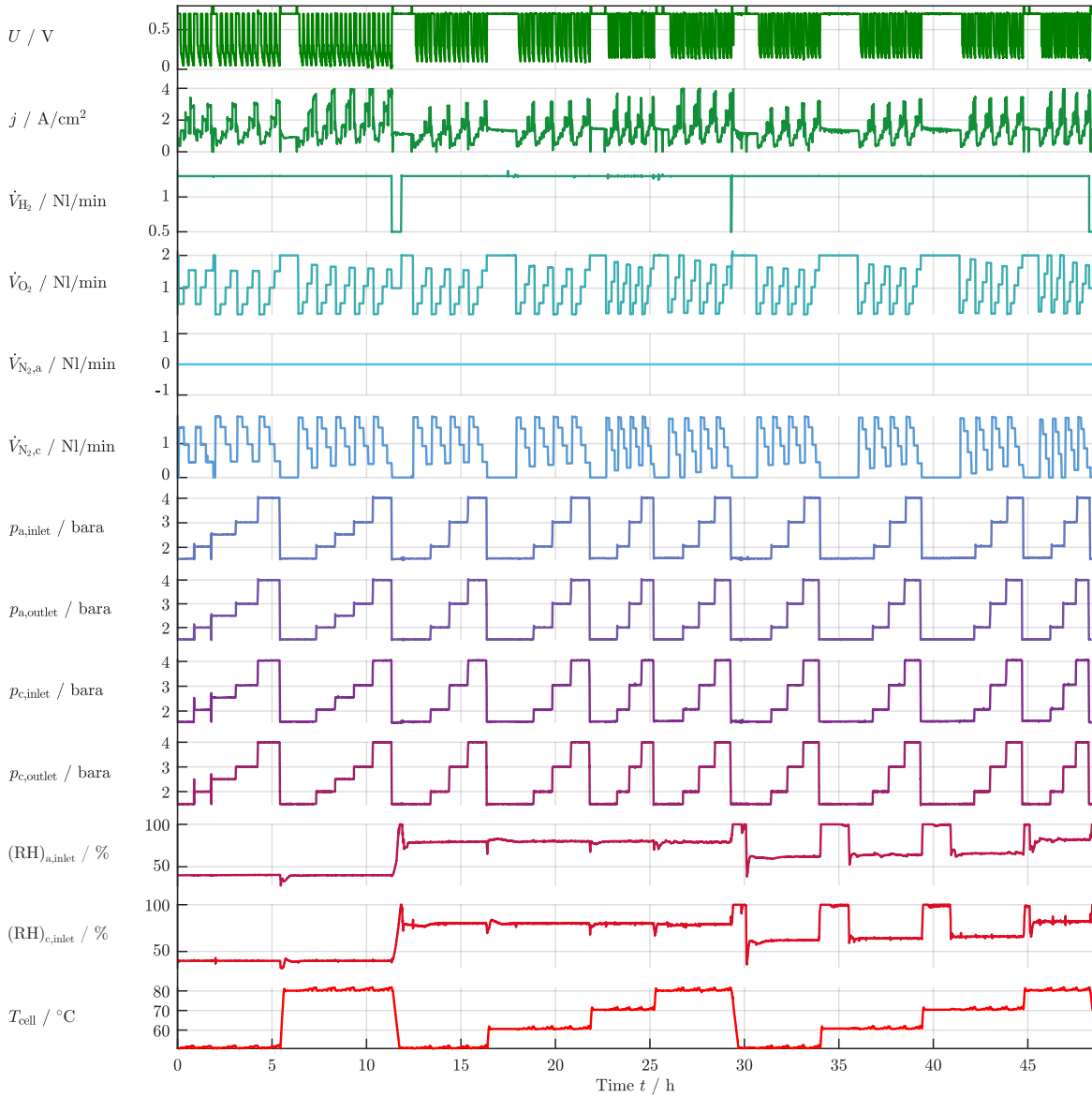


**Figure 3.22:** Extract of the fuel cell operating parameters over time during the SLC experiments in  $\text{H}_2/\text{O}_2$  mode.

ECMs were fitted to these experimental spectra and as a supplemental tool to aim at a better deconvolution and visualization of the physicochemical processes, the DRT was also computed (see section 3.2.4). Table 3.1 summarizes of the values taken by the operating parameters in the main experiments.

Finally, SLC measurements were performed according to the method proposed by Baker et al. [112] and TLC measurements according to Göbel et al. [134]. The SLC measurements were carried out for four pressure levels ( $p_{\text{out,total}} = 1.5, 2, 3, 4 \text{ bar}_a$ ), three humidity levels ( $rH = 30, 80, 100\%$ ), four temperature levels ( $T = 50, 60, 70, 80^\circ\text{C}$ ) and four oxygen mole fractions ( $x_{\text{O}_2} = 0.02, 0.05, 0.1, 0.15$ ). To reach stable operating parameters, the same methods as explained above were used. Thereafter, the cell was held potentiostatically at  $0.7 \text{ V}$  for  $8 \text{ min}$  at given pressure, humidity, temperature and concentration before jumping to the limiting current by setting the voltage progressively to

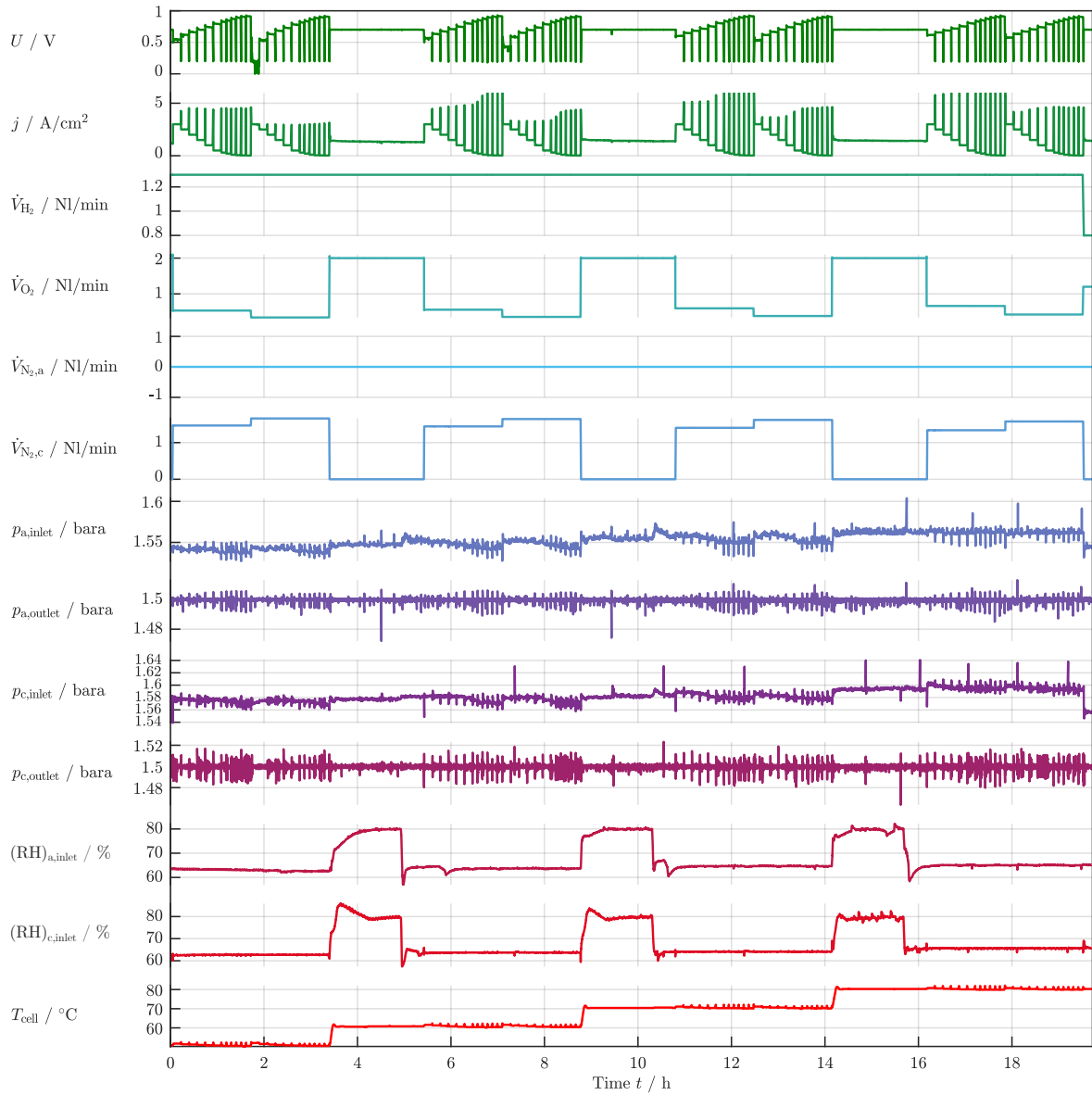


**Figure 3.23:** Extract of the fuel cell operating parameters over time during the TLC experiments in  $\text{H}_2/\text{O}_2$  mode.

0.3 V for 5 min, 0.2 V for 5 min and 0.15 V for 5 min. Figure 3.22 shows a cutout of this procedure which points out the systematic parameter variations that were performed during this experiments in the same way as in the previous test runs. The TLC measurements were carried out for  $x_{\text{O}_2} = 0.16$  and  $x_{\text{O}_2} = 0.25$  at  $p_{\text{out,total}} = 1.5 \text{ bar}_a$  by conditioning the cell current for 10 min at high load or 5 min at low load and jumping to the limiting current for 10 s by potentiostatic operation. Figure 3.23 shows the time traces of this TLC experiment for four different cell temperatures from  $50^\circ\text{C}$  to  $80^\circ\text{C}$  where the two different oxygen mole fraction levels can clearly be identified as well as the long stabilization times after changing the temperature. Furthermore, a zoom on the electric quantities is depicted in Fig. 3.24a for an SLC measurement and in Fig. 3.24b for an TLC measurement. The first zoom clearly shows that the limiting current strongly

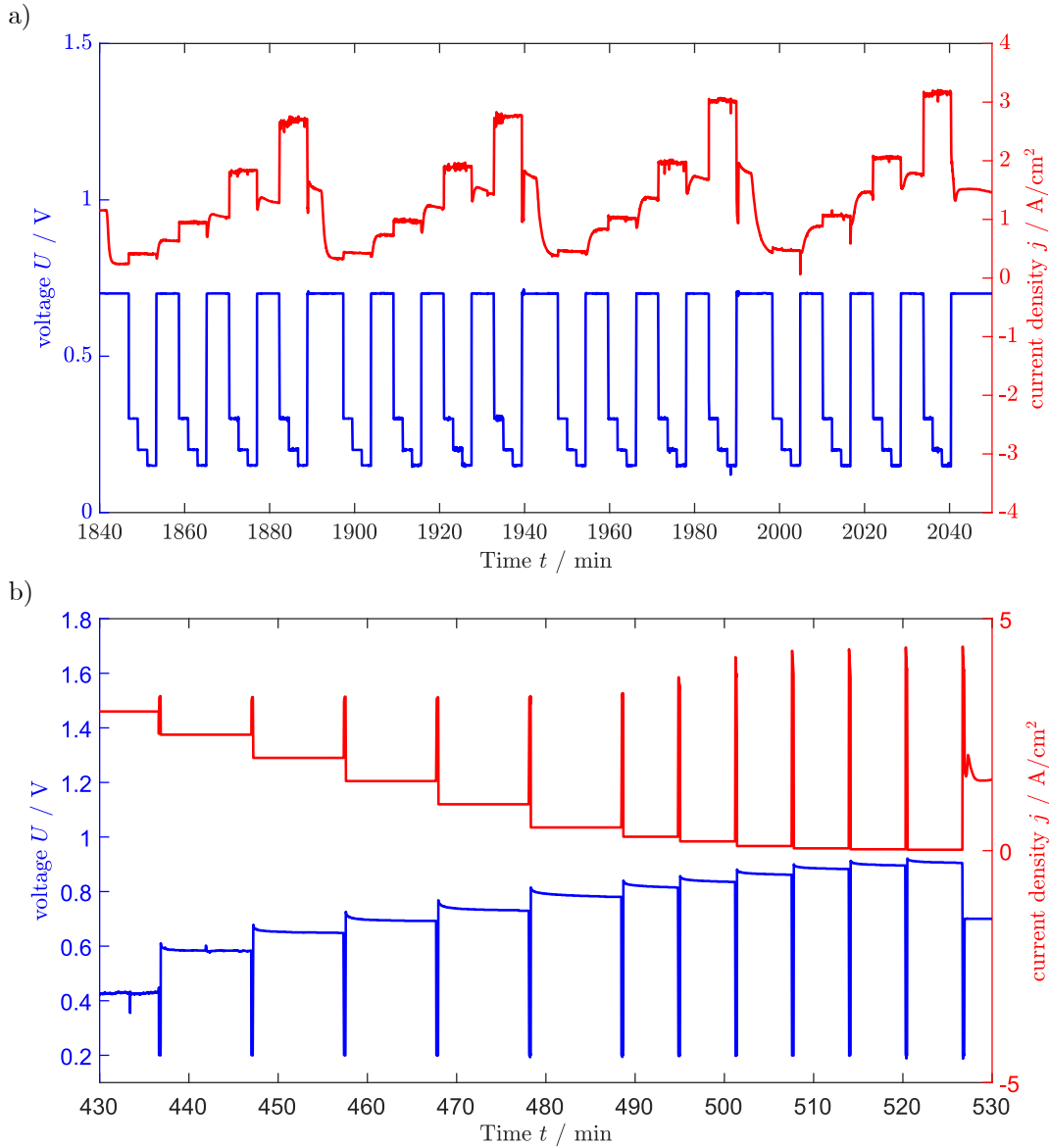


**Figure 3.24:** a) Exemplary time trace of  $U$  and  $j$  during an SLC run. The increasing current density over when operating at low potential shows the progressive increase of  $p_{\text{O}_2}$ . b) Exemplary time trace of  $U$  and  $j$  during an TLC run. The decrease of the conditioning current density over time leads to an increase of the limiting current density.

increases with increasing oxygen mole fraction as expected. The second zoom confirms that the limiting current decreases when the conditioning current increases, which is most probably due to the higher liquid water saturation in the porous media at higher loads.

### Data quality and SOH parameters

A complete overview on how good data quality was ensured is given in the supplementary data of the second publication in section A.2, especially in Fig. S3. Several CVs were recorded along the main DOE test run as described above at  $p_{\text{total}} \approx 1 \text{ bar}_a$  and  $T = 40 \text{ }^\circ\text{C}$  with fully saturated gas ( $RH = 100 \%$ ). This allowed to track SOH parameters

and prove that no significant ageing happened during the experiments. Based on this, the ECSA and double layer  $C_{dl}$  as well as the hydrogen crossover rate  $j_{H_2, crossover}$  were evaluated. The first two quantities are indicators for the cathode electrode health, whereas the hydrogen crossover rate is relevant to determine the membrane health. Furthermore, some specific polarization data and EIS spectra were measured several times to confirm that performance was reproducible and constant in time. Lastly, apart from the limiting current measurements, all other measurements were conducted twice at least.





## 4 Published Work

In this chapter, the journal articles published within this PhD thesis are presented in chronological order of publication, which is also logical from the thematic point of view and therefore allows for seamless transitions. Since the ultimate goal was to propose a simple but enhanced model capable of accurately simulating both steady-state performance and EIS signatures of differential PEM fuel cells, characterizing material properties was necessary aside from developing the simulation tool. Thus, the reader will find experimental as well as theoretical content within these articles. It is worth to mention that systematic parameter variations were carried out in a full factorial fashion in order to get consistent datasets whenever it was possible and needed (see Chapter 3). Further, high measurement quality was ensured by long stabilization times after changing the operating conditions and before doing the actual measurement, and the EIS spectra underwent the Kramers-Kronig test [137,138]. Some test runs were repeated multiple times to guarantee reproducibility and regular SOH checks were performed to make sure that the samples did not degrade significantly during the test runs.

Unless running state-of-the-art fuel cells at extreme conditions, the cathode reaction kinetics represents the major loss contribution at typical automotive operating conditions over a wide load range. They are still subject to research activities as no definitive consensus was reached concerning the mechanistic description and proper parameterization of the ORR process. Hence, the focus of this work is the cathode contribution, which cannot be accessed directly by simple in situ techniques such as polarization curves or EIS since at least hydrogen crossover as well as ohmic losses coming from proton transport in the PEM and CCL must be known in order to access the ORR kinetics. Therefore, the characterization of ionomer properties was addressed in the first publication presented in section 4.1 before the anode and cathode kinetics were investigated in the following publication presented in section 4.2. The HOR and ORR were parameterized based on steady-state polarization data and the influence of the relative humidity on the cathode kinetics was investigated. Further, oxygen mass transport contributions based mainly on limiting current measurements were discussed and deviations of the ORR from the Tafel model at high currents observed, pointing out that there are more complex mechanisms at play. Lastly, a model for the cathode kinetics comprising the ORR and a poisoning reaction of the platinum surface by oxides was proposed in the third publication in section 4.3. This model is enhanced compared with a BV or Tafel approach but still simple to parameterize and reconciles steady-state and EIS behavior of PEM fuel cells.

## 4.1 Full Factorial In Situ Characterization of Ionomer Properties in Differential PEM Fuel Cells

The first publication of this thesis covers the characterization of the most relevant ionomer phase properties [23]. Based on differential cell measurements, macro-homogeneous models for both hydrogen permeation through the membrane and ionomer conductivity of the PEM and the CCL were parameterized. To gather the data, the relative humidity  $RH$  and temperature  $T$  were varied in  $H_2/N_2$  configuration and voltammetry as well as EIS measurements were carried out for a full factorial grid of  $RH$  and  $T$  ranging from 30% to 100%  $RH$  and from 50°C to 80°C. Beforehand, the influence of  $RH$ ,  $T$ , and the hydrogen partial pressure  $p_{H_2}$  on the permeation properties was determined and a comparative study of LSV and CV was performed for two different MEAs: one with a 50- $\mu\text{m}$ -thick membrane and the baseline sample with a 18- $\mu\text{m}$ -thick membrane. It was shown thereby that under all the investigated conditions, LSV and CV yield identical results. Further, these voltammetry measurements were validated by online gas analysis.

Then, parameter dependencies of the ionomer conductivity were quantified by fitting a blocking TLM (no cathode reaction kinetics, infinite charge transfer resistance) to the  $H_2/N_2$  EIS spectra. This TLM contains constant phase elements (CPEs) instead of capacities to account for the rising deviation from the ideal behavior at low  $RH$  caused by increasing inhomogeneities in the catalyst layer. Using an Arrhenius-like prefactor for the temperature dependency and a power law for the effect of humidity, activation energies of 20  $\text{kJ mol}^{-1}$ , 7  $\text{kJ mol}^{-1}$ , and 9  $\text{kJ mol}^{-1}$  were determined for the hydrogen permeation coefficient,  $\Psi_{H_2}$ , the proton conductivity of the PEM,  $\sigma_{\text{PEM}}$ , and the proton conductivity of the CCL,  $\sigma_{\text{CCL}}$ , respectively.

Additionally,  $H_2/O_2$  measurements under load were performed to investigate the influence of water production on the ionomer conductivities by EIS measurements. The parameters of an iterative TLM which incorporates the non-uniform distribution of potential and current in the through-plane direction were fitted. This model gets essential when the ratio of the proton resistance to the charge transfer resistance,  $R_p/R_{\text{ct}}$ , increases, e.g. when the humidity decreases and the cell current increases. In this case, the assumption  $R_p^{\text{eff}} = R_p/3$  does not hold anymore. Finally, it was shown that based on the resistances under load and the parameterized models, the actual equivalent layer  $RH$  can be estimated. Further, it was shown that a subtraction of the protonic loss contributions from polarization curves based on resistances gathered from  $H_2/N_2$  measurements leads to the largest errors at cold and dry conditions.

This publication was written by the first author and commented by the three co-authors. The CV, LSV and EIS (both  $H_2/N_2$  and  $H_2/O_2$ ) experiments were designed by the first author and carried out by the first author under the advice of M. Hanauer and U. Berner. Niklas Hensle, who performed his bachelor thesis under the supervision of the first author, supported the first author with the spectrometry measurements and some of the voltammetry measurements in Figs. 3 and 4. The test station used was newly commissioned and completely automated by the first author for this work. Data analysis and interpretation were performed by the first author and results were discussed with the three co-authors.

The publication was submitted to the *Journal of The Electrochemical Society* on February 20, 2021, and published on August 5, 2021. The permanent web link to the article is <http://dx.doi.org/10.1149/1945-7111/ac1812>.

© The Electrochemical Society. Reproduced by permission of IOP Publishing Ltd. All rights reserved.

C. Gerling, M. Hanauer, U. Berner, and K. A. Friedrich, "Full factorial in situ characterization of ionomer properties in differential PEM fuel cells." *J. Electrochem. Soc.*, **168**, 0845 (2021).

© The Electrochemical Society. Reproduced by permission of IOP Publishing Ltd. All rights reserved.

*Journal of The Electrochemical Society*, 2021 **168** 084504  
1945-7111/2021/168(8)/084504/14/\$40.00 © 2021 The Electrochemical Society ("ECS"). Published on behalf of ECS by IOP Publishing Limited



## Full Factorial In Situ Characterization of Ionomer Properties in Differential PEM Fuel Cells

Christophe Gerling,<sup>1,2,z</sup> Matthias Hanauer,<sup>1</sup> Ulrich Berner,<sup>1</sup> and K. Andreas Friedrich<sup>2,3</sup>

<sup>1</sup>Robert Bosch GmbH, Corporate Research, Renningen 71272, Germany

<sup>2</sup>Institute for Building Energetics, Thermotechnology and Energy Storage (IGTE), University of Stuttgart, Stuttgart 70569, Germany

<sup>3</sup>Institute of Engineering Thermodynamics, German Aerospace Center (DLR), Stuttgart 70569, Germany

The performance optimization of membrane electrode assemblies of PEM fuel cells requires accurate characterization and modelling of the relevant mechanisms. In this paper, the ionomer conductivities and permeation properties are characterized in situ in a differential cell setup by varying the operating conditions in a full factorial fashion in H<sub>2</sub>/N<sub>2</sub> mode. Voltammetry methods are validated against online gas analysis and then used to record H<sub>2</sub> crossover. The membrane and cathode catalyst layer (CCL) resistances are deconvoluted by fitting transmission line models (TLM) to electrochemical impedance spectroscopy (EIS) data. Based on this, we estimate activation energies of 20 kJ mol<sup>-1</sup> for the H<sub>2</sub> permeation, 7 kJ mol<sup>-1</sup> for the membrane resistance and 9 kJ mol<sup>-1</sup> for the ionomer resistance in the CCL. Through EIS measurements under load (H<sub>2</sub>/O<sub>2</sub>), we also evaluate the change in the ionomer resistances in course of water production. This effect is most pronounced under cold and dry conditions and implies that a subtraction of the protonic loss contributions from polarization curves only based on EIS measurements obtained in H<sub>2</sub>/N<sub>2</sub> mode is not possible.

© 2021 The Electrochemical Society ("ECS"). Published on behalf of ECS by IOP Publishing Limited. [DOI: [10.1149/1945-7111/ac1812](https://doi.org/10.1149/1945-7111/ac1812)]

Manuscript submitted February 20, 2021; revised manuscript received July 22, 2021. Published August 5, 2021.

Supplementary material for this article is available [online](#)

Apart from design considerations on the PEMFC stack level such as the geometry of the manifolds, the style of the flow fields and the materials and coatings of the bipolar plates, the most important lever for optimizing PEMFC stacks regarding performance and lifetime lies in tuning the membrane electrode assembly (MEA) that still represents up to 50% of the fuel cell costs.<sup>1,2</sup> For this purpose, the influence on the performance induced by materials and process parameters as well as the effects of the operating conditions must be well understood. In recent years, measurements on small-scale single cells under so-called differential conditions (entry cell state = exit cell state) have greatly increased in importance.<sup>3-7</sup> These setups make it possible to focus on the MEA by minimizing unwanted along-the-channel and flow field effects, thus unravelling pure through-plane physics (aside from possible channel/land effects) and enabling the parameterization of macro-homogeneous layer properties, which is crucial for accurate and predictive models.

Regarding performance optimization, one significant path is the fabrication of thinner membranes to reduce proton conduction induced losses, but this comes at the cost of increased gas permeation and reduced lifetime.<sup>8,9</sup> Therefore, the gas permeances and ionomer conductivities are the two focal points in this work, and we want to characterize them using simple in situ techniques. Firstly, understanding the gas permeation properties is important since they do not only affect the open circuit voltage (OCV, see Fig. 1a) and more generally the reaction kinetics on the cell and stack level,<sup>10,11</sup> but they also influence the operation of the anode loop (on the system level) which accumulates N<sub>2</sub> over time.<sup>12</sup> Moreover, oxygen crossover can be beneficial to hinder CO poisoning of the anode electrode on one hand side,<sup>13</sup> but membrane ageing can be accelerated by hydrogen and oxygen crossover through chemical degradation involving the formation of radicals on the other hand side.<sup>14</sup> Secondly, understanding the protonic conductivities of the bulk membranes and the catalyst layers is of great interest, too, since they generate a major part of the performance loss during operation<sup>15-17</sup> and they are highly coupled to all the other important cell mechanisms (electrode kinetics, heat and water generation and transport). Figure 1b shows an example of the large contribution (160 mV at 2 A cm<sup>-2</sup>) of the electronic and protonic resistances on a

measured polarization curve under dry conditions. These contributions are dominated by the ionomer resistance of the membrane and of the cathode electrode and thus must be quantified.

Although the lowering of the OCV (deviation from the theoretical voltage calculated by the Nernst equation) is a complex topic and the level of contribution of fuel and oxidant crossover is still not completely understood, it is clear that there are mainly two effects at play: gas crossover and oxidation reactions within the cathode catalyst layer (CCL).<sup>10,11,18</sup> Between fuel and oxidant crossover, H<sub>2</sub> permeation is the most important contribution since O<sub>2</sub> permeates less and does not affect the state of the anode significantly. Dicks and Larminie described the internal currents created by crossover and by the membrane shorts, both shifting the polarization curve and thus lowering the OCV.<sup>19</sup> Figure 1a shows a schematic Tafel plot of both the hydrogen oxidation reaction (HOR, normally happening within the anode) and the oxygen reduction reaction (ORR) occurring at the cathode. The diffusion-limited HOR creates an internal current within the cathode that shifts the apparent OCV to lower values. Due to the very small  $p_{\text{H}_2, \text{CCL}}$ , the hypothetical exchange current density of the HOR becomes lower than the one of the ORR (shift on the current axis) and the equilibrium potential is shifted from 0 V to more positive potentials (shift on the voltage axis due to low partial pressure in the Nernst equation). Later, Zhang et al. concluded that at standard conditions (25 °C, 1 atm) the mixed potential due to the cathodic O<sub>2</sub>/H<sub>2</sub>O reaction potential (1.229 V<sub>NHE</sub>) and the anodic platinum surface oxidation reaction potential (Pt + H<sub>2</sub>O ↔ PtO + 2H<sup>+</sup> + 2e<sup>-</sup>,  $E_{\text{eq}} = 0.88$  V<sub>NHE</sub>) may cause more than twice as much voltage drop at OCV (135 mV at 80 °C) as the hydrogen crossover (56 mV for a Nafion® 112 based MEA at the same conditions) in a real cell.<sup>20</sup> More recently, Reimer et al. analyzed the time dependency of OCV due to oxide formation in half cells and concluded that platinum oxide plays an important role, even though in real cells crossover might highly influence the oxide layers.<sup>18</sup> In turn, other works focused on understanding and modeling hydrogen crossover and electrical membrane short currents, claiming that these effects are predominant at OCV.<sup>10,11</sup> In the past, different authors also investigated the permeation and diffusivity properties of H<sub>2</sub> and O<sub>2</sub> in solid polymer electrolytes (ex-situ) as functions of equivalent weight (EW), water content and temperature. They used permeability cells with pressure monitoring and gas chromatography<sup>21-23</sup> and electrochemical methods in microelectrode setups<sup>24,25</sup> or electrolysis cells.<sup>26</sup>

<sup>z</sup>E-mail: [christophe.gerling@de.bosch.com](mailto:christophe.gerling@de.bosch.com)

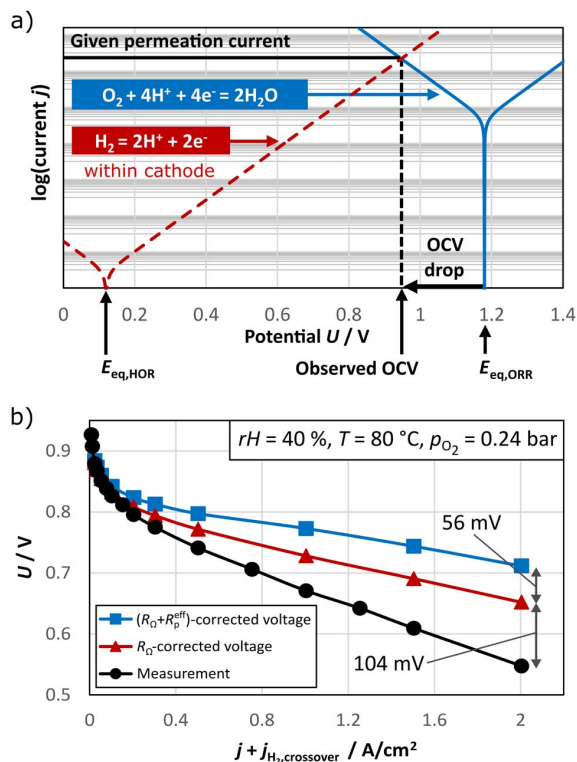


**Figure 1.** (a) Schematic representation of the internal current induced in the CCL by  $H_2$  crossover and the mixed potential. (b) Measured polarization curve at hot and dry conditions with the associated protonic loss corrections.

Lately, Baik et al. conducted permeation measurements in a real fuel cell setup by means of mass spectrometry for  $N_2$ <sup>27</sup> and  $H_2$ <sup>28</sup> and thereafter even under load.<sup>29</sup> All this shows that various techniques and materials have been used, consequently leading to a certain scatter in the experimental data. To our knowledge, Bernardi and Verbrugge were among the first to implement  $H_2$  and  $O_2$  crossover in a cell simulation model,<sup>30</sup> whereas other fundamental cell or electrode (CCL) models<sup>31–33</sup> did not take crossover effects into account. In 2004, Weber and Newman fitted experimental permeation data for vapor-equilibrated as well as for liquid-equilibrated membranes<sup>34</sup> which are still widely used in the modeling literature. In their physical membrane model, they postulated that the total transport of a given species within a membrane is composed of two mechanisms occurring in parallel if the membrane is simultaneously in contact with vapor and liquid water.<sup>35</sup>

The proton conductivity has been investigated even more widely in the literature and thus summarizing the efforts that have been made to understand and measure it would go beyond the scope of this work. Nevertheless, it is worth mentioning that Weber and Newman fitted experimental data for the vapor-equilibrated and liquid-equilibrated conductivities in the same way as they did for the permeances (see above). Also, Kusoglu et al. summarized a great amount of information on PFSA membranes<sup>8</sup> and Vetter et al. published a comprehensive review of MEA properties with a strong focus on performance modeling that shows the huge scatter in available data for each attribute.<sup>36</sup> Albeit protonic resistances of membranes and catalyst layers have been measured in specific ex situ setups<sup>37–40</sup> as well as in real cells using diverse electrical and electrochemical techniques, the electrochemical impedance spectroscopy (EIS) methods are greatly attractive for our purposes. These techniques are usually employed to investigate Ohmic losses and

polarization processes with different time constants.<sup>16,41</sup> Multiple authors showed that EIS under  $H_2/N_2$  conditions (blocking cathode by eliminating the kinetics) is an effective technique for characterizing in situ both the bulk membrane conductivity and the catalyst layer conductivity by fitting the measurements to simple transmission line models (TLM),<sup>42,43</sup> and they showed that EIS can be employed for monitoring catalyst layer degradation, too.<sup>44</sup> Furthermore, there have been studies on the impact of through-plane and in-plane inhomogeneities on the impedance response,<sup>42,44–46</sup> which can be caused by an inhomogeneous distribution of ionomer and catalyst, by heterogeneous layer thicknesses (due to the processing or to irregular MEA clamping) or by transport issues (along-the-channel effects, concentration profiles). Recently, Obermaier et al. built models for  $H_2/N_2$  impedance that take into account the pore radii and ionomer distribution within the CCL, which increases the fitting accuracy at medium and high frequencies. They also integrated parallel adsorption (sulfonate groups on the catalyst) and side reactions ( $H_2$  crossover oxidation for instance), leading to a good agreement with the experimental data at low frequencies.<sup>47</sup>

The major motivation for this work is addressing the big scatter in available data, the lack of full factorial studies and the resulting need for established standard characterization procedures (in-situ). We first show a comparison and validation of two voltammetry methods that can be used for measuring the hydrogen crossover. Secondly, we demonstrate the parameterization of ready-to-use models for both the hydrogen permeation coefficient and the ionomer conductivities (bulk and cathode catalyst layer) in a full factorial fashion for the temperature and the relative humidity. Our models are then compared to well-known parameterizations from the literature. Finally, we investigate the changes in the ionomer resistances when operating the cell under load.

## Experimental

**Cell assembly and test bench.**—Two different MEAs were used in this work: a Gore® PRIMEA® MEA (W.L. Gore & Associates, Elkton, MD, USA) with a membrane thickness of  $18 \mu m$  ( $0.4 \text{ mg}_{Pt} \text{ cm}^{-2}$  on the cathode and  $0.05 \text{ mg}_{Pt} \text{ cm}^{-2}$  on the anode side) and an MEA with  $50 \mu m$  membrane thickness (Nafion® N212,  $0.4 \text{ mg}_{Pt} \text{ cm}^{-2}$  on the cathode and  $0.2 \text{ mg}_{Pt} \text{ cm}^{-2}$  on the anode side) for comparison (only in the permeation study). Unless stated otherwise, we worked with MEAs as single cells with an active area of  $12 \text{ cm}^2$ . In order to prepare those, we cut  $25 \text{ cm}^2$  MEAs and welded them into polyethylene naphthalate (PEN) frames at  $100^\circ C$  to get better mechanical properties and enhance the handling. The thereby obtained cells, completed by a gas diffusion layer (GDL) from SGL® Carbon (Sigracet® 22BB) on top of each catalyst layer, were placed into a Baltic FuelCells quickConnect® cell holder with graphite straight channel flow fields.

As a test station we employ a FuelCon Evaluator C50 test bench that allows to control the cathode and anode gas streams separately: flow rates by mass flow controllers, dew points by two heated bubblers and gas temperature by heated gas lines. At the cell outlet, the gases are cooled down to remove the water and two valves adjust the system pressure. The cell temperature is regulated by gold-coated copper plates that are located directly behind the graphite flow fields and flowed through by a thermal fluid whose temperature is controlled by a Huber Ministat 125 thermostat. A thermocouple (type K) that is fixed onto the back of the graphite plate of the flow field measures the cell temperature. The equivalent clamping pressure of 1.3 MPa on the active area is obtained by a pneumatic cylinder.

We ensure high measurement precision by using a four-point measurement setup with twisted pair cables, where the connection of the sense cables is realized very close to the electrodes by contacting the graphite whilst the load cables are connected to the copper plates farther away. The load from our test station enables currents up to 100 A ( $=8.33 \text{ A cm}^{-2}$ ) and we use a Gamry reference 3000 plus Booster 30 K device for our EIS measurements. For our tests under

load, we chose to take the test station load for the current offset (DC current) and the impedance device to apply the AC signal for the sake of simpler software implementation and because it permits us to reach higher cell currents. Beforehand, we made sure that the test station load does not interfere with our measurements in the frequency range that is relevant for typical EIS ( $f < 20$  kHz).

**Measurement and characterization techniques.**—The permeation coefficients as well as the protonic conductivities (PEM and porous electrodes) are highly affected by the water content of the ionomer and by the temperature. For this reason we conducted full factorial parameter variations under system-relevant conditions ( $rH = 30\%$  to  $rH = 100\%$  and  $T = 50$  °C to  $T = 80$  °C, leading to 32 operating conditions) in our  $H_2/N_2$  experiments. Prior to these testings, our MEAs were conditioned in the  $H_2$ /air mode at  $p_{\text{total}} = 1.5$  bar<sub>a</sub>,  $rH = 100\%$ ,  $T = 50$  °C and with  $H_2$ /air flows of 1300/2000 sccm according to the procedure described by Harzer et al.<sup>5</sup> 0.6 V during 45 min, OCV during 5 min, and 0.85 V during 10 min. After repeating this cycle ten times (10 h conditioning time), the cell performance was stable. For each condition (temperature and humidity) of the characterization, the cell was stabilized for 2 h before starting the measurement in order to ensure a steady state and homogeneous distributions over the whole cell area. Therefore, we can assume that the ionomer phase and the gas phase were in thermodynamic equilibrium, whereas this assumption does not necessarily hold when operating the cell under load. It is worth mentioning here that the activation energies for the ionomer processes may be slightly dependent on the water activity and on the investigated temperature range<sup>34</sup> but that these effects were neglected in our work.

Our measurements were not carried out at standard conditions and we did not adjust the operating conditions to keep a constant anode potential in our studies. Anyway, since we were only interested in the current offsets of the voltammograms (red lines in Figs. 2a and 2b) for  $j_{H_2, \text{crossover}}$  ( $H_2$  crossover from the anode to the cathode and oxidation) and in the EIS response of the cell for the ionomer resistances ( $R_{\text{PEM}}$  and  $R_p$ ) we did not need to correct the potential for the Nernstian shift.

For determining the hydrogen permeation through our membranes, we carried out voltammetry measurements across a wide range of operating parameters. At given conditions, three to five cyclic voltammograms (CV) were recorded (extracted properties are averaged) and the first one was always discarded from the analysis. Additionally, either we repeated each run at least twice or we conducted a linear sweep voltammetry (LSV) measurement under the same conditions (see below). Figure 2a shows a typical cyclic voltammogram at  $p_{\text{total}} = 1.0$  bar<sub>a</sub>,  $rH = 100\%$  and  $T = 40$  °C where the cell voltage was swept from 70 mV to 900 mV (to probe the capacitive behavior of the Pt/C catalyst) by applying a sweep rate of  $100 \text{ mV s}^{-1}$  (step rate of 2 mV), with the CCL acting as working electrode and the anode catalyst layer (ACL) as counter and reference electrode. The anode was continuously flushed with 500 sccm hydrogen and the nitrogen flow on the cathode side (500 sccm) was stopped right before the measurement. From our CV measurements we could also extract the double layer capacity  $C_{\text{dl}}$  from the  $\approx 400$  mV to  $\approx 600$  mV region (purely capacitive) and the electrochemical surface area (ECSA, or roughness factor  $rf$  in  $\text{m}^2_{\text{Pt}}/\text{m}^2_{\text{geo}}$  or in  $\text{m}^2_{\text{Pt}}/\text{g}_{\text{Pt}}$  by converting with the electrode loading) by integrating the hydrogen adsorption and desorption peaks (see gray areas in Fig. 2a) and assuming a specific charge of  $210 \mu\text{C cm}_{\text{Pt}}^{-2}$  for a hydrogen monolayer ( $H_{\text{UPD}}$ ) on polycrystalline platinum (see specific literature<sup>48–50</sup> for more details).

Our LSV measurements were carried out under similar conditions but they consist of a single slow voltage sweep from 0.07 V to 0.35 V with a sweep rate of  $0.5 \text{ mV s}^{-1}$ . Figure 2b depicts such a measurement at  $p_{\text{total}} = 1.5$  bar<sub>a</sub>,  $rH = 70\%$  and  $T = 70$  °C. Since

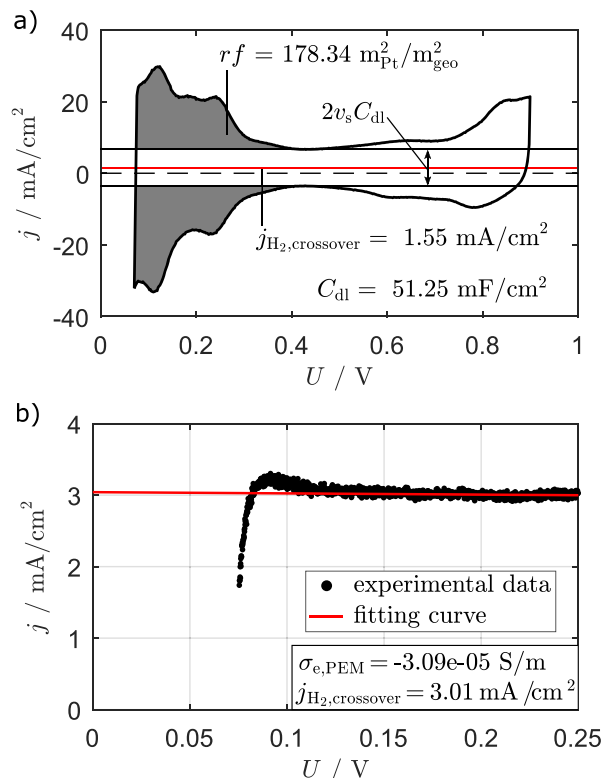


**Figure 2.** a) CV at  $rH = 100\%$ ,  $T = 40$  °C and  $p_{\text{total}} = 1.0$  bar<sub>a</sub>, recorded with a sweep rate of  $100 \text{ mV s}^{-1}$  from 70 mV to 900 mV. The roughness factor  $rf$ ,  $H_2$  crossover current  $j_{H_2, \text{crossover}}$  and double layer capacitance  $C_{\text{dl}}$  are also shown. b) LSV at  $rH = 70\%$ ,  $T = 70$  °C and  $p_{\text{total}} = 1.5$  bar<sub>a</sub>, recorded with a sweep rate of  $0.5 \text{ mV s}^{-1}$  from 70 mV to 250 mV. The y-axis offset of the red fit line indicates  $j_{H_2, \text{crossover}}$ .

the height of the hydrogen desorption peak and the charging of the double layer depend on the sweep rate they disappear almost completely (a small peak due to desorption can still be observed below 0.1 V) during such a measurement. A linear fit to the region 150 mV to 250 mV of this diagram provides the  $H_2$  crossover current (y-axis intercept) and the electronic resistance of the PEM (inverse slope of the linear fit). Here, the slope is so close to zero that an exact evaluation is not possible, meaning that the resistance is very high and therefore the shorts can be neglected. Also, some of our LSV experiments were conducted in combination with online gas analysis by mass spectrometry (MS, electron ionization quadrupole mass spectrometer OmniStar® GSD 320 OC2 from Pfeiffer Vakuum) of the cathode outlet stream to cross-validate the voltammetry techniques. For this purpose, a supplementary vapor-liquid separator (5 °C) was installed directly at the cell outlet to remove the water from the gas stream before entering the mass spectrometer.

For characterizing the ionomer conductivities, we varied the operating parameters (humidity and temperature) and conducted potentiostatic EIS measurements under  $H_2/N_2$  conditions (blocking cathode). We tested measurements at a DC potential of 0.5 V vs anode (no hydrogen adsorption or desorption<sup>51</sup>) with several perturbation amplitudes (between 3 mV rms and 12 mV rms) and they all showed identical results, meaning that any of those values can be chosen. Each measurement was repeated twice to ensure quasi-stationarity and the frequency range to acquire the spectra was  $f = 100$  kHz to  $f = 1$  Hz with ten points per decade. To investigate the influence of operating the cell under load and thus producing

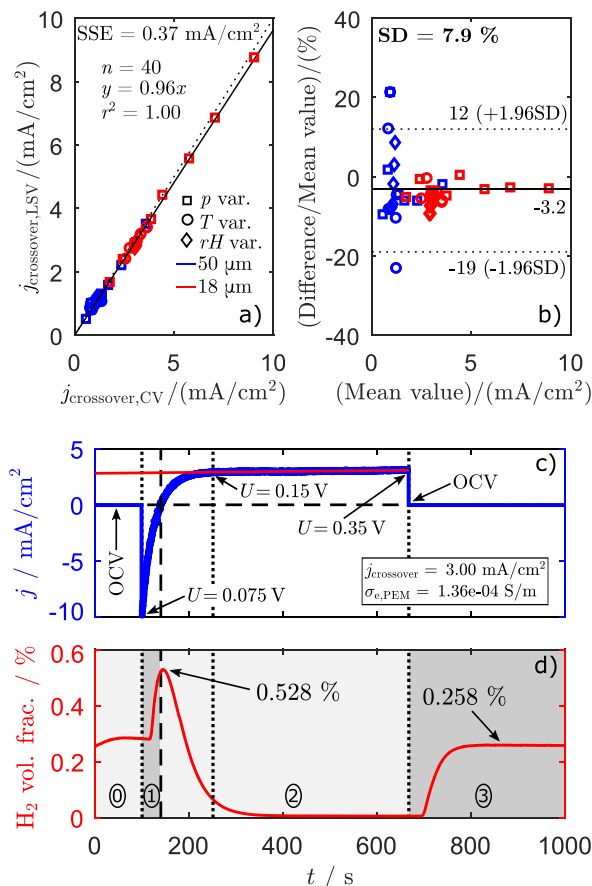


**Figure 3.** Comparison and validation of the voltammetry techniques. (a) and (b) Correlation plot and Bland-Altman plot<sup>53</sup> of  $j_{\text{crossover}}$  measured by LSV and CV for one parameter variation at a time. The red symbols are the values of the 18 μm membrane and the blue symbols the values of the 50 μm membrane. In (a), the linear fit of the data (solid line) and the bisecting line (dotted line) are also represented. In (b), the solid line represents the mean difference between the LSV and the CV values over all the data points and the (mean difference  $\pm 1.96$ -SD) lines (dotted) are also drawn. (c) and (d) exhibit a coupled LSV and mass spectrometry (cathode exhaust) measurement for the 18 μm membrane. The conditions were  $rH = 70\%$ ,  $T = 70$  °C and  $p_{\text{total}} = 1.5$  bar<sub>a</sub> and the LSV scan rate was  $0.5$  mV s<sup>-1</sup> from 70 mV to 350 mV.

water within the cathode, EIS was also conducted in H<sub>2</sub>/O<sub>2</sub> mode for current densities from  $j = 2$  A cm<sup>-2</sup> to  $j = 0.02$  A cm<sup>-2</sup>. Here, the experiments were carried out in pseudo-galvanostatic mode (called hybrid mode) by fixing the DC current and superposing the AC input signal as a voltage wave with 10 mV rms amplitude. Differential conditions were obtained by using high flow rates of 1300 sccm at the anode (dry H<sub>2</sub> flow) and 2000 sccm at the cathode (dry O<sub>2</sub> flow), thus enabling low utilizations (<13% at the anode and <5% at the cathode) and therefore avoiding gradients along the gas channels. Furthermore, channel-land inhomogeneities (or across-the-channel effects) may also arise under load but these were reduced in this study by the use of pure oxygen only and, additionally, by our particularly narrow lands (0.24 mm) on the cathode side. On the anode side such issues are less important because of the high diffusivity of hydrogen, therefore the lands can be wider to enhance heat and electrical transport. Hence, in-plane inhomogeneities were minimized, focusing the study on the through-plane layer physics.

All our EIS measurements were recorded with a system pressure of 1.5 bar<sub>a</sub>. More information about the EIS spectra and the models used for the analysis is given below.

## Results and Discussion

**Hydrogen permeation.**—First, we made sure that the CV and LSV techniques provide similar results regarding hydrogen crossover values and therefore also permeation coefficients. Figure 3a shows a correlation plot for the hydrogen crossover values acquired by CV and LSV (40 CV and 40 LSV measurements in our 25 cm<sup>2</sup> setup) during multiple parameter studies for two different MEAs. The first one is our reference state-of-the-art Gore® MEA with 18 μm PEM thickness (red symbols) and the second one is an MEA with 50 μm PEM thickness (Nafion® N212, blue symbols) used for comparison. Here, the relative humidity, temperature and pressure have been varied one by one and CV as well as LSV have been carried out in each point. The linear fit shows that there is a very high correlation between the data of both measurement techniques for both our MEAs. Even though there is very little deviation of the slope from 1 (0.96), indicating that the LSV values are slightly lower than those of the CV, this indicates that both methods produce valid results regarding the permeation properties. Thus, for our full factorial parameterization, we only use CV to shorten the measurement duration. Moreover, our MEAs showed very high electronic PEM resistances ( $R_{\text{PEM,electrical}} \gg 600$  Ωcm<sup>2</sup>) during our begin of life (no membrane thinning, no pinholes) characterizations, which proves that the cells were properly mounted and that no GDL fiber damaged the membrane, making LSV tests unnecessary. The Bland-Altman representation<sup>52,53</sup> (or mean-difference plot) of our data in Fig. 3b completes this analysis. Such a plot is useful when comparing two measurement techniques since having a good correlation does not necessarily stand for a good match between the data points. In our case it shows the difference between the CV and the LSV values (in percentage referenced by the mean value) vs the mean values and allows to confirm that LSV generally gives slightly lower results than CV. Also, this diagram demonstrates an increasing scatter of the deviation at low crossover values which might point out a decreasing accuracy.

We depict a combined LSV-MS experiment in Figs. 3c and 3d. During the measurement, the anode side was fed with 500 sccm H<sub>2</sub> and the cathode gas stream was held constant at 200 sccm N<sub>2</sub>. The cathode outlet flow was cooled down to 5 °C in order to condense and remove the water before entering the mass spectrometer. Starting from the beginning of the measurement at 75 mV at the cathode, one recognizes three important Sections that are numbered consecutively. In part 1, the cell potential is forced below the equilibrium potential leading to negative currents and thus an increase in the hydrogen concentration in the gas outlet due to the hydrogen evolution reaction. In part 2, the potential passes the OCV and the current becomes positive (the H<sub>2</sub> from crossover is oxidized within the CCL) so that the hydrogen concentration within the gas outlet drops toward zero. The third part marks the end of the LSV measurement, where the current gets back to zero and the hydrogen concentration tends slowly toward a stable value that reflects the permeation flux through the membrane. At steady-state, hydrogen concentrations in the gas stream were recorded for three different nitrogen flows (not shown here) of 200 sccm, 500 sccm and 1000 sccm and gave an average crossover flow of  $(5.3 \pm 0.2) \cdot 10^{-1}$  sccm, where the uncertainty is based on those of the mass flow controllers taken for the worst case (smallest flow rate) and on the precision of the mass spectrometer. This value can be transformed with the ideal gas law and Faraday's law and corresponds to a crossover value of  $3.1 \pm 0.1$  mA cm<sup>-2</sup> ( $5.3 \cdot 10^{-1}$  sccm corresponds to a concentration of 0.27% for a nitrogen flow of 200 sccm). This is comparable to the values measured by voltammetry methods at the same conditions and thus allows us to confirm that in H<sub>2</sub>/N<sub>2</sub> mode

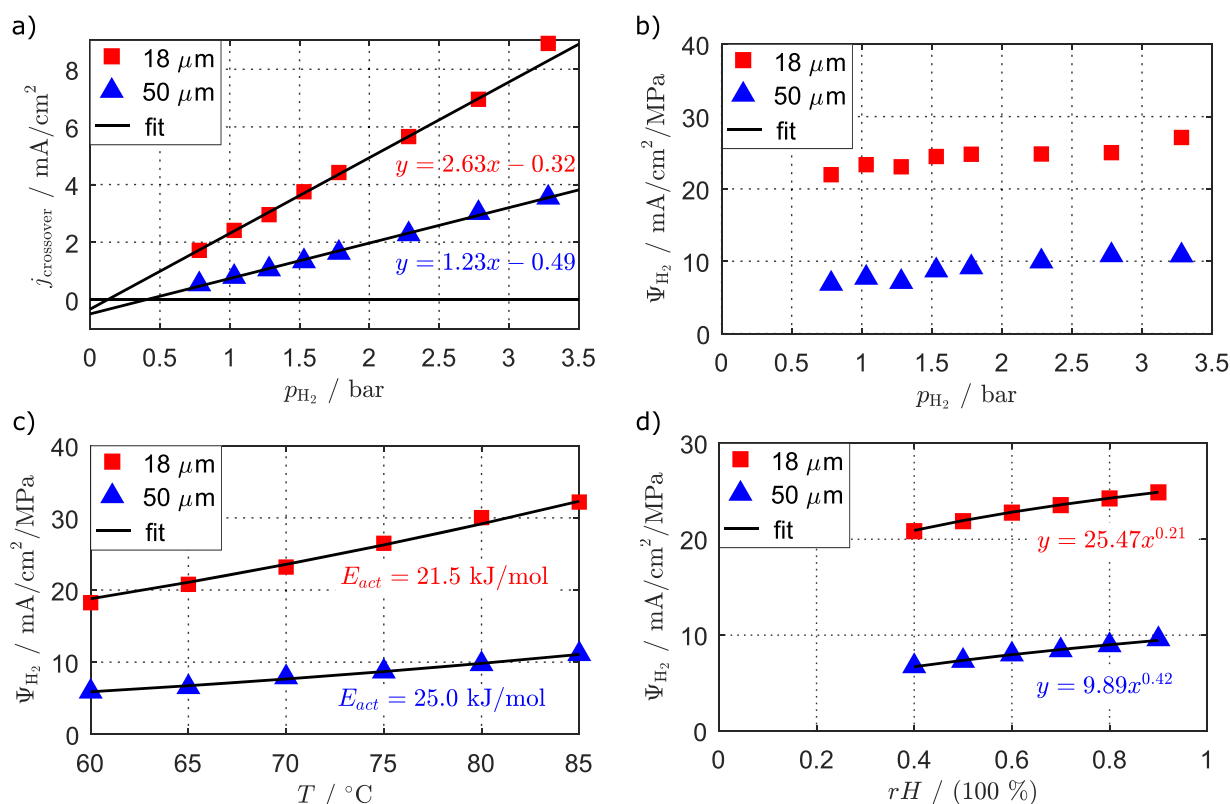
both methods (LSV/CV and MS) yield similar and thus acceptable results. However, voltammetry methods can neither measure  $N_2$  permeation or  $O_2$  permeation ( $N_2/O_2$  cell characterizations would lead to potential induced electrode degradation) accurately nor can they be used under load. For this reason, using mass spectrometry additionally could clearly be advantageous since it allows to characterize the complete permeation behavior of the membrane in situ with one single setup (for instance MS on the anode side for  $O_2$  and  $N_2$  permeation and CV/LSV on the cathode side for  $H_2$  permeation). In this study we were mainly interested in the hydrogen crossover and therefore we did not conduct further MS experiments.

In the literature, the permeation of a certain gas species  $i$  over its partial pressure  $p_i$  is usually modelled as a linear function (thickness and area specific) as follows:<sup>12</sup>

$$N_i = -\Psi_i \nabla p_i, \quad [1]$$

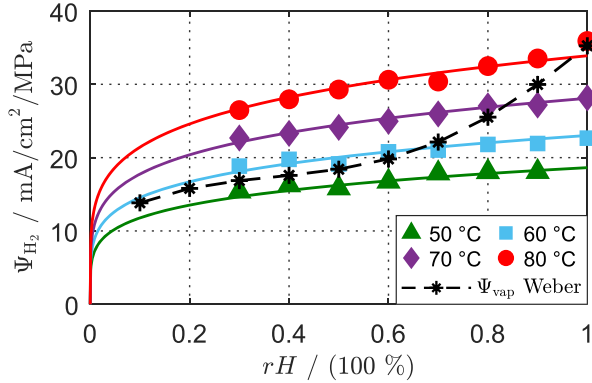
with  $N_i$  the flux of the species  $i$  in  $\text{mol}/(\text{cm}\cdot\text{s})$ ,  $\Psi_i$  its permeation coefficient (or permeance) in  $\text{mol}/(\text{cm}\cdot\text{s}\cdot\text{bar})$  and  $p_i$  its partial pressure gradient over the membrane in bar (assumption of  $p_{H_2, \text{CCL}} \approx 0$ ). The permeation coefficient is often modelled as  $\Psi = S \cdot D$ , with  $D$  being the diffusion coefficient (Fick's first law) and  $S$  the solubility (Henry's law). Figures 4a to 4d show our parameter variations used in the analysis of Figs. 3a and 3b, whereas each value corresponds to an average of the according LSV and CV measurements (see Fig. S1 available at [stacks.iop.org/JES/168/084504/mmedia](https://stacks.iop.org/JES/168/084504/mmedia) of the supplementary material for the set of CV and LSV diagrams corresponding to our pressure variation and

Fig. S2a to Fig. S2c for the thickness-normalized values of our pressure, temperature and humidity variations around the baseline conditions). To carry out the  $H_2$  pressure variations we adapted the system pressure symmetrically (identical total pressure on anode and cathode and negligible pressure drop along the channels to exclude the possibility of convective transport) between 1.0 bar<sub>a</sub> and 3.5 bar<sub>a</sub> by regulating the backpressure valves. As can be seen in Fig. 4a, the hydrogen crossover flux in our study can also be described by a linear function of the partial pressure on the anode side  $p_{H_2}$  (as in the literature) for both MEAs at baseline conditions (70% rH and 70 °C). However, our fitting curves do not go exactly through the origin and exhibit a small negative y-axis intercept, which is also shown by the slight non-constancy of the permeation coefficient over partial pressure depicted in Fig. 4b for the same dataset. Since this effect is small and as we carried out all our other permeation measurements at one given pressure of 1.5 bar<sub>a</sub> (our relevant system pressure), we chose to neglect it. Further, we reproduced the pressure variation for our 18  $\mu\text{m}$  baseline MEA over an even wider  $p_{H_2}$  range by carrying out both system pressure variation and  $H_2$  diluting at constant system pressure (see Fig. S2d). Even though the reproducibility is good (highest deviation in the relevant range is 12% at  $p_{H_2} = 0.75\text{bar}$ , decreasing rapidly with increasing pressure), the origin of the fitting curve is almost zero and shows that even small deviations at very low crossover fluxes are likely to shift the axis intercept away from zero. Hence, the permeation coefficient can be considered to be constant over the relevant  $p_{H_2}$  range within the experimental accuracy.



**Figure 4.** Crossover flux and permeation coefficients for one parameter variation at a time around the conditions  $rH = 70\%$ ,  $T = 70^\circ\text{C}$  and  $p_{\text{total}} = 1.5 \text{ bar}_a$ . The values are averaged between the CV and the LSV measured value at each point for both MEAs. The permeances were calculated by  $\Psi_{H_2} = j_{\text{crossover}}/p_{H_2}$  and the solid lines represent the locally fitted models. (a)  $H_2$  crossover flux over  $p_{H_2}$ . (b) Corresponding permeances. (c) Calculated permeance for the  $T$  variation. (d) Calculated permeance for the  $rH$  variation.





**Figure 5.** Full factorial study of the permeance over temperature and relative humidity measured by CV for the Gore® MEA. The symbols represent the experimental data and the lines the fitted model (global fit over all the conditions). Also, the Weber parameterization for  $T = 80\text{ °C}$  has been added for comparison (vapor equilibrated permeance).<sup>34</sup>

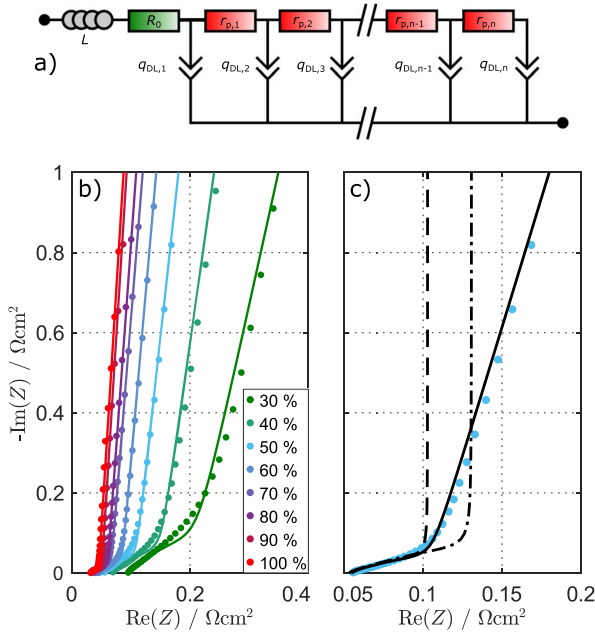


**Figure 6.** (a) Equivalent circuit model (ECM) used for fitting  $\text{H}_2/\text{N}_2$  EIS spectra. (b) Measured spectra (dots) and CNLS fit (solid lines) for each  $rH$  (from 30% to 100%) at  $T = 80\text{ °C}$ . The inductive parts are discarded from this plot. (c) Zoom on the  $rH = 50\%$  condition. The dashed line represents a simulated spectrum where all the parameters but the CPE exponent are the same ( $n_{\text{CPE}} = 1$ ) to behave as an ideal capacitance). The dash-dot line represents a fitting result with an ideal capacitance ( $n_{\text{CPE}} = 1$ ) and shows that this leads to large errors on  $R_p$ .

So far, the most heavily used parameterization of the permeation coefficient of  $\text{H}_2$  through a Nafion® membrane in the vapor-equilibrated state was given by Weber and Newman<sup>34</sup> as (in  $\text{mol}\cdot\text{cm}^{-1}\cdot\text{s}^{-1}\cdot\text{bar}^{-1}$ )

$$\Psi_{\text{vap}} = (0.29 + 2.2f_v) \cdot 10^{-11} \exp \left[ \frac{E_{\text{H}_2}}{R} \left( \frac{1}{T_{\text{ref}}} - \frac{1}{T} \right) \right], \quad [2]$$

with  $f_v$  the dimensionless water content,  $E_{\text{H}_2} = 21\text{ kJ mol}^{-1}$  and  $T_{\text{ref}} = 303\text{ K}$ , and in the liquid-equilibrated state as

$$\Psi_{\text{liq}} = 1.8 \cdot 10^{-11} \exp \left[ \frac{E_{\text{H}_2}}{R} \left( \frac{1}{T_{\text{ref}}} - \frac{1}{T} \right) \right], \quad [3]$$

independent of the water content ( $\lambda = 22$ ) and with a slightly lower activation energy  $E_{\text{H}_2} = 18\text{ kJ mol}^{-1}$ . Globally, although our membranes are from different suppliers (we do not expect identical materials), they show comparable behavior as the ratio of the measured fluxes correspond quite well to the ratio of the membrane thicknesses ( $50/18 = 2.78$ ). However, there are some deviations at large pressures, where the  $18\text{ }\mu\text{m}$  membrane shows less crossover than the  $50\text{ }\mu\text{m}$  in proportion to their thickness. This might be due to the reinforcement of the thinner membrane that acts as a supplementary barrier to permeation fluxes (see also Fig. S2a).

Figure 4c shows a temperature variation and Fig. 4d a relative humidity variation for both membranes around our baseline conditions ( $p_{\text{total}} = 1.5\text{ bar}_a$ ,  $rH = 70\%$  and  $T = 70\text{ °C}$ ). Here it is obvious that both membranes do not behave the same way because even though the fitted activation energies are consistent with the previously cited literature values for vapor-equilibrated membranes, their dependency on humidity differs by a factor of 2. The slope of the  $50\text{ }\mu\text{m}$  curve in the log-log diagram  $\log(\Psi_{\text{H}_2}) = f(\log(rH))$  is therefore twice as high as the slope of the  $18\text{ }\mu\text{m}$  curve (not shown here). Overall, the deviations in the permeance of both membranes are the largest for high pressure conditions, low temperatures and/or low relative humidities. The full factorial parameterization (Arrhenius-like ansatz) of the permeance for the  $18\text{ }\mu\text{m}$  membrane over temperature and humidity (measured at  $p_{\text{total}} = 1.5\text{ bar}_a$ ) is depicted in Fig. 5 and is ready-to-use for modeling purposes. The lines represent the global model that has been fitted to the measurement points and is in excellent agreement with the experimental data. The expression of this model (in  $\text{A cm}^{-2}\text{ MPa}^{-1}$ ) is given by

$$\Psi_{\text{H}_2} = \left( 21.33 \frac{\text{A}}{\text{cm}^2\text{MPa}} \right) (rH)^{0.20} \exp \left( -\frac{18.9\text{ kJ mol}^{-1}}{RT} \right) \quad [4]$$

This enables the calculation of the crossover flux for given conditions and thus also the estimation of the shift in the polarization current under the following two assumptions: the  $\text{H}_2$  permeation flux remains approximately constant when the cell is operated under load and all the molecules that cross the PEM are oxidized within the CCL. The first assumption holds especially when the following two effects are either negligible (low current densities) or if they compensate each other: the  $\text{H}_2$  partial pressure drop within the ACL due to the HOR that leads to less crossover, and the slightly increasing membrane hydration (at most conditions) due to the produced water that leads to more crossover. The second assumption is justified by the high potentials of the cathode and accordingly excludes the possibility of a characterization of  $\text{H}_2$  crossover under load by means of mass spectrometry. Furthermore, the importance of knowing the exact crossover amount decreases with increasing current density since its influence on the polarization drops. Thus, developing new characterization techniques to measure  $\text{H}_2$  crossover precisely under load does not seem rewarding.

Figure 5 also compares our model with the corresponding curve of  $\Psi_{\text{vap}}$  from Weber for  $T = 80\text{ °C}$  ( $\Psi_{\text{liq}} \approx 53.3\text{ mA/cm}^2/\text{MPa}$  is not represented). This curve was calculated with the Eq. 2 and the Springer water uptake isotherm<sup>31</sup> (measured at  $T = 30\text{ °C}$  and close to the Weber isotherm,<sup>34</sup> with only a small temperature influence), converted with Faraday's law and expressed for a  $18\text{ }\mu\text{m}$  thick membrane. This model is typically used in the modeling literature. One can see that neither the absolute values nor the slopes match those of our fitted model, the values are in the same order of magnitude though and therefore lie within the limits of permeation in liquid water and dry Teflon (see Fig. S3 in the supplementary material for some typical permeation values). Transforming this

diagram into a log-log plot (not shown) results in one single slope of our curves  $\log(\Psi_{H_2}) = f(\log(rH))$  of 0.2 and the temperature simply shifts the curves along the permeance axis. In this representation, the Weber data exhibits two slopes: 0.17 up to  $rH = 50\%$  and then 1.3 for the high relative humidities. This emphasizes the need for individual characterizations to accurately model different materials.

**Ionomer conductivities from  $H_2/N_2$  EIS.**—For characterizing the ionomer resistances, we carried out EIS under  $H_2/N_2$  conditions. As mentioned above, this mode of operation allows a homogeneous distribution of the physical properties within each functional layer because of the equilibrium between the ionomer phase and the gas phase, whose properties can be well controlled and adjusted by the test station. Moreover, the fact that this technique is also applied under  $H_2/N_2$  operation made it possible to carry out the measurements within the same experimental run as the measurements of the permeation properties. Flushing the cathode with  $N_2$  instead of an  $O_2$ -containing mixture inhibits faradaic currents (no reaction kinetics apart from the crossover reaction) within the cathode, thus simplifying considerably the impedance response. In addition, the anode impedance can generally be neglected. An adequate equivalent circuit model (ECM) for fitting and modelling such cell operations is shown in Fig. 6a. It is composed of an inductance  $L$  (mainly for the cables and the setup) in series with a resistor  $R_\Omega$  (or  $R_0$ ) for the electrical resistance and a blocking transmission line for the impedance response of the CCL. It is worth mentioning that in our case, the fitted values for  $L$  are almost constant at around  $8.7 \cdot 10^{-9}$  H (standard deviation is  $3.9 \cdot 10^{-10}$  H) for all the measured conditions.

The high-frequency Ohmic resistance  $R_\Omega$  is the  $x$ -axis intercept of a spectrum in the Nyquist plot (no phase shift) and contains the membrane resistance  $R_{PEM}$  as well as the electronic resistances (bulk and contact resistances) of the setup. We measured  $R_{electronic} = 15 \text{ m}\Omega \text{ cm}^2$  for these electronic resistances by recording steady-state voltage drops and impedances of the system {anode flow field || anode GDL || cathode GDL || cathode flow field} for different clamping pressures and temperatures (see Fig. S4). Therefore, we can determine the membrane contribution from the high-frequency resistance as  $R_{PEM} = R_\Omega - 15 \text{ m}\Omega \text{ cm}^2$ . Our equivalent baseline clamping pressure was 1.3 MPa, even though higher clamping pressures are possible with the setup and might improve the performance by further reducing the contact resistances. However, we decided that this was the best compromise since higher forces might damage the MEA (GDL fibers through the PEM) or the rather sensitive graphite flow field. Further, higher pressures might cause large deformations of the GDLs, thus penetrating and blocking the gas channels. Moreover, the absolute values of the electronic contact and bulk resistances are of minor importance in this study since we subtract them when determining  $R_{PEM}$ .

In the particular case of  $H_2/N_2$  EIS the charge transfer resistance  $R_{ct}$  tends to be infinitely high, thus leaving only distributed proton resistance in the upper branch of the TLM (electronic resistance of the carbon phase of the CCL is neglected) and the capacitive part of the porous electrode in each branch, modeled by a constant phase element (CPE) in our case. In the literature, ideal capacitances were usually used instead of constant phase elements (ideal behavior of the I/C interface). The spectra resulting from such a model therefore exhibit a  $45^\circ$  slope in the Nyquist plane ( $\text{Re}(Z) = -\text{Im}(Z)$ ) at high frequencies due to the frequency-dependent penetration depth of the AC signal, and a vertical line (the imaginary part increases at constant real part) at lower frequencies.<sup>42–44,51</sup> The projection of the length of the  $45^\circ$  slope on the real axis yields  $R_p/3 = R_p^{eff}$ .<sup>3,43</sup> Fig. 6b shows the EIS spectra (dots) we obtained for our whole humidity range at  $T = 80^\circ \text{C}$  and the according CNLS fitting results (solid lines) to the TLM presented in Fig. 6a. For the sake of clarity, the high-frequency inductivities have been discarded from this plot. As expected, the intersect with the  $x$ -axis shifts to higher values and the length of the  $45^\circ$  slope increases with decreasing humidity.

Spectra with an ideal behavior are also depicted exemplarily in Fig. 6c (dashed line and dash-dot line) along with our actual fit (solid line) and differ only in the value of  $R_p$ . Eikerling and Kornyshev showed the equivalence of modeling the CCL EIS response based on the system of differential equations yielding analytical solutions for some special cases, and the transmission-line-based modeling.<sup>15</sup> In the case of infinite charge transfer and negligible electronic resistances in the CCL, the impedance response is given by

$$Z_{TLM}(\omega) = \sqrt{\frac{R_p}{i\omega C_{DL}}} \coth \sqrt{i\omega C_{DL} R_p} \quad [5]$$

However, as can be seen in Figs. 6b and 6c, our spectra do not show an ideal behavior. Several authors showed the impact of inhomogeneous layer properties on the EIS signatures either by physical modeling<sup>45,54</sup> or by computing iteratively the EIS response<sup>42,55</sup> (TLM approach) for both the  $H_2/O_2$  and the  $H_2/N_2$  configuration. They calculated the impedance with different capacity and resistivity profiles in through-plane direction and Gaumont et al. even connected several TLMs with different layer thicknesses to model in-plane inhomogeneities.<sup>44</sup> They emphasized that such heterogeneous properties mainly affect the slope and the length of the proton transport response.<sup>56</sup> More recently, Obermaier et al. stated that the deviations from the  $90^\circ$  inclination at low frequencies mainly come from the EIS response of the mix of several pores with different sizes (non-homogeneous pore size distribution).<sup>47</sup> They took this distribution as well as possible side reactions and adsorption processes, into account and got fitting results that outperformed all the previous models from the literature. For our purposes though, their approaches are too complex since they need to be fed with pore size distributions, and therefore they are not suited for rapid in situ characterization of the effective ionomer resistances. In our cases the slopes were very close to  $45^\circ$  at high frequencies and to overcome the issues of the deviation from  $90^\circ$  at lower frequencies we chose constant phase elements within our TLM instead of ideal capacities (see above). This approach is quite simple and as can be seen in Fig. 6b, the model fits the experimental data correctly even though there are some deviations at dry conditions that lead to higher uncertainty on  $R_p$ . For comparison we also determined  $R_p$  graphically by taking the intercept of the  $x$ -axis and the linear fit to the low-frequency branch and subsequently subtracting  $R_\Omega$  (see Makharia et al.<sup>43</sup>). The results from this graphical evaluation differed by 10%–20% from the results of our TLM fit. However, we trust the model more especially at wet conditions since the  $R_p$  values obtained graphically depend on the chosen frequency range for the linear fit (the impedance at low frequencies is in fact not perfectly linear in the Nyquist representation) and small deviations in the slope of this fit can lead to significant relative errors on  $R_p$ . Compared to a traditional TLM approach the exponent  $n_{CPE}$  is the only free parameter added in this model. When  $n_{CPE} = 1$  the component acts as a pure capacity and when  $n_{CPE} = 0$  it acts as a resistance ( $n_{CPE} > 0.9$  in all our cases). Figure 6c shows that the error on  $R_p$  can get very large when using ideal capacities in the fitting procedure and that the value of  $R_p$  is strongly dependent on the chosen frequency range, thus emphasizing the utility of the CPEs in the TLM. The analytical solution of our slightly adapted model is

$$Z_{TLM}(\omega) = \sqrt{\frac{R_p}{Q(i\omega)^n}} \coth \sqrt{R_p Q(i\omega)^n}, \quad [6]$$

with  $n = n_{CPE}$  and  $Q$  being assimilated to  $C_{DL}$  from now on in this work. Figure 7a illustrates the fitted double layer capacity and the constant phase exponent over the relative humidity from the spectra shown in Fig. 6b, and the double layer capacity from our CV experiments at the same conditions for comparison. This shows clearly that an increasing humidity has a positive effect on both quantities. On one hand, the double layer increases, which is

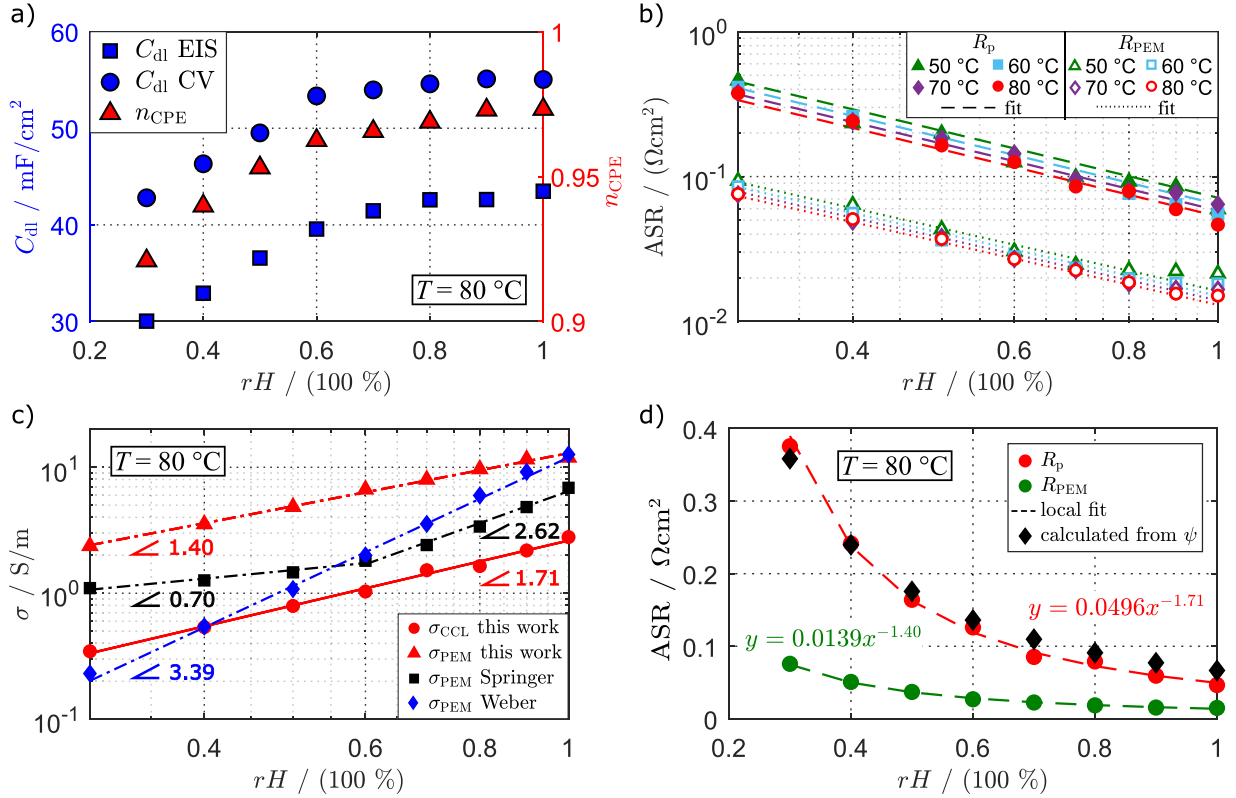


**Figure 7.** (a) Double layer capacitance  $C_{dl}$  from CV and from  $\text{H}_2/\text{N}_2$  EIS and constant phase element exponent  $n_{CPE}$  from  $\text{H}_2/\text{N}_2$  EIS vs  $rH$  at  $T = 80^\circ\text{C}$ . (b) Area specific resistances (ASR) of the membrane ( $R_{PEM}$ ) and the CCL ( $R_p$ ) for a full factorial EIS run over  $T$  and  $rH$ . The symbols are the measured data, the dashed lines show the global fit of  $R_p$  and the dotted lines the fit of  $R_{PEM}$ . (c) Calculated conductivities from the measurements at  $T = 80^\circ\text{C}$  and local fitting curve (lines) for the PEM (bulk) and the CCL (sheet) and data from Springer et al.<sup>31</sup> ( $T = 30^\circ\text{C}$ ) and Weber et al.<sup>34</sup> ( $T = 80^\circ\text{C}$ ) for comparison. (d) Measured  $R_p$  and  $R_{PEM}$  (dots), local fits (dashed lines) and  $R_p$  obtained from the fitting of the “structural parameter”  $\psi$ .

supposedly due to better contacting of the electronic and the electrolyte phase, and on the other hand the exponent tends toward 1 at high humidities, which means that the CPE behaves almost like an ideal capacity. We assume the cause of the latter effect to be more homogeneous properties of the CCL. The double layer capacity of the CV experiments shows a similar trend; however there seems to

be an approximately constant offset to the values measured by EIS. The results of the full factorial run for both  $R_p$  and  $R_{PEM}$  and the global models that have been fitted to the data can be seen in Fig. 7b (see Fig. S6 for the individual fits and Table I for the parameters). It can be observed that the models globally match the data well. For the membrane resistance, the global fit yields

**Table I.** Parameters extracted from local fits of semi-empirical power laws  $ASR = a \cdot rH^{-b}$  to the experimental data and fitted structural parameters. The exponent  $-b$  represents the slope of the curve  $ASR = f(rH)$  in the double logarithmic diagram.

$T$	Classical TLM approach				
	$a_{R_{PEM}}$	$b_{R_{PEM}}$	$a_{R_p}$	$b_{R_p}$	$\psi$
(°C)	( $\text{m}\Omega\text{cm}^2$ )	(—)	( $\text{m}\Omega\text{cm}^2$ )	(—)	(—)
50	17.6	1.34	209.9	1.06	0.076
60	15.5	1.35	80.1	1.52	0.114
70	14.7	1.32	62.3	1.49	0.141
80	13.9	1.40	49.6	1.71	0.148
New approach with “TLM + R-CPE” for 50 °C and 60 °C					
$T$	$a_{R_{PEM}}$	$b_{R_{PEM}}$	$a_{R_p}$	$b_{R_p}$	$\psi$
(°C)	( $\text{m}\Omega\text{cm}^2$ )	(—)	( $\text{m}\Omega\text{cm}^2$ )	(—)	(—)
50	17.6	1.34	62.2	1.57	0.164
60	15.5	1.35	53.2	1.72	0.155
70	14.7	1.32	58.4	1.52	0.151
80	13.9	1.40	49.4	1.59	0.170

$$R_{\text{PEM}} = (1.20 \text{ m}\Omega\text{cm}^2)(rH)^{-1.44} \exp\left(\frac{7.0 \text{ kJ mol}^{-1}}{RT}\right) \quad [7]$$

and shows very good agreement with experimental data, although at very high relative humidity the slope of the experimental curves decrease (effect increases with decreasing temperature), leading to slightly higher model errors. According to Weber and Newman,<sup>34</sup> the low activation energy could be explained by only low contribution from the vehicle mechanism in the vapor-equilibrated transport mode, and that it is even smaller than for the Grotthuss mechanism ( $11 \text{ kJ mol}^{-1}$ ) might be due to another effect: Arrhenius-like activation behavior countered by the change in the water sorption isotherm with the temperature (less water volume fraction at high temperatures).

For determining  $R_p$  properly, we had to adapt our model for the low temperature conditions and developed an approach based on two interleaved optimization loops. The reason for this is that, unlike at high temperatures as shown in Fig. 6b, the spectra at low temperatures exhibit another process that affects the evaluation of  $R_p$  when fitting only with a TLM model. This process has a very high activation energy (high resistance at cold conditions and almost absent at warm conditions) and can also be seen in  $\text{H}_2/\text{H}_2$  mode (see Fig. S5) at the same operating conditions. We have observed that it depends on the sample history (it is reversible thus not linked to degradation) and generally do not observe it under load. Additional control experiments showed that this effect originates from CO poisoning of the anode in course of the long experimentation time (we use hydrogen 5.0 and nitrogen 5.0). The slow decrease of the ECSA on the anode side due to CO adsorption on the catalyst leads to an increase of the charge transfer resistance which then gets visible in the spectra. The fact that CO poisoning is strongly temperature and time dependent<sup>57,58</sup> fits to our observation of a high activation energy in our measurements. Moreover, oxygen crossover plays a major role in keeping the anode catalyst clean (CO oxidation)<sup>13</sup> and explains why the process is only present (or at least significant) in absence of oxygen in the system ( $\text{H}_2/\text{H}_2$  or  $\text{H}_2/\text{N}_2$ ). Therefore, we strongly recommend regular recovery steps or short measurement times for future measurements under oxygen free conditions and will discuss this point further in the context of a characterization of the anode kinetics (HOR) in a forthcoming publication. In order to separate this undesired effect from the contribution of the  $R_p$  in the present dataset, we added an R-CPE element representing the anode charge transfer process in series with the TLM for the  $T = 50 \text{ }^\circ\text{C}$  and  $T = 60 \text{ }^\circ\text{C}$  conditions and fitted all the 32 spectra at the same time. The outer loop optimized the Arrhenius-like law  $R_p = a \cdot rH^{-b} \cdot \exp(E_{\text{act}}/(RT))$  for the constants  $a$ ,  $b$  and  $E_{\text{act}}$ , and passed the parameters to the inner loop to fix  $R_p$  in the individual EIS fits which optimized the ECM parameters. In the inner loop, the residual arrays of each single ECM fit were minimized. In the outer loop, we concatenated these single residual arrays to one overall residual array that was minimized. This permitted to find the optimum over the whole operating condition range and yielded the following parameterization for the proton resistance in the CCL:

$$R_p = (2.20 \text{ m}\Omega\text{cm}^2)(rH)^{-1.53} \exp\left(\frac{9.4 \text{ kJ mol}^{-1}}{RT}\right) \quad [8]$$

This demonstrates that the ionomers in the PEM and the CCL behave comparably, although the humidity dependency of the CCL appears to be a bit more pronounced. We used these parameters from our global fit as initial guesses for new individual fits of the spectra where every parameter was free apart from the double layer capacity and the CPE exponent from the TLM. The resulting resistances are

the symbols in Fig. 7b. Without taking into account the increased anode impedance at low temperatures and by fitting each spectrum individually (anode resistance effectively contained in  $R_p$ ), an activation energy of  $30 \text{ kJ mol}^{-1}$  would have been determined and would lead to erroneous conclusions. The results of the single fits to semi-empirical power laws  $\text{ASR} = a \cdot rH^{-b}$  for each temperature without fitting the additional process (classical TLM approach, “TLM data”) and the individual fits based on our adapted approach (“TLM+RQ” for  $50 \text{ }^\circ\text{C}$  and  $60 \text{ }^\circ\text{C}$ , and “TLM data 2” for  $70 \text{ }^\circ\text{C}$  and  $80 \text{ }^\circ\text{C}$ , respectively) are shown in Fig. S6 and the parameters are listed in Table I.

In Fig. 7c we expressed the effective conductivities obtained from  $\sigma_{\text{PEM}} = L_{\text{PEM}}/R_{\text{PEM}}$  ( $L_{\text{PEM}} = 18 \text{ } \mu\text{m}$ ) and  $\sigma_{\text{CCL}} = L_{\text{CCL}}/R_p$  ( $L_{\text{CCL}} = 13 \text{ } \mu\text{m}$ ) in a log-log plot in order to compare them with some well-known literature models and we displayed the slopes of the curves. Of course, these models depend on the chosen water uptake isotherm and therefore have to be analyzed carefully. The discrepancies in the slopes and the absolute values of the conductivities emphasize again the risk of simply relying on literature models and point out the need for material-specific characterization. Compared to the literature models, the conductivity of the Gore® membrane is globally higher even though the dependency on the relative humidity is lower. Heinzmann et al. also showed conductivity values in the same order of magnitude but with higher slopes (2.58–2.59) in the log-log plot  $\log \sigma = f(\log(rH))$  for Nafion® 112 and 117.<sup>17</sup> The membrane conductivity of their commercial Greenerity® H500EL2 MEA showed a humidity dependency comparable to ours (slope of 1.56), although its values were lower. Also, their CCL conductivity showed a much higher humidity dependency (slope of 2.90, comparable to that of Nafion®), pointing out that the materials used were not identical. The authors assumed a lower equivalent weight (EW) to be the reason. Also, they suggested that the smaller slopes and lower conductivities of their membrane might be caused by the reinforcement.

In our case, the slopes of the bulk and electrode conductivities are rather close. This might imply that the ionomers used in the PEM and CCL behave very similar and irrespective of the reinforcement. The fact that the reinforcement does not visibly impact the permeation process either, as discussed above, consolidates this statement. We are thus tempted to assume that their conductivities are simply related by a structural parameter  $\psi = \epsilon/\tau$ ,<sup>17,44</sup> which is the ratio of CCL porosity to tortuosity and can be estimated by

$$R_p = \frac{L_{\text{CCL}}}{L_{\text{PEM}}} \cdot \frac{R_{\text{PEM}}}{\psi} \rightarrow \psi = \frac{\sigma_{\text{CCL}}}{\sigma_{\text{PEM}}} \quad [9]$$

The example shown in Fig. 7d for  $T = 80 \text{ }^\circ\text{C}$  demonstrates that this yields indeed a good fit for a given temperature. However, the corresponding activation energies of the PEM and the CCL conductivities differ slightly and cause a small temperature dependency of this estimated structure factor (see Table I). Although this does not prove that the ionomer used in the PEM and CCL is the same, it indicates at least that their properties are alike. The global structure parameter is  $\psi = 0.155$ , averaged over all the 32 conditions based on the calibrated Arrhenius-like laws.

In this part, we have parameterized an Arrhenius-like ansatz containing also the dependency on the humidity for both  $R_{\text{PEM}}$  and  $R_p$ . In the next part, we will discuss the influence of operating the cell under load on the ionomer resistances.

**Ionomer conductivities under load.**—Knowing the ionomer resistances under well-controlled humidity and temperature conditions is very important for CCL optimization as well as for tracking degradation. However, these resistances might change when generating and transporting water and heat during real fuel cell operation. This effect must be understood in order to clarify whether

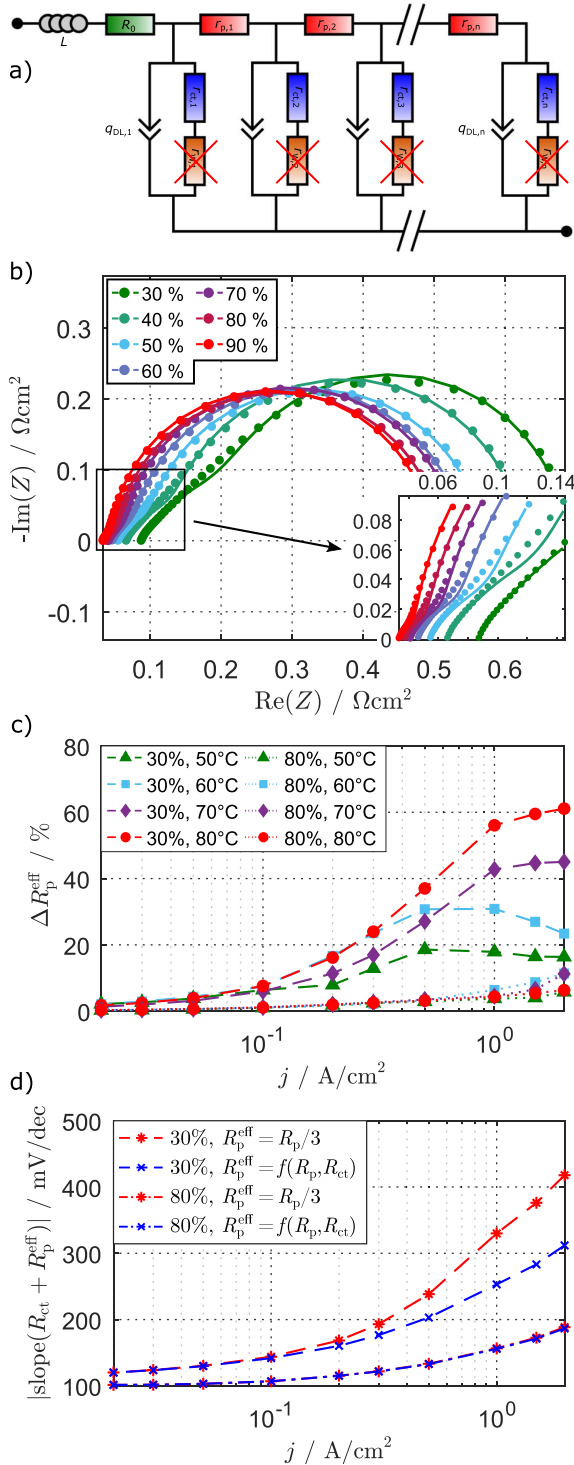


**Figure 8.** (a) ECM for  $\text{H}_2/\text{O}_2$  operation. Mass transport resistances (orange  $r_{w,i}$ ) are discarded. (b)  $rH$  variation under load at  $j = 0.1 \text{ A cm}^{-2}$  and  $T = 80 \text{ }^\circ\text{C}$ . The measured data (dots) and the individual fits (solid lines) are shown. The inductive parts are discarded from this plot. (c) Error on  $R_p^{\text{eff}}$  when calculating  $R_p^{\text{eff}} = R_p/3$  (low current model) instead of  $R_p^{\text{eff}} = f(R_p, R_{\text{ct}})$  (high current model). (d) Hypothetical equivalent local slopes of the Tafel plot caused by the ORR and  $\text{H}^+$  transport in the active layer at  $T = 80 \text{ }^\circ\text{C}$ .  $R_{\text{ct}}$  and  $R_p$  are fitted,  $R_p^{\text{eff}}$  is calculated according to (c).

knowing the resistances under equilibrium conditions is sufficient to carry out loss analyses under load (parameterizing the cathode kinetics for instance). Furthermore, investigating this can shed light on the operando water transport.

For this purpose, we recorded EIS spectra under  $\text{H}_2/\text{O}_2$  conditions for varying  $rH$ ,  $T$  and the current density  $j$ , again in a full factorial fashion. Flushing the cathode with pure oxygen minimizes the mass transport contributions over a large current density range. Therefore, we neglect oxygen transport resistances in our modeling approach. For some conditions, a small low-frequency shoulder appears in the EIS spectra (see Fig. S7) that is probably linked to mass transport at high current densities and has been discarded in this study. However, this shoulder can be fitted by a Warburg term in practice. Regarding the high amount of collected data, we targeted very short fitting durations and therefore discarded a differential-equations-based model. Here again, we opted for a TLM approach (see Fig. 8a), while this time the charge transfer resistance is not infinitely high and the individual branches thus contain R-CPE elements, leading to a closed loop in the impedance spectra at  $0.1 \text{ A cm}^{-2}$  (see Fig. 8b).

In the literature, analytical models derived from the differential equations (charge conservation and Ohmic drop in the electrolyte) or simple Randles circuits are generally used for fitting EIS data.<sup>15,17,59–62</sup> The analytical solution for the case of homogeneously distributed resistances and capacitances (homogeneously working CCL due to small currents or high humidities in our case) is well-known and is identical to the TLM with an infinite number of branches.<sup>15,51</sup> By replacing the ideal capacities by CPEs we get:

$$Z(\omega) = \frac{R_p}{\sqrt{Q(\omega)^n R_p + \frac{R_p}{R_{\text{ct}}}}} \times \coth \sqrt{R_p Q(\omega)^n + \frac{R_p}{R_{\text{ct}}}} \quad [10]$$

In this low current density case, we have  $R_p^{\text{eff}} = R_p/3$ , with  $R_p^{\text{eff}}$  being the effective resistive contribution of the proton transport within the CCL to a measured polarization curve at the same conditions. Nevertheless, the utilization of the catalyst layer drops when the cell is operated at high currents or dry conditions since the reaction front moves toward the membrane (ratio  $R_p/R_{\text{ct}}$  increases). In this case, the previously described model is not valid because the charge transfer resistance is not distributed equally over the CCL anymore. Neyerlin et al. described in detail the calculation of the profiles of current and electrolyte potential under these circumstances and how this affects the effective proton resistance  $R_p^{\text{eff}}$  of the CCL.<sup>63</sup> Based on these results, Gaumont et al. calculated the impedance iteratively for the high current regime (TLM approach) and showed the increasing deviations with the traditionally employed analytical expression for  $jR_p/b > 1$ .<sup>51</sup> Generally, the EIS response of a transmission line resembling the one depicted in Fig. 8a and composed of  $m$  elements, from the membrane interface ( $x = 0$ ) to the GDL interface ( $x = L_{\text{CCL}}$ ), can be calculated iteratively as follows ( $1 < k < m$ ).<sup>44,51,55</sup>

$$\begin{cases} Z_1 = z_{\text{ct},1}\delta x + r_{p,1}\delta x \\ Z_{k+1} = \left( \frac{1}{Z_k} + \frac{1}{z_{\text{ct},k+1}\delta x} \right)^{-1} + r_{p,k+1}\delta x \end{cases} \quad [11]$$

With constant properties (resistivity and double layer capacity) over the CCL thickness we simply have  $r_p\delta x = R_p/m$  and  $q_{\text{dl}}\delta x = Q/m$ . By introducing a CPE approach instead of ideal capacities again, we have:

$$z_{ct,k} = \left[ \left( \frac{b}{i(x_k)} \right)^{-1} + q_{dl,k}(i\omega)^n \right]^{-1}$$

$$= \left[ \frac{1 + q_{dl,k}(i\omega)^n r_{ct,k}}{r_{ct,k}} \right]^{-1} \quad [12]$$

Here,  $b$  is the Tafel slope. In order to solve this, the through-plane current distribution  $i(x)$  has to be calculated in the steady-state:<sup>51,63</sup>

$$i(x) = \frac{j}{L_{CCL}} \frac{\theta}{\tan(\theta)} \left( 1 + \tan^2 \left[ \theta \left( 1 - \frac{x}{L_{CCL}} \right) \right] \right) \quad [13]$$

where  $\theta$  is a solution of  $2\theta \tan(\theta) = R_p/R_{ct}$ . Finally, the effective proton resistance of the CCL during operation is also a function of  $R_p$  and  $R_{ct}$ , derived by Neyerlin<sup>63</sup> as

$$R_p^{\text{eff}} = \frac{R_p}{2\theta \tan(\theta)} \ln \left[ \frac{\theta}{\tan(\theta)} (1 + \tan^2 \theta) \right] \quad [14]$$

which approaches  $R_p^{\text{eff}} = R_p/3$  in the low current regime. In Fig. 8c, we show the relative error on  $R_p^{\text{eff}}$  when using this low current approximation over the whole current range. It is obvious here that the error is the highest for hot and dry conditions, reaching up to 60%. For the  $rH=80\%$  conditions, even at the highest current density  $j=2 \text{ A cm}^{-2}$ , the largest error does not exceed 10%. The fact that dry conditions are critical is also shown in Fig. 8d, where the effective slopes of the  $R_{\Omega}$ -corrected performance curves in the Tafel plot are depicted for the  $T=80^\circ\text{C}$  conditions. This plot shows that the  $\approx 10\%$  error on  $R_p^{\text{eff}}$  at  $rH=80\%$  does not influence the slope, whereas the  $\approx 60\%$  error on  $R_p^{\text{eff}}$  at  $rH=30\%$  leads to more than  $100 \text{ mV dec}^{-1}$  error on the slope at  $2 \text{ A cm}^{-2}$ . The fact that the 10% error at high humidities does not influence the slope at all is due to the low values taken by  $R_p$ . Thus, at humid conditions, even larger errors on  $R_p$  have no significant influence on the performance analysis.

Gaumont et al. showed that this iterative approach perfectly matches the general solution of the system of differential equations obtained numerically with a finite differences solver in MATLAB.<sup>51</sup> Also, it is worth mentioning that we compared these results with an even more elaborate model containing also Fick's diffusion law for the  $\text{O}_2$  transport resistance in the CCL and even in the GDL through a Robin type boundary. This model implements a Butler-Volmer description for the reaction kinetics instead of the Tafel approximation (see Chapter 5 from Kulikovskiy's book<sup>54</sup>). In the case of very high diffusivities, the mass transport resistances drop sharply and the simulated spectra then perfectly match those obtained from the two other models described above. Although the effects of the presence of liquid water on the potential and current distribution are neglected, the iterative model we used is, to our knowledge, the most accurate one for rapid EIS fitting under  $\text{H}_2/\text{O}_2$  conditions. Heinzmann et al. also implemented a Warburg term in series to account for mass transport effects at high currents or low  $\text{O}_2$  partial pressures, but they modeled the porous electrode with the low current analytical solution of the transmission line.<sup>17</sup>

Thanks to the above-described impedance model, we tracked the changes in the ionomer resistances over the current density in a full factorial way. We varied  $rH$  between 30% and 90%,  $T$  between  $50^\circ\text{C}$  and  $80^\circ\text{C}$  and the current density  $j$  between  $0.02 \text{ A cm}^{-2}$  and  $2 \text{ A cm}^{-2}$ . The results of this study are depicted in Fig. 9 for  $50^\circ\text{C}$  and  $80^\circ\text{C}$ , whereas the results for  $60^\circ\text{C}$  and  $70^\circ\text{C}$  can be found in Fig. S8. In general, both resistances decrease faster at cold conditions with rising current density. We believe that three combining effects are at play: the higher water uptake by the ionomer at lower temperatures, the faster saturation of the gas phase

when producing a given quantity of water, and the slower water removal (lower desorption and evaporation rate as well as lower diffusion coefficients). Moreover, as can be seen, taking the parameterized resistances from the  $\text{H}_2/\text{N}_2$  study at low humidities ( $rH < 60\%$ ) to correct the polarization curves would lead to an inaccurate analysis. This is not an issue for the membrane resistance since  $R_{\text{PEM}}$  can be measured easily during operation by either one of two methods. The first one is continuously logging a certain high frequency, which is an approximation since the operating-condition-dependent frequency of the  $x$ -axis intercept can lead to up to 20% relative error on  $R_{\Omega}$  when evaluating  $\text{Re}(Z(1 \text{ kHz}))$  (intercept happens between 5 kHz and 10 kHz with our setup). The second and more suitable method is recording more extensive high-frequencies EIS spectra at given discrete current densities. The latter technique is also valid for  $R_p$ , but only at small current densities because complete spectra are needed in order to properly separate  $R_p$  from  $R_{ct}$  (time constants are merging) in the high current regime. To get at least a quick rough approximation of the change in the conductivities over the current density, one could record a spectrum at a low current and another at a high current and interpolate logarithmically (curves in Figs. 9c and 9d are linear on a logarithmic current scale). As can be seen, this technique also yields better results with increasing humidity.

For all the recorded conditions,  $R_{\text{PEM}}$  seems to converge to its value measured at  $rH=100\%$  in the  $\text{H}_2/\text{N}_2$  study without ever dropping below. However,  $R_p$  tends to drop below its value at  $rH=100\%$  for most of the conditions (apart from hot and dry conditions), most likely indicating the presence of liquid water within the CCL. Based on the calibration curves obtained under well-controlled conditions from the  $\text{H}_2/\text{N}_2$  tests (data given in Table I), we can estimate the effective relative humidity during real fuel cell operation ( $\text{H}_2/\text{O}_2$ ). Gaumont et al. did this to study along-channel effects on the ionomer resistances related to current, stoichiometry and gas humidification in a segmented cell setup.<sup>51</sup> To our knowledge, this has never been applied to single differential cells before.

Nonetheless, regarding the thickness of the electrolyte (bulk membrane), it is critical in our opinion to evaluate effective humidities for the PEM in this manner since substantial gradients in the water distribution may arise in the through-plane direction during operation, caused essentially by the production of water in the CCL, the electroosmotic drag and the water backdiffusion. Accordingly, the local water content of the membrane might deviate from the effective content calculated by the EIS resistances. Hence, we discard this approach and prefer to work with the effective proton resistance  $R_{\text{PEM}}$  of the membrane. For the thinner CCL, we assume a homogeneous water distribution since the ionomer is in contact with the gas phase and the liquid phase through the whole layer thickness. This leads to a more homogeneous water distribution in the CCL in comparison to the PEM, which we assume is only in contact with the fluid phases at its boundaries. Thus, we can carry out such analyses of equivalent humidities in the CCL. Figure 10 depicts the current at which the proton resistance in the CCL corresponds to the fully saturated state ( $rH=100\%$  in the  $\text{H}_2/\text{N}_2$  mode) depending on the relative humidity in the gas channel, for the four temperatures used in our work. A plot of  $R_p$  vs.  $rH$  (example in Fig. 7d) shows small slopes (curve gets flat) at high humidities, meaning that an important change in the humidity leads only to a small change in the resistance. This means in turn that the values depicted in Fig. 10 are subject to high uncertainties since small errors in the evaluation of  $R_p$  lead to large errors in the calculation of the effective  $rH$  and therefore in the currents. Nevertheless, this Fig. emphasizes the huge influence of the temperature on the operation of the cell. At low temperatures, the CCL is rapidly well-humidified, independently of the relative humidity of the gas supply. On the contrary, at high temperatures the humidity of the CCL seems to change only little during operation, meaning that if the gas supply is rather dry, then the CCL will also stay dry within a large range of current densities. Such analyses in combination with analyses of the mass transport

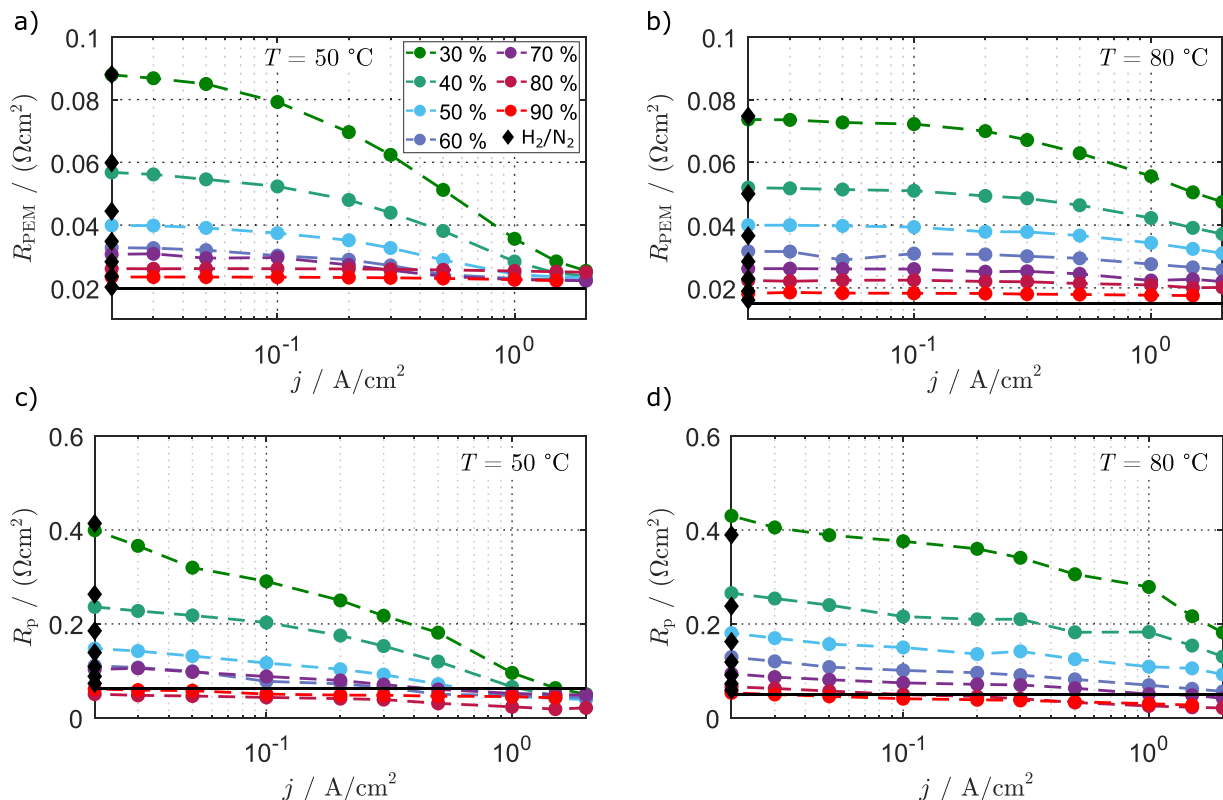


**Figure 9.** Representation of the ionomer resistances  $R_{PEM}$  and  $R_p$  obtained under load for several gas stream humidities ( $rH = 30\%$  to  $rH = 90\%$ ). The values have been obtained by fitting to the ECM shown in Fig. 8a. For  $R_{PEM}$ ,  $15\text{ m}\Omega\text{cm}^2$  caused by contact and bulk resistances of the setup are subtracted. The black diamonds represent the resistances from the  $\text{H}_2/\text{N}_2$  operation and the black solid lines the  $rH = 100\%$  conditions. (a) Membrane resistances at  $T = 50\text{ }^\circ\text{C}$ , (b) Membrane resistances at  $T = 80\text{ }^\circ\text{C}$ , (c) CCL proton resistances at  $T = 50\text{ }^\circ\text{C}$  and (d) CCL proton resistances at  $T = 80\text{ }^\circ\text{C}$ .

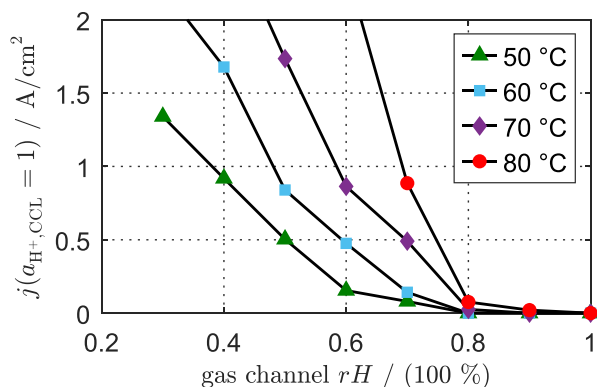


**Figure 10.** Estimation of the current densities at which the equivalent relative humidity in the CCL reaches 100% depending on the gas channel humidity and the temperature.

contributions can be very helpful in finding optimized operating conditions (tradeoff between current density and humidification) regarding performance and ageing.

### Conclusions

In this study, we extensively investigated the ionomer permeation and conductivity properties of PEMFC single cells. We carried out voltammetry and EIS measurements for this purpose and addressed

the lack of simple full factorial in situ characterization on real cell setups in the literature.

One-at-a-time parameter variations confirmed the equivalence of the LSV and the CV methods regarding  $\text{H}_2$  crossover based on a statistical analysis and permitted to understand the influence of the operating conditions ( $rH$ ,  $T$ ,  $p_{\text{H}_2}$ ) on permeation through the PEM. The two techniques were further validated against a mass spectrometric quantification of the hydrogen crossover flux. A full factorial experiment served to fit an empirical law consisting of an Arrhenius-type prefactor for the temperature influence and a power law for the dependency on humidity. This can be used to correct polarization curves for hydrogen crossover during performance loss analyses or can even be implemented directly into simulation models.

Subsequently, we also conducted EIS studies under well-controlled temperature and humidity conditions ( $\text{H}_2/\text{N}_2$ ) in a full factorial fashion. These spectra allowed us to extract the ionomer resistance of the membrane and of the cathode catalyst layer separately by fitting a blocking transmission line model. We slightly adjusted this model by replacing the capacities with constant phase elements to take into account the deviations from the ideal behavior at low frequencies due to inhomogeneities within the catalyst layer. Besides, we reported a non-negligible anode process that gets significant at low temperatures and alters the values of  $R_p$ . Therefore, we connected an R-CPE element in series with our TLM to capture this contribution in a global optimization loop in which all the spectra were fitted simultaneously. Our models showed a good match with the experimental data and the use of CPEs in our TLM turned out to be particularly important for low humidities. Based on the obtained resistances we calibrated ready-to-use models

for the ionomer resistances, which is especially relevant for modeling purposes.

Furthermore, we conducted EIS measurements under load to investigate the influence of the produced water on the ionomer resistances. Here, again, we used a transmission line model to determine the ionomer resistances. In contrast to the H<sub>2</sub>/N<sub>2</sub> study, we selected an iterative model ("high current model") that allows to account for the non-uniform through-plane distribution of the electrolyte potential and the current density, which gets substantial with decreasing humidities and increasing cell current. This model enables very short fitting durations compared to a modelling approach based on the complete full boundary value problem for which an analytical solution is not known and hence has to be solved numerically. With this evaluation of the ionomer resistances over the cell current, the huge influence of the temperature and the gas channel humidity became apparent. At high temperatures, the resistances decrease rather slowly over current density, whereas at low temperatures they drop sharply and seem to converge to one given value that is independent of the gas channel humidity. Moreover, we could estimate the current density at which the protonic resistance of the CCL corresponds to a fully saturated state depending on the temperature and the gas channel humidity. This opens the door to optimizing the operating conditions regarding cell performance.

Finally, the comparison between our calibrated models (permeation and protonic resistances) and data from literature (for similar yet not identical materials) showed differences in the absolute values and in the trends regarding humidity, even though the activation energies are comparable. This emphasizes the need to apply rapid and proper in situ characterization for the specific materials of interest when creating PEMFC models.

#### Acknowledgments

The authors thank SGL® Carbon for providing the gas diffusion layer samples and Gore® for helpful discussions. Niklas Hensle is gratefully acknowledged for his support in carrying out the permeation measurements.

#### ORCID

Christophe Gerling  <https://orcid.org/0000-0002-7918-6973>

#### References

- L. Carrette, K. A. Friedrich, and U. Stimming, "Fuel Cells-Fundamentals and Applications." *Fuel Cells*, 1, 5 (2001).
- Y. Wang, D. F. Ruiz Diaz, K. S. Chen, Z. Wang, and X. C. Adroher, "Materials, technological status, and fundamentals of PEM fuel cells—A review." *Mater. Today*, 32, 178 (2020).
- K. C. Neyerlin, W. Gu, J. Jome, and H. A. Gasteiger, "Determination of Catalyst Unique Parameters for the Oxygen Reduction Reaction in a PEMFC." *J. Electrochem. Soc.*, 153, A1955 (2006).
- D. R. Baker, D. A. Caulk, K. C. Neyerlin, and M. W. Murphy, "Measurement of Oxygen Transport Resistance in PEM Fuel Cells by Limiting Current Methods." *J. Electrochem. Soc.*, 156, B991 (2009).
- G. S. Harzer, J. N. Schwämmlein, A. M. Damjanović, S. Ghosh, and H. A. Gasteiger, "Cathode Loading Impact on Voltage Cycling Induced PEMFC Degradation: A Voltage Loss Analysis." *J. Electrochem. Soc.*, 165, F3118 (2018).
- M. Heinzmann, A. Weber, and E. Ivers-Tiffée, "Advanced impedance study of polymer electrolyte membrane single cells by means of distribution of relaxation times." *Journal of Power Sources*, 402, 24 (2018).
- R. Alink, R. Singh, P. Schneider, K. Christmann, J. Schall, R. Keding, and N. Zamel, "Full Parametric Study of the Influence of Ionomer Content, Catalyst Loading and Catalyst Type on Oxygen and Ion Transport in PEM Fuel Cell Catalyst Layers." *Molecules*, 25, 1523 (2020).
- A. Kusoglu and A. Z. Weber, "New Insights into Perfluorinated Sulfonic-Acid Ionomers." *Chem. Rev.*, 117, 987 (2017).
- S. J. Peighambaroust, S. Rowshanzamir, and M. Amjadi, "Review of the proton exchange membranes for fuel cell applications." *International Journal of Hydrogen Energy*, 35, 9349 (2010).
- S. A. Vilekar and R. Datta, "The effect of hydrogen crossover on open-circuit voltage in polymer electrolyte membrane fuel cells." *Journal of Power Sources*, 195, 2241 (2010).
- C. Francia, V. S. Ijeri, S. Specchia, and P. Spinelli, "Estimation of hydrogen crossover through Nafionmembranes in PEMFCs." *Journal of Power Sources*, 196, 1833 (2011).
- R. K. Ahluwalia and X. Wang, "Buildup of nitrogen in direct hydrogen polymer-electrolyte fuel cell stacks." *Journal of Power Sources*, 171, 63 (2007).
- F. Sapountzi, M. N. Tsampas, and C. G. Vayenas, "Electrocatalysis and electrochemical promotion of CO oxidation in PEM fuel cells: the role of oxygen crossover." *Topics in Catalysis*, 44, 461 (2007).
- V. A. Sethuraman, J. W. Weidner, A. T. Haug, S. Motupally, and L. V. Protsailo, "Hydrogen Peroxide Formation Rates in a PEMFC Anode and Cathode." *J. Electrochem. Soc.*, 155, B50 (2008).
- M. Eikerling and A. A. Kornyshev, "Electrochemical impedance of the cathode catalyst layer in polymer electrolyte fuel cells." *Journal of Electroanalytical Chemistry*, 475, 107 (1999).
- N. Wagner and K. A. Friedrich, "Application of Electrochemical Impedance Spectroscopy for Fuel Cell Characterization: PEFC and Oxygen Reduction Reaction in Alkaline Solution." *Fuel Cells*, 9, 237 (2009).
- M. Heinzmann, A. Weber, and E. Ivers-Tiffée, "Impedance modelling of porous electrode structures in polymer electrolyte membrane fuel cells." *Journal of Power Sources*, 444, 227279 (2019).
- U. Reimer, Y. Cai, R. Li, D. Froning, and W. Lehnert, "Time Dependence of the Open Circuit Potential of Platinum Disk Electrodes in Half Cell Experiments." *J. Electrochem. Soc.*, 166, F3098 (2019).
- J. Larminie and A. Dicks, *Fuel cell systems explained* (Wiley, Chichester, West Sussex) 2nd ed. (2003).
- J. Zhang, Y. Tang, C. Song, J. Zhang, and H. Wang, "PEM fuel cell open circuit voltage (OCV) in the temperature range of 23C to 120C." *Journal of Power Sources*, 163, 532 (2006).
- T. Sakai, H. Takenaka, N. Wakabayashi, Y. Kawami, and E. Torikai, "Gas permeation properties of solid polymer electrolyte (SPE) membranes." *J. Electrochem. Soc.*, 132, 1328 (1985).
- Tetsuo Sakai, Hiroyasu Takenaka, and Eiichi Torikai, "Gas diffusion in the dried and hydrated Nafions." *J. Electrochem. Soc.*, 133, 88 (1986).
- K. Broka and P. Ekdunge, "Oxygen and hydrogen permeation properties and water uptake of Nafion 117 membrane and recast film for PEM fuel cell." *Journal of applied electrochemistry*, 27, 117 (1997).
- Felix N. Büchi, M. Wakizoe, and S. Srinivasan, "Microelectrode investigation of oxygen permeation in perfluorinated proton exchange membranes with different equivalent weights." *J. Electrochem. Soc.*, 143, 927 (1996).
- P. Gode, G. Lindbergh, and G. Sundholm, "In-situ measurements of gas permeability in fuel cell membranes using a cylindrical microelectrode." *Journal of Electroanalytical Chemistry*, 518, 115 (2002).
- Z. Ogumi, Z. Takehara, and S. Yoshizawa, "Gas permeation in SPE method: I. Oxygen permeation through Nafion and NEOSEPTA." *J. Electrochem. Soc.*, 131, 769 (1984).
- K. D. Baik and M. S. Kim, "Characterization of nitrogen gas crossover through the membrane in proton-exchange membrane fuel cells." *International Journal of Hydrogen Energy*, 36, 732 (2011).
- K. D. Baik, B. K. Hong, and M. S. Kim, "Effects of operating parameters on hydrogen crossover rate through Nafion membranes in polymer electrolyte membrane fuel cells." *Renewable Energy*, 57, 234 (2013).
- A. Jung, J. Oh, K. Han, and M. S. Kim, "An experimental study on the hydrogen crossover in polymer electrolyte membrane fuel cells for various current densities." *Applied Energy*, 175, 212 (2016).
- D. M. Bernardi and M. W. Verbrugge, "A mathematical model of the solid-polymer-electrolyte fuel cell." *J. Electrochem. Soc.*, 139, 2477 (1992).
- T. E. Springer, "Polymer Electrolyte Fuel Cell Model." *J. Electrochem. Soc.*, 138, 2334 (1991).
- T. F. Fuller, "Solid-polymer-electrolyte fuel cells." *PhD thesis*, Lawrence Berkeley Lab., CA (United States of America) (1992).
- M. Eikerling and A. Kornyshev, "Modelling the performance of the cathode catalyst layer of polymer electrolyte fuel cells." *Journal of Electroanalytical Chemistry*, 453, 89 (1998).
- A. Z. Weber and J. Newman, "Transport in Polymer-Electrolyte Membranes." *J. Electrochem. Soc.*, 151, A311 (2004).
- A. Z. Weber and J. Newman, "Transport in Polymer-Electrolyte Membranes." *J. Electrochem. Soc.*, 150, A1008 (2003).
- R. Vetter and J. O. Schumacher, "Experimental parameter uncertainty in proton exchange membrane fuel cell modeling. Part I: Scatter in material parameterization." *Journal of Power Sources*, 438, 227018 (2019).
- T. E. Springer, M. S. Wilson, and S. Gottesfeld, "Modeling and experimental diagnostics in polymer electrolyte fuel cells." *J. Electrochem. Soc.*, 140, 3513 (1993).
- H. Iden, A. Ohma, and K. Shinohara, "Analysis of Proton Transport in Pseudo Catalyst Layers." *J. Electrochem. Soc.*, 156, B1078 (2009).
- K. Cooper, "Characterizing through-plane and in-plane ionic conductivity of polymer electrolyte membranes." *ECS Trans.*, 41, 1371 (2011).
- Z. Siroma, J. Hagiwara, K. Yasuda, M. Inaba, and A. Tasaka, "Simultaneous measurement of the effective ionic conductivity and effective electronic conductivity in a porous electrode film impregnated with electrolyte." *Journal of Electroanalytical Chemistry*, 648, 92 (2010).
- N. Wagner, T. Kaz, and K. A. Friedrich, "Investigation of electrode composition of polymer fuel cells by electrochemical impedance spectroscopy." *Electrochimica Acta*, 53, 7475 (2008).
- M. C. Lefebvre, R. B. Martin, and P. G. Pickup, "Characterization of ionic conductivity profiles within proton exchange membrane fuel cell gas diffusion electrodes by impedance spectroscopy." *Electrochemical and Solid State Letters*, 2, 259 (1999).



43. R. Makharia, M. F. Mathias, and D. R. Baker, "Measurement of Catalyst Layer Electrolyte Resistance in PEMFCs Using Electrochemical Impedance Spectroscopy." *J. Electrochem. Soc.*, **152**, A970 (2005).
44. T. Gaumont, G. Maranzana, O. Lottin, J. Dillet, S. Didierjean, J. Pauchet, and L. Guétaz, "Measurement of protonic resistance of catalyst layers as a tool for degradation monitoring." *International Journal of Hydrogen Energy*, **42**, 1800 (2017).
45. D. Gerteisen, "Impact of inhomogeneous catalyst layer properties on impedance spectra of polymer electrolyte membrane fuel cells." *J. Electrochem. Soc.*, **162**, F1431 (2015).
46. T. Reshetenko and A. Kulikovskiy, "Impedance spectroscopy study of the PEM fuel cell cathode with nonuniform nafion loading." *J. Electrochem. Soc.*, **164**, E3016 (2017).
47. M. Obermaier, A. S. Bandarenka, and C. Lohri-Tymozhynsky, "A Comprehensive Physical Impedance Model of Polymer Electrolyte Fuel Cell Cathodes in Oxygen-free Atmosphere." *Sci. Rep.*, **8**, 4933 (2018).
48. T. Biegler, D. A. J. Rand, and R. Woods, "Limiting oxygen coverage on platinumized platinum; relevance to determination of real platinum area by hydrogen adsorption." *Journal of Electroanalytical Chemistry and Interfacial Electrochemistry*, **29**, 269 (1971).
49. S. Trasatti and O. A. Petrii, "Real surface area measurements in electrochemistry." *Journal of Electroanalytical Chemistry*, **327**, 353 (1992).
50. W. Li and A. M. Lane, "Resolving the HUPD and HOPD by DEMS to determine the ECSA of Pt electrodes in PEM fuel cells." *Electrochemistry Communications*, **13**, 913 (2011).
51. T. Gaumont, G. M. Olivier Lottin, J. Dillet, L. Guétaz, and J. Pauchet, "In Operando and Local Estimation of the Effective Humidity of PEMFC Electrodes and Membranes." *J. Electrochem. Soc.*, **164**, F1535 (2017).
52. J. M. Bland and D. G. Altman, "Statistical methods for assessing agreement between two methods of clinical measurement." *The Lancet*, **327**, 307 (1986).
53. R. Klein. Bland-Altman and Correlation Plot, 2020. <https://www.mathworks.com/matlabcentral/fileexchange/45049-bland-altman-and-correlation-plot>.
54. A. A. Kulikovskiy, "Analytical Models for PEM Fuel Cell Impedance." *Self-publishing, Eisma* 121 (2018), Self-publishing, Eisma.
55. X. Ren and P. G. Pickup, "Simulation and analysis of the impedance behavior of electroactive layers with non-uniform conductivity and capacitance profiles." *Electrochimica Acta*, **46**, 4177 (2001).
56. T. Gaumont, "Résistance protonique d'électrodes de piles à combustible à membrane (PEMFC): effets de l'humidité et des dégradations." *PhD thesis*, (2017).
57. J. Kim, "Characterization of CO tolerance of PEMFC by ac impedance spectroscopy." *Solid State Ionics*, **140**, 313 (2001).
58. N. Wagner and E. Gülzow, "Change of electrochemical impedance spectra (EIS) with time during CO-poisoning of the Pt-anode in a membrane fuel cell." *Journal of Power Sources*, **127**, 341 (2004).
59. T. E. Springer, T. A. Zawodzinski, M. S. Wilson, and S. Gottesfeld, "Characterization of polymer electrolyte fuel cells using AC impedance spectroscopy." *J. Electrochem. Soc.*, **143**, 587 (1996).
60. S. Cruz-Manzo and R. Chen, "An electrical circuit for performance analysis of polymer electrolyte fuel cell stacks using electrochemical impedance spectroscopy." *J. Electrochem. Soc.*, **160**, F1109 (2013).
61. S. Cruz-Manzo and R. Chen, "A generic electrical circuit for performance analysis of the fuel cell cathode catalyst layer through electrochemical impedance spectroscopy." *Journal of Electroanalytical Chemistry*, **694**, 45 (2013).
62. J. J. Giner-Sanz, E. M. Ortega, and V. Pérez-Herranz, "Mechanistic equivalent circuit modelling of a commercial polymer electrolyte membrane fuel cell." *Journal of Power Sources*, **379**, 328 (2018).
63. K. C. Neyerlin, W. Gu, J. Jome, A. Clark, and H. A. Gasteiger, "Cathode Catalyst Utilization for the ORR in a PEMFC." *J. Electrochem. Soc.*, **154**, B279 (2007).

## 4.2 PEM Single Cells under Differential Conditions: Full Factorial Parameterization of the ORR and HOR Kinetics and Loss Analysis

In the second publication [24], the characterization of the macro-homogeneous layer properties started in the first publication was pursued. Based on differential cell measurements, the focus was set on the parameterization of the anode (HOR) and cathode (ORR) kinetics, followed by a loss analysis and critical discussion of the relevance of oxygen mass transport. First, EIS signatures of the proton pump mode ( $\text{H}_2/\text{H}_2$  configuration) were investigated at OCV by carrying out systematic variations of the relative humidity  $RH$ , the temperature  $T$  and the gas concentration  $x_{\text{H}_2}$  by diluting hydrogen with nitrogen. This was complemented by DRT analyses and clearly showed processes with distinct time constants that are strongly dependent on both humidity and hydrogen concentration. The high-frequency loop is in fact composed of at least two separate processes and was assigned to the combination of HOR kinetics and proton transport. The low-frequency loop is expected to be linked to the interplay of the charge transfer resistance  $R_{\text{ct}}$  and the proton transport resistance  $R_{\text{p}}$  in the TLM caused by slow water management effects combined with hydrogen transport contributions, even though it could not be finally assigned. Then, the importance to clean the catalyst from adsorbates to get meaningful data was emphasized and a new CO recovery protocol for both electrodes was introduced. By sweeping the cell voltage between -0.9 V and 0.9 V, this protocol oxidates parasitic adsorbates alternately in both electrodes. This permitted an accurate parameterization of the linear HOR kinetics and an activation energy of  $18 \text{ kJ mol}^{-1}$  was found.

After this, based on the ionomer resistances and hydrogen permeation coefficients parameterized in the first publication shown in section 4.1, steady-state polarization curves were corrected for the ohmic contributions and hydrogen crossover and the low-current parts of these corrected curves were used to fit the parameters of a simple Tafel model for the ORR kinetics. With the  $\text{H}_2/\text{O}_2$  dataset made of a full factorial variation of  $RH$ ,  $T$ ,  $p_{\text{O}_2}$  and  $j$ , an activation energy of  $71 \text{ kJ mol}^{-1}$  was determined for the effective ORR exchange current density, a reaction order  $\gamma$  of 0.5 and a transfer coefficient  $\alpha_c$  of 1, representing a Tafel slope (TS) of around -70 mV/dec. Moreover, it was demonstrated that the ORR kinetics are mostly independent of the relative humidity.

Finally,  $\text{O}_2$  mass transport was examined by both SLC and TLC measurements and a model for the oxygen transport resistance  $R_{\text{O}_2,\text{SLC}}$  which has an activation energy of  $11 \text{ kJ mol}^{-1}$  was parameterized. Based on all the previous results, a loss contribution analysis was critically discussed. It was concluded that the accuracy of the loss correction decreases with increasing current density and thus a potential-dependent change of the Tafel slope could not clearly be proven. However, the data showed that such effects do not need to be taken into account for cathodic half-cell potentials above 0.8 V. Nevertheless, it was pointed out that, even at low current densities, discrepancies between a steady-state polarization-based and a capacitive EIS-based evaluation of the TS contain information about more complex mechanisms at play.

This publication was written by the first author and commented by the three co-authors. The polarization curves as well as all the other experiments (CV, LSV, EIS, limiting current, heliox and  $H_2/H_2$  measurements) were designed by the first author and carried out by the first author under the advice of M. Hanauer and U. Berner. The test station used was newly commissioned and completely automated by the first author for this work. Data analysis and interpretation were performed by the first author and results were discussed with the three co-authors. The open access article is distributed under the terms of the Creative Commons Attribution Non-Commercial No Derivatives 4.0 International License (CC BY-NC-ND 4.0) and may be accessed at <http://dx.doi.org/10.1149/1945-7111/ac44ba>.

C. Gerling, M. Hanauer, U. Berner, and K. A. Friedrich, "PEM single cells under differential conditions: full factorial parameterization of the ORR and HOR kinetics and loss analysis." *J. Electrochem. Soc.*, **169**, 0145 (2022).



## PEM Single Cells under Differential Conditions: Full Factorial Parameterization of the ORR and HOR Kinetics and Loss Analysis

Christophe Gerling,<sup>1,2,z</sup> Matthias Hanauer,<sup>1</sup> Ulrich Berner,<sup>1</sup> and K. Andreas Friedrich<sup>2,3</sup>

<sup>1</sup>Robert Bosch GmbH, Corporate Research, Robert-Bosch-Campus 1, Renningen 71272, Germany

<sup>2</sup>Institute for Building Energetics, Thermotechnology and Energy Storage (IGTE), University of Stuttgart, Pfaffenwaldring 6, Stuttgart 70569, Germany

<sup>3</sup>Institute of Engineering Thermodynamics, German Aerospace Center (DLR), Pfaffenwaldring 38-40, Stuttgart 70569, Germany

The anode and cathode kinetics are parameterized based on differential cell measurements. Systematic parameter variations are evaluated to disentangle the dependencies of the electrochemical impedance spectroscopy (EIS) signatures in H<sub>2</sub>/H<sub>2</sub> mode. We introduce a new CO recovery protocol for both electrodes that enables to accurately characterize the hydrogen oxidation reaction (HOR) kinetics. Then, we demonstrate that a compact Tafel kinetics law captures the oxygen reduction reaction (ORR) kinetics for a full factorial grid of conditions, covering a wide range of relative humidities (*rH*), temperatures, oxygen partial pressures and current densities. This yields the characteristic activation energy and effective reaction order, and we reconcile models that make different assumptions regarding the *rH* dependency. Moreover, we analyze O<sub>2</sub> transport contributions by steady-state and transient limiting current techniques and heliox measurements. Although the rising uncertainty of loss corrections at high current densities makes it impossible to unambiguously identify an intrinsic potential-dependent change of the Tafel slope, our data support that such effect needs not be considered for steady-state cathodic half-cell potentials above 0.8 V.

© 2022 The Author(s). Published on behalf of The Electrochemical Society by IOP Publishing Limited. This is an open access article distributed under the terms of the Creative Commons Attribution Non-Commercial No Derivatives 4.0 License (CC BY-NC-ND, <http://creativecommons.org/licenses/by-nc-nd/4.0/>), which permits non-commercial reuse, distribution, and reproduction in any medium, provided the original work is not changed in any way and is properly cited. For permission for commercial reuse, please email: [permissions@iopublishing.org](mailto:permissions@iopublishing.org). [DOI: [10.1149/1945-7111/ac44ba](https://doi.org/10.1149/1945-7111/ac44ba)]



Manuscript submitted September 20, 2021; revised manuscript received December 9, 2021. Published January 5, 2022.

Supplementary material for this article is available [online](#)

As of today, the lifetime and costs of PEM fuel cells are still the most important barriers to a wide commercialization. Within the cost, the membrane electrode assemblies (MEA) represent up to 50% of the total expenses (40% for the electrodes alone).<sup>1</sup> Thus, one way of optimization lies in enhancing the MEAs which requires understanding the influence of the operating parameters on the performance. The most important physicochemical processes limiting the performance are the cathode and anode kinetics, the Ohmic contribution, and finally the species transport from the gas channel to the triple phase boundaries (TPB).<sup>2-4</sup> This leads to a polarization curve described by

$$U_{\text{cell}} = U_0 - \eta_{\text{ORR}} - \eta_{\text{HOR}} - \eta_{\text{MT}} - j \cdot (R_{\Omega} + R_{\text{p}}^{\text{eff}}) \quad [1]$$

with  $U_0$  the equilibrium cell voltage,  $\eta_{\text{ORR}}$  and  $\eta_{\text{HOR}}$  the overpotential of the cathode and anode kinetics (ORR for oxygen reduction reaction and HOR for hydrogen oxidation reaction), and  $\eta_{\text{MT}}$  the voltage drop due to mass transport contributions. The Ohmic contribution from  $(R_{\Omega} + R_{\text{p}}^{\text{eff}})$  is proportional to the current density and contains proton transport in the polymer electrolyte membrane (PEM) and the catalyst layers (CL), electron transport and all the contact resistances. Even though these mechanisms are strongly overlapping in full cell configurations, they are generally addressed separately in the literature, making it difficult to find consistent parameter sets for given material combinations. Moreover, different measurement setups or techniques often lead to discrepancies in the results, which is shown in the scatter in the available data,<sup>5</sup> and material parameterizations become increasingly outdated, as recently discussed by Dickinson and Smith for membrane properties.<sup>6</sup> For these reasons, there is a need for fast in situ characterization workflows to parameterize state-of-the-art materials. We started to address this need in our previous publication concerning the parameterization of the hydrogen permeation and the ionomer conductivities in a full factorial manner, where we also investigated the changes in these properties under load due to the product water.<sup>7</sup>

In this work, we continue our investigations with a special focus on the parameterization of the ORR and HOR based on the most comprehensive dataset in the literature to our knowledge. Polarization data and electrochemical impedance spectroscopy (EIS) were recorded for over 1400 operating conditions (see Fig. 1 and detailed description of the test run below).

Albeit the hydrogen sorption and reaction kinetics on platinum and alloy catalysts have been widely studied, the HOR is often neglected in full cell studies for the sake of simplicity, justified by the high rates of the kinetics. Nevertheless, the anode is usually low-loaded with platinum and thus the HOR overpotential is not necessarily negligible. So far, in full cells and gas diffusion electrodes in three-electrode setups, the HOR has mainly been studied by voltammetry and polarization techniques,<sup>8-14</sup> or by EIS. The EIS response of an H<sub>2</sub>/H<sub>2</sub> cell generally exhibits two capacitive semicircles: the high frequency (HF) loop that is usually assigned to the charge transfer and proton conduction within the catalyst layer,<sup>9,15-17</sup> and the low frequency (LF) loop that is sometimes assigned to hydrogen chemisorption (independent of the partial pressure).<sup>15,16</sup> In contradiction with these findings and based on proton pumping measurements under load with only nitrogen on the cathode side, Huth et al. argued that the HF loop represents the anodic oxidation of hydrogen and the LF loop the reduction of protons to H<sub>2</sub> on the cathode side.<sup>10</sup> Also, Heinzmann et al. identified three processes in their H<sub>2</sub>/H<sub>2</sub> measurements with symmetrical electrodes using the distribution of relaxation times (DRT), all three being strongly dependent on the hydrogen partial pressure.<sup>18</sup> In this work, we show an extensive characterization of the performance of our MEA under H<sub>2</sub>/H<sub>2</sub> conditions with EIS at open circuit voltage (OCV) and polarization data. Therein, we vary the relative humidity *rH*, the temperature *T* and the hydrogen partial pressure  $p_{\text{H}_2}$  individually. Additionally, we introduce an effective recovery technique to oxidize parasitic CO within both electrodes almost simultaneously that allows us to access the kinetics without influence of surface poisoning. This permits us to discuss in detail the performance signatures of the proton pump operation mode and the correction for the anode contributions under fuel cell (H<sub>2</sub>/O<sub>2</sub>) mode.

Among the loss mechanisms, the sluggish oxygen reduction reaction (ORR) on the cathode side still represents the most

<sup>z</sup>E-mail: [christophe.gerling@de.bosch.com](mailto:christophe.gerling@de.bosch.com)

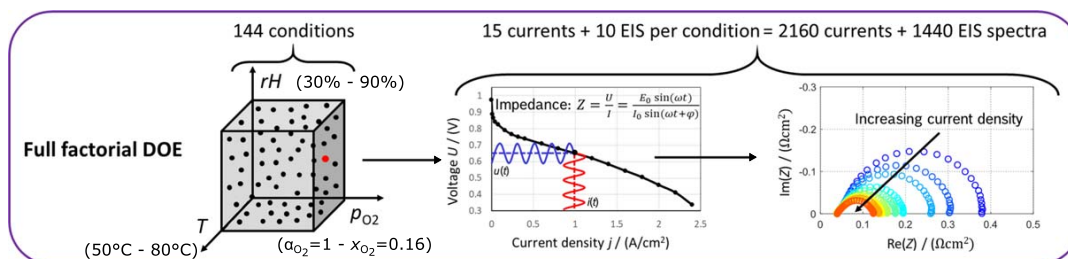


**Figure 1.** Schematic of our full factorial design of experiments in fuel cell mode. For each condition, polarization (16 currents) and EIS (10 currents) data were recorded.

important contribution to the overpotential under system relevant operating conditions. However, even though the ORR has been widely studied in the literature, it is still subject to research activities and there is no consensus concerning its modeling and parameterization yet. We aim at addressing these issues by meticulously analyzing our extensive dataset. This is challenging nonetheless since several loss mechanisms overlap in a full cell setup, making it difficult to properly extract pure ORR kinetics over a wide range of current densities. In the most simple approach, the ORR is described by Tafel kinetics with one intrinsic slope given by  $-\ln(10)RT/(\alpha F)$ , where  $\alpha \approx 1$ .<sup>19</sup> This is equivalent to 60–70 mV/dec at typical fuel cell operation temperatures. However, rotating disc electrode (RDE) and microelectrode measurements showed that  $\alpha$  can decrease to 0.5 at potentials below 0.8 V, confirmed by different modeling studies.<sup>20–22</sup> This change in the slope has been explained by more complex ORR kinetics including changes in the platinum surface coverage and potential-dependent changes of the rate limiting step and various descriptions were integrated in physical models of full cells.<sup>23–26</sup> Despite the difficulty to capture this effect in full cell measurements (the  $jR$ -corrected voltages are usually higher than 750 mV with loadings  $> 0.2 \text{ mg}_{\text{Pt}} \text{ cm}_{\text{geo}}^{-2}$ ), Subramanian et al. were able to parameterize a coverage-dependent model that was in agreement with their data by using an MEA with a low-loaded cathode.<sup>27</sup> Besides these effects, it is known that the proton conduction within the electrodes of full cells can also lead to a doubling of the apparent Tafel slope in the high current regime.<sup>3,28</sup> The analyses in full cells are therefore usually carried out for low current densities with pure  $\text{O}_2$  at  $rH=100\%$  and the data are corrected by the protonic loss contributions  $j \cdot (R_{\Omega} + R_{\text{p}}^{\text{eff}})$ . This

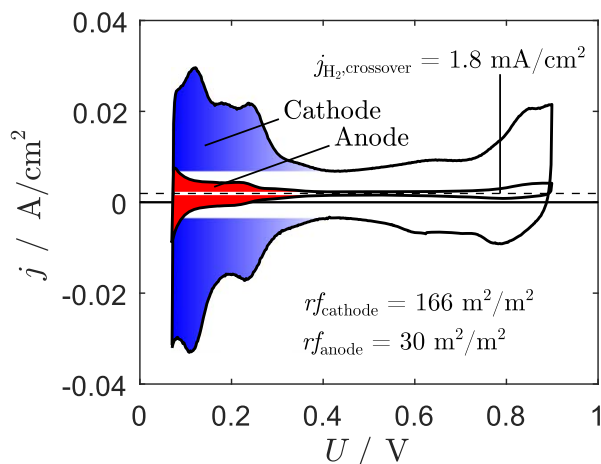


**Figure 2.** CV of the cathode (blue) and the anode (red) at  $rH=100\%$ ,  $T=40^\circ\text{C}$  and  $p_{\text{total}}=1.0 \text{ bar}_a$ , recorded with a sweep rate of  $100 \text{ mV s}^{-1}$  from 70 mV to 900 mV. The extracted roughness factors  $rf$  and the  $\text{H}_2$  crossover current  $j_{\text{H}_2, \text{crossover}}$  are also shown.

enables to guarantee a homogeneous distribution of the ORR within the CCL and to limit mass transport issues. In this work, we will also cover such conditions and present a full factorial parameterization of the ORR based on a simple Tafel law. The necessity of a more sophisticated ORR model will also be discussed. We will further investigate the influence of the relative humidity on the ORR by comparing a  $p_{\text{H}_2\text{O}}$ -dependent and a  $p_{\text{H}_2\text{O}}$ -independent model.

For estimating the  $\text{O}_2$  mass transport contribution to the overall performance loss, the low frequency signatures of the cell impedance can be investigated.<sup>18,29</sup> To do this, several methods have been used in the literature, including fitting simple Randles circuits or transmission line models (TLM) containing a mass transport element (often Warburg) either in series with the charge transfer resistance<sup>30–32</sup> or with the whole circuit,<sup>33–36</sup> or fitting more sophisticated physical models exhibiting analytical solutions under specific assumptions.<sup>37</sup> However, the low frequency domain might also contain other mechanisms that overlap frequency-wise (slow water management contributions for instance), making the analysis challenging. Another technique is the limiting current measurement, where low  $\text{O}_2$  concentrations are usually used in order to analyze the transport resistance.<sup>38</sup> Although the measurement principle is straightforward, limiting current data requires careful analysis because  $\text{O}_2$  mass transport strongly depends on the CCL and GDL water household. This can manifest itself as a steady increase of the mass transport resistance in course of rising  $\text{O}_2$  concentration and hence rising limiting current density and water production,<sup>39</sup> which may result in the overestimation of mass transport induced voltage drops for lower current densities. An evaluation of how the transport resistance evolves in operation was only done recently by transient limiting current experiments.<sup>40</sup> We will use both limiting current techniques in this work to discuss the influence of oxygen transport on the performance.

In summary, the main goal of this work is to systematically extend our previously published full factorial in situ characterization approach<sup>7</sup> to disentangle further loss contributions. We thus aim at proposing a seamless parameterization chain based on in situ techniques that can be applied to a material combination of choice. In this paper we will show the parameterization of ready-to-use models for the HOR and ORR with the relative humidity, the temperature and the partial pressures as parameters. Our findings will also be compared to results from the literature. Finally, we will discuss the mass transport contributions and perform a global loss analysis.

## Experimental

**Setup.**—In this work we used  $12 \text{ cm}^2$  Gore® PRIMEA® MEAs (W.L. Gore & Associates, Elkton, MD, USA) with a membrane thickness of  $18 \mu\text{m}$  and platinum loadings of  $0.4 \text{ mg}_{\text{Pt}} \text{ cm}^{-2}$  in the cathode and  $0.05 \text{ mg}_{\text{Pt}} \text{ cm}^{-2}$  in the anode. Figure 2 superposes typical cathode and anode voltammograms for such an MEA. The roughness factors  $rf$  were calculated by integrating the colored  $\text{H}_{\text{UPD}}$  areas and averaging over the adsorption and desorption processes (see also Fig. S1 of the supplementary material, available at [stacks.iop.org/JES/169/014503/mmedia](https://stacks.iop.org/JES/169/014503/mmedia)). The results were  $rf_{\text{cathode}} = 166 \pm 11 \text{ m}_{\text{Pt}}^2 \text{ m}_{\text{geo}}^{-2}$  and

$r_{\text{anode}} = 30 \pm 3 \text{ m}_{\text{Pt}}^{-2} \text{ m}_{\text{geo}}^{-2}$ , determined over at least 10 CVs of each electrode.

The 12 cm<sup>2</sup> MEAs were laminated into polyethylene naphthalate frames at about 100 °C. The MEAs were sandwiched between Sigracet® 22BB gas diffusion layers (GDL) from SGL® Carbon and mounted in a differential cell setup from Baltic FuelCells (quickConnect®) with straight graphite flow fields. The equivalent clamping pressure on the active area was about 1.3 MPa.

For all our tests we employ a fully automated FuelCon Evaluator C50 test station. The cell temperature is measured by a type K thermocouple and regulated by a Huber Ministat 125 thermostat. For the EIS measurements, a Gamry reference 3000 plus Booster 30 K device in combination with the test station load were used and high precision was ensured by using a four-point measurement setup. More information about our setup is given in our previous publication.<sup>7</sup>

**Design of experiments and techniques.**—Our full factorial test run was carried out in four stages:

1. Cell conditioning.
2. Proton pump (H<sub>2</sub>/H<sub>2</sub>) and blocking cathode (H<sub>2</sub>/N<sub>2</sub>) experiments including CV and EIS measurements.
3. Fuel cell (H<sub>2</sub>/O<sub>2</sub>) experiments including polarization curves and EIS. Second separate run with heliox (O<sub>2</sub> and He mixtures in the cathode).
4. Separate test run in H<sub>2</sub>/O<sub>2</sub> mode for limiting current measurements.

The conditioning was done in the H<sub>2</sub>/air mode at  $p_{\text{total}} = 1.5 \text{ bar}_a$ ,  $rH = 100\%$ ,  $T = 50 \text{ °C}$ , and with H<sub>2</sub>/air flows of 1300/2000 sccm, according to the procedure described by Harzer et al.:<sup>41</sup> 0.6 V during 45 min, OCV during 5 min, and 0.85 V during 10 min. The cell performance was stable after repeating this ten times ( $\approx 10 \text{ h}$ ) and then operating the cell at 0.3 V for 2 h.

The proton pump and blocking cathode measurements allowed us to characterize the proton conductivities, the hydrogen permeation coefficient and also the anode resistance in a full factorial manner under system relevant conditions. We varied the operating conditions from  $rH = 30\%$  to  $rH = 100\%$  and  $T = 50 \text{ °C}$  to  $T = 80 \text{ °C}$  at  $p_{\text{total}} = 1.5 \text{ bar}_a$ , leading to 32 operating conditions. For each of these conditions, EIS and CVs were recorded in H<sub>2</sub>/N<sub>2</sub> mode and EIS and polarization curves in H<sub>2</sub>/H<sub>2</sub> mode. The sequence was as follows for each humidity/temperature condition:

1. Setting the temperature and the dew point (from low to high dew points) in H<sub>2</sub>/N<sub>2</sub> mode and letting the cell equilibrate for 2 h before starting the measurements in order to ensure a steady state.
2. Carrying out the polarization curves and the potentiostatic EIS at OCV in H<sub>2</sub>/H<sub>2</sub> mode (proton pump) for the anode impedance from  $f = 100 \text{ kHz}$  to  $f = 0.1 \text{ Hz}$  with 10 points per decade and an amplitude of 4 mV.
3. Switching back to H<sub>2</sub>/N<sub>2</sub> mode, waiting for 10 min and carrying out potentiostatic EIS for  $R_{\Omega}$  and  $R_p$ . Then, recording CVs to determine the hydrogen permeation properties, the roughness factor  $r_f$  (or electrochemical surface area, ECSA) and the double layer capacity. This step was explained in detail in our previous publication.<sup>7</sup> Hereafter, going back to the first step with the next humidity and temperature condition.

In a second measurement campaign in H<sub>2</sub>/H<sub>2</sub> mode we also implemented recovery steps to avoid CO-poisoning of the catalyst layers (see below for further details).

The main test run in fuel cell mode was done with 7 humidity conditions, from  $rH = 30\%$  to  $rH = 100\%$ , 4 temperatures ( $T = 50 \text{ °C}$  to  $T = 80 \text{ °C}$ ), 4 concentrations on the cathode side ( $x_{\text{O}_2}^{\text{dry}} = 1$ ,  $x_{\text{O}_2} = 0.5$ ,  $x_{\text{O}_2} = 0.25$ ,  $x_{\text{O}_2} = 0.16$ ), and 16 current densities

( $j = 2 \text{ A cm}^{-2}$  to  $j = 4 \text{ mA cm}^{-2}$ ), leading to 1792 operating points. For our EIS measurements we chose 10 currents out of the 16 ( $j = 2 \text{ A cm}^{-2}$  to  $j = 20 \text{ mA cm}^{-2}$ ), leading to 1120 spectra. The constant dry flow rates were 1300 sccm on the anode side and 2000 sccm on the cathode side and the system pressure was  $p_{\text{total}} = 1.5 \text{ bar}_a$ , leading to pressure drops  $\Delta p < 100 \text{ mbar}$  for all the conditions. To vary  $p_{\text{O}_2}$  we mixed O<sub>2</sub> with N<sub>2</sub> ahead of the humidification bubbler, and we also conducted heliox measurements in a separate experiment for  $rH = 30\%$  and  $rH = 80\%$ . The run was carried out in the order of increasing dew points and from high currents to low currents. Whenever adjusting the temperature or the dew point, the cell was stabilized in H<sub>2</sub>/air at 0.7 V for 2 h. The currents at which we performed EIS were stabilized for 25 min prior to the measurement to ensure high measurement quality, and the other currents were held for 5 min. The impedance measurements were carried out in hybrid mode with 11 mV AC amplitude from  $f = 100 \text{ kHz}$  to  $f = 0.1 \text{ Hz}$  and with 10 points per decade. We also calculated the distribution of relaxation times to deconvolute the physicochemical processes, given by

$$Z_{\text{DRT}}(f) = R_{\Omega} + \int_{-\infty}^{+\infty} \frac{\gamma \ln(\tau)}{1 + i2\pi f\tau} d(\ln \tau) \quad [2]$$

For this, we used the tool by Wang et al.<sup>42</sup> which we have adapted to allow an automated evaluation of multiple spectra at the same time (See Figs. S2a to S2d).

Finally, we performed steady-state limiting current (SLC) measurements according to the method proposed by Baker et al.<sup>38</sup> and transient limiting current (TLC) measurements as proposed by Göbel et al.<sup>40</sup> We chose to carry out the SLC measurements for 4 pressure levels ( $p_{\text{total}} = 1.5, 2, 3, 4 \text{ bar}_a$ ), 3 humidity levels ( $rH = 30, 80, 100\%$ ), 4 temperature levels ( $T = 50, 60, 70, 80 \text{ °C}$ ) and 4 concentrations ( $x_{\text{O}_2} = 0.02, 0.05, 0.1, 0.15$ ). For stabilizing the operating conditions, the same procedures and times as mentioned above were used. Before going to the limiting current, the cell was held at 0.7 V for 8 min at given pressure, humidity, temperature and concentration. Then, the voltage was set to 0.3 V for 5 min, 0.2 V for 5 min and 0.15 V for 5 min and the limiting current was determined from these three operating points. The TLC measurements were carried out for  $x_{\text{O}_2} = 0.16$  and  $x_{\text{O}_2} = 0.25$  at  $p_{\text{total}} = 1.5 \text{ bar}_a$  by conditioning the cell current for 10 min and going to the limiting current for 10 s in the potentiostatic mode. Since in limiting current operation the conditions were not differential anymore, we considered a log-averaged O<sub>2</sub> concentration to calculate the transport resistance  $R_{\text{MT}}$ .

An overview on how we ensured good measurement quality (state-of-health checks and Kramers-Kronig test) is given in the supplementary material of this work (see Fig. S3). Furthermore, we show the methodology used to extract the kinetic parameters for the anode and cathode kinetics based on a flowchart in Fig. 11 in the appendix.

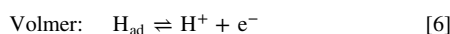
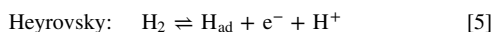
## Results and Discussion

**Ionomer properties.**—In order to carry out loss analyses, the Ohmic resistance  $R_{\Omega}$  containing the electronic losses and the protonic losses of the membrane, as well as the effective protonic resistance of the CCL  $R_p^{\text{eff}}$ , have to be known for each condition. These two resistances cause a voltage loss that is proportional to the cell current density as  $\Delta U = j \cdot (R_{\Omega} + R_p^{\text{eff}})$ . Further, it is essential to correct the cell current for the hydrogen crossover current  $j_{\text{H}_2, \text{crossover}}$  for accurate Tafel analyses of the ORR at small current densities. We characterized these ionomer properties extensively in our previous publication and provide a brief summary of the parameterized models in the supplementary material (see Fig. S4).<sup>7</sup> Also, the EIS spectra of an  $rH$ -variation under load for two currents and their DRTs are shown exemplarily in Fig. S5 to illustrate the importance of the ionomer humidification on the performance.

**Anode contribution.**—Since the Pt-loading in our anode is eight times lower than the loading in the cathode, we did not expect the anode overpotential to be completely negligible during normal fuel cell operation, even though the Pt-area specific exchange current density of the HOR is several orders of magnitude higher than the one of the ORR. Thus, we carried out measurements in the H<sub>2</sub>/H<sub>2</sub> configuration to investigate the anode contribution to the overall cell performance. Due to the fast diffusion of H<sub>2</sub> from the channel to the ACL and the thinness ( $\approx 2 \mu\text{m}$ ) of the electrode in our system, we neglect mass transport and assume that the anode impedance is limited by proton transport within the ACL and by the electrochemical oxidation of hydrogen according to



In previous works, the H<sub>2</sub> kinetics was generally assumed to be describable by a sequence of two out of the three following reaction pathways:



There have been many studies focusing on nailing down the exact reaction mechanism and trying to find out whether the hydrogen adsorption on the metal or the electron transfer step is dominant (see references in Table I). The latest research of Stühmeier et al. showed that a Tafel-Volmer mechanism is most likely to occur within the anode of PEM fuel cells at small overpotentials.<sup>14</sup> However, the HOR is often described by a single Butler-Volmer (BV) law in the modeling literature for the sake of simplicity. Moreover, since the kinetics are typically operating in the linear regime over a large current density range, the Butler-Volmer expression can even be linearized. Thus, the overall voltage loss contribution from the anode reaction (in fact including the effect of proton transport limitations in the ACL) is written as

$$\eta_{\text{anode}} = \frac{RT}{Fj_{\text{a,eff}}^0(\alpha_c + \alpha_a)} j \quad [7]$$

where both the current density  $j$  and the effective exchange current density  $j_{\text{a,eff}}^0$  are referenced to the geometrical surface area. The sum of anodic and cathodic transfer coefficients ( $\alpha_c + \alpha_a$ ) cannot be determined from the linear regime and is set to unity in this case.<sup>14</sup> Table I summarizes various parameterizations of the HOR/HER from the literature that were referenced to the platinum surface area for the sake of comparableness ( $r_f = 30 \text{ m}_{\text{Pt}}^2/\text{m}_{\text{geo}}^2$  for our measurements). However, due to the likely inhomogeneous through-plane-distribution of the reaction rate, this approach to reference the exchange current density presumably introduces errors and makes the comparison between values from different sources difficult. The above expression of the overpotential leads to the impedance of the charge transfer process

$$\frac{\partial \eta_{\text{anode}}}{\partial j} = R_{\text{anode}} = \frac{RT}{Fj_{\text{a,eff}}^0} \rightarrow j_{\text{a,eff}}^0 = \frac{1}{R_{\text{anode}}} \cdot \frac{RT}{F} \quad [8]$$

which does not depend on the current density. This means that the exchange current density can be parameterized by EIS and that measurements at OCV are sufficient. Further, it means that the Tafel slope (symmetry factor) is not accessible from these measurements and that we get no information regarding the rate limiting step.

Figure 3a shows the EIS at OCV and Fig. 3b the corresponding DRT of a relative humidity variation at 80 °C with pure H<sub>2</sub> on both sides. As can be seen from these typical H<sub>2</sub>/H<sub>2</sub> spectra, two main

processes are identified, which confirms previous literature findings.<sup>9,15–17</sup> Apparently, both processes exhibit a strong humidity dependency. For the high-frequency loop, this dependency is believed to come from the proton transport resistance of the catalyst layer,<sup>18</sup> or from a water dependency in the hydrogen kinetics itself.<sup>53</sup> However, EIS and DRT results from a humidity variation with a low  $p_{\text{H}_2, \text{anode}}$  (see Figs. S6a to S6b) show that the high frequency loop in fact contains two processes with separate time constants and that only the one occurring at the highest frequencies seems to be humidity-dependent. This hints at combined  $rH$ -dependent proton transport and  $rH$ -independent electrode kinetics, thus confirming the former hypothesis. In Fig. 3c we fitted the HF loop ( $R_{\text{p1A}} = R_{\text{HF}}$ ) to the low-frequency real part of the transmission line model

$$Z = \sqrt{R_{\text{p}}R_{\text{ct}}} \coth\left(\frac{R_{\text{p}}}{R_{\text{ct}}}\right) \quad [9]$$

and assumed that the cathode impedance (counter electrode) is negligible (due to its eight times higher ECSA), which was previously discussed in the literature for comparable counter electrodes.<sup>52</sup> Here,  $R_{\text{ct}}$  represents the kinetics charge transfer resistance and  $R_{\text{p}}$  the proton resistance of the catalyst layer. The Fig. shows the resistance over  $rH$  at 80 °C for three different H<sub>2</sub> concentrations on the anode side ( $x_{\text{H}_2, \text{A}} = 0.75$ ,  $x_{\text{H}_2, \text{A}} = 0.5$  and  $x_{\text{H}_2, \text{A}} = 0.25$ , obtained by diluting with N<sub>2</sub>). We further assumed that the proton resistance is a fraction of the cathode proton resistance we characterized in blocking cathode configuration<sup>7</sup> and found  $R_{\text{p, anode}} = 0.18 \cdot R_{\text{p, cathode}}$ , reflecting approximately the ratio of anode to cathode thickness ( $2/13 \approx 0.15$ ). The HF loop is therefore well explained by a combination of proton transport and charge transfer limitations as given by Eq. 9. It is worth noting that we generally found  $R_{\text{ct}}$  to be in the same order of magnitude or smaller ( $1 \text{ m}\Omega \text{ cm}^2 < R_{\text{ct}} < 30 \text{ m}\Omega \text{ cm}^2$ ) than  $R_{\text{p}}$  ( $7 \text{ m}\Omega \text{ cm}^2 < R_{\text{p}} < 60 \text{ m}\Omega \text{ cm}^2$ ). In this limit  $R_{\text{p}} > R_{\text{ct}}$ , Eq. 9 simplifies to  $Z = \sqrt{R_{\text{p}} \cdot R_{\text{ct}}}$ , such that the true exchange current density  $j_{\text{a,ct}}^0 = RT/(F \cdot R_{\text{ct}})$  is related to the apparent exchange current density by  $j_{\text{a,ct}}^0 = j_{\text{a,eff}}^0 \cdot \sqrt{R_{\text{p}}/R_{\text{ct}}}$ .

Even though Neyerlin et al.<sup>52</sup> explained that with pure hydrogen the gas-phase related transport resistances are expected to be very small in the proton pump measurements with state-of-the-art diffusion media (high diffusion coefficient  $D_{\text{H}_2} \approx 0.5 \text{ cm}^2/\text{s}$ ),<sup>52</sup> Heinzmann et al. recently showed that low-frequency EIS loop depends on the partial pressure and assigned it to H<sub>2</sub> mass transport from the channel to the reaction sites.<sup>18</sup> We also see this  $p_{\text{H}_2}$ -dependency of the LF loop (see below); however, the influence of  $rH$  is just as strong in our case. In the literature, this dependency on  $rH$  was attributed to ionomer dry out effects caused by the electroosmotic drag.<sup>54,55</sup> Based on these analyses, we believe that the interplay of  $R_{\text{p}}$  and  $R_{\text{ct}}$  in the transmission line causes the combined  $rH$  and  $p_{\text{H}_2}$  influence on the low-frequency loop. The other hypotheses of the low frequency process being linked to H<sub>2</sub> adsorption or desorption processes,<sup>15,16</sup> or to the HER,<sup>10</sup> could not be validated yet. Further parameter variations in the H<sub>2</sub>/H<sub>2</sub> configuration can be seen in the supplementary material (Figs. S6 and S7).

When trying to characterize the temperature dependency of the anode kinetics, we were initially puzzled by a far too high apparent activation energy of  $E_{\text{act}} > 70 \text{ kJ mol}^{-1}$  in our first two H<sub>2</sub>/H<sub>2</sub> measurement campaigns. We already observed this high  $T$ -dependency during the H<sub>2</sub>/N<sub>2</sub> characterization in our previous publication<sup>7</sup>. After identifying an undesired and highly  $T$ -dependent anodic contribution via EIS, we chose to account for it through an additional R-CPE element in order to achieve a clean parameterization of the ionomer resistance  $R_{\text{p}}$ . We also found that this spurious process was correlated to long stabilization times ( $> 2 \text{ h}$ ) prior to the measurements and that it was in fact due to CO poisoning of the catalyst layer. This poisoning effect is absent in the normal fuel cell configuration since O<sub>2</sub> crossover from the cathode to the anode helps

**Table I. HOR and/or HER data from the literature. Data obtained from measurements in acidic and in alkaline media as well as in full PEM fuel cells. In PEMFCs, the  $j_0$  values are given for  $p_{\text{H}_2} \approx 1$  bar and the information on the catalyst are only given for the working electrode if not mentioned otherwise (A stands for anode and C stands for cathode).**

Catalyst	Electrolyte	$T$ (°C)	$j_{\text{a,eff}}^0$ (mA cm $_{\text{Pt}}^{-2}$ )	$E_{\text{act}}$ (kJ mol $^{-1}$ )	Tafel slope (mV/dec)	Year / References
5wt% Pt/C	96% H $_3$ PO $_4$	160	144	17	43 <sup>a)</sup>	1975 / <sup>43</sup>
Mono- & Polycrystalline Pt	HClO $_4$	25	1.7–3		30	1987 / <sup>44</sup>
Polycrystalline Pt	0.01 N HClO $_4$	25	2.48		118 <sup>b)</sup>	1989 / <sup>45</sup>
	0.01 N—0.1 N H $_2$ SO $_4$		1.75–1.16			
	0.1 N H $_3$ BO $_3$		$\ll$ 0.01			
	0.08 N NaOH		0.55			
Monocrystalline Pt	0.5 M H $_2$ SO $_4$	25	$\approx$ 1–1.5		32–35	1992 / <sup>46</sup>
Monocrystalline Pt	0.05 M H $_2$ SO $_4$	60	0.83–1.35 <sup>c)</sup>	9.5–18 <sup>c)</sup>	28–112 <sup>c)</sup>	1997 / <sup>47</sup>
1.7 mg cm $^{-2}$ symmetrical	PEMFC (N112)	50	7 <sup>d)</sup>			1999 / <sup>15</sup>
20wt% Pt/C, 0.5 mg cm $^{-2}$	1 M H $_2$ SO $_4$	25	1			2001 / <sup>48</sup>
47wt% Pt/C, 0.05–0.4 mg cm $^{-2}$	PEMFC (900EW)	60	$\approx$ 27 <sup>e)</sup>	9.5	33	2004 / <sup>49</sup>
10wt% Pt $_{\text{nanop}}$ /C	0.10 M H $_2$ SO $_4$	25	$\approx$ 20		30	2004 / <sup>50</sup>
0.7 mg cm $^{-2}$ symmetrical	PEMFC (N117)	40–70	2.6 mA/mg $_{\text{Pt}}$ <sup>f)</sup>	50–55		2005 / <sup>17</sup>
Polycrystalline Pt	0.15 M HClO $_4$	25	1.08			2006 / <sup>8</sup>
50wt% Pt/C, 0.35/0.5 mg cm $^{-2}$ (A/C)	PEMFC (1100EW)	80	7–36 A/mg $_{\text{Pt}}$ <sup>g)</sup>			2007 / <sup>51</sup>
5wt% Pt/C, 0.003 mg cm $^{-2}$	PEMFC	80	235–600		70–140	2007 / <sup>52</sup>
Symmetrical, Pt/C	HT-PEM (PBI/H $_3$ PO $_4$ )	80–140	550–1450			2009 / <sup>10</sup>
46wt% Pt/C, 0.007 mg cm $^{-2}$	0.1 M KOH	21	0.57	30	120	2010 / <sup>11</sup>
4.7wt% Pt/C, 0.002 mg cm $^{-2}$	PEMFC	40–80	120–260	16	124–149	2014 / <sup>12</sup>
0.2/0.4 mg cm $^{-2}$ (A/C)	PEMFC	80	$\approx$ 19 A/mg $_{\text{Pt}}$ <sup>h)</sup>			2018 / <sup>18</sup>
4.8wt% Pt/C, 1.2–1.6 $\mu$ g cm $^{-2}$	PEMFC	30–90	88–580	25	135–144	2021 / <sup>14</sup>
0.05/0.4 mg cm $^{-2}$ (A/C)	PEMFC	40–80	170–408 <sup>i)</sup>	17.8 <sup>i)</sup>		This work

a) Determined with  $2.3RT/(2F)$  for 160 °C. b) Determined with  $2.3RT/(0.5F)$  for 25 °C. c) Dependent on the different Pt facets. d) Determined by  $j_0 = RT/(zFR_a)$ , with  $R_a$  being the resistance of the HF loop. e) Data taken from<sup>47</sup> for Pt(110) ( $j_0 = 1.35$  mA cm $_{\text{Pt}}^{-2}$ ) and adjusted to match the observed polarization curves. f) Calculated based on the HF loop at 60 °C. Since  $rf$  is not given, data is mass specific. g) Based on the polarization curves slopes for 60%  $rH$  and 100%  $rH$  (12 m $\Omega$ cm $^2$  and 2.5 m $\Omega$ cm $^2$ ). Values obtained by considering the ratio of loadings of the electrodes. Since  $rf$  is not given, data is mass specific. h) Estimated for  $\approx (0.4/(0.4 + 0.2)) \cdot 12$  m $\Omega$ cm $^2$  at OCV in H $_2$ /H $_2$ ,  $T = 80$  °C,  $p_{\text{H}_2} = 0.67$  bar and  $rH = 70\%$ . i) Values obtained for our final test run containing micropolarization curves, EIS and recovery steps to keep the catalyst layers clean. Calculated for  $rf=30$  m $_{\text{Pt}}^2$ /m $_{\text{geo}}^2$  obtained by CV measurements.

keeping the anode catalyst clean. It also perfectly explains the observed high  $T$ -dependency.<sup>56</sup> We refer to the supplementary material for a more detailed discussion.

To get a clean dataset we reproduced H $_2$ /H $_2$  EIS and micropolarization measurements and introduced recovery steps after each operating condition to keep the catalyst layers clean. To do so, we carried out CV measurements from  $-0.9$  V to  $0.9$  V to oxidize the CO layer in both the anode and cathode electrode by diluting H $_2$  in N $_2$  and stopping the flow before starting the measurements. Such a CV measurement is shown in Fig. 4a, where the CO peaks are highlighted by the gray areas and disappear completely after the second cycle. We chose  $rH = 100\%$  in this test run to keep the ionomer resistances as low as possible and therefore make the evaluation of the kinetics as precise as possible. In Fig. 4b we show the micropolarization curves of a hydrogen partial pressure variation at  $rH = 100\%$  and  $T = 40$  °C and Fig. 4c displays corresponding EIS at OCV. The polarization curves show a perfectly linear behavior in the range that we used for the parameter fitting; however, the HOR direction (negative voltage and current in this case) shows nonlinearities at higher overpotentials for the low H $_2$  concentrations. In this special case, this behavior is not linked to the anodic overpotential-dependent limiting current observed in the literature (most probably potential-independent rate limiting Tafel step),<sup>12,14</sup> but rather to mass transport contributions because of the dropping stoichiometry ( $\lambda < 4$ ). In the Nyquist plot of the EIS measurements at OCV, we can only observe one loop at high partial pressures. With decreasing partial pressures, several capacitive processes and a low-frequency inductive feature appear. According to detailed analyses of these EIS features (see Fig. S8), the high-frequency loop has an activation energy of around 20 kJ mol $^{-1}$  which is much higher than for the low-frequency capacitive loop ( $\approx 2$  kJ mol $^{-1}$ ) and for the low-frequency inductive loop ( $\approx 4$  kJ mol $^{-1}$ ). Moreover, the

size of the inductive loop is inversely proportional to  $p_{\text{H}_2}$  (exponent  $\approx -1.0$ ) and therefore stronger pressure-dependent than the capacitive loops (exponent  $\approx -0.8$ ).

However, for fitting our simple kinetics model we chose to evaluate the polarization curves. The according procedure for extracting the parameters is shown in the appendix in Fig. 11. Figure 5a shows an Arrhenius plot of the HOR/HER exchange current density for three different concentrations and the corresponding Ohmic resistance used for the performance corrections. The resulting activation energies are virtually independent of  $p_{\text{H}_2}$  and lie in the range 15 kJ mol $^{-1}$  to 18 kJ mol $^{-1}$ , which is close to the value from Durst et al.<sup>12</sup> Fig. 5b shows the partial pressure dependency of the exchange current density (apparent reaction order with respect to  $p_{\text{H}_2} \approx 0.4$ ) at  $T = 40$  °C. This is in line with the results of Stühmeier et al.<sup>14</sup> At lower partial pressures the apparent exchange current density deviates from the expected behavior and gets too small. This effect partially comes from the presence of the other effects that are also visible in the EIS response as mentioned above. If we analyze only the high-frequency loops from the EIS (triangles in Fig. 5b), the exchange current densities are closer to the regression curve but still too low. This effect may come from a change in the influence of the ionomer contribution on the effective anode resistance when the charge transfer resistance rises due to lower  $p_{\text{H}_2}$ , such that the approximation  $R_p > R_{\text{ct}}$  of Eq. 9 is not justified anymore. Another possible explanation is a change in the mechanisms of the kinetics at very low partial pressures. However, the current parameterization of the hydrogen kinetics is already sufficiently accurate in the range of operating conditions that are meaningful for typical PEM operation. Hence, we chose to exclude all the data points recorded at  $p_{\text{H}_2} < 0.1$  bar in our final fitting and obtained the expression



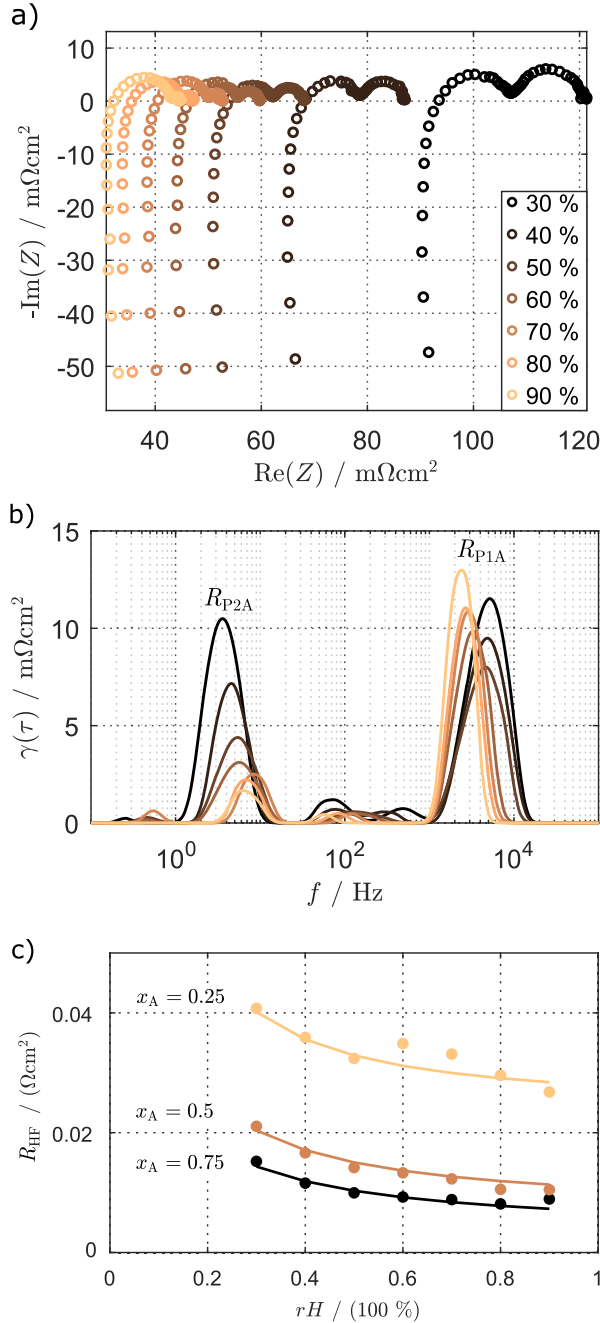


**Figure 3.** a) EIS for a variation of  $rH$  in  $H_2/H_2$  mode at OCV ( $U_{\text{cell}} = 0$  V) and  $T = 80$  °C with pure  $H_2$  on both sides ( $x_{H_2}^{\text{dry}} = 1$ ). b) DRT corresponding to a). c) Transmission line model based fits of the HF loop resistance  $R_{P1A}$  in  $H_2/H_2$  mode at OCV and  $T = 80$  °C with pure  $H_2$  in the cathode for three  $H_2$  concentrations in the anode  $x_A$ .

$$j_{a,\text{eff}}^0 = (1.57 \cdot 10^{-2} \text{ A/cm}^2_{\text{pV}}) \cdot \left( \frac{p_{H_2}}{p_{\text{ref}}} \right)^{0.36} \exp\left( -\frac{17.8 \text{ kJ mol}^{-1}}{RT} \right) \quad [10]$$

which was normalized by the roughness factor  $30 \text{ m}_{\text{Pt}}^2 \text{ m}_{\text{geo}}^{-2}$  (see above). The correlation plot in Fig. 5c demonstrates the model and the measured values match quite well apart from the points that were excluded from

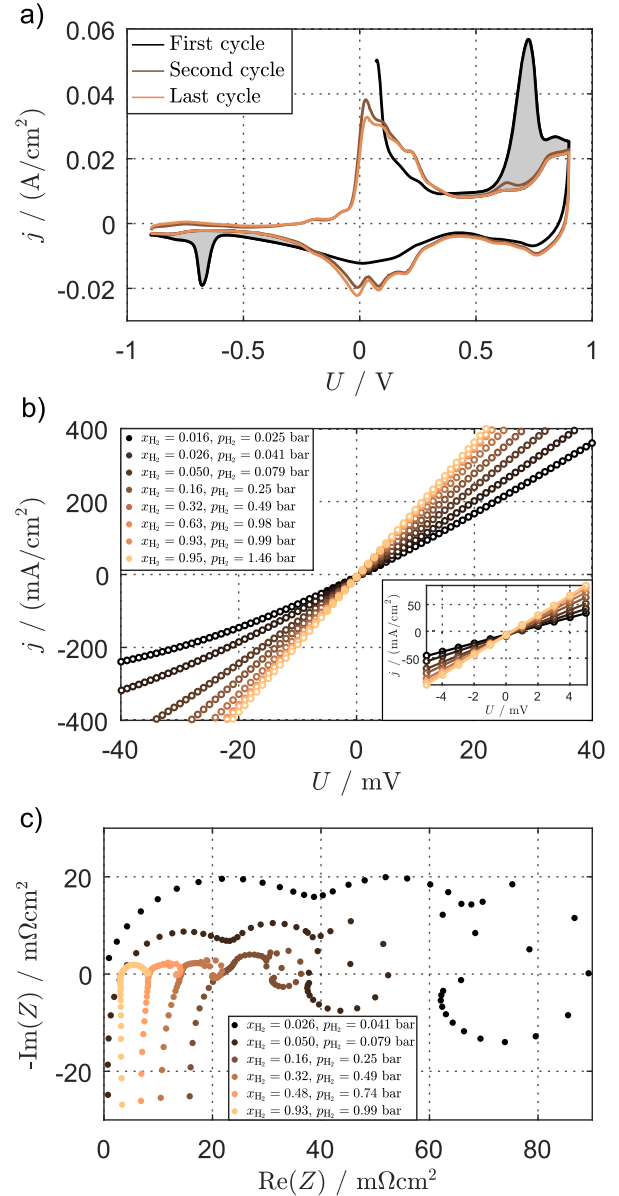


**Figure 4.** a) CO recovery step: combined CV of the anode and cathode catalyst layer during proton pump operation with 2.7%  $H_2$  in the dry ( $H_2, N_2$ ) mixture at  $p_{\text{total}} = 1.5$  bar,  $rH = 100\%$  and  $T = 40$  °C. The scan was carried out with  $100 \text{ mV s}^{-1}$  from  $-0.9$  V to  $0.9$  V after stopping the gas streams. In this case, the conditions were held over 10 h before the measurement to exaggerate the poisoning effect and demonstrate the efficacy of the method. After the 2<sup>nd</sup> cycle, the CO peaks have completely disappeared. b) Micropolarization curves for a  $p_{H_2}$  variation at  $T = 40$  °C where the inset represents a zoom on the voltage zone used for parameterization. c) EIS at OCV for a  $p_{H_2}$  variation at the same conditions as in d). The curves are shifted along the  $x$ -axis for the sake of visibility.

the fitting. Further, the resulting fit parameters are close to the values from the literature for proton pumping experiments (see Table I).<sup>12,14,52</sup> Nevertheless, we emphasize that if we consider the true exchange current density  $j_{a,\text{ct}}^0 = (j_{a,\text{eff}}^0)^2 \cdot R_p \cdot F / (RT)$  instead of the apparent exchange current density  $j_{a,\text{eff}}^0$ , the activation energy becomes  $23.4 \text{ kJ mol}^{-1}$  and the reaction order with respect to hydrogen doubles

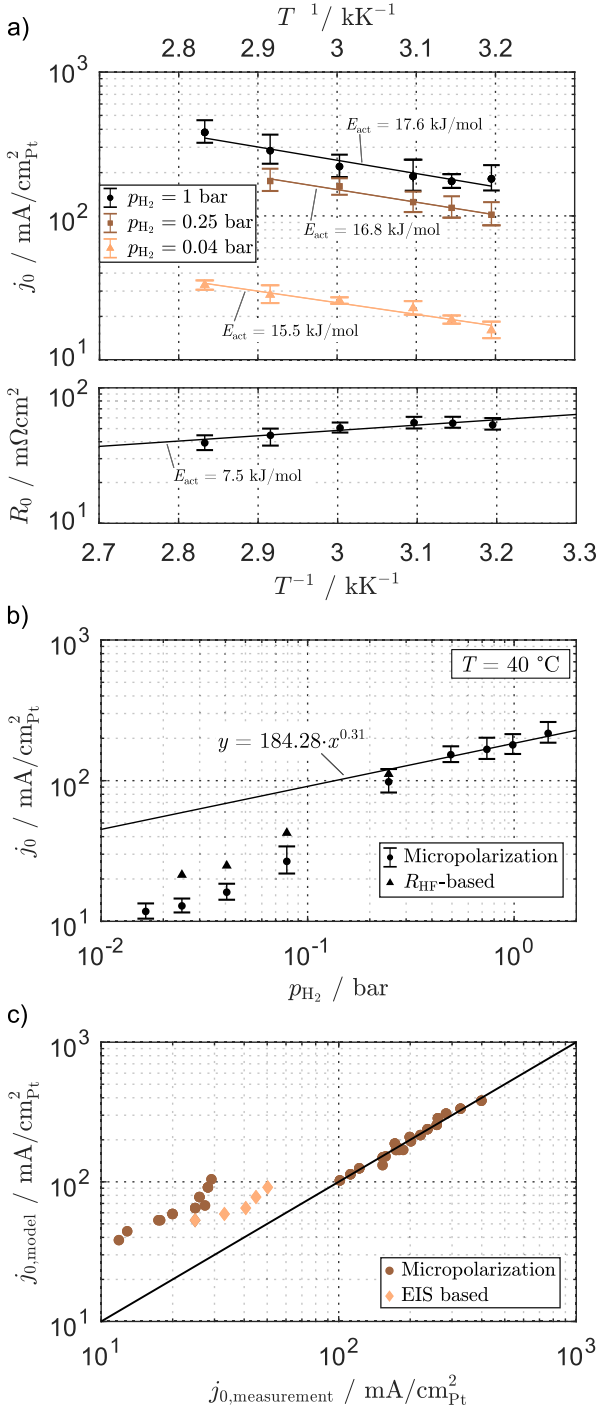


**Figure 5.** a) Arrhenius plot of the HOR/HER specific current density for three  $H_2$  concentrations and corresponding high-frequency resistance below. b) Double-logarithmic plot of the specific current density over  $p_{H_2}$  at  $T = 40$  °C. The error bars in a) and b) have been determined over at least two measurements. c) Correlation plot of the specific exchange current density obtained from the fitted model versus the values calculated based on our measurements. In all the plots,  $j_0 = j_{a,eff}^0$ .

from 0.36 to 0.72. Further, the true exchange current density is two to three times higher ( $j_{a,ct}^0 \approx 1 \text{ A cm}_{Pt}^{-2}$ ) than the apparent exchange current density ( $j_{a,eff}^0 \approx 0.4 \text{ A cm}_{Pt}^{-2}$ ) at the same conditions.

With this evaluation we obtain a ready-to-use model for the anode kinetics that can directly be implemented into simulation models or used for loss contribution analyses. Furthermore, we emphasize the importance of our CO recovery procedure for getting accurate data and that caution is required even when working at high cell temperatures since surface poisoning effects can easily be overlooked.

**Cathode kinetics.**—The ORR is the major loss process under the most relevant operating conditions. Thus, well-parameterized models are needed for the ORR to accurately predict the performance in fuel cell operation. As mentioned in the introduction, this is still subject to research as there is no consensus regarding its mechanistic description. However, simple Tafel kinetics is typically employed since the overpotential  $\eta_{ORR}$  is high and can be expressed as a logarithmic function of the current density according to

$$\eta_{ORR} = \frac{RT}{\alpha_c F} \cdot \ln \frac{j}{j_{c,eff}^0} \quad [11]$$

where the cathodic transfer coefficient  $\alpha_c$  is the product of the symmetry factor  $\beta$  and the number of transferred electrons  $z$ , and  $j_{c,eff}^0$  is the effective exchange current density. This leads to the impedance expression of the charge transfer process

$$\frac{\partial \eta_{ORR}}{\partial j} = R_{ct} = \frac{RT}{\alpha_c F j} = \frac{b}{j} \quad [12]$$

that does not depend on the exchange current density  $j_{c,eff}^0$  and thus not on  $p_{O_2}$ . This expression directly links the intrinsic Tafel slope  $b$  (slope of the curves  $U_{jR-free}$  versus  $\ln(j + j_{H_2,crossover})$ ) to the size of the charge transfer loop in the Nyquist spectra. In contrast to the anode kinetics (see Eqs. 7 and 8), EIS cannot be used to determine the exchange current density, yet would enable direct characterization of  $b$ . However, this is complicated by the impact of slow Pt oxidation kinetics on the apparent Tafel slope in steady-state measurements.<sup>57</sup> These oxidation mechanisms lead to low-frequency inductive features in the EIS spectra and discrepancies are therefore observed between an EIS-based evaluation of  $b$  through the high-frequency charge transfer resistance  $R_{ct}$  by  $b = j \cdot R_{ct}$  and a steady-state-based evaluation of  $b$  through the slope of the polarization curve in the Tafel plot. The first approach yields Tafel slopes  $b \geq 100$  mV/dec (see Fig. S5), and the second approach yields slopes  $b \approx 70$  mV/dec (see below). We will analyze this effect in a forthcoming paper. In the present work, we aim for a simple representation of the ORR kinetics and understanding of its limits by parameterizing a Tafel law like shown in Eq. 11 using exclusively polarization data at low currents.

We evaluated the kinetics overpotential  $\eta_{ORR}$  by subtracting the  $jR$ -free voltage from the equilibrium voltage  $U_0$  according to

$$\begin{aligned} \eta_{ORR} &= U_0 - U_{measurement} + j \cdot (R_p^{eff} + R_\Omega) \\ &= U_0 - U_{jR-free} \end{aligned} \quad [13]$$

where the  $jR$ -correction was made based on the evaluation of EIS spectra under load as described in our previous publication.<sup>7</sup> In the literature, the ORR parameters are most often obtained from measurements gathered under fully saturated conditions<sup>19</sup> and a full factorial parameterization containing data at varying  $rH$  does not exist to our knowledge; however, some authors discussed the influence of  $rH$  on the ORR performance. Xu et al. found out that their CCL performs badly at elevated temperature and dry conditions even after correcting the data for the effective protonic resistance.<sup>58,59</sup> In contrast to these findings, Neyerlin et al. and Liu et al. saw a way smaller influence of  $rH$  on the  $jR$ -free performance.<sup>60,61</sup> Even though the humidity influence on the ORR initially appeared to be small in our dataset (see Fig. S9a), we

investigated different modeling approaches. Firstly, we used an approach where the water activity was set to unity as it is usually the case in literature studies which we call here the 'water-independent' approach. There, the equilibrium voltage  $U_0$  can be calculated by the Nernst equation according to

$$U_0 = 1.23 \text{ V} - (0.9 \cdot 10^{-3} \text{ VK}^{-1})(T - 298 \text{ K}) + \frac{RT}{2F} \ln \left[ \left( \frac{p_{\text{H}_2}}{p_{\text{ref}}} \right) \left( \frac{p_{\text{O}_2}}{p_{\text{ref}}} \right)^{\frac{1}{2}} \right] \quad [14]$$

The exchange current density contains the dependencies on temperature and on oxygen partial pressure through the activation energy  $E_{\text{act}}$  and the reaction order  $\gamma$ , respectively, and was expressed as

$$j_{\text{c,eff}}^0 = rf \cdot j_{\text{c,ref}}^0 \cdot \left( \frac{p_{\text{O}_2}}{p_{\text{ref}}} \right)^\gamma \exp \left[ \frac{-E_{\text{act}}}{RT} \left( 1 - \frac{T}{T_{\text{ref}}} \right) \right] \quad [15]$$

with  $rf$  the roughness factor of the cathode electrode in  $\text{m}_{\text{Pt}}^2 \text{m}_{\text{geo}}^{-2}$  and  $j_{\text{c,ref}}^0$  the reference exchange current density in  $\text{A cm}_{\text{Pt}}^{-2}$ . In our second approach that we call in the following 'water-dependent' we accounted for the actual partial pressure of water in the gas phase  $p_{\text{H}_2\text{O}}$  in the Nernst equation instead of setting the activity to unity and thus calculated the cell equilibrium voltage by

$$\tilde{U}_0 = 1.23 \text{ V} - (0.9 \cdot 10^{-3} \text{ VK}^{-1})(T - 298 \text{ K}) + \frac{RT}{2F} \ln \left[ \left( \frac{p_{\text{H}_2\text{O}}}{p_{\text{ref}}} \right)^{-1} \left( \frac{p_{\text{H}_2}}{p_{\text{ref}}} \right) \left( \frac{p_{\text{O}_2}}{p_{\text{ref}}} \right)^{\frac{1}{2}} \right] \quad [16]$$

We further added a possible water dependency in the exchange current density through a power law for  $p_{\text{H}_2\text{O}}$  therein with the supplementary parameter  $n$ . This change yields

$$\tilde{j}_{\text{c,eff}}^0 = rf \cdot j_{\text{c,ref}}^0 \cdot \left( \frac{p_{\text{H}_2\text{O}}}{p_{\text{ref}}} \right)^n \cdot \left( \frac{p_{\text{O}_2}}{p_{\text{ref}}} \right)^\gamma \times \exp \left[ \frac{-E_{\text{act}}}{RT} \left( 1 - \frac{T}{T_{\text{ref}}} \right) \right] \quad [17]$$

Therefore, the basic model for saturated conditions contains the four fitting parameters  $\alpha_c$ ,  $E_{\text{act}}$ ,  $\gamma$ , and  $j_{\text{c,ref}}^0$ , and the modified  $p_{\text{H}_2\text{O}}$ -dependent model adds a fifth parameter,  $n$ . It can easily be shown algebraically however that for  $n = 0.5$  both models are in fact

**Table II. Exchange current density parameters extracted from globally fitting all the polarization points  $U_{jR\text{-free}}$  for  $j \leq 0.1 \text{ A cm}^{-2}$ . The conditions where no  $n$  is given were fitted with the  $p_{\text{O}_2}$ -independent model (water activity set to unity in  $U_0$  and  $j_{\text{c,eff}}^0$ ). The symmetry factor was fixed at  $\alpha_c = 1$ .**

$\alpha_c$ (—)	$j_{\text{c,ref}}^0 \cdot 10^8$ ( $\text{A/cm}_{\text{Pt}}^2$ )	$\gamma$ (—)	$n$ (—)	$E_{\text{act}}$ ( $\text{kJ mol}^{-1}$ )
<i>p</i> <sub>H<sub>2</sub>O</sub> -dependent model without the <i>rH</i> = 90% conditions				
1.0	2.13	0.49	0.51	68.74
<i>p</i> <sub>H<sub>2</sub>O</sub> -dependent model with all conditions				
1.0	1.82	0.50	0.41	73.41
<i>p</i> <sub>H<sub>2</sub>O</sub> -independent model with all the <i>rH</i> conditions				
1.0	2.05	0.50	—	69.52
<i>p</i> <sub>H<sub>2</sub>O</sub> -independent model only with <i>rH</i> = 80% conditions				
1.0	2.15	0.51	—	71.27
<i>p</i> <sub>H<sub>2</sub>O</sub> -independent model only with <i>rH</i> = 90% conditions				
1.0	1.81	0.54	—	70.88

identical. Thus, a noticeable water dependency is only observed if  $n \neq 0.5$ .

We depict the method to get the kinetic parameters schematically in Fig. 11 of the appendix. If not mentioned otherwise, the reference conditions for all fitted models were  $T_{\text{ref}} = 80 \text{ }^\circ\text{C}$  and  $p_{\text{ref}} = 1 \text{ bar}$ . We took  $j = j_{\text{measured}} + j_{\text{H}_2\text{crossover}}$  for the global fitting and excluded  $j > 0.1 \text{ A cm}_{\text{geo}}^{-2}$  in most cases. To verify the meaningfulness of the latter condition and see the influence of one-at-a-time parameter variations, we performed local fits at given humidity, temperature or current density (see Table S1 and Table S2 of the supplementary material) prior to the global fit over all the conditions simultaneously. These local fits confirmed that the parameters are constant and the Tafel slope was captured properly for  $j \leq 0.1 \text{ A cm}^{-2}$ . The model for the  $\text{H}_2$  permeation coefficient  $\Psi_{\text{H}_2}$  and the corresponding measurements are summarized in Fig. S4c over  $T$  and  $rH$  and the resulting crossover current taken for the current correction is shown in Fig. S4d for our standard condition  $p_{\text{total}} = 1.5 \text{ bar}_a$ . Since the membranes of our samples showed very high electrical resistances ( $\geq 600 \text{ } \Omega \text{ cm}^2$ ) we neglected electrical membrane shorts.

Optimized parameters from the global fit simultaneously over all the operating conditions are shown in Table II. It can be seen that the activation energy is around  $70 \text{ kJ mol}^{-1}$ , the reference exchange current density is around  $2 \cdot 10^{-8} \text{ A cm}_{\text{Pt}}^{-2}$ , the reaction order is around 0.5 and the exponent of the power law for the water partial pressure dependency is between 0.4 and 0.5. Moreover, the fit results from cases in which  $\alpha_c$  was not fixed to 1 (not shown in the table) yielded results that were very close to those of the fitting procedures in which  $\alpha_c$  was fixed to 1, matching our expectations of Tafel slopes around  $70 \text{ mV/dec}$  (see above). Figures 6a and 6b show the good agreement between the fitted local exchange current densities (symbols,  $\alpha_c = 1$ ) and the global model (black lines) for an  $rH$  variation with the  $p_{\text{H}_2\text{O}}$ -dependent model at  $T = 50 \text{ }^\circ\text{C}$  and  $T = 80 \text{ }^\circ\text{C}$  (Fig. 6a) and with the  $p_{\text{H}_2\text{O}}$ -independent model (Fig. 6b) at the same conditions. The  $rH = 90\%$  conditions are outliers and thus were excluded from the fitting (probably partial flooding of the electrode). In Fig. 6c and Fig. 6d we depict a  $p_{\text{O}_2}$  variation for four different temperature and humidity combinations for the  $p_{\text{H}_2\text{O}}$ -dependent model and the  $p_{\text{H}_2\text{O}}$ -independent model, respectively (see Fig. S9b for a similar plot in the heliox case). The slopes in the double-logarithmic plots of this Fig. represent the reaction order  $\gamma$  (for the  $p_{\text{O}_2}$  variation) and the exponent of the  $p_{\text{H}_2\text{O}}$  influence  $n$  ( $rH$  variation). Both models seem to fit the data well. This is not surprising, as  $n \approx 0.5$  means that both models are essentially equivalent and there is effectively no influence of  $rH$  on the ORR. Thus, the exchange current density can be parameterized as

$$\tilde{j}_{\text{c,eff}}^0 = rf \cdot (2.13 \cdot 10^{-8} \text{ A/cm}_{\text{Pt}}^2) \left( \frac{p_{\text{H}_2\text{O}}}{p_{\text{ref}}} \right)^{0.51} \left( \frac{p_{\text{O}_2}}{p_{\text{ref}}} \right)^{0.49} \times \exp \left[ \frac{-68.7 \text{ kJ mol}^{-1}}{RT} \left( 1 - \frac{T}{T_{\text{ref}}} \right) \right] \quad [18]$$

if the Nernst equation contains the effective water partial pressure, or as

$$j_{\text{c,eff}}^0 = rf \cdot (2.15 \cdot 10^{-8} \text{ A/cm}_{\text{Pt}}^2) \left( \frac{p_{\text{O}_2}}{p_{\text{ref}}} \right)^{0.51} \times \exp \left[ \frac{-71.3 \text{ kJ mol}^{-1}}{RT} \left( 1 - \frac{T}{T_{\text{ref}}} \right) \right] \quad [19]$$

if the water activity is set to unity in the Nernst equation.

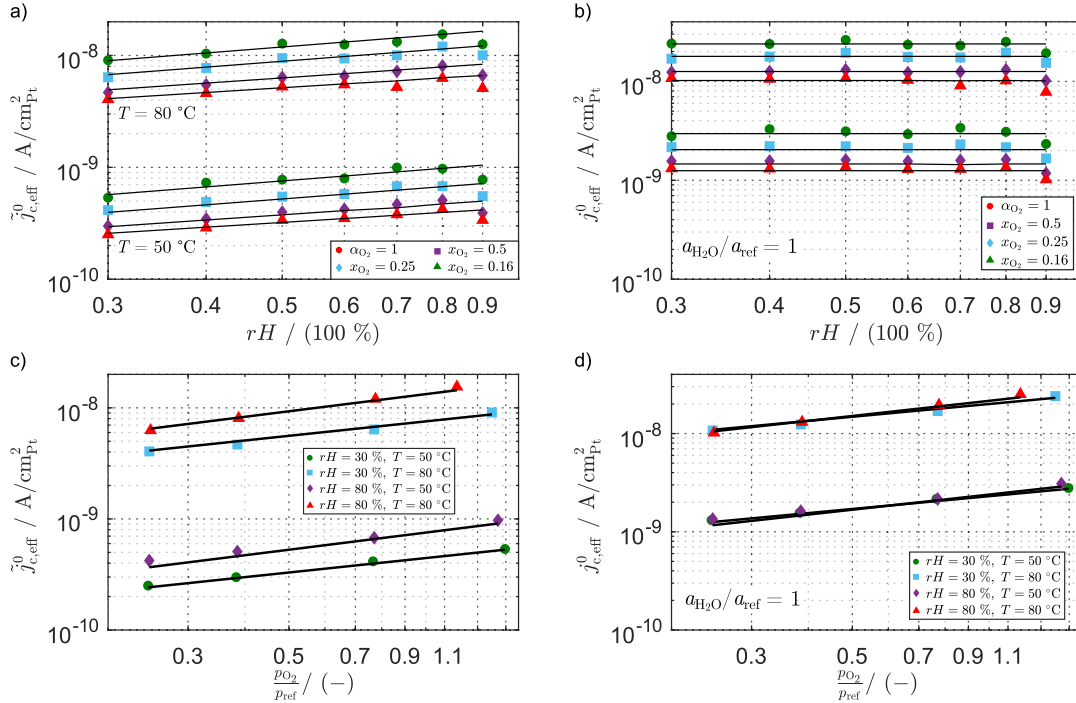


**Figure 6.** Local exchange current densities (symbols) and global model (lines) for the  $\{O_2-N_2\}$  measurements. a)  $p_{H_2O}$ -dependent model for  $T = 50\text{ }^\circ\text{C}$  and  $T = 80\text{ }^\circ\text{C}$  over the relative humidity  $rH$ . Both the Nernst voltage  $\tilde{U}_0$  and  $J_{c,eff}^0$  depend on the water partial pressure. b) Same as in a) for the  $p_{H_2O}$ -independent model where liquid water is assumed in the Nernst voltage and in the expression of the model of  $J_{c,eff}^0$  (activity is set to unity) instead of using  $p_{H_2O}$  in the gas phase. c) Same as in a) for a  $p_{O_2}$  variation at four different temperature and humidity levels. d) Same as in c) for the  $p_{H_2O}$ -independent model.

Figure 7a depicts the measured exchange current density versus the modeled exchange current density for the  $p_{H_2O}$ -dependent model and Fig. 7b for the  $p_{H_2O}$ -independent model. The measured  $U_{jR-free}$  cell voltage versus the modeled cell voltage is also shown for both model variants in Figs. 7c and 7d. Even though both models yield very good agreement with the experimental data, the water-dependent model seems to slightly outperform the water-independent model, which is not surprising considering the additional degree of freedom in the fitting procedure. Figure S9c to S9f additionally depict the good match between measured  $U_{jR-free}$  polarization curves and the according model curves at four different  $rH$  and  $T$  combinations (exemplarily for the water-dependent model). Furthermore, we checked our specific values against the data published by Neyerlin et al.<sup>19</sup> that still represent a reliable reference to date for Pt/C catalysts. This comparison is given in Table III: first, we compared the exchange current density parameters referenced to  $80\text{ }^\circ\text{C}$  and 1 bar; second, we compared the  $jR$ -free cell voltage referenced to  $80\text{ }^\circ\text{C}$  1 bar and 0.9 V. The equation for the latter was given as in Eq. 20:<sup>19</sup>

$$U_{jR-free} = 0.9\text{ V} - \frac{RT}{\alpha_c F} \ln \left[ \frac{j + j_{crossover}}{r_f \cdot j_{0,ref}^{0.9V} \cdot \left(\frac{p_{H_2}}{p_{ref}}\right)^{\alpha_c/2} \cdot \left(\frac{p_{O_2}}{p_{ref}}\right)^m \cdot \exp\left[\frac{-E_{ref}^{0.9V}}{RT} \left(1 - \frac{T}{T_{ref}}\right)\right]} \right] \quad [20]$$

Table III shows that there is a good agreement between the reference from the literature and our measurements. Hence, we have an accurate ready-to-use model for the ORR mechanism in our full cell described by a simple Tafel law with an intrinsic slope determined by  $\alpha_c = 1$ . This model can reasonably be applied over a wide range of current densities ( $U_{jR-free} > 0.8\text{ V}$ ) and, according to the

literature, more complex models with ORR intermediates only gain importance with low-loaded cathodes or at lower potentials.<sup>27</sup> Subramanian et al. parameterized oxide-coverage-dependent ORR kinetics to model their  $jR$ -corrected performance curves measured with a cathode loading of  $0.06\text{ mg cm}^{-2}_{geo}$ .<sup>27</sup> This model contains a change in the apparent Tafel slope at around 0.75 V to 0.8 V and they ruled out mass transport effects in their measurement based on limiting current measurements. In our data, we also see deviations from the ORR model below 0.8 V. These effects could also result from more complex ORR kinetics, from inaccurate  $jR$  corrections at high current densities (decreasing fitting quality with decreasing CCL utilization), or from mass transport contributions. A more detailed discussion regarding these observations is given below.

**Mass transport contributions.**—Investigating the contribution to the cell resistance of  $O_2$  mass transport from the gas channels to the catalytic surface of the Pt particles is essential for modeling purposes since it usually contributes to the overpotential at operating conditions that are relevant from a system point of view (medium to high current densities). Furthermore, the importance of this contribution grows as the roughness factor decreases,<sup>62</sup> which is a main target to pursue for cost-reductions. In this work, we want to clarify whether  $O_2$  transport contributions are relevant in the ORR parameterization to ensure that the parameters are free of unwanted effects. For this purpose, both the steady-state limiting current (SLC) technique and the transient limiting current (TLC) technique are used and discussed. The principle of the first method lies in measuring the limiting current density with strongly diluted oxygen to avoid high currents and therefore much water production (dry transport resistance), whereas the principle of the second method lies in recording a limiting current density for an arbitrarily conditioned cell state by going to a low cell voltage only for a few seconds ( $< 10\text{ s}$ ) in order not to significantly change the cell state. In our case, the TLC was measured along polarization curves for different operating

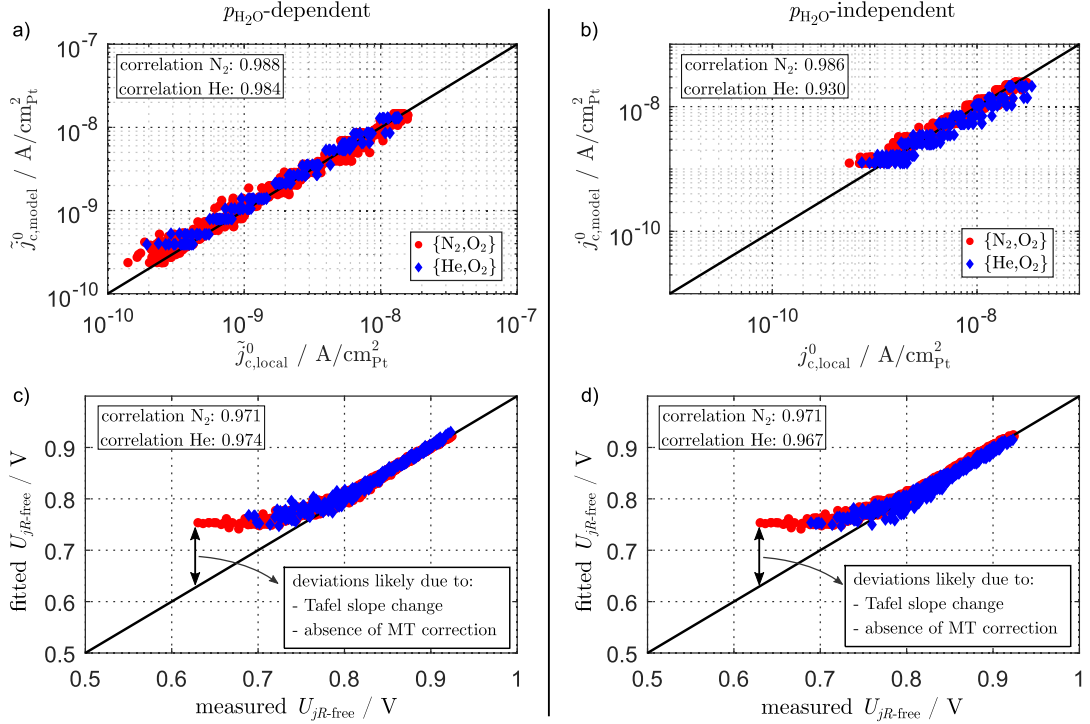


**Figure 7.** a) Correlation plot of the ORR exchange current density  $j_{c,\text{eff}}^0$  (local measurement vs. model) with the  $p_{\text{H}_2\text{O}}$ -dependent model. b) Same as in a) with the  $p_{\text{H}_2\text{O}}$ -independent model ( $j_{c,\text{eff}}^0$ ). In a) and b), the local exchange current density was calculated for all the currents  $j < 1 \text{ A cm}^{-2}$ . c) Correlation plot of  $U_{\text{measurement}} = U_{jR-\text{free}}$  vs.  $U_{\text{model}} = U_0 - \eta_{\text{ORR,model}}$  for all the conditions (and current densities) with the  $p_{\text{H}_2\text{O}}$ -dependent model. d) Same as in c) with the  $p_{\text{H}_2\text{O}}$ -independent model. The plots a) and b) contain each 783  $\{\text{O}_2, \text{N}_2\}$  data points and 168  $\{\text{O}_2, \text{He}\}$  data points and the plots c) and d) contain each 1117  $\{\text{O}_2, \text{N}_2\}$  data points and 240  $\{\text{O}_2, \text{He}\}$  data points.

**Table III.** Comparison of our reference data ( $rH = 80\%$ ) with the data of Neyerlin et al.<sup>19</sup> The parameters were acquired by fitting Eq. 15 and Eq. 20 to our data.

Parameter	Neyerlin <sup>19</sup>	This work	
		$\{\text{O}_2, \text{N}_2\}$	$\{\text{O}_2, \text{He}\}$
Exchange current density parameters			
$j_{c,\text{ref}}^0 \cdot 10^8 \text{ (A/cm}^2_{\text{Pt}})$	2.47	2.15	2.45
$\gamma$ (—)	0.54	0.51	0.62
$E_{\text{act}}$ (kJ mol <sup>-1</sup> )	67	71.27	68.62
$U_{jR-\text{free}}$ parameters			
$j_{0,\text{ref}}^{0.9V} \cdot 10^4 \text{ (A/cm}^2_{\text{Pt}})$	2.47	2.11	2.49
$m$ (—)	0.79	0.75	0.87
$E_{\text{act}}^{0.9V}$ (kJ mol <sup>-1</sup> )	10	10.85	10.89

parameters to investigate the impact of current density on the transport resistance.

We measured steady-state limiting currents for strongly diluted  $\text{O}_2$  in  $\text{N}_2$  gas streams and different temperature and humidity levels according to the method described by Baker et al.<sup>38</sup> During this procedure, the cell was operated up to the  $\text{O}_2$  mass transport limitation (vertical part of the polarization curve at high currents) by jumping to cell voltages below 0.3 V in the potentiostatic mode. Low oxygen concentrations are used to avoid high limiting currents and therefore much liquid water production that would alter the measured transport resistance in the gas phase. From this limiting current density the oxygen transport resistance (in s/m) from the channel to the electrode can be calculated by

$$R_{\text{O}_2, \text{MT}} = \frac{p_{\text{O}_2}^{\text{channel}} \cdot 4 \cdot F}{R \cdot T \cdot j_{\text{lim}}} \quad [21]$$

Since the conditions were not perfectly differential during the limiting current measurements, we chose to use a log-mean  $\text{O}_2$  partial pressure in the gas channel which was calculated based on the inlet and the outlet mole fraction. The outlet mole fraction was estimated by

$$x_{\text{O}_2}^{\text{outlet}} = \frac{\dot{n}_{\text{O}_2}^{\text{inlet}} - j_{\text{lim}} / (4 \cdot F)}{\dot{n}_{\text{O}_2}^{\text{inlet}} + \dot{n}_{\text{N}_2} + \dot{n}_{\text{H}_2\text{O}}^{\text{inlet}} + j_{\text{lim}} / (4 \cdot F)} \quad [22]$$

with  $\dot{n}$  being the molar fluxes and under the assumption that the product water is completely in the gas phase on the cathode side,  $\dot{n}_{\text{H}_2\text{O}}^{\text{outlet}} = \dot{n}_{\text{H}_2\text{O}}^{\text{inlet}} + j_{\text{lim}} / (2 \cdot F)$ . Based on such an  $\text{O}_2$  transport resistance from limiting current experiments, it is possible to estimate the voltage drop during a polarization curve by considering both the effect on the Nernst voltage and the drop of the exchange current density of the ORR:

$$\Delta U_{\text{O}_2, \text{MT}}(j) = \frac{RT}{F} \left( \frac{1}{4} + \frac{\gamma_{\text{ORR}}}{\alpha_{\text{ORR}}} \right) \ln \left( \frac{p_{\text{O}_2}^{\text{in}} - \frac{RT}{4F} \cdot R_{\text{O}_2} \cdot j}{p_{\text{O}_2}^{\text{in}}} \right) \quad [23]$$

Here,  $\gamma_{\text{ORR}} = 0.5$  is the ORR reaction order and  $\alpha_{\text{ORR}} = 1$  the ORR transfer coefficient. In Fig. 8a we depict the measured transport resistance  $R_{\text{O}_2, \text{MT}}$  over the limiting current density  $j_{\text{lim}} \propto \alpha_{\text{O}_2}$  for 80% and 100%  $rH$  and four temperatures ( $T = 50 \text{ }^\circ\text{C}$  to  $T = 80 \text{ }^\circ\text{C}$ ). As expected, the resistance grows with decreasing temperature, which can be attributed to the decreasing diffusion coefficients. Also, the

80%- $rH$  resistances seem to be located in an intermediate range between dry conditions and fully saturated conditions as they converge to very low values at low limiting currents and to similar values as for 100%  $rH$  at high limiting currents. We also observed such a transition behavior between a dry and a wet plateau in our transient limiting current measurements (see Fig. 8c). Such behavior is known in the literature for some GDLs.<sup>39,40,63,64</sup> As the resistances are below  $1 \text{ s cm}^{-1}$  even at fully saturated gas and low temperature conditions, the loss contributions will be very small at typical operating conditions.

In Fig. 8b we show the voltage drop occasioned by  $\text{O}_2$  transport over the current density for four different temperature and humidity combinations, which reflects the higher transport resistances of the fully saturated conditions. Owing to the fact that the loss contribution initially increases linearly, it is very small in the low current density range ( $j < 0.5 \text{ A cm}^{-2}$ ) no matter the temperature and partial pressure. In the range that is interesting for our ORR investigations, the voltage drop does not exceed 3 mV and is therefore not significant for the ORR parameterization. Subramanian et al. used such SLC measurements as an argument to exclude the possibility of  $\text{O}_2$ -transport-related effects in the change of the apparent Tafel slope they observed experimentally (mainly with their low-loaded cathode).<sup>27</sup> However, according to us there are two uncertainties coming with such considerations. First, the resistance from the SLC experiment does not correspond to the resistance along the polarization curve since it is a function of saturation and temperature of the porous media and therefore depends on current density. This is indicated in Fig. 8c, where the transient limiting current measurements show the significant influence of the pre-polarization current on the mass transport resistance. Secondly, we might underestimate the resistance and mainly characterize the GDL resistance because the oxygen concentration may drop toward zero at the CL/GDL boundary during limiting current operation such that the catalytic reaction concentrates near that interface. Thus, the measured resistance may not contain the CCL resistance that is effective during a normal polarization curve in the non-transport-limited region. Moreover, even though  $R_{\text{O}_2, \text{MT}}$  in the SLC case (Fig. 8a) seems to converge to similar values as the wet plateaus in the TLC case (Fig. 8c) at high limiting currents (and thus high  $\text{O}_2$  concentrations), the TLC resistances are higher than the SLC resistances at low currents, indicating a different water management in the cell. This effect was also observed by Göbel et al.<sup>40</sup> but is not yet well enough understood. Therefore, the polarization curve corrections based on limiting current techniques have to be interpreted with caution. However, mass transport corrections of the performance based on both the SLC and the TLC technique are discussed below. For the SLC method we parameterized a model of the transport resistance  $R_{\text{O}_2, \text{MT}}$  by fitting it to the values measured for the highest  $\text{O}_2$  concentration (highest limiting current and thus highest resistance)  $x_{\text{O}_2} = 0.15$ , over all the humidity, temperature, and total pressure levels (see above for the values). For this model we got

$$R_{\text{O}_2, \text{SLC}} = (8.74 \cdot 10^{-1} \text{ s/cm}) (rH)^{0.07} \left( \frac{p_{\text{total}}}{p_{\text{ref}}} \right)^{0.87} \times \exp \left( \frac{10.7 \text{ kJ mol}^{-1}}{RT} \right) \quad [24]$$

with  $p_{\text{ref}} = 1 \text{ bar}_a$ . The good match between this model and the measured data is shown in Fig. 9.

**Loss contributions analysis.**—Finally, we show typical  $jR$ -corrected polarization curves for the  $\text{N}_2$  and the He cases in Fig. 10a ( $T = 50^\circ\text{C}$ ,  $rH = 80\%$ ) and Fig. 10b ( $T = 80^\circ\text{C}$ ,  $rH = 80\%$ ) for all our  $\text{O}_2$ -concentration levels in the Tafel representation. These polarization curves show that the kinetics part at low currents can be accurately described by a Tafel slope of around 70 mV/dec, which meets our expectations. Moreover, the use of

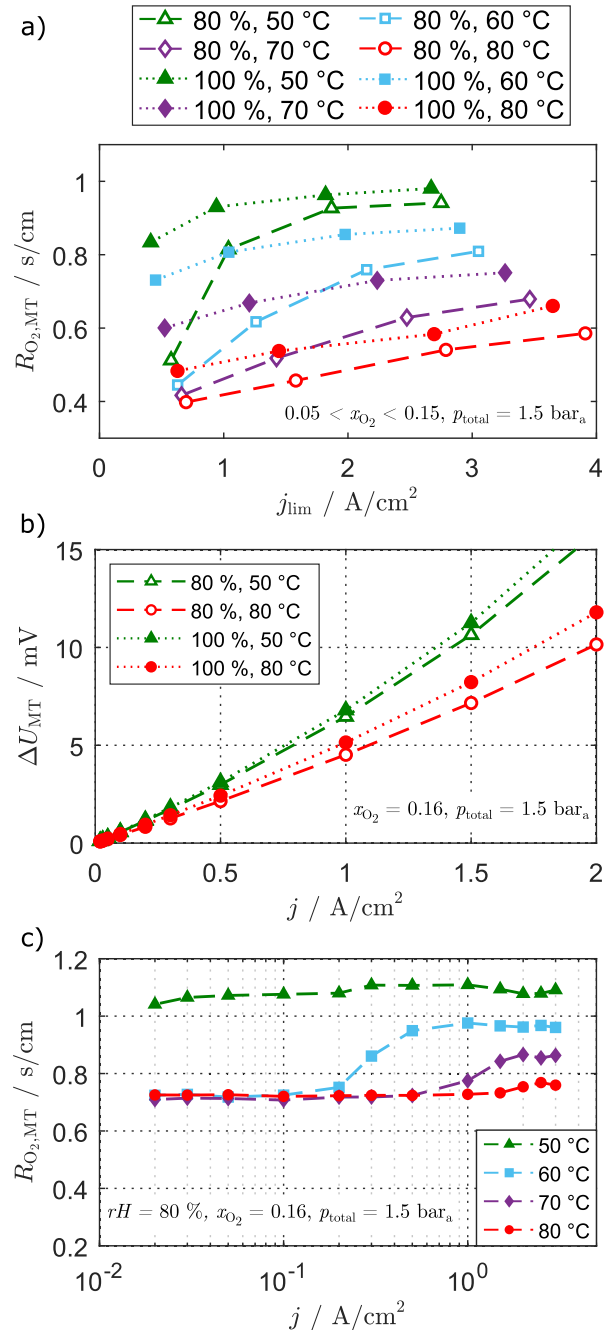


**Figure 8.** a) Oxygen mass transport resistance  $R_{\text{O}_2, \text{MT}}$  from steady-state limiting current measurements in fuel cell configuration depending on the limiting current density for different temperature and humidity conditions at  $p_{\text{total}} = 1.5 \text{ bar}_a$ . The variation of the limiting current was achieved by varying the oxygen mole fraction in the gas stream. b) Voltage loss contribution from  $\text{O}_2$  transport over the current density for four different humidity and temperature combinations, estimated for  $x_{\text{O}_2} = 0.16$ . c)  $R_{\text{O}_2, \text{MT}}$  from transient limiting current measurements over the conditioning current density at  $rH = 80\%$ ,  $p_{\text{total}} = 1.5 \text{ bar}_a$  and  $x_{\text{O}_2} = 0.16$  for four temperatures.

helium instead of nitrogen does not seem to influence the kinetics part ( $j \leq 0.2 \text{ A cm}^{-2}$  at  $T = 50^\circ\text{C}$  and  $j \leq 0.5 \text{ A cm}^{-2}$  at  $T = 80^\circ\text{C}$ ) and starts to have an influence at current densities above  $0.3 \text{ A cm}^{-2}$ . While the heliox curves clearly show less voltage loss at high current

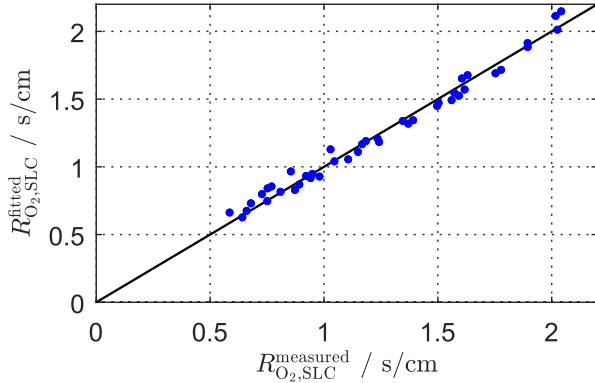


**Figure 9.** Correlation plot of  $R_{O_2,SLC}^{measured}$  versus  $R_{O_2,SLC}^{fitted}$  for  $x_{O_2} = 0.15$  and all the  $rH$ ,  $T$  and  $p_{total}$  levels.

densities, deviations from ideal Tafel behavior still remain in this region. Plausible explanations would be either pressure-independent transport effects (platinum-near effects that are unaffected by the use of heliox) or intrinsic changes of the ORR Tafel slope. Interestingly, the deviations are more important at cold conditions, where the diffusion coefficients are the lowest and two-phase issues (liquid water) the most pronounced. Also, the  $x_{O_2} = 1$  curves are parallel to the  $x_{O_2} = 0.5$  curves with nitrogen but the distance between the  $x_{O_2}^{dry} = 1$  curves and the  $x_{O_2} = 0.5$  curves with helium decreases over the current density. One explanation for this effect could be a different water management with the helium mixture since the diffusion coefficient of water in helium is roughly ten times higher than the one of water in nitrogen ( $3.1 \cdot 10^{-4} \text{ m}^2 \text{ s}^{-1}$  for He against  $3.9 \cdot 10^{-5} \text{ m}^2 \text{ s}^{-1}$  for  $N_2$  at 300 K) and the thermal conductivity of helium is roughly six times higher than the one of

nitrogen ( $157 \text{ mWm}^{-1} \text{ K}^{-1}$  for He against  $26 \text{ mWm}^{-1} \text{ K}^{-1}$  for  $N_2$  at 300 K and 2 bar).<sup>65</sup> Fig. 10c exhibits a typical polarization curve for  $x_{O_2} = 0.16$  with its according  $jR$  correction, anode correction based on our parameterization of the HOR, and mass transport correction based either on the SLC method (curve i) or on the TLC method (curve ii). One can see that even for this humid condition ( $rH = 80\%$ ), the major loss mechanism apart from the ORR still comes from the protonic losses in the membrane and cathode catalyst layer over a wide range of current densities. Figure 10c further confirms that voltage losses from anode kinetics and mass transport are negligible at the lowest current densities used for the parameterization of the ORR kinetics. Across our full factorial DOE, the voltage losses from these effects at  $j = 1 \text{ A cm}^{-2}$  do not exceed 5 mV ( $\approx 4.6 \text{ mV}$  at  $T = 50^\circ \text{C}$  and  $\approx 2.5 \text{ mV}$  at  $T = 80^\circ \text{C}$ , anode kinetics) and 7 mV (mass transport, based on SLC measurements), respectively. At higher current densities however, these losses gain in importance and thus meaningful characterization is needed in order not to draw wrong conclusions. Even though the Ohmic contributions and the HOR kinetics are properly accounted for, the mass transport loss correction brings uncertainties in the analysis: while the SLC-corrected curve predicts a deviation from the Tafel line beyond  $0.5 \text{ A cm}^{-2}$ , the TLC-corrected curve lies on the Tafel line over the whole current density range. Further measurement techniques such as EIS could be brought into play to strengthen the investigation of mass transport contributions. Nevertheless, the model for  $R_{O_2}$  parameterized by SLC measurements (see Eq. 24) can be employed to delimit the performance range in which the ORR obeys a simple Tafel law for sure, which corresponds to steady-state cathodic half-cell potentials above 0.8 V in our case as shown in Fig. 10d.

## Conclusions

In this work, we extensively studied the hydrogen and oxygen kinetics as well as oxygen mass transport contributions in a

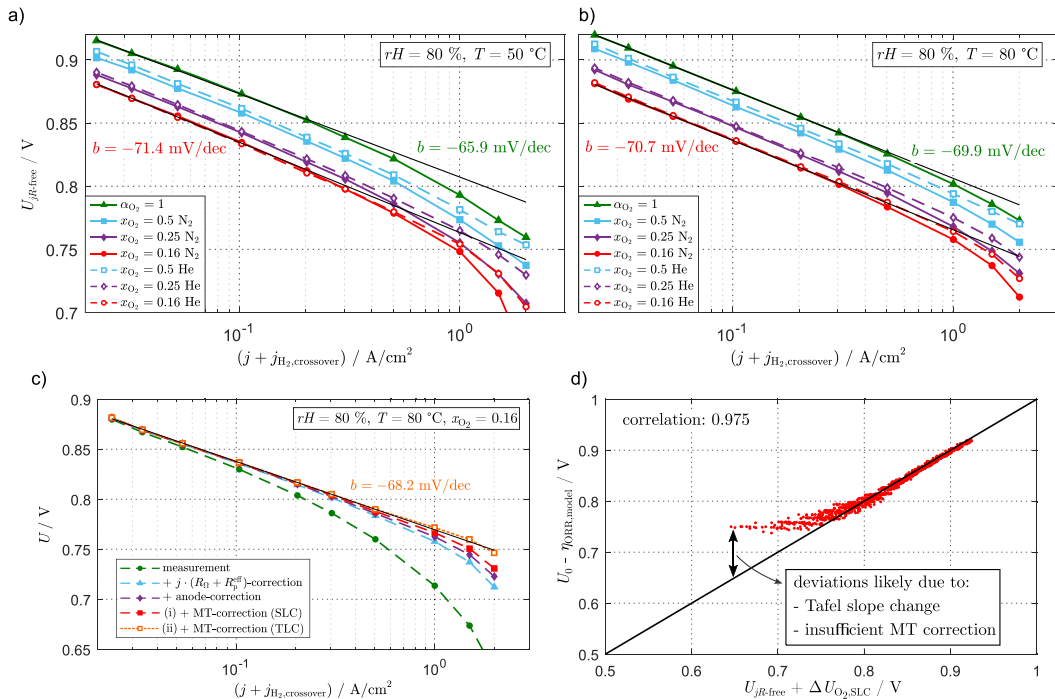


**Figure 10.** Polarization curves in the Tafel representation. a)  $jR$ -free curves for our four  $O_2$  concentrations in the  $\{O_2, N_2\}$ -mixture and comparison with the same concentrations in the  $\{O_2, He\}$ -mixture at  $rH = 80\%$  and  $T = 50^\circ \text{C}$ . b) Same as in a) but at  $rH = 80\%$  and  $T = 80^\circ \text{C}$ . c) Polarization curve for  $x_{O_2} = 0.16$  at  $rH = 80\%$  and  $T = 80^\circ \text{C}$  with its different levels of loss-corrections. d) Correlation plot of  $U_{\text{measurement}} + j \cdot (R_p^{\text{eff}} + R_\Omega) + \Delta U_{O_2,SLC}$  vs.  $U_{\text{model}} = U_0 - \eta_{\text{ORR,model}}$  for all the conditions with the  $p_{H_2O}$ -independent model. The mass transport correction was calculated by Eqs. 23 and 24.

differential PEM fuel cell with a state-of-the-art MEA based on an unprecedentedly large dataset. Systematic parameter variations ( $rH$ ,  $T$ ,  $p_{O_2}$ ,  $p_{H_2}$ ,  $j$ ) were conducted and polarization data and EIS were recorded.

EIS in the Proton pumping mode ( $H_2/H_2$ ) allowed us to better understand the performance signatures. With the help of DRT and by fitting a classical TLM to the data, we assigned the high-frequency loop to a combination of  $H_2$  kinetics (strongly  $p_{H_2}$  dependent) and proton transport in the catalyst layer (strongly  $rH$  dependent). We pointed out that the definition of the effective exchange current density therefore depends on the conductivity of the ionomer in the anodic catalyst layer. Even though we could not finally assign the low-frequency loop to a specific process, we showed that it is strongly influenced by both  $p_{H_2}$  and  $rH$ . We further found that CO surface poisoning can, in the absence of oxygen, severely impede the HOR kinetics and distort its characterization when overlooked, even at high temperatures. We introduced a fast and simple recovery procedure to oxidize parasitic CO almost simultaneously in both electrodes. This allowed us to get an accurate parameterization of the HOR (linearized Butler-Volmer consideration) in our full cell that can be used for loss contribution analyses and physical cell models.

Subsequently, a full factorial parameterization of the ORR mainly based on steady-state data obtained in the  $H_2/O_2$  mode with  $\{O_2, N_2\}$  or  $\{O_2, He\}$  mixtures on the cathode side provided a simple and accurate parameterization of the ORR kinetics based on a simple Tafel law with an exchange current density depending on  $p_{O_2}$  and temperature. Detailed analysis of its humidity dependency and comparison of  $p_{H_2O}$ -dependent and  $p_{H_2O}$ -independent models showed that it is justified to simply assume a constant water activity in modeling approaches even under dry conditions.

Furthermore, we quantified the oxygen mass transport contributions to the overall cell voltage through steady-state and transient limiting current measurements. In combination with the previously developed models of the HOR and ORR, this permitted a

quantitative analysis of the different loss mechanisms occurring in the cell and confirmed that the anode and mass transport contributions do not interfere with an ORR parameterization based on current densities  $j \leq 0.1 \text{ A cm}^{-2}$ . For the whole range of conditions covered by our full-factorial test procedure, the simple Tafel law accurately captures the (steady-state) ORR kinetics down to cathodic half-cell potentials of 0.8 V, without the need to account for intrinsic changes of the ORR Tafel slope. In the region of lower half-cell potentials and thus typically high current densities, the analysis becomes limited by uncertainties in the accounting of mass transport effects. This is because readily available techniques are not able to probe mass transport alone without at the same time affecting the internal state of the porous structures (water and heat management), as demonstrated by our comparison of steady-state and transient limiting current data, and our observations on heliox measurements.

However, our large set of EIS data revealed systematic trends on the dynamical response of the ORR reaction that are not covered by the simple Tafel law, even at low current densities. Further, observed discrepancies between Tafel slopes from polarization-based data and EIS-based evaluations hint at more complex electrode kinetics and shall be addressed in our next publication.

**Acknowledgments**

The authors thank SGL® Carbon for providing the gas diffusion layer samples and Gore® for helpful discussions.

**Appendix**

The flowchart in Fig. 11 shows the methods we use to fit our kinetics parameters depending on the electrode being investigated and whether an analytical expression of the overpotential  $\eta$  is known. Since in this work we employed simple Tafel kinetics for the ORR, which yields such an analytical relation for  $\eta_{ORR}$ , we only needed the paths that are inside the frame. However, our general

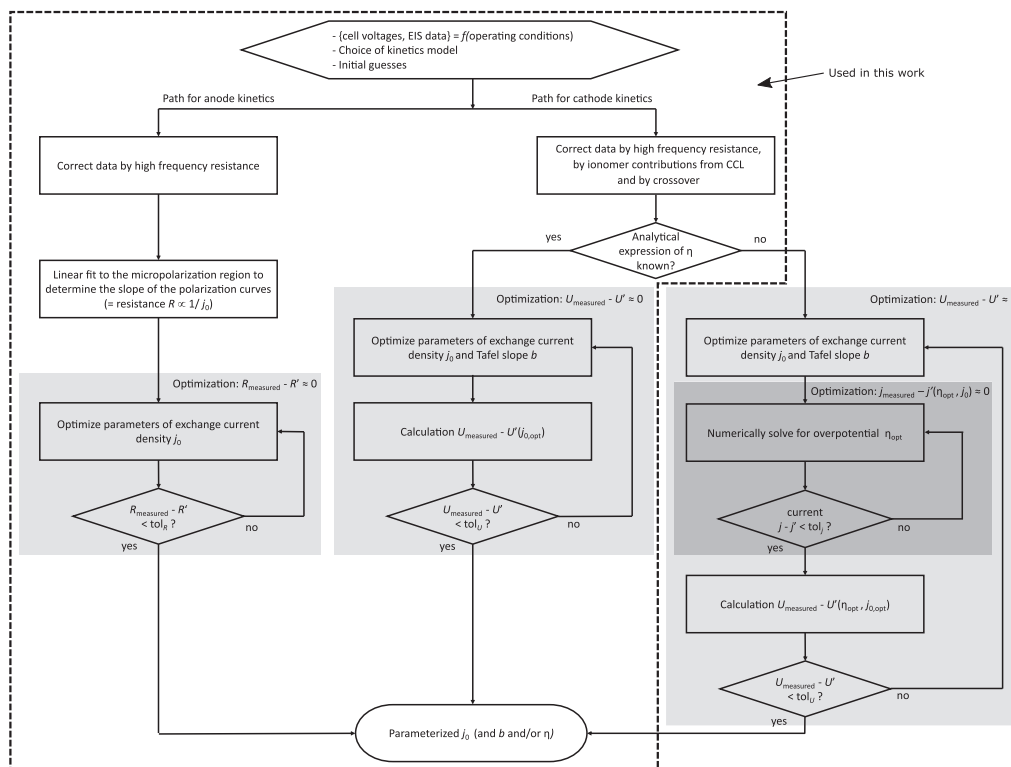


Figure 11. Flowchart representing the routines used in this work to extract kinetics parameters.



approach enables also to test other formulations of the ORR, which is not in the scope of this publication.

### ORCID

Christophe Gerling  <https://orcid.org/0000-0002-7918-6973>

### References

1. Y. Wang, D. F. Ruiz Diaz, K. S. Chen, Z. Wang, and X. C. Adroher, "Materials, technological status, and fundamentals of PEM fuel cells - A review." *Mater. Today*, **32**, 178 (2020).
2. T. E. Springer, "Polymer Electrolyte Fuel Cell Model." *J. Electrochem. Soc.*, **138**, 2334 (1991).
3. M. Eikerling and A. Kornyshev, "Modelling the performance of the cathode catalyst layer of polymer electrolyte fuel cells." *Journal of Electroanalytical Chemistry*, **453**, 89 (1998).
4. L. Carrette, K. A. Friedrich, and U. Stimming, "Fuel Cells - Fundamentals and Applications." *Fuel Cells*, **1**, 5 (2001).
5. R. Vetter and J. O. Schumacher, "Experimental parameter uncertainty in proton exchange membrane fuel cell modeling. Part I: Scatter in material parameterization." *Journal of Power Sources*, **438**, 227018 (2019).
6. E. J. F. Dickinson and G. Smith, "Modelling the Proton-Conductive Membrane in Practical Polymer Electrolyte Membrane Fuel Cell (PEMFC) Simulation: A Review." *Membranes*, **10**, 310 (2020).
7. C. Gerling, M. Hanauer, U. Berner, and K. A. Friedrich, "Full factorial in situ characterization of ionomer properties in differential PEM fuel cells." *J. Electrochem. Soc.*, **168**, 0845 (2021).
8. A. F. Innocente and A. C. D. Ângelo, "Electrocatalysis of oxidation of hydrogen on platinum ordered intermetallic phases: Kinetic and mechanistic studies." *Journal of Power Sources*, **162**, 151 (2006).
9. D. Malevich, E. Halliop, B. Peppley, J. Pharoah, and K. Karan, "Effect of Relative Humidity on Electrochemical Active Area and Impedance Response of PEM Fuel Cell." *ECS Trans.*, **16**, 1763 (2019).
10. A. Huth, B. Schaar, and T. Oeckermann, "A proton pump concept for the investigation of proton transport and anode kinetics in proton exchange membrane fuel cells." *Electrochimica Acta*, **54**, 2774 (2009).
11. W. Sheng, H. A. Gasteiger, and Y. Shao-Horn, "Hydrogen Oxidation and Evolution Reaction Kinetics on Platinum: Acid vs Alkaline Electrolytes." *J. Electrochem. Soc.*, **157**, B1529 (2010).
12. J. Durst, C. Simon, F. Hasché, and H. A. Gasteiger, "Hydrogen oxidation and evolution reaction kinetics on carbon supported Pt, Ir, Rh, and Pd electrocatalysts in acidic media." *J. Electrochem. Soc.*, **162**, F190 (2014).
13. V. Briega-Martos, A. Ferre-Vilaplana, E. Herrero, and J. M. Feliu, "Why the activity of the hydrogen oxidation reaction on platinum decreases as pH increases." *Electrochimica Acta*, **354**, 136620 (2020).
14. B. M. Stühmeier, M. R. Pietsch, J. N. Schwämmlein, and H. A. Gasteiger, "Pressure and Temperature Dependence of the Hydrogen Oxidation and Evolution Reaction Kinetics on Pt Electrocatalysts via PEMFC-based Hydrogen-Pump Measurements." *J. Electrochem. Soc.*, **168**, 064516 (2021).
15. M. Ciureanu and H. Wang, "Electrochemical Impedance Study of Electrode-Membrane Assemblies in PEM Fuel Cells: I. Electro-oxidation of H<sub>2</sub> and H<sub>2</sub>/CO Mixtures on Pt-Based Gas-Diffusion Electrodes." *J. Electrochem. Soc.*, **146**, 4031 (1999).
16. M. Ciureanu, S. D. Mikhailenko, and S. Kaliaguine, "PEM fuel cells as membrane reactors: kinetic analysis by impedance spectroscopy." *Catal. Today*, **82**, 195 (2003).
17. A. G. Hombrados, L. González, M. A. Rubio, W. Agila, E. Villanueva, D. Guinea, E. Chinarro, B. Moreno, and J. R. Jurado, "Symmetrical electrode mode for PEMFC characterisation using impedance spectroscopy." *Journal of Power Sources*, **151**, 25 (2005).
18. M. Heinzmann, A. Weber, and E. Ivers-Tiffée, "Advanced impedance study of polymer electrolyte membrane single cells by means of distribution of relaxation times." *Journal of Power Sources*, **402**, 24 (2018).
19. K. C. Neyerlin, W. Gu, J. Jorne, and H. A. Gasteiger, "Determination of Catalyst Unique Parameters for the Oxygen Reduction Reaction in a PEMFC." *J. Electrochem. Soc.*, **153**, A1955 (2006).
20. A. Holewinski and S. Lincic, "Elementary mechanisms in electrocatalysis: revisiting the ORR Tafel slope." *J. Electrochem. Soc.*, **159**, H864 (2012).
21. J. Huang, J. Zhang, and M. Eikerling, "Unifying theoretical framework for deciphering the oxygen reduction reaction on platinum." *Phys. Chem. Chem. Phys.*, **20**, 11776 (2018).
22. A. M. Gómez, "Marín and E. A. Ticianelli. A reviewed vision of the oxygen reduction reaction mechanism on Pt-based catalysts." *Current Opinion in Electrochemistry*, **9**, 129 (2018).
23. B. P. Setzler and T. F. Fuller, "A physics-based impedance model of proton exchange membrane fuel cells exhibiting low-frequency inductive loops." *J. Electrochem. Soc.*, **162**, F519 (2015).
24. I. V. Zenyuk, "P. K. Das, and A. Z. Weber. Understanding Impacts of Catalyst-Layer Thickness on Fuel-Cell Performance via Mathematical Modeling." *J. Electrochem. Soc.*, **163**, F691 (2016).
25. Georg A. Futter, Pawel Gazdzicki, K. Andreas Friedrich, and Arnulf Latz, "and Thomas Jahnke. Physical modeling of polymer-electrolyte membrane fuel cells: Understanding water management and impedance spectra." *Journal of Power Sources*, **391**, 148 (2018).
26. A. Goshtasbi, P. García-Salaberri, J. Chen, K. Talukdar, and D. G. Sanchez, "and Tulga Ersal. Through-the-Membrane Transient Phenomena in PEM Fuel Cells: A Modeling Study." *J. Electrochem. Soc.*, **166**, F3154 (2019).
27. N. P. Subramanian, T. A. Greszler, J. Zhang, W. Gu, and R. Makharia, "Pt-oxide coverage-dependent oxygen reduction reaction (ORR) kinetics." *J. Electrochem. Soc.*, **159**, B531 (2012).
28. A. A. Kulikovskiy and A. Physically, "Based Analytical Polarization Curve of a PEM Fuel Cell." *J. Electrochem. Soc.*, **161**, F263 (2014).
29. T. E. Springer, T. A. Zawodzinski, M. S. Wilson, and S. Gottesfeld, "Characterization of polymer electrolyte fuel cells using AC impedance spectroscopy." *J. Electrochem. Soc.*, **143**, 587 (1996).
30. D. Malevich, E. Halliop, B. A. Peppley, J. G. Pharoah, and K. Karan, "Investigation of Charge-Transfer and Mass-Transport Resistances in PEMFCs with Microporous Layer Using Electrochemical Impedance Spectroscopy." *J. Electrochem. Soc.*, **156**, B216 (2009).
31. S. Cruz-Manzo and R. Chen, "A generic electrical circuit for performance analysis of the fuel cell cathode catalyst layer through electrochemical impedance spectroscopy." *Journal of Electroanalytical Chemistry*, **694**, 45 (2013).
32. S. Cruz-Manzo and R. Chen, "An electrical circuit for performance analysis of polymer electrolyte fuel cell stacks using electrochemical impedance spectroscopy." *J. Electrochem. Soc.*, **160**, F1109 (2013).
33. N. Wagner, "Characterization of membrane electrode assemblies in polymer electrolyte fuel cells using ac impedance spectroscopy." *Journal of applied electrochemistry*, **32**, 859 (2002).
34. N. Wagner, T. Kaz, and K. A. Friedrich, "Investigation of electrode composition of polymer fuel cells by electrochemical impedance spectroscopy." *Electrochimica Acta*, **53**, 7475 (2008).
35. N. Wagner and K. A. Friedrich, "Application of Electrochemical Impedance Spectroscopy for Fuel Cell Characterization: PEFC and Oxygen Reduction Reaction in Alkaline Solution." *Fuel Cells*, **9**, 237 (2009).
36. M. Heinzmann, A. Weber, and E. Ivers-Tiffée, "Impedance modelling of porous electrode structures in polymer electrolyte membrane fuel cells." *Journal of Power Sources*, **444**, 227279 (2019).
37. A. A. Kulikovskiy, "Analytical Models for PEM Fuel Cell Impedance." *Self-publishing, Eisma* (2018).
38. D. R. Baker, "D. A. Caulk, K. C. Neyerlin, and M. W. Murphy. Measurement of Oxygen Transport Resistance in PEM Fuel Cells by Limiting Current Methods." *J. Electrochem. Soc.*, **156**, B991 (2009).
39. D. A. Caulk and D. R. Baker, "Heat and Water Transport in Hydrophobic Diffusion Media of PEM Fuel Cells." *J. Electrochem. Soc.*, **157**, B1237 (2010).
40. M. Göbel et al., "Transient limiting current measurements for characterization of gas diffusion layers." *Journal of Power Sources*, **402**, 237 (2018).
41. Gregor S. Harzer, Jan N. Schwämmlein, Ana Marija Damjanović, Sourov Ghosh, and Hubert, "A. Gasteiger. Cathode Loading Impact on Voltage Cycling Induced PEMFC Degradation: A Voltage Loss Analysis." *J. Electrochem. Soc.*, **165**, F3118 (2018).
42. T. H. Wan, M. Saccoccio, C. Chen, and F. Ciucci, "Influence of the Discretization Methods on the Distribution of Relaxation Times Deconvolution: Implementing Radial Basis Functions with DRTools." *Electrochimica Acta*, **184**, 483 (2015).
43. W. Vogel, L. Lundquist, P. Ross, and P. Stonehart, "Reaction pathways and poisonsII: The rate controlling step for electrochemical oxidation of hydrogen on Pt in acid and poisoning of the reaction by CO." *Electrochimica Acta*, **20**, 79 (1975).
44. K. Seto and A. Iannelli, "B.e Love, and J. Lipkowski. The influence of surface crystallography on the rate of hydrogen evolution at Pt electrodes." *Journal of electroanalytical chemistry and interfacial electrochemistry*, **226**, 351 (1987).
45. R. Notoya and A. Matsuda, "Determination of the rate of the discharge step of hydrogen ion on a hydrogen-platinum electrode in aqueous solutions by the galvanostatic transient method." *The Journal of Physical Chemistry*, **93**, 5521 (1989).
46. H. Kita, S. Ye, and Y. Gao, "Mass transfer effect in hydrogen evolution reaction on Pt single-crystal electrodes in acid solution." *Journal of Electroanalytical Chemistry*, **334**, 351 (1992).
47. N. M. Marković, B. N. Grgur, and P. N. Ross, "Temperature-dependent hydrogen electrochemistry on platinum low-index single-crystal surfaces in acid solutions." *The Journal of Physical Chemistry B*, **101**, 5405 (1997).
48. L. Giorgi, A. Pozio, C. Bracchini, R. Giorgi, and S. Turtu, "H<sub>2</sub> and H<sub>2</sub>/CO oxidation mechanism on Pt/C, Ru/C and Pt-Ru/C electrocatalysts." *Journal of applied electrochemistry*, **31**, 325 (2001).
49. H. A. Gasteiger, J. E. Panels, and S. G. Yan, "Dependence of PEM fuel cell performance on catalyst loading." *Journal of Power Sources*, **127**, 162 (2004).
50. S. Chen and A. Kucernak, "Electrocatalysis under Conditions of High Mass Transport: Investigation of Hydrogen Oxidation on Single Submicron Pt Particles Supported on Carbon." *The Journal of Physical Chemistry B*, **108**, 13984 (2004).
51. K. C. Neyerlin, W. Gu, J. Jorne, A. Clark, and H. A. Gasteiger, "Cathode Catalyst Utilization for the ORR in a PEMFC." *J. Electrochem. Soc.*, **154**, B279 (2007).
52. K. C. Neyerlin, W. Gu, J. Jorne, and H. A. Gasteiger, "Study of the Exchange Current Density for the Hydrogen Oxidation and Evolution Reactions." *J. Electrochem. Soc.*, **154**, B631 (2007).
53. K. Wiezell, P. Gode, and G. Lindbergh, "Steady-State and EIS Investigations of Hydrogen Electrodes and Membranes in Polymer Electrolyte Fuel Cells." *J. Electrochem. Soc.*, **153**, A749 (2006).
54. N. Holmström, K. Wiezell, and G. Lindbergh, "Studying Low-Humidity Effects in PEFCs Using EIS: I. Experimental." *J. Electrochem. Soc.*, **159**, F369 (2012).
55. K. Wiezell, N. Holmström, and G. Lindbergh, "Studying low-humidity effects in PEFCs using EIS II. modeling." *J. Electrochem. Soc.*, **159**, F379 (2012).

*Journal of The Electrochemical Society*, 2022 **169** 014503

56. J. Kim, "Characterization of CO tolerance of PEMFC by ac impedance spectroscopy." *Solid State Ionics*, **140**, 313 (2001).
57. M. Mathias, D. Baker, J. Zhang, Y. Liu, and W. Gu, "Frontiers in Application of Impedance Diagnostics to H<sub>2</sub>-Fed Polymer Electrolyte Fuel Cells." *ECS Trans.*, **13**, 129 (2008).
58. H. Xu, Y. Song, H. R. Kunz, and J. M. Fenton, "Effect of Elevated Temperature and Reduced Relative Humidity on ORR Kinetics for PEM Fuel Cells." *J. Electrochem. Soc.*, **152**, A1828 (2005).
59. H. Xu, H. R. Kunz, and J. M. Fenton, "Analysis of proton exchange membrane fuel cell polarization losses at elevated temperature 120C and reduced relative humidity." *Electrochimica Acta*, **52**, 3525 (2007).
60. K. C. Neyerlin, H. A. Gasteiger, C. K. Mittelsteadt, J. Jorne, and W. Gu, "Effect of Relative Humidity on Oxygen Reduction Kinetics in a PEMFC." *J. Electrochem. Soc.*, **152**, A1073 (2005).
61. Y. Liu, M. W. Murphy, D. R. Baker, W. Gu, C. Ji, J. Jorne, and H. A. Gasteiger, "Proton Conduction and Oxygen Reduction Kinetics in PEM Fuel Cell Cathodes: Effects of Ionomer-to-Carbon Ratio and Relative Humidity." *J. Electrochem. Soc.*, **156**, B970 (2009).
62. A. T. S. Freiberg, M. C. Tucker, and A. Z. Weber, "Polarization loss correction derived from hydrogen local-resistance measurement in low Pt-loaded polymer-electrolyte fuel cells." *Electrochemistry Communications*, **79**, 14 (2017).
63. D. R. Baker and D. A. Caulk, "Limiting Current as a Tool to Study Oxygen Transport in PEM Fuel Cells." *ECS Trans.*, **50**, 35 (2013).
64. C. Simon, D. Kartouzian, D. Mueller, F. Wilhelm, and H. A. Gasteiger, "Impact of microporous layer pore properties on liquid water transport in PEM fuel cells: carbon black type and perforation." *J. Electrochem. Soc.*, **164**, F1697 (2017).
65. O. E. Herrera, D. P. Wilkinson, and W. Mérida, "Anode and cathode overpotentials and temperature profiles in a PEMFC." *Journal of Power Sources*, **198**, 132 (2012).

### 4.3 Experimental and Numerical Investigation of the Low-Frequency Inductive Features in Differential PEM Fuel Cells: Ionomer Humidification and Platinum Oxide Effects

In the third publication, the low-frequency inductive features in the EIS response of differential PEMFC were studied by measurements and numerical simulation [25]. These low-frequency features are hard to capture properly in the experiments and cause discrepancies between the local polarization curve slopes and the capacitive parts of EIS since they occur at frequencies even lower than the low-frequency real-axis intercept of the spectra in the Nyquist plane. To start, previous literature regarding this topic was summarized and two main sources of the low-frequency inductive loops were identified: firstly, slow water management contributions which increase the ionomer conductivity when operating the fuel cell; secondly, complex cathode reaction kinetics involving the ORR and platinum oxidation and reduction. Other effects such as HOR reaction intermediates might also play a role, but they do not represent the favored path to follow and along-the-channel effects could be discarded in this work by the setup.

Then, a new simple way of modeling the cathode kinetics was presented including the ORR and a platinum oxidation-reduction mechanism which leads to inductive loops as it affects the effective ECSA through the fraction of platinum oxide coverage and thus the apparent TS. These equations were integrated into a macro-homogeneous 1D through-plane finite element method (FEM) model reaching from the anode side of the PEM to the cathode gas channel. This model contains coupled electron and ion transport within the ionomer and the carbon phase, oxygen diffusion within the porous media and platinum oxidation kinetics within the CCL, all coupled through the ORR sinks and sources. Since this model can handle both the steady-state and transient behavior, it was used to simulate polarization curves, EIS spectra and cyclic voltammograms and a significant sensitivity investigation was carried out. The latter is shown in the supplementary material which can be found in section A.3. Thereafter, the results from the systematic parameter variations in H<sub>2</sub>/O<sub>2</sub> mode of the second publication (see section 4.2 [24]) were used to evaluate the discrepancies between the local polarization curve slopes and capacitive parts of EIS and the inductive contributions were thereby computed from our experimental data.

Based on the ionomer resistances under load from the first publication [23] (see section 4.1), the contributions of slow platinum oxide reactions and ionomer humidification were disentangled and it was shown that the latter matters the most at medium to high loads. Thus, the contribution of 30 mV/dec to 40 mV/dec at small currents mainly comes from kinetics effects. Furthermore, it was demonstrated that the inductive contributions reach over 150 mV/dec at high load and that they are strongly dependent on the current density ( $j$ ) and on the relative gas humidity ( $RH$ ), whereas temperature ( $T$ ) and oxygen partial pressure ( $p_{O_2}$ ) play a minor role. Finally, the FEM model was parameterized for wet conditions based on this dataset and gives an unprecedented match with both steady-state and EIS data, thus bringing performance and impedance signatures of PEMFC together.

This publication was written by the first author and commented by the three co-authors. The enhanced kinetics model consisting of both an ORR and a PtOx mechanism was developed by the first author and M. Hanauer and the final FEM model containing the PEM and the CCL layers with the associated physics was implemented and calibrated by the first author. The simulations were carried out by the first author. The test station used was newly commissioned and completely automated by the first author for this work. Data analysis and interpretation were performed by the first author and results were discussed with the three co-authors. The open access article is distributed under the terms of the Creative Commons Attribution Non-Commercial No Derivatives 4.0 International License (CC BY-NC-ND 4.0) and may be accessed at <http://dx.doi.org/10.1149/1945-7111/acb3ff>.

C. Gerling, M. Hanauer, U. Berner, and K. A. Friedrich, "Experimental and Numerical Investigation of the Low-Frequency Inductive Features in Differential PEM Fuel Cells: Ionomer Humidification and Platinum Oxide Effects." *J. Electrochem. Soc.*, **170**, 0145 (2023).



## Experimental and Numerical Investigation of the Low-Frequency Inductive Features in Differential PEMFCs: Ionomer Humidification and Platinum Oxide Effects

Christophe Gerling,<sup>1,2,z</sup> Matthias Hanauer,<sup>1</sup> Ulrich Berner,<sup>1</sup> and K. Andreas Friedrich<sup>2,3</sup>

<sup>1</sup>Robert Bosch GmbH, Corporate Research, Renningen 71272, Germany

<sup>2</sup>Institute for Building Energetics, Thermotechnology and Energy Storage (IGTE), University of Stuttgart, Stuttgart 70569, Germany

<sup>3</sup>Institute of Engineering Thermodynamics, German Aerospace Center (DLR), Stuttgart 70569, Germany

The low-frequency inductive features in PEMFC are studied by differential measurements and numerical simulation. Systematic parameter variations are conducted and the discrepancies between the local polarization curve slopes and the capacitive loops of electrochemical impedance spectra (EIS) are evaluated to compute the inductive contributions. These contributions, primarily slow platinum oxide kinetics and ionomer humidification, are disentangled and we show that the latter is more relevant at medium to high currents, leaving mainly kinetics contributions of around  $35 \text{ mV dec}^{-1}$  at small currents. We demonstrate that the inductivity reaches over  $150 \text{ mV dec}^{-1}$  at high load and that it strongly depends on the current density ( $j$ ) and on the relative gas humidity ( $RH$ ), whereas temperature ( $T$ ) and oxygen partial pressure ( $p_{\text{O}_2}$ ) play a minor role. A new approach for modeling the combination of the oxygen reduction reaction and platinum oxidation leading to inductive loops is presented and integrated into a 1D through-plane model which we parameterize based on our large dataset. We present a comprehensive parameter study with this model. Its current version contains platinum oxide kinetics and electron, proton as well as oxygen transport and yields a good match with both steady-state and EIS data.

© 2023 The Author(s). Published on behalf of The Electrochemical Society by IOP Publishing Limited. This is an open access article distributed under the terms of the Creative Commons Attribution Non-Commercial No Derivatives 4.0 License (CC BY-NC-ND, <http://creativecommons.org/licenses/by-nc-nd/4.0/>), which permits non-commercial reuse, distribution, and reproduction in any medium, provided the original work is not changed in any way and is properly cited. For permission for commercial reuse, please email: [permissions@iopublishing.org](mailto:permissions@iopublishing.org). [DOI: [10.1149/1945-7111/acb3ff](https://doi.org/10.1149/1945-7111/acb3ff)]



Manuscript submitted September 22, 2022; revised manuscript received December 1, 2022. Published January 25, 2023.

Supplementary material for this article is available [online](#)

The optimization of PEM fuel cells lifetime and costs in view of wide commercialization requires strong understanding of the membrane electrode assembly (MEA) performance signatures. Thus, in situ and in operando methods to characterize the physicochemical processes are strongly needed in the PEMFC development. In the past, mainly polarization curves complemented by electrochemical impedance spectroscopy (EIS) were employed as operando techniques. While steady-state polarization measurements are done by recording the cell voltage at different loads or vice-versa, the EIS technique uses a small sinusoidal current (galvanostatic) or voltage (potentiostatic) signal to record the system's response for a range of frequencies. However, polarization measurements alone are insufficient to separate the loss mechanisms and even though EIS is widely used in PEM characterization, it is still not fully understood. In Figs. 1a (Nyquist plot) and 1b (Bode representation) we show a representative EIS spectrum at high load and cold and dry conditions. There, the high-frequency (HF) inductive part due to the setup is visible below the axis intercept at approximately 10 kHz, which represents the Ohmic resistance (membrane and electronic resistance). The capacitive part that contains the proton transport resistance in the electrodes, charge transfer resistances and mass transport contributions is visible from approximately 10 kHz to 1 Hz. Recently, the distribution of relaxation times (DRT) was applied additionally to EIS to deconvolute the capacitive processes and generate better initial guesses for equivalent circuit model (ECM) fitting.<sup>1</sup> However, this method is also limited when the time constants in the system are very close or even overlap with each other. Thus, separating the reaction kinetics from oxygen and water transport processes happening at medium to low frequencies in PEMFC might be challenging under some conditions, making the analysis of EIS complex.

As can be seen in Fig. 1a, a low-frequency (LF) inductive loop is detected in EIS below 1 Hz. As a consequence, the axis intercept at approximately 1 Hz, which is typically used in EIS analyses, differs

from the actual differential resistance of the polarization curve (=local slope, black ellipse with red contour). This causes discrepancies between polarization-curve-based and EIS-based evaluation of the oxygen reduction reaction (ORR) Tafel slope  $b_{\text{ORR}} = \partial \eta_{\text{ORR}} / \partial \ln j$ , with  $j$  the current density and  $\eta_{\text{ORR}}$  the kinetics overpotential. This LF loop is still subject to research and has previously been attributed to side reactions and intermediates of the ORR, to platinum surface oxide (PtOx) formation and dissolution, to platinum poisoning by CO, or to changes in the ionomer hydration due to slow water dynamics, see the references in Table I.

However, to the best of our knowledge, there has been no attempt to quantify the contributions based on a consistent experimental dataset in combination with simulation since these effects were mostly treated separately in the past. Ionomer hydration effects were investigated by physical modeling by Kosakian et al.,<sup>17</sup> by Kulikovskiy<sup>18</sup> and by Wiezell et al. in combination with humidity-dependent anode contributions.<sup>12-15</sup> An EIS model containing platinum oxide effects was proposed early by Mathias et al.,<sup>6</sup> though it was fed with constant parameters and validated only by a single experimental spectrum. Setzler et al. analyzed the LF inductive behavior and the discrepancy between steady-state polarization and capacitive EIS response for various operating conditions based on experimental data and physical cell modeling.<sup>9</sup> Nevertheless, their platinum oxide kinetics were rather complex and their model did not match the experimental data at high loads. Also, their model did not predict an influence of water management on the LF inductive features, which is puzzling since most other comparable physical models do.<sup>14,16,17,29</sup> Futter et al. proposed an along-the-channel model that takes into account both water management phenomena and platinum oxide effects on the LF inductive signatures, but they observed a large mismatch between experimental and numerical spectra at low frequencies.<sup>29</sup> Lately, Schiefer et al. managed to record EIS down to 5 mHz in a differential cell and used a negative DRT analysis to unravel two processes with separate time constants within the LF inductive loops of their spectra:<sup>30</sup> one process was dominant at high cell voltage and the other one at low humidity. They could however not unambiguously assign the time constants to physico-chemical processes.

<sup>z</sup>E-mail: [christophe.gerling@de.bosch.com](mailto:christophe.gerling@de.bosch.com)

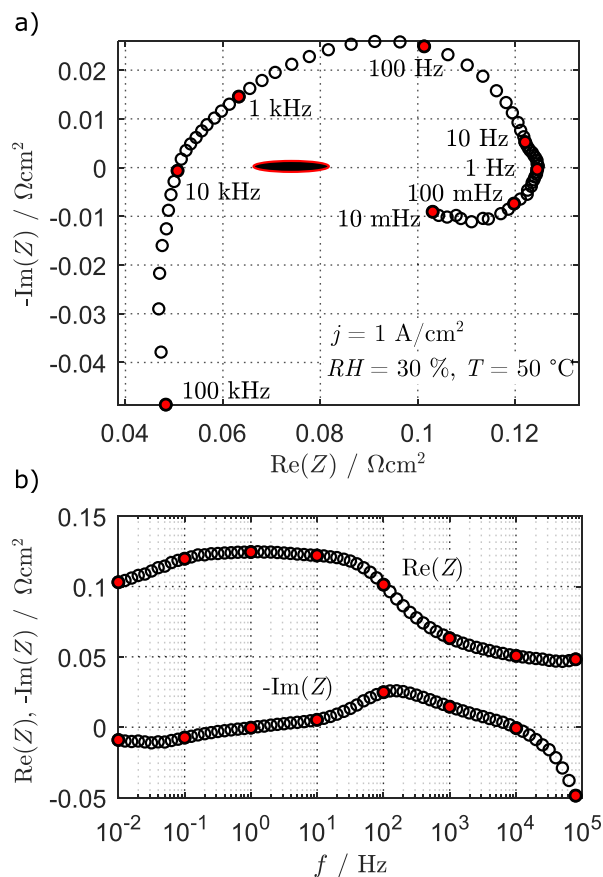


**Figure 1.** (a) Nyquist plot of an EIS spectrum recorded at  $j = 1 \text{ A/cm}^2$ ,  $RH = 30\%$  and  $T = 50 \text{ }^\circ\text{C}$  (dry conditions) from 100 kHz to 10 mHz. Some frequencies are highlighted by the filled red symbols and the steady-state differential resistance is shown by the black ellipse with red contour. (b) Corresponding Bode diagram showing the real and imaginary parts over the frequency  $f$ . See Fig. S1 in the supplementary material for the corresponding EIS at hot and dry conditions.

Finally, Meyer and Zhao showed that they could control the size of their inductive loops by making the oxygen volume flow oscillate at the same frequencies as the current during galvanostatic EIS.<sup>31</sup> The low-frequency limits of their spectra converged to the steady-state differential resistances of their polarization curves.

In this work, we aim at disentangling the different contributions of the LF inductive loop based on the extensive test run of our previous works.<sup>32,33</sup> We evaluate the absolute values of the inductive contributions by subtracting the local slopes of the polarization curves (calculated by numerical derivation) from the low-frequency real-axis-intercept of the capacitive EIS that occurs at approximately 1 Hz. With this knowledge and our previous study of the ionomer resistances,<sup>32</sup> we separate the humidification from the PtOx contributions and parameterize a simple ORR model containing platinum poisoning effects that result in a low-frequency inductive loop. We integrate this mechanism into a simplified 1D through-plane MEA model which matches the experimental data well. Thus, this model goes beyond simple Tafel law kinetics in order to reconcile steady-state performance and EIS signatures of PEM fuel cells. We also use this model for an extensive parameter study (see Figs. S6 to S29 in the supplementary material).

### Experimental

**Setup and procedures.**—We used Gore® PRIMEA® MEAs (W. L. Gore & Associates, Elkton, MD, USA) with 18  $\mu\text{m}$  membrane

thickness and loadings of 0.4/0.05  $\text{mg}_{\text{Pt}} \text{ cm}^{-2}$  in the cathode/anode. They were sandwiched between Sigracet® 22BB gas diffusion layers (GDL) from SGL® Carbon and mounted in a 12  $\text{cm}^2$  differential cell setup from Baltic FuelCells (quickConnect®) with an equivalent clamping pressure of about 1.3 MPa. In this setup, the combination of high gas flow rates (differential conditions, cell inlet = cell outlet) and the flowfield structure on the cathode side with wide channels (channel/land ratio of approximately 0.7/0.3) leads to negligible in-plane gradients during operation. We conditioned the cells in  $\text{H}_2/\text{air}$  configuration at  $p_{\text{total}} = 1.5 \text{ bar}_a$ ,  $RH = 100\%$ ,  $T = 50 \text{ }^\circ\text{C}$ , and with  $\text{H}_2/\text{air}$  flows of 1300/2000 sccm, as described by Harzer et al.<sup>34</sup>

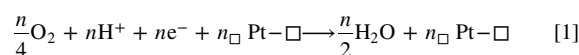
The same full factorial test runs under  $\text{H}_2/\text{O}_2$  and  $\text{H}_2/\text{N}_2$  conditions to record polarization test curves and EIS spectra as in our previous publications were used here.<sup>32,33</sup> The parameter ranges are summarized in Table II. For our EIS measurements we chose 10 currents out of the 16, which lead to 1120 spectra. We set constant dry flow rates of 1300/2000 sccm in the anode/cathode at the system pressure  $p_{\text{total}} = 1.5 \text{ bar}_a$  to get low pressure drops ( $\Delta p < 100 \text{ mbar}$ ) for all the conditions. The run was carried out in the order of increasing dew points and from high currents to low currents. Whenever adjusting the temperature or the dew point, the cell was stabilized in  $\text{H}_2/\text{air}$  at 0.7 V for 2 h. The currents at which we performed EIS were stabilized for at least 25 min prior to the measurement to ensure high measurement quality. We recorded most of our EIS in the range of  $f = 100 \text{ kHz}$  to  $f = 100 \text{ mHz}$  with 10 points per decade but some selected conditions were also recorded down to  $f = 10 \text{ mHz}$  (see Fig. 1).

More information about our setup and tests and how we ensured good measurement quality (state-of-health checks and Kramers-Kronig analyses) is given in our previous publications.<sup>32,33</sup>

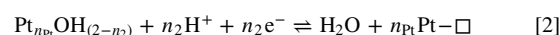
### Model

**Model description.**—In this work we aim at using a pragmatic approach for kinetics modeling and therefore propose a simple model based on two reactions. In the past, Setzler et al. published an extended ORR modeling approach and implemented it into a physical MEA model which yielded meaningful results, even though their spectra showed large deviations at high loads or low oxygen concentration.<sup>9</sup> Further, their oxide growth model is quite complex and thus not suited for our applications since we want a model that can be parameterized with a minimal amount of simple in situ experiments. Our model resembles the one of Mathias et al.<sup>6</sup> in the way that we also have a single step representing the slow platinum poisoning effect through oxides, even though we further simplify it by keeping only a single Tafel equation for the ORR rather than using a two-step mechanism with OH intermediates.

We model the ORR as a single non-reversible electron transfer step comparable to the well-known ORR Tafel approximation (only the cathodic branch), although containing the need for free platinum sites in the rate determining step:



where  $\text{Pt}-\square$  represents an active platinum site. The oxidation of the platinum surface is represented in a general way by



For simplicity, we will restrict our analysis in the following to the special case  $n_2 = 1$ . Based on the reaction given in Eq. 1 the rate of the ORR step  $\nu_1$  can be written as follows:

$$\nu_1 = k'_1 [\text{O}_2]^{\frac{n}{4}} [\text{H}^+]^n \cdot \exp\left(\frac{-\Delta G_1^\ddagger - (1-\beta)nF\Delta\phi}{RT}\right) \theta_{\square}^{n_{\square}} \quad [3]$$

with  $k'_1$  the rate constant,  $\Delta G_1^\ddagger$  the Gibbs free energy of activation of the ORR step,  $\Delta\phi = \phi_e - \phi_p$  the difference between the electrode

**Table I.** Overview of the most relevant literature regarding the low-frequency inductive loop and/or the bias between the slope of the polarization curve and the LF limit of the capacitive impedance.

Attributed physics	System/Model	Source/Year
Kinetics intermediates and/or platinum oxides	Half cells/ORR model	Antoine et al. <sup>2</sup> /2001
	Single cells	Mathias et al. <sup>3,7</sup> /2006
	Half cells/ORR and HOR model	Kuhn et al. <sup>4</sup> /2006
	Single cells/0D cell model	Roy et al. <sup>5</sup> /2007
	Single cells/ORR model	Mathias et al. <sup>6</sup> /2008
	Single cells and stacks/ECM modeling	Cruz-Manzo et al. <sup>7,8</sup> /2013
	Single cells/1D cell model	Setzler et al. <sup>9</sup> /2015
	ORR model PEM stacks/ECM modeling	Kulikovsky <sup>10</sup> /2015 Giner-Sanz et al. <sup>11</sup> /2018
Water and/or Ionomer dynamics	Single cells/1D model	Wiezell et al. <sup>12-15</sup> /2006-2012
	2D along-the-channel 1-phase isothermal model	Bao and Bessler <sup>16</sup> /2015
	Single cells/2D across-the-channel 1-phase non-isothermal model	Kosakian et al. <sup>17</sup> /2020
	CCL model	Kulikovsky <sup>18</sup> /2022
Combined effects/Others	Single cells (CO poisoning)	Wagner et al. <sup>19</sup> /2004
	Segmented cell (water dynamics and along-the-channel effects)	Schneider et al. <sup>20-23</sup> /2007-2008
	Segmented cell/2D along-the-channel model (along-the-channel effects)	Maranzana et al. <sup>24</sup> /2012
	Single cells/ ECM modeling	Pivac et al. <sup>25,26</sup> /2016-2017
	Single cells/ECM modeling (O <sub>2</sub> transport effects in CCL)	Pivac et al. <sup>27</sup> & Meyer et al. <sup>28</sup> /2018-2020
	2D along-the-channel 2-phase non-isothermal model (water dynamics and platinum oxides)	Futter et al. <sup>29</sup> /2018
	Single cells/ECM modeling & negative DRT (water dynamics, kinetics intermediates, anode contribution)	Schiefer et al. <sup>30</sup> /2020
	Single cells (concentration oscillations)	Meyer et al. <sup>31</sup> /2021

**Table II. Values taken by the parameters during our experimental run.<sup>33</sup> The values for  $x_{\text{O}_2}$  and  $j$  only apply for the test run in fuel cell mode.**

Parameter	Values
RH / %	{30, 40, 50, 60, 70, 80, 90, 100}
$T / ^\circ\text{C}$	{50, 60, 70, 80}
$x_{\text{O}_2}^{\text{dry}}$ or $x_{\text{O}_2} / -$	{1} or {0.5, 0.25, 0.16}
$j / \text{A/cm}^2$	{2, 1.5, 1, 0.5, 0.3, 0.2, 0.1, 0.05, 0.03, 0.02}

and the electrolyte potentials,  $\beta$  the symmetry coefficient,  $n$  the number of transferred electrons,  $[\text{O}_2]$  and  $[\text{H}^+]$  the activity of oxygen and protons, respectively, and  $\theta_{\square}$  the fraction of platinum sites free from oxides. As we want to express the rate constant as a function of the overpotential  $\eta = \Delta\phi - \Delta\phi_{\text{eq}}$ , we introduce the equilibrium condition

$$\Delta\phi_{\text{eq}} = -\frac{\Delta G_{1,\text{ref}}}{2F} - \frac{RT}{2F} \ln\left(\frac{[\text{H}_2\text{O}]}{[\text{O}_2]^{1/2}[\text{H}^+]^2}\right) \quad [4]$$

with  $\Delta G_{1,\text{ref}}$  the molar Gibbs free energy of reaction at standard conditions and  $[\text{H}_2\text{O}]$  the activity of water. With this, the reaction rate of the ORR can be rewritten as

$$\nu_1 = k_1[\text{H}^+]^{\beta n}[\text{O}_2]^{m/4}[\text{H}_2\text{O}]^{(1-\beta)n/2} \cdot \exp\left(\frac{-(1-\beta)nF}{RT}\eta\right)\theta_{\square}^{n_{\square}} \quad [5]$$

where  $k_1$  is defined such that it includes constants and an Arrhenius-type temperature dependency with the activation energy  $E_{\text{act},1}$ . Using a similar approach for the poisoning reaction, assuming  $\beta_2 = 1/2$ , introducing  $\Delta G_{1,\text{ref}}$ , and keeping both the cathodic and anodic branches, the reaction rate  $\nu_2$  can be expressed as follows:

$$\nu_2 = k_2' \left[ \theta_{\square}^{n_{\text{Pt}}} [\text{H}_2\text{O}] \exp\left(\frac{-\Delta G_2^{\ddagger} + \Delta G_{2,\text{ref}} + \frac{1}{2}F\Delta\phi}{RT}\right) - \left(\frac{1-\theta_{\square}}{n_{\text{Pt}}}\right) [\text{H}^+] \exp\left(\frac{-\Delta G_2^{\ddagger} - \frac{1}{2}F\Delta\phi}{RT}\right) \right] \quad [6]$$

where  $\Delta\phi$  must again be substituted since we want to express the kinetics as a function of the overpotential  $\eta$ . Thus, we transform Eq. 6 by implementing Eq. 4 and rearranging to

$$\nu_2 = k_2[\text{H}^+]^{1/2} \left[ \theta_{\square}^{n_{\text{Pt}}} [\text{O}_2]^{1/8} [\text{H}_2\text{O}]^{3/4} \exp\left(\frac{F}{RT}\Delta U_{\text{eq}}\right) \exp\left(\frac{F}{2RT}\eta\right) - \left(\frac{1-\theta_{\square}}{n_{\text{Pt}}}\right) [\text{O}_2]^{-1/8} [\text{H}_2\text{O}]^{1/4} \exp\left(-\frac{F}{2RT}\eta\right) \right] \quad [7]$$

with  $\Delta U_{\text{eq}} = -\Delta G_{1,\text{ref}}/(2F) + \Delta G_{2,\text{ref}}/F$  the difference of the reference equilibrium potentials of both reactions. We neglect the temperature dependency of  $\Delta U_{\text{eq}}$  and handle it as a fitting parameter. From this point on we set the proton activity  $[\text{H}^+]$  to unity. Further, we define the reaction rate constant  $k_2$  as

$$k_2 = k_{2,\text{ref}} \cdot \exp\left[\frac{-E_{\text{act},2}}{RT} \left(1 - \frac{T}{T_{\text{ref}}}\right)\right] \quad [8]$$

even though we set  $E_{\text{act},2} = 0 \text{ kJ mol}^{-1}$  in this study. According to this,  $k_{2,\text{ref}}$  is the only fitting parameter in Eq. 8. In order to transform  $\nu_2$  from Eq. 7 to a current density  $j_2$ ,  $k_2$  and therewith  $k_{2,\text{ref}}$  are expressed in  $\text{A/cm}^2$ .

We convert the reaction rate from Eq. 5 to a current density and re-organize the coefficients in the following way:

$$j_1 = n \cdot \nu_1 = j_{\text{c,eff}}^0 \exp\left(\frac{-(1-\beta)nF}{RT}\eta\right) \quad [9]$$

where  $j_{\text{c,eff}}^0$  is the effective or apparent exchange current density of the ORR which is given by

$$j_{\text{c,eff}}^0 = rf \cdot j_{\text{c,ref}}^0 \cdot [\text{O}_2]^{\gamma} \cdot [\text{H}_2\text{O}]^m \cdot \theta_{\square}^{n_{\square}} \cdot \exp\left[\frac{-E_{\text{act},1}}{RT} \left(1 - \frac{T}{T_{\text{ref}}}\right)\right] \quad [10]$$

with the roughness factor  $rf$ , the reference exchange current density  $j_{\text{c,ref}}^0$ , the activation energy  $E_{\text{act},1}$  and the exponents  $\gamma$ ,  $m$  for the dependencies on the activities of the species. These parameters can be fitted independently of each other and allow therefore for more flexibility. In the steady-state, the coverage is constant in time, leading to

$$\frac{\partial\theta_{\square}}{\partial t} = 0 \rightarrow \nu_2 = 0 \quad [11]$$

Thus, the total current  $j$  equals the ORR current  $j_1$ . With this, it is possible to write the equation of the steady-state coverage

$$\frac{\theta_{\square}^{n_{\text{Pt}}}}{1-\theta_{\square}} = \frac{1}{n_{\text{Pt}}} [\text{O}_2]^{-1/4} [\text{H}_2\text{O}]^{-1/2} \exp\left(-\frac{F}{RT}\Delta U_{\text{eq}}\right) \exp\left(-\frac{F}{RT}\eta\right) \quad [12]$$

and to discuss the asymptotic behavior of the model. In the low current limit ( $j \rightarrow 0$ , index "LC"), the denominator  $1 - \theta_{\square}$  of Eq. 12 approaches unity since the platinum surface is almost completely covered by oxides ( $\theta_{\square} \rightarrow 0$ ). By summarizing the first four terms of Eq. 12 in the constant  $C_1$  and bringing the exponent  $n_{\text{Pt}}$  to the right side of the equation we get the approximation for the free platinum surface fraction:

$$\theta_{\square}|_{j \rightarrow 0} = C_1 \cdot \exp\left(-\frac{F}{n_{\text{Pt}}RT}\eta\right) \quad [13]$$

This expression can be incorporated into the steady-state total current density equation which consists only in the ORR contribution and thus transforms to the low current form

$$j_{\text{LC}} = C_2 \cdot \exp\left(-\frac{F}{RT} \left((1-\beta)n + \frac{1}{n_{\text{Pt}}}\right)\eta\right) \quad [14]$$

In this case, the apparent steady-state Tafel slope  $b_{\text{LC}}$  is given by

$$b_{\text{LC}} = -\frac{RT}{\left((1-\beta)n + \frac{1}{n_{\text{Pt}}}\right)F} \quad [15]$$

In the opposite limit, at high current ( $j \rightarrow +\infty$ , index "HC"), the electrode potential and the oxide coverage of the platinum surface decrease such as

$$\theta_{\square}|_{j \rightarrow +\infty} = 1 \quad [16]$$

which means that the complete active platinum surface is available for the ORR, leading to the high current form

$$j_{\text{HC}} = C_3 \cdot \exp\left(-\frac{(1-\beta)nF}{RT}\eta\right) \quad [17]$$

and thus to the apparent Tafel slope at high currents  $b_{\text{HC}}$

$$b_{\text{HC}} = -\frac{RT}{(1-\beta)nF} \quad [18]$$



We see that Eqs. 15 and 18 only differ in the term  $1/n_{Pt}$  which comes from the oxide formation and relaxation at low load and which we expect to cause the low-frequency inductive behavior of  $30 \text{ mV dec}^{-1}$  to  $50 \text{ mV dec}^{-1}$  that we observe experimentally (see below). At high load, where the apparent Tafel slope is solely influenced by the actual ORR step, this term disappears. This means that carrying out polarization and EIS measurements at small currents is enough to fix the product  $(1 - \beta)n$  as well as  $n_{Pt}$ :

- $(1 - \beta)n \approx 0.66$  from the capacitive part of the EIS that represents  $-100 \text{ mV dec}^{-1}$  to  $-120 \text{ mV dec}^{-1}$ .
- $n_{Pt} \approx 2.5 - 3.3$  from the inductive part of the EIS that represents  $30 \text{ mV dec}^{-1}$  to  $50 \text{ mV dec}^{-1}$ .

To compute polarization curves and EIS spectra and to fit the parameters of the model described above to our experimental data we built a simple 1D through plane performance model in the commercial software COMSOL Multiphysics (Version 6.0). The aim of this model is to propose an improved description of PEMFC performance and EIS compared to models containing Butler-Volmer or Tafel description of the ORR while still being easier to parameterize and to handle than complete MEA models which also solve energy and water management. The justification for not representing in-plane effects, i.e. along- and across-the-channel gradients, lies in the differential operating conditions and the test cell setup with wide gas channels on the cathode side (see the setup and procedures above). Variations of the cathode flow around our baseline conditions (see experimental) showed no influence on the cell response, thus we discarded along-the-channel effects. Small channel-land effects cannot completely be discarded, particularly at high cell currents where liquid water is present in the porous structures. However, the latter effects mainly affect oxygen transport which is represented in a simplified manner through effective diffusion coefficients in this 1D approach.

The model is represented schematically in Fig. 2a and contains three domains: the membrane (PEM), the cathode catalyst layer (CCL) and the cathode gas diffusion layer (CGDL). Neither the anode catalyst layer (ACL) nor the cathode gas channel (CGC) are modeled. Hence, the model reaches from the ACL/PEM boundary to the CGDL/CGC boundary. Four partial differential Eqs. are solved in the model: two Eqs. based on the current conservation and Ohm's law for the proton and for the electron potentials  $\phi_p$  (PEM and CCL) and  $\phi_e$  (CCL and CGDL), one equation for the free platinum surface fraction  $\theta_{\square}$  (only in the CCL), and one equation for the oxygen mole fraction  $x_{O_2}$  (CCL and CGDL) based on Fick's law of diffusion. These Eqs. were implemented as follows for the CCL:

$$\frac{C_{dl}}{L_{CCL}} \cdot \frac{\partial \Delta \phi}{\partial t} + \nabla(-\sigma_p \nabla \phi_p) = -\frac{n \cdot \nu_1 + \nu_2}{L_{CCL}} \quad [19]$$

$$\frac{C_{dl}}{L_{CCL}} \cdot \frac{\partial \Delta \phi}{\partial t} + \nabla(-\sigma_e \nabla \phi_e) = \frac{n \cdot \nu_1 + \nu_2}{L_{CCL}} \quad [20]$$

$$\frac{\Gamma}{L_{CCL}} \cdot \frac{\partial \theta_{\square}}{\partial t} = -\frac{\nu_2 \cdot n_{Pt}}{L_{CCL} \cdot F} \quad [21]$$

$$\epsilon_p C \frac{\partial x_{O_2}}{\partial t} + \nabla(-CD_{O_2} \nabla x_{O_2}) = -\frac{n \cdot \nu_1}{L_{CCL} \cdot 4 \cdot F} \quad [22]$$

Since the model is considered as being macro-homogeneous, the material properties are distributed homogeneously over the layer thicknesses and the source terms on the right side of the Eqs. need to be volumetric. In these equations,  $C_{dl}$  is the double layer capacitance in  $\text{mF cm}^{-2}$ ,  $\Gamma$  the total quantity of surface platinum atoms in  $\text{mol}_{Pt}/\text{cm}^2_{geo}$ ,  $\epsilon_p$  the porosity of the porous layer,  $C$  the total gas concentration in  $\text{mol}/\text{m}^3$  and  $D_{O_2}$  the effective diffusion coefficient of oxygen in  $\text{m}^2 \text{ s}^{-1}$ . As can be seen, the mixed conductive nature of

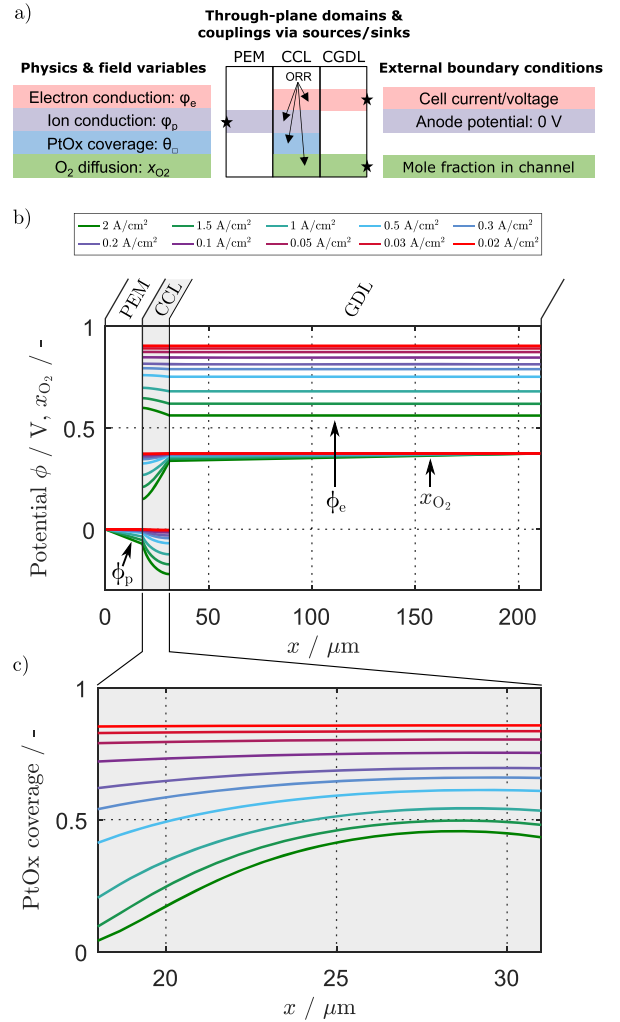


**Figure 2.** (a) Schematic representation of our physical 1D through-plane model as implemented in COMSOL Multiphysics 6.0. The domains and corresponding physics plus external boundary conditions (black stars) are shown. (b) Exemplary distribution of the electrode potential  $\phi_e$ , the electrolyte potential  $\phi_p$  and the oxygen mole fraction  $x_{O_2}$  over the layer thickness for the baseline parameterization at  $RH = 80\%$ ,  $T = 80^\circ \text{ C}$ ,  $x_{O_2}^{dry} = 0.5$  and different cell currents. Model parameters are consistent with Table III, with one exception: The electrode conductivity  $\sigma_{e,CCL}$  has been set unphysically low (5 S/m) to show its influence on the potential distribution. (c) Corresponding distribution of the platinum oxide coverage in the CCL.

the electrode is modeled, which is necessary to reproduce experimental performance curves and EIS accurately. We set the electron conductivity very high to create only negligible losses ( $>500 \text{ S m}^{-1}$ ) and took the proton conductivities  $\sigma_p$  from our previous characterization study.<sup>32</sup> The latter can be calculated based on the area specific resistances (ASR) shown in Fig. S4 and the layer thicknesses  $L$  given in Table III by  $\sigma_p = L/ASR$ .

So far, we did not model the water management (transport and ionomer hydration) explicitly in order to avoid too high complexity and only took the experimental data with high relative humidities for the parameterization and validation (see below). Particularly the EIS contributions of slow ionomer hydration/dehydration due to water management are not computed in the current model version. However, the impact of water management on the effective ionomer conductivities and thus on the performance is taken into account implicitly by employing the effective conductivities from our

**Table III. Baseline parameters of the presented model.**

Table III. Baseline parameters of the presented model.		
Design		
$L_{\text{PEM}}$ ( $\mu\text{m}$ )	18	
$L_{\text{CCL}}$ ( $\mu\text{m}$ ), $\epsilon_p$ (—)	13, 0.4	
$L_{\text{GDL}}$ ( $\mu\text{m}$ ), $\epsilon_p$ (—)	180, 0.8	
$rf$ ( $\text{m}_p^2/\text{m}_{\text{geo}}^2$ )	166	
$C_{\text{dl}}$ & $C_{\text{dl,CV}}$ ( $\text{mF}/\text{cm}_{\text{geo}}^2$ )	30 & 50	
Operating conditions		
$RH$ (%)	80	
$T$ ( $^{\circ}\text{C}$ )	80	
$x_{\text{O}_2}^{\text{dry}}$ (—)	1	
$P$ ( $\text{bar}_a$ )	1.5	
Diffusion properties (at $T = 80^{\circ}\text{C}$ )		
$D_{\text{O}_2\text{GDL}}$ ( $\text{cm}^2/\text{s}$ )	$3.0 \cdot 10^{-2}$	
$D_{\text{O}_2\text{CCL}}$ ( $\text{cm}^2/\text{s}$ )	$3.4 \cdot 10^{-4}$	
Kinetic properties		
	Tafel + PtOx	Tafel <sup>33</sup>
$n_{\text{O}_2}$ (—)	0.5	0.5
$n$ (—)	2	2
$n_{\text{Pt}}$ (—)	2.5	—
$n_{\square}$ (—)	1	—
$\beta$ (—)	0.66	0.5
$\Gamma$ ( $\text{mol}/\text{cm}_{\text{geo}}^2$ )	$1.44 \cdot 10^{-7}$	—
$\Delta U_{\text{eq}}$ (V)	0.42	—
$j_{\text{c,ref}}^0$ ( $\text{A}/\text{cm}_{\text{Pt}}^2$ )	$1.92 \cdot 10^{-6}$	$2.13 \cdot 10^{-8}$
$k_{2,\text{ref}}$ ( $\text{A}/\text{cm}_{\text{geo}}^2$ )	$7.07 \cdot 10^{-7}$	—
$\gamma$ (—)	0.54	0.51
$m$ (—)	0.50	0.49
$E_{\text{act},1}$ (kJ/mol)	60.5	68.7
$E_{\text{act},2}$ (kJ/mol)	0	—

experiments as functions of the gas channel relative humidity, the temperature and the current density. This means that no through-plane distribution of the conductivities is considered and especially that the membrane behaves like a purely Ohmic element (linear potential profile over the PEM). On this PEM layer, only the following equation is solved:

$$\nabla(-\sigma_p \nabla \phi_p) = 0 \quad [23]$$

Finally, on the GDL layer, electron and oxygen transport were computed respectively according to

$$\nabla(-\sigma_e \nabla \phi_e) = 0 \quad [24]$$

and

$$\epsilon_p C \frac{\partial x_{\text{O}_2}}{\partial t} + \nabla(-CD_{\text{O}_2} \nabla x_{\text{O}_2}) = 0 \quad [25]$$

The external boundary conditions for our simulations were the following:

- Dirichlet boundary  $\phi_e = \phi_p = 0$  V at the anode—membrane interface (ACL—PEM) as an approximation of the anode half-cell potential.
- Neumann boundary  $j = j^{\text{setpoint}}$  at the cathode gas diffusion layer—cathode gas channel interface (CGDL—CGC) to match the current setpoints of our experiments. For the EIS calculations we used the dynamic Neumann boundary condition  $j = j(t)$  and for the cyclic voltammetry simulations we used the dynamic Dirichlet boundary condition  $U = U(t)$ .
- Dirichlet boundary  $x_{\text{O}_2} = x_{\text{O}_2}^{\text{setpoint}}$  at the CGDL—CGC interface representing the oxygen mole fraction in the gas channel to match our experiments.

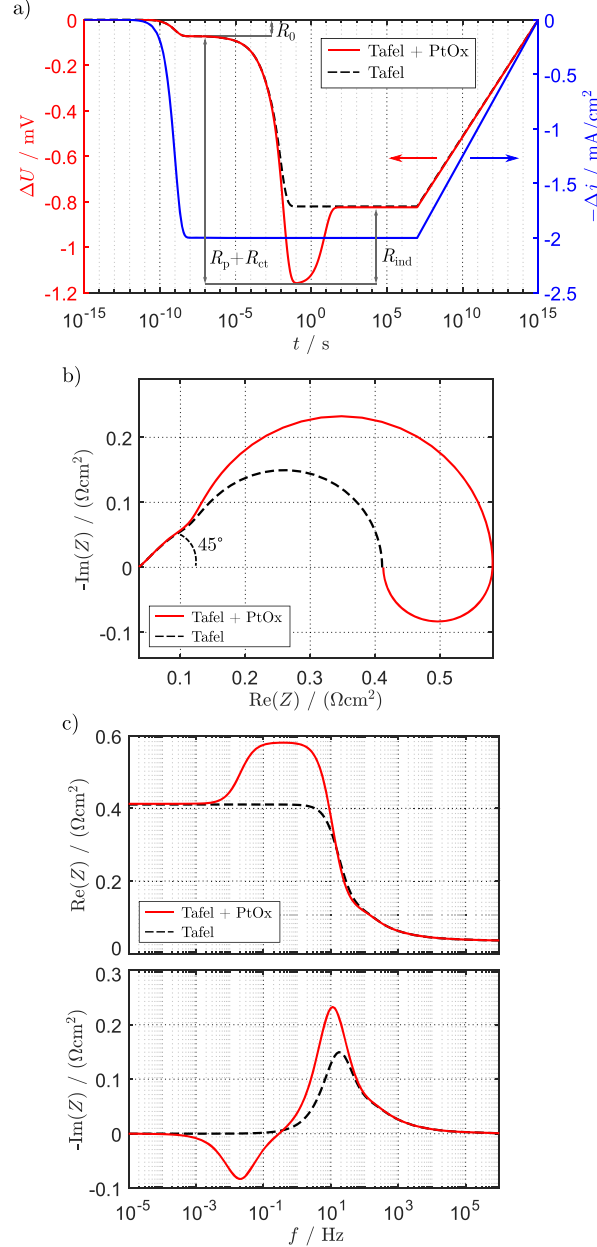


**Figure 3.** (a) Time traces of a galvanostatic EIS simulation at  $j=0.1$  A/cm<sup>2</sup>,  $T=80^{\circ}\text{C}$ ,  $RH=80\%$  and  $x_{\text{O}_2}^{\text{dry}}=1$  for our baseline parameterization without considering mass transport contributions and setting  $\sigma_{\text{p,CCL}}=0.5$  S/m and  $\sigma_{\text{p,PEM}}=5$  S/m. The excitation current (blue line, exponential step at  $t=10^{-15}$  s), the potential response for a Tafel law (dashed black line) and for our new model (solid red line) and the corresponding resistance assessment are shown. (b) Resulting EIS spectra in the Nyquist plane. (c) Resulting EIS spectra in the Bode plot.

**Computation of EIS and polarization curves.**—Polarization curves were simulated galvanostatically to match the currents selected during our experiments. In Figs. 2b and 2c we show typical through-plane distributions of the field variables of our model for the different current setpoints. This was simulated with our baseline parameterization given in Table III at  $RH=80\%$ ,  $T=80^{\circ}\text{C}$  and  $x_{\text{O}_2}^{\text{dry}}=0.5$ . Only the electronic conductivity  $\sigma_{\text{e,CCL}}$  has been lowered in this example to show its influence on the potential distribution

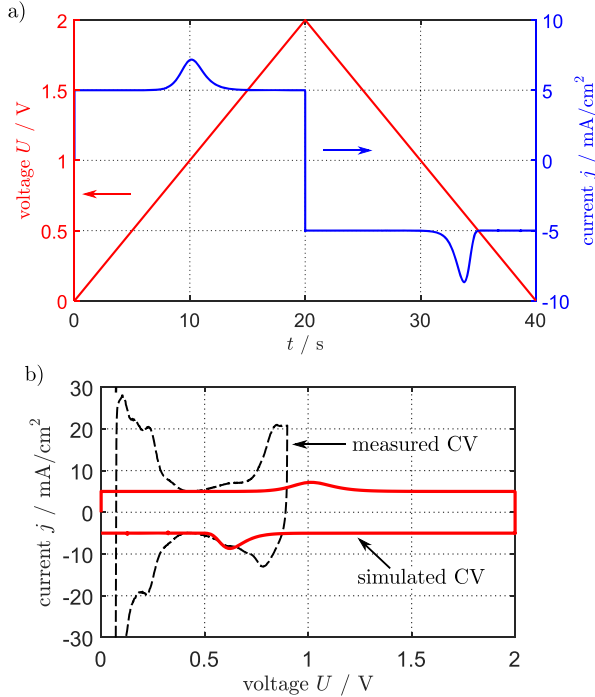


**Figure 4.** (a) Time traces of a cyclic voltammetry simulation (potentiostatic ramp up and ramp down) at 100 mV/s,  $T = 50\text{ }^{\circ}\text{C}$  and  $RH = 80\%$ . (b) Corresponding cyclic voltammogram in the representation  $j$  vs  $U$  (solid red line) and exemplary experimental CV (dashed black line). Hydrogen adsorption and the explicit dynamics of fast Pt oxidation effects are not modeled (see main text).

within the CCL. It can be observed that all the trends are linear within the PEM and the GDL layers; however, these trends are non-linear within the mixed-conducting CCL because of the sources and sinks due to the ORR. It is also interesting to notice that at current densities above  $0.5\text{ A cm}^{-2}$  in Fig. 2c the platinum oxide coverage drops toward zero at the PEM/CCL interface even though it remains almost as high as 50% at the CCL/CGDL interface. Thus, even at typical high current densities, the catalyst is not completely oxide free and the effective exchange current density and Tafel slope of the ORR are distributed inhomogeneously over the CCL. Note that this effect comes from the fact that all the kinetics locally depend on the difference between the electrolyte and the electrode potentials. Therefore, even if  $\sigma_{\text{e,CCL}}$  is not lowered, the effect remains almost as pronounced as in Fig. 2c. In the latter more realistic case, the electrode potential is constant through the CCL but the electrolyte potential is still strongly inhomogeneous due to the relatively low ionomer conductivity of the CCL in comparison with its electronic conductivity.

EIS spectra were simulated by applying a small current step on top of the DC load as described by Bessler.<sup>35</sup> The steady-state solution of each DC load was computed before performing an exponential current step  $j_{\text{step}} = 2\text{ mA cm}^{-2}$  according to

$$j(t) = j_{\text{DC}} + j_{\text{step}} \cdot \left[ 1 - \exp\left(-\frac{t}{\tau}\right) \right] \quad [26]$$

with  $\tau = 10^{-9}$  s. The simulated time window was defined from  $10^{-15}$  s to  $10^7$  s with a logarithmic time step distribution with 10 points per decade. After the simulation, a point was added artificially at  $t = 10^{15}$  s to slowly bring the system back to its original state. Then, the DC state was subtracted from the time trace of  $j(t)$  and  $\phi_{\text{e}}(t)|_{\text{GDL/GC}} = U(t)$  as shown exemplarily in Fig. 3a (only displacement from steady-state point remaining) and the Fourier transform of

these signals into the frequency domain was computed, followed by complex division to obtain the impedance:<sup>35</sup>

$$Z^*(\omega) = U^*(\omega)/j^*(\omega) \quad [27]$$

In the example shown in Fig. 3a, mass transport contributions were not taken into account and the protonic conductivities were set to  $\sigma_{\text{p,PEM}} = 5\text{ S m}^{-1}$  and  $\sigma_{\text{p,CCL}} = 0.5\text{ S m}^{-1}$ . The associated impedance responses are shown in Figs. 3b (Nyquist) and 3c (Bode), where the red curves originate from our new kinetics model and the black curves come from a Tafel kinetics model for the ORR. It is apparent that in contrast to the Tafel kinetics, our new description leads to an inductive loop. Since both EIS spectra converge to the same value for  $f \rightarrow 0$  Hz, the effective differential resistance (local slope of the polarization curve) of both models is equivalent. Regarding only the kinetics, both models yield approximately  $b = -70\text{ mV dec}^{-1}$ :

- Tafel: high-frequency capacitive loop of  $-70\text{ mV dec}^{-1}$ .
- New kinetics with PtOx: high-frequency capacitive loop of  $-110\text{ mV dec}^{-1}$  to  $-100\text{ mV dec}^{-1}$  and low-frequency inductive loop of  $30\text{ mV dec}^{-1}$  to  $40\text{ mV dec}^{-1}$ .

This step method to compute EIS has already been used in the PEMFC context by Kosakian et al.,<sup>17</sup> who showed its equivalency to the sine wave technique that requires a complete transient study for each frequency of the spectrum and is therefore way more demanding for computational time. The Fourier transform of the non-equispaced signals in time (logarithmic distribution) was calculated by the method which was first proposed by Wiese and Weil and also used by Bessler and Kosakian et al. for instance (see the corresponding publications for more details<sup>17,35,36</sup>).

Additionally, we carried out cyclic voltammetry (CV) simulations by ramping the voltage up and down at  $100\text{ mV s}^{-1}$  (red curve) and recording the current response (blue curve) as shown exemplarily in Fig. 4a. Since we model neither hydrogen sorption nor desorption kinetics, only one oxidation and one reduction peak coming from the slow platinum oxidation kinetics can be seen above 0.5 V in the resulting simulated CV in Fig. 4b (red curve). Fast kinetics effects, i.e. features which are present in the capacitive loop of the EIS, are not disentangled and thus taken into account implicitly through the parameterization of the ORR step. We added an experimental CV for comparison (dashed black line) to point out the limitations of our model compared to other more sophisticated models that match the experimental CVs better,<sup>9,37</sup> however, as shown in the results below, this model offers a good compromise between accuracy and simplicity as it is easier to parameterize than other literature models and fits both experimentally gathered steady-state polarization curves and EIS spectra well. Hence, it helps understanding the commonly known discrepancies between steady-state and dynamic performance signatures of PEM fuel cells.

## Results and Discussion

**Bias between steady-state and EIS evaluation.**—In our previous work, we focused on the cathode kinetics which cause a major loss contribution at relevant operating points.<sup>33</sup> We parameterized models based on polarization curves that were corrected for the Ohmic contributions  $R_0$  and  $R_{\text{p}}^{\text{eff}}$  and demonstrated that neither oxygen transport nor anode contributions significantly affect the characterization of the ORR at low current densities. Due to the sluggish kinetics of the ORR, the overpotentials are usually quite high even at low loads and thus simple Tafel kinetics are assumed to take place according to

$$\eta_{\text{ORR}} = -\frac{RT}{\alpha_{\text{c}}F} \cdot \ln \frac{j}{j_{\text{c,eff}}^0} \quad [28]$$

where  $\eta_{\text{ORR}}$  is the kinetic overpotential,  $\alpha_{\text{c}}$  the transfer coefficient ( $= (1 - \beta)n$ ),  $j$  the current density and  $j_{\text{c,eff}}^0$  the effective exchange

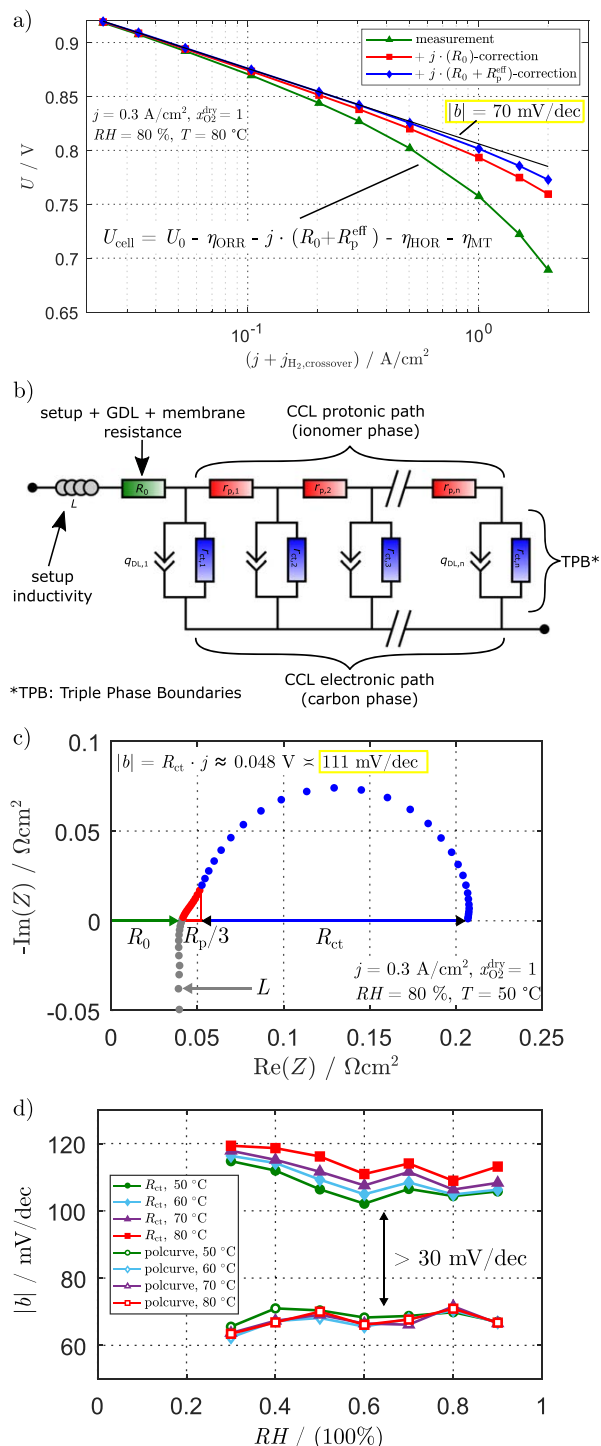


**Figure 5.** (a) Steady-State polarization curve with Ohmic corrections and corresponding ORR Tafel analysis. (b) Equivalent circuit model (ECM) of the cell in  $H_2/O_2$  configuration. (c) Representative EIS spectrum measured at  $0.3 \text{ A cm}^{-2}$  and corresponding Tafel slope resulting from  $R_{ct}$  (yellow box). (d) Tafel slope  $|b|$  over the relative humidity based on the slope of the polarization curve for  $j \leq 0.2 \text{ A cm}^{-2}$  (hollow symbols) and based on the slope obtained by the charge transfer resistance  $R_{ct}$  recorded at  $j = 0.1 \text{ A cm}^{-2}$  (full symbols).

current density. Our ORR parameterization was consistent with previous literature findings that were also based on steady-state investigations and we found  $\alpha_c = 1$ , leading to Tafel slopes  $b = -RT/(\alpha_c F) \approx -70 \text{ mV dec}^{-1}$ . This is depicted in Fig. 5a, where the blue curve which is corrected for the ionomer contributions yields a slope of around  $-70 \text{ mV dec}^{-1}$  at small to medium current densities and slightly higher slopes at high current densities due to combined anode and oxygen transport contributions (see our previous publication<sup>33</sup>).

Nevertheless, we pointed out that these kind of models show inconsistencies with EIS-based determination of the Tafel slope, which is directly linked to the charge transfer resistance  $R_{ct}$  by

$$\frac{\partial \eta_{ORR}}{\partial j} = -\frac{RT}{\alpha_c F j} = \frac{b}{j} = -R_{ct} \quad [29]$$

EIS data usually yield slopes that are higher, which is also illustrated in Fig. 5: in Fig. 5b we show a transmission line model (TLM) that is typically used to evaluate the impedance response of PEM fuel cells under the assumption of negligible oxygen transport and anode resistance, thus that the impedance is dominated by the membrane and the cathode contributions. The parameters of this ECM can be fitted to match a low-current-density spectrum like the one shown exemplarily in Fig. 5c, measured from 100 kHz to 0.1 Hz and cut at 1 Hz. According to Eq. 29, the absolute Tafel slope  $|b|$  is obtained by multiplying the diameter of the semicircle in Fig. 5c ( $\approx 160 \text{ m}\Omega\text{cm}^2$ ) with the current density ( $0.3 \text{ A cm}^{-2}$ ) and results in  $0.048 \text{ V} \cdot \ln(10) \cdot 1000 = 111 \text{ mV dec}^{-1}$ .

The bias between the slope of the corrected polarization curve and  $R_{ct}$  therefore represents around  $30$  to  $40 \text{ mV dec}^{-1}$  at small current densities and is depicted depending on  $RH$  and  $T$  in Fig. 5d. Overall, these discrepancies can be explained by the presence of low-frequency inductive features occurring below  $0.1 \text{ Hz}$  that are not visible in the spectrum in Fig. 5c. In steady-state, the local slope of the polarization curve must equal the low-frequency impedance where the Nyquist plot intercepts the real axis (differential cell resistance, in theory when the frequency  $f$  converges to  $0 \text{ Hz}$ ). However, as seen above in Fig. 1, the EIS spectra show low-frequency inductive features besides the capacitive contributions at frequencies below  $0.1 \text{ Hz}$ , which has been demonstrated early by Mathias et al.<sup>38</sup> This proves that typical EIS investigations limited to frequencies above  $0.1 \text{ Hz}$  or  $1 \text{ Hz}$  in the literature are incomplete and that the equivalent circuit in Fig. 5b is unable to describe the whole frequency range of PEMFC operation. At higher current densities, this bias between steady-state polarization and capacitive EIS gets even larger and our findings are therefore in agreement with those of Schiefer et al.,<sup>30</sup> who reported inductive loops the size of up to 50% of the capacitive loops. Hence, the LF inductive behavior plays a major role in PEMFC performance and needs to be understood.

According to our summarized literature overview in Table I containing both experimental and theoretical studies, two explanations to the low frequency inductive behavior are prominent. On the one hand, slow ionomer humidification effects that decrease the ionomer resistance in course of increased water production when increasing the current may be responsible. On the other hand, nontrivial ORR kinetics with intermediates or platinum oxidation phenomena at high cathode half-cell potentials may be another source of LF inductivities. A large number of investigations have been carried out in the last 20 years and yet, to our knowledge, there has not been an attempt to properly apportion these contributions based on a combined experimental and numerical approach. In simulation studies, the inductive loops are mostly investigated with models containing either detailed cathode kinetics (ORR with intermediates and/or platinum oxide kinetics) or water dynamics effects. Some models consider both effects, but the validation to experimental data is often insufficient. This lack might be due to the difficulty of measuring EIS at frequencies as low as  $100 \text{ mHz}$  down

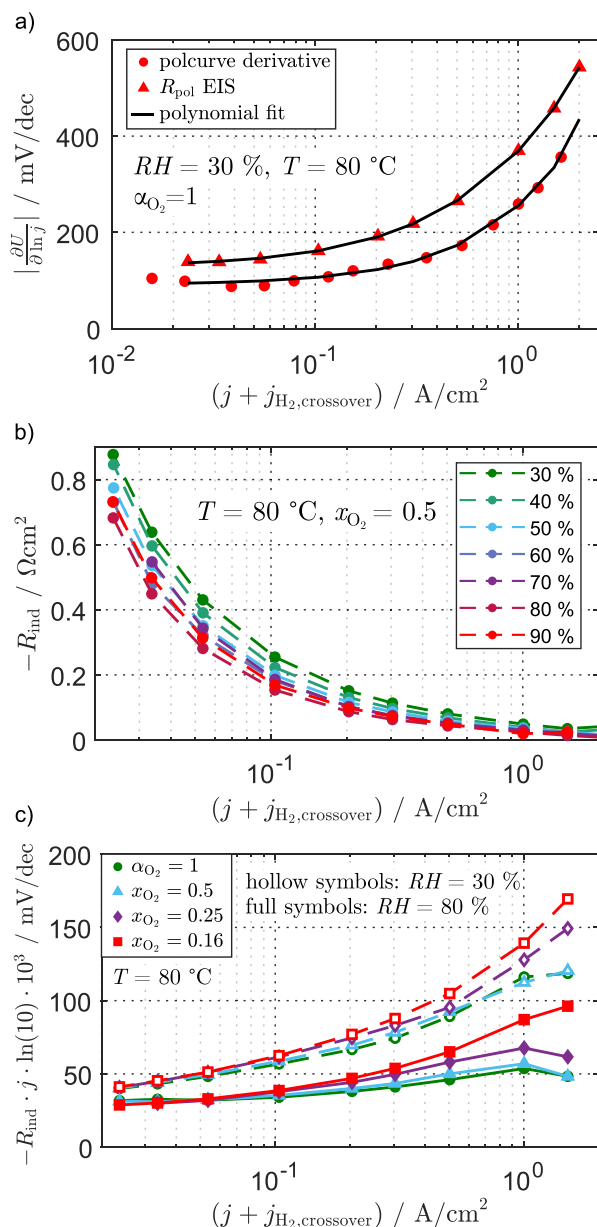


**Figure 6.** (a) Local slope of the polarization curve over the current density at  $RH = 30\%$ ,  $T = 80\text{ °C}$  and  $\alpha_{\text{O}_2} = 1$  based on the numerical derivative of the polarization curve and based on the low-frequency  $x$ -axis intercept of the EIS spectra ( $f \approx 1\text{ Hz}$ ). (b) Low-frequency inductive contribution  $-R_{\text{ind}}$  over the current density at  $T = 80\text{ °C}$  and  $x_{\text{O}_2} = 0.5$  for a variation of  $RH$ , computed for each condition by calculating the difference of the two curves shown exemplarily in (a). (c) Representation of the inductive contribution in  $\text{mV/dec}$  over the current density  $j$  depending on the relative humidity and the oxygen concentration at  $T = 80\text{ °C}$ .

to 1 mHz because of instabilities in course of the long measurement durations.

Subramanian et al. managed to parameterize a simple steady-state model for the ORR extended by oxide coverage effects solely by fitting polarization data.<sup>39</sup> They stuck to their steady-state description of the potential-dependent change in the electrochemical surface area (ECSA) and did not investigate the dynamical cell response, even though their model would certainly yield inductive effects due to the PtOx kinetics. Moreover, such a parameterization is

challenging, too, since in medium to high-loaded cathodes the half-cell potential is usually high in typical operating ranges and therefore a change in the apparent Tafel slope cannot be unambiguously discerned (see our previous publication<sup>35</sup>). Meyer et al.<sup>31</sup> recently showed that the size of the inductive loop during galvanostatic EIS can be controlled by provoking oscillations in the oxygen mass flow at the same frequencies as the current oscillations. They observed only small incomplete inductive semicircles during their normal EIS and were capable of getting completely closed loops by oscillating with the mass flow controllers; however, in our case we clearly see the inductive behavior even at the lowest currents (highest stoichiometries  $\lambda \gg 10$ , differential conditions) and mass flow variations revealed no influence on the size of our inductive features. We thus discard this hypothesis and other along-the-channel effects and only investigate the two first assumptions in more detail in the next sections.

**Evaluation of the low-frequency inductive loop.**—To quantify the low-frequency inductive part of the EIS spectra we computed two quantities. The first one was the local slope of the steady-state polarization curve, obtained by numerical derivation and expressed in  $\text{mV/dec}$  by

$$\left| \frac{\partial U}{\partial \ln j} \right| = \left| \frac{\Delta U}{\Delta \ln j} \right| \cdot \ln(10) \cdot 1000 \quad [30]$$

The second was the low-frequency real-axis-intercept of the capacitive part of the EIS spectra (capacitive polarization resistance), where  $\text{Im}(Z)=0$  and  $f \approx 1\text{ Hz}$ . Its equivalent local slope in  $\text{mV/dec}$  was computed via

$$\left| \frac{\partial U}{\partial \ln j} \right| = R_{\text{pol}} \cdot j \cdot \ln(10) \cdot 1000 \quad [31]$$

Figure 6a depicts these two quantities over the current density for hot and dry conditions with pure oxygen in the dry cathode gas ( $T = 80\text{ °C}$ ,  $RH = 30\%$  and  $\alpha_{\text{O}_2}$ ). As can be seen, the capacitive part of the EIS yields higher slopes than the polarization curve derivative over the whole current density range. The amount of the discrepancies are however dependent on the operating conditions (see Fig. S2). The inductive contribution is then simply defined as the difference between the two corresponding polynomial fitting curves and can be expressed as a negative differential resistance in  $\Omega \text{cm}^2$  as shown in Fig. 6b. This simple and rapid technique gives the size of the inductive contribution but misses the frequency information, which is needed to determine the time constants of the processes. The parameter study in Figs. S6 to S29 shows the quantities that affect the time constant of the inductive loop caused by the PtOx kinetics according to our new model. Some of these parameters also strongly affect the performance and EIS response and can therefore be fitted, others are taken from the literature or estimated in order to give meaningful results (see parameterization below).

From Fig. 6b it gets clear that the behavior of the inductive contribution is non-linear with the current density and that there is a non-negligible dependency on the relative humidity, with low  $RH$  leading to higher LF inductivities even at the lowest load point. Figure 6c depicts the LF inductive contribution in terms of a slope in  $\text{mV/dec}$  and shows that there is no significant dependency on the oxygen partial pressure at small to medium current densities; at high currents, however, such a dependency can be observed as the inductive contribution slightly increases with decreasing oxygen partial pressure at both high and low humidity. This observation is discussed in more details below. Since the slope of the curves at dry conditions is higher than the slope of the curves at humid conditions, we speculate that all the curves merge at current densities even lower than  $0.02\text{ A cm}^{-2}$ . Furthermore, this Fig. demonstrates that even though the inductive features are the smallest at low current densities, they decrease the local slopes of the polarization curve

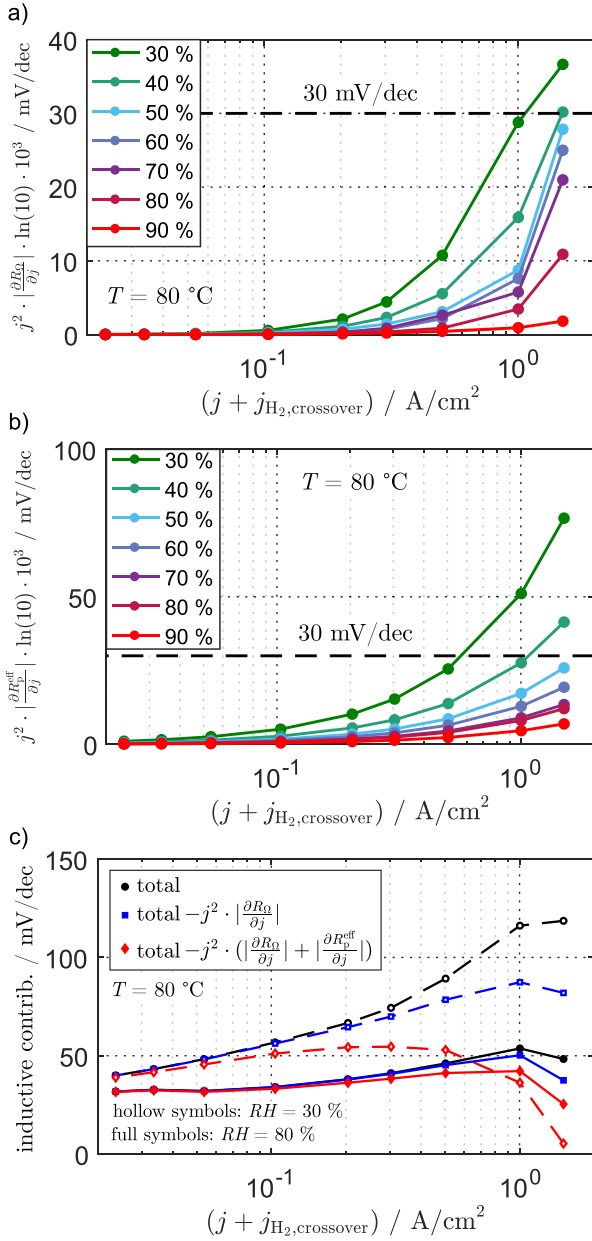


**Figure 7.** (a) Low-frequency contribution of the membrane humidification dynamics over the current density for varying gas channel humidity levels at  $T = 80\text{ }^\circ\text{C}$ . (b) Same as in (a) but for the CCL humidification contribution. (c) Size of the low-frequency inductive contribution over the current density at  $T = 80\text{ }^\circ\text{C}$  for wet ( $RH = 80\%$ , solid black line) and dry ( $RH = 30\%$ , dashed black line) conditions and corresponding corrections by the LF membrane contributions (blue lines) and by the LF membrane and CCL contributions (red lines).

by up to almost  $50\text{ mV dec}^{-1}$  depending on the operating conditions. Then, the inductive contribution increases with increasing current density. The lower the gas humidity and the oxygen partial pressure are, the faster the inductive loop increases with current density (higher slope of the curves in Fig. 6c at low  $RH$  and low  $p_{\text{O}_2}$ ). Additional conditions can be found in the Figs. S2 and S3.

Based on the assumption that the overpotentials caused by proton transport in the membrane and in the cathode catalyst layer follow Ohms law, which is a sufficiently good compromise between

complexity and accuracy, we have

$$|\eta_{\text{PEM}}| = R_{\text{PEM}} \cdot j \quad [32]$$

for the membrane, with  $\eta_{\text{PEM}}$  the potential drop caused by the membrane,  $R_{\text{PEM}}$  the high-frequency membrane resistance and  $j$  the cell current density. For the CCL we have

$$|\eta_{\text{CCL}}^{\text{H}^+}| = R_p^{\text{eff}} \cdot j \quad [33]$$

with  $\eta_{\text{CCL}}^{\text{H}^+}$  the potential drop due to proton transport in the CCL and  $R_p^{\text{eff}}$  the effective CCL sheet resistance that follows  $R_p^{\text{eff}} \approx (1/3) \cdot R_p$ . The resistances  $R_{\text{PEM}}$  and  $R_p$  are inversely proportional to the conductivity of the corresponding layer.<sup>32</sup> Considering the results of our previous publication<sup>32</sup> we can compute the absolute value of the impedance caused by proton transport in the membrane according to

$$\left| \frac{\partial \eta_{\text{PEM}}}{\partial j} \right| = R_{\text{PEM}} + j \cdot \frac{\partial R_{\text{PEM}}}{\partial j} \quad [34]$$

It is important to note that the membrane resistance  $R_{\text{PEM}}$  is included in the high-frequency intercept  $R_\Omega$  of the EIS spectra, which comprises also the electronic bulk and contact resistances of the setup. However, the latter contributions are assumed to be constant and do therefore not affect the derivative term (last term) in Eq. 34. Thus, we have

$$j \cdot \frac{\partial R_{\text{PEM}}}{\partial j} = j \cdot \frac{\partial R_\Omega}{\partial j} \quad [35]$$

which represents the contribution from the changing membrane resistance during operation caused by the production of water and thus ionomer hydration. In this work we do not attempt to quantify time constants for this process but assume that it entirely contributes to the evaluated LF inductive loop. Its inductive nature is confirmed by the fact that its sign is always negative in our case because the resistance  $R_{\text{PEM}}$  decreases with increasing current density. Moreover, this contribution is expected to appear at low frequencies in the EIS since it is linked to slow water management effects. With thicker membranes, however, the sign could supposedly become positive in some cases where the EOD contribution dries out the membrane at higher currents.

Taking the ionomer resistances as a function of the current density from our previous publication<sup>32</sup> shown in Fig. S4, we can compute their derivatives numerically and determine the terms of Eq. 35. Then, based on these low-frequency (LF) terms we calculate equivalent Tafel slopes  $b_{\text{ionomer}}^{\text{LF}} = j^2 \cdot (\partial R_\Omega / \partial j)$ . These Tafel slopes contribute to the complete apparent Tafel slope of the polarization curve and can be presented in mV/dec as in Fig. 7a by calculating  $j^2 \cdot |(\partial R_\Omega / \partial j)| \cdot \ln(10) \cdot 1000$ . Therefore, these contributions are proportional to  $j^2$ . We see that the low-frequency membrane contribution due to changes in the humidification is negligible at low current densities since it only gets visible above  $0.2\text{ A cm}^{-2}$  for dry conditions ( $RH = 30\%$ ) and even higher current densities for wet conditions. At  $RH = 30\%$  we barely reach  $30\text{ mV dec}^{-1}$  at  $1\text{ A cm}^{-2}$  and at  $RH = 90\%$  we do not see any contribution at all. Following the same logic for the proton resistance in the cathode catalyst layer we get

$$\left| \frac{\partial \eta_{\text{CCL}}^{\text{H}^+}}{\partial j} \right| = R_p^{\text{eff}} + j \cdot \frac{\partial R_p^{\text{eff}}}{\partial j} \quad [36]$$

The contribution of the second term of this equation to the apparent Tafel slope is illustrated as  $j^2 \cdot |(\partial R_p^{\text{eff}} / \partial j)| \cdot \ln(10) \cdot 1000$  in Fig. 7b similarly to the membrane contribution ( $\alpha j^2$ ). Even though this CCL

contribution is generally higher than the one of the membrane, it is still negligible below  $0.2 \text{ A cm}^{-2}$  at any conditions. Hence, even the sum of both ionomer hydration contributions remains very small at current densities below  $0.2 \text{ A cm}^{-2}$ . Especially the inductive loop of  $30\text{--}40 \text{ mV dec}^{-1}$  at the smallest current density in Fig. 7c cannot be explained by such contributions. The diagrams corresponding to Figs. 7a and 7b for  $T = 50 \text{ }^\circ\text{C}$  can be found in Fig. S5.

The total LF inductive contribution over the current density (black curves) for dry ( $RH = 30\%$ , dashed lines and hollow symbols) and wet ( $RH = 80\%$ , solid lines and full symbols) conditions and the corresponding curves minus the ionomer hydration contributions are depicted in Fig. 7c. The blue curves with the square markers represent the total inductivity minus the membrane contribution, and the red curves with the diamond markers represent the total inductivity minus both membrane and CCL contribution. Thus the red curves supposedly contain mainly the LF inductivity caused by the PtOx kinetics, representing  $30\text{--}40 \text{ mV dec}^{-1}$  at very small currents. All the solid curves start with an almost completely flat slope at small currents and overlap over a wide range, highlighting again that the ionomer humidification does not significantly influence the LF inductive loop at humid conditions. Yet, the dashed curves have a steeper slope at small to medium current densities and begin diverging at  $0.1 \text{ A cm}^{-2}$ , proving that ionomer humidification effects on the LF inductive features cannot be neglected at dry conditions. Since particularly the dashed red curve exhibits a small positive slope at low currents, we believe that another small humidity-dependent effect is contained in the LF inductive loop, which leads to the gap of  $10 \text{ mV dec}^{-1}$  between the  $RH = 30\%$  and the  $RH = 80\%$  conditions. One explanation might be the presence of an additional ionomer humidification term coming from the transmission line structure of the CCL which is not considered in Eq. 36. Such a term was recently derived by Kulikovskiy under the assumption that the CCL conductivity increases linearly with the current density.<sup>18</sup> This term provoked an inductive contribution in  $\text{mV/dec}$  increasing linearly with  $j$ , in contrast to the second term of Eq. 36 which leads to a contribution proportional to  $j^2$  as shown above.

Other humidity-dependent effects could also be envisaged, for example related to the humidification of the anode catalyst layer (ACL). Some authors assumed an influence of water activity on the anode reaction kinetics (HOR, hydrogen oxidation reaction),<sup>14,15</sup> which would also lead to LF inductive effects. We could neither confirm nor deny the presence of such contributions from the ACL based on the current dataset. However, in our previous publication we showed that the anode contribution to the performance is generally very small,<sup>33</sup> therefore we do not believe that such contributions could be responsible for the gap observed between the wet and dry conditions.

Finally, as already mentioned for Fig. 6c, the wet and dry curves are very close to each other and might converge at very low current densities in Fig. 7c according to the trend. Since mainly PtOx kinetics contributions are present at such low load, this means that the relative humidity has only little or no influence at all on them, which is supported by our model (see Fig. S20). At higher current densities, both red curves eventually drop, which is linked to the decreasing presence of platinum oxides due to the lower cathode half-cell potentials.

Considering that the ORR follows simple Tafel kinetics in each point as in Eq. 28, the kinetics overpotential can be written in a simplified manner as

$$\eta_{\text{ORR}} = b \ln \frac{j}{j_0} \quad [37]$$

where  $b$  is the Tafel slope,  $j$  the current density and  $j_0$  the effective exchange current density. As explained above, Tafel kinetics with a constant intrinsic Tafel slope  $b$  do not lead to LF inductive processes in the EIS spectra. Thus, a model as ours that takes into account the slow poisoning effect of platinum oxide formation happening within

the CCL at high cell voltages is needed to investigate the LF contributions of the ORR kinetics. If one assumes that neither  $b$  nor  $j_0$  are constant over the current density, the total impedance caused by the ORR can be written as

$$\frac{\partial \eta_{\text{ORR}}}{\partial j} = \frac{b}{j} + \frac{\partial b}{\partial j} \ln \left( \frac{j}{j_0} \right) - \frac{b}{j_0} \frac{\partial j_0}{\partial j} \quad [38]$$

where the first term  $b/j$  equals  $-R_{\text{ct}}$  which is the well-known charge transfer resistance from the Tafel law. The two other terms depend on the change in the Tafel slope and the exchange current density over the current density and can be determined by a more sophisticated model as presented in this work. In the next section, our model is parameterized and validated with experimental data and the behavior of  $b_{\text{apparent}}$  as well as  $j_{0,\text{effective}}$  is investigated for our baseline conditions.

**Model parameterization and validation.**—A complete variation of all the relevant model parameters and their influence on the steady-state polarization curves, the EIS response and the cyclic voltammetry is shown in Figs. S6 to S29 in the supplementary material and gives some deep insights into our model. The focus of this section, however, is the parameterization and validation. In Fig. 8 we depict the experimental and simulated Ohmic-contributions-corrected steady-state polarization curves used in the fitting procedure (Figs. a and c) and the respective simulated platinum oxide coverage (Figs. b and d). Here, no mass transport contributions were taken into account in the model and only currents up to  $0.2 \text{ A cm}^{-2}$  were used in the fitting procedure. Further, we did not consider low relative humidity conditions here since our model does not account for the water management effects discussed above. To simulate dry conditions accurately, a complete MEA model would be needed, which goes beyond the scope of this work. To summarize, we used both EIS and steady-state polarization data at  $RH = 80\%$  and  $j \leq 0.2 \text{ A cm}^{-2}$  to parameterize the model. We fixed the values of  $\Gamma$  and  $k_{2,\text{ref}}$  by adjusting them to three requirements: (1) being physically meaningful (i.e. with the order of magnitude of  $\Gamma$  being in line with a Pt atomic surface density of  $2.17 \cdot 10^{-9} \text{ mol/cm}^2_{\text{Pt}}$ ), (2) matching the  $0.6 \text{ V}$  shoulder in the experimental CV, (3) yielding a consistent time constant of the inductive process in the EIS (between  $10 \text{ mHz}$  and  $1 \text{ Hz}$ <sup>30</sup>). However, based on this dataset we could not precisely determine the time constant and solely focused on the absolute contribution of the low-frequency inductive features as mentioned above. We thus considered all the fast capacitive kinetics effects equivalently in the parameterization of the ORR step and the slow inductive kinetics effects equivalently in the PtOx parameterization.

In Figs. 8a and 8b we show an oxygen mole fraction variation at  $T = 50 \text{ }^\circ\text{C}$  and  $T = 80 \text{ }^\circ\text{C}$  and in Figs. 8c and 8d a variation of temperature for  $x_{\text{O}_2}^{\text{dry}} = 1$  and  $x_{\text{O}_2} = 0.16$ . The model matches the experimental points well for currents up to  $0.5 \text{ A cm}^{-2}$  and the deviation gets only larger at higher currents, probably because of inaccuracies in the protonic loss correction as well as mass transport issues that were not accounted for. Further, even though the apparent Tafel slope increases continuously with increasing current density due to the decreasing oxide coverage, it is almost impossible to detect any change with the naked eye until corrected cell voltages of around  $0.75 \text{ V}$  (corresponding to remaining coverages of about 10% to 30%), which confirms that simple steady-state models with a single Tafel slope and exchange current density can easily fit such polarization data at low to medium current density. It is known, however, as mentioned previously, that simple Butler-Volmer and Tafel models cannot reproduce both the steady-state and the dynamic response observed in PEMFC as there are discrepancies in the resulting Tafel slopes between the polarization curves and the EIS response. Our new simple model aims at resolving this issue. Thus, we also computed EIS spectra for all the operating points to tune the parameters even further and improve results. As can be seen

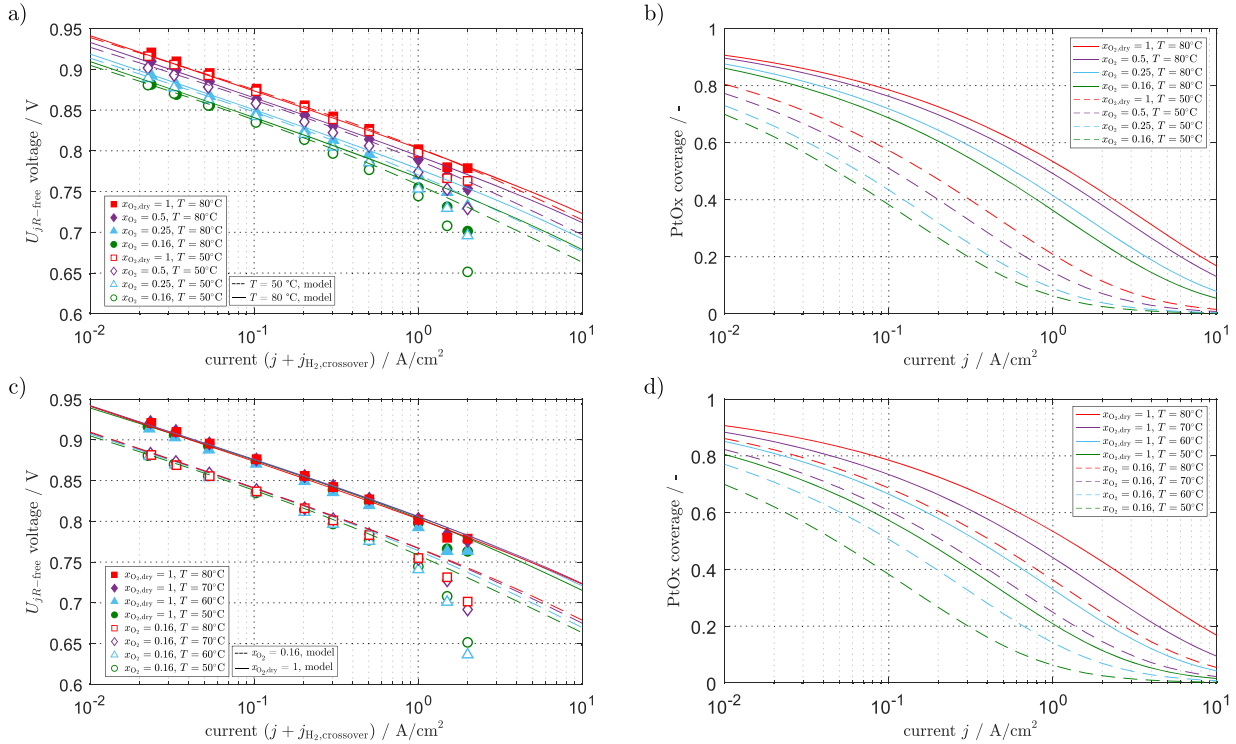


**Figure 8.** (a) Experimental (symbols) and simulated (lines) polarization curves in the Tafel representation for a variation of  $x_{O_2}$  at  $T = 50^\circ C$  and  $T = 80^\circ C$ . (b) Corresponding curves of the platinum oxide coverage. (c) Experimental (symbols) and simulated (lines) polarization curves in the Tafel representation for a variation of  $T$  at  $x_{O_2}^{dry} = 1$  and  $x_{O_2} = 0.16$ . (d) Corresponding curves of the platinum oxide coverage. All the data were gathered at  $RH = 80\%$  and the simulations were carried out without considering mass transport contributions.

in Fig. 9, the simulated capacitive parts of the EIS spectra also match the experiments well up to  $0.5 \text{ A cm}^{-2}$  and deviations can only be observed above this current density as the simulated resistances seem to be too low.

Figure 10a displays the results of our parameterization for our baseline condition ( $RH = 80\%$ ,  $T = 80^\circ C$ ,  $x_{O_2}^{dry} = 1$ ). The experimental  $R_{ct}$  was obtained by fitting a transmission line model (TLM) to our EIS as explained in our previous publication<sup>33</sup> and the corresponding  $|R_{ind}|$  was obtained as explained above and shown in Fig. 6a. Model responses are represented by the solid lines and the dashed line represents the model results plus the low-frequency inductive contribution from the ionomer humidification effects determined in Fig. 7. The good agreement between model and experiment for both the high-frequency capacitive  $R_{ct}$  and the low-frequency inductive  $|R_{ind}|$  is emphasized in Fig. 10a. The match of the capacitive charge transfer resistance is good over the complete current density range and the match of the inductive part caused by the PtOx kinetics (solid line) is good for currents up to  $0.5 \text{ A cm}^{-2}$ . Above these currents, the model prediction for the inductive contribution is slightly too small because of the other effects that are not taken into account including the slow ionomer humidification (see explanation above). We can take this effect into account nonetheless by adding it to the model prediction (dashed line, see the investigation of the ionomer behavior above). This yields better results at high current densities even though the match is not perfect, probably because of the decreasing accuracy in determining the ionomer contributions at high current densities caused by two reasons: the decreasing fitting quality and the increasing error of the numerical derivation due to the limited number of sampled load points. However, owing to the good agreement of this new simple model with our consistent dataset we can say that we made a step forward in reconciling steady-state and EIS signatures in PEM fuel cells.

Based on computed polarization curves corrected by the Ohmic contribution,  $U_{jR-free} = f(j)$ , an apparent differential Tafel slope of the cathode kinetics can be determined by numerical derivation according to

$$|b_{\text{apparent}}| = \left| \frac{\partial U_{jR-free}}{\partial \ln j} \right| \quad [39]$$

and given this apparent slope  $b_{\text{apparent}}$ , the effective exchange current density of the ORR can be calculated using

$$j_{0,\text{effective}} = \frac{j}{rf} \cdot 10^{\frac{\eta}{b_{\text{apparent}}}} \quad [40]$$

These two quantities are depicted in Fig. 10b as functions of the current density  $j$  at our baseline conditions. As previously shown in the literature, for example based on microkinetic modeling of the ORR, both  $|b_{\text{apparent}}|$  and  $j_{0,\text{effective}}$  increase with increasing current density and thus decreasing cathode half-cell potential.<sup>40</sup> In our case, the absolute apparent Tafel slope curve starts between  $60$  and  $70 \text{ mV dec}^{-1}$  at low load with a flat slope and tends to increase toward  $90 \text{ mV dec}^{-1}$  while the slope gets steeper with increasing load. Comparably, the effective exchange current density increases by almost three orders of magnitude over the investigated current range, from  $10^{-9} \text{ A/cm}^2_{Pt}$  to  $10^{-6} \text{ A/cm}^2_{Pt}$ . For comparison, the effective exchange current density we found in our previous publication for the ORR based on the Tafel approximation lies at around  $2.15 \cdot 10^{-8} \text{ A/cm}^2_{Pt}$ , with  $\alpha_c = 1$  leading to  $|b| = 70 \text{ mV dec}^{-1}$  at  $T = 80^\circ C$ . Such values are attained at approximately  $0.2 \text{ A cm}^{-2}$  with our new model.

**Mass transport contributions.**—In this Section we took mass transport contributions into account through Fick's law of diffusion



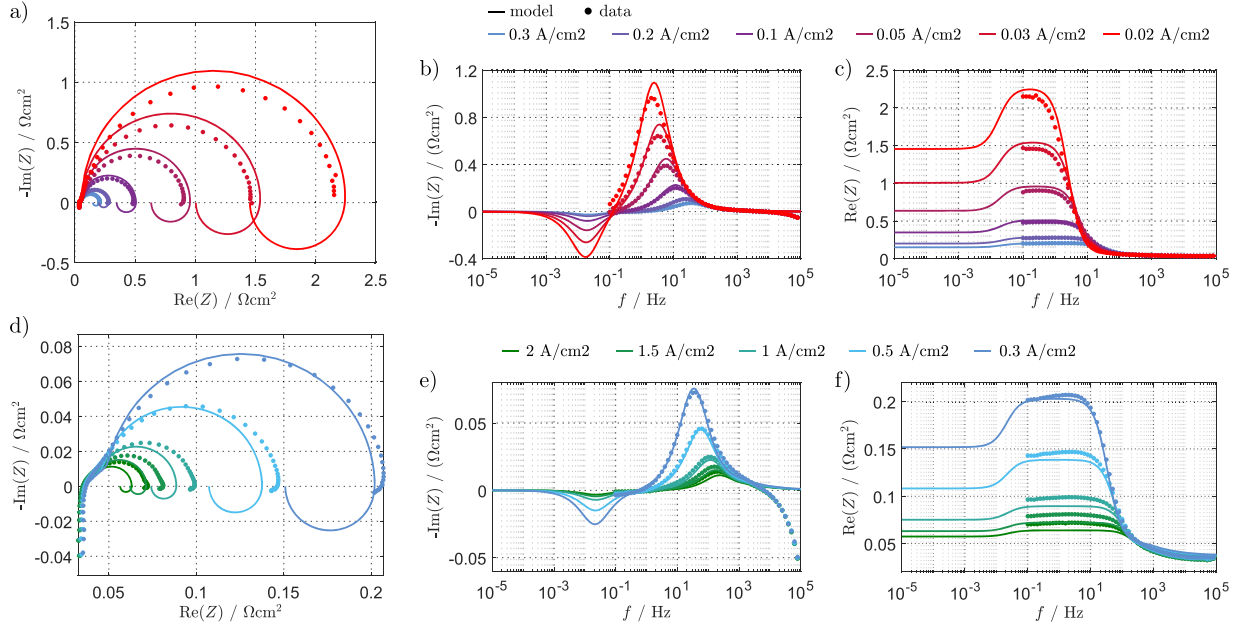


**Figure 9.** Experimental (dots) and simulated (lines) EIS spectra at  $RH = 80\%$ ,  $T = 80^\circ\text{C}$  and  $x_{\text{O}_2}^{\text{dry}} = 1$  for the cell currents shown in the polarization curves in Fig. 8. (a) and (d) Nyquist representations. (b), (c), (e) and (f) Bode representations. All the data were gathered at  $RH = 80\%$  and the simulations were carried out without considering mass transport contributions.

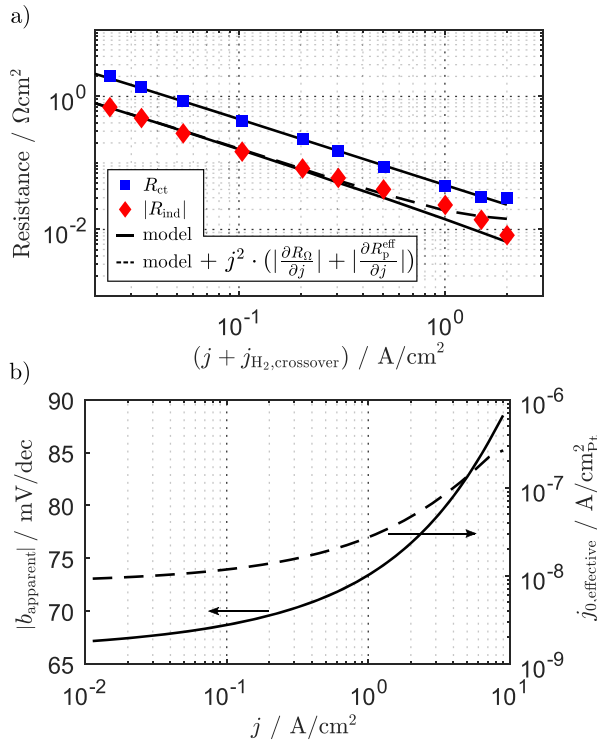


**Figure 10.** (a) Experimental (symbols) and simulated (lines) charge transfer resistance  $R_{\text{ct}}$  and inductive contribution  $|R_{\text{ind}}|$  over the current density  $j$  at  $RH = 80\%$ ,  $T = 80^\circ\text{C}$  and  $x_{\text{O}_2}^{\text{dry}} = 1$ . The experimental  $R_{\text{ct}}$  was obtained by fitting EIS data to an equivalent circuit model and  $|R_{\text{ind}}|$  was obtained as described in Fig. 6a. The lines correspond to our model without mass transport contributions and the dashed line was added including the ionomer contributions determined in Fig. 7. (b) Corresponding apparent Tafel slope  $|b|$  and effective exchange current density  $j_0$ .

(see model description above) to further improve the match between the experiments and simulations. We focused on the  $T = 50^\circ\text{C}$  and  $T = 80^\circ\text{C}$  conditions and determined independent oxygen diffusion coefficients for the GDL and the CCL by fitting the high current density parts of the polarization curves at  $T = 80^\circ\text{C}$  and respecting the proportionality  $D \propto T^{3/2}$ :

- $T = 50^\circ\text{C}$ :  $D_{\text{O}_2,\text{GDL}} = 2.6 \cdot 10^{-2} \text{ cm}^2 \text{ s}^{-1}$ ,  $D_{\text{O}_2,\text{CCL}} = 2.8 \cdot 10^{-4} \text{ cm}^2 \text{ s}^{-1}$
- $T = 80^\circ\text{C}$ :  $D_{\text{O}_2,\text{GDL}} = 3.0 \cdot 10^{-2} \text{ cm}^2 \text{ s}^{-1}$ ,  $D_{\text{O}_2,\text{CCL}} = 3.2 \cdot 10^{-4} \text{ cm}^2 \text{ s}^{-1}$

These values lie in the same orders of magnitude as values determined previously in the literature for instance by Kulikovskiy.<sup>41</sup> The complete set of parameters for this enhanced model is depicted in Table III. As shown in Fig. 11, considering these mass transport features leads to simulated EIS that correspond better to the experiments at high currents as there are only small deviations even at  $j \geq 0.5 \text{ A cm}^{-2}$ . Further, the polarization curves in Fig. 12a match the measurements well even at high current densities, pointing out again that this model is suited for modeling both steady-state performance and EIS features of PEM fuel cells despite its simplicity. Comparing the new oxide coverage in Fig. 12b with the previous, mass transport free coverage in Fig. 8b indicates that this parameter remains almost unaffected by the change in the model at small and medium loads. Differences can be observed at high currents since the oxide coverage is lower than before due to the lower cathode half-cell potential. This effect increases with decreasing oxygen partial pressure.

Finally, the EIS spectra of a  $p_{\text{O}_2}$  variation at  $j = 0.2 \text{ A cm}^{-2}$  in Fig. 13 highlight that even though it is impossible to probe partial pressure effects on the local slope of polarization data at such small current densities, EIS is capable of sensing these contributions. Our model containing mass transport contributions predicts an increasing capacitive loop with decreasing oxygen partial pressure due to the increasing oxygen mass transport resistance and is in accordance with the experimental data. Further, the model predicts a slightly lower inductive contribution at lower partial pressure, which is in

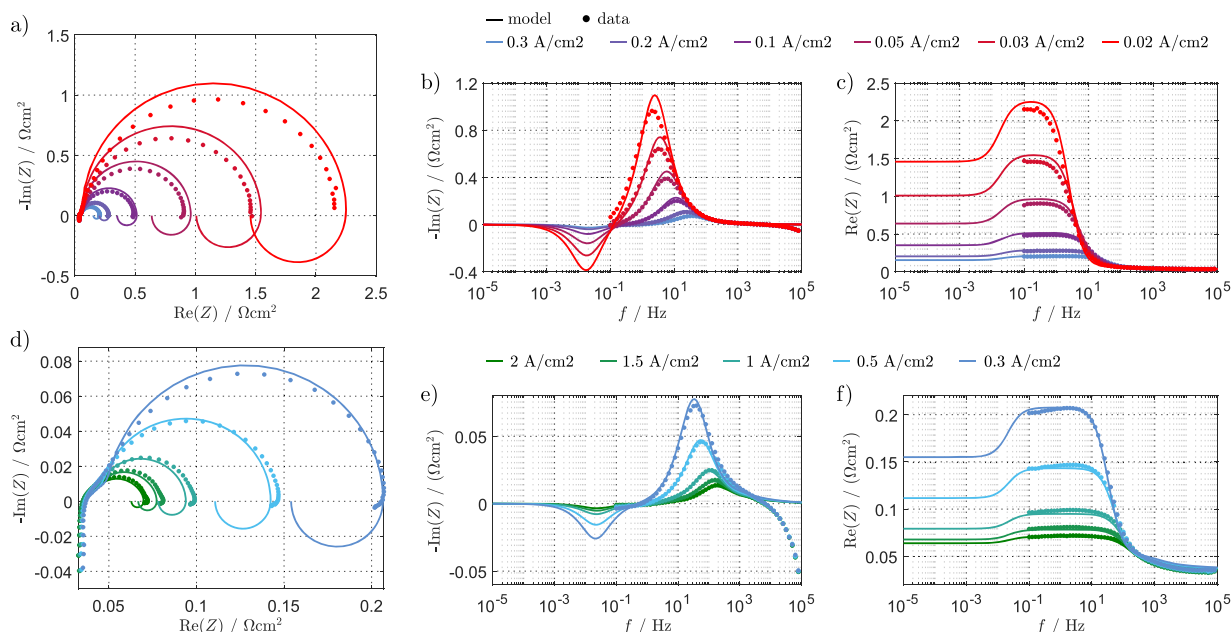


**Figure 11.** Experimental (dots) and simulated (lines) EIS spectra at  $RH = 80\%$ ,  $T = 80^\circ\text{C}$  and  $x_{\text{O}_2}^{\text{dry}} = 1$  for the cell currents shown in the polarization curves in Fig. 8. (a) and (d) Nyquist representations. (b), (c), (e) and (f) Bode representations. All the data were gathered at  $RH = 80\%$  and the simulations were carried out considering oxygen mass transport through GDL and CCL by Fick's law of diffusion.

agreement with our expectation because the half-cell potential gets lower with decreasing partial pressures and so does the oxide coverage. However, above  $0.1\text{ A cm}^{-2}$ , the data in Fig. 6c show

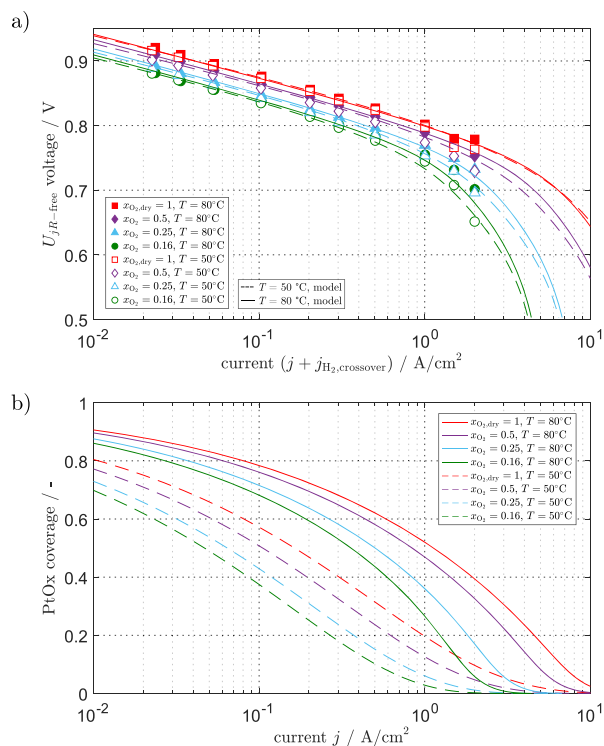


**Figure 12.** (a) Experimental (symbols) and simulated (lines) polarization curves in the Tafel representation of a variation of  $x_{\text{O}_2}$  at  $T = 50^\circ\text{C}$  and  $T = 80^\circ\text{C}$  for  $RH = 80\%$  considering mass transport contributions by Fick's law. (b) Corresponding curves of the platinum oxide coverage.

slightly higher inductive contributions at lower partial pressures, which is not linked to the platinum oxide kinetics and thus cannot be simulated by the model. Such behavior could probably be explained by a beneficial transport effect that is strongest at small partial pressures (not integrated in our model), for instance due to an improvement in the oxygen diffusion through a more humidified ionomer film. Pivac et al. investigated LF inductive features based on a specially developed equivalent circuit model (ECM) and stated that such an improvement in the transport properties of oxygen to the catalyst provoke LF inductive contributions.<sup>26,27</sup> In principle, our new kinetics model can be integrated into a complete MEA simulation model to replace the typically used Butler-Volmer of Tafel approaches for the ORR kinetics. Such a model would allow to account for the most important effects including water management and local catalyst-near effects. Nevertheless, this would add much complexity as it would need additional comprehensive representations of the following effects: heat transport, water and proton transport within the ionomer phase, two-phase water flow within the porous media and catalyst-near transport effects through the ionomer/water film. Therefore, this would go beyond the scope of this work whose purpose of providing a simple model for the cathode reaction kinetics that represents a good compromise between complexity and accuracy is fulfilled.

### Conclusions

In this work we investigated the low-frequency inductive phenomena in differential PEM fuel cells based on both a numerical simulation model and a large experimental dataset. The latter has been acquired by varying the operating conditions  $RH$ ,  $T$ ,  $p_{\text{O}_2}$  and  $j$  systematically and recording steady-state polarization curves as well as the corresponding EIS spectra. In the first part we explained that the discrepancies between the polarization curve slopes and the slopes from EIS based on the capacitive parts of the spectra are caused by the low-frequency inductive features (positive imaginary part) of  $30\text{ mV dec}^{-1}$  to over  $200\text{ mV dec}^{-1}$  depending on the operating conditions. Since measuring EIS at very low frequencies is very challenging and time-consuming, EIS spectra are typically recorded at frequencies higher than  $0.1\text{ Hz}$ , thus missing these low-

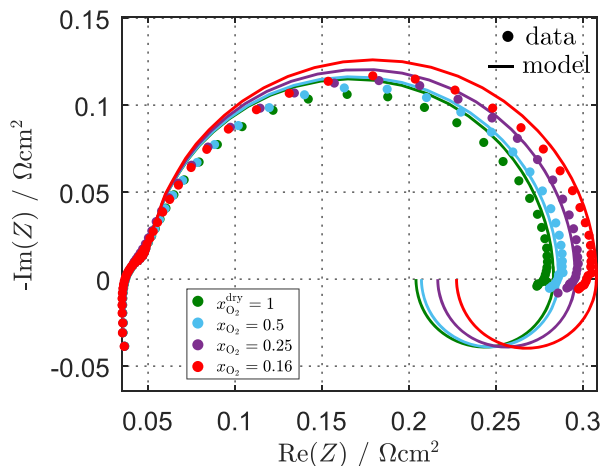


**Figure 13.** Nyquist plot of a  $x_{O_2}$  variation at  $j = 0.2 \text{ A cm}^{-2}$ ,  $T = 80 \text{ °C}$  and  $RH = 80\%$ . The dots represent the measurement points and the lines the model results considering mass transport by Fick's law.

frequency inductive contributions. In order to explain them we summarized previous literature sources which allowed us to narrow down the possible interpretations to complex cathode kinetics involving intermediates or platinum oxidation, and slow water management dynamics that influence the ionomer hydration and thus its conductivity.

We calculated the absolute inductive contributions by subtracting the low-frequency real-axis-intercepts ( $f \approx 1 \text{ Hz}$ ) of the capacitive EIS from the local slopes of the polarization curves which we obtained by numerical derivation. Therewith, we investigated the influence of the operating conditions on the inductive loop in a full factorial fashion, which was done for the first time to our knowledge. We found that the size of the inductive loop strongly depends on the current density and the relative humidity; however, the effect of temperature and oxygen partial pressure is minor but not negligible. Thus, the inductive loop (in  $\Omega\text{cm}^2$ ) is largest at low load even though its influence on the slope of the polarization curve is proportional to the current density and therefore increases with increasing load. Further, decreasing the relative humidity increases the inductive loop and decreasing the oxygen partial pressure increases it at high current density. Based on our previous characterization of the ionomer resistances as a function of the current density depending on the relative humidity we could quantify the inductive contributions originating from slow ionomer hydration. We pointed out that these contributions play almost no role at all at wet conditions and are important only at medium to high currents at dry conditions. Hence, we could prove that the inductive effects at small current density come almost exclusively from ORR kinetics effects within the cathode electrode, even though we observed a small additional process of  $\leq 10 \text{ mV dec}^{-1}$  at dry conditions that is not proportional to the current density.

Finally, we proposed a new approach to model the cathode kinetics following a single-step Tafel equation for the oxygen reduction reaction and an additional equation for the platinum oxidation reaction. The latter influences the effective exchange current density of the ORR step through the fraction of available platinum surface, therefore also affecting the apparent Tafel slope. We integrated this approach into a dynamic, isothermal, one-dimensional through-plane FEM model reaching from the anode side of the membrane to the cathode gas channel. By using the current-step method we got one complete EIS spectrum per computation and we simulated cyclic voltammetry responses by switching off the ORR and imposing a succession of voltage ramp up and ramp down. Based on this fast model we performed an extensive parameter study that helps understanding the influence of

each quantity on the steady-state and EIS response. We parameterized the model for high relative humidity conditions based on both polarization and EIS data and despite the good match between simulation and experiment over a wide range of operating conditions, the polarization curves showed deviations at high current densities. We attributed these deviations to oxygen transport in the porous media and minimized them by adding Fickian diffusion physics in the GDL and CCL. Our validation study based on this final model showed an improved match between simulation and experiment for both polarization curves and EIS spectra, highlighting that our model approach is well-suited for PEMFCs. According to this, we proposed a simple model which presents a good compromise between complexity, parameterability and accuracy and which brings the reconciliation of steady-state performance and EIS signatures in differential PEM fuel cells one step forward. In future works, this model could be complemented by ionomer hydration dynamics in order to simulate also dry conditions, or it may directly be integrated into complete MEA models in order to get even deeper and more precise insights into PEMFC performance.

#### Acknowledgments

The authors thank SGL® Carbon for providing the gas diffusion layer samples and Gore® for helpful discussions.

#### ORCID

Christophe Gerling  <https://orcid.org/0000-0002-7918-6973>

K. Andreas Friedrich  <https://orcid.org/0000-0002-2968-5029>

#### References

- M. Heinzmann, A. Weber, and E. Ivers-Tiffée, "Impedance modelling of porous electrode structures in polymer electrolyte membrane fuel cells." *J. Power Sources*, **444**, 227279 (2019).
- O. Antoine, Y. Bultel, and R. Durand, "Oxygen reduction reaction kinetics and mechanism on platinum nanoparticles inside Nafion®." *J. Electroanalytical Chem.*, **499**, 85 (2001).
- D. R. Baker, D. A. Caulk, K. C. Neyerlin, and M. W. Murphy, "Measurement of oxygen transport resistance in PEM fuel cells by limiting current methods." *J. Electrochem. Soc.*, **156**, B991 (2009).
- H. Kuhn, A. Wokaun, and G. G. Scherer, "Exploring single electrode reactions in polymer electrolyte fuel cells." *Electrochimica Acta*, **52**, 2322 (2007).
- S. K. Roy, M. E. Orazem, and B. Tribollet, "Interpretation of low-frequency inductive loops in PEM fuel cells." *J. Electrochem. Soc.*, **154**, B1378 (2007).
- M. Mathias, D. Baker, J. Zhang, Y. Liu, and W. Gu, "Frontiers in application of impedance diagnostics to H<sub>2</sub>-Fed polymer electrolyte fuel cells." *ECS Trans.*, **13**, 129 (2008).
- S. Cruz-Manzo and R. Chen, "An electrical circuit for performance analysis of polymer electrolyte fuel cell stacks using electrochemical impedance spectroscopy." *J. Electrochem. Soc.*, **160**, F1109 (2013).
- S. Cruz-Manzo and R. Chen, "A generic electrical circuit for performance analysis of the fuel cell cathode catalyst layer through electrochemical impedance spectroscopy." *J. Electroanalytical Chem.*, **694**, 45 (2013).
- B. P. Setzler and T. F. Fuller, "A physics-based impedance model of proton exchange membrane fuel cells exhibiting low-frequency inductive loops." *J. Electrochem. Soc.*, **162**, F519 (2015).
- A. A. Kulikovskiy, "Analysis of Damjanović kinetics of the oxygen reduction reaction: stability, polarization curve and impedance spectra." *J. Electroanalytical Chem.*, **738**, 130 (2015).
- J. J. Giner-Sanz, E. M. Ortega, and V. Pérez-Herranz, "Mechanistic equivalent circuit modelling of a commercial polymer electrolyte membrane fuel cell." *J. Power Sources*, **379**, 328 (2018).
- K. Wiezell, P. Gode, and G. Lindbergh, "Steady-State and EIS investigations of hydrogen electrodes and membranes in polymer electrolyte fuel cells." *J. Electrochem. Soc.*, **153**, A749 (2006).
- K. Wiezell, P. Gode, and G. Lindbergh, "Steady-state and EIS investigations of hydrogen electrodes and membranes in polymer electrolyte fuel cells." *J. Electrochem. Soc.*, **153**, A759 (2006).
- K. Wiezell, N. Holmström, and G. Lindbergh, "Studying low-humidity effects in PEMFCs using EIS II. Modeling." *J. Electrochem. Soc.*, **159**, F379 (2012).
- N. Holmström, K. Wiezell, and G. Lindbergh, "Studying low-humidity effects in PEMFCs using EIS: I. Experimental." *J. Electrochem. Soc.*, **159**, F369 (2012).
- C. Bao and W. G. Bessler, "Two-dimensional modeling of a polymer electrolyte membrane fuel cell with long flow channel. Part II. Physics-based electrochemical impedance analysis." *J. Power Sources*, **278**, 675 (2015).
- A. Kosakian, L. Padilla Urbina, A. Heaman, and M. Secanell, "Understanding single-phase water-management signatures in fuel-cell impedance spectra: a numerical study." *Electrochimica Acta*, **350**, 136204 (2020).

*Journal of The Electrochemical Society*, 2023 **170** 014504

18. A. Kulikovskiy, "Effect of proton conductivity transients on PEM fuel cell impedance: formation of a low-frequency inductive loop." *Electrochem. Commun.*, **140**, 107340 (2022).
19. N. Wagner and E. Gülzow, "Change of electrochemical impedance spectra (EIS) with time during CO-poisoning of the Pt-anode in a membrane fuel cell." *J. Power Sources*, **127**, 341 (2004).
20. I. A. Schneider, P. Boillat, A. Wokaun, and G. G. Scherer, "Formation of low frequency inductive loops in polymer electrolyte fuel cell (PEFC) impedance spectra under sub-saturated conditions." *ECS Meeting Abstracts* (2007).
21. I. A. Schneider, D. Kramer, A. Wokaun, and G. G. Scherer, "Oscillations in gas channels." *J. Electrochem. Soc.*, **154**, B770 (2007).
22. I. A. Schneider, S. A. Freunberger, D. Kramer, A. Wokaun, and G. G. Scherer, "Oscillations in gas channels." *J. Electrochem. Soc.*, **154**, B383 (2007).
23. I. A. Schneider, M. H. Bayer, A. Wokaun, and G. G. Scherer, "Impedance response of the proton exchange membrane in polymer electrolyte fuel cells." *J. Electrochem. Soc.*, **155**, B783 (2008).
24. G. Maranzana, J. Mainka, O. Lottin, J. Dillet, A. Lamibrac, A. Thomas, and S. Didierjean, "A proton exchange membrane fuel cell impedance model taking into account convection along the air channel: on the bias between the low frequency limit of the impedance and the slope of the polarization curve." *Electrochimica Acta*, **83**, 13 (2012).
25. I. Pivac and F. Barbir, "Inductive phenomena at low frequencies in impedance spectra of proton exchange membrane fuel cells—a review." *J. Power Sources*, **326**, 112 (2016).
26. I. Pivac, B. Šimić, and F. Barbir, "Experimental diagnostics and modeling of inductive phenomena at low frequencies in impedance spectra of proton exchange membrane fuel cells." *J. Power Sources*, **365**, 240 (2017).
27. Ivan Pivac, Dario Bežmalinović, and Frano Barbir, "Catalyst degradation diagnostics of proton exchange membrane fuel cells using electrochemical impedance spectroscopy." *Int. J. Hydrogen Energy*, **43**, 13512 (2018).
28. Q. Meyer, I. Pivac, F. Barbir, and C. Zhao, "Detection of oxygen starvation during carbon corrosion in proton exchange membrane fuel cells using low-frequency electrochemical impedance spectroscopy." *J. Power Sources*, **470**, 228285 (2020).
29. G. A. Futter, P. Gazdzicki, K. Andreas Friedrich, A. Latz, and T. Jahnke, "Physical modeling of polymer-electrolyte membrane fuel cells: understanding water management and impedance spectra." *J. Power Sources*, **391**, 148 (2018).
30. A. Schiefer, M. Heinzmann, and A. Weber, "Inductive low-frequency processes in PEMFC-impedance spectra." *Fuel Cells*, **20**, 499 (2020).
31. Q. Meyer and C. Zhao, "Air perturbation-induced low-frequency inductive electrochemical impedance arc in proton exchange membrane fuel cells." *J. Power Sources*, **488**, 229245 (2021).
32. C. Gerling, M. Hanauer, U. Berner, and K. Andreas Friedrich, "Full factorial in situ characterization of ionomer properties in differential PEM fuel cells." *J. Electrochem. Soc.*, **168**, 084504 (2021).
33. C. Gerling, M. Hanauer, U. Berner, and K. Andreas Friedrich, "PEM single cells under differential conditions: full factorial parameterization of the ORR and HOR kinetics and loss analysis." *J. Electrochem. Soc.*, **169**, 014503 (2022).
34. G. S. Harzer, J. N. Schwämmlein, A. Marija Damjanović, S. Ghosh, and H. A. Gasteiger, "Cathode loading impact on voltage cycling induced PEMFC degradation: a voltage loss analysis." *J. Electrochem. Soc.*, **165**, F3118 (2018).
35. W. G. Bessler, "Rapid impedance modeling via potential step and current relaxation simulations." *J. Electrochem. Soc.*, **154**, B1186 (2007).
36. H. Wiese and K. Georg Weil, "An efficient fourier transform algorithm for frequency domains of several decades using logarithmically spaced time samples." *IEEE Transactions on Acoustics, Speech, and Signal Processing*, **36**, 1096 (1988).
37. G. Maranzana, A. Lamibrac, J. Dillet, S. Abbou, S. Didierjean, and O. Lottin, "Startup (and shutdown) model for polymer electrolyte membrane fuel cells." *J. Electrochem. Soc.*, **162**, F694 (2015).
38. M. Mathias, D. Baker, W. Gu, M. Murphy, and K. C. Neyerlin, "Low frequency impedance of polymer electrolyte fuel cells." *ECS Meeting Abstracts*, *MA2005-01 1519* (2006).
39. N. P. Subramanian, T. A. Greszler, J. Zhang, W. Gu, and R. Makharia, "Pt-oxide coverage-dependent oxygen reduction reaction (ORR) kinetics." *J. Electrochem. Soc.*, **159**, B531 (2012).
40. J. Huang, J. Zhang, and M. Eikerling, "Unifying theoretical framework for deciphering the oxygen reduction reaction on platinum." *Phys. Chem. Chem. Phys.*, **20**, 11776 (2018).
41. A. Kulikovskiy, "Analytical low-current impedance of the cathode side of a PEM fuel cell." *J. Electroanalytical Chem.*, **823**, 335 (2018).
42. E. L. Redmond, B. P. Setzler, F. M. Alamgir, and T. F. Fuller, "Elucidating the oxide growth mechanism on platinum at the cathode in PEM fuel cells." *Phys. Chem. Chem. Phys.*, **16**, 5301 (2014), 2018.

# 5 Significance of the Studies in the Literature Context

Currently in the PEM literature, even though there are still some recent steady-state and EIS modeling studies either yielding full MEA models [89, 141] or focusing on specific cell effects [90], there is a lack of studies combining both proper experimental characterization and the development of user-friendly models. Furthermore, even recent models often rely on parameterizations which become increasingly outdated, as deplored for instance by Dickinson and Smith [22]. Even worse, parameters not seldom originate from several different sources working with different materials in their studies and in detailed/sophisticated models sometimes many parameters are only estimated. Vetter and Schumacher also pointed out the important scatter in material parameterizations that are available in the literature [141, 142], making the choice of the right material laws even more difficult. As a consequence, PEMFC function is still not completely understood. Despite all this, literature works increasingly focus on optimization and cost reduction

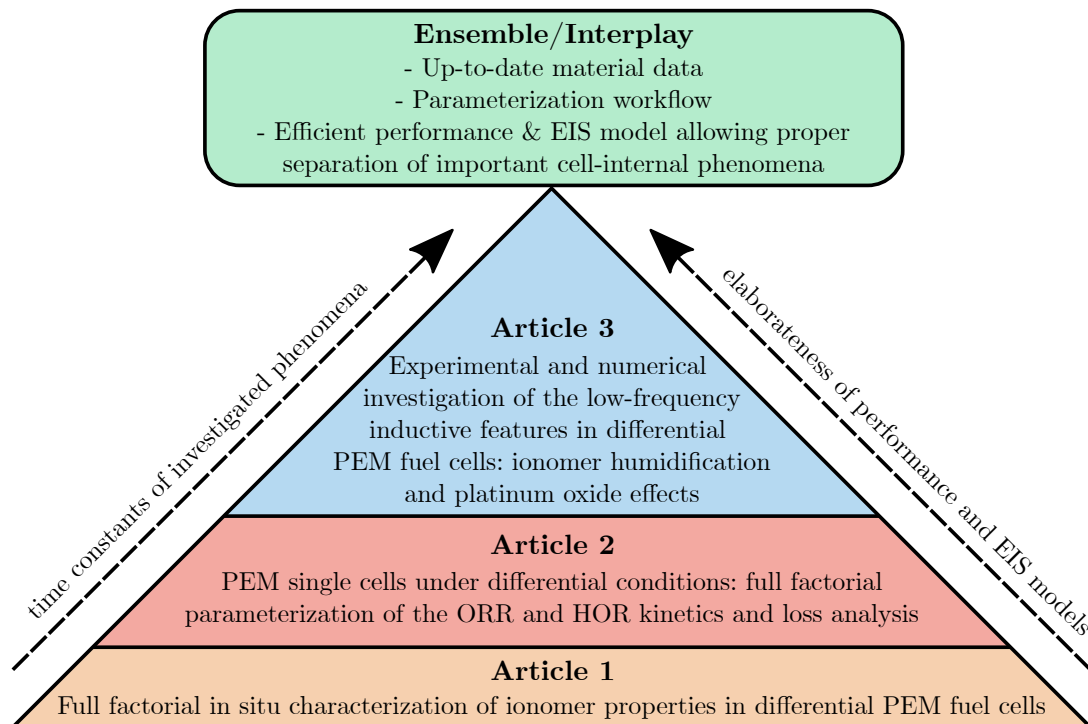


**Figure 5.1:** Structure of this cumulative doctoral thesis and interplay of the publications.

through novel materials as well as understanding aging phenomena.

This work aimed at addressing the proper characterization of important material laws and proposing meaningful models for cell performance and EIS. Whenever possible, the parameters were varied systematically in a full factorial fashion and control measurements were carried out to ensure good measurement quality, which is an important attribute of this work since the availability of sufficient proper data is often the bottleneck in literature studies. As it was already mentioned previously, the order of the publications followed a clear meaningful thread towards the parameterization of a model for differential cells with the focus on an enhanced ORR modeling approach. This is also shown in Fig. 5.1 which shows how the papers built upon each other.

In the first paper, important ionomer properties were investigated and quantified as these are always important to understand performance signatures. As explained in section 3.2, hydrogen crossover yields a small shift in the cell current density. However, even only a small shift that is not accounted for might lead to erroneous interpretations in Tafel analyses. Thus, hydrogen permeation was characterized by voltammetry techniques. Also, proton conductivity of the membrane and the catalyst layer play a major role in the polarization processes with increasing importance at dry conditions. Therefore, these properties were measured and investigated intensively by EIS techniques. Then, based on these results, the actual investigation of the ORR kinetics was started in the second paper, complemented by an investigation of the anode contributions and followed by a first loss separation analysis which also contains an estimation of oxygen transport losses by limiting current techniques. It came out that the correction of performance signatures by the ionomer contribution is important before the quantification of the kinetics and that at low current densities, the anode contributions only play a very small role. At high currents, however, deviations from the models were observed that could not be solely attributed to mass transport issues. Moreover, it was pointed out that an EIS-based evaluation of Tafel slopes leads to discrepancies with respect to the classical polarization-based Tafel analysis. Thus, it was concluded that more sophisticated kinetic laws for the ORR are needed, which was addressed in the third publication. There a new simple model of the ORR combined with PtOx kinetics was proposed that reproduces the half-cell potential-dependent change in the Tafel slope as well as the low-frequency inductive loop in EIS linked to slow PtOx relaxation, which was quantified in a full factorial fashion experimentally. This model was also complemented by Fick's law of diffusion to take oxygen transport within the GDL and CCL into account, which is a process of high time constants. Hence, from a global point of view, it can be said that aside from the logic behind the order of publication, there is also a tendency going from the processes with the lowest time constants to those with the highest time constants.

In order to contextualize the final performance and EIS model that came out of this work, it is necessary to discuss previous literature modeling approaches. The simplest model of the steady-state performance is the one given in (3.1) which is a 0D model containing the most important contributions to voltage loss and is often used for both differential and non-differential cells. The parameters of this model can be obtained experimentally as explained all along in this work. For the cathode kinetics, such models often used Tafel or Butler-Volmer representations with one intrinsic slope of -70 mV/dec, even though some rare studies aim at capturing the oxide coverage effects on the catalyst, e.g. by scaling the ECSA and thus the effective exchange current density by the fraction

of free platinum surface such as Subramanian et al. [80]. More advanced studies employ 1D *through-plane* models that resolve the distribution of the field variable through the layer depths. Often, the anode is neglected, the membrane represented as a simple resistor and the focus is set on the cathode side (CCL). When pure oxygen is used and losses caused by reactant transport are negligible, the equations that come into play are charge conservation and Ohm's law as presented in (5.1). Of course, these equations must be used in their transient form to access EIS:

$$\frac{C_{\text{dl}}}{L_{\text{CCL}}} \cdot \frac{\partial \eta}{\partial t} + \nabla(-\sigma_p \cdot \nabla \phi_p) = S_{\text{ct}}, \quad (5.1)$$

with  $C_{\text{dl}}$  the double layer capacity,  $L_{\text{CCL}}$  the CCL thickness,  $\eta$  the kinetics overpotential,  $\sigma_p$  the protonic conductivity and  $S_{\text{ct}}$  the source term from finite charge transfer. The latter is, as previously, a kinetics law such as the ones of Tafel or Butler-Volmer. If the oxygen transport resistance cannot be ignored, Fick's law of diffusion must be added to the problem:

$$\epsilon_p \cdot C \cdot \frac{\partial x_{\text{O}_2}}{\partial t} + \nabla(-C \cdot D_{\text{O}_2} \cdot \nabla x_{\text{O}_2}) = \frac{S_{\text{ct}}}{4 \cdot F}, \quad (5.2)$$

where  $C$  is the concentration,  $x_{\text{O}_2}$  the oxygen mole fraction and  $\epsilon_p$  the layer porosity. This can also be solved in the GDL if the latter is modeled explicitly, or the losses caused there can be computed via an adapted boundary condition. This system of partial differential equations admits an analytical solution for the steady-state and sometimes even for the EIS when some specific simplifications are made, i.e. if proton and/or oxygen transport is fast [58, 143]. If both conditions apply at the same time, i.e. at low cell currents and well humidified conditions, the general expression of the well-known TLM for EIS spectra is obtained [110]:

$$Z(\omega) = R_{\Omega} + \frac{R_p}{\sqrt{C_{\text{dl}} \cdot i \cdot \omega \cdot R_p + \frac{R_p}{R_{\text{ct}}}}} \coth \sqrt{R_p \cdot C_{\text{dl}} \cdot i \cdot \omega + \frac{R_p}{R_{\text{ct}}}}. \quad (5.3)$$

However, at high current densities or dry conditions, the ratio  $R_p/R_{\text{ct}}$  increases, leading to a decreasing catalyst layer utilization and then, due to the current dependency of  $R_{\text{ct}}$ , this model does not apply anymore. Another effect that can play a significant role is inhomogeneous distribution of the properties through the layer thickness. For both these cases, the equations do not admit simple analytical solutions and must therefore be solved numerically.

The next step towards more complex models capturing more effects in the literature is often to add more layers, e.g. model the anode side and separate the GDL into GDB and MPL, and to add more equations to capture further physics such as water transport in all phases and energy transport. Such models are referred to as *complete MEA models*. Furthermore, more dimensions can be added by a channel and land separation or by explicit modeling of the gas channel dimension, which are called *across-the-channel* and *along-the-channel*, respectively. However, this was out of the scope of this work which focused on providing a simple 1D through-plane model which can be parameterized with manageable effort and is capable of capturing both steady-state and EIS signatures properly. To do so, as mentioned above, a new simple model of the ORR containing PtOx kinetics was implemented as explained in detail in the third publication (section 4.3). The

additional PDE for the oxide coverage was implemented as:

$$\frac{\Gamma}{L_{\text{CCL}}} \cdot \frac{\partial \theta_{\square}}{\partial t} = S_{\text{PtOx}}, \quad (5.4)$$

with  $\Gamma$  the molar quantity of available active surface platinum,  $\theta_{\square}$  the fraction of free platinum surface and  $S_{\text{PtOx}}$  the platinum oxide source term. Before, such simple 1D models mainly used Tafel or BV formulations in the literature, which cannot reconcile steady-state and EIS signatures as they contain one single intrinsic Tafel slope and thus yield too small  $R_{\text{ct}}$  and no low-frequency inductive loop. However, even in the model of this work, very fast oxide coverage effects were contained effectively in the capacitive  $R_{\text{ct}}$  and not modeled explicitly by micro-kinetics which are very challenging to parameterize. Thus, this model represents a meaningful compromise between accuracy and complexity and can be seen as a valuable addition to the existing literature models from Kulikovsky for instance. Moreover, models in the literature are seldom parameterized and validated for a consistent full factorial dataset coming from one set of materials as it was done in this work, which enhances its quality.

However, one important weakness of this model is that ionomer humidification was considered in a simplified way by applying the local equivalent conductivities of membrane and catalyst layer for each simulated load point as they were measured experimentally by EIS techniques at high frequencies and fitted by TLM approaches. Hence, the slow transient load-dependent contributions of water management coming from  $\partial R/\partial j$  which yield low-frequency inductive features as demonstrated in the last publication were not taken into account. These slow contributions were estimated based on the measured resistance values. However, the final model was not able to account for these physics and thus was only suited for modeling high humidity conditions. To solve this issue pragmatically, an additional PDE can be added to represent the conductivity dynamics within the PEM and the CCL, as demonstrated recently by Kulikovsky [90]. Coupled with a function giving the layer conductivity based on the relative humidity and the current density as an enhancement of the previous method, this provides the low-frequency inductive contributions coming from slow ionomer hydration. In the end, the final model is based on the following PDEs:

$$\frac{C_{\text{dl}}}{L_{\text{CCL}}} \cdot \frac{\partial \Delta \phi}{\partial t} + \nabla(-\sigma_p \nabla \phi_p) = -\frac{n \cdot \nu_1 + \nu_2}{L_{\text{CCL}}} \quad (5.5)$$

$$\frac{C_{\text{dl}}}{L_{\text{CCL}}} \cdot \frac{\partial \Delta \phi}{\partial t} + \nabla(-\sigma_e \nabla \phi_e) = \frac{n \cdot \nu_1 + \nu_2}{L_{\text{CCL}}} \quad (5.6)$$

$$\frac{\Gamma}{L_{\text{CCL}}} \cdot \frac{\partial \theta_{\square}}{\partial t} = -\frac{\nu_2 \cdot n_{\text{Pt}}}{L_{\text{CCL}} \cdot F} \quad (5.7)$$

$$\epsilon_p \cdot C \cdot \frac{\partial x_{\text{O}_2}}{\partial t} + \nabla(-C \cdot D_{\text{O}_2} \cdot \nabla x_{\text{O}_2}) = -\frac{n \cdot \nu_1}{L_{\text{CCL}} \cdot 4 \cdot F} \quad (5.8)$$

$$\tau_p \cdot \frac{\partial \sigma}{\partial t} + \sigma = \sigma^0 \quad (5.9)$$

The first four equations are explained in detail in the third publication contained in section 4.3. In the last equation, which was newly added to the set of previous PDEs,  $\tau_p$  represents the time constant of the process, which is chosen above 10 s for both the



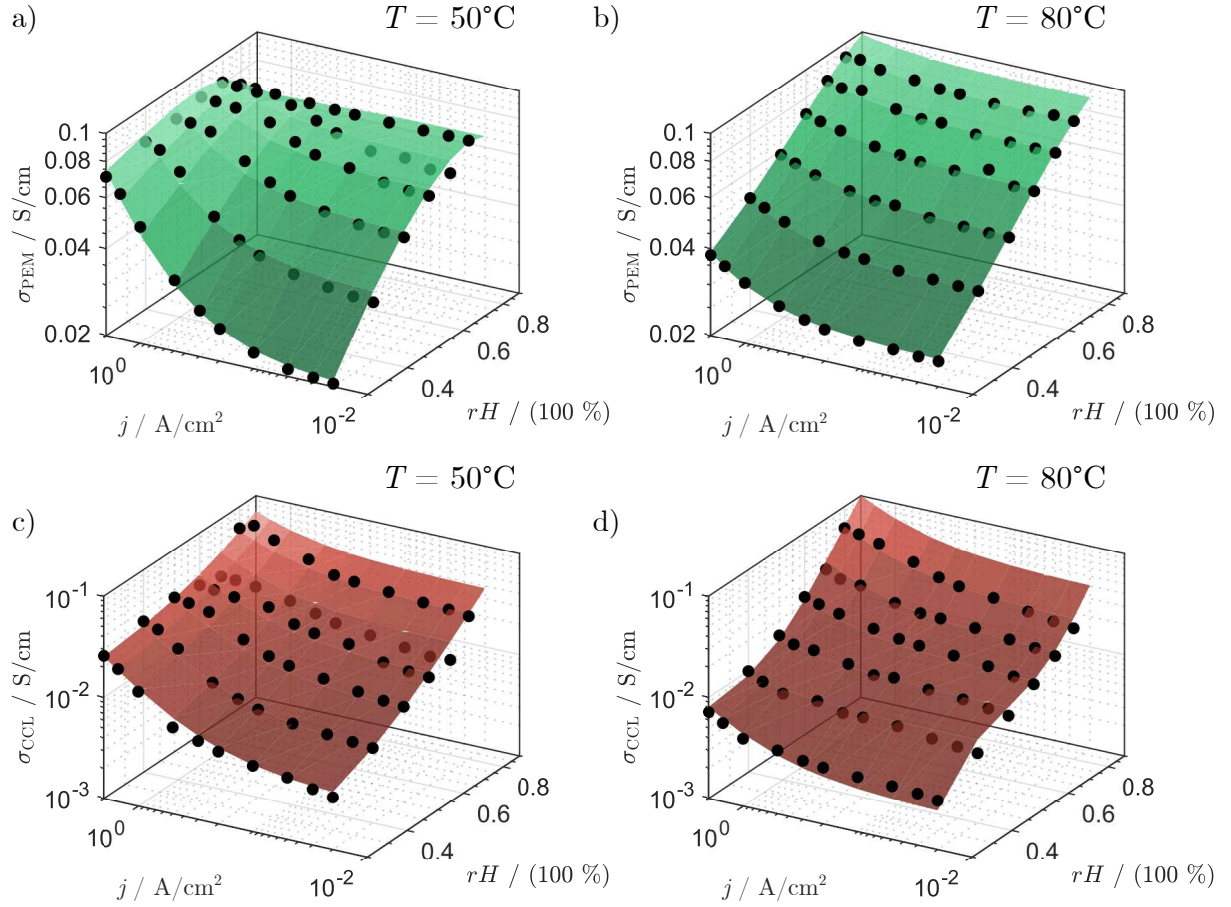


**Figure 5.2:** Conductivities  $\sigma_{\text{PEM}}$  and  $\sigma_{\text{CCL}}$  depending on the cell current and the relative humidity for 50°C (a and c) and 80°C (b and d). The black dots represent the values determined from measurement with the help of a TLM and the surfaces represent the model fit.

PEM and the CCL but cannot be properly determined from the data available in this work. Furthermore,  $\sigma$  represents the field variable for the conductivity and  $\sigma^0$  the steady-state conductivity depending on the current density and the relative humidity at given temperature. The latter was parameterized by fitting a polynomial to the data as given by

$$\begin{aligned} \sigma^0(j, RH) = & p_{00} + p_{01} \cdot j + p_{10} \cdot RH + p_{20} \cdot (RH)^2 + p_{30} \cdot (RH)^3 \\ & + p_{11} \cdot j \cdot RH + p_{21} \cdot j \cdot (RH)^2, \end{aligned} \quad (5.10)$$

where  $\sigma^0$  is given in S/cm,  $j$  is in A/cm<sup>2</sup> and  $RH$  is dimensionless between 0 and 1. The parameters obtained from the equation fitting to the data are given in Table 5.1 and the fitting results are shown in Fig. 5.2 for 50°C and 80°C. It can be seen that fitted surfaces match the experimental data (black dots) well.

It can be seen in Fig. 5.3 that in addition to the results shown in the third paper in section 4.3, the model is now able to capture low-humidity effects coming from the slow ionomer hydration physics and matches the experiments quite well. As expected, the spectra at low current densities are unspectacular as solely  $R_p$  is affected at high frequencies and everything else seems to be similar to the wet conditions shown in the

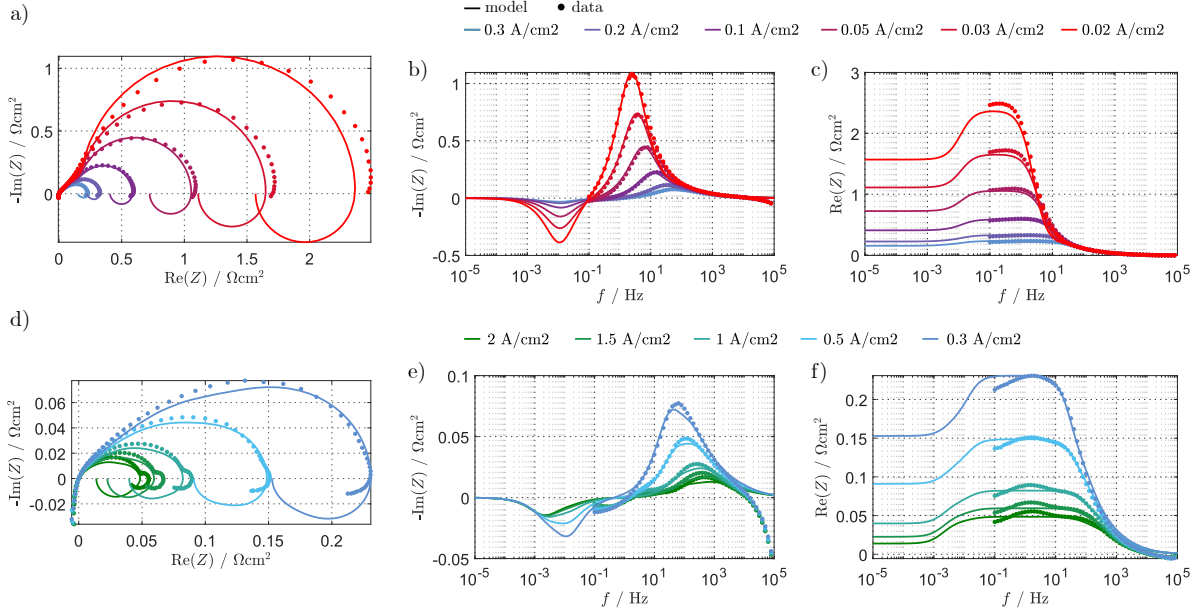


**Figure 5.3:** Experimental (dots) and simulated (lines) EIS spectra at  $RH = 30\%$ ,  $T = 80\text{ }^\circ\text{C}$  and  $x_{\text{O}_2}^{\text{dry}} = 1$  at different cell current densities. a) and d) Nyquist representations. b), c), e) and f) Bode representations. All the data were gathered at  $RH = 30\%$  and the simulations were carried out considering oxygen mass transport through GDL and CCL by Fick's law of diffusion as well as ionomer humidification transients. The spectra were shifted on the real axis for the sake of clarity.

third publication. It is important to notice that the spectra have been shifted on the real axis by their respective  $R_\Omega$  value so that they all have the same axis intercept of  $0\text{ }\Omega\text{ cm}^2$  for the sake of visibility. Moreover, the inductive loop does not seem to be affected by the low humidity. At current densities above  $0.1\text{ A/cm}^2$ , however, the capacitive loop is strongly affected by the decrease in relative humidity, which is due to the decreasing catalyst utilization caused by the low proton conductivity. Also, the inductive loop which is now composed of the PtOx relaxation as well as of the ionomer hydration features is larger than at wet conditions. Figure 5.4 demonstrates the good match between experiment and simulation for both  $R_{\text{ct}}$  and  $|R_{\text{ind}}|$  at dry (a) and at wet (b) conditions. It gets clear that the model is now able to predict the size of the low-frequency inductive loop properly and got better even at the wet conditions at high current density compared

**Table 5.1:** Fitted parameters of eq. (5.10) for the PEM and CCL at  $50^\circ\text{C}$  and  $80^\circ\text{C}$ .

	$T$ $^\circ\text{C}$	$p_{00}$ S/cm	$p_{01}$ S·cm/A	$p_{10}$ S/cm	$p_{20}$ S/cm	$p_{30}$ S/cm	$p_{11}$ S·cm/A	$p_{21}$ S·cm/A
$\sigma_{\text{PEM}}^0$ (S/cm)	50	-1.48e-2	3.27e-2	8.00e-2	1.82e-1	-1.91e-1	-8.93e-3	-3.55e-2
	80	1.53e-2	6.12e-3	-3.65e-2	2.74e-1	-1.58e-1	5.59e-3	-7.97e-3
$\sigma_{\text{CCL}}^0$ (S/cm)	50	2.16e-3	1.02e-2	1.34e-7	1.22e-7	4.86e-2	4.24e-7	7.75e-3
	80	-4.68e-2	2.29e-2	3.00e-1	-5.69e-1	3.80e-1	-1.04e-1	1.26e-1

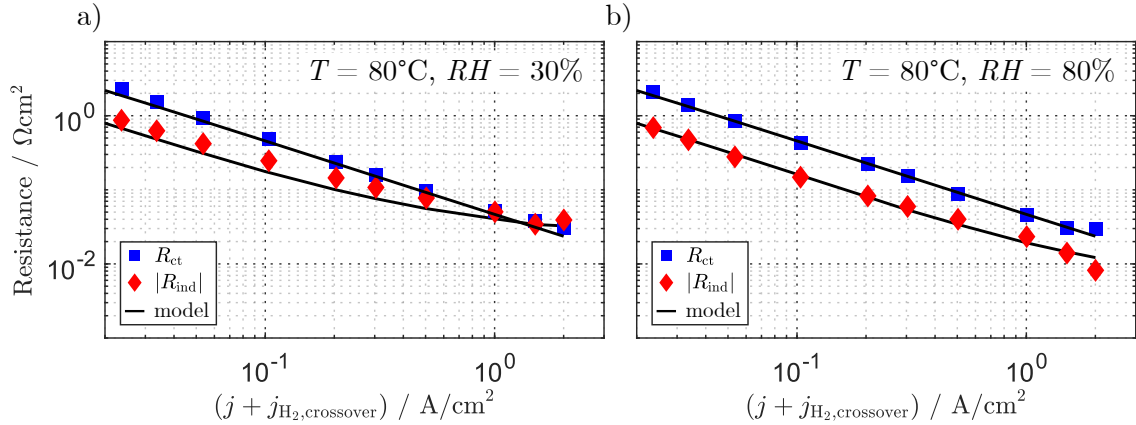


**Figure 5.4:** Experimental (symbols) and simulated (lines) charge transfer resistance  $R_{ct}$  and inductive contribution  $|R_{ind}|$  over the current density  $j$  at  $T = 80^\circ\text{C}$  and  $x_{\text{O}_2}^{\text{dry}} = 1$  for  $RH = 30\%$  (a) and  $RH = 80\%$  (b). The experimental  $R_{ct}$  was obtained by fitting EIS data to an ECM and  $|R_{ind}|$  was obtained as described in section 4.3.

with the result given in section 4.3. Regardless of the relative humidity, the size of the inductive loop changes linearly with the current density at low loads in the double logarithmic representation. This behavior comes principally from the oxide kinetics. At wet conditions, the curve remains linear even at higher currents and starts deviating from this behavior only at current densities above  $0.5 \text{ A/cm}^2$ . At low humidity, the ionomer hydration effects are present starting from current densities above  $0.1 \text{ A/cm}^2$ . As already discussed in the publication, there is small offset of the inductive contribution between dry and wet conditions even at the lowest current densities. Here, it gets obvious that it can neither be tackled by the PtOx kinetics nor by the physics representing ionomer hydration dynamics. This is not an issue however considering the small impact of this offset on the performance and thus on the analyses performed in this work.

It is also worth mentioning that the model now predicts a growing inductive loop with decreasing oxygen partial pressure as it was observed in the experiments (see below) but could not be explained so far. Nevertheless, the accuracy of the model decreases with decreasing partial pressure and temperature at high current density, which might come from the strong coupling between all PDEs at such low CCL utilization. Understanding these effects and providing better parameterizations for such conditions would need separate in-depth studies and would therefore go beyond the scope of this work. Furthermore, as mentioned in the last paper, the time constants of the inductive loop processes were only estimated as they could not be determined exactly based on the experimental methods used here. Determining them precisely would require special studies which was not needed in this work to reach the targets of developing a model capable of predicting steady-state performance as well as capacitive EIS precisely and quantify low-frequency inductive contributions meaningfully. This model yields important insights that are needed to understand the complex low-frequency behavior and therefore the observed discrepancies between polarization-curve-based Tafel analysis and Tafel slopes originating from the capacitive charge transfer resistance in EIS.

Based on this model, it is possible to carry out loss separation analyses based on both steady-state overpotentials from polarization behavior and on differential resistances

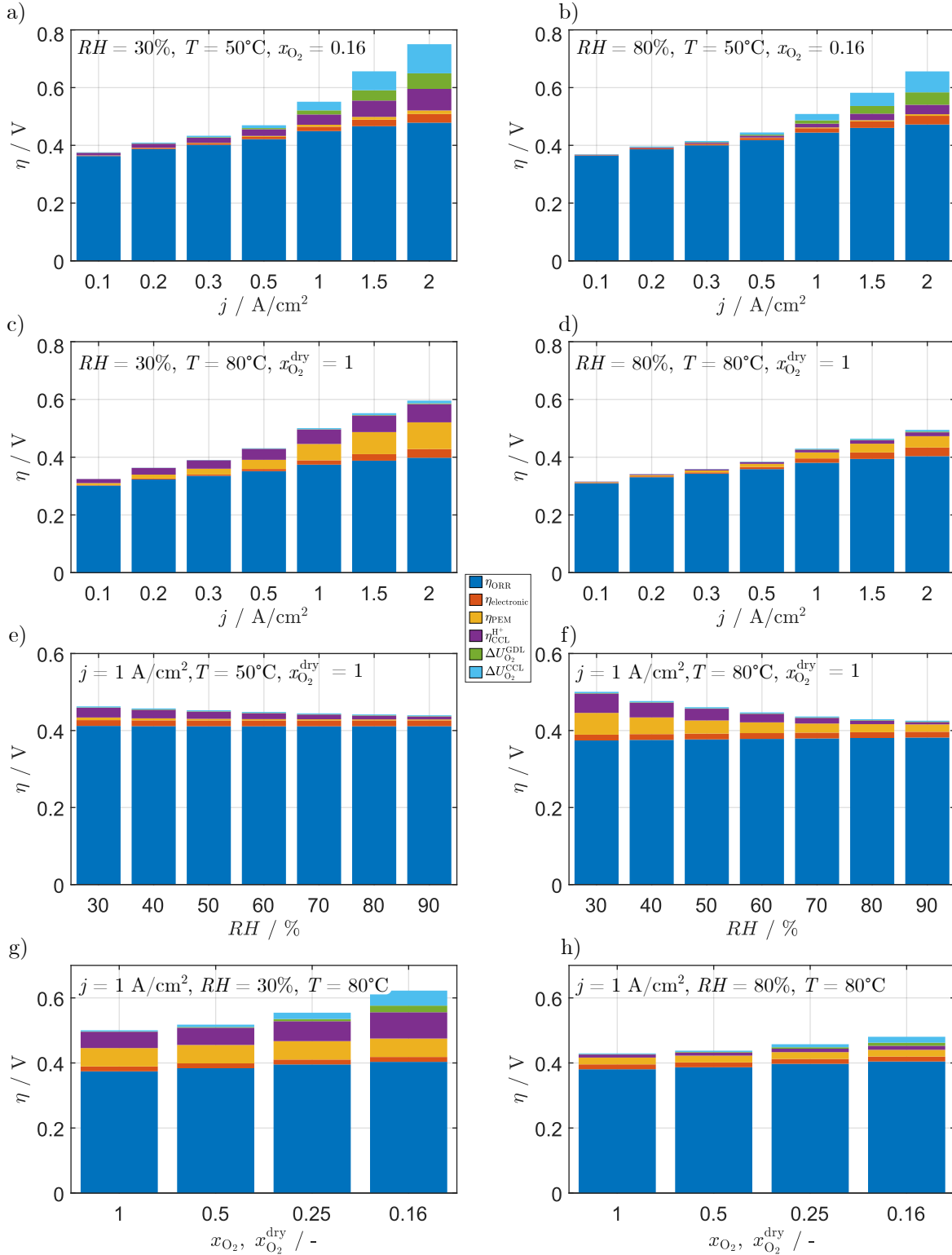


**Figure 5.5:** Loss separation based on the steady-state overpotentials for selected operation points. The overpotentials  $\eta_{ORR}$ ,  $\eta_{electronic}$ ,  $\eta_{PEM}$ ,  $\eta_{CCL}^{H+}$ ,  $\Delta U_{O_2}^{GDL}$  and  $\Delta U_{O_2}^{CCL}$  were obtained by activating the mechanisms one by one in the model which was parameterized in this work.

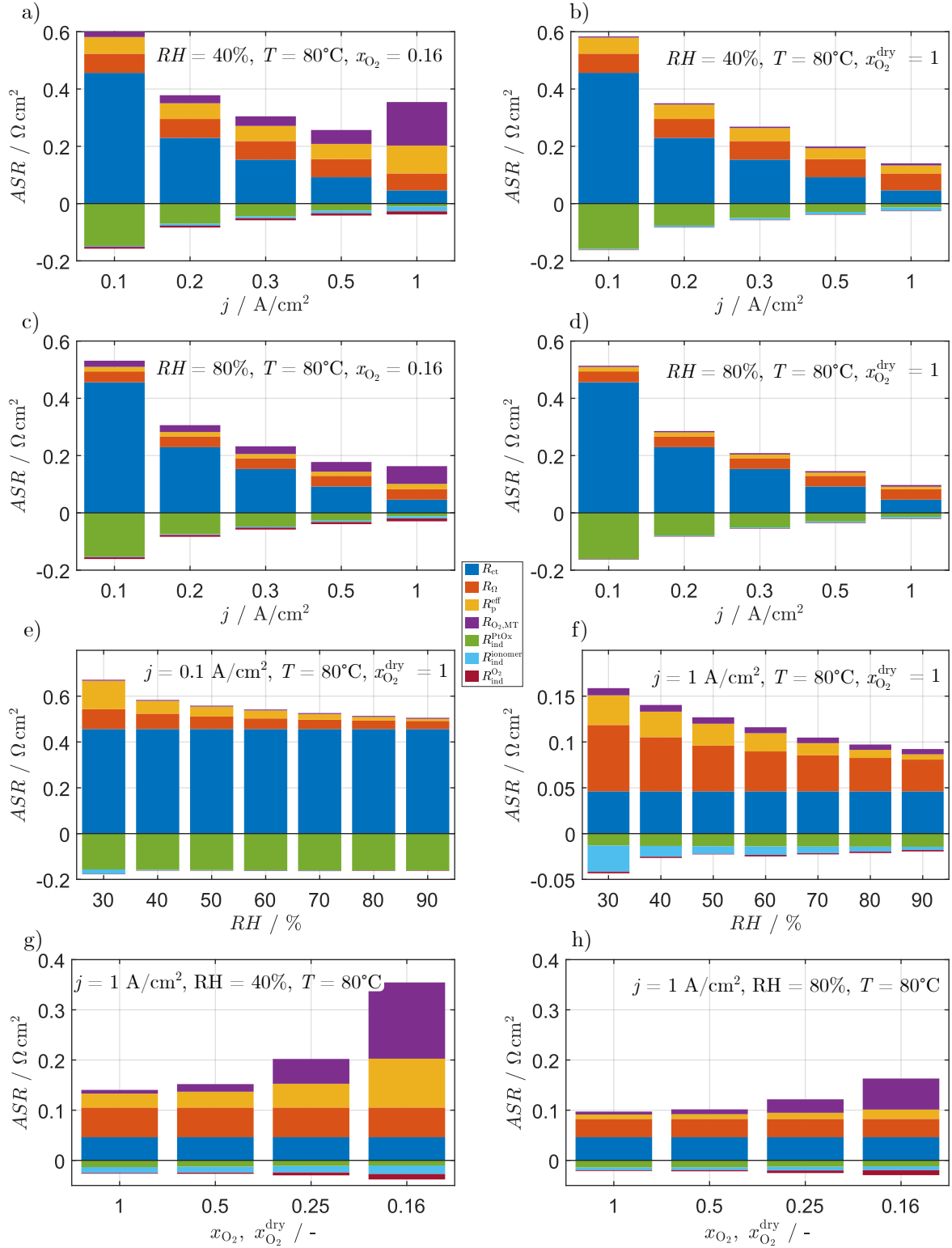


**Figure 5.6:** Differential resistance separation based on EIS for selected operation points. The resistances  $R_{ct}$ ,  $R_{\Omega}$ ,  $R_p^{eff}$ ,  $R_{O_2,MT}$ ,  $R_{ind}^{PtOx}$ ,  $R_{ind}^{ionomer}$  and  $R_{ind}^{O_2}$  were obtained by activating the mechanisms one by one in the model which was parameterized in this work.

from EIS spectra. An example of the first is depicted in Fig. 5.5 for important operating conditions and an example of the second is given in Fig. 5.6. It is important to emphasize that the loss separation was obtained by repeating each simulation at given conditions multiple times and deactivating one physics at a time, i.e. by setting unphysically high transport properties in order to reach a negligible impact on the cell behavior. This is the simplest way to probe the effect of a single transport mechanism. Furthermore, the anode contribution to the performance is not taken into account in this analysis as the ACL operates in the linear regime with a resistance  $\ll 10 \text{ m}\Omega \text{ cm}^2$ , leading to a very small potential drop even at high current density. The overpotentials shown in Fig. 5.5 confirm the original postulate of this work saying that the cathode kinetics yield by far the most important overpotential at any typical operating condition with state-of-the-art materials. It can be seen however that this contribution increases only slowly with increasing current density as compared to the other contributions. Voltage drop caused by oxygen transport from the channel to the electrode seems to play a significant role only above  $1 \text{ A/cm}^2$  even at low oxygen partial pressures and is highest at cold conditions. At dry conditions, the effective protonic resistance of the CCL seems to be slightly higher at low temperature, while the membrane resistance is much higher at warm than at cold conditions. The relative humidity and oxygen partial pressure variations in Fig. 5.5 permit to quantify the influence of those parameters, however they do not yield any surprising result.

Figure 5.6 depicts a similar analysis based on a decomposition of EIS spectra, i.e. from the differential resistance point of view, which corresponds to the local slope of the steady-state polarization curve. From the two first diagrams a and b, the strong coupling of the effects within the catalyst layer gets clear: the oxygen concentration has a strong impact on both  $R_p^{\text{eff}}$  and  $R_{\text{O}_2, \text{MT}}$  in the capacitive part as well as on the low-frequency inductive part. This demonstrates that it is challenging and probably not meaningful to consider the effects separately. From the comparison of the two latter diagrams with the third and fourth diagrams c and d it can be learned that oxygen transport is less important at high humidity conditions, i.e. when the CCL utilization is still high. Then, the humidity variations at  $0.1 \text{ A/cm}^2$  and  $1 \text{ A/cm}^2$  in e and f show similar behavior but on a different scale and prove two facts: again, that oxygen mass transport contributions are higher at low humidity conditions, and that low-frequency inductive signatures coming from slow ionomer hydration are large only at high current densities and low humidity. The oxygen partial pressure variation in the two last diagrams g and h confirms the previous statements and strongly emphasizes the importance of the oxygen partial pressure on both the capacitive and the inductive loop, which is higher the lower the relative humidity is.

## 6 Conclusion and Outlook

In this doctoral thesis, characterization methods to determine macro-homogeneous material properties were elucidated and performance models which reproduce steady-state as well as EIS behavior were developed. The focus was set on understanding the role of the main operating parameters which are the relative humidity, temperature, oxygen partial pressure and current density. Especially the ORR kinetics occurring on the cathode side was investigated in detail since it leads to the highest performance drop at most operating conditions and is still subject to discussions in the literature. Therefore, special care was taken to gather a comprehensive and consistent dataset where the operating parameters were varied systematically in a full factorial manner whenever possible. This is one attribute that particularly distinguishes this work from others in the literature, where the quantity and quality of available data are sometimes lacking and thus authors fall back on diverse other sources to feed their models with material parameters. In the experiments of this work, long hold times for stabilization of each point and regular state-of-health checks by reproducing polarization curves as well as cyclic voltammetry guaranteed high data quality. To do so, a subscale test station from FuelCon was commissioned and fully automated in order to allow for proper and reproducible testing of the state-of-the-art MEA materials which were mounted in a differential cell setup from Baltic FuelCells. The latter was used to minimize the influence of design parameters and operate the cells as homogeneously as possible since the characterization of macro-homogeneous layer properties requires a differential approach, i.e. no in-plane gradients. Thus, all the considerations in this work were 0D or 1D through-plane. Since several loss mechanisms such as electrode kinetics, proton and oxygen transport overlap during fuel cell operation, the ORR overpotential is not directly accessible. Therefore, the performance needed to be investigated integrally.

In the first publication, ionomer-related properties were characterized extensively by voltammetry and EIS techniques. A study in  $\text{H}_2/\text{N}_2$  configuration, i.e. with a blocked working electrode, proves the equivalency of CV and LSV regarding the determination of the transport-limited hydrogen crossover based on a statistical analysis for one-factor-at-a-time variations of the hydrogen partial pressure on the anode side  $p_{\text{H}_2}$ , the relative humidity  $rH$  and the temperature  $T$ . This was completed by a small study with online gas analysis of the cathode exhaust stream which also shows consistent results with the LSV measurements. Furthermore, the absolute pressure variation and hydrogen partial pressure variation by mixing  $\text{H}_2$  and  $\text{N}_2$  showed that crossover indeed obeys a simple permeation law in which the crossover flux increases linearly with increasing  $p_{\text{H}_2}$ . Recording several CVs in both  $\text{H}_2/\text{N}_2$  and  $\text{N}_2/\text{H}_2$  configurations allowed to determine the roughness factors of the cathode and anode electrodes by integration of the hydrogen sorption and desorption peaks and taking the average of both values for each electrode. Then, a

second even larger measurement campaign with full factorial parameter variations in a broad space served to measure the hydrogen crossover rates at all conditions and thus to parameterize a model of the permeation coefficient which was used afterwards in modeling. This model consists of an Arrhenius-type prefactor and an exponential dependency on  $RH$  and an activation energy of 20 kJ/mol was found. Even though the permeation coefficient is in the same order of magnitude as typical literature parameterizations, the  $RH$ -dependency is slightly different.

Subsequently this measurement campaign was also used to record EIS at each condition and therewith extract the ohmic resistance  $R_{\Omega} = R_0$  and the protonic resistance of the cathode electrode  $R_p$  at well-defined equilibrium conditions. This was done by fitting the parameters of a blocking cathode TLM containing constant phase elements instead of capacitances in order to compensate the increasing deviation from the ideal behavior with decreasing humidity. To deconvolute  $R_w$  into the membrane resistance  $R_{PEM}$  and the electronic resistance  $R_{\text{electronic}}$ , measurements without a CCM, i.e. only with two GDLs facing each other with the MPL side, were conducted to approximate the electronic contact and bulk resistances to  $15 \text{ m}\Omega \text{ cm}^2$ . Then, a model similar to the one for the permeation coefficient was parameterized for both quantities and yields 7 and 9 kJ/mol for  $R_{PEM}$  and  $R_p$ , respectively. Again, these models point out differences with respect to previous literature parameterizations even though the values lie in the same orders of magnitude and thus show the necessity to properly characterize new materials instead of falling back to outdated literature values. Through a third measurement campaign containing EIS measurements under load in  $\text{H}_2/\text{O}_2$  mode, the change of the ionomer resistances due to water production was analyzed. This water production causes the resistances to decrease with increasing current density and is most pronounced at cold and dry operating conditions. The implication of this effect is that the correction of polarization curves by the ohmic loss contributions based only on EIS measurements obtained in  $\text{H}_2/\text{N}_2$  mode should be considered carefully as this might lead to important deviations at dry conditions. Again, a TLM-based approach was used to fit the EIS spectra; however, an iterative high current density model was selected which is able to capture both uniform and non-uniform electrode utilization. The latter is relevant at high  $R_p$  and low charge transfer resistance  $R_{ct}$ , i.e. mostly at dry conditions and high current density. This evaluation of the ionomer resistances depending on the current points out the massive influence of  $RH$  and  $T$  on the cell performance. At high cell temperatures, there is a slow decrease of the resistances over the current density, while at low temperatures the resistances drop sharply since less water can be uptaken by the gas phase and converge to one specific resistance which is independent of  $RH$ . This effect was emphasized by tracking the current density at which  $R_p$  reaches its saturation value (i.e.  $RH = 100\%$ ) in  $\text{H}_2/\text{N}_2$  mode depending on  $RH$  and  $T$ . This last  $\text{H}_2/\text{O}_2$  measurement campaign represents the main dataset of this work and contains also the measurements that were used in the next publications, thus it laid the foundation for deeper investigations of the kinetics and oxygen mass transport losses.

In the second publication, the goal of complete parameterization of a meaningful model for differential PEMFC behavior with a special focus on the ORR was pursued further. The hydrogen and oxygen kinetics (HOR and ORR, respectively) as well as oxygen mass transport contributions were investigated deeply based on polarization and EIS data. On the one hand, a dataset containing variations of  $RH$ ,  $T$ ,  $p_{\text{H}_2}$  and  $j$  in proton pump mode ( $\text{H}_2/\text{H}_2$ ) was used for the analysis of the anode contributions. On the other hand, the



main H<sub>2</sub>/O<sub>2</sub> dataset from the previous publication containing systematic variations of  $RH$ ,  $T$ ,  $p_{O_2}$  and  $j$  was used for the analyses of the ORR and the loss contribution separation. First, EIS in H<sub>2</sub>/H<sub>2</sub> configuration allowed to visualize and quantify the proton pump performance signatures. By employing DRT and by fitting the parameters of a classical TLM, the strongly  $p_{H_2}$ - and  $RH$ -dependent high-frequency loop was assigned to a combination of HOR kinetics and proton transport in the catalyst layer. This leads to an effective exchange current density which actually depends on the conductivity of the ionomer in the catalyst layer. Even though the low-frequency loop could not be unambiguously assigned to a specific process, it was shown that it is strongly dependent on both  $p_{H_2}$  and  $RH$  as well. Moreover, it was noticed that in the absence of O<sub>2</sub>, CO surface poisoning can strongly impede HOR kinetics and lead to erroneous characterizations when overlooked. The effect is small at 80°C but severe at 50°C. To counter this, a fast and simple recovery procedure to oxidize parasitic CO almost simultaneously in both electrodes based on voltammetry was implemented. This made a poison-free parameterization of the anode loss contribution possible based on linearized Butler-Volmer kinetics which yields an activation energy of 18 kJ/mol. Depending on  $T$  and  $p_{H_2}$ , the effective exchange current density lies between 170 and 408 mA/cm<sub>Pt</sub><sup>2</sup>, meaning that the effective resistance is always way below 10 mΩ cm<sup>2</sup> and thus that the anode contributes only marginally to the performance loss with the state-of-the-art materials used in this study.

Then, a full factorial parameterization of the ORR kinetics based on a simple Tafel law with an exchange current density depending on  $p_{O_2}$  and  $T$  was conducted. For this purpose, steady-state polarization curves obtained in fuel cell mode with {O<sub>2</sub>, N<sub>2</sub>} or {O<sub>2</sub>, He} mixtures on the cathode side came into play. These curves were corrected by the ionomer contributions characterized in the first publication. Additionally, the humidity dependency of the ORR was investigated by the comparison of a  $p_{H_2O}$ -dependent with a  $p_{H_2O}$ -independent model. The comparison shows that assuming a constant water activity of 1 is justified for the characterization and modeling of the ORR based on Tafel kinetics even under dry conditions. An activation energy of approximately 70 kJ/mol and a reaction order of 0.5 were found, which are in accordance with previous literature findings. Furthermore, oxygen mass transport contributions to the overall cell voltage were quantified by steady-state and transient limiting current measurements. In combination with the previously developed models for the ohmic and kinetic losses, this permits a quantitative loss separation and confirms that for the whole range of conditions covered by the dataset, the simple Tafel law with one intrinsic slope is sufficient to capture the (steady-state) ORR kinetics down to half-cell potentials of 0.8 V. At lower half-cell potentials, however, the analysis becomes limited by uncertainties in the accounting of mass transport effects. This is the case because available methods are not able to probe oxygen transport alone without affecting the internal state of the cell at the same time, as demonstrated by the comparison of SLC and TLC measurements. Nevertheless, the dataset reveals systematic trends on the capacitive EIS response of the ORR that are not covered by the Tafel law even at low current densities. Further, discrepancies between Tafel slopes from polarization-based data and EIS-based evaluations hint at more complex electrode kinetics, which were addressed in the last publication.

In the third publication, the low-frequency inductive phenomena in differential PEMFCs were investigated based on both numerical simulation and experimental techniques involv-

ing the main  $\text{H}_2/\text{O}_2$  dataset. First it was explained that the discrepancies between the polarization curve slopes and the slopes obtained from  $R_{\text{ct}}$  evaluation considering a Tafel law are caused by the low-frequency inductive features (positive imaginary part) in EIS of 30 to over 150 mV/dec depending on the operating conditions. An analysis of previous literature permitted to narrow down the possible origins of the inductive features to more complex cathode kinetics involving platinum oxides and to slow water management dynamics that influence the ionomer conductivity. Then, the absolute inductive contributions were computed by subtracting the low-frequency real-axis-intercepts ( $f \approx 1$  Hz) of capacitive EIS from the local slopes of the polarization curves which were obtained by numerical derivation. Therewith, the influence of the operating conditions on the inductive loop could be investigated in a full factorial fashion. This showed that the size of the inductive loop is strongly dependent on  $RH$  and  $j$ ; however, there is also a small but non-negligible effect of  $T$  and  $p_{\text{O}_2}$ . Thus, the inductive loop (in  $\Omega\text{cm}^2$ ) is largest at low load, even though its influence on the local slope is proportional to the current density and thus increases with increasing  $j$ . Further, decreasing  $RH$  or  $p_{\text{O}_2}$  increases the inductive loop strongly at high currents. Based on the previous full factorial characterization of the ionomer resistances, the inductive contributions originating from slow ionomer hydration could be estimated and thus allowed a separation between these effects and kinetic contributions. It could be shown that these ionomer contributions play almost no role at high  $RH$  conditions and are only important starting from medium currents at dry conditions. Hence, this is proof that the inductive effects at small current density originate almost exclusively from ORR-linked effects within the CCL, even though a small additional process of  $\leq 10$  mV/dec that is not proportional to  $j$  was observed at dry conditions. A new approach to model the cathode kinetics was proposed following a single-step Tafel law for the ORR and an additional equation for the slow platinum poisoning reaction by surface oxides which results in an inductive loop. This model assumes that the poisoning influences the effective exchange current density of the ORR and thus also its apparent Tafel slope through the fraction of available platinum surface. This approach was then integrated into a dynamic, isothermal, one-dimensional through-plane FEM model which is able to simulate polarization curves as well as EIS by using the current-step method, complemented by CV simulations obtained by switching off the ORR and imposing a succession of voltage ramp up and ramp down. Based on this fast model, an extensive parameter study could be performed. The model for the kinetics was parameterized for high  $RH$  conditions based on both polarization and EIS data. After adding Fickian diffusion physics in the GDL and CCL, the final model shows an unprecedented match between simulation and experiment for both polarization curves and EIS spectra. Hence, a new simple model is proposed which presents a good compromise between complexity, parameterability and accuracy and at the same time brings the reconciliation of steady-state performance and EIS signatures in differential PEMFCs one significant step forward.

In Chapter 5, aside from recapitulating the link between the publications of this work and their significance in the current literature context, the model from the third publication which builds on all the previous results of this work was successfully extended by physics representing the slow ionomer hydration dynamics. This was done to enable accurate simulations at dry conditions, which were not possible until then. To do so, functions representing the PEM and CCL conductivities depending on the relative humidity and the current density were needed. This was obtained by fitting polynomials

to the experimental data which were previously evaluated by TLM techniques. This resulted in the final model of this work which demonstrates that dry conditions can also be simulated meaningfully and even that the match between experimental and modeled inductive contributions is better at high  $RH$ . Moreover, a  $p_{O_2}$  dependency of the inductive loop as it was observed in the experiments is now obtained in the model, caused by the complex interplay of oxygen and proton transport as well as the oxidation state within the CCL. Finally, the model was employed for a new comprehensive loss analysis based on both steady-state overpotentials and differential resistances from EIS with a higher degree of separation into individual contributions than known from literature. This study permitted to elucidate the most important loss mechanisms in state-of-the-art PEMFCs depending on the operating conditions. It can therefore be stated that in the end the most important targets of this work are achieved. Beyond that, further interesting open points were discussed, which can be given as an outlook of this work.

In future works, critical operating conditions at which the model accuracy decreases compared with the baseline conditions and parameterization procedures tailored for such conditions should be investigated in more detail, e.g. at low  $p_{O_2}$ , low  $T$  or low  $RH$ . However, the catalyst utilization might be strongly inhomogeneous at such conditions. Thus, it would be necessary to examine whether a model as proposed in this work can compute such conditions accurately or if complete MEA models containing detailed water and energy management are needed. One point that needs to be analyzed is the representation of anode drying effects caused by electroosmotic drag (EOD). Furthermore, experimental techniques are needed to properly deconvolute the low-frequency inductive processes and calibrate their time constants as they are not accessible based on the experiments of this work and thus were estimated. For this purpose, so-called negative DRT represents a promising approach, even though measuring EIS at frequencies below 1 Hz remains technically challenging. Finally, besides investigating MEA performance, the model of this work can serve as a basis for physical aging modeling. Moreover, it can be integrated into complete cell models for the sake of upscaling towards stack and system simulation with the ultimate goal of improving efficiency, lifetime and costs. Hence, such models are essential in fuel cell and fuel cell system engineering in the effort of reaching a large-scale market entry.



## 7 Bibliography

- [1] *UN Population Division Data Portal*. <https://population.un.org/dataportal/home>, accessed on November 6<sup>th</sup> 2022
- [2] H. Ritchie, M. Roser, and P. Rosado. *CO<sub>2</sub> and greenhouse gas emissions*. *Our World in Data*, 2020. <https://ourworldindata.org/co2-and-greenhouse-gas-emissions>, accessed on April 19<sup>th</sup> 2023
- [3] L. Carrette, K. A. Friedrich, and U. Stimming. Fuel Cells - Fundamentals and Applications. *Fuel Cells*, 1(1):5–39, June 2001.
- [4] J. Larminie and A. Dicks. *Fuel cell systems explained*. 2nd ed., John Wiley & Sons, 2003.
- [5] *Global energy-related CO<sub>2</sub> emissions by sector*. <https://www.iea.org/data-and-statistics/charts/global-energy-related-co2-emissions-by-sector>, accessed on April 19<sup>th</sup> 2023
- [6] S. Pardhi, S. Chakraborty, D.-D. Tran, M. El Baghdadi, S. Wilkins, and O. Hegazy. A Review of Fuel Cell Powertrains for Long-Haul Heavy-Duty Vehicles: Technology, Hydrogen, Energy and Thermal Management Solutions. *Energies*, 15(24):9557, December 2022.
- [7] *Europäische Energie- und Klimaziele*. <https://www.umweltbundesamt.de/daten/klima/europaeische-energie-klimaziele>, accessed on November 4<sup>th</sup> 2022
- [8] *Klimaschutzpaket der EU-Kommission*. <https://www.bundesregierung.de/breg-de/themen/europa/fit-for-55-eu-1942402>, accessed on November 4<sup>th</sup> 2022
- [9] *Net Zero by 2050*. <https://www.iea.org/reports/net-zero-by-2050>, accessed on November 4<sup>th</sup> 2022
- [10] *Verbrenner-Verbot: EU beschließt CO<sub>2</sub>-Flottenziele für neue Pkw*. <https://www.adac.de/news/aus-fuer-verbrenner-ab-2035/>, accessed on November 4<sup>th</sup> 2022
- [11] *EU-Umweltrat: Nur noch CO<sub>2</sub>-frei fahren*. <https://www.bundesregierung.de/breg-de/themen/europa/verbrennermotoren-2058450>, accessed on November 4<sup>th</sup> 2022
- [12] C. H. Hamann and W. Vielstich. *Elektrochemie*. 4th ed., John Wiley & Sons, 2005

- 
- [13] *Honda Clarity Fuel Cell kommt nach Europa.* <https://www.honda.de/cars/world-of-honda/news-events/2016-11-30-honda-clarity-fuel-cell-kommt-nach-europa.html>, accessed on November 3<sup>th</sup> 2022
- [14] *Mirai.* <https://www.toyota.de/neuwagen/mirai>, accessed on November 3<sup>th</sup> 2022
- [15] *Der Hyundai NEXO.* <https://www.hyundai.de/modelle/nexo/>, accessed on November 3<sup>th</sup> 2022
- [16] *Mercedes-Benz GLC F-CELL.* <https://www.mercedes-benz.de/passengercars/mercedes-benz-cars/models/glc/glc-f-cell/der-neue-glc-f-cell/module.html>, accessed on November 3<sup>th</sup> 2022
- [17] *Wasserstofffahrzeuge.* <https://h2.live/wasserstoffautos/>, accessed on November 3<sup>th</sup> 2022
- [18] *Filling up with H<sub>2</sub>.* <https://h2.live/en/>, accessed on November 4<sup>th</sup> 2022
- [19] *Hydrogen Stations in France in November 2022.* <https://www.glpautogas.info/en/hydrogen-stations-france.html>, accessed on November 4<sup>th</sup> 2022
- [20] *Ländervergleich: Frankreich - Deutschland.* <https://www.laenderdaten.info/laendervergleich.php?country1=FRA&country2=DEU>, accessed on November 4<sup>th</sup> 2022
- [21] Y. Wang, D. F. Ruiz Diaz, K. S. Chen, Z. Wang, and X. C. Adroher. Materials, technological status, and fundamentals of PEM fuel cells – A review. *Materials Today*, 32:178–203, January 2020.
- [22] E. J. F. Dickinson and G. Smith. Modelling the Proton-Conductive Membrane in Practical Polymer Electrolyte Membrane Fuel Cell (PEMFC) Simulation: A Review. *Membranes*, 10(11):310, October 2020.
- [23] C. Gerling, M. Hanauer, U. Berner, and K. A. Friedrich. Full Factorial In Situ Characterization of Ionomer Properties in Differential PEM Fuel Cells. *Journal of The Electrochemical Society*, 168(8):084504, August 2021.
- [24] C. Gerling, M. Hanauer, U. Berner, and K. A. Friedrich. PEM Single Cells under Differential Conditions: Full Factorial Parameterization of the ORR and HOR Kinetics and Loss Analysis. *Journal of The Electrochemical Society*, 169(1):014503, January 2022.
- [25] C. Gerling, M. Hanauer, U. Berner, and K. A. Friedrich. Experimental and Numerical Investigation of the Low-Frequency Inductive Features in Differential PEMFCs: Ionomer Humidification and Platinum Oxide Effects. *Journal of The Electrochemical Society*, 170(1):014504, January 2023.
- [26] M. Pan, C. Pan, C. Li, and J. Zhao. A review of membranes in proton exchange membrane fuel cells: Transport phenomena, performance and durability. *Renewable and Sustainable Energy Reviews*, 141:110771, May 2021.

- [27] A. Kusoglu and A. Z. Weber. New Insights into Perfluorinated Sulfonic-Acid Ionomers. *Chemical Reviews*, 117(3):987–1104, February 2017.
- [28] A. Z. Weber and J. Newman. Transport in Polymer-Electrolyte Membranes. *Journal of The Electrochemical Society*, 150(7):A1008, 2003.
- [29] J. Biesdorf. *Neutron radiography of Polymer Electrolyte Fuel Cells: From conventional towards energy selective neutron imaging*. PhD thesis, ETH Zurich, 2016.
- [30] J. Wind, R. Späh, W. Kaiser, and G. Böhm. Metallic bipolar plates for PEM fuel cells. *Journal of Power Sources*, 105(2):256–260, 2002.
- [31] X. Li and I. Sabir. Review of bipolar plates in PEM fuel cells: Flow-field designs. *International Journal of Hydrogen Energy*, 30(4):359–371, March 2005.
- [32] Y. Yoon, W. Lee, G. Park, T. Yang, and C. Kim. Effects of channel and rib widths of flow field plates on the performance of a PEMFC. *International Journal of Hydrogen Energy*, 30(12):1363–1366, September 2005.
- [33] J.-K. Kuo, T.-H. Yen, and C.-K. Chen. Three-dimensional numerical analysis of PEM fuel cells with straight and wave-like gas flow fields channels. *Journal of Power Sources*, 177(1):96–103, February 2008.
- [34] C. Bao and W. G. Bessler. Two-dimensional modeling of a polymer electrolyte membrane fuel cell with long flow channel. Part I. Model development. *Journal of Power Sources*, 275:922–934, February 2015.
- [35] S. Shimpalee, S. Greenway, and J. W. Van Zee. The impact of channel path length on PEMFC flow-field design. *Journal of Power Sources*, 160(1):398–406, September 2006.
- [36] S. Shimpalee and J. Vanzee. Numerical studies on rib & channel dimension of flow-field on PEMFC performance. *International Journal of Hydrogen Energy*, 32(7):842–856, May 2007.
- [37] S.-S. Hsieh and K.-M. Chu. Channel and rib geometric scale effects of flowfield plates on the performance and transient thermal behavior of a micro-PEM fuel cell. *Journal of Power Sources*, 173(1):222–232, November 2007.
- [38] D. Jeon. The effect of serpentine flow-field designs on PEM fuel cell performance. *International Journal of Hydrogen Energy*, 33(3):1052–1066, February 2008.
- [39] X.-D. Wang, W.-M. Yan, Y.-Y. Duan, F.-B. Weng, G.-B. Jung, and C.-Y. Lee. Numerical study on channel size effect for proton exchange membrane fuel cell with serpentine flow field. *Energy Conversion and Management*, 51(5):959–968, May 2010.
- [40] W.-M. Yan, C.-H. Yang, C.-Y. Soong, F. Chen, and S.-C. Mei. Experimental studies on optimal operating conditions for different flow field designs of PEM fuel cells. *Journal of Power Sources*, 160(1):284–292, September 2006.

- [41] H. Heidary, M. J. Kermani, S. G. Advani, and A. K. Prasad. Experimental investigation of in-line and staggered blockages in parallel flowfield channels of PEM fuel cells. *International Journal of Hydrogen Energy*, 41(16):6885–6893, May 2016.
- [42] R. Roshandel, F. Arbabi, and G. K. Moghaddam. Simulation of an innovative flow-field design based on a bio inspired pattern for PEM fuel cells. *Renewable Energy*, 41:86–95, May 2012.
- [43] B.-T. Tsai, C.-J. Tseng, Z.-S. Liu, C.-H. Wang, C.-I. Lee, C.-C. Yang, and S.-K. Lo. Effects of flow field design on the performance of a PEM fuel cell with metal foam as the flow distributor. *International Journal of Hydrogen Energy*, 37(17):13060–13066, September 2012.
- [44] A. Su, F. Weng, C. Hsu, and Y. Chen. Studies on flooding in PEM fuel cell cathode channels. *International Journal of Hydrogen Energy*, 31(8):1031–1039, July 2006.
- [45] S.-S. H. and Y.-J. Huang. Measurements of current and water distribution for a micro-PEM fuel cell with different flow fields. *Journal of Power Sources*, 183(1):193–204, August 2008.
- [46] A. P. Manso, F. F. Marzo, J. Barranco, X. Garikano, and M. Garmendia Mujika. Influence of geometric parameters of the flow fields on the performance of a PEM fuel cell. A review. *International Journal of Hydrogen Energy*, 37(20):15256–15287, October 2012.
- [47] H. Liu, P. Li, D. Juarez-Robles, K. Wang, and A. Hernandez-Guerrero. Experimental Study and Comparison of Various Designs of Gas Flow Fields to PEM Fuel Cells and Cell Stack Performance. *Frontiers in Energy Research*, 2, 2014.
- [48] A. Azarafza, M. S. Ismail, M. Rezakazemi, and M. Pourkashanian. Comparative study of conventional and unconventional designs of cathode flow fields in PEM fuel cell. *Renewable and Sustainable Energy Reviews*, 116:109420, December 2019.
- [49] *Engineering ToolBox*. Standard state and enthalpy of formation, gibbs free energy of formation, entropy and heat capacity. [https://www.engineeringtoolbox.com/standard-state-enthalpy-formation-definition-value-Gibbs-free-energy-entropy-molar-heat-capacity-d\\_1978.html](https://www.engineeringtoolbox.com/standard-state-enthalpy-formation-definition-value-Gibbs-free-energy-entropy-molar-heat-capacity-d_1978.html). accessed on January 14<sup>th</sup> 2023
- [50] M. W. Chase and National Information Standards Organization (US). *NIST-JANAF thermochemical tables*, volume 9. American Chemical Society Washington, DC, 1998.
- [51] A J. Bard and L R. Faulkner. *Electrochemical methods: fundamentals and applications*. 2nd ed., John Wiley & Sons, 2001.
- [52] D. M. Bernardi and M. W. Verbrugge. Mathematical model of a gas diffusion electrode bonded to a polymer electrolyte. *AIChE journal*, 37(8):1151–1163, 1991.



- [53] K. C. Neyerlin, W. Gu, J. Jorne, and H. A. Gasteiger. Determination of Catalyst Unique Parameters for the Oxygen Reduction Reaction in a PEMFC. *Journal of The Electrochemical Society*, 153(10):A1955, 2006.
- [54] A. A. Kulikovskiy. The regimes of catalyst layer operation in a fuel cell. *Electrochimica Acta*, 55(22):6391–6401, September 2010.
- [55] A. A. Kulikovskiy. A model for local impedance of the cathode side of PEM fuel cell with segmented electrodes. *Journal of the Electrochemical Society*, 159(7):F294, 2012.
- [56] A. A. Kulikovskiy. A physical model for catalyst layer impedance. *Journal of Electroanalytical Chemistry*, 669:28–34, March 2012.
- [57] A. A. Kulikovskiy. Analytical solutions for polarization curve and impedance of the cathode catalyst layer with fast oxygen transport in a PEM fuel cell. *Journal of the Electrochemical Society*, 161(8):E3171, 2014.
- [58] A. A. Kulikovskiy. A PhysicallyBased Analytical Polarization Curve of a PEM Fuel Cell. *Journal of The Electrochemical Society*, 161(3):F263–F270, 2014.
- [59] A. A. Kulikovskiy. A simple and accurate fitting equation for half of the faradaic impedance arc of a PEM fuel cell. *Journal of Electroanalytical Chemistry*, 738:108–112, February 2015.
- [60] T. Reshetenko and A. A. Kulikovskiy. Variation of PEM fuel cell physical parameters with current: Impedance spectroscopy study. *Journal of The Electrochemical Society*, 163(9):F1100, 2016.
- [61] T. Reshetenko and A. A. Kulikovskiy. Impedance spectroscopy study of the PEM fuel cell cathode with nonuniform nafion loading. *Journal of The Electrochemical Society*, 164(11):E3016–E3021, 2017.
- [62] B. M. Stühmeier, M. R. Pietsch, J. N. Schwämmlein, and H. A. Gasteiger. Pressure and Temperature Dependence of the Hydrogen Oxidation and Evolution Reaction Kinetics on Pt Electrocatalysts via PEMFC-based Hydrogen-Pump Measurements. *Journal of The Electrochemical Society*, 168(6):064516, June 2021.
- [63] K. C. Neyerlin, W. Gu, J. Jorne, and H. A. Gasteiger. Study of the Exchange Current Density for the Hydrogen Oxidation and Evolution Reactions. *Journal of The Electrochemical Society*, 154(7):B631, 2007.
- [64] A. Huth, B. Schaar, and T. Oekermann. A “proton pump” concept for the investigation of proton transport and anode kinetics in proton exchange membrane fuel cells. *Electrochimica Acta*, 54(10):2774–2780, April 2009.
- [65] W. Sheng, H. A. Gasteiger, and Y. Shao-Horn. Hydrogen Oxidation and Evolution Reaction Kinetics on Platinum: Acid vs Alkaline Electrolytes. *Journal of The Electrochemical Society*, 157(11):B1529, 2010.

- [66] J. Durst, C. Simon, F. Hasché, and H. A. Gasteiger. Hydrogen oxidation and evolution reaction kinetics on carbon supported Pt, Ir, Rh, and Pd electrocatalysts in acidic media. *Journal of The Electrochemical Society*, 162(1):F190, 2014.
- [67] V. Briega-Martos, A. Ferre-Vilaplana, E. Herrero, and J. M. Feliu. Why the activity of the hydrogen oxidation reaction on platinum decreases as pH increases. *Electrochimica Acta*, 354:136620, September 2020.
- [68] B. Andraus. Proton-conducting polymer membranes in fuel cell humidification aspects. *Solid State Ionics*, 168(3-4):311–320, March 2004.
- [69] K. Wiezell, P. Gode, and G. Lindbergh. Steady-State and EIS Investigations of Hydrogen Electrodes and Membranes in Polymer Electrolyte Fuel Cells. *Journal of The Electrochemical Society*, 153(4):A749, 2006.
- [70] K. Wiezell, P. Gode, and G. Lindbergh. Steady-State and EIS Investigations of Hydrogen Electrodes and Membranes in Polymer Electrolyte Fuel Cells. *Journal of The Electrochemical Society*, 153(4):A759, 2006.
- [71] N. Holmström, K. Wiezell, and G. Lindbergh. Studying Low-Humidity Effects in PEFCs Using EIS: I. Experimental. *Journal of The Electrochemical Society*, 159(8):F369, 2012.
- [72] K. Wiezell, N. Holmström, and G. Lindbergh. Studying low-humidity effects in PEFCs using EIS II. modeling. *Journal of the Electrochemical Society*, 159(8):F379, 2012.
- [73] A. Parthasarathy, S. Srinivasan, A. J. Appleby, and C. R. Martin. Temperature dependence of the electrode kinetics of oxygen reduction at the platinum/Nafion<sup>®</sup> interface: a microelectrode investigation. *Journal of the Electrochemical Society*, 139(9):2530, 1992.
- [74] A. Holewinski and S. Linic. Elementary mechanisms in electrocatalysis: revisiting the ORR Tafel slope. *Journal of The Electrochemical Society*, 159(11):H864, 2012.
- [75] M. Markiewicz, C. Zalitis, and A. Kucernak. Performance measurements and modelling of the ORR on fuel cell electrocatalysts – the modified double trap model. *Electrochimica Acta*, 179:126–136, October 2015.
- [76] V. Briega-Martos, E. Herrero, and J. M. Feliu. Effect of pH and Water Structure on the Oxygen Reduction Reaction on platinum electrodes. *Electrochimica Acta*, 241:497–509, July 2017.
- [77] A. Damjanovic and V. Brusic. Electrode kinetics of oxygen reduction on oxide-free platinum electrodes. *Electrochimica Acta*, 12(6):615–628, June 1967.
- [78] A. Damjanovic, M. A. Genshaw, and J. O’M. Bockris. The Role of Hydrogen Peroxide in Oxygen Reduction at Platinum in H<sub>2</sub>SO<sub>4</sub> Solution. *Journal of The Electrochemical Society*, 114(5):466, 1967.

- [79] A. Damjanovic. Progress in the Studies of Oxygen Reduction during the Last Thirty Years. *Electrochemistry in Transition*, pages 107–126. Springer US, 1992.
- [80] N. P. Subramanian, T. A. Greszler, J. Zhang, W. Gu, and R. Makharia. Pt-oxide coverage-dependent oxygen reduction reaction (ORR) kinetics. *Journal of The Electrochemical Society*, 159(5):B531, 2012.
- [81] O. Antoine, Y. Bultel, and R. Durand. Oxygen reduction reaction kinetics and mechanism on platinum nanoparticles inside Nafion<sup>®</sup>. *Journal of Electroanalytical Chemistry*, 499(1):85–94, February 2001.
- [82] I. A. Schneider, P. Boillat, A. Wokaun, and G. G. Scherer. Formation of Low Frequency Inductive Loops In Polymer Electrolyte Fuel Cell (PEFC) Impedance Spectra Under Sub-Saturated Conditions. *ECS Meeting Abstracts*, 2007.
- [83] I. A. Schneider, M. H. Bayer, A. Wokaun, and G. G. Scherer. Impedance Response of the Proton Exchange Membrane in Polymer Electrolyte Fuel Cells. *Journal of The Electrochemical Society*, 155(8):B783, 2008.
- [84] G. Maranzana, J. Mainka, O. Lottin, J. Dillet, A. Lamibrac, A. Thomas, and S. Didierjean. A proton exchange membrane fuel cell impedance model taking into account convection along the air channel: On the bias between the low frequency limit of the impedance and the slope of the polarization curve. *Electrochimica Acta*, 83:13–27, November 2012.
- [85] C. Bao and W. G. Bessler. Two-dimensional modeling of a polymer electrolyte membrane fuel cell with long flow channel. Part II. Physics-based electrochemical impedance analysis. *Journal of Power Sources*, 278:675–682, March 2015.
- [86] I. Pivac and F. Barbir. Inductive phenomena at low frequencies in impedance spectra of proton exchange membrane fuel cells A review. *Journal of Power Sources*, 326:112–119, September 2016.
- [87] I. Pivac, B. Šimić, and F. Barbir. Experimental diagnostics and modeling of inductive phenomena at low frequencies in impedance spectra of proton exchange membrane fuel cells. *Journal of Power Sources*, 365:240–248, October 2017.
- [88] Q. Meyer and C. Zhao. Air perturbation-induced low-frequency inductive electrochemical impedance arc in proton exchange membrane fuel cells. *Journal of Power Sources*, 488:229245, March 2021.
- [89] A. Kosakian, L. P. Urbina, A. Heaman, and M. Secanell. Understanding single-phase water-management signatures in fuel-cell impedance spectra: A numerical study. *Electrochimica Acta*, 350:136204, August 2020.
- [90] A. A. Kulikovskiy. Effect of proton conductivity transients on PEM fuel cell impedance: Formation of a lowfrequency inductive loop. *Electrochemistry Communications*, 140:107340, July 2022.

- [91] N. Wagner and M. Schulze. Change of electrochemical impedance spectra during CO poisoning of the Pt and PtRu anodes in a membrane fuel cell (PEFC). *Electrochimica Acta*, 48(25-26):3899–3907, November 2003.
- [92] N. Wagner and E. Gülzow. Change of electrochemical impedance spectra (EIS) with time during CO-poisoning of the Pt-anode in a membrane fuel cell. *Journal of Power Sources*, 127(1-2):341–347, March 2004.
- [93] S. K. Roy, M. E. Orazem, and B. Tribollet. Interpretation of Low-Frequency Inductive Loops in PEM Fuel Cells. *Journal of The Electrochemical Society*, 154(12):B1378, 2007.
- [94] M. Mathias, D. Baker, W. Gu, M. Murphy, and K. C. Neyerlin. Low Frequency Impedance of Polymer Electrolyte Fuel Cells. *ECS Meeting Abstracts*, MA2005-01(41):1519, 2006.
- [95] M. Mathias, D. Baker, J. Zhang, Y. Liu, and W. Gu. Frontiers in Application of Impedance Diagnostics to H<sub>2</sub>-Fed Polymer Electrolyte Fuel Cells. *ECS Transactions*, 13(13):129–152, December 2019.
- [96] R. M. Darling and J. P. Meyers. Kinetic Model of Platinum Dissolution in PEMFCs. *Journal of The Electrochemical Society*, 150(11):A1523, 2003.
- [97] E. L. Redmond, B. P. Setzler, F. M. Alamgir, and T. F. Fuller. Elucidating the oxide growth mechanism on platinum at the cathode in PEM fuel cells. *Physical Chemistry Chemical Physics*, 16(11):5301, 2014.
- [98] B. P. Setzler and T. F. Fuller. A physics-based impedance model of proton exchange membrane fuel cells exhibiting low-frequency inductive loops. *Journal of The Electrochemical Society*, 162(6):F519, 2015.
- [99] A. A. Kulikovskiy. Analysis of Damjanovi kinetics of the oxygen reduction reaction: Stability, polarization curve and impedance spectra. *Journal of Electroanalytical Chemistry*, 738:130–137, February 2015.
- [100] G. A. Futter, P. Gazdzicki, K. A. Friedrich, A. Latz, and T. Jahnke. Physical modeling of polymer-electrolyte membrane fuel cells: Understanding water management and impedance spectra. *Journal of Power Sources*, 391:148–161, July 2018.
- [101] A. Schiefer, M. Heinzmann, and A. Weber. Inductive LowFrequency Processes in PEMFC Impedance Spectra. *Fuel Cells*, March 2020.
- [102] H. S. Wroblowa, Y.-C.-Pan, and G. Razumney. Electroreduction of oxygen. *Journal of Electroanalytical Chemistry and Interfacial Electrochemistry*, 69(2):195–201, April 1976.
- [103] J. X. Wang, J. Zhang, and R. R. Adzic. Double-Trap Kinetic Equation for the Oxygen Reduction Reaction on Pt(111) in Acidic Media. *The Journal of Physical Chemistry A*, 111(49):12702–12710, December 2007.

- [104] M. Moore, A. Putz, and M. Secanell. Investigation of the ORR using the double-trap intrinsic kinetic model. *Journal of the Electrochemical Society*, 160(6):F670, 2013.
- [105] J. Huang, J. Zhang, and M. Eikerling. Unifying theoretical framework for deciphering the oxygen reduction reaction on platinum. *Physical Chemistry Chemical Physics*, 20(17):11776–11786, 2018.
- [106] A. M. Gómez-Marín and E. A. Ticianelli. A reviewed vision of the oxygen reduction reaction mechanism on Pt-based catalysts. *Current Opinion in Electrochemistry*, 9:129–136, June 2018.
- [107] A. M. Gómez-Marín and J. M. Feliu. Oxygen reduction at platinum electrodes: The interplay between surface and surroundings properties. *Current Opinion in Electrochemistry*, 9:166–172, June 2018.
- [108] J. Huang and M. Eikerling. Modeling the oxygen reduction reaction at platinum-based catalysts: A brief review of recent developments. *Current Opinion in Electrochemistry*, 13:157–165, February 2019.
- [109] T. Gaumont, G. Maranzana, O. Lottin, J. Dillet, S. Didierjean, J. Pauchet, and L. Guétaz. Measurement of protonic resistance of catalyst layers as a tool for degradation monitoring. *International Journal of Hydrogen Energy*, 42(3):1800–1812, January 2017.
- [110] T. Gaumont, G. Maranzana, O. Lottin, J. Dillet, L. Guétaz, and J. Pauchet. In Operando and Local Estimation of the Effective Humidity of PEMFC Electrodes and Membranes. *Journal of The Electrochemical Society*, 164(14):F1535–F1542, 2017.
- [111] P. Zihrul, I. Hartung, S. Kirsch, G. Huebner, F. Hasché, and H. A. Gasteiger. Voltage Cycling Induced Losses in Electrochemically Active Surface Area and in H<sub>2</sub>/Air-Performance of PEM Fuel Cells. *Journal of The Electrochemical Society*, 163(6):F492–F498, 2016.
- [112] D. R. Baker, D. A. Caulk, K. C. Neyerlin, and M. W. Murphy. Measurement of Oxygen Transport Resistance in PEM Fuel Cells by Limiting Current Methods. *Journal of The Electrochemical Society*, 156(9):B991, 2009.
- [113] D. R. Baker and D. A. Caulk. Limiting Current as a Tool to Study Oxygen Transport in PEM Fuel Cells. *ECS Transactions*, 50(2):35–45, March 2013.
- [114] F. B. Spingler, A. Phillips, T. Schuler, M. C. Tucker, and A. Z. Weber. Investigating fuel-cell transport limitations using hydrogen limiting current. *International Journal of Hydrogen Energy*, 42(19):13960–13969, May 2017.
- [115] A. T. S. Freiberg, M. C. Tucker, and A. Z. Weber. Polarization loss correction derived from hydrogen local-resistance measurement in low Pt-loaded polymer-electrolyte fuel cells. *Electrochemistry Communications*, 79:14–17, June 2017.

- [116] T. Schuler, A. Chowdhury, A. T. Freiberg, B. Sneed, F. B. Spingler, M. C. Tucker, K. L. More, C. J. Radke, and A. Z. Weber. Fuel-cell catalyst-layer resistance via hydrogen limiting-current measurements. *Journal of The Electrochemical Society*, 166(7):F3020–F3031, 2019.
- [117] T. Reshetenko and A. A. Kulikovskiy. PEM fuel cell characterization by means of the physical model for impedance spectra. *Journal of The Electrochemical Society*, 162(7):F627, 2015.
- [118] T. Reshetenko and A. A. Kulikovskiy. A model for extraction of spatially resolved data from impedance spectrum of a PEM fuel cell. *Journal of The Electrochemical Society*, 165(5):F291–F296, 2018.
- [119] S. Cruz-Manzo and R. Chen. An electrical circuit for performance analysis of polymer electrolyte fuel cell stacks using electrochemical impedance spectroscopy. *Journal of The Electrochemical Society*, 160(10):F1109–F1115, 2013.
- [120] S. Cruz-Manzo and R. Chen. A generic electrical circuit for performance analysis of the fuel cell cathode catalyst layer through electrochemical impedance spectroscopy. *Journal of Electroanalytical Chemistry*, 694:45–55, April 2013.
- [121] J. J. Giner-Sanz, E. M. Ortega, and V. Pérez-Herranz. Mechanistic equivalent circuit modelling of a commercial polymer electrolyte membrane fuel cell. *Journal of Power Sources*, 379:328–337, March 2018.
- [122] M. Heinzmann, A. Weber, and E. Ivers-Tiffée. Impedance modelling of porous electrode structures in polymer electrolyte membrane fuel cells. *Journal of Power Sources*, 444:227279, December 2019.
- [123] M. Heinzmann and A. Weber. Impedance based performance model for polymer electrolyte membrane fuel cells. *Journal of Power Sources*, 558:232540, February 2023.
- [124] F. A. de Bruijn, V. A. T. Dam, and G. J. M. Janssen. Review: Durability and Degradation Issues of PEM Fuel Cell Components. *Fuel Cells*, 8(1):3–22, February 2008.
- [125] P. Ren, P. Pei, Y. Li, Z. Wu, D. Chen, and S. Huang. Degradation mechanisms of proton exchange membrane fuel cell under typical automotive operating conditions. *Progress in Energy and Combustion Science*, 80:100859, September 2020.
- [126] Y. Yu, H. Li, H. Wang, X.-Z. Yuan, G. Wang, and M. Pan. A review on performance degradation of proton exchange membrane fuel cells during startup and shutdown processes: Causes, consequences, and mitigation strategies. *Journal of Power Sources*, 205:10–23, May 2012.
- [127] D. Qiu, L. Peng, X. Lai, M. Ni, and W. Lehnert. Mechanical failure and mitigation strategies for the membrane in a proton exchange membrane fuel cell. *Renewable and Sustainable Energy Reviews*, 113:109289, October 2019.

- [128] J. Mitzel, Q. Zhang, P. Gazdzicki, and K. A. Friedrich. Review on mechanisms and recovery procedures for reversible performance losses in polymer electrolyte membrane fuel cells. *Journal of Power Sources*, 488:229375, March 2021.
- [129] Q. Zhang, C. Harms, J. Mitzel, P. Gazdzicki, and K. A. Friedrich. The challenges in reliable determination of degradation rates and lifetime in polymer electrolyte membrane fuel cells. *Current Opinion in Electrochemistry*, 31:100863, February 2022.
- [130] H. Wang, X.-Z. Yuan, and H. Li. *PEM Fuel Cell Diagnostic Tools*. CRC Press, August 2011.
- [131] T. Biegler, D. A. J. Rand, and R. Woods. Limiting oxygen coverage on platinumized platinum; relevance to determination of real platinum area by hydrogen adsorption. *Journal of Electroanalytical Chemistry and Interfacial Electrochemistry*, 29(2):269–277, 1971.
- [132] W. Li and A. M. Lane. Resolving the HUPD and HOPD by DEMS to determine the ECSA of Pt electrodes in PEM fuel cells. *Electrochemistry Communications*, 13(9):913–916, September 2011.
- [133] D. A. Caulk and D. R. Baker. Heat and Water Transport in Hydrophobic Diffusion Media of PEM Fuel Cells. *Journal of The Electrochemical Society*, 157(8):B1237, 2010.
- [134] M. Göbel, S. Kirsch, L. Schwarze, L. Schmidt, H. Scholz, J. Haumann, M. Klages, J. Scholta, H. Markötter, S. Alrwashdeh, I. Manke, and B. R. Müller. Transient limiting current measurements for characterization of gas diffusion layers. *Journal of Power Sources*, 402:237–245, October 2018.
- [135] O. E. Herrera, D. P. Wilkinson, and W. Mérida. Anode and cathode overpotentials and temperature profiles in a PEMFC. *Journal of Power Sources*, 198:132–142, January 2012.
- [136] A. Leonide. *SOFC modelling and parameter identification by means of impedance spectroscopy*. PhD thesis, Karlsruher Institut für Technologie, KIT Scientific Publishing, Karlsruhe, 2010.
- [137] B. A. Boukamp. A linear Kronig-Kramers transform test for immittance data validation. *Journal of the electrochemical society*, 142(6):1885–1894, 1995.
- [138] M. Schönleber, D. Klotz, and E. Ivers-Tiffée. A Method for Improving the Robustness of linear Kramers-Kronig Validity Tests. *Electrochimica Acta*, 131:20–27, June 2014.
- [139] Ting Hei Wan, Mattia Saccoccio, Chi Chen, and Francesco Ciucci. Influence of the Discretization Methods on the Distribution of Relaxation Times Deconvolution: Implementing Radial Basis Functions with DRTtools. *Electrochimica Acta*, 184:483–499, December 2015.

- [140] G. S. Harzer, J. N. Schwämmlein, A. M. Damjanović, S. Ghosh, and H. A. Gasteiger. Cathode Loading Impact on Voltage Cycling Induced PEMFC Degradation: A Voltage Loss Analysis. *Journal of The Electrochemical Society*, 165(6):F3118–F3131, 2018.
- [141] R. Vetter and J. O. Schumacher. Experimental parameter uncertainty in proton exchange membrane fuel cell modeling. Part I: Scatter in material parameterization. *Journal of Power Sources*, 438:227018, October 2019.
- [142] R. Vetter and J. O. Schumacher. Experimental parameter uncertainty in proton exchange membrane fuel cell modeling. Part II: Sensitivity analysis and importance ranking. *Journal of Power Sources*, 439:126529, November 2019.
- [143] A. A. Kulikovskiy. *Analytical Models for PEM Fuel Cell Impedance*. Self-publishing, Eisma, 2018.



# A Supplementary Material

## A.1 Supplementary Information Publication I

Supplementary material for:  
Full factorial in-situ characterization of ionomer properties in  
differential PEM fuel cells

Christophe Gerling<sup>1,2</sup>, Matthias Hanauer<sup>1</sup>, Ulrich Berner<sup>1</sup>,  
and K. Andreas Friedrich<sup>2,3</sup>

<sup>1</sup> Robert Bosch GmbH, Corporate Research, Robert-Bosch-Campus 1, Renningen 71272, Germany

<sup>2</sup> Institute for Building Energetics, Thermotechnology and Energy Storage (IGTE), University of  
Stuttgart, Pfaffenwaldring 6, Stuttgart 70569, Germany

<sup>3</sup> Institute of Engineering Thermodynamics, German Aerospace Center (DLR), Pfaffenwaldring 38-40,  
Stuttgart 70569, Germany

E-mail: christophe.gerling@de.bosch.com

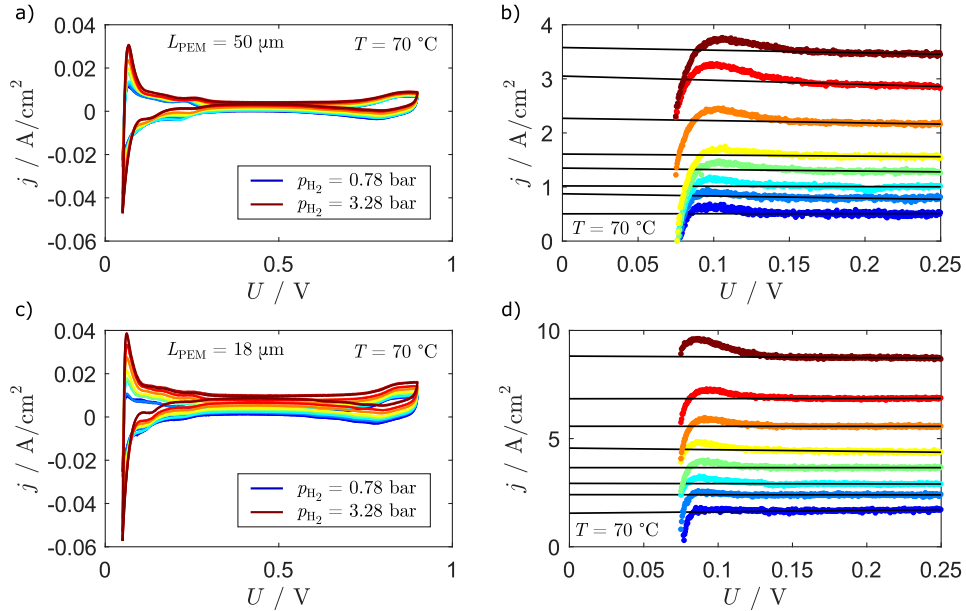


**Figure S1:** CV and LSV measurements used to determine  $j_{\text{crossover}} = f(p_{H_2, \text{anode}})$  shown in Figure 4a. a) and b) are the measurements from the MEA with 50 μm PEM thickness and c) and d) are the measurements from the MEA with 18 μm PEM thickness.

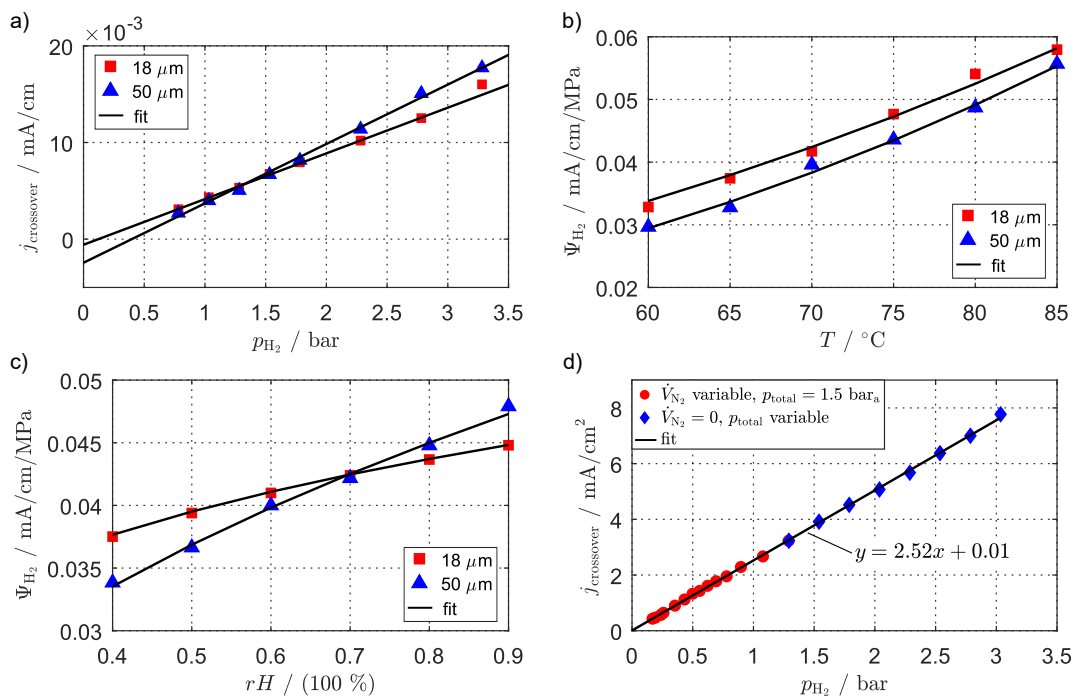


**Figure S2:** a) to c) Thickness-normalized values of Figure 4a, Figure 4c and Figure 4d respectively. d) Plot of the reproduction of the measurement  $j_{\text{crossover}} = f(p_{\text{H}_2, \text{anode}})$ . The data were acquired at  $rH = 70 \%$  and  $T = 70 ^\circ\text{C}$  as described in the experimental section of the paper.

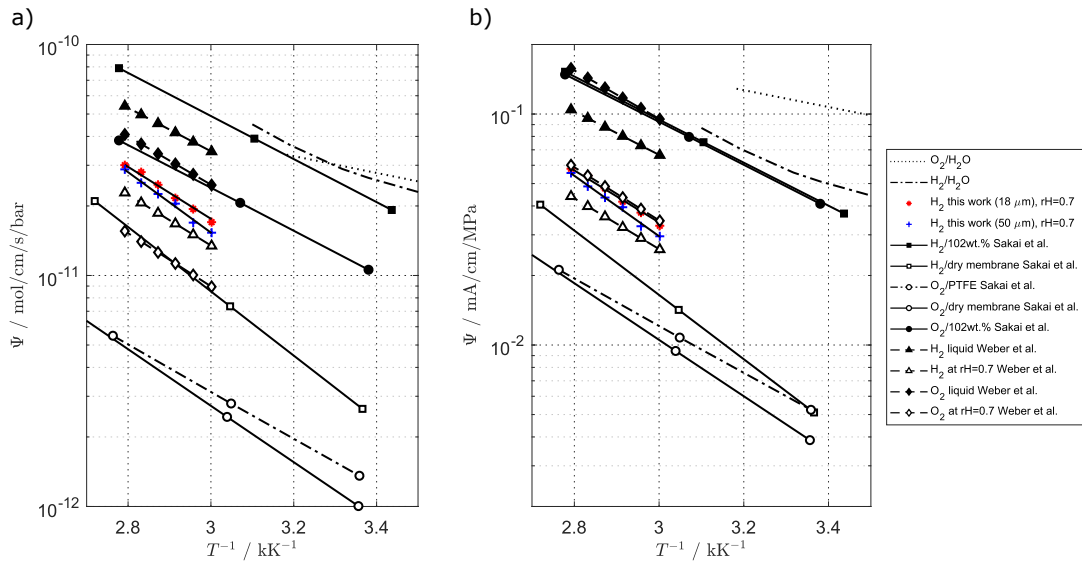


**Figure S3:** Measured permeation coefficients (in-house) for  $\text{H}_2$  at  $rH = 70\%$  over  $T$  of this work, compared with measured permeation coefficients of Sakai et al. [1, 2] for Nafion<sup>®</sup> N117 and fitted models of Weber et al. [3]. a) Values as chemical fluxes. b) Values as electrochemical fluxes corresponding to the values of a) that were converted into electrochemical quantities by Faraday's law ( $2F$  for  $\text{H}_2$  and  $4F$  for  $\text{O}_2$ ). In b), the  $\text{H}_2$  and  $\text{O}_2$  values for Nafion<sup>®</sup> correspond well, showing that the molar flux of Oxygen is approximately half the flux of hydrogen.

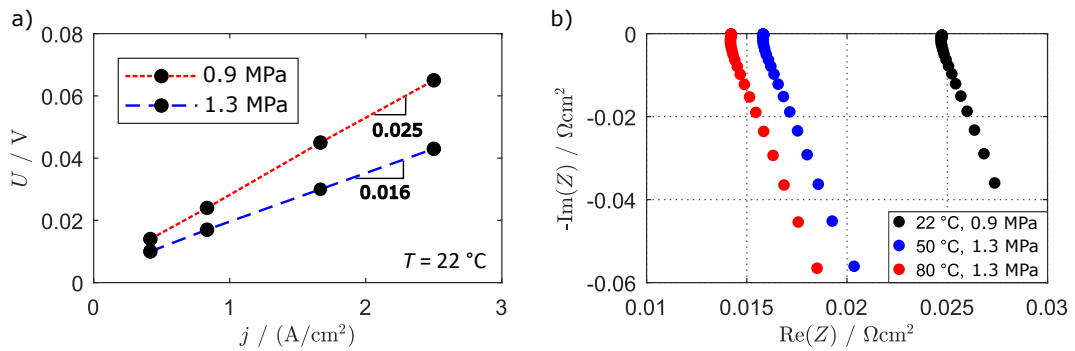


**Figure S4:** Approximation of the contact and bulk resistances of the setup for getting  $R_{\text{PEM}}$  out of  $R_0$  (also called  $R_\Omega$ ) by characterizing the system (anode flow field|anode GDL+MPL|cathode MPL+GDL|cathode flow field). a) Potential drop measurement over the current density for two clamping pressures at ambient temperature. b) Impedance measurements for different temperatures and clamping pressures.

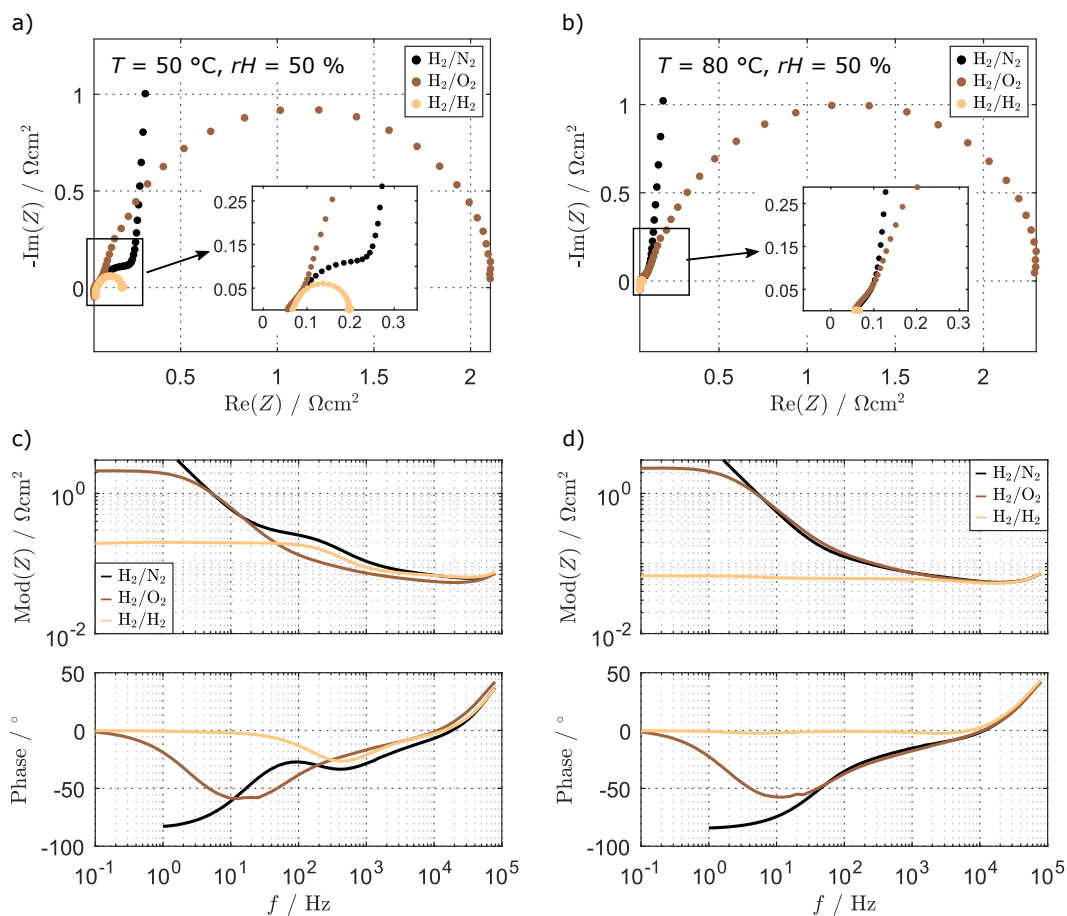


**Figure S5:** Comparison of  $\text{H}_2/\text{N}_2$ ,  $\text{H}_2/\text{H}_2$  ("proton pump" mode at OCV) and  $\text{H}_2/\text{O}_2$  ( $j = 20 \text{ mA}/\text{cm}^2$ ) EIS at  $T = 50^\circ\text{C}$  and  $T = 80^\circ\text{C}$ . a) and b) show the Nyquist representations and c) and d) the associated Bode plots. This shows that there is a process in the  $\text{H}_2/\text{N}_2$  and  $\text{H}_2/\text{H}_2$  modes with a high activation energy (pronounced at cold conditions and low at high temperatures) that seems to be absent in the  $\text{H}_2/\text{O}_2$  mode. This process has to be taken into account when fitting  $R_p$  from the  $\text{H}_2/\text{N}_2$  EIS data.

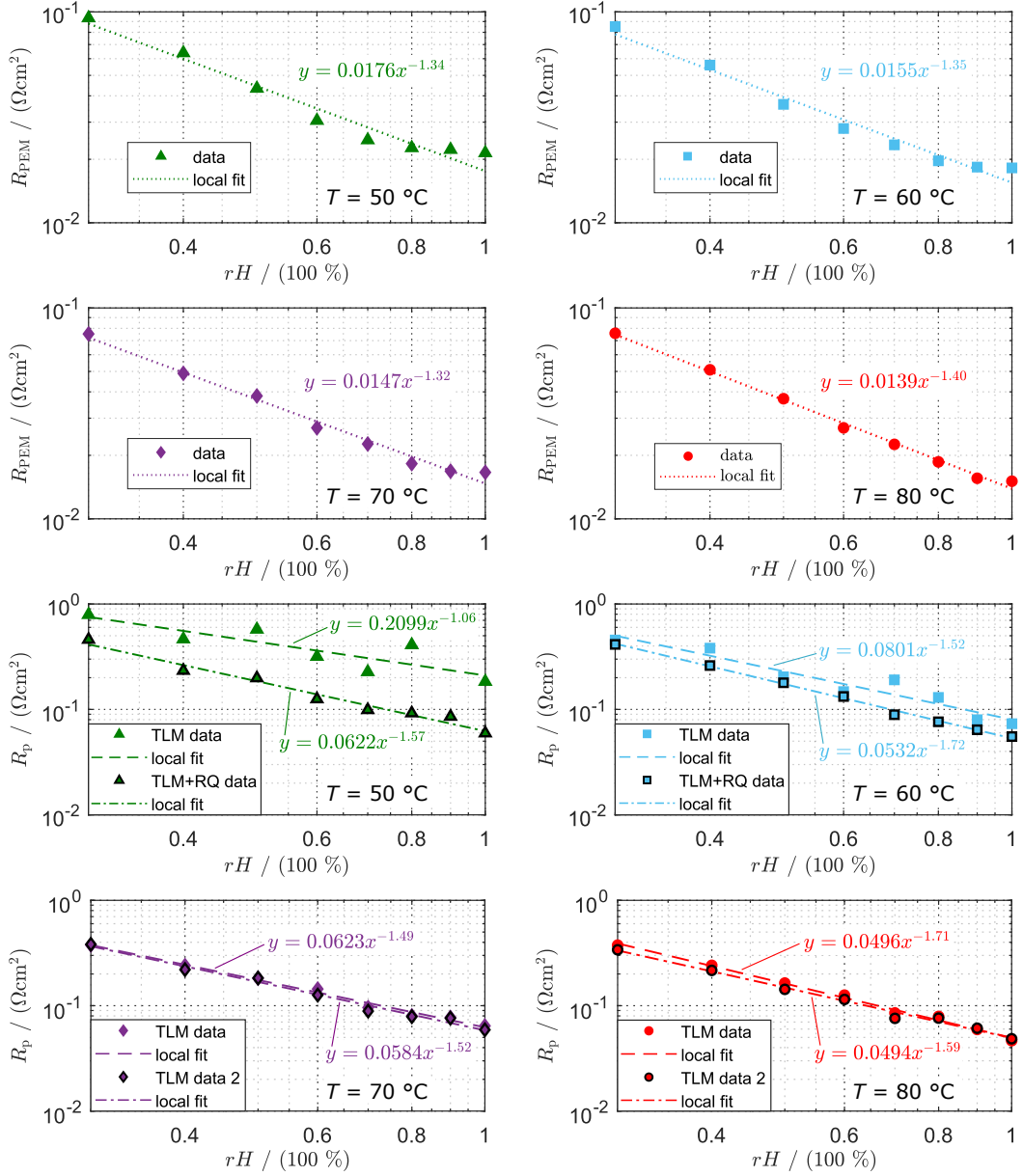


**Figure S6:** Detailed view of  $R_{PEM}$  and  $R_p$  and their local fits to semi-empirical power laws. The values are listed in Table 1. In all four  $R_p$  plots, "TLM data" represent the initial fitting results to the "blocking" TLM. The "TLM+RQ data" and "TLM data 2" represent the values obtained from individual fits with initial guesses taken from the global fit to all the spectra simultaneously as described in the results section of the paper. At low temperatures ( $T = 50 \text{ }^\circ\text{C}$  and  $T = 60 \text{ }^\circ\text{C}$ ), the RQ-element served to fit the additional process.

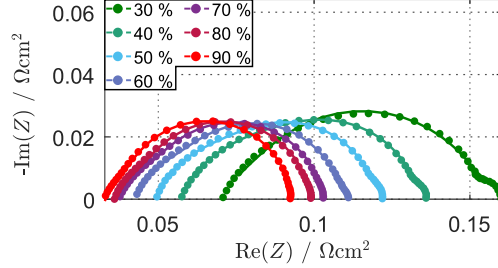


**Figure S7:** EIS spectra of an  $rH$  variation under load at  $j = 1 \text{ A/cm}^2$ ,  $T = 80 \text{ }^\circ\text{C}$  and  $p_{\text{total}} = 1.5 \text{ bar}_a$  ( $V_{\text{H}_2} = 1300 \text{ sccm}$ ,  $V_{\text{O}_2} = 2000 \text{ sccm}$ ). Both the measured data (dots) and the individual fits (solid lines) are shown. Here, the low-frequency shoulders were fitted with a Warburg term placed in series with our TLM model, but they were discarded from the discussions in the results part of the paper.

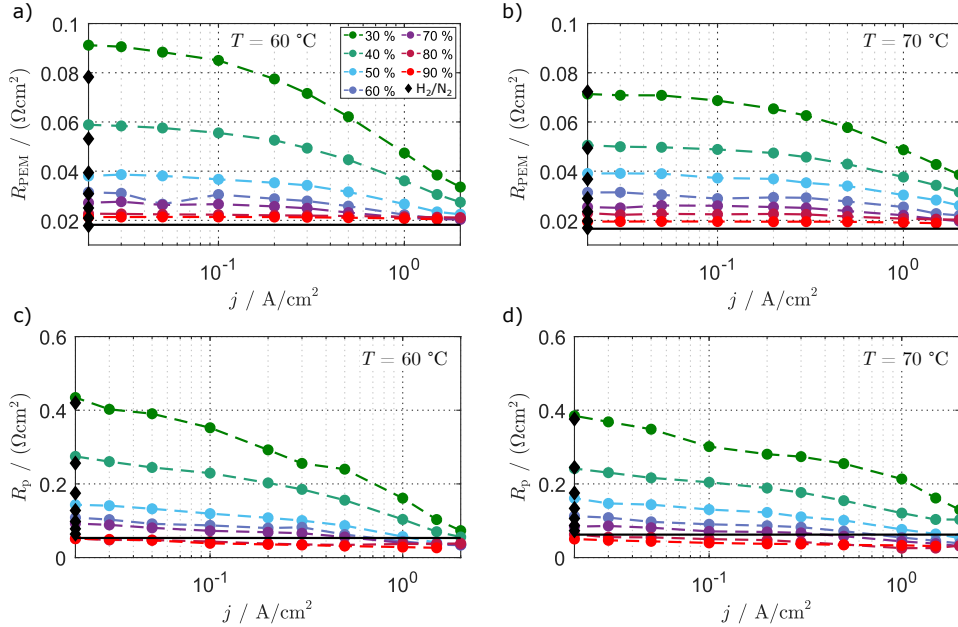


**Figure S8:** Representation of the ionomer resistances  $R_{\text{PEM}}$  and  $R_p$  obtained under load for several gas stream humidities ( $rH = 30\%$  to  $rH = 90\%$ ). The values have been obtained by fitting EIS spectra under load to the ECM shown in Figure 8a. For  $R_{\text{PEM}}$ , we subtracted the  $15 \text{ m}\Omega\text{cm}^2$  caused by contact and bulk resistances of the setup like in our  $\text{H}_2/\text{N}_2$  study. The black diamonds represent the resistances from the  $\text{H}_2/\text{N}_2$  operation and the black solid lines the  $rH = 100\%$  conditions. a) Shows the membrane resistances at  $T = 60 \text{ }^\circ\text{C}$ , b) the membrane resistances at  $T = 70 \text{ }^\circ\text{C}$ , c) the CCL proton resistance at  $T = 60 \text{ }^\circ\text{C}$  and d) the CCL proton resistance at  $T = 70 \text{ }^\circ\text{C}$ .

## References

- [1] Tetsuo Sakai, Hiroyasu Takenaka, Noboru Wakabayashi, Yoji Kawami, and Eiichi Torikai. Gas permeation properties of solid polymer electrolyte (SPE) membranes. *Journal of the Electrochemical society*, 132(6):1328, 1985.
- [2] Tetsuo Sakai, Hiroyasu Takenaka, and Eiichi Torikai. Gas diffusion in the dried and hydrated Nafions. *Journal of the Electrochemical society*, 133(1):88, 1986.
- [3] Adam Z. Weber and John Newman. Transport in Polymer-Electrolyte Membranes. *Journal of The Electrochemical Society*, 151(2):A311, 2004.



## A.2 Supplementary Information Publication II

### Supplementary material for: PEM single cells under differential conditions: full factorial parameterization of the ORR and HOR kinetics and loss analysis

Christophe Gerling<sup>1,2</sup>, Matthias Hanauer<sup>1</sup>, Ulrich Berner<sup>1</sup>,  
and K. Andreas Friedrich<sup>2,3</sup>

<sup>1</sup> Robert Bosch GmbH, Corporate Research, Robert-Bosch-Campus 1, Renningen 71272, Germany

<sup>2</sup> Institute for Building Energetics, Thermotechnology and Energy Storage (IGTE), University of Stuttgart, Pfaffenwaldring 6, Stuttgart 70569, Germany

<sup>3</sup> Institute of Engineering Thermodynamics, German Aerospace Center (DLR), Pfaffenwaldring 38-40, Stuttgart 70569, Germany

E-mail: christophe.gerling@de.bosch.com

#### Experimental: materials, techniques and measurement quality

##### Materials

Figure S1 shows typical cyclic voltammograms of the cathode and anode electrode of the 12 cm<sup>2</sup> Gore<sup>®</sup> PRIMEA<sup>®</sup> MEAs (W.L. Gore & Associates, Elkton, MD, USA) we used in this work (CVs are the same as in Fig 2 in the body of this work). The platinum loadings are of 0.4 mg<sub>Pt</sub>/cm<sup>2</sup> in the cathode and 0.05 mg<sub>Pt</sub>/cm<sup>2</sup> in the anode.

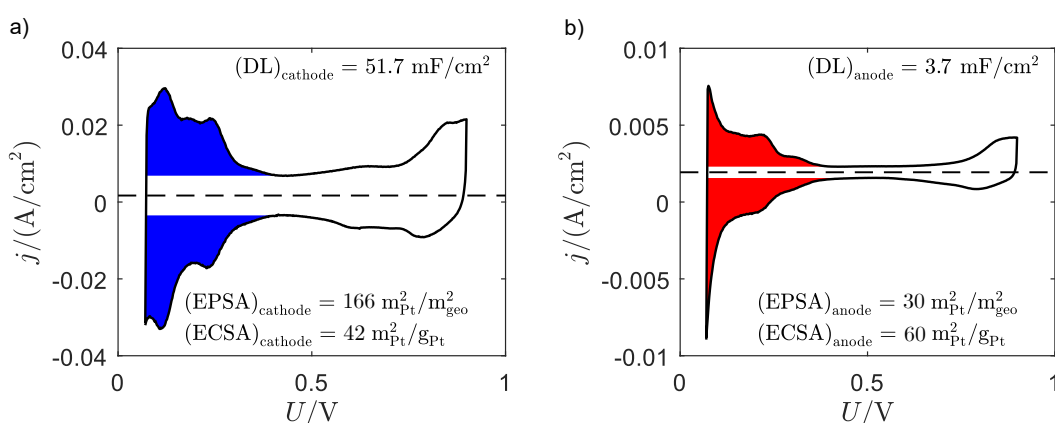


**Figure S1:** a) CV of the cathode and b) on the anode side. The conditions were  $rH = 100\%$ ,  $T = 40\text{ }^\circ\text{C}$  and  $p_{\text{total}} = 1.0\text{ bar}_a$ , recorded with a sweep rate of 100 mV/s from 70 mV to 900 mV.



## EIS and DRT

Figures S2a and S2b show some typical EIS spectra and their according DRTs, which are in accordance with previous literature results [1] since four or five peaks are visible in the  $\text{H}_2/\text{O}_2$  configuration depending on the operating conditions. From the lowest frequency peak P1 to the highest frequency peak P5 we have: oxygen mass transport (P1), ORR kinetics (P2) and proton transport in the catalyst layer (P3 to P5). Of course, if the time constants of the processes are very close or even completely overlapping, this DRT technique is also limited. However, it can be very helpful to get a better understanding of the influence of parameter changes. The low-frequency inductive features were discarded in this study, though they will be the main focus of our next publication. Figures S2c and S2d show the variation of the regularization parameter  $\lambda$  for two current densities. Setting  $\lambda$  too low leads to non-deconvoluted processes, whereas a too high  $\lambda$  can lead to misinterpretation due to erroneous peaks coming from the measurement noise [1]. For our analyses we chose  $\lambda = 1 \cdot 10^{-5}$ .

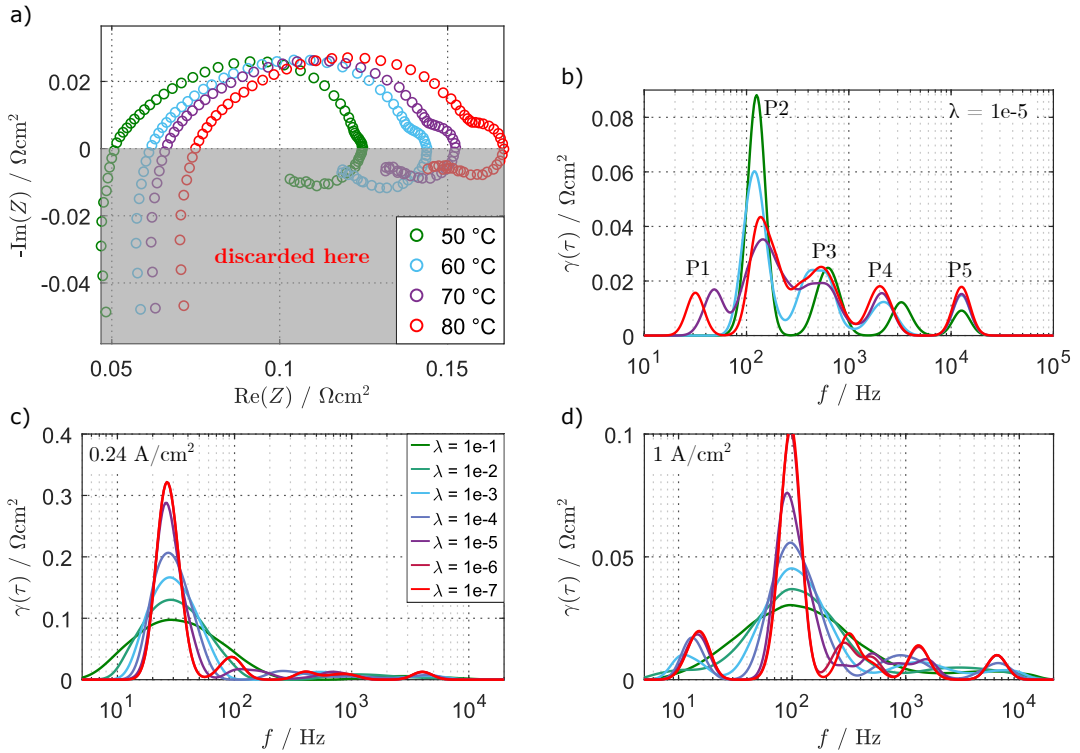


**Figure S2:** a) EIS and b) according DRT of the capacitive part for a  $T$ -variation with pure  $\text{O}_2$  at  $rH = 30 \%$  and  $j = 1 \text{ A/cm}^2$ . c) Variation of the regularization parameter  $\lambda$  at  $j = 0.25 \text{ A/cm}^2$  and d)  $j = 1 \text{ A/cm}^2$ . The measurements in c) and d) were made in a  $25 \text{ cm}^2$  differential cell with pure  $\text{O}_2$  at  $rH = 70 \%$  and  $T = 80 \text{ }^\circ\text{C}$ .

### Measurement quality and degradation tracking

To make sure that our samples did not degrade during the measurements, we built in several CV measurements between the different relative humidity levels of our main DOE in fuel cell mode. These CVs were recorded as described in the experimental subsection of this publication, but at ambient pressure conditions ( $p_{\text{total}} \approx 1 \text{ bar}_a$ ), fully saturated gas ( $rH = 100 \%$ ) and  $T = 40 \text{ }^\circ\text{C}$ . The according diagrams are shown in Fig S3a, where it is apparent that there is no degradation of the cathode catalyst layer as all the CVs almost perfectly overlap. Figure S3b shows the detailed evaluation of the ECSA ( $= r f_{\text{cathode}}/\text{Pt loading}$ ) along our experiments based on the integration of the hydrogen adsorption and desorption peaks. The active surface area remains almost constant, only exhibiting a slight increase at the beginning (performance was stable). Figure S3c shows that the double layer capacity and the hydrogen crossover also stayed approximately constant, proving that there was neither significant electrode nor membrane degradation (thinning or pinholes). Additionally, we repeated some measurements (mainly the  $rH = 80 \%$  condition) several times on different samples to make sure that our polarization curves and EIS are reproducible, which was the case for the current density range we are interested in ( $j \leq 2 \text{ A/cm}^2$ ). Above  $2 \text{ A/cm}^2$  and depending on the operating parameters we observed some discrepancies that may have different origins: mass transport issues due to variations in the GDL samples or their alignment, or water transport hysteresis effects that are strongly dependent on the sample history. We show some EIS reproduction measurements (4 measurements on 3 samples) in Figs S3e and S3f, where the lines are the average curves and the error bars represent the minimal and maximal values of the 4 measurements. The spread is the largest for the highest current density and the lowest oxygen concentration at low frequencies (in the mass transport dominated part), indicating that the above assumption is correct. Furthermore, apart from our limiting current measurements, all the other measurements were at least conducted twice and CVs were conducted before and after each test to track the state-of-health of our samples and to ensure high data quality.

Finally, it is worth mentioning that all our EIS spectra passed the linear Kramers-Kronig test according to Boukamp [2] as implemented by Schönleber et al. [3] to ensure linearity, causality and time-invariance of our data. If these requirements are met by the EIS data, the real part of the impedance and the imaginary part are linked by the following relations:

$$Z_{\text{Re}}(\omega) = \frac{2}{\pi} \cdot \int_0^\infty \frac{\omega' \cdot Z_{\text{Im}}(\omega')}{\omega^2 - \omega'^2} d\omega' \quad (1)$$

$$Z_{\text{Im}}(\omega) = \frac{-2}{\pi} \cdot \int_0^\infty \frac{\omega \cdot Z_{\text{Re}}(\omega')}{\omega^2 - \omega'^2} d\omega' \quad (2)$$

The major criteria to evaluate the quality of the EIS data is then given by the residuals of the Kramers-Kronig test. The residuals obtained from the linear K-K test for our test run under load (over 1400 spectra) are shown in Fig S3d and were calculated by

$$\Delta_{\text{Re}}(\omega) = \frac{Z_{\text{Re,meas}}(\omega) - Z_{\text{Re,model}}(\omega)}{|Z(\omega)|} \quad (3)$$

$$\Delta_{\text{Im}}(\omega) = \frac{Z_{\text{Im,meas}}(\omega) - Z_{\text{Im,model}}(\omega)}{|Z(\omega)|} \quad (4)$$

for the real part and for the imaginary part, respectively.

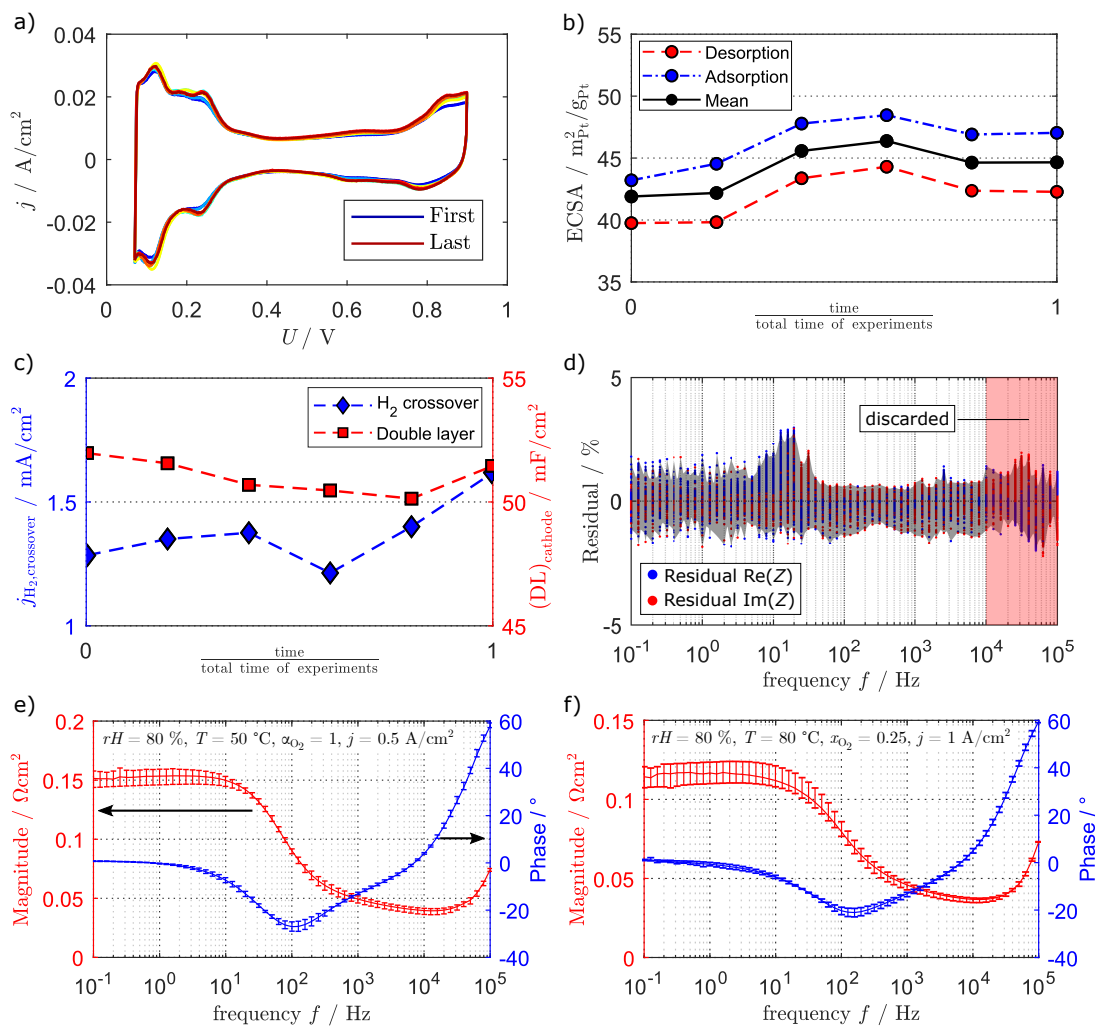


**Figure S3:** a) CV of the cathode in course of our H<sub>2</sub>/O<sub>2</sub> DOE at  $rH = 100\%$ ,  $T = 40\text{ }^\circ\text{C}$  and  $p_{\text{total}} = 1\text{ bar}_a$ , recorded with a sweep rate of  $100\text{ mV/s}$  from  $70\text{ mV}$  to  $900\text{ mV}$ . b) ECSA, c) H<sub>2</sub> crossover and double layer capacity extracted from the CV measurements in a). d) Kramers-Kronig residuals calculated for all our H<sub>2</sub>/O<sub>2</sub> EIS spectra. e) and f) Bode plots of H<sub>2</sub>/O<sub>2</sub> EIS for two conditions. The error bars represent the maximal deviations of the four spectra from the average spectrum.

### Ionomer properties: hydrogen crossover and proton conductivities

In our previous work, we focused on characterizing both the ionomer conductivities and the permeation properties in situ on a real cell setup in a full factorial manner for the operating conditions (relative humidity  $rH$ , temperature  $T$  and current density  $j$ ) [4]. We validated the voltammetry techniques cyclic voltammetry and linear sweep voltammetry (LSV) techniques against online gas analysis and then primarily used CV to parameterize  $H_2$  permeation depending on the relative humidity and temperature as

$$\Psi_{H_2} = \left( 21.33 \frac{\text{A}}{\text{cm}^2 \text{MPa}} \right) (rH)^{0.20} \exp \left( -\frac{18.9 \text{ kJ/mol}}{RT} \right) \quad (5)$$

This expression can directly be implemented in a physical model and can be used to correct our polarization curves and other measurements for the current shift. The crossover currents for the case of  $p_{\text{total}} = 1.5 \text{ bar}_a$  are shown in Fig S4d for a grid of conditions defined by four temperatures and seven humidities. Even though the crossover changes during operation under load (decreasing  $p_{H_2}$  within the ACL due to  $H_2$  consumption and changing membrane hydration due to product water), we do not take this effect into account. At small currents, where the shift in the current affects mainly the fitting of the ORR exchange current density and its Tafel slope, we consider that the constant crossover value is accurate enough for our purposes.

Then, we parameterized the membrane and cathode catalyst layer protonic resistances by fitting a transmission line model (TLM) containing constant phase elements (CPE) instead of ideal capacities to our  $H_2/N_2$  EIS. The expression of this model is  $Z(\omega) = \sqrt{R_p}/(Q(i\omega)^n) \coth \sqrt{R_p} Q(i\omega)^n$ . The CPEs were needed since the low frequency part of the spectra deviates increasingly from the ideal behavior with decreasing humidity (non-homogeneous distribution effects). Based on this, we calibrated the following model for  $R_p$ :

$$R_p = (2.20 \text{ m}\Omega\text{cm}^2)(rH)^{-1.53} \exp \left( \frac{9.4 \text{ kJ/mol}}{RT} \right) \quad (6)$$

To parameterize  $R_{\text{PEM}}$  we took the high frequency resistance  $R_0 = R_\Omega$  and subtracted  $15 \text{ m}\Omega\text{cm}^2$  that are due to the electronic resistance (bulk conductivity and contact resistance) of the GDLs and the setup. Based on this we got

$$R_{\text{PEM}} = (1.20 \text{ m}\Omega\text{cm}^2)(rH)^{-1.44} \exp \left( \frac{7.0 \text{ kJ/mol}}{RT} \right) \quad (7)$$

These parameterizations are represented in Figs S4a to S4c along with the measurements (black dots) and one can see that the global models match the datasets well. Through EIS measurements under load ( $H_2/O_2$ ), we also investigated the change in the ionomer resistances in operation due to reaction water. Especially under cold and/or dry conditions this effect is very important and implies that a subtraction of the proton resistances from the performance based on the  $H_2/N_2$  resistances is generally not sufficient. Therefore, all the  $j \cdot (R_\Omega + R_p^{\text{eff}})$ -free results shown in this paper are based on the effective protonic resistance  $R_p^{\text{eff}}$  under load obtained after fitting the according EIS spectra to the TLM model described in our previous publication [4]. The EIS of two  $rH$ -variations under load (one at low and one at high current) are shown exemplarily in Fig S5.

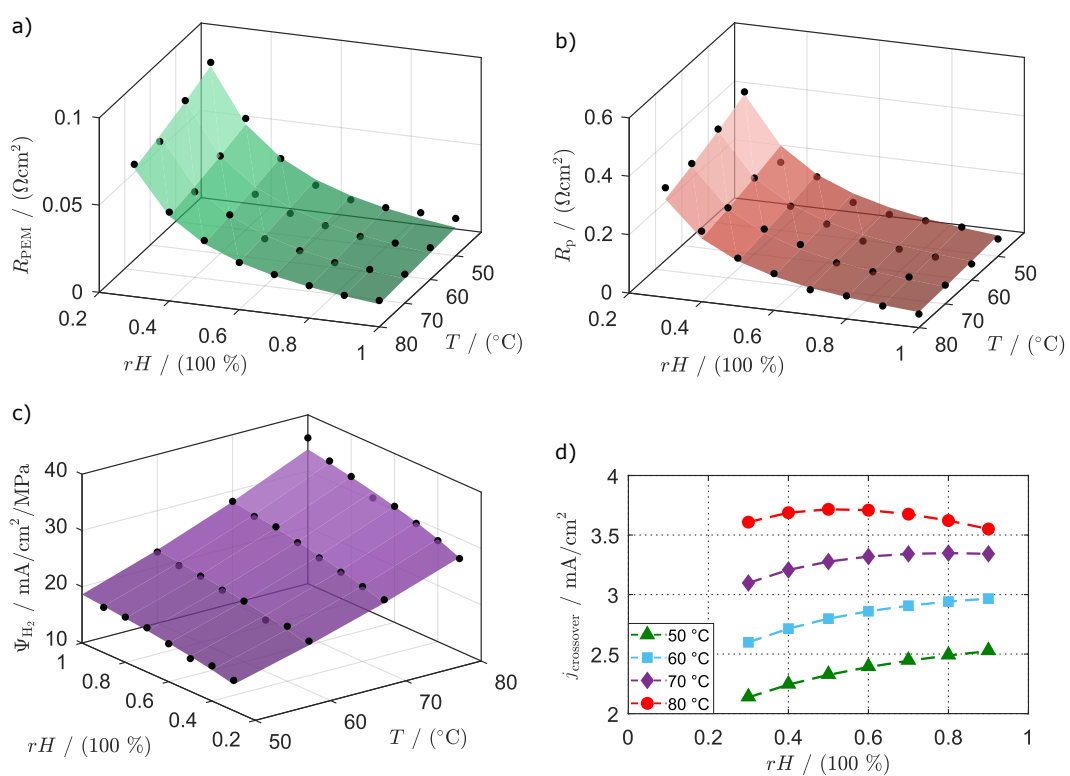


**Figure S4:** a) Membrane resistance calculated by  $R_{PEM} = R_{\Omega} - 15 \text{ m}\Omega\text{cm}^2$  over  $rH$  and  $T$  (black dots) from EIS and globally fitted model (surface). b) CCL proton resistance  $R_p$  over  $rH$  and  $T$  (black dots) from EIS and globally fitted model (surface). c) Measured permeation coefficient over  $rH$  and  $T$  (black dots) from CV measurements and globally fitted Arrhenius-like model (surface). d) Hydrogen crossover values calculated for correcting performance data based on our parameterization of the permeation coefficient. The values are calculated for  $p_{\text{total}} = 1.5 \text{ bar}_a$  and  $x_{\text{H}_2}^{\text{dry}} = 1$ . All the plots show values obtained for our 18  $\mu\text{m}$ -thick membrane.

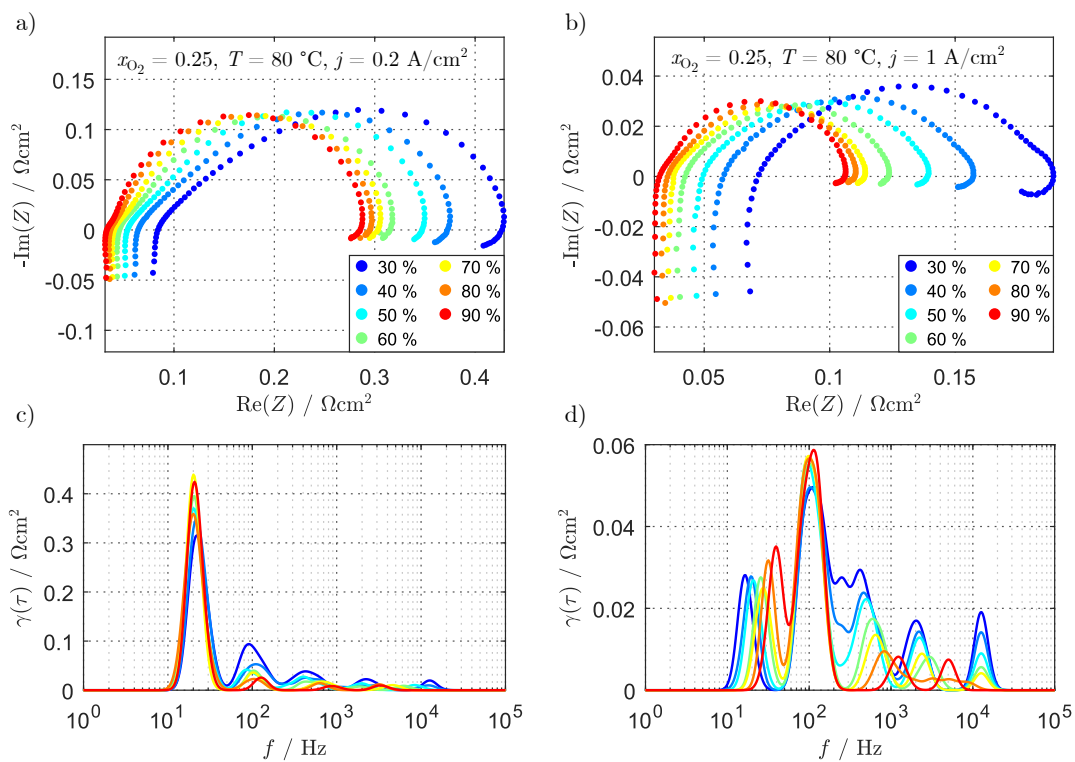


**Figure S5:** EIS spectra and according DRTs in  $\text{H}_2/\text{O}_2$  mode recorded under load at  $j = 0.2 \text{ A/cm}^2$  (a and c) and  $j = 1 \text{ A/cm}^2$  (b and d) for  $rH$  between 30 % and 90 %. All the spectra were recorded at  $p_{\text{total}} = 1.5 \text{ bar}_a$ ,  $T = 80^\circ\text{C}$  and  $x_{\text{O}_2} = 0.25$  according to the description in the experimental part.

**Anode characterization in H<sub>2</sub>/H<sub>2</sub> mode: effect of CO poisoning**

*Preliminary remarks:* The results presented in this section originate from test runs which were subject to CO poisoning in course of very long stabilization times. The parameter dependencies are interesting to investigate nonetheless. This dataset also enabled us to understand the influence of catalyst poisoning on the performance signatures better and, therefore, to derive a CO recovery step of the anode and cathode electrodes simultaneously that is useful for characterization in oxygen-free conditions.

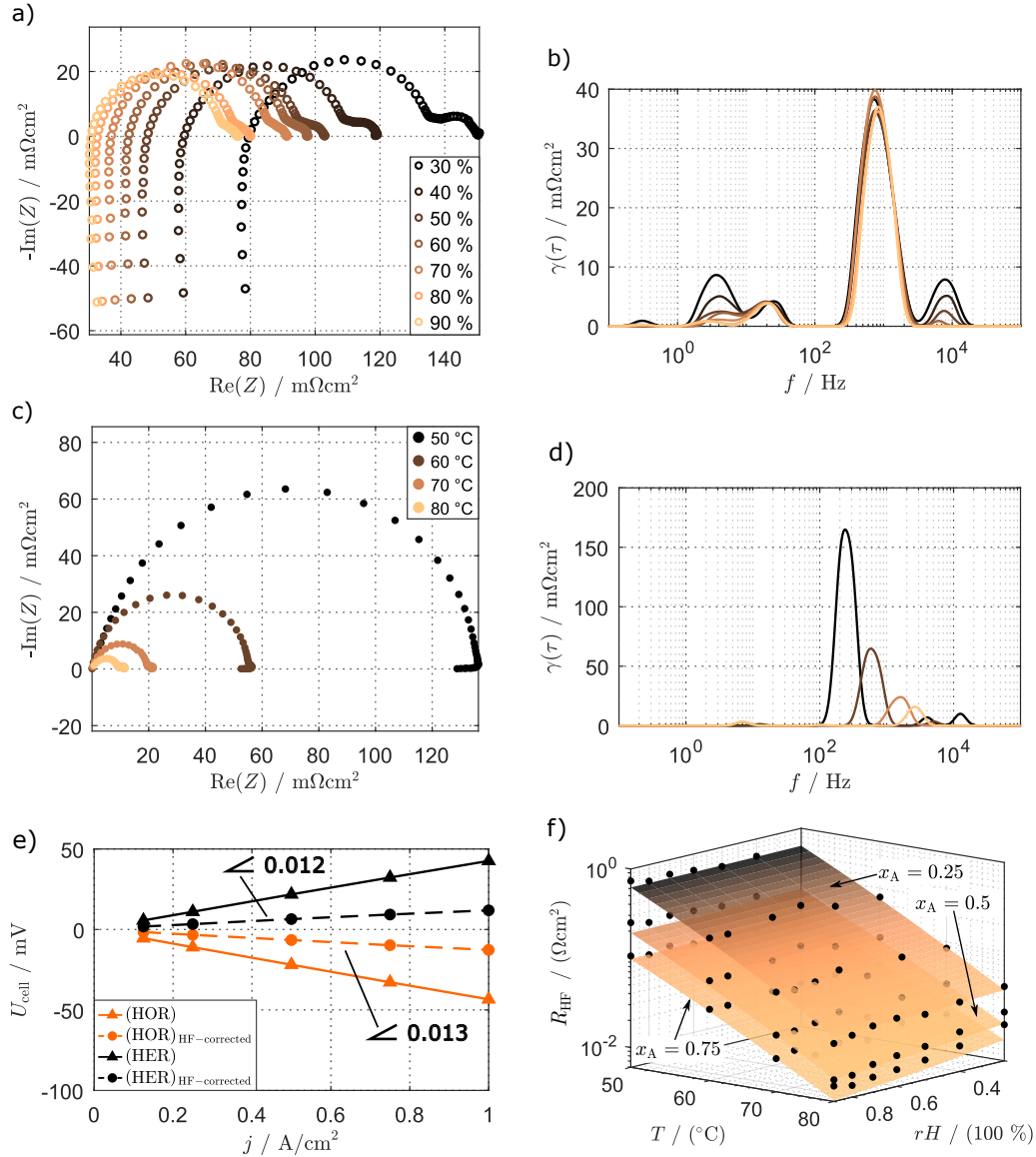
First, the fact that the proton pump showed such bizarre behavior (high activation energy and partial pressure dependency) only when using long stabilization times ( $> 2$  h) prior to the measurements potentially could hint at different effects: CL poisoning [5] only occurring in H<sub>2</sub>/N<sub>2</sub> or H<sub>2</sub>/H<sub>2</sub> configuration due to the absence of O<sub>2</sub> crossover which is helpful to oxidize the parasitic CO in the anode [6]; or a slow change in the ionomer behavior caused by an activation/deactivation process in the presence/absence of current [7]. When operating the cell under load, a stable performance was not obtained and the shape of the EIS was changed reversibly, with the HF loop changing its size and a relaxing back to the original state at low frequencies. Degradation mechanisms of the CLs could be excluded since the  $rf$  and  $j_{\text{H}_2, \text{crossover}}$  did not change along the experiments and the performance in H<sub>2</sub>/O<sub>2</sub> was not altered.

Then, the multiple CVs we carried out in between the H<sub>2</sub>/H<sub>2</sub> measurements at different operating conditions showed an additional peak between 0.6 V and 0.9 V and thus allowed us to confirm the hypothesis of adsorbed CO that poisons the CL surface by blocking the active sites. The fact that CO poisoning is strongly temperature dependent [8] could explain the activation energy (high resistance at low temperatures) we measured. Also, the influence of time and CO concentration on the hydrogen kinetics in Pt electrodes and in PEM fuel cells (steady-state performance and EIS response) was widely studied in the literature and was in accordance with our observations [5, 8–11]. Since the anode loading is lower than the cathode loading, the effect of poisoning was worse on the anode side in our experiments. Furthermore, we only carried out CVs on the cathode side during our test runs (which regularly oxidized the CO), meaning that CO accumulated in the anode over time and was never oxidized. Thus, we had an explanation of the high  $E_{\text{act}}$  and the high  $p_{\text{H}_2}$  dependency of the kinetics loop.

The parameter variations in Figs S6 and S7 complete our analysis presented in the main part of this paper. Figures S6a to S6b represent the EIS and DRT for a  $rH$  variation with a low  $p_{\text{H}_2, \text{anode}}$  and confirms, as discussed in the main part, that the HF loop effectively contains two processes: proton transport within the CLs and HOR/HER kinetics, with only the proton transport being  $rH$ -dependent. Figures S6c and S6d show the EIS and DRT of a temperature variation with pure H<sub>2</sub> on both sides and point out the unexpectedly high activation energy caused by the CO poisoning effect. In Fig S6e, the polarization curves at  $T = 80$  °C are perfectly linear and show resistances that are not unusual for the proton pumping mode despite the fact that both electrodes were blocked by CO. To emphasize this effect we show a parameterization of the HF loop of the EIS depending on  $rH$ ,  $T$  and  $p_{\text{H}_2, \text{anode}}$  for the poisoned electrodes in Fig S6f and the expression of  $R_{\text{HF}}$  that was obtained is

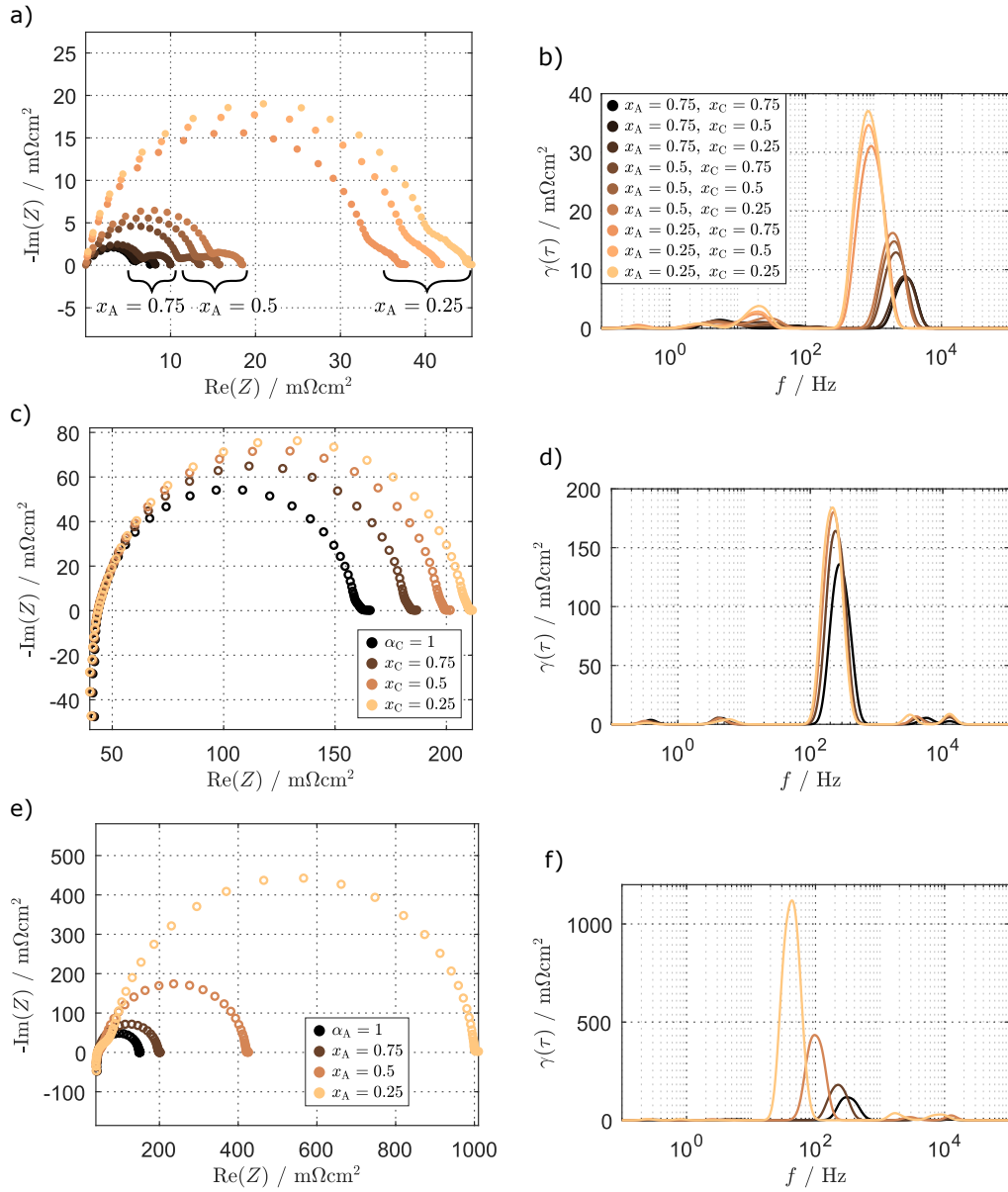
$$R_{\text{HF}} = (4.36 \cdot 10^{-14} \text{ m}\Omega\text{cm}^2) \left( \frac{p_{\text{H}_2}}{p_{\text{ref}}} \right)^{-1.60} \exp \left( \frac{95 \text{ kJ/mol}}{RT} \right) \quad (8)$$

In Fig S7a we show a hydrogen partial pressure variation for both sides and in Fig S7b the according DRT. There, one can observe that both processes seem to be partial pressure dependent, even though the high-frequency process shows a higher dependency than the low-frequency process. The very high influence of the partial pressure on the anode side confirms that the anode contribution dominates the impedance, which is not surprising considering the loadings (see above). Figures S7c to S7d depict partial pressure variations on the cathode side and Figs S7e to S7f on the anode side (Figs S7e and S7f) for  $T = 50$  °C.

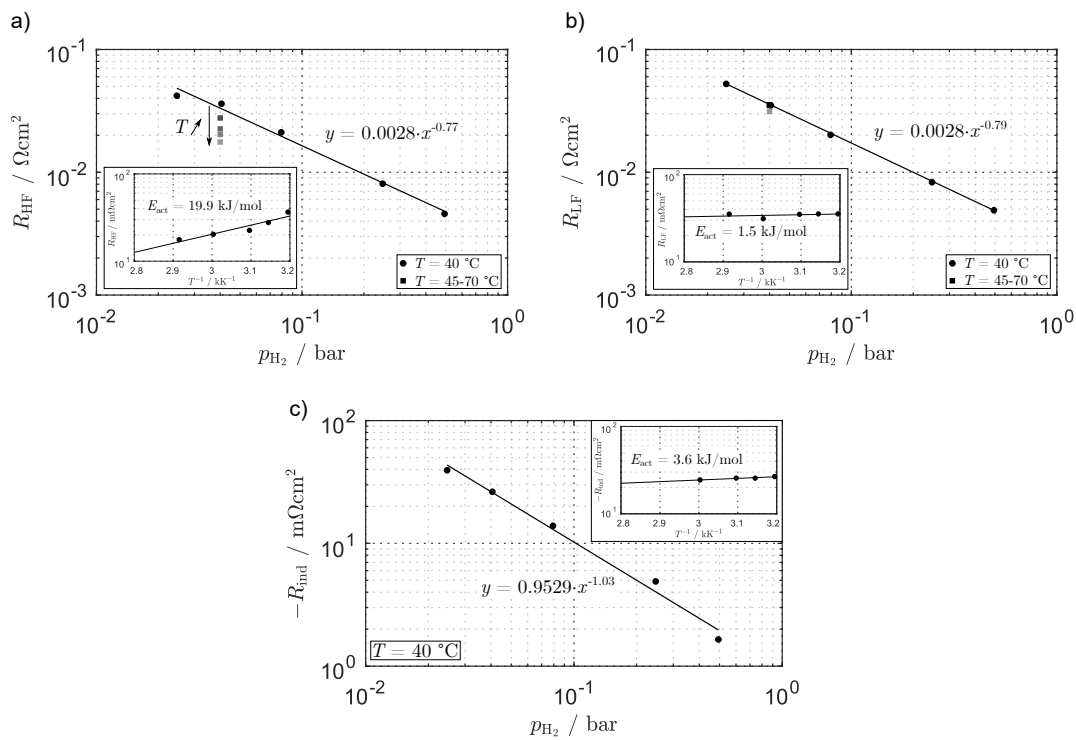


**Figure S6:** a) and b)  $rH$ -variation at OCV and  $T = 80\text{ }^{\circ}\text{C}$  with  $x_A = x_C = 0.16$ . c) and d) EIS for a  $T$ -variation at OCV with pure  $\text{H}_2$  on both sides. The spectra are shifted by  $-R_{\Omega}$  on the  $x$ -axis. b) and d) show the corresponding DRT to a) and c) respectively. e)  $\text{H}_2/\text{H}_2$  polarization curves at  $T = 80\text{ }^{\circ}\text{C}$  and  $rH = 100\%$ . f) Global parameterization (surfaces) of the high frequency loop of the  $\text{H}_2/\text{H}_2$  EIS over  $rH$ ,  $T$  and  $x_A$  with pure hydrogen on the cathode side.





**Figure S7:** a) and b) Separate  $p_{\text{H}_2}$ -variation on each side at OCV ( $U_{\text{cell}} = 0 \text{ V}$ ),  $rH = 80 \%$  and  $T = 80 \text{ }^\circ\text{C}$ .  $x_A$  and  $x_C$  represent the molar fraction of  $\text{H}_2$  in the  $\{\text{H}_2, \text{N}_2, \text{H}_2\text{O}\}$  mixture on the anode and cathode side respectively. The spectra are shifted by  $-R_\Omega$  on the x-axis. c) and d)  $p_{\text{H}_2}$ -variation on the cathode side at  $rH = 70 \%$ ,  $T = 50 \text{ }^\circ\text{C}$  and  $x_A = 0.75$ . e) and f)  $p_{\text{H}_2}$ -variation on the anode side at  $rH = 70 \%$ ,  $T = 50 \text{ }^\circ\text{C}$  and  $x_C = 0.5$ . b), d) and f) show the DRT corresponding to a), c) and e) respectively.

Anode characterization by  $\text{H}_2/\text{H}_2$  measurements: final test run containing recovery steps


**Figure S8:** a) Resistance of the high-frequency loop for a Hydrogen pressure variation in proton pump mode at OCV,  $T = 40 \text{ }^\circ\text{C}$  and  $p_{\text{total}} = 1.5 \text{ bar}$ . The square symbols represent a temperature variation locally at  $p_{\text{H}_2} = 0.04 \text{ bar}$  and the inset represents these points in an Arrhenius plot (19.9 kJ/mol). Even though the activation energy is similar as for the micropolarization analysis at higher  $\text{H}_2$  pressures, the slope (-0.77) in the log-log plot showing the dependency to  $p_{\text{H}_2}$  is higher (0.77 against 0.3 to 0.5). b) Same as in a) but for the low-frequency loop of the EIS at OCV. The order of magnitude of the resistances is the same as for the HF resistance and the partial pressure dependency (-0.79) is comparable but the activation energy (1.5 kJ/mol) is very small. c) Same analysis as in a) and b) but for the low-frequency inductive loop

## Cathode kinetics (ORR)

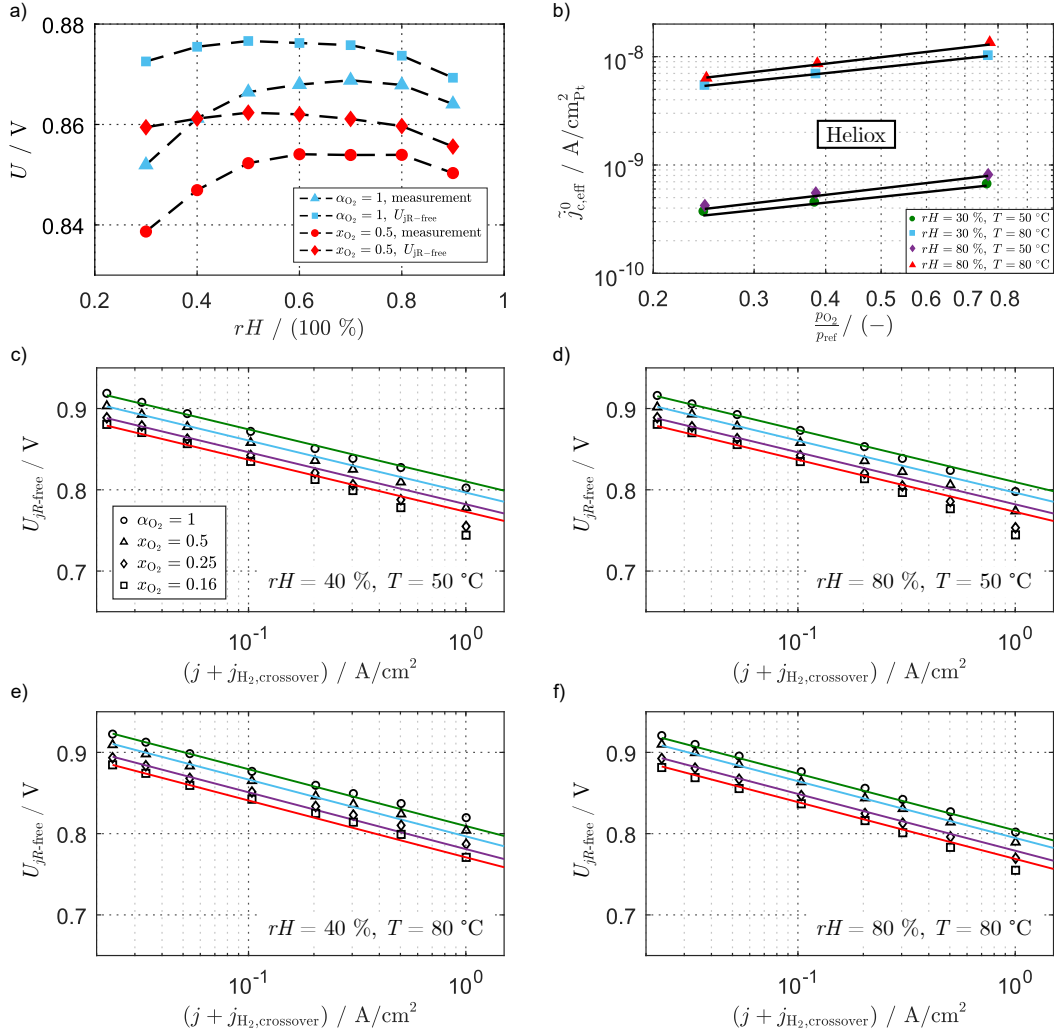


**Figure S9:** a) Measured cell potential at the current density  $j = 0.1 A/cm^2$  over the relative humidity  $rH$  for  $x_{O_2}^{dry} = 1$  and  $x_{O_2} = 0.5$  and corresponding  $(j \cdot (R_\Omega + R_p^{eff}))$ -corrected potential. The curves are averaged over the four temperature levels to smoothen the trends. b) Local exchange current densities (symbols) and global model (lines) for a  $p_{O_2}$  variation at four different temperature and humidity levels for the  $\{O_2, He\}$  case (heliox). The  $p_{H_2}$ -dependent model was used. c) to f) Polarization curves in  $H_2/O_2$  mode corrected for the protonic and electronic resistance contribution  $j \cdot (R_\Omega + R_p^{eff})$  (symbols) and corresponding model of the ORR kinetics (Tafel law) from our full factorial parameterization (lines). c)  $rH = 30\%$ ,  $T = 50^\circ C$ . d)  $rH = 80\%$ ,  $T = 50^\circ C$ . e)  $rH = 30\%$ ,  $T = 80^\circ C$ . f)  $rH = 80\%$ ,  $T = 80^\circ C$ .

**Table S1:** Exchange current density parameters extracted from fitting each current density  $j$  separately. The transfer coefficient  $\alpha_c$  was fixed to 1 in all the cases and the values marked with \* were held constant during the fitting.

Parameter\Current	0.02 A/cm <sup>2</sup>	0.03 A/cm <sup>2</sup>	0.05 A/cm <sup>2</sup>	0.1 A/cm <sup>2</sup>	0.2 A/cm <sup>2</sup>	0.3 A/cm <sup>2</sup>	0.5 A/cm <sup>2</sup>	1 A/cm <sup>2</sup>
<i>p</i> H <sub>2</sub> O-dependent model without the <i>rH</i> = 90 % conditions								
$\tilde{j}_{c,ref} \cdot 10^8$ (A/cm <sup>2</sup> <sub>Pt</sub> )	2.14	2.17	2.15	2.06	1.81	1.75	1.81	1.95
$\gamma$ (-)	0.50	0.50	0.49	0.49	0.48	0.54	0.64	0.82
$n$ (-)	0.53	0.53	0.52	0.47	0.34	0.26	0.23	0.30
$E_{act}$ (kJ/mol)	66.54	67.31	68.32	72.81	82.66	90.03	97.05	103.40
<i>p</i> H <sub>2</sub> O-dependent model without the <i>rH</i> = 90 % conditions and fixing the activation energy								
$\tilde{j}_{c,ref} \cdot 10^8$ (A/cm <sup>2</sup> <sub>Pt</sub> )	2.06	2.12	2.14	2.22	2.32	2.55	2.98	3.63
$\gamma$ (-)	0.50	0.50	0.50	0.49	0.48	0.54	0.64	0.82
$n$ (-)	0.50	0.51	0.52	0.53	0.56	0.60	0.68	0.85
$E_{act}$ (kJ/mol)	68.74*	68.74*	68.74*	68.74*	68.74*	68.74*	68.74*	68.74*
<i>p</i> H <sub>2</sub> O-independent model with all the <i>rH</i> conditions								
$j_{c,ref}^0 \cdot 10^8$ (A/cm <sup>2</sup> <sub>Pt</sub> )	2.00	2.03	2.05	2.12	2.23	2.40	2.58	2.52
$\gamma$ (-)	0.50	0.51	0.50	0.50	0.50	0.56	0.66	0.85
$E_{act}$ (kJ/mol)	68.22	68.68	69.56	71.64	75.74	79.61	85.12	95.12
<i>p</i> H <sub>2</sub> O-independent model only with <i>rH</i> = 80 % conditions								
$j_{c,ref}^0 \cdot 10^8$ (A/cm <sup>2</sup> <sub>Pt</sub> )	2.16	2.13	2.13	2.16	2.16	2.16	2.13	1.88
$\gamma$ (-)	0.50	0.51	0.51	0.53	0.55	0.59	0.67	0.78
$E_{act}$ (kJ/mol)	70.64	70.05	71.37	73.03	75.93	79.36	82.58	91.44
<i>p</i> H <sub>2</sub> O-independent model only with <i>rH</i> = 90 % conditions								
$j_{c,ref}^0 \cdot 10^8$ (A/cm <sup>2</sup> <sub>Pt</sub> )	1.75	1.75	1.83	1.91	2.02	2.15	2.25	2.27
$\gamma$ (-)	0.53	0.53	0.54	0.56	0.58	0.66	0.75	1.05
$E_{act}$ (kJ/mol)	70.03	69.42	71.34	72.70	75.86	79.66	84.47	96.87

**Table S2:** Exchange current density parameters extracted from fitting  $j \leq 0.1 \text{ A/cm}^2$  for each gas channel relative humidity  $rH$  separately or for each oxygen mole fraction  $x_{\text{O}_2}$  separately. The transfer coefficient  $\alpha_c$  was fixed to 1 in all the cases.

Parameter \ $rH$	30 %	40 %	50 %	60 %	70 %	80 %	90 %
$p_{\text{H}_2\text{O}}$ -dependent model for each $rH$ level							
$\tilde{j}_{c,\text{ref}}^0 \cdot 10^8 \text{ (A/cm}_{\text{Pt}}^2)$	0.75	0.89	1.07	1.13	1.20	1.32	1.18
$\gamma (-)$	0.43	0.48	0.51	0.50	0.55	0.51	0.54
$E_{\text{act}}$ (kJ/mol)	91.88	90.60	91.47	91.06	88.60	93.07	92.69
$p_{\text{H}_2\text{O}}$ -independent model for each $rH$ level							
$\tilde{j}_{c,\text{ref}}^0 \cdot 10^8 \text{ (A/cm}_{\text{Pt}}^2)$	1.99	2.05	2.19	2.12	2.08	2.15	1.81
$\gamma (-)$	0.43	0.48	0.51	0.50	0.55	0.51	0.54
$E_{\text{act}}$ (kJ/mol)	70.09	68.80	69.68	69.25	66.81	71.27	70.88
$p_{\text{H}_2\text{O}}$ -dependent model for the heliox conditions							
$\tilde{j}_{c,\text{ref}}^0 \cdot 10^8 \text{ (A/cm}_{\text{Pt}}^2)$	1.17					1.51	
$\gamma (-)$	0.56					0.62	
$E_{\text{act}}$ (kJ/mol)	89.30					90.43	
$p_{\text{H}_2\text{O}}$ -independent model for the heliox conditions							
$\tilde{j}_{c,\text{ref}}^0 \cdot 10^8 \text{ (A/cm}_{\text{Pt}}^2)$	3.10					2.45	
$\gamma (-)$	0.56					0.62	
$E_{\text{act}}$ (kJ/mol)	67.49					68.62	
Parameter \ $\text{O}_2$ mole fraction	$x_{\text{O}_2}^{\text{dry}} = 1$	$x_{\text{O}_2} = 0.5$	$x_{\text{O}_2} = 0.25$	$x_{\text{O}_2} = 0.16$			
$p_{\text{H}_2\text{O}}$ -dependent model for each $\text{O}_2$ concentration							
$\tilde{j}_{c,\text{ref}}^0 \cdot 10^8 \text{ (A/cm}_{\text{Pt}}^2)$	2.20	1.65	1.07	0.82			
$n (-)$	0.44	0.44	0.38	0.34			
$E_{\text{act}}$ (kJ/mol)	70.31	72.99	75.13	75.03			
$p_{\text{H}_2\text{O}}$ -dependent model for each $\text{O}_2$ concentration w/o $rH = 90 \%$							
$\tilde{j}_{c,\text{ref}}^0 \cdot 10^8 \text{ (A/cm}_{\text{Pt}}^2)$	2.63	1.92	1.25	0.96			
$n (-)$	0.55	0.54	0.48	0.44			
$E_{\text{act}}$ (kJ/mol)	65.28	68.37	70.46	70.74			
$p_{\text{H}_2\text{O}}$ -independent model for each $\text{O}_2$ concentration							
$\tilde{j}_{c,\text{ref}}^0 \cdot 10^8 \text{ (A/cm}_{\text{Pt}}^2)$	2.38	1.78	1.25	1.02			
$E_{\text{act}}$ (kJ/mol)	67.71	70.39	69.76	68.07			

**References**

- [1] M. Heinzmann, A. Weber, and E. Ivers-Tiffée. Advanced impedance study of polymer electrolyte membrane single cells by means of distribution of relaxation times. *Journal of Power Sources*, 402:24–33, 2018.
- [2] B. A. Boukamp. A linear Kronig-Kramers transform test for immittance data validation. *Journal of the electrochemical society*, 142(6):1885–1894, 1995.
- [3] M. Schönleber, D. Klotz, and E. Ivers-Tiffée. A Method for Improving the Robustness of linear Kramers-Kronig Validity Tests. *Electrochimica Acta*, 131:20–27, 2014.
- [4] C. Gerling, M. Hanauer, U. Berner, and K. A. Friedrich. Full factorial in situ characterization of ionomer properties in differential PEM fuel cells. *Journal of The Electrochemical Society*, 168(8):084504, 2021.
- [5] N. Wagner and M. Schulze. Change of electrochemical impedance spectra during CO poisoning of the Pt and PtRu anodes in a membrane fuel cell (PEFC). *Electrochimica Acta*, 48(25-26):3899–3907, 2003.
- [6] F. Sapountzi, M. N. Tsampas, and C. G. Vayenas. Electrocatalysis and electrochemical promotion of CO oxidation in PEM fuel cells: the role of oxygen crossover. *Topics in Catalysis*, 44(3):461–468, 2007.
- [7] R. Hiesgen, Tobias. Morawietz, M. Handl, M. Corasaniti, and K. A. Friedrich. Insight into the structure and nanoscale conductivity of fluorinated ionomer membranes. *Journal of The Electrochemical Society*, 161(12):F1214, 2014.
- [8] J. Kim. Characterization of CO tolerance of PEMFC by ac impedance spectroscopy. *Solid State Ionics*, 140(3-4):313–325, 2001.
- [9] W. Vogel, L. Lundquist, P. Ross, and P. Stonehart. Reaction pathways and poisons-II: The rate controlling step for electrochemical oxidation of hydrogen on Pt in acid and poisoning of the reaction by CO. *Electrochimica Acta*, 20(1):79–93, 1975.
- [10] M. Ciureanu, S.D. Mikhailenko, and S. Kaliaguine. PEM fuel cells as membrane reactors: kinetic analysis by impedance spectroscopy. *Catalysis Today*, 82(1-4):195–206, 2003.
- [11] N. Wagner and E. Gülzow. Change of electrochemical impedance spectra (EIS) with time during CO-poisoning of the Pt-anode in a membrane fuel cell. *Journal of Power Sources*, 127(1-2):341–347, 2004.



### A.3 Supplementary Information Publication III

**Supplementary material for:  
Experimental and numerical investigation of the low-frequency  
inductive features in differential PEM fuel cells: ionomer  
humidification and platinum oxide effects**

**Christophe Gerling<sup>1,2</sup>, Matthias Hanauer<sup>1</sup>, Ulrich Berner<sup>1</sup>,  
and K. Andreas Friedrich<sup>2,3</sup>**

<sup>1</sup> Robert Bosch GmbH, Corporate Research, Robert-Bosch-Campus 1, Renningen 71272, Germany

<sup>2</sup> Institute for Building Energetics, Thermotechnology and Energy Storage (IGTE), University of Stuttgart,  
Pfaffenwaldring 6, Stuttgart 70569, Germany

<sup>3</sup> Institute of Engineering Thermodynamics, German Aerospace Center (DLR), Pfaffenwaldring 38-40, Stuttgart 70569,  
Germany

E-mail: christophe.gerling@de.bosch.com

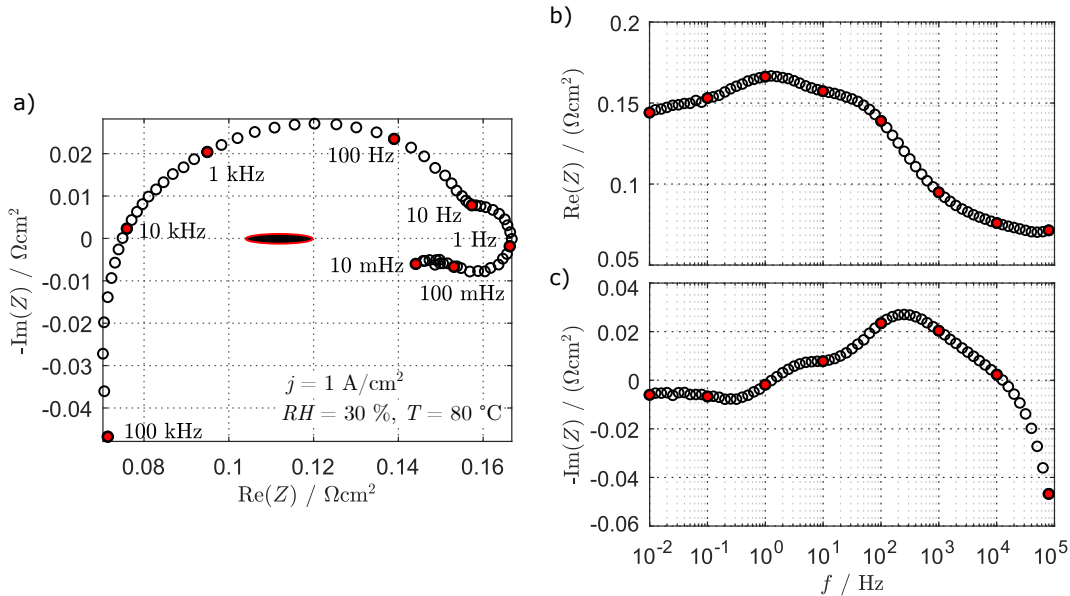


**Figure S1:** a) Nyquist plot of an EIS spectrum recorded at  $j = 1 \text{ A/cm}^2$ ,  $RH = 30\%$  and  $T = 80^\circ\text{C}$  (dry conditions) from 100 kHz to 10 mHz. Some frequencies are highlighted by the filled symbols and the steady-state differential resistance is shown by the black ellipse with red contour. b) According Bode plot of the real part of the impedance. c) According Bode plot of the imaginary part of the impedance.



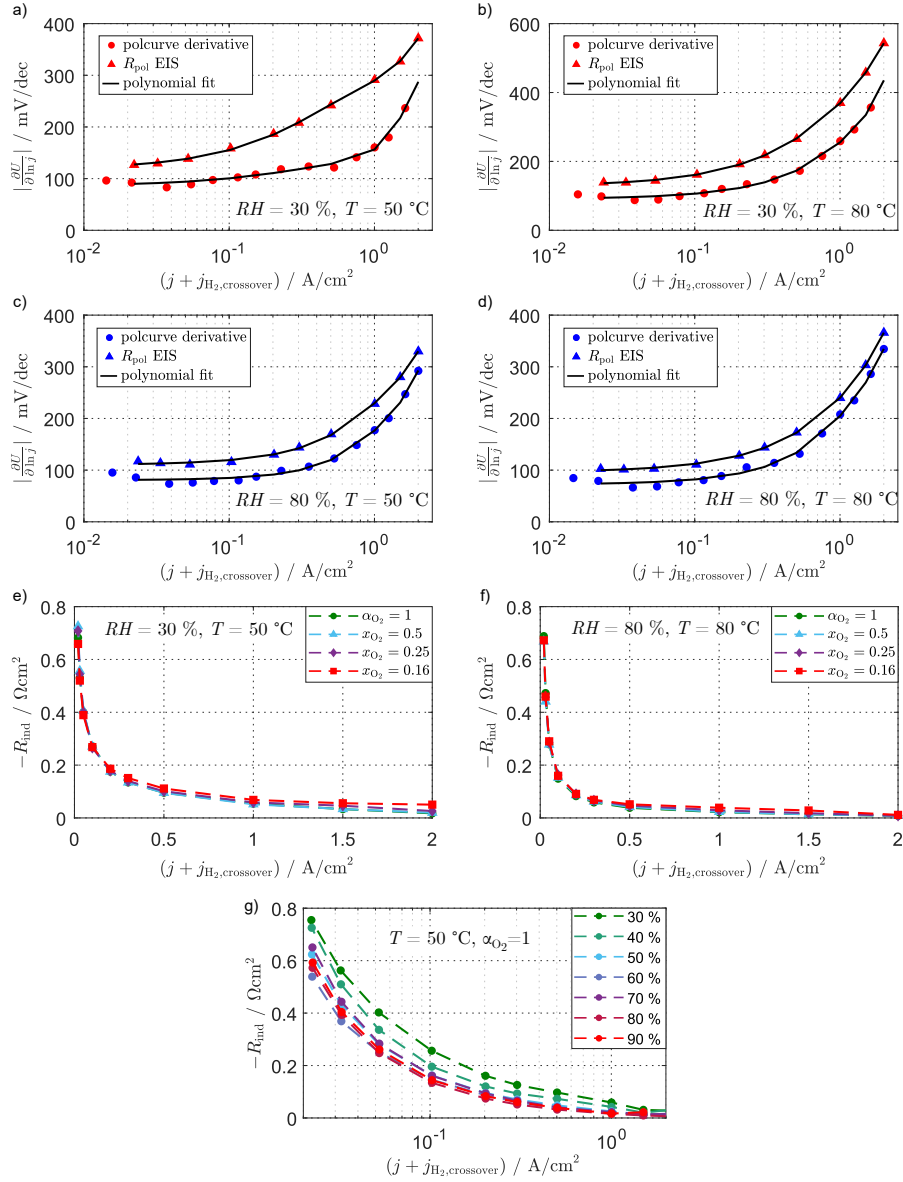


**Figure S2:** a) Local slope of the polarization curve over the current density at  $RH = 30\%$ ,  $T = 50\text{ }^\circ\text{C}$  and  $x_{\text{O}_2}^{\text{dry}} = 1$  based on the numerical derivative of the polarization curve and on the low-frequency  $x$ -axis intercept of the EIS spectra ( $f \approx 1\text{ Hz}$ ). b) Same as in a) for  $RH = 30\%$  and  $T = 80\text{ }^\circ\text{C}$ . c) Same as in a) for  $RH = 80\%$  and  $T = 50\text{ }^\circ\text{C}$ . d) Same as in a) for  $RH = 80\%$  and  $T = 80\text{ }^\circ\text{C}$ . e) Size of the low-frequency inductive contribution ( $= -R_{\text{ind}}$ ) depending on the current density  $j$  at  $RH = 30\%$  and  $T = 50\text{ }^\circ\text{C}$ , calculated based on the difference of the polarization curve derivatives and the low-frequency  $x$ -axis intercepts. f) Same as in e) for  $RH = 80\%$  and  $T = 80\text{ }^\circ\text{C}$ . g) Inductive contribution  $-R_{\text{ind}}$  over the current density at  $T = 50\text{ }^\circ\text{C}$  and  $x_{\text{O}_2}^{\text{dry}} = 1$  for a variation of  $RH$ .

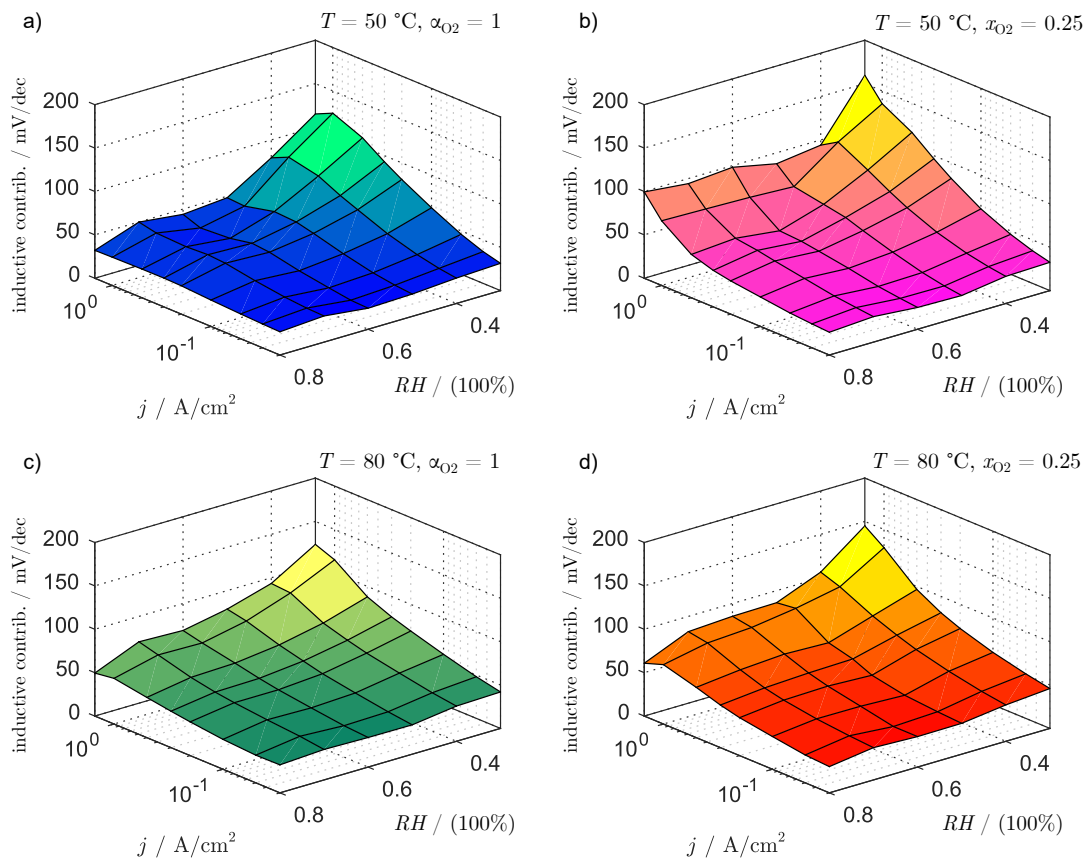


**Figure S3:** 3D representations of the inductive contribution in mV/dec depending on the current density  $j$  and on the relative humidity  $RH$  for different temperatures and oxygen concentrations. This was computed based on the difference between the numerical derivative of the polarization curve and the low-frequency polarization resistance (low-frequency  $x$ -axis intercept in the Nyquist plot at approximately 1 Hz).

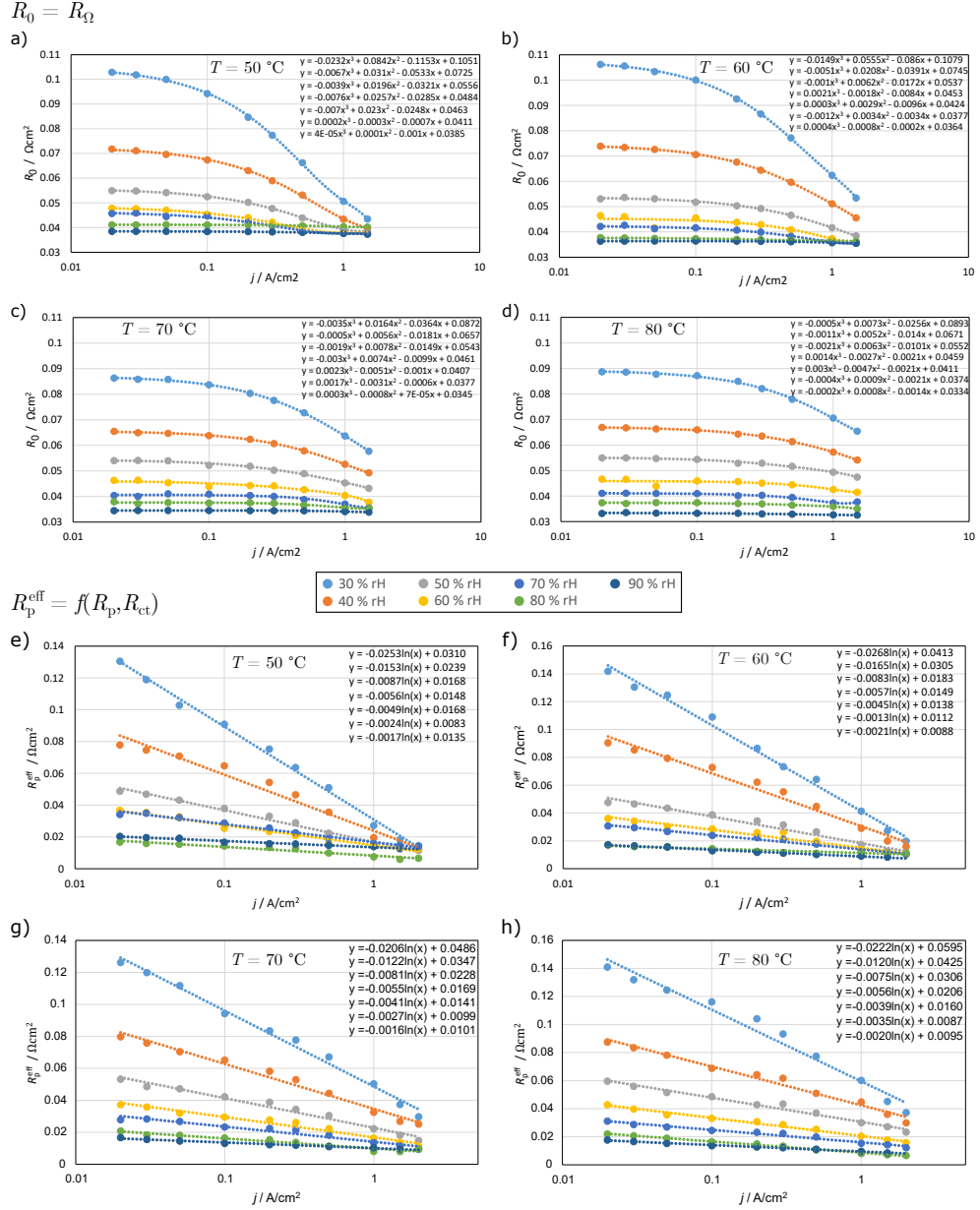


**Figure S4:** High-frequency resistance  $R_\Omega$  and effective CCL proton resistance  $R_p^{\text{eff}}$  depending on the cell current density for  $x_{\text{O}_2}^{\text{dry}} = 1$  and RH from 30% to 90%.

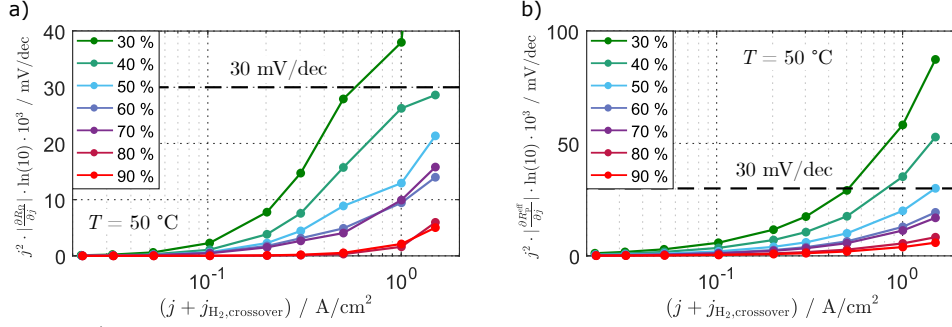


**Figure S5:** a) Low-frequency contribution of the membrane humidification dynamics over the current density for varying gas channel humidity levels at  $T = 50$  °C. b) Same as in a) for the CCL humidification contribution.

### Parameter variation with the FEM model

The Figures S6 to S29 show a variation of the most important parameters of the presented FEM model. The baseline parameterization is given in Table S1 and deviates only if specifically mentioned in the caption of the concerned figure. From Figure S6 to S21, Fickian diffusion contributions were eliminated by setting unphysically high effective diffusion coefficients in both the cathode catalyst layer (CCL) and the gas diffusion layer (GDL). Furthermore, the ionomer conductivities were set unphysically high unless mentioned otherwise.

**Table S1:** Baseline model parameters.

Design	
$L_{PEM}$ ( $\mu\text{m}$ )	18
$L_{CCL}$ ( $\mu\text{m}$ ), $\epsilon_p$ (-)	13, 0.4
$L_{GDL}$ ( $\mu\text{m}$ ), $\epsilon_p$ (-)	180, 0.8
$rf$ ( $\text{m}_{Pt}^2/\text{m}_{geo}^2$ )	166
$C_{dl}$ ( $\text{mF}/\text{cm}_{geo}^2$ )	30
Operating conditions	
$rH$ (%)	80
$T$ (°C)	80
$x_{O_2}^{dry}$ (-)	1
$P$ ( $\text{bar}_a$ )	1.5
Diffusion properties (at $T = 80$ °C)	
$D_{O_2,GDL}$ ( $\text{cm}^2/\text{s}$ )	$3.0 \cdot 10^{-2}$
$D_{O_2,CCL}$ ( $\text{cm}^2/\text{s}$ )	$3.4 \cdot 10^{-4}$
Kinetic properties	
$n_{O_2}$ (-)	0.5
$n$ (-)	2
$n_{Pt}$ (-)	2.5
$n_{\square}$ (-)	1
$\beta$ (-)	0.66
$\Gamma$ ( $\text{mol}/\text{cm}_{geo}^2$ )	$1.44 \cdot 10^{-7}$
$\Delta U_{eq}$ (V)	0.42
$j_{c,ref}^0$ ( $\text{A}/\text{cm}_{Pt}^2$ )	$1.92 \cdot 10^{-6}$
$k_{2,ref}$ ( $\text{A}/\text{cm}_{geo}^2$ )	$7.07 \cdot 10^{-7}$
$\gamma$ (-)	0.54
$m$ (-)	0.50
$E_{act,1}$ (kJ/mol)	60.5

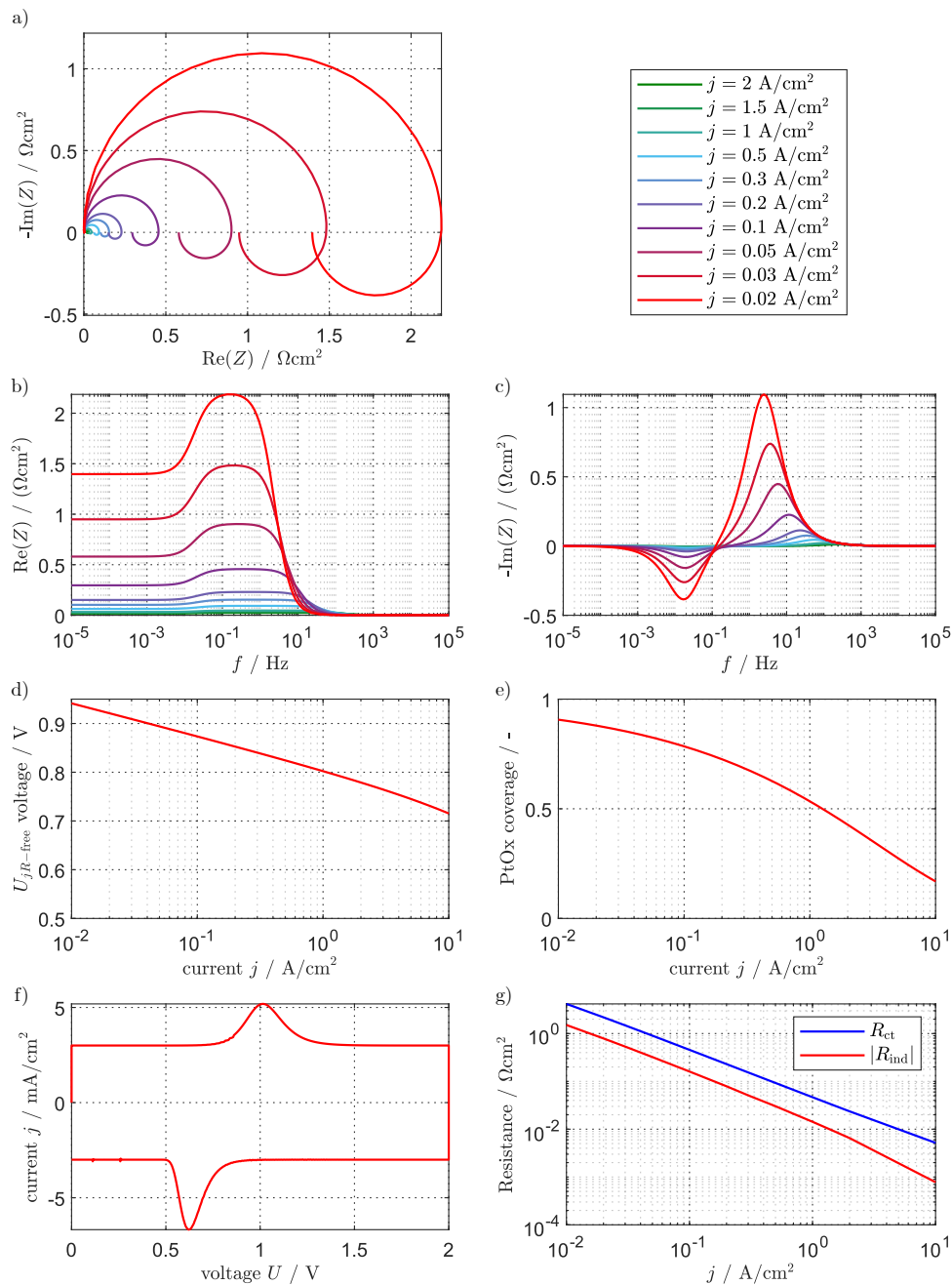


**Figure S6:** Variation of the current density  $j$  in our FEM model with otherwise baseline parameterization. a) Nyquist plot. b) and c) Corresponding Bode plots. d) Polarization curve (Tafel plot). e) Platinum oxide coverage. f) Cyclic voltammetry. g)  $R_{\text{ct}}$  and  $|R_{\text{ind}}|$ .

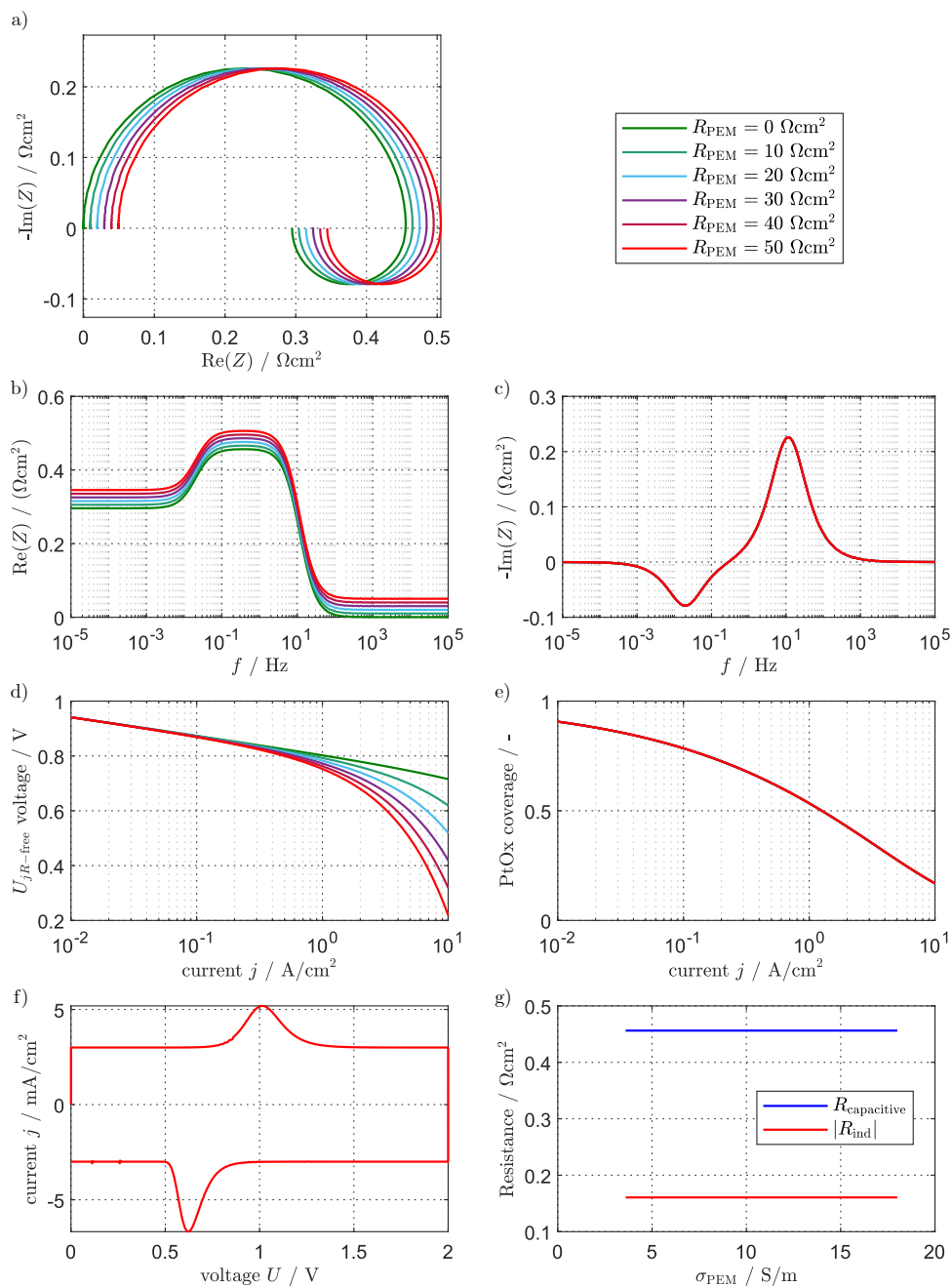


**Figure S7:** Variation of  $R_{PEM}$  in our FEM model with otherwise baseline parameterization. a) Nyquist plot at  $j = 0.1 \text{ A}/\text{cm}^2$ . b) and c) Corresponding Bode plots. d) Polarization curve (Tafel plot). e) Platinum oxide coverage. f) Cyclic voltammometry. g)  $R_{\text{capacitive}}$  and  $|R_{\text{ind}}|$ .

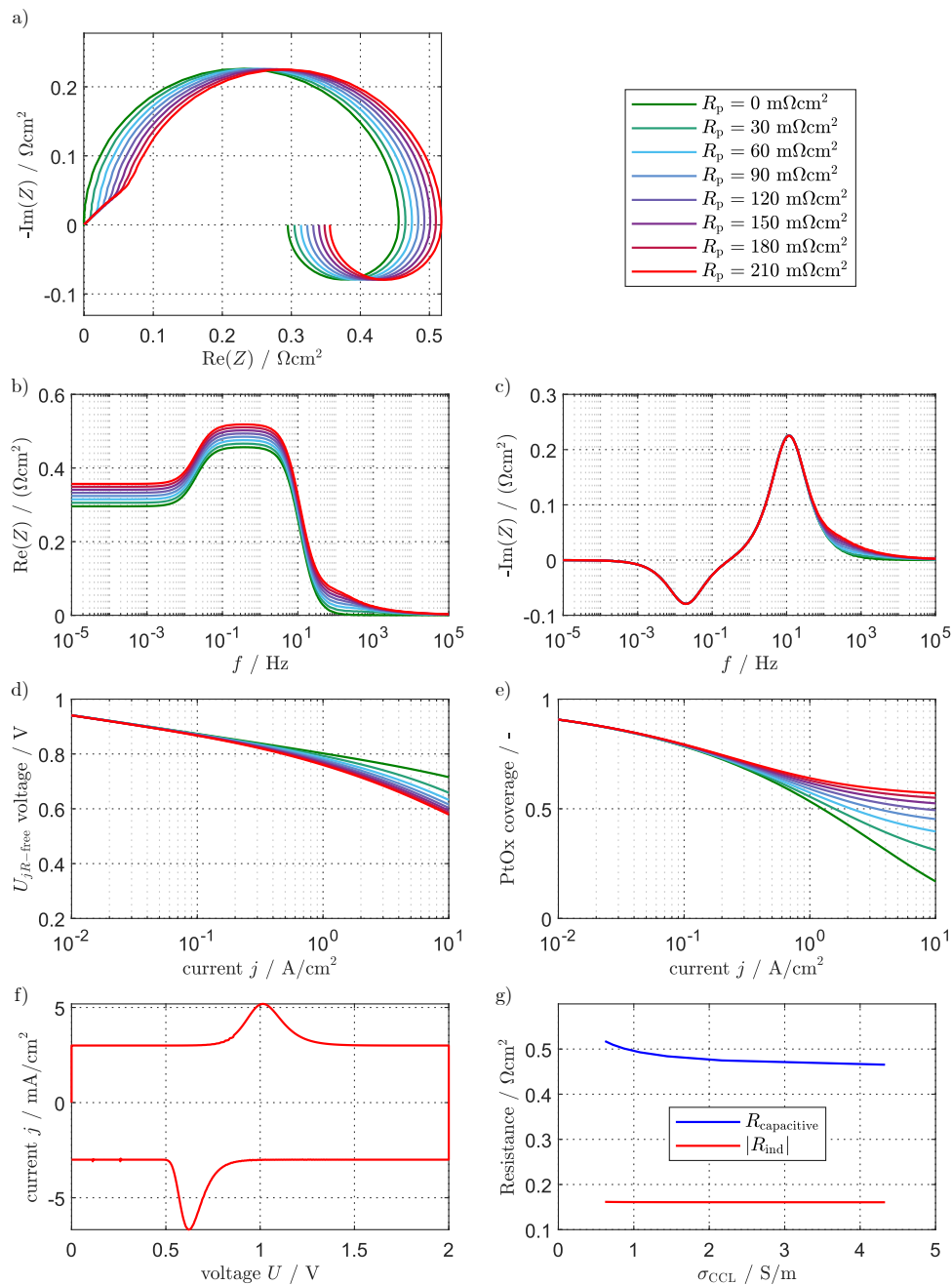


**Figure S8:** Variation of  $R_p$  in our FEM model with otherwise baseline parameterization. a) Nyquist plot at  $j = 0.1 \text{ A}/\text{cm}^2$ . b) and c) Corresponding Bode plots. d) Polarization curve (Tafel plot). e) Platinum oxide coverage. f) Cyclic voltammetry. g)  $R_{\text{capacitive}}$  and  $|R_{\text{ind}}|$ .

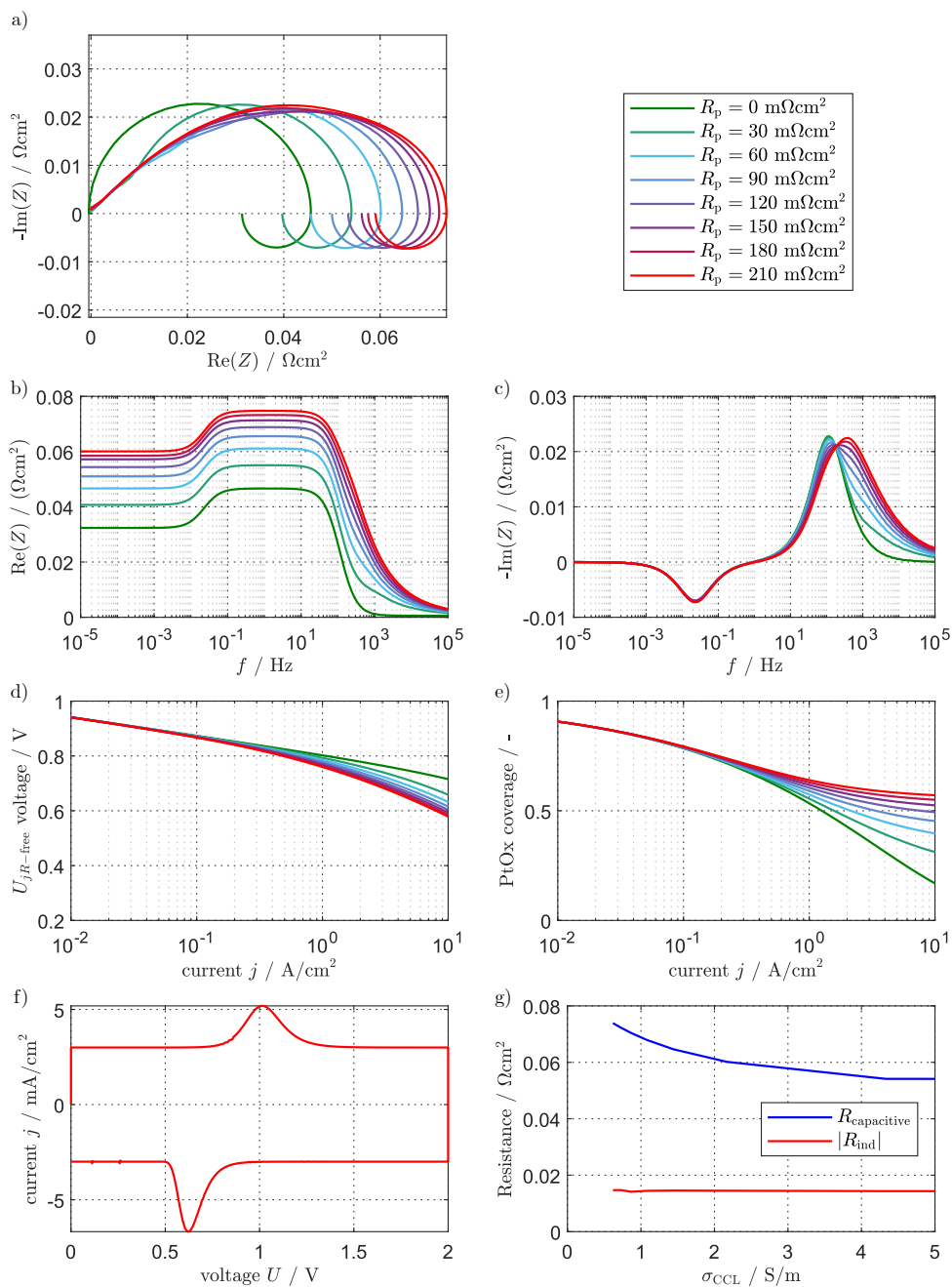


**Figure S9:** Variation of  $R_p$  in our FEM model with otherwise baseline parameterization. a) Nyquist plot at  $j = 1 \text{ A}/\text{cm}^2$ . b) and c) Corresponding Bode plots. d) Polarization curve (Tafel plot). e) Platinum oxide coverage. f) Cyclic voltammety. g)  $R_{\text{capacitive}}$  and  $|R_{\text{ind}}|$ .



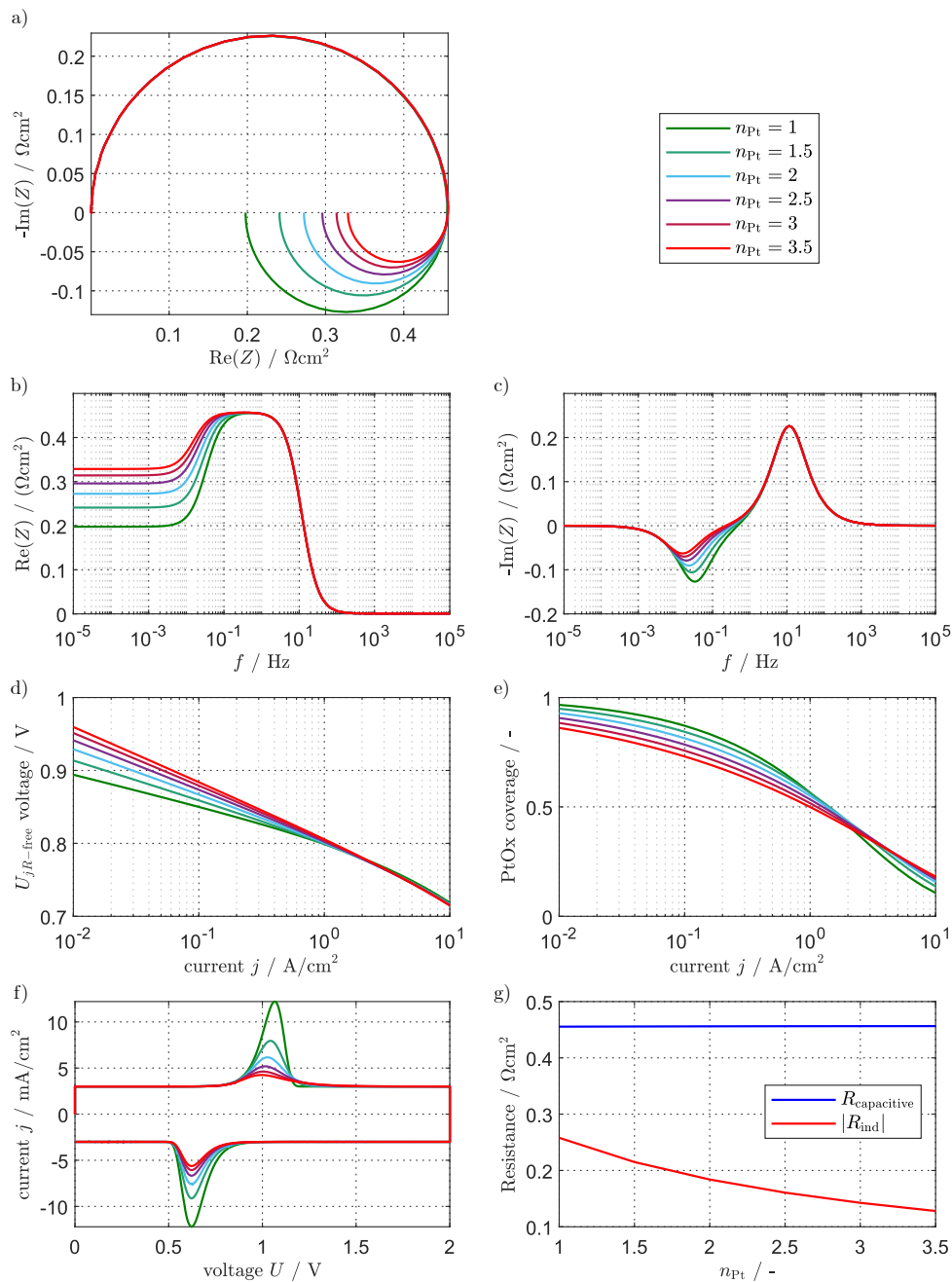


**Figure S10:** Variation of  $n_{Pt}$  in our FEM model with otherwise baseline parameterization. a) Nyquist plot at  $j = 0.1 \text{ A}/\text{cm}^2$ , b) and c) Corresponding Bode plots. d) Polarization curve (Tafel plot). e) Platinum oxide coverage. f) Cyclic voltammetry. g)  $R_{\text{capacitive}}$  and  $|R_{\text{ind}}|$ .

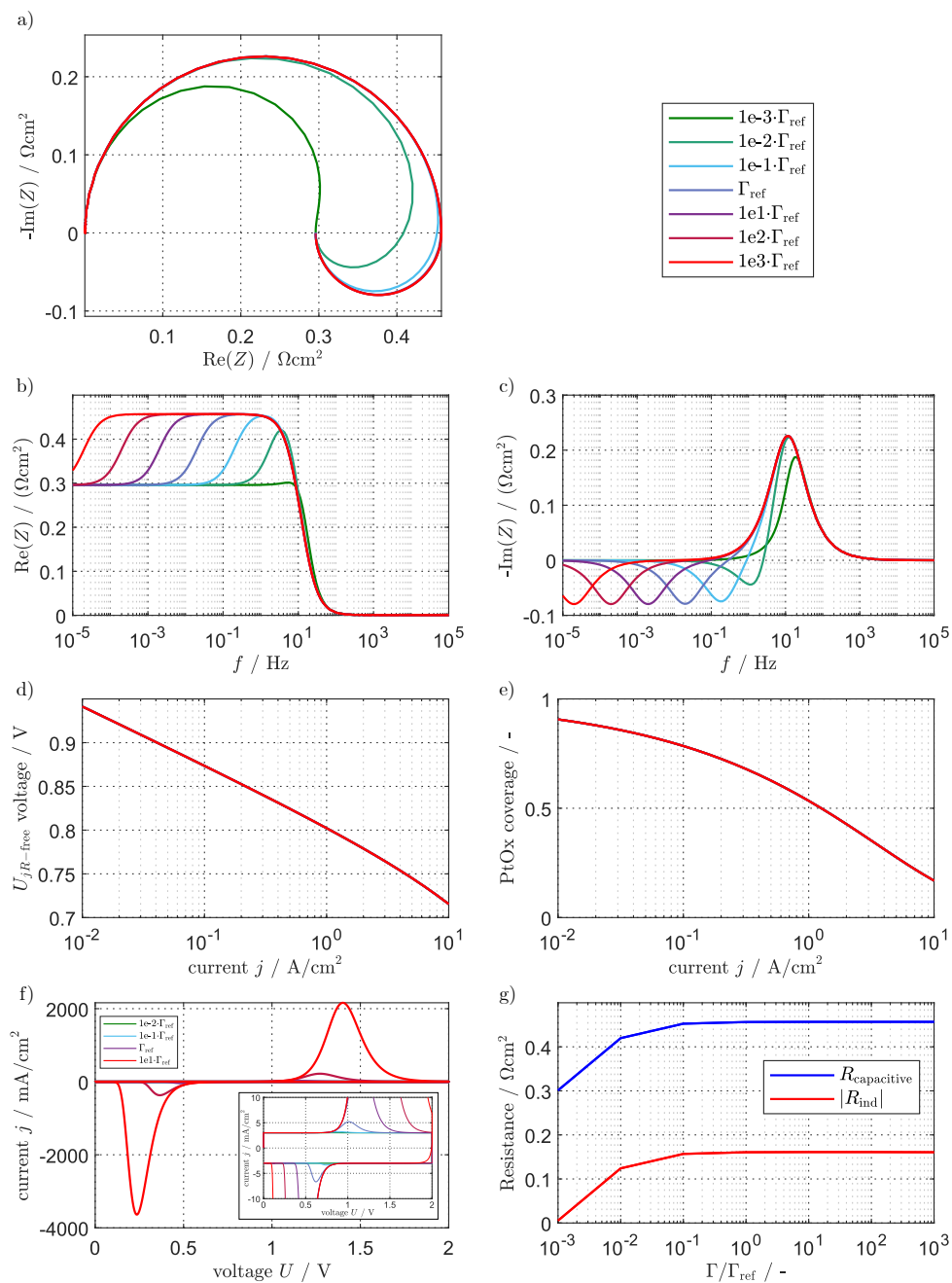


**Figure S11:** Variation of  $\Gamma$  in our model with otherwise baseline parameterization. a) Nyquist plot at  $j = 0.1 \text{ A/cm}^2$ . b) and c) Corresponding Bode plots. d) Polarization curve (Tafel plot). e) Platinum oxide coverage. f) Cyclic voltammetry. g)  $R_{\text{capacitive}}$  and  $|R_{\text{ind}}|$ .

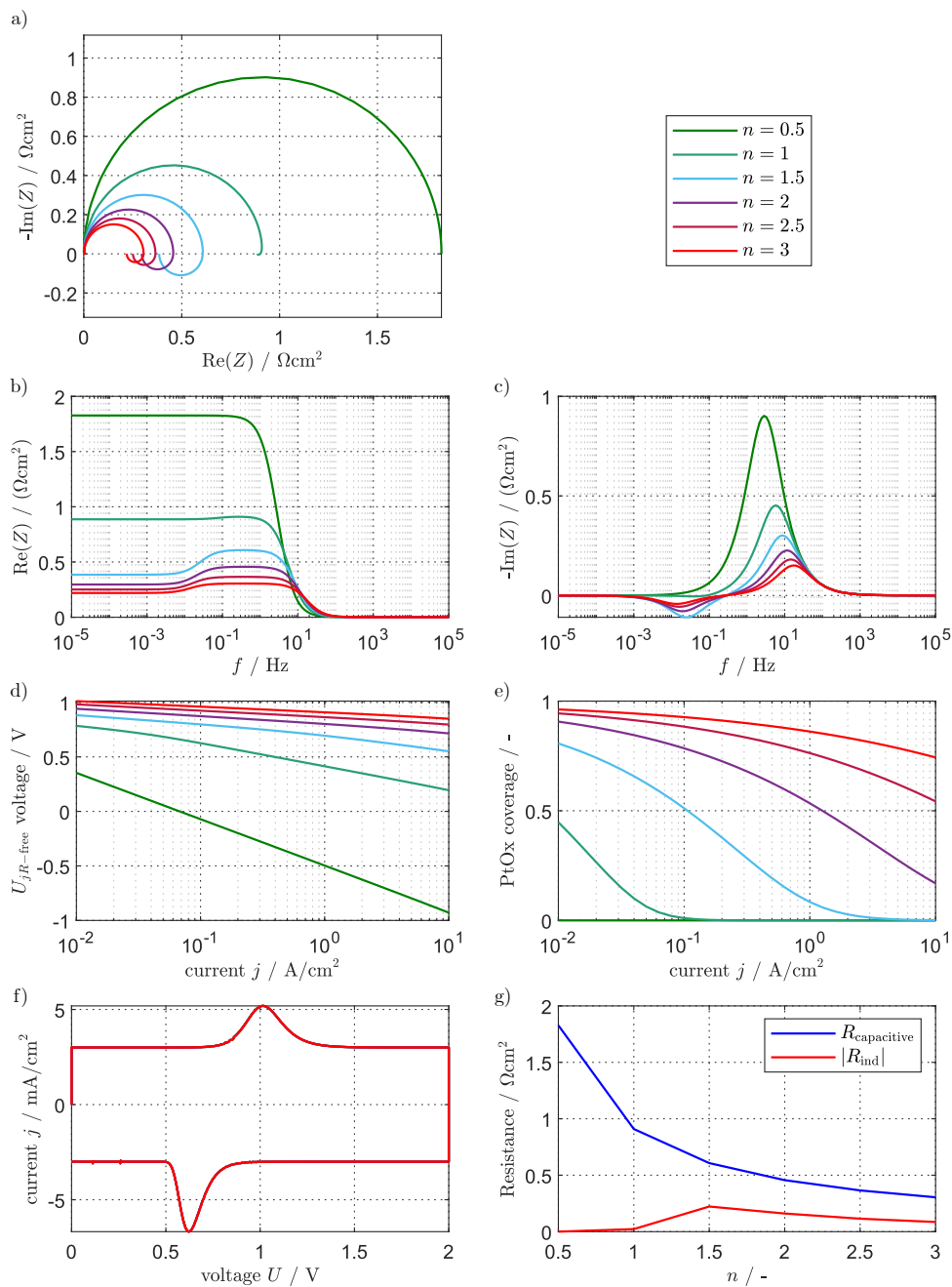


**Figure S12:** Variation of  $n$  in our model with otherwise baseline parameterization. a) Nyquist plot at  $j = 0.1 \text{ A/cm}^2$ . b) and c) Corresponding Bode plots. d) Polarization curve (Tafel plot). e) Platinum oxide coverage. f) Cyclic voltammetry. g)  $R_{\text{capacitive}}$  and  $|R_{\text{ind}}|$ .

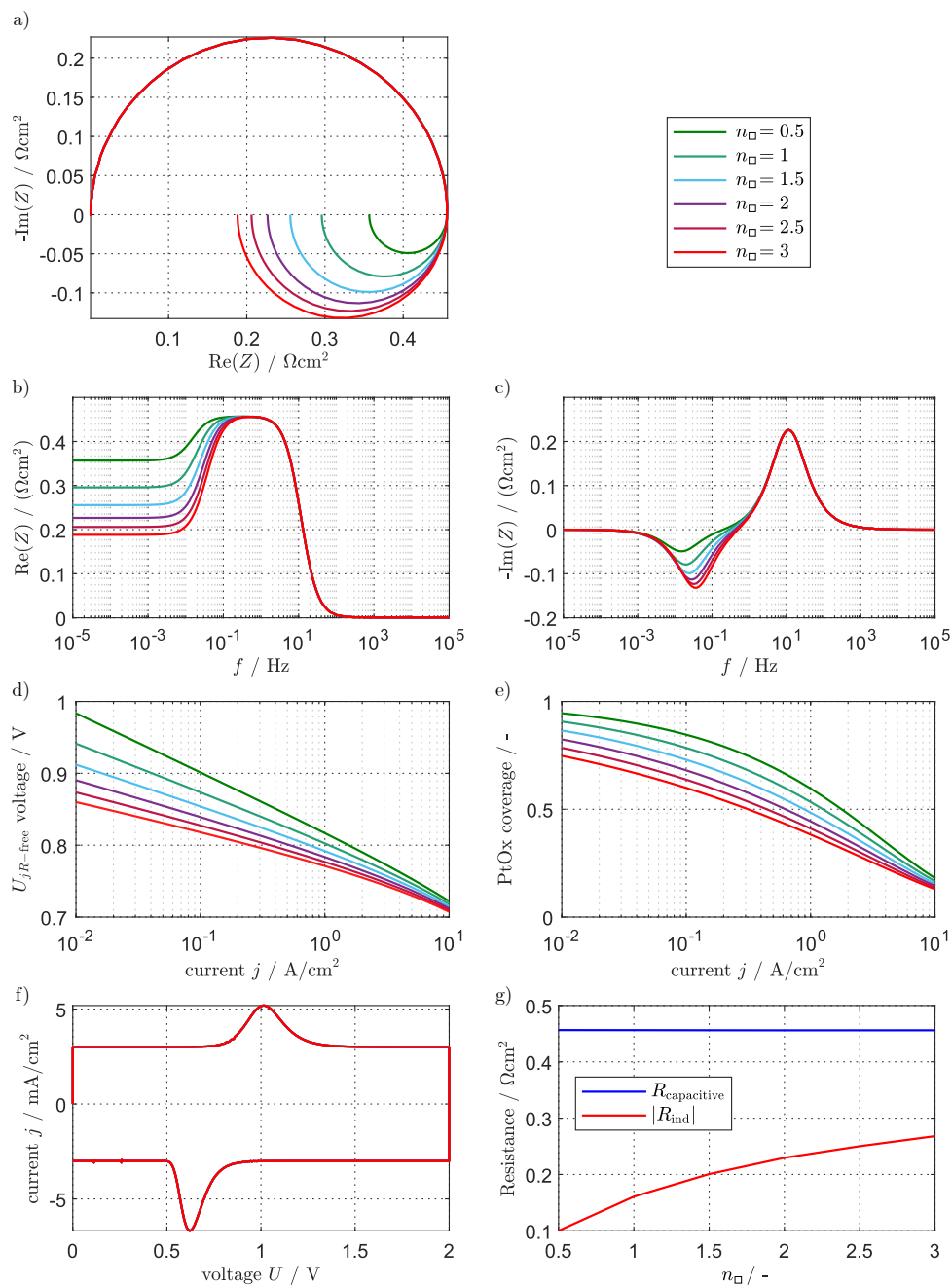


**Figure S13:** Variation of  $n_{\text{ox}}$  in our model with otherwise baseline parameterization. a) Nyquist plot at  $j = 0.1 \text{ A}/\text{cm}^2$ . b) and c) Corresponding Bode plots. d) Polarization curve (Tafel plot). e) Platinum oxide coverage. f) Cyclic voltammetry. g)  $R_{\text{capacitive}}$  and  $|R_{\text{ind}}|$ .

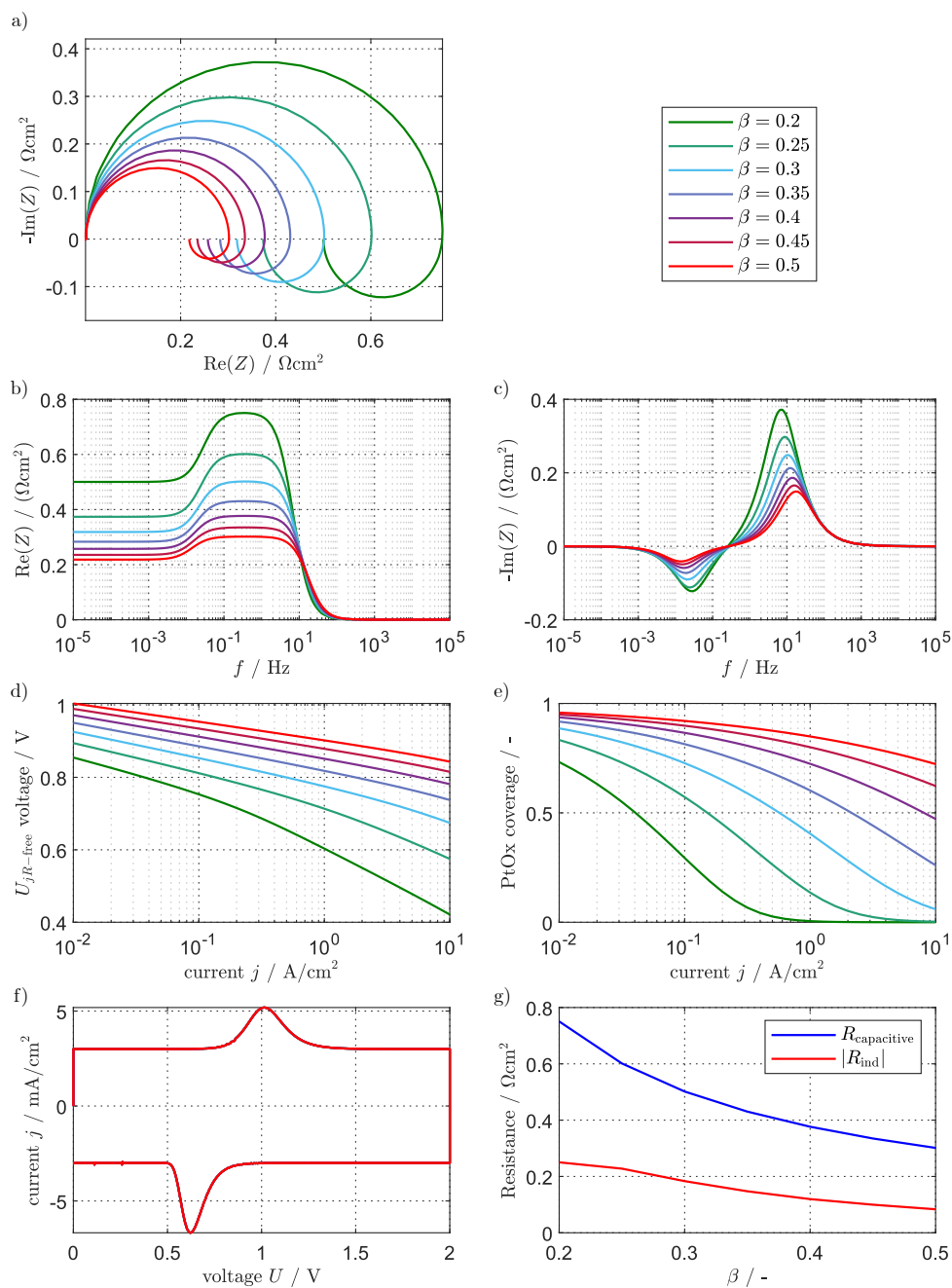


**Figure S14:** Variation of  $\beta$  in our model with otherwise baseline parameterization. a) Nyquist plot at  $j = 0.1 \text{ A/cm}^2$ . b) and c) Corresponding Bode plots. d) Polarization curve (Tafel plot). e) Platinum oxide coverage. f) Cyclic voltammetry. g)  $R_{\text{capacitive}}$  and  $|R_{\text{ind}}|$ .

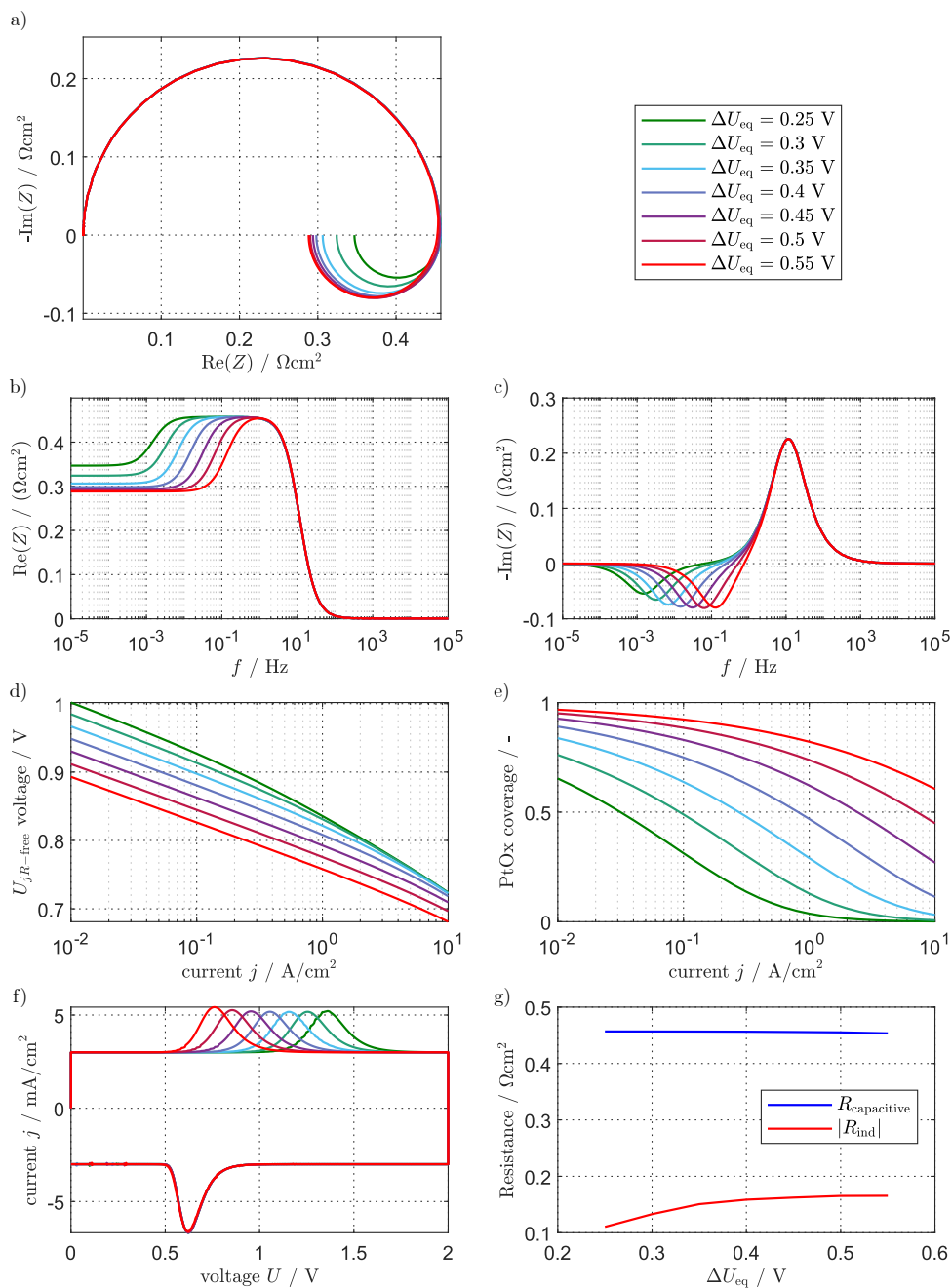


**Figure S15:** Variation of  $\Delta U_{\text{eq}}$  in our model with otherwise baseline parameterization. a) Nyquist plot at  $j = 0.1 \text{ A/cm}^2$ . b) and c) Corresponding Bode plots. d) Polarization curve (Tafel plot). e) Platinum oxide coverage. f) Cyclic voltammety. g)  $R_{\text{capacitive}}$  and  $|R_{\text{ind}}|$ .

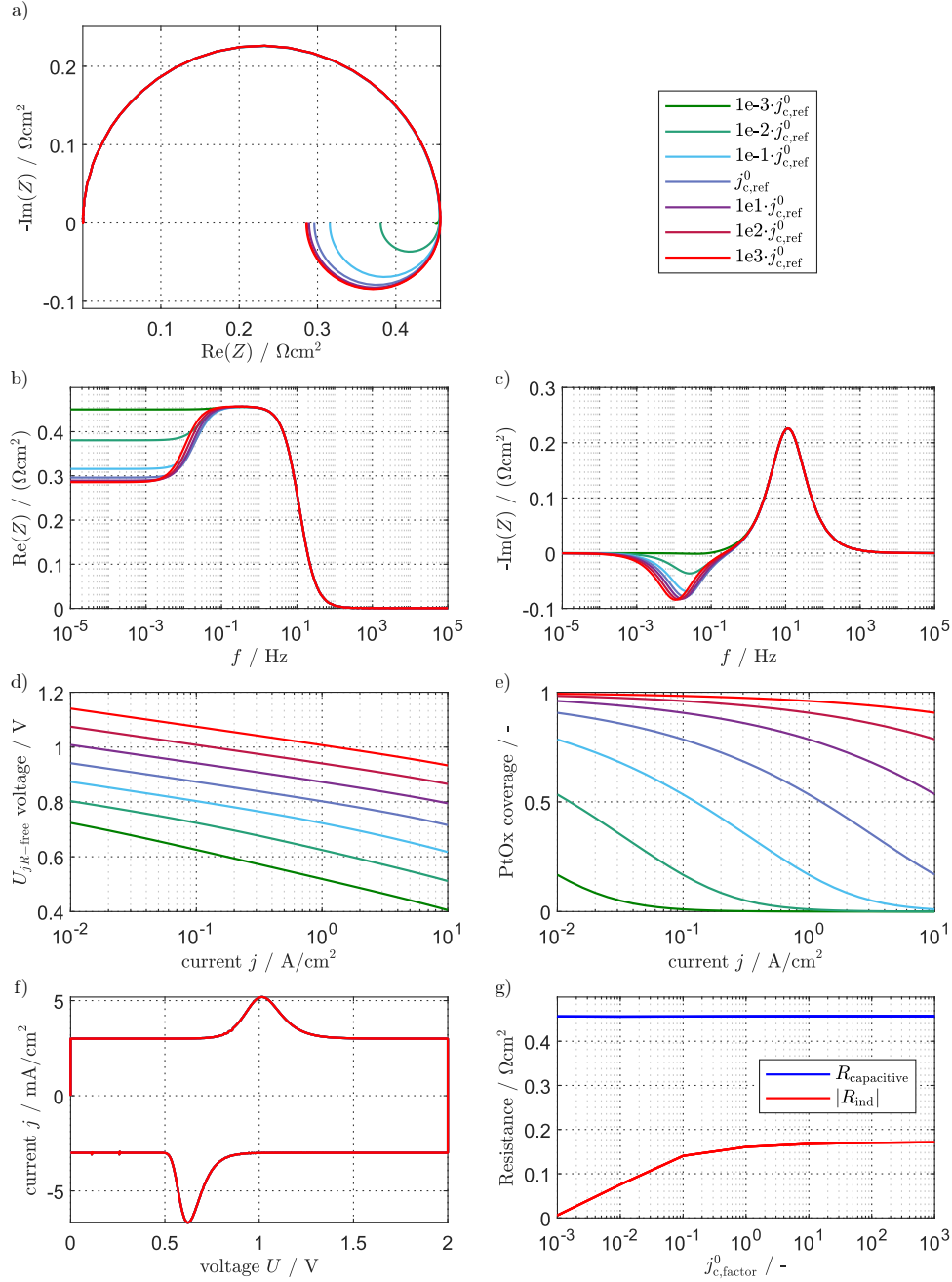


**Figure S16:** Variation of  $j_{c,ref}^0$  in our model with otherwise baseline parameterization. a) Nyquist plot at  $j = 0.1 \text{ A}/\text{cm}^2$ . b) and c) Corresponding Bode plots. d) Polarization curve (Tafel plot). e) Platinum oxide coverage. f) Cyclic voltammetry. g)  $R_{\text{capacitive}}$  and  $|R_{\text{ind}}|$ .

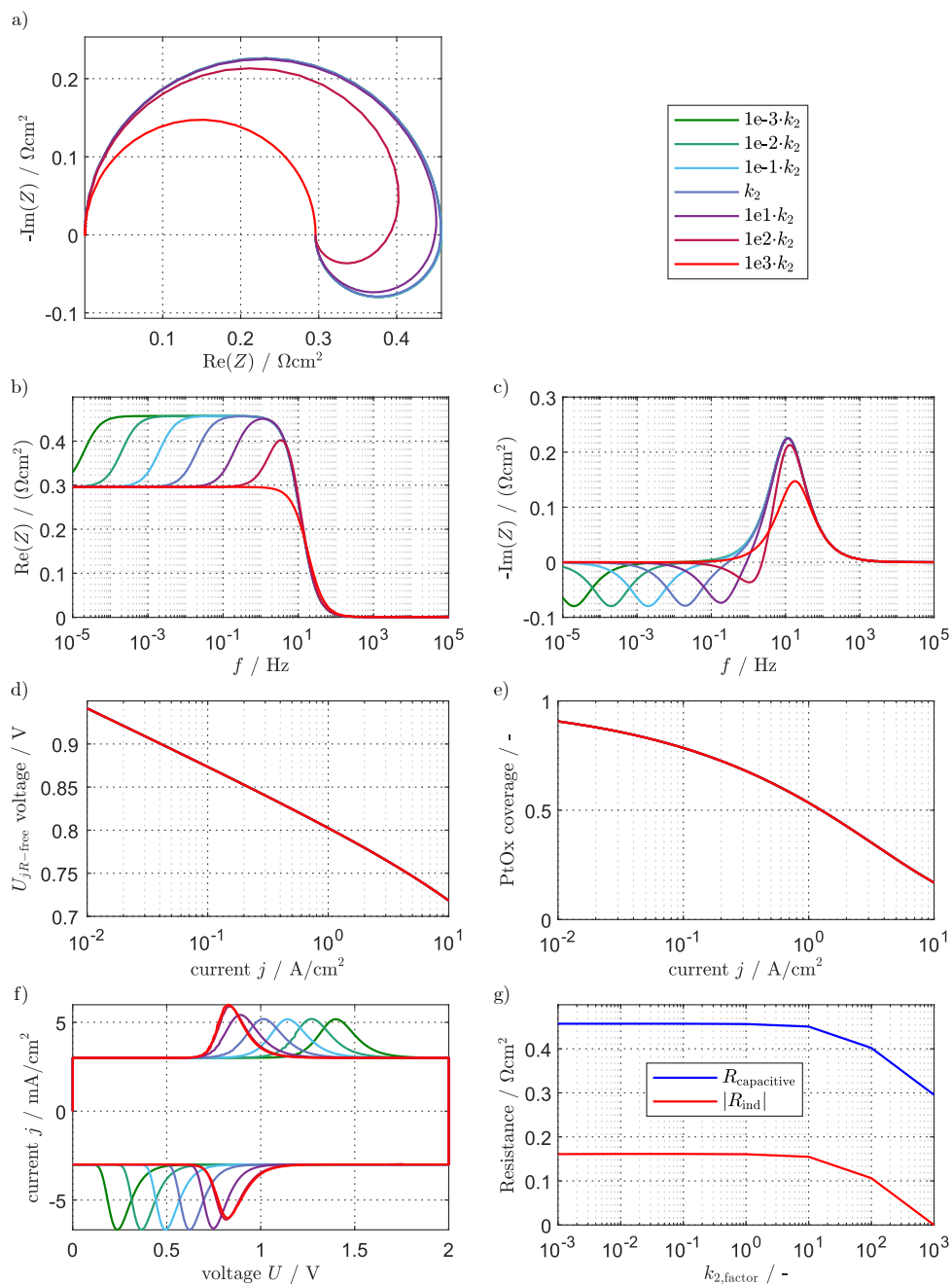


**Figure S17:** Variation of  $k_2$  in our model with otherwise baseline parameterization. a) Nyquist plot at  $j = 0.1 \text{ A}/\text{cm}^2$ . b) and c) Corresponding Bode plots. d) Polarization curve (Tafel plot). e) Platinum oxide coverage. f) Cyclic voltammetry. g)  $R_{\text{capacitive}}$  and  $|R_{\text{ind}}|$ .



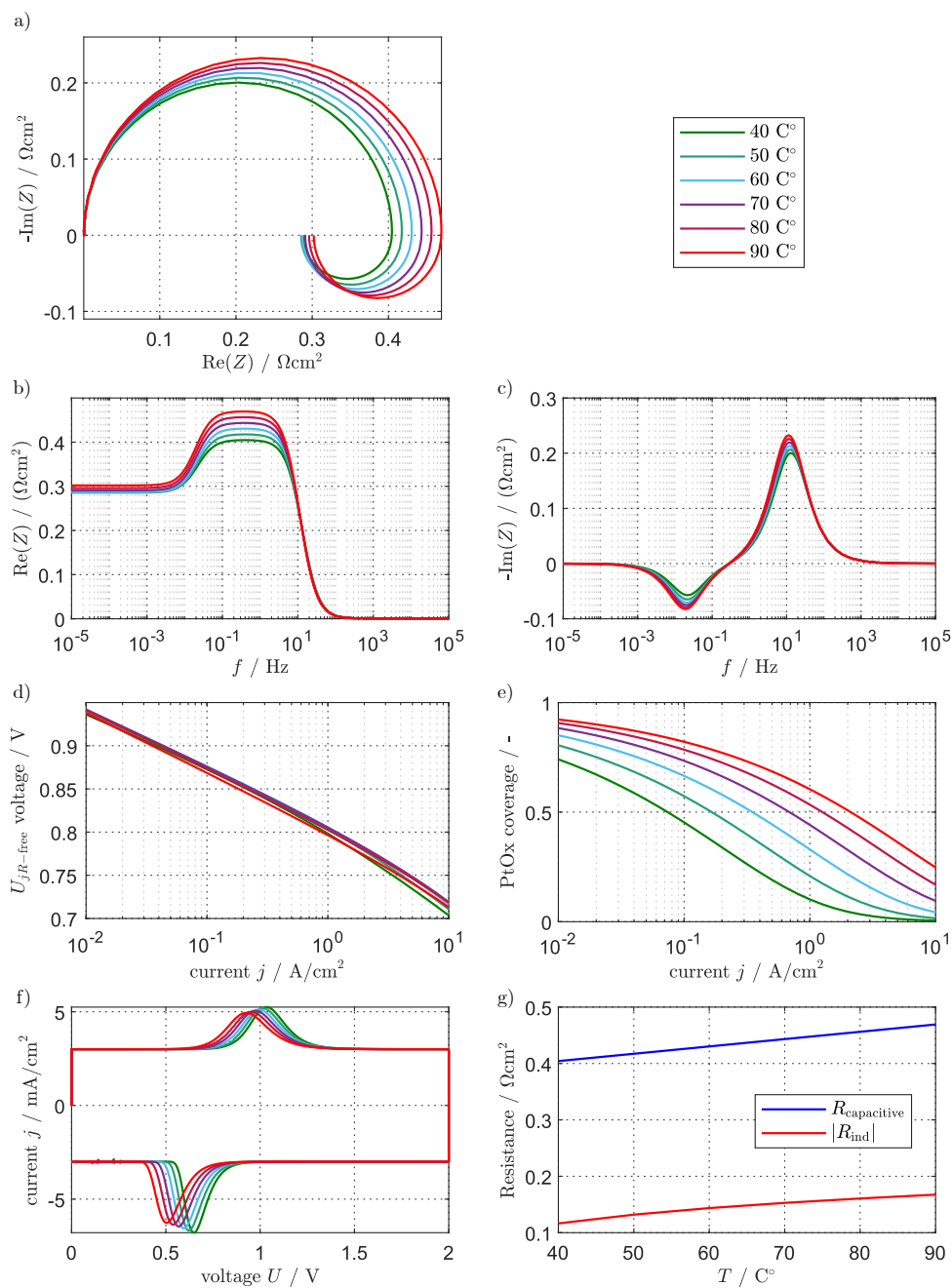


**Figure S18:** Variation of  $T$  in our model with otherwise baseline parameterization. a) Nyquist plot at  $j = 0.1 \text{ A/cm}^2$ . b) and c) Corresponding Bode plots. d) Polarization curve (Tafel plot). e) Platinum oxide coverage. f) Cyclic voltammetry. g)  $R_{\text{capacitive}}$  and  $|R_{\text{ind}}|$ .

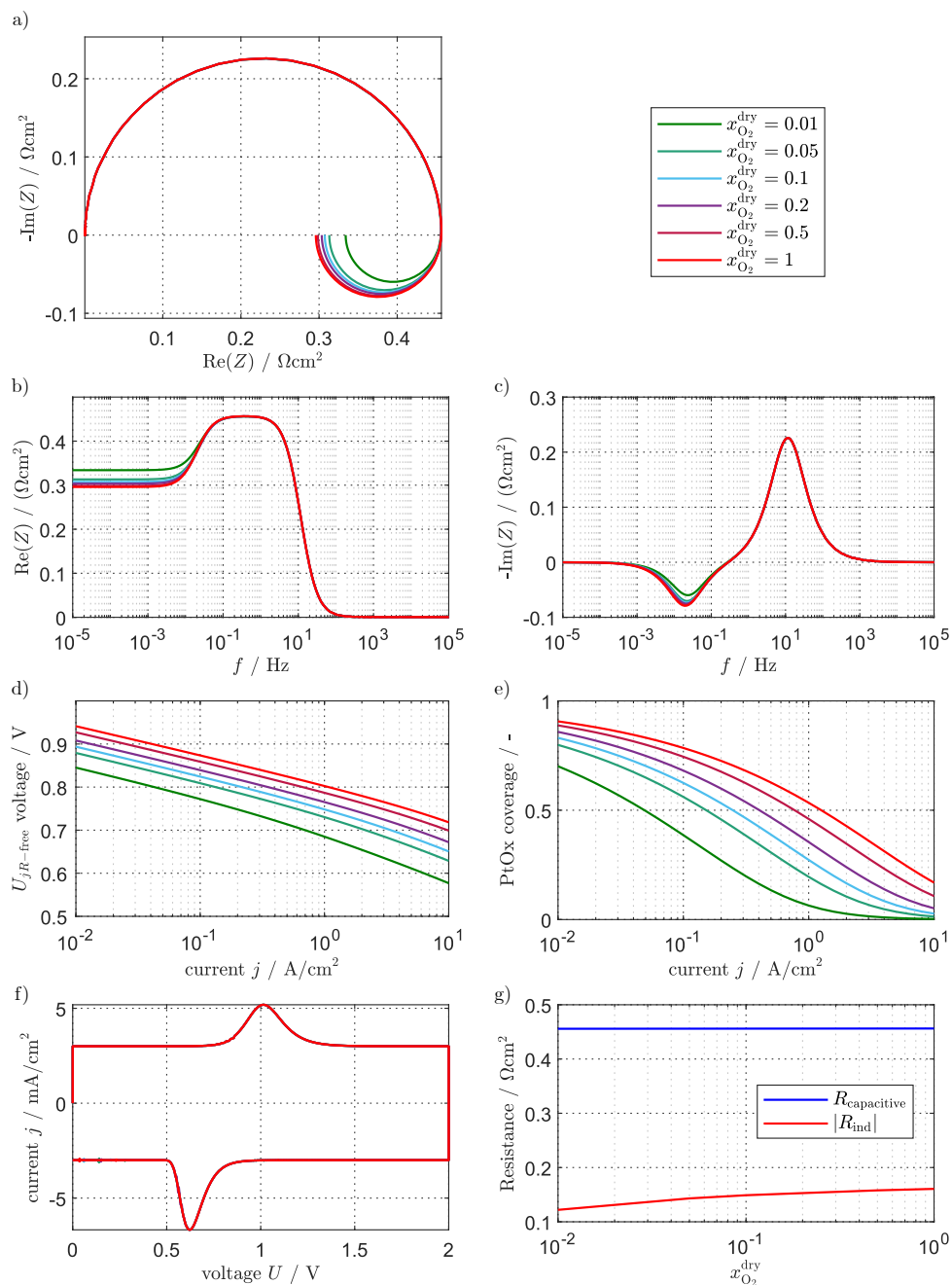


**Figure S19:** Variation of  $x_{O_2}^{dry}$  in our model with otherwise baseline parameterization. a) Nyquist plot at  $j = 0.1 \text{ A}/\text{cm}^2$ . b) and c) Corresponding Bode plots. d) Polarization curve (Tafel plot). e) Platinum oxide coverage. f) Cyclic voltammetry. g)  $R_{\text{capacitive}}$  and  $|R_{\text{ind}}|$ .

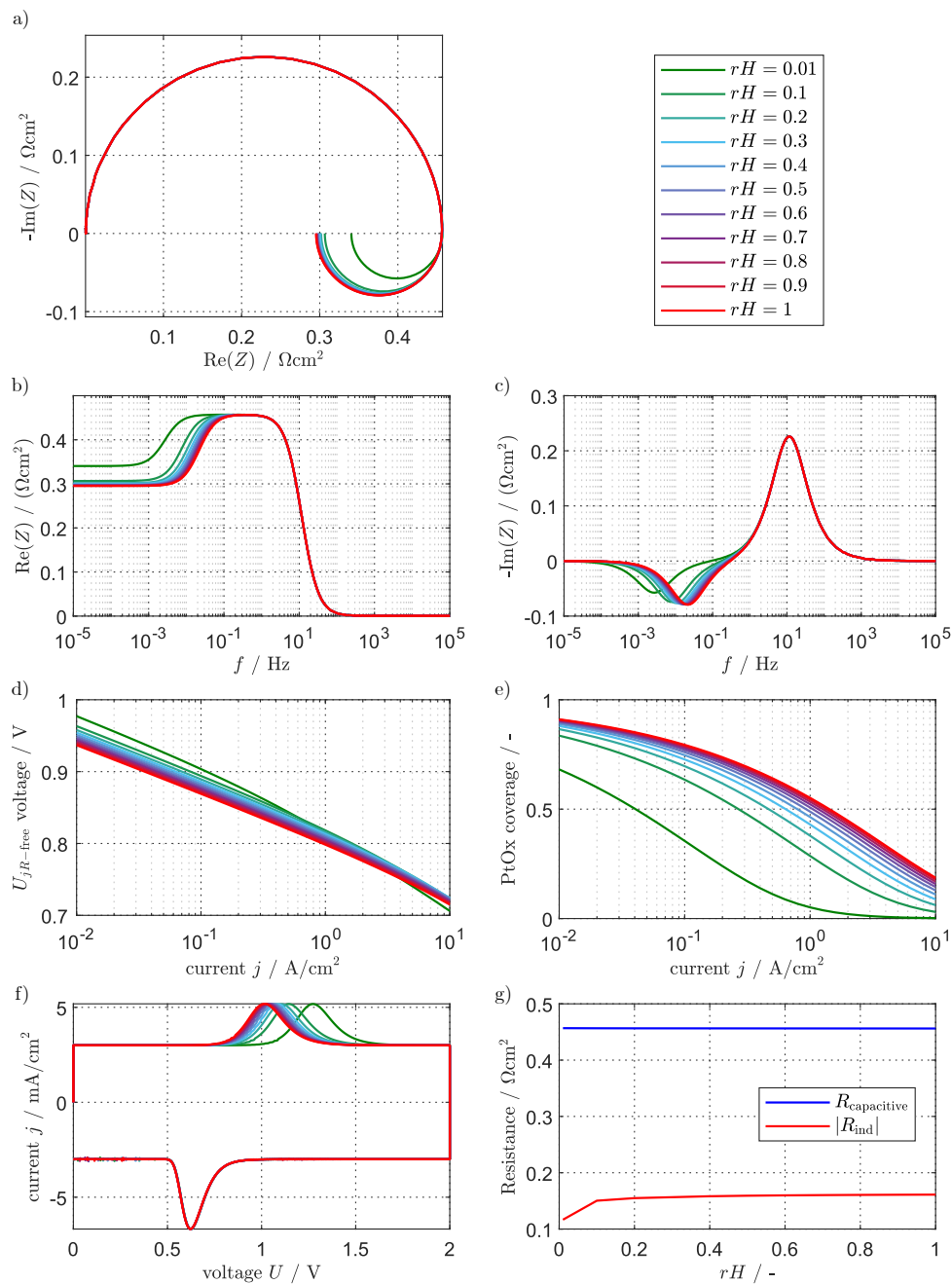


**Figure S20:** Variation of  $RH$  in our model with otherwise baseline parameterization. a) Nyquist plot at  $j = 0.1 \text{ A/cm}^2$ . b) and c) Corresponding Bode plots. d) Polarization curve (Tafel plot). e) Platinum oxide coverage. f) Cyclic voltammety. g)  $R_{\text{capacitive}}$  and  $|R_{\text{ind}}|$ .

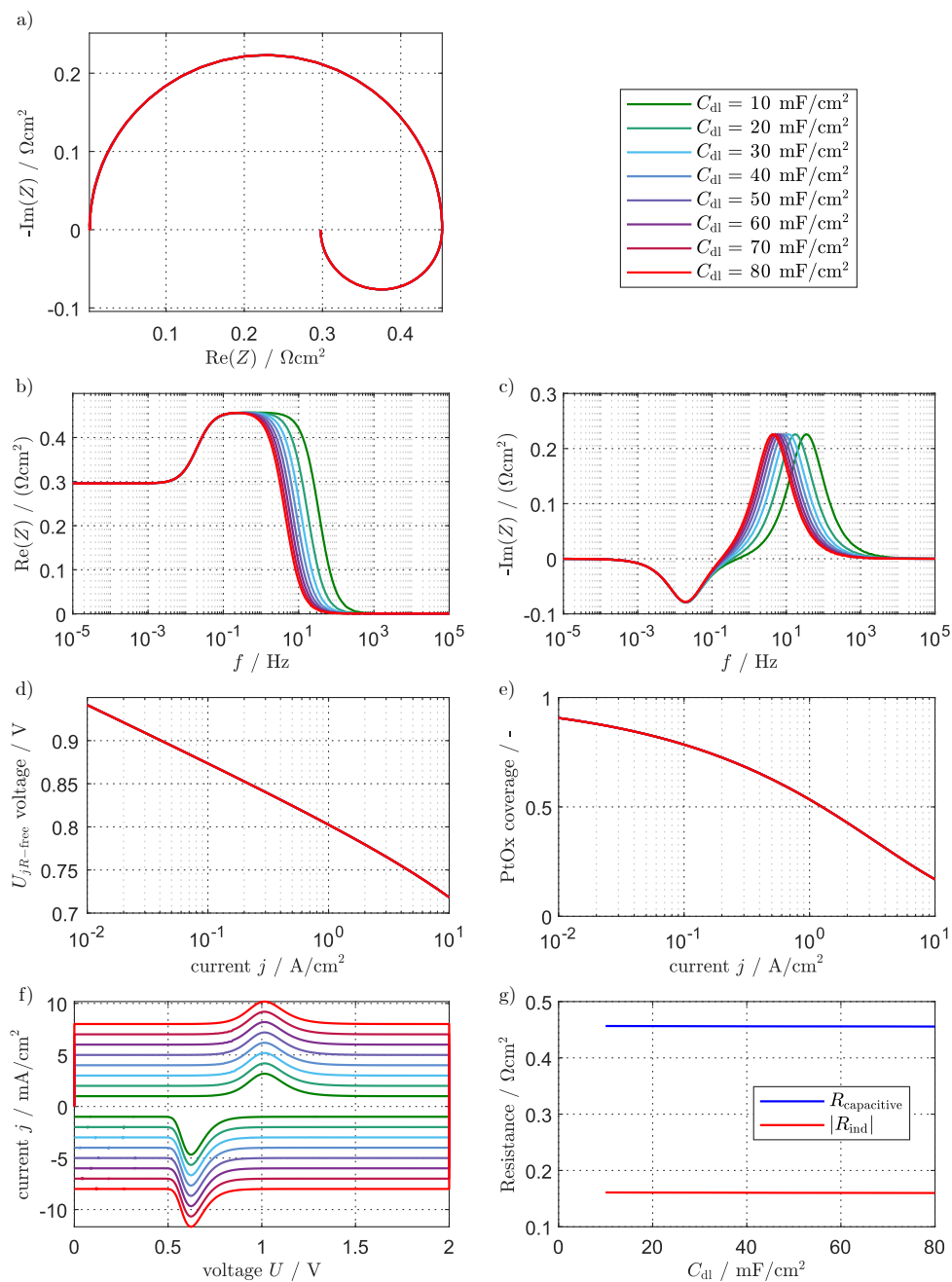


**Figure S21:** Variation of  $C_{dl}$  in our model with otherwise baseline parameterization. a) Nyquist plot at  $j = 0.1 \text{ A}/\text{cm}^2$ . b) and c) Corresponding Bode plots. d) Polarization curve (Tafel plot). e) Platinum oxide coverage. f) Cyclic voltammety. g)  $R_{\text{capacitive}}$  and  $|R_{\text{ind}}|$ .

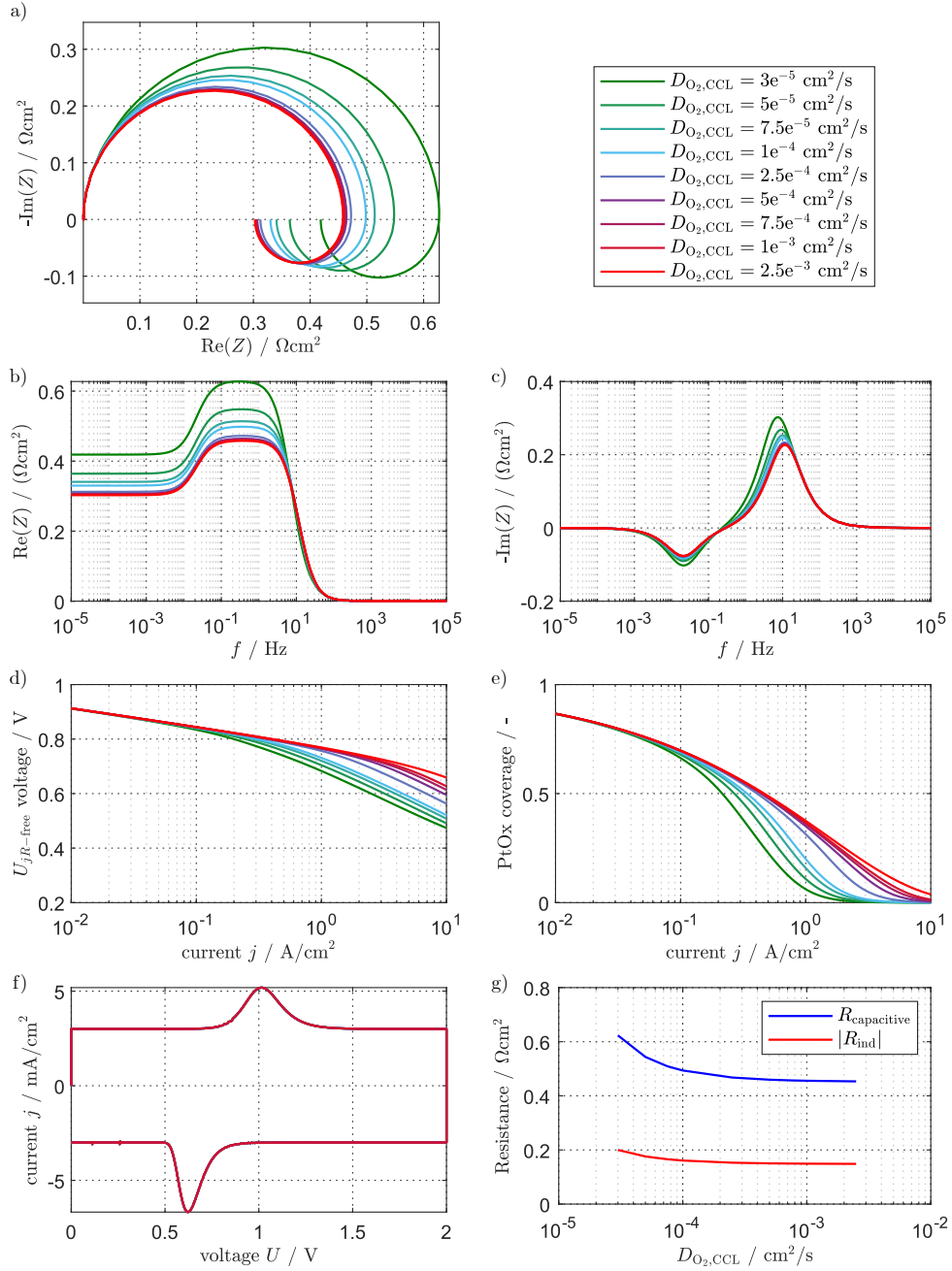


**Figure S22:** Variation of  $D_{O_2,CCL}$  in our model for  $x_{O_2}^{dry} = 0.25$  with otherwise baseline parameterization. GDL diffusivity was set unphysically high. a) Nyquist plot at  $j = 0.1 \text{ A}/\text{cm}^2$ . b) and c) Corresponding Bode plots. d) Polarization curve (Tafel plot). e) Platinum oxide coverage. f) Cyclic voltammetry. g)  $R_{\text{capacitive}}$  and  $|R_{\text{ind}}|$ .

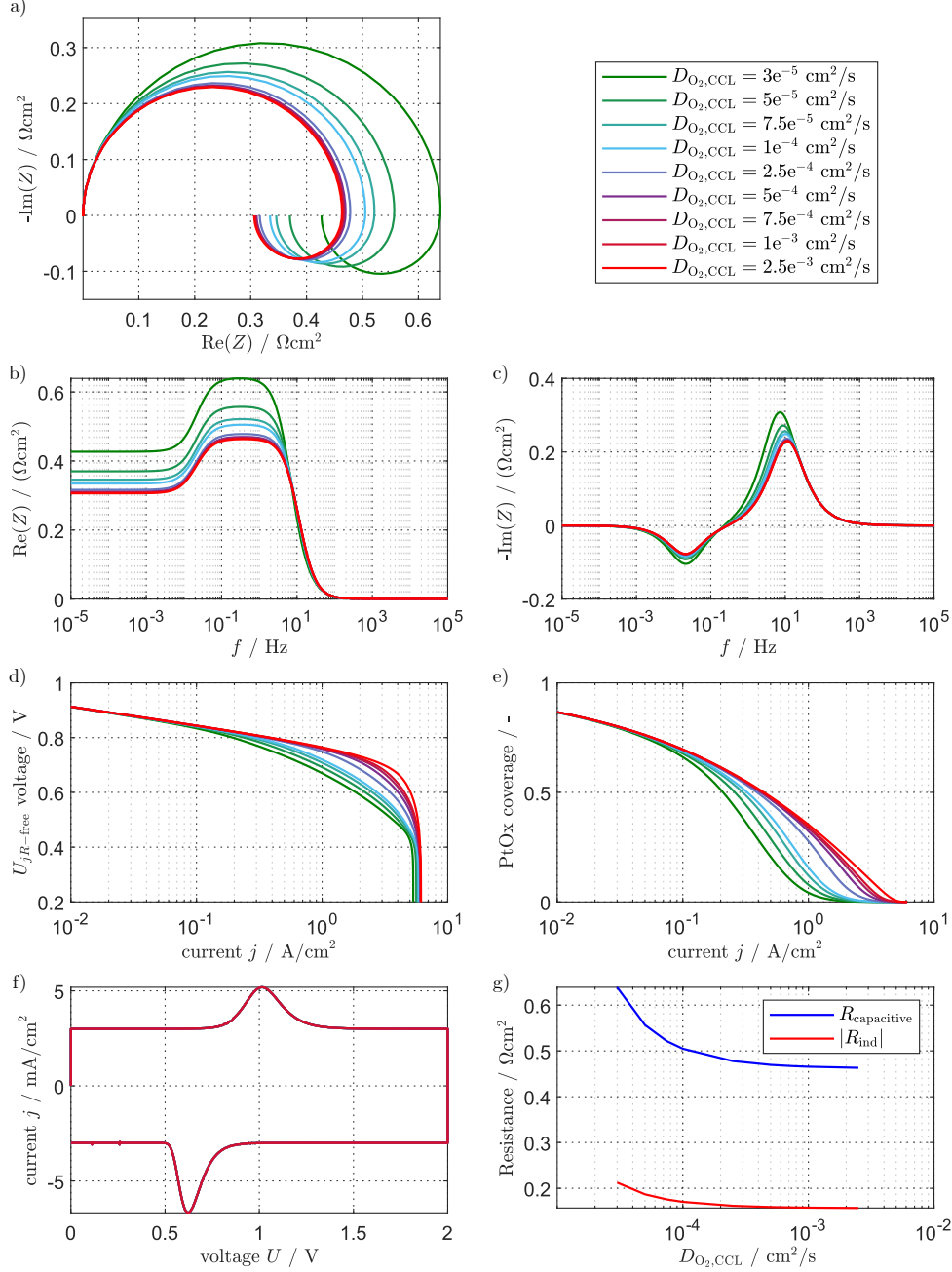


**Figure S23:** Variation of  $D_{O_2,CCL}$  in our model for  $x_{O_2}^{dry} = 0.25$  with otherwise baseline parameterization. GDL diffusivity was set to its baseline value. a) Nyquist plot at  $j = 0.1 \text{ A}/\text{cm}^2$ . b) and c) Corresponding Bode plots. d) Polarization curve (Tafel plot). e) Platinum oxide coverage. f) Cyclic voltammetry. g)  $R_{\text{capacitive}}$  and  $|R_{\text{ind}}|$ .

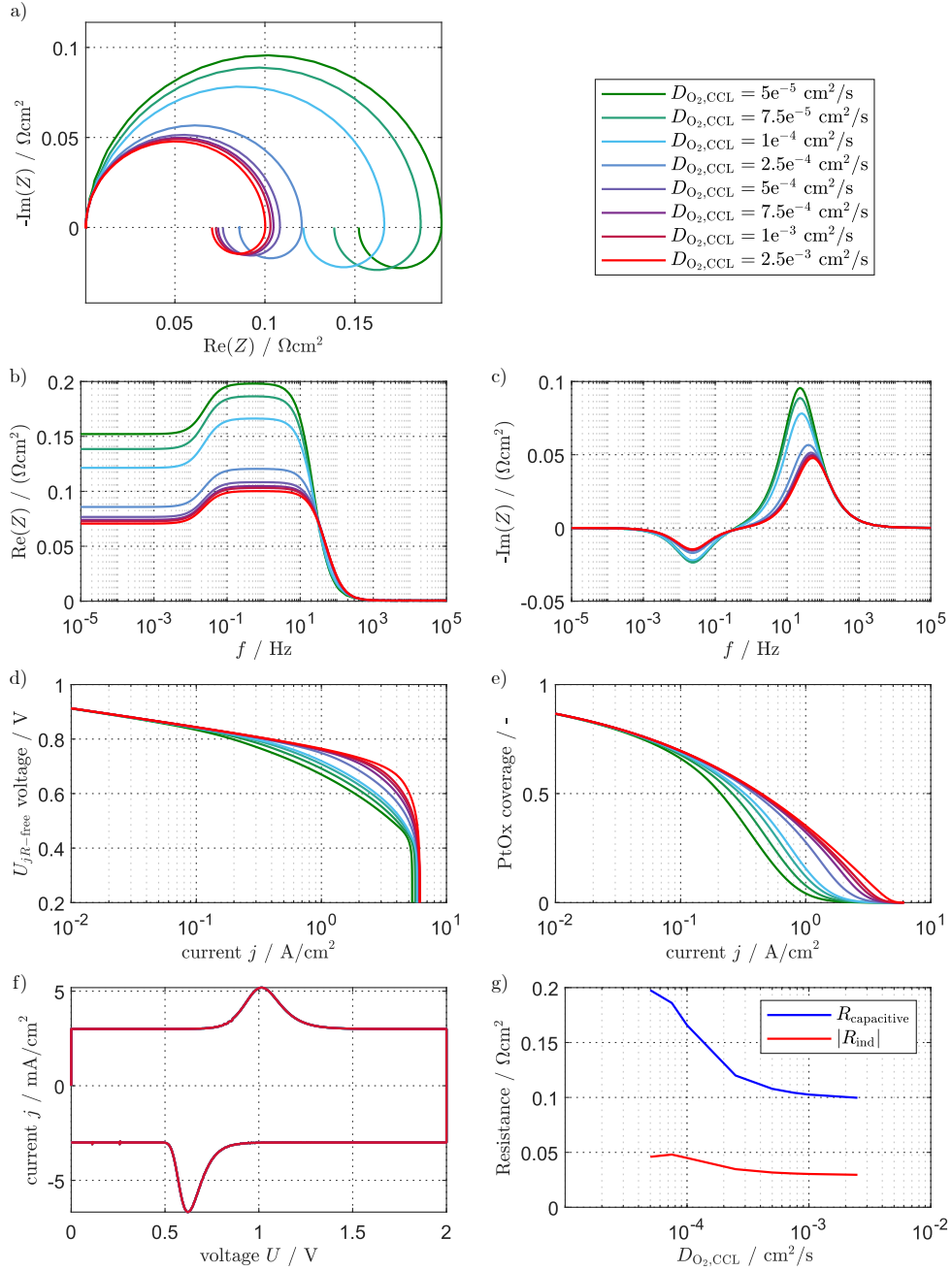


**Figure S24:** Variation of  $D_{O_2,CCL}$  in our model for  $x_{O_2}^{dry} = 0.25$  with otherwise baseline parameterization. GDL diffusivity was set unphysically high. a) Nyquist plot at  $j = 0.5$  A/cm<sup>2</sup>. b) and c) Corresponding Bode plots. d) Polarization curve (Tafel plot). e) Platinum oxide coverage. f) Cyclic voltammetry. g)  $R_{\text{capacitive}}$  and  $|R_{\text{ind}}|$ .

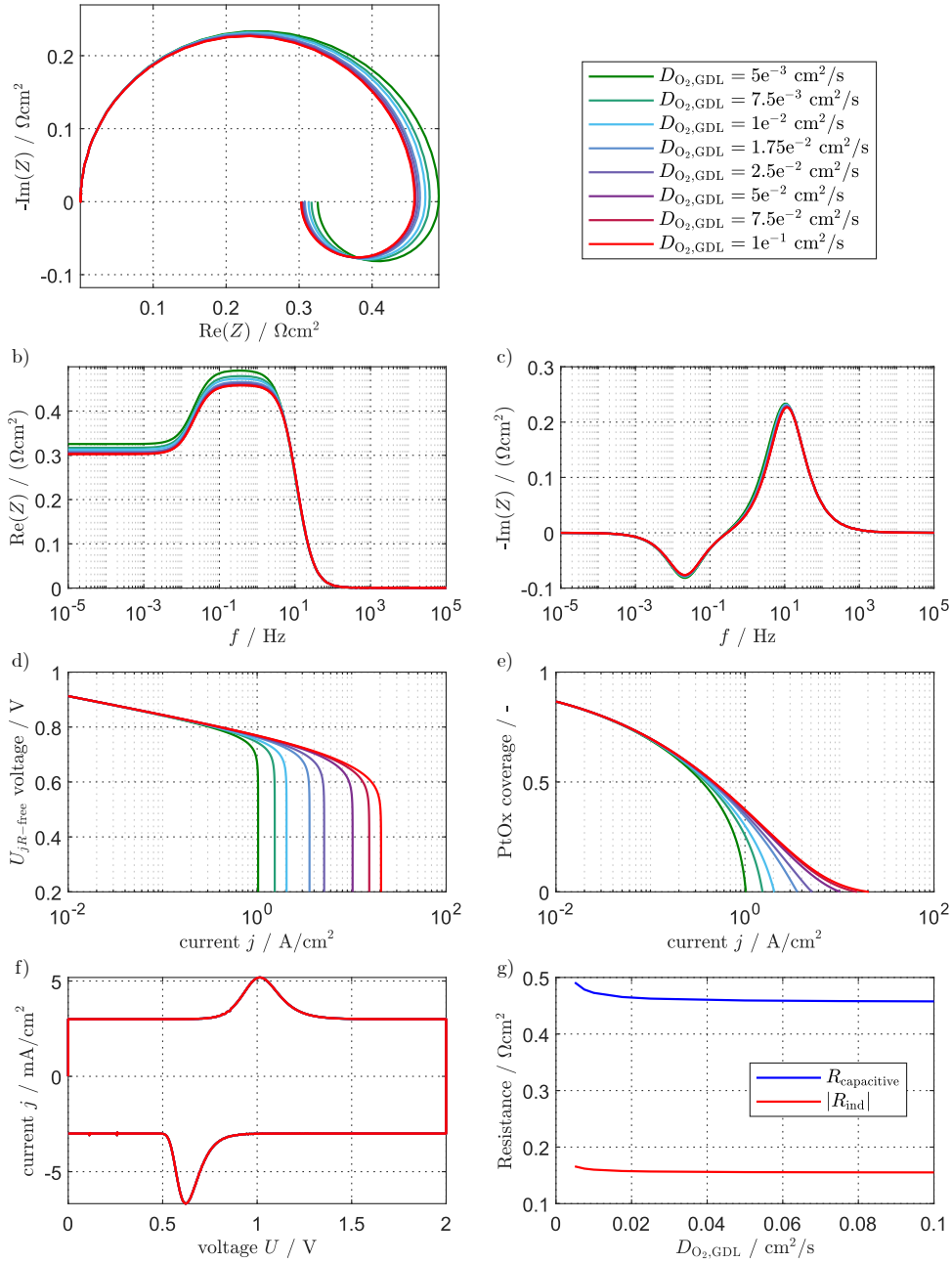


**Figure S25:** Variation of  $D_{\text{O}_2,\text{GDL}}$  in our model for  $x_{\text{O}_2}^{\text{dry}} = 0.25$  with otherwise baseline parameterization. CCL diffusivity was set unphysically high. a) Nyquist plot at  $j = 0.1$   $\text{A}/\text{cm}^2$ . b) and c) Corresponding Bode plots. d) Polarization curve (Tafel plot). e) Platinum oxide coverage. f) Cyclic voltammetry. g)  $R_{\text{capacitive}}$  and  $|R_{\text{ind}}|$ .



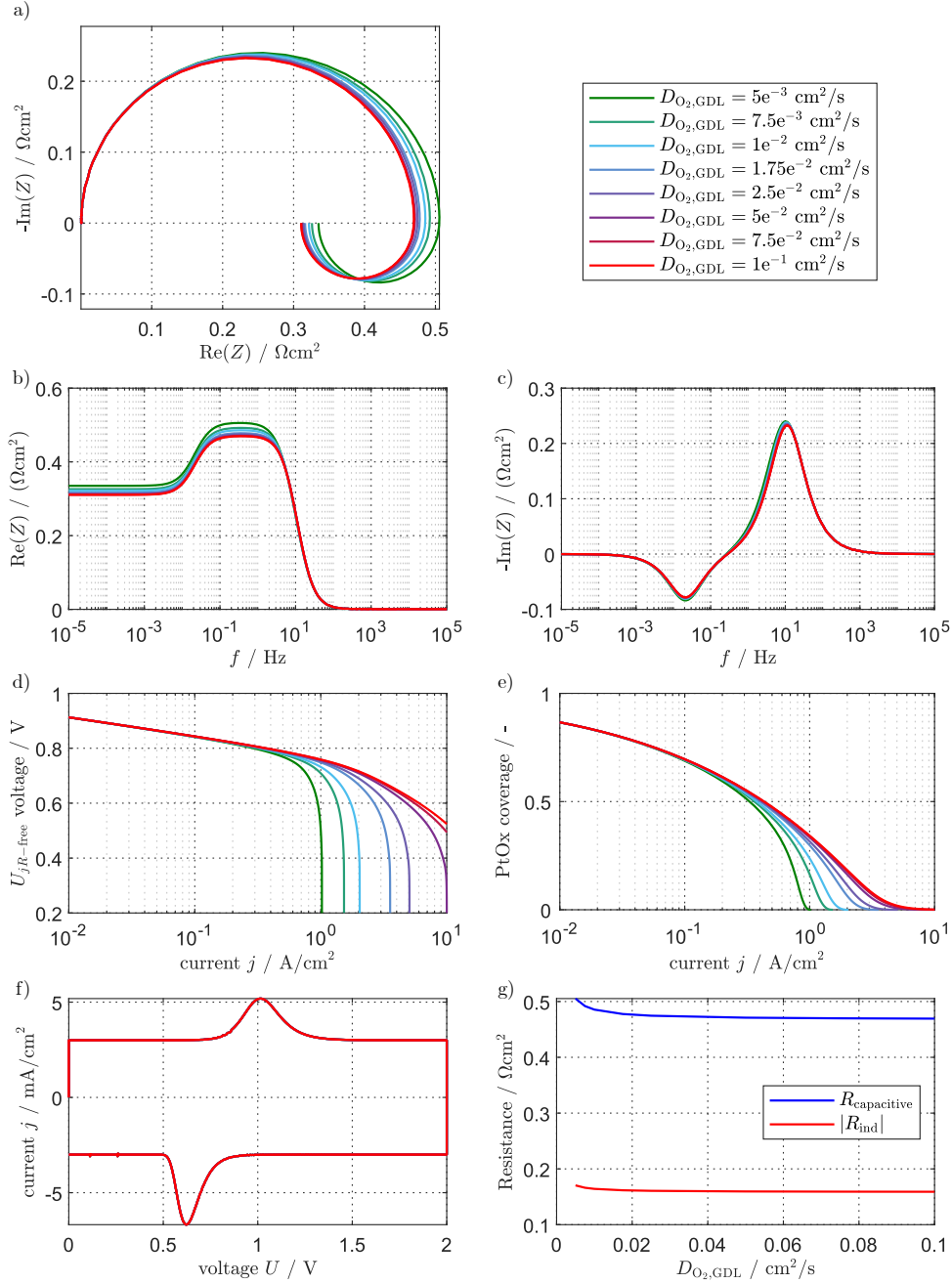


**Figure S26:** Variation of  $D_{O_2,GDL}$  in our model for  $x_{O_2}^{dry} = 0.25$  with otherwise baseline parameterization. CCL diffusivity was set to its baseline value. a) Nyquist plot at  $j = 0.1 \text{ A}/\text{cm}^2$ . b) and c) Corresponding Bode plots. d) Polarization curve (Tafel plot). e) Platinum oxide coverage. f) Cyclic voltammetry. g)  $R_{\text{capacitive}}$  and  $|R_{\text{ind}}|$ .

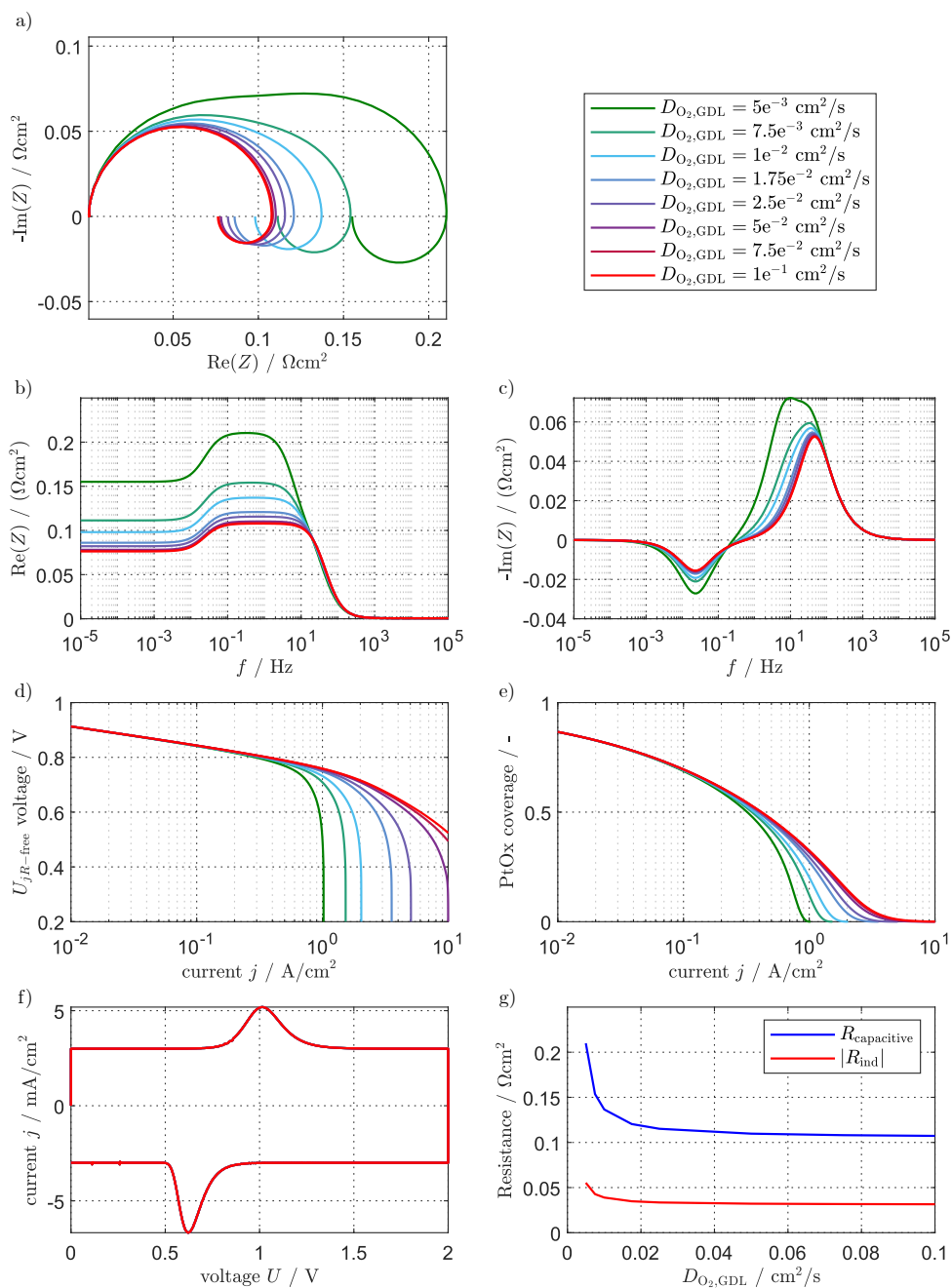


**Figure S27:** Variation of  $D_{O_2,GDL}$  in our model for  $x_{O_2}^{dry} = 0.25$  with otherwise baseline parameterization. CCL diffusivity was set unphysically high. a) Nyquist plot at  $j = 0.5 \text{ A/cm}^2$ . b) and c) Corresponding Bode plots. d) Polarization curve (Tafel plot). e) Platinum oxide coverage. f) Cyclic voltammetry. g)  $R_{\text{capacitive}}$  and  $|R_{\text{ind}}|$ .

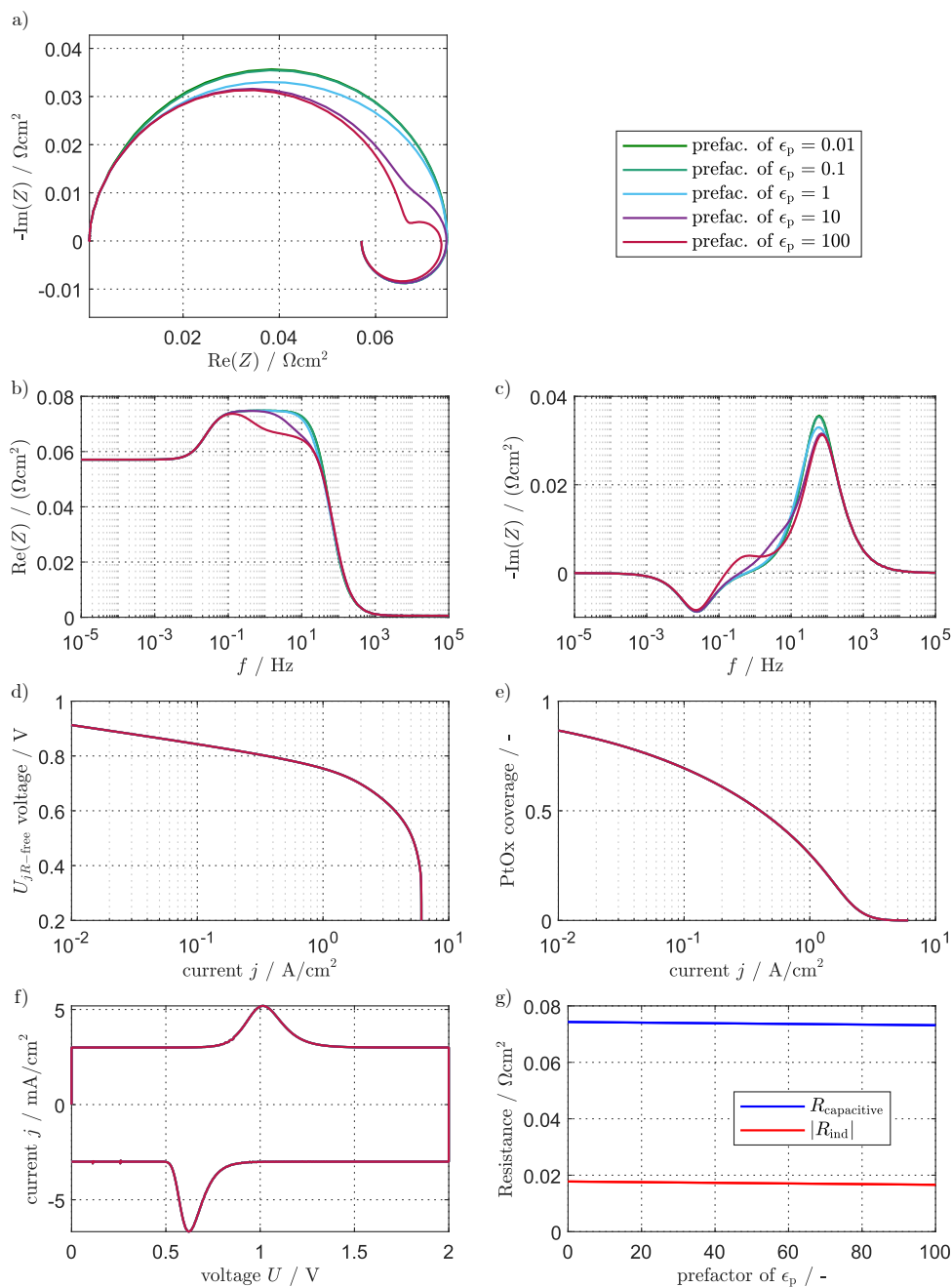


**Figure S28:** Variation of  $\epsilon_p$  of the CCL in our model for  $x_{\text{O}_2}^{\text{dry}} = 0.25$  with otherwise baseline parameterization. a) Nyquist plot at  $j = 1 \text{ A/cm}^2$ . b) and c) Corresponding Bode plots. d) Polarization curve (Tafel plot). e) Platinum oxide coverage. f) Cyclic voltammetry. g)  $R_{\text{capacitive}}$  and  $|R_{\text{ind}}|$ .

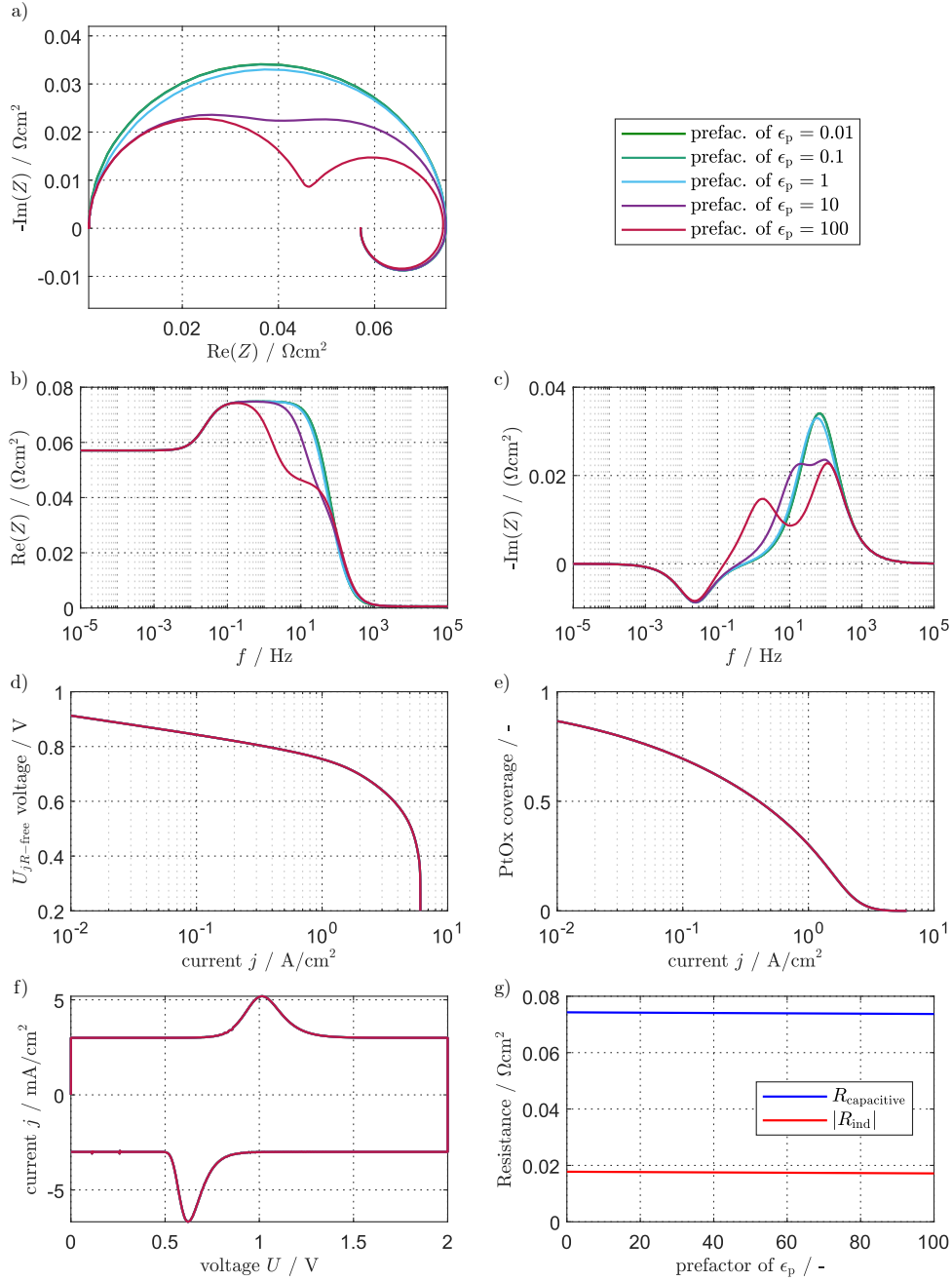


**Figure S29:** Variation of  $\epsilon_p$  of the GDL in our model for  $x_{O_2}^{dry} = 0.25$  with otherwise baseline parameterization. a) Nyquist plot at  $j = 1 \text{ A/cm}^2$ . b) and c) Corresponding Bode plots. d) Polarization curve (Tafel plot). e) Platinum oxide coverage. f) Cyclic voltammetry. g)  $R_{\text{capacitive}}$  and  $|R_{\text{ind}}|$ .

# Publications and Supervised Theses

## Peer-reviewed journal articles

- C. Gerling, M. Hanauer, U. Berner, and K. A. Friedrich, "Full Factorial In Situ Characterization of Ionomer Properties in Differential PEM Fuel Cells." *J. Electrochem. Soc.*, **168**, 0845 (2021).
- C. Gerling, M. Hanauer, U. Berner, and K. A. Friedrich, "PEM Single Cells Under Differential Conditions: Full Factorial Parameterization of the ORR and HOR Kinetics and Loss Analysis." *J. Electrochem. Soc.*, **169**, 0145 (2022).
- C. Gerling, M. Hanauer, U. Berner, and K. A. Friedrich, "Experimental and Numerical Investigation of the Low-Frequency Inductive Features in Differential PEM Fuel Cells: Ionomer Humidification and Platinum Oxide Effects." *J. Electrochem. Soc.*, **170**, 0145 (2023).

## Conference contributions

Oral presentations - First author = presenting author

- C. Gerling, M. Hanauer, U. Berner, and K. A. Friedrich, "PEMFC Model Parameterization by Means of Differential Cell Polarization and Electrochemical Impedance Spectroscopy." *ECS Prime 2020 Meeting*, online conference, October 2020.
- C. Gerling, M. Hanauer, U. Berner, and K. A. Friedrich, "Full Factorial Characterization of PEMFC Properties in Differential Cells." *ModVal 17*, online conference, April 2021.

Poster presentations - First author = presenting author

- C. Gerling, M. Hanauer, U. Berner, and K. A. Friedrich, "Between physical complexity and simplicity: Nailing down the cathodic activation overpotential in a small-scale PEM fuel cell.", *Bosch PhD Conference 2019*, Renningen, September 2019.

## Supervised Theses

- N. Hensle, "Experimentelle und Simulative Studie der Wasserstoff-Permeation in PEM-Brennstoffzellen", Bachelor thesis, Hochschule Offenburg, February 2019.
- V. Sanabria, "Characterization of PEMFC Electrode Activation Overpotential by Means of Electrochemical Impedance Spectroscopy", Master thesis, Otto von Guericke University Magdeburg, September 2019.
- T. Heidrich, "Entwicklung von Modellen zur Simulation und Effizienzoptimierung von PEM-Brennstoffzellen-Stacks", Bachelor thesis, DHBW Baden-Württemberg, September 2022.



## Christophe Gerling

PEM Fuel Cell Stack Development Engineer

Date & Place of Birth 16.05.1994 in Haguenau (France)  
 Nationality French

Phone +49 711 811 248 22  
 Email christophe.gerling@de.bosch.com



### Work Experience

---

- 10/2021 - today **Robert Bosch GmbH**, Stuttgart-Feuerbach (Germany)  
PEM Fuel Cell Stack Development Engineer
- 05/2018 – 09/2021 **Robert Bosch GmbH**, Renningen (Germany)  
PhD Candidate (Topic: *Experimental Characterization and Numerical Simulation of Differential PEM Fuel Cells*)
- 09/2017 – 03/2018 **Robert Bosch GmbH**, Renningen (Germany)  
Master/diploma thesis (Topic: *Hydrogen Recirculation of Fuel Cell Systems*)
- 10/2016 – 10/2017 **University of Applied Sciences Offenburg**, Offenburg (Germany)  
Seminar work in the *Projekt Schluckspecht* (Topic: *CFD Calculation of the Aerodynamics of the Schluckspecht 3 vehicle*)
- 05/2016 – 08/2016 **Safran Landing Systems**, Molsheim (France)  
Internship
- 06/2015 – 08/2015 **Michelin**, Karlsruhe (Germany)  
Internship

### Education

---

- 05/2018 – today **University of Stuttgart**, Stuttgart (Germany)  
PhD Candidate at the Institute for Building Energetics, Thermotechnology and Energy Storage (IGTE)  
Supervisor: Prof. Dr. K. Andreas Friedrich (German Aerospace Center, DLR)
- 10/2016 – 03/2018 **University of Applied Sciences Offenburg**, Offenburg (Germany)  
Three-semester study program leading to a double diploma (Ingénieur/M.Sc.)  
Degree: "Master of Science Mechanical Engineering"
- 09/2012 – 03/2018 **Institut National des Sciences Appliquées**, Strasbourg (France)  
Studies in Mechanical Engineering  
Degree: "Diplôme d'Ingénieur en Génie mécanique"
- until 06/2012 **Lycée André Maurois**, Bischwiller (France)  
Baccalauréat (equivalent to the Abitur in Germany)